Department of Civil and Environmental Engineering

University College Cork

Bridge-vehicle interaction for structural health monitoring: potentials, applications, and limitations

by

Vesna Jaksic

Head of School of Engineering

Prof Nabeel Riza B.S. EE (IIT), M.S. EE (Caltech) PhD EE (Caltech)

Supervisor

Dr Vikram Pakrashi BE, PhD

A Thesis submitted to the National University of Ireland, Cork

In part candidature for the degree of Doctor of Philosophy

October 2013

Contents

List of Figures

CHAPTER 4

CHAPTER 5

APPENDIX A

APPENDIX B1

List of Tables

CHAPTER 6

APPENDIX A

List of Acronyms

AAFT	Amplitude Adjusted Fourier Transform
AR	Autoregressive
ARMA	Autoregressive Moving Average
BF	Bottom Flange
BRI	Bridge Roughness Index
C3	Third-order Autocovariance
CDR	Crack Depth Ratio
COR	Correlation exponent
CoV	Coefficient of Variation
CWT	Continuous Wavelet Transform
DVs	Delay Vectors
DVV	Delay Vector Variance
ECG	Electrocardiogram
EEG	Electro Encephalogram
EKF	Extended Kalman Filters
ER	Entropy Ratio
EU	European Union
FE	Finite Element
FEM	Finite Element Model
fMRI	functional Magnetic Resonance Imaging
FRF	Frequency Response Function
H	Hurst
HRV	Heart Rate Variability
iAAFT	iterative Amplitude Adjusted Fourier Transform
IRI	International Roughness Index
ISO	International Organization for Standardization

K-L	Kozachenko-Leonenko
KTH	Royal Institute of Technology, Stockholm, Sweden
LDV	Laser Doppler Vibrometer
MAC	Modal Assurance Criterion
MC	Master Curve
MCK	Master Curve - Kurtosis
MCS	Master Curve - Skewnes
MP	Monitoring Point
MRPT	Minimum Rank Perturbation Theory
MSE	Mean Square Error
PSD	Power Spectral Density
REV	Deviation due to time Reversibility
RMS	Root Mean Square
RMSE	The Root Mean Squared Error (here quantification of deviation of DVV scatter plot)
RSR	Road Surface Roughness
RSV	Remote Sensing Vibrometer
R/S	Range (of data)/Standard Deviation (of data)
SA	Swedish Steel Arrow train
SDOF	Single Degree Of Freedom
SG	Strain Gauge(s)
SHM	Structural Health Monitoring
STD	Standard Deviation
TCM	Traditional Chinese Medicine
TF	Top Flange
WTB	Wind Turbine Blade
ΔRMSE	The Root Mean Squared Error Deviation

Declaration

The author hereby declares that the thesis entitled ‘Bridge-vehicle interaction for structural health monitoring: potentials, applications, and limitations’ and the work presented in it are my own except where references have been provided. I confirm that the thesis has not been submitted to any other university for a degree in whole or in part.

The author confirms that the library may, for academic purposes, lend or copy this thesis upon request.

Vesna Jaksic

____

This thesis is dedicated to my husband Aleksandar and my children Tara, Danica and Bratislav

Abstract

Structural Health Monitoring (SHM) is an integral part of infrastructure maintenance and management systems due to socio-economic, safety and security reasons.

The behaviour of a structure under vibration depends on structure characteristics. The change of structure characteristics may suggest the change in system behaviour due to the presence of damage(s) within. Therefore the consistent, output signal guided, and system dependable markers would be convenient tool for the online monitoring, the maintenance, rehabilitation strategies, and optimized decision making policies as required by the engineers, owners, managers, and the users from both safety and serviceability aspects.

SHM has a very significant advantage over traditional investigations where tangible and intangible costs of a very high degree are often incurred due to the disruption of service. Additionally, SHM through bridge-vehicle interaction opens up opportunities for continuous tracking of the condition of the structure. Research in this area is still in initial stage and is extremely promising.

This PhD focuses on using bridge-vehicle interaction response for SHM of damaged or deteriorating bridges to monitor or assess them under operating conditions. In the present study, a number of damage detection markers have been investigated and proposed in order to identify the existence, location, and the extent of an open crack in the structure. The theoretical and experimental investigation has been conducted on Single Degree of Freedom linear system, simply supported beams. The novel Delay Vector Variance (DVV) methodology has been employed for characterization of structural behaviour by time-domain response analysis. Also, the analysis of responses of actual bridges using DVV method has been for the first time employed for this kind of investigation.

Acknowledgements

My professional and personal acknowledgements go to everyone who made this thesis possible.

This work has been supported by the Irish Research Council through EMBARK Iniative, a programme funded by the Irish Government under the National Development Plan. I would like to express my profound thanks to the Council for their support in the critical situation at the beginning of my PhD and financial assistance throughout my research.

I would like to thank **Prof. Dr. Alistair Borthwick** for the use of the facilities of the Civil and Environmental Engineering Department. I am grateful to **Dr. Michael Creed, Prof. Gerard Kiely, Prof. Patrick Fitzpatrick**, and **Prof. Alan Kelly** for their support.

I would like to express my profound gratitude to my project supervisor **Dr. Vikram Pakrashi.** His devotion, enthusiasm, support, understanding, and the exchange of ideas were always stimulating and were encouraging me all the way throughout my study. Going through three years of PhD ‘rollercoaster ride’ along with family enlargement requires strength and balance, which I was lucky to get from my supervisor. In the process Vikram has become my friend and, occasionally, psychiatrist.

I am indebted to **Prof. Dr Biswajit Basu**, **Prof. Dr. Alan O’ Connor**, and **Dr. Kevin Ryan**, for the use of the facilities of the Civil, Structural and Environmental Engineering, Trinity College Dublin, for experimental work on this thesis and for the stimulating discussions during preparation of the thesis and related publications.

I am indebted to **Dr. Shaikh Faruque Ali** from the Department of Applied Mechanics, Indian Institute of Technology Madras, for his interest in my work and fruitful collaboration.

I would like to thank **Prof. Dr Danilo P. Mandic** and **Dr Andreas Amann** for their help in developing of my understanding of Delay Vector Varianace Method.

I am grateful to **Prof. Dr Raid Karoumi** from The Royal Institute of Technology KTH (Kungliga Tekniska högskolan), Stockholm, Sweden, and **Dr Nora Ann Nolan** for providing valuable data for the research.

I would like to thank **Dr. Cheng-I Hsieh**, Department of Bioenvironmental Systems Engineering, National Taiwan University, Taipei, and **Dr Matteo Sottocornola**, Waterford Institute of Technology, Department of Chemical & Life Sciences, for their friendship and support.

I would like to acknowledge all who have contributed to this work with discussions, ideas and moral support during this project, and especially **John Keane**, **Anthony O'Sullivan**, **Paul Cahill**, and **Ciaran Hanley** for their permanent help and friendship.

I would also like to thank my father **Blagoje Nedeljković** for his unconditional love and support. My great thanks go to my husband **Aleksandar Jakšić** for his support, encouragement, and love. Finally my thanks go to my children for providing me with the love and laughter and my mother-in-law for her great help.

"You have your way. I have my way. As for the right way, the correct way, and the only way, it does not exist."

Friedrich Nietzsche

Chapter 1

Introduction and Literature Review

1.1 Motivation

An increasing demand for improved transport infrastructure in today's world ensures that lifelines of society are unaffected and trade between the countries increase leading to economic development and competitiveness. For example, European Union (EU) creates the largest single market for trade and investment in the world, hence it is important that intra- and extra-EU trade become sustainable and grow to the benefit of all member states. The existing road infrastructure is strategic in achieving these goals. A significant number of bridges within the EU road network have been built in the post-war period (from 1945 to 1965). Since then the loading conditions in many of these bridges have changed, leading, together with the climate change, to the infrastructure deterioration [1]. As structures age and degrade, the need for monitoring integrity to ensure their safe operation increases. The increased requirements for managing aging bridges have a significant financial burden on operating costs and increase the risk of un-scheduled major maintenance and repair. Structural Health Monitoring (SHM) approach can improve this situation. SHM addresses the monitoring of a structure in terms of static and dynamic responses, including the diagnoses of the onset of anomalous structural behaviour [2]. Therefore, SHM allows optimised and targeted infrastructure maintenance management leading to significant transformation of benefits to infrastructure owners and end-users.

1.2 Structural Health Monitoring

The aim of the SHM techniques is to accurately monitor structural response due to real-time loading conditions, detect damage in the structure, and report the location, extent and in certain cases, the nature of this damage. Hence, SHM is not only important for the various structural and safety issues of the structures, but is also critical for the prioritisation of the time and nature of investment in a structure or a network of structures. SHM can be a practical tool for remote monitoring of in service structures aiming to improve the prediction of safety level and system performance while reducing maintenance costs. Non-destructive structural damage detection, in this regard, is becoming an important aspect of integrity assessment for aging, extreme event affected, or inaccessible structures [3-6].

Therefore SHM is rapidly becoming an integral part of infrastructure maintenance and management systems. SHM of bridge structures is extremely important in this regard due to obvious socio-economic, safety, and security reasons.

1.3 Damage Detection

One of the main objectives of SHM is to detect damage at reasonably early stage for aerospace, civil, and mechanical engineering infrastructures. For the purpose of this thesis, damage is defined as changes, either intentional or unintentional, to the material and/or geometric properties of structural systems, including changes to the boundary conditions and system connectivity, which adversely affect the current or future performance of that system [7].

The problem of detecting the damage in structural systems has been the subject of numerous studies [8-11]. The traditional non-destructive damage detection methods are visual or instrumental methods, e.g. ultrasound, X-radiography, Eddy covariance, radar, etc [12-16]. The majority of the methods require taking out of service the structure under observation. Some of the methods require that the approximate location of damage is known. Therefore the inspection procedure can be time consuming and expensive, especially if structure is located in inaccessible locations. Hence the development of damage detection techniques that could preserve and improve current safety and reliability levels and reduce the cost is required. Also application of novel techniques on the structure response data such as Delay Vector Variance (DVV) method or other statistical methods can reduce data efficiently to a single marker. Reduction of data is major challenge in damage detection. Such detection directly affects numerous aspects such as: serviceability [17], structural assessment [18-20], service life prediction [21, 22], deterioration monitoring [23], ratings of public structures in a network [24], cost optimization [25] etc.

SHM, in general, can be approached as a four stage problem [26]:

1) Detection of the existence of damage,
2) Detection of damage location,
3) Quantification of severity of damage, and
4) Prediction of the remaining service life of the structure.

This thesis will focus on the first three stages of diagnostics, considering that prediction of the structure service life is relatively ‘decoupled’ from the first three stages [27].

1.3.1 Vibration Based Damage Detection

The use of vibration data for damage detection as the basis for SHM is a popular approach. The change of structural characteristics such as mass, stiffness and / or damping can indicate the presence of damage in the structure. This can cause the change of vibration responses due to operational or testing loads. Vibration based damage detection can be defined mathematically as nonlinear inverse problem where the changed vibration responses are known and the parameters that determine location and extent of damage causing those changes are variables to be identified [27].

Early investigations in damage detection from vibration data tended to be based on changes in natural frequencies alone. Doebling [7] in his review paper refers to Lifshiz and Rotem [28] as the first authors who suggested the use of vibration data for damage detection. They used the changes in dynamic moduli obtained from extensional and torsional stress-strain curves as indicators of damage in the form of delaminations in the composite specimen under dynamic loading. Over the years, methods for damage detection developed incorporating more sophisticated laboratory techniques and computer simulations.

1.3.1.1 Methods Based on Natural Frequency Shifts

Damage diagnostics based on natural frequencies is the first and by far the most investigated vibration-based method [29]. Adams et al. [30] and Cawley and Adams [31] use the ratio in frequency changes in two different modes as the function of damage position. The method uses finite element model (FEM) which requires high precision from both model and experimental results. However, the estimated magnitude of the damage is reported to be inaccurate. Stubbs and Osegueda [32] used fractional changes of the natural frequencies as damage indicators and included better estimates of damage severity by further developing the sensitivity approach. Armon et al. [33] introduced rank-ordering procedure based on fractional eigenfrequency shifts providing the method that is more robust with respect to measurement errors and model uncertainties. Friswell et al. [34] introduced statistical analysis for the identification of the best damage scenario (forward method). Frequency-based methods using fractional changes in some format are incorporated in modern approaches such as neural networks [35, 36] and genetic algorithms [37]. The identification of the changes in natural frequencies of a freely vibrating damaged beam with respect to its undamaged state remains popular damage identification method [3, 27, 38, 39]. However, these changes are often negligible and the method performs poorly when measurements are contaminated by noise.

1.3.1.2 Methods Based on Mode Shapes

West [40] uses spatial information to improve damage detection by correlating mode shapes of the damaged and undamaged structure applying the Modal Assurance Criterion (MAC). MAC is a statistical indicator that is most sensitive to large differences and relatively insensitive to the small differences in the mode shapes [41]. Yuen [42] suggests the use of rotational mode shapes to characterize the presence of damage. Rizos et al. [43] suggest the use of the mode shape information at only two locations of cantilever beam. Pandey et al. [44] propose the use of curvature mode shapes arguing that displacement mode shapes are insensitive to the presence of local damage. Numerous studies propose the use of strain mode shapes that could be directly obtained from strain gauge measurements [45-48].

The use of mode shapes in simulations can provide information on the location and severity of damage, but experimentally identified modes lack measurement accuracy. Also, either approximate location(s) of potential damage(s) or very large number of sensors is needed for mode shape identification, which poses a practical limitation. To enhance the potential of damage detectability using mode shape Ratcliffe [49] proposes the application of a Laplace operator on mode shape data. Stubbs and Kim [50] propose a damage index obtained from integrations of mode shapes and use it as a pattern recognition technique. Cornwell et al. [51] revisit the integral damage index describing in terms of modal strain energy and extend the approach for plate type structures. Yoo et al. [52] compare several damage indicators derived from the MAC and conclude, based on finite element (FE) simulations of the crack plate, that the use of absolute values of differences of mode shapes is the best damage index.

Some researchers regard mode shapes and related quantities capable of providing spatial information not readily available from natural frequencies, thus increasing the chances of obtaining the location and severity of damage. Others argue that the mode shapes are very little affected by the presence of local damage and that the changes are virtually indistinguishable from experimental errors. Doebling et al. [7] conclude that the both sides are partially correct and that the advantages of using mode shape information depend upon the type of structure under consideration. A truss would be good example for successful application of mode shape methods, since local damages on joints or individual members may result in large modal displacement in a large region [53, 54].

However, successful detection of the presence and the location of damage through spatial analysis has gained considerable importance recently as it has become possible to reliably measure the deflected static [5] and dynamic shapes [55] of a damaged structure using modern equipment such as Laser Doppler Vibrometer (LDV). The global change of mode shape (particularly the first natural mode shape) is small for a damaged structure in comparison to its undamaged situation. However, the measurement of the first natural mode shape is comparatively easier and less prone to measurement noise than the higher modes [10].

1.3.1.3 Methods Based on Frequency Response Functions

The peak magnitudes or anti-resonance in Frequency response function (FRF) could provide spatial information for damage diagnostics. Swamidas and Cheng [56] use strain FRFs as indicators of fatigue crack initiation and growth in tubular t-joints. Perchard and Swamidas [57] suggest that displacement FRFs and strain FRFs can provide combined information for crack detection from peak and off–peak region. Fritzen et al. [58] propose the use of FRFs in a model based solution to the inverse problem using orthogonalisation strategy to reduce the number of damage parameters and improve numerical conditioning. Lopes et al. [59] describe detection technique using neural networks in which training phase is based on FRFs computed from finite element model previously updated using experimental FRFs from undamaged structure. The method is experimentally validated by successfully detecting damage in the welded joint of metallic structure. Sampaio et al. [60] perform comparative studies of FRF based methods and suggest that the strain energy obtained directly from FRFs can be used as damage indicator.

1.3.1.4 Methods Based on Matrices of Structural Parameters

Another family of methods uses structural matrices to identify damage by determining the degrees of freedom that correspond to the elements in an identified error or perturbation matrix. Mannan and Richardson [61] propose the estimation of mass, stiffness, and damping matrices from measured modal data; by comparing them with corresponding matrices of undamaged state they obtain damage location. Hyoung and Bartkowicz [62] discuss the influence of noise level, number of damaged sites, number of measurement points, and number of modes in different matrix based detection procedures. They conclude that the number of measurement points is the most relevant factor for the accuracy of the investigated methods. Pandey and Biswas [63] use the first three measured natural frequencies and mode shapes to estimate flexibility matrices for the intact and damaged structure. The damage indicator is calculated from difference between these two flexibility matrices. More elaborate matrix based techniques are derived from model updating methods in which the matrices of analytical model are corrected to match experimental modal data by minimizing the norm of the corresponding perturbation matrices [8]. Zimmerman and co-workers have published numerous investigations on detection methodology using structural matrices. They propose the Minimum Rank Perturbation Theory (MRPT) that produces perturbation matrices of the same rank as the number of modes used [64, 65]. Many developments have followed from this method, including the use of changes in the damping matrix as damage indicator [66]. Damage location using subspace recognition [67] and hybrid expansion-reduction method based on linear matrix inequalities [68] are just some of the recent developments.

1.3.1.5 Time Domain Methods

Time domain methods represent alternative to modal parameter methods for damage diagnostic procedure. The advantage of using time domain techniques, i.e. using time response measurements directly, relates to avoidance of implicit data reduction of modal analysis methods, which may cause the loss of important information about the dynamic response of the structure. Also, unlike modal analysis approaches, time domain methods are not limited by any assumption of linearity. On the other hand, the main disadvantage is that model based time domain methods may require considerable computational effort for calculation of time response. Qian et al. [69] propose a method that uses autoregressive–moving–average (ARMA) models, a statistical analysis of time series to estimate damage parameters. They present results in terms of equivalent eigenfrequencies. Ostachowicz and Krawczuk [70] propose crack identification method from the maximum amplitudes of time responses. They investigate double-sided crack, occurring in the case of cyclic loadings, and single-sided crack, which in principle occurs as a result of fluctuating loadings of cantilever beam. Banks et al. [71] develop non destructive damage diagnostic procedure using parameterized partial differential equations and Galerkin approximation techniques. The iterative method is based on enhanced least-square error minimization. The method proves to be successful in detecting small geometric defects. Masri et al. [72] propose a neural network based detection scheme by use of vibration measurements from a "healthy" system to train a neural network for identification purposes. Subsequently, the trained network is fed comparable vibration measurements from the same structure under different episodes of response in order to monitor the health of the structure. They show that proposed damage detection methodology is capable of detecting relatively small changes in the structural parameters, even when the vibration measurements are noise polluted. Seibold and Weinert [73] consider a probabilistic time-domain method based on parameter estimation using a series of the extended Kalman filters (EKF), taking nonlinearities into account to locate cracks in rotors. Cattarius and Inman [74] propose a time domain method independent of modal parameters and analytical models, to characterize small differences between the responses of damaged and undamaged linear structure. A number of researchers have also investigated the possibility of using autoregressive (AR) and ARMA coefficients obtained from time records for damage diagnostics [75-77]. Trendafilova [78] considers use of pure time series analysis for damage diagnosis in vibrating structures by the state space methodology and discusses a number of possible methods to extract damage sensitive features from the state space representation of the attractor of a vibrating system. The discussed methods can be divided into two groups: methods that use non-linear dynamic characteristics and methods based on the statistical characteristics of the distribution of points on the attractor.

1.3.2 Model Based and Model Independent Damage Detection

There are two distinctive vibration based damage detection techniques, model based and model independent damage detection techniques. The advantages of model independent damage detection technique relate to the avoidance of modelling errors and computational costs of numerical simulations. However, the majority of these methods developed to date can provide only stage 1 and 2 damage identification. In order to advance no-model methods to quantify the severity of damage (stage 3), a mathematical model of the structure is necessary. The use of the mathematical structure describing the dynamic system permits application of model based parameter identification methods, which could reduce the amount of experimental data required. The theoretical model can be used for inexpensive simulations with slight variation of system physical parameters, external influences, boundary conditions, etc. The model can also be used to optimize the number of sensors and their most appropriate locations for structure monitoring. Hence, in order to understand the governing mechanism of structural damage and to identify the parameter to be measured damaged models are needed.

In connection with model used for any online monitoring procedure it is important to find acceptable balance of simplicity and accuracy. The choice of the damage model is driven by the problem of quantification of damage effects, which can be forward or inverse. The forward problem refers to either quantifying the effects of a damage of known extent on the dynamic characteristic of the structure or predicting a nonlinear signature spectrum that would indicate presence of damage. The inverse problem, i.e. localising and quantifying a crack from the structure responses, is usually based on simplified linear models where the effect of the damage is represented by a local change of model characteristics [34].

The modelling of cracks in beam structures and rotating shafts is a popular research topic. The models fall into three main categories: local stiffness reduction; discrete spring models; and complex models in two or three dimensions.

1) The smeared crack model considers the local loss of inertia due to the presence of a crack. Simplified smeared crack models have been used by numerous researchers [79, 80]; some consider the sudden stiffness change within the vicinity of the crack as a damage model [3, 81].

2) The lumped crack model assumes the effects of the damage to be localized at the position of damage and substitutes the effects of damage with equivalent structural members like a rotational spring. This method is the most popular among researchers [82-86]. The lump crack model stands as natural choice to be used and as such is employed in this thesis.

3) The continuous crack models are derived from the stationarity of hybrid functionals using the energy concepts and model the damage from the principles of elasticity. The first published continuous beam model was proposed by Christides and Barr [87] and later improved by Shen and Pierre [88, 89]. More detailed continuous crack models are based on the so-called Hu-Washizu-Barr method [90, 91].

The choice of a damage model depends on the objective of the modelling. In general, a simplified model that represents the basic characteristics of a cracked member at an acceptable computational time and cost is the most convenient one.

1.3.3 Dynamic Quantities for Damage Detection

The choice of dynamic quantities used in the monitoring process is very important for the purpose of damage detection. Friswell and Penny [92] provide a review of damage location methods in terms of the measured data used. There are three basic types of data used in measurement of dynamics: time domain, frequency domain, and the modal model. Structural vibration responses are generally collected as time series by various sensors such as accelerometers, strain gauges, laser Doppler vibrometers, etc. Frequency responses are calculated from time series usually by numerical Fourier transform. The obtained frequency data are further used as source for estimation of modal parameters through curve fitting, i.e. the natural frequencies, damping ratios and mode shapes. Hence, some potentially useful information can be lost with each step due to reduction of data. Therefore it would be best to use time series data as the number of data points is the highest. For linear system there is no loss of information going from time domain to frequency domain. Also, there is the advantage that the data may be averaged easily and so the effect of random noise is reduced [92].

The use of frequency response functions (FRF) or modal parameters is equivalent for most of the cases as they contain the same information [92]. For this reason many recent publications focus on diagnostic methods based on modal parameters, e.g. natural frequencies, mode shapes, modal strain energy, strain mode shapes, etc. The disadvantages of this approach are that the assumption of linearity inherent in modal methods may introduce error in damage identification procedure and that the effects of small changes (i.e. natural frequency shifts and local changes in mode shapes) could be masked by experimental uncertainties and/or data reduction [27].

The majority of damage evaluation techniques are based on time domain response of the structure. However, these techniques can not be employed without bridge temporary closure. On the other hand, vibration data obtained from the structure in its operational condition are essential for the successful SHM technique. Moreover the presence of noise in measured vibration data is identified to be a very important factor in terms of a successful damage detection scheme. Therefore, for a robust damage detection process, a method should be able to perform in the presence of considerable noise within the signal [10].

1.4 Bridge-Vehicle Interaction for SHM

Generally, damages or alterations to a structure tend to change its dynamic characteristics. Often, the presence of damage in a structure only affects the change in local dynamic characteristics of the system, and significant changes are not observed in the global dynamic response. Consequently, methodologies are developed to capture the local change through some marker to estimate the presence, the location, and the severity of damage. In this regard damage detection employing bridge-vehicle interaction is of considerable interest since the structure can be kept in operation throughout the process [93].

Identification of the location (stage 2) and the extent of damage (stage 3) in beam type structures are an important example of SHM. The possibility of using response of damaged or deteriorating bridges [2, 7, 11, 94] and the bridge-vehicle interaction [11, 85, 95-98] for SHM has been theoretically and experimentally investigated.

Pesterev and Bergman [99] propose a method for solving the problem of dynamic response of an elastic structure carrying a moving oscillator with arbitrarily varying speed. Lee et al. [96] experimentally investigate possible application of bridge–vehicle interaction data for identifying the loss of bending rigidity by continuously monitoring the operational modal parameters. Majumdar and Manohar [100] propose time domain damage descriptor to reflect the changes in bridge behaviour due to damage occurrence, i.e. the loss of local stiffness. Bilello et al. [101] observe the dynamic response of a small-scale bridge model and compare the findings with Euler–Bernoulli beam theory. Bilello and Bergman [85] consider the response of a smooth surface damaged Euler–Bernoulli beam traversed by a moving mass, theoretically and experimentally, where the damage is modelled through rotational springs. They observe an increase in structural damage sensitivity under the effect of a moving interacting load. Law and Zhu [97] study dynamic behaviour of damaged reinforced concrete bridge under moving loads using as a model a simply supported beam with open and breathing cracks. They observe that the phase space is distorted due to the presence of the crack as compared with an undamaged phase space. Bu et al. [98] propose damage assessment approach from the dynamic response of a passing vehicle through a damage index considering different vehicle models, vehicle speed, sampling frequency, vehicle and bridge mass and stiffness ratios, road surface roughness, measurement noise, and model error. Poor road surface roughness is observed to be a bad detector for damage in their approach. Zhu and Law [102] provide similar numerical studies emphasizing the importance of bridge–vehicle interaction based damage detection in concrete bridges. Pakrashi et al. [11] perform experimental investigation of simply supported beam with moving load subjected to different level of damage where they observe that the wavelet transformed phase spaces for damaged and undamaged cases differ distinctly at the high scale.

The bridge-vehicle interaction approach allows the bridges to be monitored or assessed under operating conditions. This is a very significant advantage over more traditional intrusive, semi-intrusive, or non-intrusive investigations where considerable tangible and intangible costs are often incurred due to the disruption of service. Additionally, SHM through bridge-vehicle interaction opens up opportunities for continuous tracking of the condition of the structure. Research in this area, although extremely promising, is relatively imature and there is a strong need for detailed analyses exploring the potentials, applications, possibilities, extensions and limitations of this approach. The thesis attempts to address these issues and intends to contribute to this research field through innovative applications of various numerical, statistical and analytical techniques.

1.5 Objectives

The broad focus of this thesis is detailed and critical investigation of the use of bridge – vehicle interaction response for SHM. Specifically, the aims of the thesis are as follows:

- Development of analytical, statistical, ad-hoc numerical techniques for detection and characterization of degradation,
- Application of the developed method on a linear and bilinear models and characterization of robust markers for SHM,
- The investigation into the presence of noise in the signal and related masking effects,
- Studies of the performance of new markers of SHM, and
- Delineation of the domain of usefulness of the markers.

1.6 Research Strategy

The research strategy is significantly dependent on numerical techniques and simulations. The research strategy includes the following:

- Development of a bridge-vehicle interaction damage models of varying complexity and detail to appropriately characterise the nature of the response.
- Qualitative isolation and characterization of the response obtained from the combination of damage and bridge-vehicle interaction models based on the fundamental nature of the interaction.
- Introduction of a pool of markers for SHM; these markers act as the basis for assessment of performance of the proposed method.

- Application of analytical, statistical, ad-hoc numerical techniques to track degradation or damage. Determination and isolation of robust SHM markers along with calibration curves for the estimation of damage extent.
- Investigation of the effects of environmental conditions change (e.g. temperature) in response data.
- Investigation of the effects of noise in the response data.
- Investigation of the efficiency of detection as a function of monitoring devices and sensors placement. Investigation into pathological cases like sensor malfunctioning.

1.7 Organisation of the Thesis

The thesis is organised in seven chapters.

Chapter 1 provides introduction and literature review.

Chapter 2 explores possibility of developing robust statistical descriptors from structural responses for detecting system properties. The frequency responses of a linear and a non-linear system due to the change of their damping ratio are statistically analysed and calibrated. The consistency and robustness of the calibration against different sampling rates and measurement noise is studied.

Chapter 3 consists of two parts. The first part is theoretical and considers possibility of using surface roughness for damage detection of bridge structure through bridge vehicle interaction. The detection and calibration of the damage from the single point observation is investigated through cumulant based statistical parameters. Detection of the damage under benchmarked and non-benchmarked cases is discussed. Practicalities behind implementing this concept are also considered. The second part of the chapter investigates possibilities of the experimental detection of a sudden structural stiffness change. By contrasting the Laser Doppler Vibrometer and accelerometer measurements their effectiveness to detect sudden stiffness change is studied. The possibility of using basic types of dynamic data (time domain and frequency domain) and wavelet analysis in the detection of the presence and the location of damage is discussed too.

Chapter 4 presents the effects of road quality and vehicle speed on damage detection (stage 2 and 3 damage identification) on bridges through consideration of bridge-vehicle interaction effects. The damaged Euler Bernoulli beam traversed by a moving oscillator is considered. The road surface roughness (RSR) of the beam, realistically classified as per ISO 8606:1995(E), is used as an aid to monitor the health of the structure in its operational condition. The aim of this chapter is to define simple, consistent, easy to implement, and robust statistical descriptors to detect and calibrate the existence, location, and extent of damage considering the effects of vehicle speed and variable RSR profiles.

Chapter 5 investigates the possibility, extent of application, and limitation of using Delay Vector Variance (DVV) method for SHM through structure vibration analysis. The DVV method is applied to analyse responses of various systems (i.e. theoretical model – Single Degree of Freedom (SDOF) system, and two experiments – SDOF oscillator and Wind turbine blade (WTB) – performed in laboratory environment) exposed to different excitation forces with varying characteristics. Effectivness of DVV method to detect change in the degree of non-linearity of the observed system output signal due to changes of system characteristics (e.g. mass, stiffness, natural frequency, etc.) is investigated.

Chapter 6 validates the use of DVV method as SHM tool by investigating its potential and limitation when applied on responses produced by bridge-vehicle interaction. Two bridge systems and their responses are analysed: 1) an impact damaged prestressed concrete bridge, and 2) single span steel-concrete composite train bridge. In the case of the first bridge responses are monitored during the rehabilitation works, while in the case of the train bridge the vibrations induced by different types of train crossing over are analysed.

Chapter 7 presents summary, conclusions, and contributions of the present research, as well as suggestions for future work.

Chapter 2

Developing Robust Descriptors from Structural Responses for Detecting System Properties

2.1 Introduction

A majority of dynamic systems can be described as or reduced to a Single Degree of Freedom (SDOF) system [95, 103-105]. The behaviour of SDOF system under vibration depends on its characteristics and the change of characteristics can imply the change in system behaviour. This may range from linear to nonlinear response, a presence or absence of damage, or both. Also, input excitations are often not available. Hence the need arises for consistent and output signal guided markers. In this chapter simple, consistent, and robust statistical descriptors are defined for the calibration of damping in linear and non-linear systems through frequency response in the presence of variability and uncertainties due to noise and sampling intervals. The work employs the frequency response of a linear system and a Duffing Oscillator simulating hardening and softening springs. The skewness and kurtosis descriptors are tested for efficiency in calibrating the nature of the system and the extent of damping with robustness against measurement noise and sampling effects.

2.1.1 Background

The identification of damping in a structural system is often a very important, but difficult problem. The main reason behind this difficulty is the lack of information regarding the energy dissipation mechanism of the system. Even when the dissipation mechanism can be acceptably modelled for practical applications as an equivalent viscous damping ratio, the identification of the extent of damping can be problematic due to the lack of information on the linearity or the non-linearity and condition of the system. For linear structures, a significant number of classical and new approaches are available to establish damping, including the use of logarithmic decrement [106], energy loss per cycle, frequency response function [105] and the analyses of vibration response in time and frequency [107] or time-frequency [108] domain.

The description or calibration of damping, even under the assumption of an equivalent viscous damping ratio is scarce for non-linear systems. In fact, within the domain of definition of equivalent viscous damping ratios, sub-critical damping of low magnitude (0-10%) tends to govern the dynamics of an extremely wide range of elastomechanical systems. The use of frequency response functions [39, 109] is good approach to characterise damping in a system. The frequency response functions, when available, tend to accurately characterize the linear or non-linear system they belong to. The shapes of the functions are affected by damping and this opens up a possibility of exploring simple, robust, and consistent descriptors to calibrate damping ratios employing the entire curve. Additionally, the frequency response functions can be directly related to the efficiency and capacity of a number of energy harvesting devices [110-112]. Consequently, an appropriate descriptor for damping calibration can be related to the performance of energy harvesters. Systems, like Duffing oscillators, also have a potential to act as vibration absorbers by tuning their dynamic characteristics [113].

This chapter explores and recommends a simple, consistent, and robust statistical descriptor to calibrate damping ratios in linear and non-linear systems, where the non-linear system is modelled as a Duffing oscillator in the form of hardening and softening springs. Noise stress tests and effects of sampling rate variability have been investigated to establish the robustness, efficiency, and consistency of the descriptors.

2.2 Frequency Response of Linear and Duffing Systems

A non-linear single degree of freedom (SDOF) system in the form of a Duffing Oscillator is considered in this work in order to establish and illustrate the proposed approach. Although a great number of studies have looked into the computational or phenomenological aspects [114, 115], a practical description of such a system through frequency response does not seem to have been approached.

The nonlinear SDOF system is a Duffing Oscillator governed by the equation:

$$\ddot{x} + 2\xi\dot{x} + x + \alpha x^3 = F\, cos(\Omega\tau) \tag{2.1}$$

where x is the non-dimensional displacement for the non-linear single degree of freedom Duffing Oscillator, ξ is the equivalent viscous damping ratio, α is a constant proportional to the cubic non-linearity of the hardening or softening dynamical system, F is the non-dimensional amplitude of the harmonic force with non-dimensional frequency ratio Ω impressed upon the system, and τ is the non-dimensional time parameter. These parameters are defined as $\xi = \frac{c}{2m\omega_n}$; $\omega_n = \sqrt{\frac{k_1}{m}}$; $\alpha = \frac{k_3 x_0^2}{k_1}$; $\Omega = \frac{\omega}{\omega_n}$; $\tau = \omega_n t$ where k_1 forms the linear part of the stiffness of the system, and k_3 the cubic non-linear part. Consequently, the term α represents the ratio of the non-linear and linear stiffness, since $x_0 = \frac{F_e}{k_1}|_{k_3=0,\ \omega=0}$ and ω is the frequency of the harmonic excitation. The term ω_n is not the natural frequency but a characteristic frequency of the linearised system. The term t is time and. c is the equivalent viscous damping coefficient. The overdots in equation 2.1 represent differentiation with respect to the non-dimensional time parameter. A range of non-dimensional frequency ratio between 0 and 2 is considered throughout the chapter. The frequency response of this non-linear system can be given as the roots of a quadratic function in the form:

$$\Omega_1 = \sqrt{\left(1 + \frac{3}{4}\alpha x^2 - 2\xi^2\right) - \frac{1}{x}\sqrt{1 - 4\xi^2 x^2 (1 - \xi^2 + \frac{3}{4}\alpha x^2)}} \tag{2.2}$$

and

$$\Omega_2 = \sqrt{\left(1 + \frac{3}{4}\alpha x^2 - 2\xi^2\right) + \frac{1}{x}\sqrt{1 - 4\xi^2 x^2 (1 - \xi^2 + \frac{3}{4}\alpha x^2)}} \tag{2.3}$$

where the subscripts of Ω represent the roots.

The Duffing Oscillator with $\alpha = 0$ behaves as a linear system. Figure 2.1 shows the response amplitude against the non-dimensional frequency for a linear case, and for situations related to non-linear coefficient value, i.e. maximum (α_{max}), critical (α_{crit}), and limit (α_{lim}), respectively. The value $|\alpha|_{max} = \frac{4}{3}\xi^2$ limits the value α can assume for a jump phenomenon to take place, $|\alpha_{crit}| < \frac{2^8}{3^{(5/2)}}\xi^3$ provides the limit of jump avoidance, and $\alpha_{lim} = 2\frac{16}{3}\frac{\xi^2(1-\xi^2)}{\xi^4}$ is the situation where the jump down frequency is equal to the natural frequency. These values of α can be readily computed and interpreted following Carrella [113]. It is clearly observed that the shapes of the curves are governed by the type of nonlinearity (hardening $\alpha > 0$ or softening $\alpha < 0$), the degree of nonlinearity, and the damping ratio. Also, the hardening and softening parts are generally not symmetrical about the linear response. This change of shape is the motivation behind this work. The next section presents the appropriate descriptors of damping ratio.

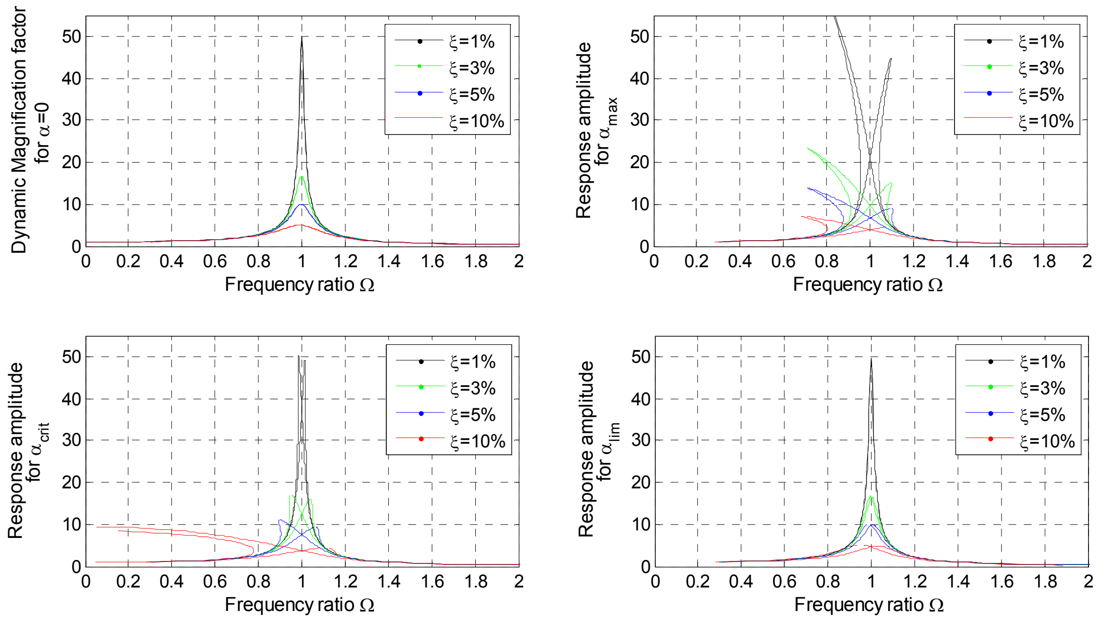

Figure 2.1 Response amplitude versus frequency ratio for linear and non-linear (Duffing).

2.3 Choice of Calibration Markers

In addition to showing the change of shape of the frequency response curves, Figure 2.1 illustrates that the frequency response curves tend to have a single significant global maximum within the domain of definition. The global maximum is being referred to here since a number of local maxima can form when the ideal curve is corrupted by measurement noise. Under these circumstances, in terms of the description of shape properties, the resemblance of the frequency response curves with probability distributions are exploited. Consequently, the statistical moments of the discretely sampled curves forming the frequency response describe the shape of the curves. Of the various simple descriptors available in this regard, the skewness and the kurtosis are chosen since the nature of the system and the damping ratio is observed to significantly affect the peakedness and the symmetry of the frequency response. The uses of these statistical descriptors have become popular in the field of structural health monitoring in recent years [86, 116, 117]. In a sense, it is attempted to relate the nature of the system and the damping ratio through a relative deviation from Gaussianity. The skewness and the kurtosis of a discretely sampled curve are computed as:

$$\lambda = \frac{\frac{1}{N}\sum_{i=1}^{N}(f_i - \mu)^3}{\left(\sqrt{\frac{1}{N}\sum_{i=1}^{N}(f_i - \mu)^2}\right)^3} \tag{2.4}$$

$$\kappa = \frac{\frac{1}{N}\sum_{i=1}^{N}(f_i - \mu)^4}{\left(\frac{1}{N}\sum_{i=1}^{N}(f_i - \mu)^2\right)^2} \tag{2.5}$$

where λ is the skewness, κ is the kurtosis, f is a discretely sampled function, N is the number of points at which the function f is discretely sampled, and μ is the mean of the function f in this regard:

$$\mu = \frac{1}{N}\sum_{i=1}^{N} f_i \tag{2.6}$$

2.4 Discussion and Results

2.4.1 Skewness and kurtosis descriptors for damping ratio calibration

Figure 2.2 presents calibration of a range of damping ratio employing skewness and kurtosis descriptors when system has linear (α_{lin}) or non-linear (α_{max},

α_{crit} and α_{lim}) behaviour in the case of softening (α_{maxsof}, $\alpha_{critsof}$ and α_{limsof}) and hardening (α_{maxhar}, $\alpha_{crithar}$ and α_{limhar}).

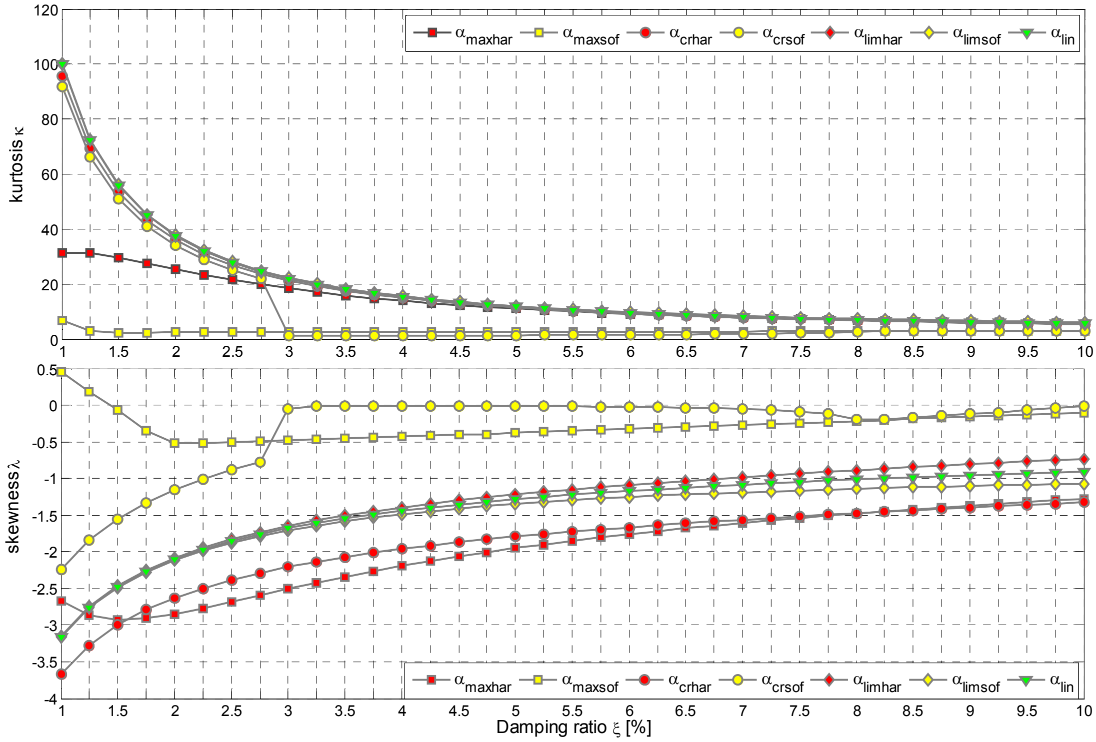

Figure 2.2 Skewness-Kurtosis based consistent calibration of damping ratios.

The values of skewness and kurtosis for observed damping ratios are given in Table 2.1. The variation of calibration is relatively high for extremely low damping ratios (less than 2%). A kurtosis based calibration of damping ratio is observed to be monotonic, consistent, and significantly independent of the system non-linearity. The level of calibration values can be easily related to the system damping, while the relative change in the region of damping under consideration allows obtaining a practical and appropriate resolution. Unless the system becomes exceptionally non-linear, these observations hold true. Consequently, a kurtosis based calibration is extremely useful. A skewness based calibration provides a consistent and monotonic calibration against damping as well (except for $\alpha_{critsof}$ between 7-10%). However, it is significantly dependent on the type and the level of non-linearity present in the system. The calibration curves are distinctly bundled according to whether the system is significantly soft, hard or more or less linear. This observation leads to the proposition of a combined skewness-kurtosis descriptor based calibration.

Table 2.1 Skewness – Kurtosis based consistent calibration of damping ratios.

$\xi(\%)$	α_{maxhar}		α_{maxsof}		$\alpha_{crithar}$		$\alpha_{critsof}$		α_{limhar}		α_{limsof}		α_{lin}	
	κ	λ	κ	λ	κ	λ	κ	λ	κ	λ	κ	λ	κ	λ
1	31.45	-2.68	6.83	0.46	95.67	-3.66	91.65	-2.25	99.99	-3.15	100.16	-3.17	100.07	-3.16
2	25.38	-2.85	2.46	-0.52	36.01	-2.63	33.94	-1.15	37.48	-2.08	37.73	-2.12	37.60	-2.10
3	18.33	-2.51	2.51	-0.48	21.20	-2.21	1.13	-0.05	21.85	-1.65	22.18	-1.71	22.01	-1.68
4	13.92	-2.20	2.57	-0.43	14.87	-1.96	1.24	-0.01	15.18	-1.40	15.57	-1.49	15.38	-1.44
5	11.10	-1.95	2.63	-0.38	11.45	-1.79	1.38	-0.01	11.55	-1.22	12.01	-1.35	11.78	-1.29
6	9.19	-1.76	2.70	-0.33	9.33	-1.67	1.57	-0.02	9.30	-1.09	9.83	-1.25	9.56	-1.17
7	7.84	-1.60	2.76	-0.27	7.89	-1.56	1.87	-0.05	7.80	-0.98	8.37	-1.19	8.07	-1.08
8	6.84	-1.48	2.81	-0.21	6.84	-1.47	2.69	-0.19	6.70	-0.89	7.33	-1.14	7.01	-1.01
9	6.07	-1.37	2.87	-0.16	6.05	-1.40	2.88	-0.12	5.88	-0.81	6.57	-1.10	6.20	-0.95
10	5.45	-1.28	2.92	-0.11	5.43	-1.33	2.93	-0.02	5.24	-0.73	5.98	-1.07	5.59	-0.91

2.4.2 Damping ratio calibration

Given the kurtosis, the damping ratio can be calibrated independent of the system. The value of skewness at that level of damping estimates the type and the degree of non-linearity of the system.

Figure 2.3 shows graphical interpretation of the function that can be used to calculate the damping ratio given the kurtosis.

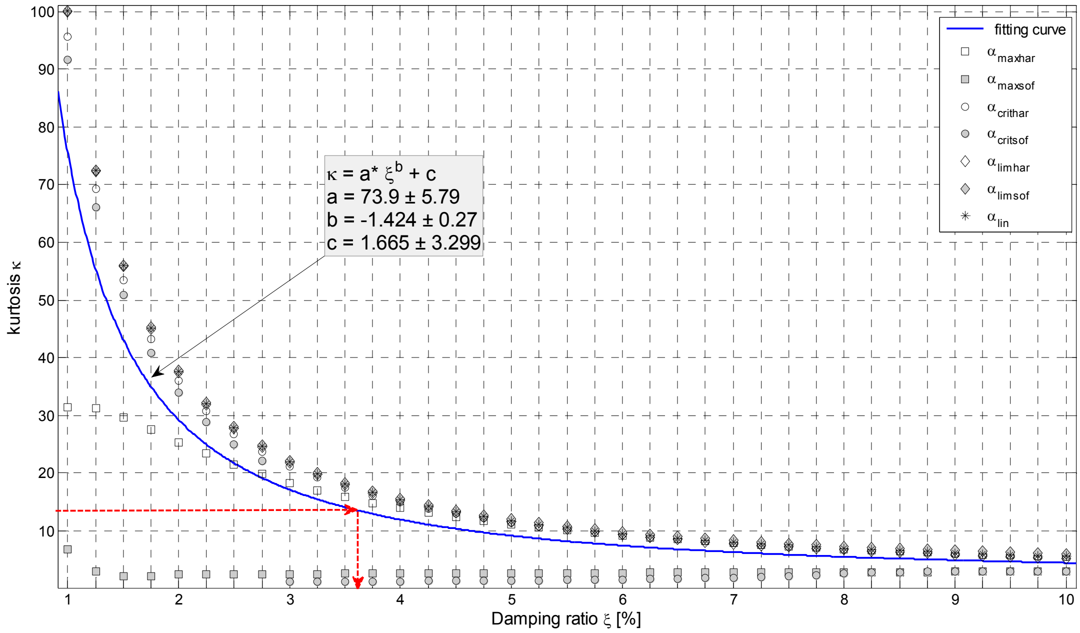

Figure 2.3 Kurtosis vs. damping ratios fitting curve.

Figure 2.4 shows three different functions that correlate damping ratio and skewness, each corresponding to the different system behaviour, i.e. $\alpha = 0$ (linear), $\alpha > 0$ (hardening), or $\alpha < 0$ (softening). The kurtosis and skewness fitting functions and goodness of their fit are shown in Table 2.2.

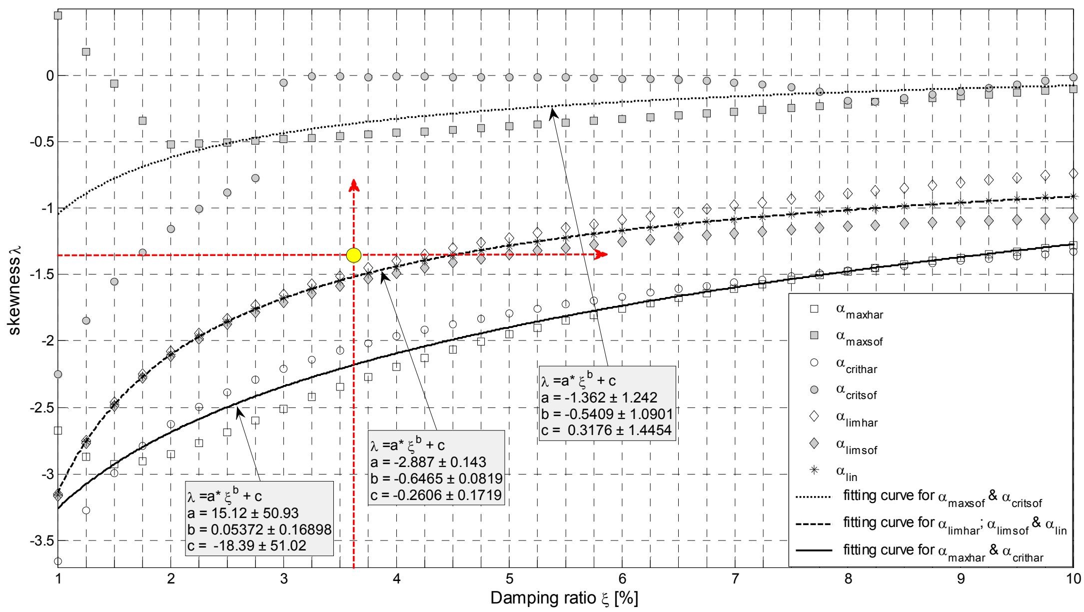

Figure 2.4 Skewness vs. damping ratios fitting curves.

Table 2.2 Skewness and Kurtosis vs. damping ratios fitting curves equations.

Case	Fitting Curve Equation	Coefficients	Root-Square (R^2)	Adjusted Root Square (adj-R^2)
Kurtosis all α cases	$\kappa = a\xi^b + c$	a = 73.9 ± 5.79 b = -1.424 ± 0.27 c = 1.665 ± 3.299	0.7168	0.7146
Skewness α_{maxsof} $\alpha_{critsof}$	$\kappa = a\xi^b + c$	a = -1.362 ± 1.242 b = -0.5409 ± 1.0901 c = 0.3176 ± 1.4454	0.304	0.2844
Skewness α_{limhar} α_{limsof} α_{lin}	$\kappa = a\xi^b + c$	a = -2.887 ± 0.143 b = -0.6465 ± 0.0819 c = -0.2606 ± 0.1719	0.9807	0.9803
Skewness α_{maxhar} $\alpha_{crithar}$	$\kappa = a\xi^b + c$	a = 15.12 ± 50.93 b = 0.05372 ± 0.16898 c = -18.39 ± 51.02	0.9517	0.9503

In order to use proposed calibration curves the kurtosis and skewness of the frequency response curve should be calculated first. The value of the calculated kurtosis is found on vertical axis of the Figure 2.3. Following the horizontal line right to where it crosses the calibration curve, draw vertical line towards horizontal axes to find corresponding damping value. When damping of the system is known, the next step is to establish the type and degree of nonlinearity. This can be done using Figure 2.4 by drawing the horizontal line from the calculated skewness value on the vertical axes and the vertical line from the previously found damping value on the horizontal axes. The place where these two lines intersect will determine nature of the system (i.e. type and degree of its nonlinearity).

The robustness of these calibrations under noise effects and variable rates of sampling will establish their usefulness as descriptors for practical purposes and for a potentially wide range of applications.

2.4.3 The effect of the noise on calibration

To establish the effect of noise, the situation where the discretely measured data is corrupted by significantly high levels of Gaussian white noise has been considered. The nature of the noise is not very important here, as the resistance of the calibrations against broadband noise is to be demonstrated. A wide range of noise levels is considered for the various calibrations, this establishes the distribution of the calibration values about the calibration values obtained from pure data. The descriptors are for all cases (α_{max}, α_{crit}, and α_{lim}) observed to be defined within tight standard deviation bands of calibration. The calibrations employing kurtosis and skewness are presented in Figure 2.5 and Figure 2.6, respectively.

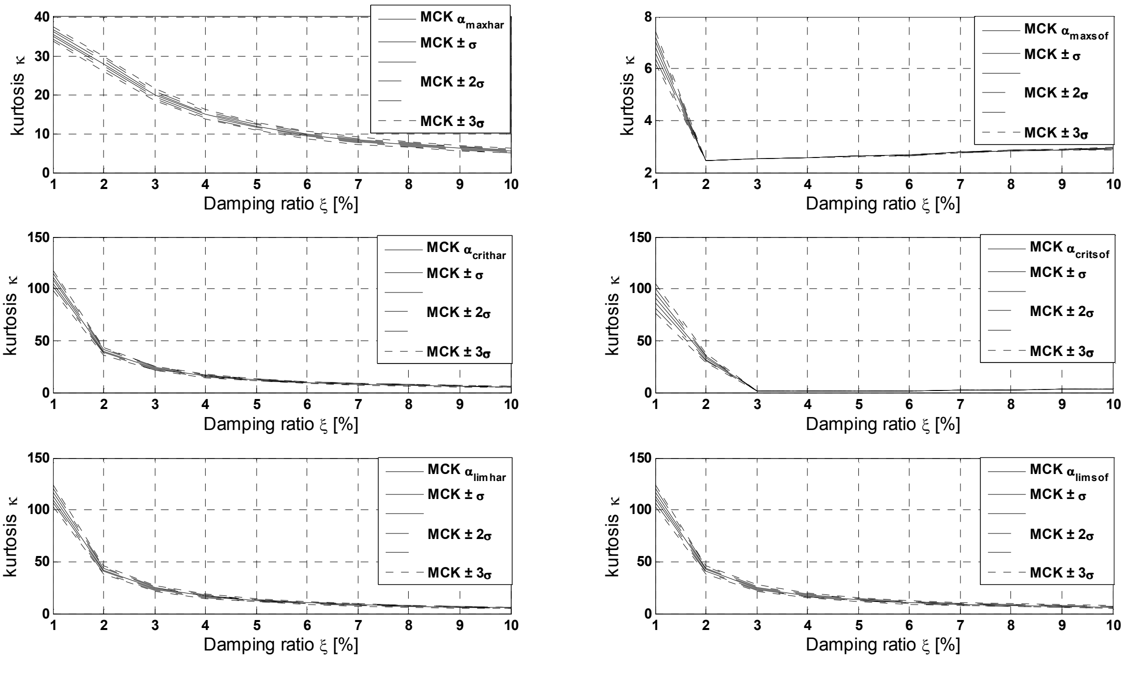

Figure 2.5 Robustness of kurtosis calibration against noise: a) α_{max}(hard), b) α_{max}(soft), c) α_{crit}(hard), d) α_{crit}(soft), e) α_{lim}(hard), and f) α_{lim}(soft).

Kurtosis calibrations tend to form a Master Curve (MCK) relatively independent on the nature and the extent of non-linearity of the system and the representative case is thus useful to appreciate how the deviation of calibrations stays within a very tight range in the presence of significant noise. It is also observed that the standard deviation bounds are smaller for a relatively higher damping ratio. This is related to how close the uniformly distributed discrete samples are in the kurtosis axis. For low damping, the separations are high even for relatively closely spaced non-dimensional frequency ratios and a measurement noise can significantly affect the shape of the curve near the global maxima. The effect reduces for higher damping as the separation in the kurtosis axis becomes relatively lesser. The calibrations of the descriptors are thus extremely robust against measurement noise.

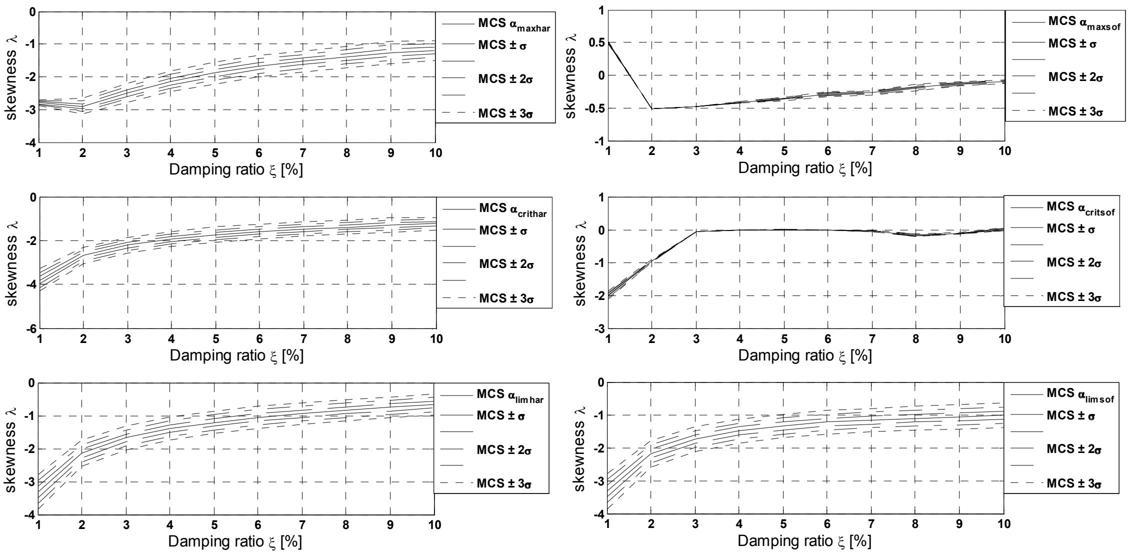

Figure 2.6 Robustness of skewness calibration against noise: a) α_{max}(hard), b) α_{max}(soft), c) α_{crit}(hard), d) α_{crit}(soft), e) α_{lim}(hard), and f) α_{lim}(soft).

2.4.4 The function of variations in sampling rate

The effects of variations in sampling rate of the non-dimensional frequency ratio are presented in Figure 2.7. Both kurtosis and skewness calibrations are considered in this regard where α_{lim} (hard) describes the non-linear system. It is observed that, barring extremely low damping ratios (as low as 1%), the calibration values are relatively independent of the discrete sampling rate covering logarithmic scales. The calibrations presented are thus extremely consistent and robust. The tests against noise and sampling rate establish a high degree of confidence on the proposed dual descriptors.

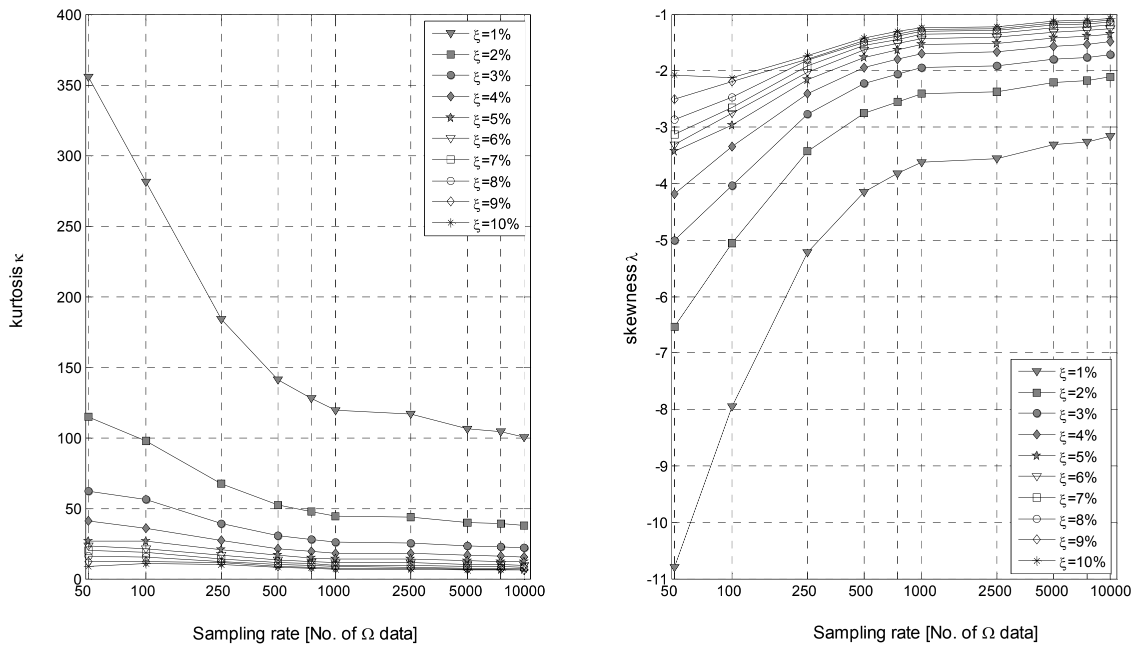

Figure 2.7 Effects of sampling frequency.

2.5 Conclusions

A skewness-kurtosis descriptor has been presented for the calibration of damping ratios in linear and non-linear systems from frequency response. The validation of the proposed descriptor has been carried out on the frequency response of a Duffing Oscillator. The calibrations are observed to be fast, simple, computationally inexpensive, consistent, and robust against measurement noise and sampling rates. The kurtosis measure tends to characterize the damping, while the skewness measure is also important for characterizing the type and the degree of non-linearity in the system. The descriptors allow rapid computation and can be applied to experimental data without the requirement of assuming a specific underlying model. The findings are general and applicable to a very broad spectrum of linear and non-linear systems and applications, including system identification, energy harvesting, and adaptive control of dynamical systems. However, there is a need to establish new markers from the specific system point of view. Real structure, e.g. a bridge, can be modelled as the SDOF system, but the characteristics of such system can be different, e.g. natural frequency, damping, stiffness, etc. Hence, the following chapter presents observation of behaviour of the specific system, i.e. damaged beam, modelled as SDOF. The model will be used to determine if the detection and calibration of damage is achievable through cumulant based statistical parameters computed on responses of the damaged beam due to passages of the load.

Chapter 3

Investigations on Indicators of Calibration of Damage

3.1 Introduction

It has been observed in the previous chapter that statistical descriptors of frequency response can be successfully used to characterize the type and the degree of non-linearity in the system, as well as to characterise the system damping. The introduction of damage in the structure will usually cause the change in damping capacity of the structure [26]. Thus the statistical parameters obtained by the analysis in previous chapter fulfil only stage 1 damage diagnostics (existence of the damage) requirements of SHM. In this chapter the attempt is made to address stage 2 and 3 damage diagnostics (location and severity of damage) requirements by employing statistical parameters on SDOF system response.

The damage detection and SHM for bridges employing bridge-vehicle interaction has created considerable interest recently. In this regard, a significant amount of work is present on the bridge-vehicle interaction models and on damage models. Surface roughness on bridges is typically used for detailed models and there are analyses relating surface roughness to the dynamic amplification of response of the bridge, the vehicle, or the ride quality.

The first part of this chapter presents the possible potential of using surface roughness for damage detection of bridge structures through bridge-vehicle interaction. The concept is introduced by considering a single point observation of the interaction of an Euler-Bernoulli beam with a breathing crack traversed by a point load. The detection and calibration of damage is investigated through cumulant based statistical parameters computed on stochastic, normalized responses of the damaged beam due to passages of the load.

However, when monitoring real structures the damage can happen suddenly; moreover the event is often masked by the noise. Therefore, the experiment on SDOF system with sudden change of system is performed in order to test the capability of SHM devices in detecting such occurrence.

The second part of the chapter is dedicated to experimental detection of sudden stiffness change. Sudden changes in the stiffness of a structure are often indicators of structural damage. Detection of such sudden stiffness change from the vibrations of structures is important for Structural Health Monitoring (SHM) and damage detection. Non-contact measurement of these vibrations is a quick and efficient way for successful detection of sudden stiffness change of a structure.

3.1.1 Background to Bridge-Vehicle Interaction Based Damage Detection Using Surface Roughness

Bridge-vehicle interaction has been theoretically and experimentally investigated by many researchers [11, 93, 95, 99, 118].

The subject of these studies are detection and identification of the location of damage and its calibration in the presence of noise, which represent key factors affecting SHM and implemented maintenance programmes [11]. In these studies the assessment, monitoring, and modelling of damage progression have usually been based on the analyses of structure responses. Narkis [82] has suggested that the use of traditional descriptors like change in natural frequencies as a marker of damage extent using pre-existing benchmark is often quite difficult in the presence of measurement noise. The use of laser-based devices [55, 119] and less expensive digital camera based methods [5, 9, 117, 120] combined with image processing techniques and wavelet based identification of possible existence, location, and the extent of damage using spatial data have been reported [121]. Most of these studies deal with the identification of damage position quite well. However, few have investigated the development of the extent of damage [55, 117].

A large number of studies have been devoted to the problem of an open crack in the simply supported beams [11, 82] in this respect and the use of wavelet analysis on the damaged modeshapes [119] or static deflected shapes [5] has successfully illustrated the potential of wavelet based analyses in identifying the damage without a pre-existing benchmark. The wavelet based detection is often masked by local extrema of high magnitude due to the presence of noise within the signal [81], where the damage is overridden by the measurement noise.

Damage identification techniques in the time domain are still more popular since the measurements are easier than obtaining the data from the spatial domain and generally more accessible. The major studies on damage identification and calibration of beams using temporal data have mostly dealt with the observation of the changes in natural frequency due to the presence of damage [3, 122-126], propagation of elastic waves [38, 83], tracking of frequency contours from different modes [127], and local attractor based detections using stochastic and chaotic excitation, where the structure is considered as a filter and the damage is described through phase space reconstruction [128-131].

Researchers are extensively looking at establishing unique markers which could be used for SHM. In this regard, using numerical and statistical techniques [76, 132] carried out on the data itself have often been observed to provide practical and good results. In this respect, Maholanobis Distance [94] has successfully been used before.

The first section of this chapter proposes the use of surface roughness for damage detection of beam-like structures through bridge vehicle interaction. Surface roughness on bridges is typically used for detailing models and analyses are present relating surface roughness to the dynamic amplification of response of the bridge, the vehicle, or to the ride quality. Abdel-Rohman and Al-Duaij [95] have found that the unevenness has a great effect on deflection and acceleration response compared with the smooth deck bridge, however, the difference in responses of hinged-hinged and simply-supported beam was negligible. O'Brien et al. [133] have investigated the International Roughness Index (IRI) and found that it is poorly correlated with dynamic amplification for roads of average roughness; instead they propose the use of the Bridge Roughness Index (BRI).

The concept presented in this chapter is demonstrated by considering the interaction of an Euler-Bernoulli beam with a breathing crack traversed by a Single Degree Of Freedom (SDOF) oscillator. The dynamic behaviour of the beam considered is modelled as bilinear damped mechanical system of SDOF since the breathing crack is considered as a nonlinear system with bilinear stiffness characteristics related to the opening and closing of crack [134]. The surface roughness of the beam is treated as a spatial representation of some broadband spectral definition. In this case a broadband Gaussian white noise [135] is considered for the purposes of demonstration. The mean removed residuals of beam response are analysed to detect damage. Uniform velocity and acceleration conditions of the traversing load are investigated. The detection and calibration of damage rely on cumulant based statistical parameters computed on stochastic, normalized responses of the damaged beam due to passages of the load. Behaviour of bilinear system is tested through changes in compression or tension stiffness of the system and acceleration coefficients. Given a spatial spectral definition of roughness, statistical estimates of response can be computed based on single point measurements. Statistical descriptions of these responses may be related to the global and local damage conditions. A successful demonstration of the concept presented in this chapter for single point measurements immediately opens up possibilities of employing multi-point measurements on a structure, monitored over a considerable period of time, for damage estimation on non-benchmarked situations.

3.2 Problem formulation

3.2.1 Undamaged Simply Supported Beam – Linear System

Three simply supported Euler-Bernouilli beams of length L with different rectangular uniform cross-sections and transverse SDOF oscillator are shown in Figure 3.1a.

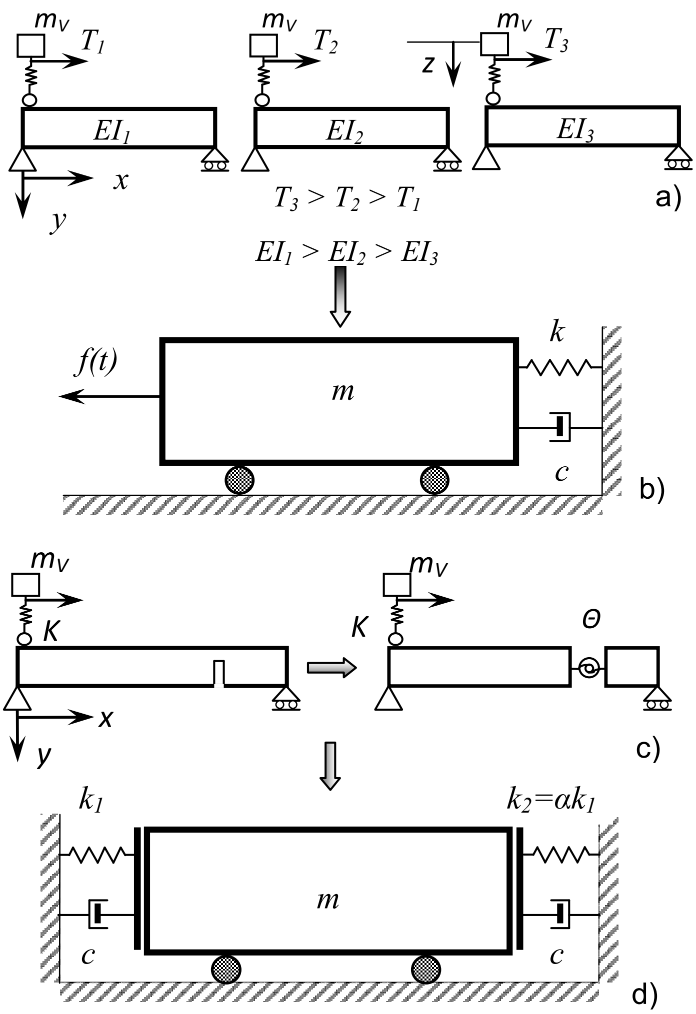

Figure 3.1 a) simply supported beams with decreasing cross section characteristics; b) SDOF – linear system; c) simply supported beam with breathing crack modelled as two beams connected by torsional spring; and d) SDOF – bilinear oscillator [134].

Equation of motion of single span bridge with rough surface (omitting the stretching in the midplane) [95] can be written as:

$$EI\frac{\partial^4 y}{\partial x^4} + c\frac{\partial y}{\partial t} + \rho A\frac{\partial^2 y}{\partial t^2} = P\delta(x - \upsilon t) \tag{3.1}$$

where E is Young's modulus of the beam, I is constant moment of inertia of the beam cross section; combined EI is flexural rigidity, y (x, t) is beam transverse deflection at the point x and time t (measured from the equilibrium position when the beam is loaded with own weight), x is the length coordinate with the origin at the left-hand end of the beam, $\bar{x} = \upsilon t$ is the position of the vehicle from the left support, c is the equivalent viscous damping coefficient, t is the time coordinate with an origin at the instant of the force arriving upon the beam, ρ is the density of the beam, A is the beam cross-section area, δ is the dynamic coefficient defined as the ratio of the maximum dynamic deflection to the static deflection at the mid-span of a beam [103], υ is the constant speed of the motion of the moving load traversing the beam. The moving load P is defined as:

$$P = m_V g + K[z - y(\bar{x}, t) - r(\bar{x})] \tag{3.2}$$

where m_V is the mass of the SDOF oscillator, g is the acceleration due to gravity, $m_V g$ is the weight of SDOF oscillator, K is the combined stiffness of vehicle's tires and springs, z is the vertical displacement of the vehicle with respect to its static equilibrium position, and r is the road surface roughness or unevenness. The second term of equation 3.2 represents the inertial force.

The vertical displacement of the SDOF oscillator with no damping with respect to its static equilibrium position may be found from:

$$m_V\ddot{z} + K[z - y(\bar{x}, t) - r(\bar{x})] = 0 \tag{3.3}$$

The solution of equation 3.1 can be obtained by the technique of separation of variables in the spatial and temporal domains as:

$$y(x,t) = \sum_{i=1}^{n} \phi_i(x) q_i(t) \tag{3.4}$$

where $\phi_i(x)$ is the orthogonal mode shape for the i^{th} mode and $q_i(t)$ is the time dependent amplitude.

By substituting equation 3.4 into equation 3.1, multiplying the left and the right side of the equation with orthogonal mode shapes and integrating over the length of the beam, a system of differential equations is obtained using the sampling property of Dirac-Delta function as:

$$\ddot{q}_i(t) + 2\xi_i\omega_i\dot{q}_i(t) + \omega_i^2 q_i(t) = f_i(t) \qquad i = 1, 2, \dots, \bar{n} \tag{3.5}$$

where ξ is the damping ratio, ω is the natural frequency, $f(t)$ is the equivalent external force, and $\bar{n}$ is the number of orthogonal modes considered.

Each of these equations of motion can be modelled by an SDOF system. For many practical purposes, it is often sufficient to consider the response from the fundamental mode [11]. Therefore the dynamic behavior of the beam considered can be modelled as linear damped mechanical system of a SDOF, presented in Figure 3.1b. The generic equation of motion for an SDOF system is:

$$m\ddot{y}(t) + c\dot{y}(t) + ky(t) = f(t) \tag{3.6}$$

where m is mass of the system, $c = 2m\omega\xi$ is equivalent viscous damping coefficient of the system, and $k = m\omega^2$ is the stiffness of SDOF system.

Considering the movement of an accelerating vehicle and comparing with equations 3.2, 3.3, 3.4, and 3.5, in this case input external force is equal to:

$$f(t) = A_0 sin(at + bt^2) + r(t) \tag{3.7}$$

A_0 is force amplitude, while a and b are velocity and acceleration coefficient, respectively.

The mean removed output removes the effects of the sinusoidal component of equation 3.7 taking into consideration only the roughness component. The effect of $r(t)$ comes only when inertial effects of vehicle are considered, in which case equation (3.6) becomes:

$$m\ddot{y}(t) + c\dot{y}(t) + ky(t) = r(t) \tag{3.8}$$

3.2.2 Damaged Simply Supported Beam – Bilinear System

A simply supported Euler-Bernouilli beam of length L with rectangular uniform cross-section having transverse crack at the distance L_C from the left support is modelled as two beams connected by torsional spring [82, 95] and is shown in Figure 3.1c. The presence of crack defines specific boundary conditions at the location of crack and equation 3.1 is valid for each segment of the beam separately on either side of the crack with appropriate boundary conditions.

The dynamic behaviour of the damaged beam can be modelled as bilinear damped mechanical system of a single degree of freedom [134, 136, 137], as shown in Figure 3.1d. Here the difference in the stiffness in compression k_1 and tension k_2 represents the change in stiffness of the crack beam. The motion of a SDOF bilinear oscillator can be expressed as:

$$\begin{cases} m\ddot{x} + c\dot{x} + \alpha kx = f(t), & 0 \le \alpha \le 1 \; and \; x \ge 0 \\ m\ddot{x} + c\dot{x} + kx = f(t), & x < 0 \end{cases} \tag{3.9}$$

Where $\alpha = k_2/k_1$ represents stiffness ratio (or stiffness reduction factor under tension). If the stiffness ratio equals one the model is linear. The input external force can be expressed by equation 3.7. The excitation force $f(t)$ incorporates effects of roughness.

3.2.3 Proposed Method and Assumptions

An Euler-Bernoulli beam with a breathing crack is traversed by a point load. This system is equivalent to SDOF bilinear oscillator (see Figure 3.1).The breathing crack is treated as a nonlinear system with bilinear stiffness characteristics related to the opening and closing of crack. The observed SDOF bilinear oscillator has constant equivalent viscous damping coefficient. The force acting on the system is combination of SDOF mass, inertia, and interaction with surface roughness. The surface roughness of the beam is essentially a spatial representation of some spectral definition and is treated as a broadband white noise in this chapter. The varying stiffness ratio conditions represent damage extent. The cumulant based statistical parameters are obtained on the mean removed residuals of beam response. The calculated statistical parameters are used for detection and calibration of damage.

Uniform non-dimensional velocity and acceleration conditions of the traversing load are investigated for the appropriateness of use.

3.3 Discussion and Results

3.3.1 Choice of Calibration Markers

The SDOF bilinear oscillator (Figure 3.1d) with a generic unit mass and constant damping coefficient ξ = 2% in all cases is analysed. The input force consists of the sinusoidal force and surface roughness effects as per equation 3.7. The response of the system (displacement, velocity and acceleration) is observed for the different stiffness conditions, k_1 and k_2, and acceleration coefficients, b, and is calculated using linear acceleration method [105]. Calculations are repeated many times employing the generated white noise to obtain statistical averages of responses. The time window size for averaging is equal to the residence time of the vehicle. We choose displacement as the response of the system in this chapter and attempt to use statistical descriptors of displacement in order to relate to nature of the system and the changes in its stiffness. It is obvious from the equations that this choice of response, if demonstrated successful, is sufficient to demonstrate the appropriateness of use of other responses like velocity and acceleration. In order to achieve this we observe a number of statistical descriptors including: the displacement mean μ, the standard deviation of displacement σ, the Mahalanobis distance to displacement means $d(\vec{x},\vec{y})$, the skewness λ, and the kurtosis κ:

$$\mu = \frac{1}{n}\sum_{i=1}^{n} x_i \qquad (3.10)$$

$$\sigma = \sqrt{\frac{1}{n}\sum_{i=1}^{n}(x_i - \mu)} \qquad (3.11)$$

$$d(\vec{x},\vec{y}) = \sqrt{\sum_{i=1}^{n} \frac{(\vec{x}_i - \vec{y}_i)^2}{\sigma_i^2}} \tag{3.12}$$

$$\lambda = \frac{\frac{1}{n}\sum_{i=1}^{n}(x_i - \mu)^3}{\left(\sqrt{\frac{1}{n}\sum_{i=1}^{n}(x_i - \mu)^2}\right)^3} \tag{3.13}$$

$$\kappa = \frac{\frac{1}{n}\sum_{i=1}^{n}(x_i - \mu)^4}{\left(\frac{1}{n}\sum_{i=1}^{n}(x_i - \mu)^2\right)^2} \tag{3.14}$$

where *n* is number of points at which the observed function is discreetly sampled.

3.3.2 System Linearity

Peng et al. [134] define restoring force of bilinear oscillator as a piecewise linear continuous function of displacement of the bilinear SDOF system, which is calculated:

$$S(x) = \begin{cases} \alpha kx & x \geq 0 \\ kx & x < 0 \end{cases} \tag{3.15}$$

Equation 3.14 describes relationship between stiffness ratio and observed system linearity. It can be also related to the equation 3.8, which represents the motion of a SDOF bilinear oscillator. For the stiffness ratio less than 1.0, i.e. where tension stiffness is lower than compression stiffness, system becomes non-linear or bilinear.

3.3.3 Calibration markers

3.3.3.1 Linear System

Figure 3.2 presents calibration of a range of stiffness employing mean and standard deviation descriptors, where the stiffness in compression and tension have the same values. The sensitivities of calibration when employing the mean and the standard deviation values are comparable. The mean and standard deviation values of displacement based calibration of system stiffness are observed to be monotonic and consistent.

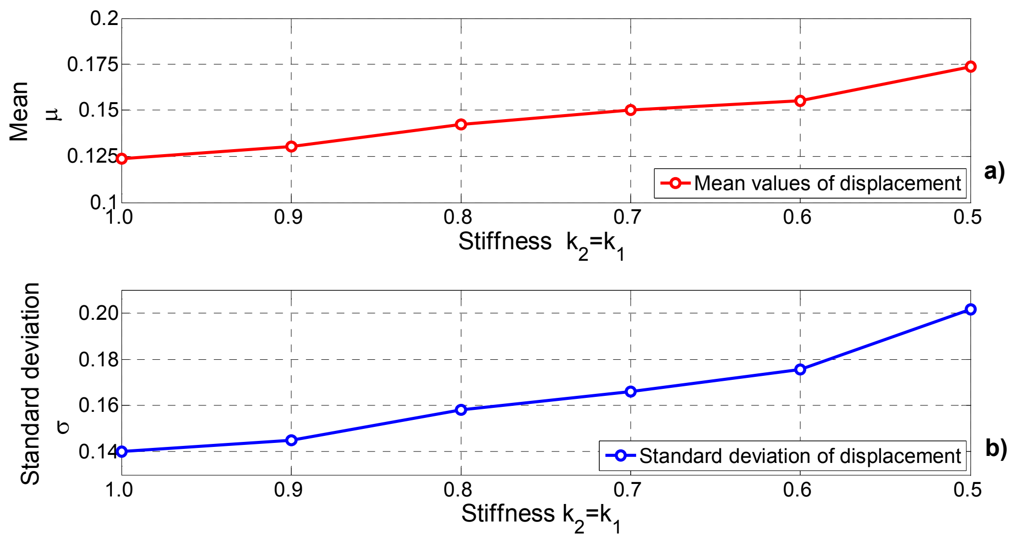

Figure 3.2 Damaged beam – SDOF Linear system (stiffness under compression and tension are equal and decreases): a) mean values and b) Standard deviation.

3.3.3.2 Bilinear System

Figure 3.3 shows the mean values and standard deviation of displacement for the system where the compression stiffness is kept constant (k_1 = 1) and the tension stiffness decreases ($1.0 \geq k_2 \geq 0.5$). This situation is similar to a bilinear formulation of a breathing crack (see equation 3.8). It is observed that the mean and the standard deviation descriptors of displacement based calibration of system stiffness remain monotonic and consistent. The sensitivities are comparable to those obtained in Figure 3.2. In both these figures, a higher degree of damage corresponds to a more rapid change in the descriptor values.

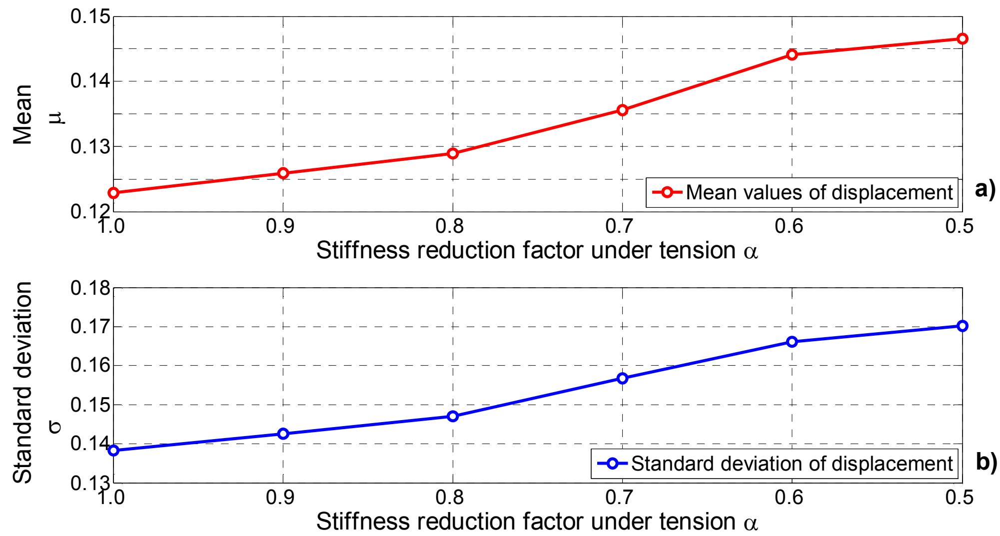

Figure 3.3 Damaged beam – SDOF Bilinear system (stiffness under compression is constant $k_1 = 1$ and stiffness under tension decreases): a) mean values and b) Standard deviation.

The bilinear system is investigated next where the compression stiffness ($k_1 = 1.0$) and the tension stiffness ($k_2 = 0.5$) remain constant while the acceleration coefficient of the input force to the system varies ($0 \leq b \leq 0.1$). The mean and the standard deviation values of displacement are shown in Figure 3.4 for this variation. It can be seen that the mean and standard deviation values of the mean-removed responses are only stable for acceleration coefficients $b \geq 0.06$. Consequently, it is important to investigate the variations in calibration significantly below and above this value for a potential application of accelerating vehicles interacting with the rough surface of a bridge for damage estimation.

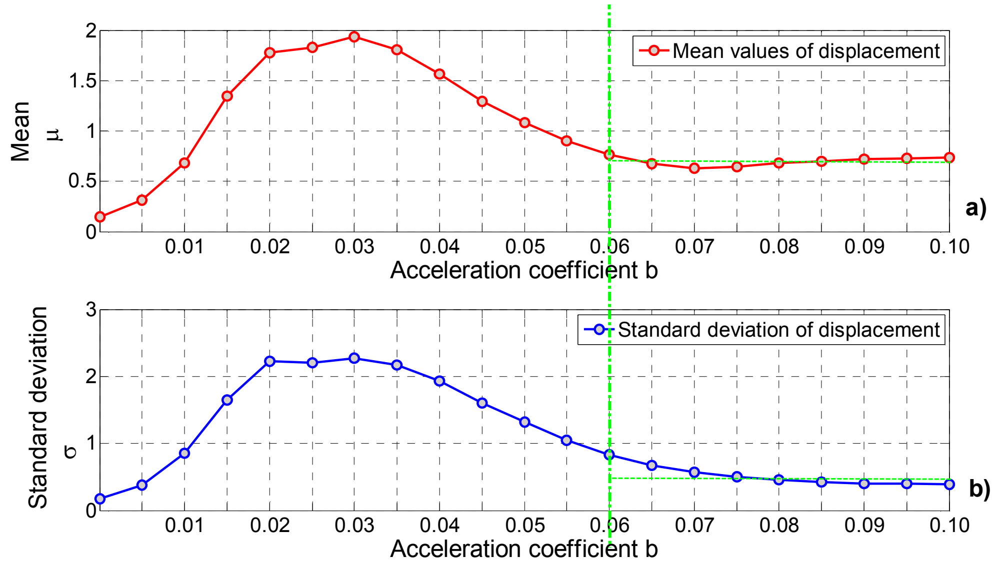

Figure 3.4 Damaged beam – SDOF Bilinear system (stiffness under compression is k_1 = 1 and under tension k_2 = 0.5): a) mean values and b) Standard deviation.

The mean and standard deviation values of mean-removed displacement output are studied next. The compression stiffness remains constant (k_1 = 1) and tension stiffness is gradually reduced for two cases of acceleration coefficient b = 0.1 (high) and b = 0.03 (low). Results are presented in Figure 3.5. In both cases the mean and standard deviation values of displacement based calibration of system stiffness remain monotonic and consistent for the whole range of stiffness ratio. Significant deviations in calibration values are not observed due to significant changes in acceleration coefficients. Consequently, for accelerating vehicles or vehicles with constant speed, a control-chart type continuous monitoring method may be employed for single point observations of mean-removed output response of bridge-vehicle interaction employing surface roughness. However, the acceleration effects are often small and in most situations correspond to a relatively uniform speed of a vehicle traversing a bridge.

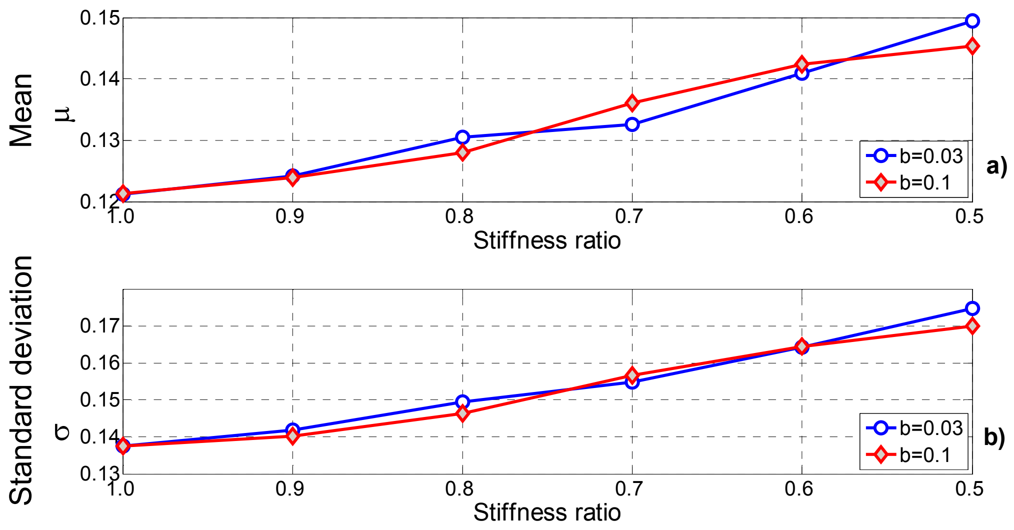

Figure 3.5 Damaged beam – SDOF Bilinear system (stiffness under compression is $k_1 = 1$ and under tension k_2 decreases): a) mean values and b) Standard deviation; for acceleration coefficient $b = 0.03$ (low) and $b = 0.1$ (high).

The possibility of using scaled output data or the use of higher cumulant based estimations for single point measurements is investigated next. In this regard, the Mahalanobis distance to displacement means is chosen as a candidate for a descriptor of damage. Statistically, it is a variance normalised Euclidian distance in this thesis. The measure has been exploited previously for experimental research [138] and full scale experiments on bridges [2]. Figure 3.6 shows Mahalanobis distance to displacement means for decreasing values of compression and tension stiffness where $k_1 = k_2$. A consistent and monotonic marker of damage is not obvious from this figure.

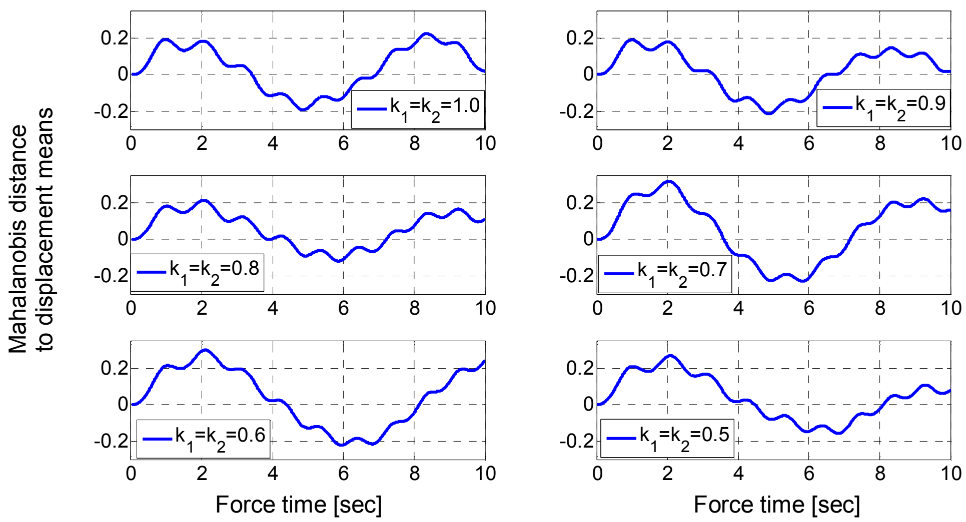

Figure 3.6 Mahalanobis distance to displacement means for system where stiffness of compression and tension are equal and changing from 1.0 to 0.5.

To assess the suitability of the use of Mahalanobis distance and higher cumulants of mean-removed single point measurements, we explore the mean and standard deviation of the Mahalanobis distance along with skewness and kurtosis (Figure 3.7).

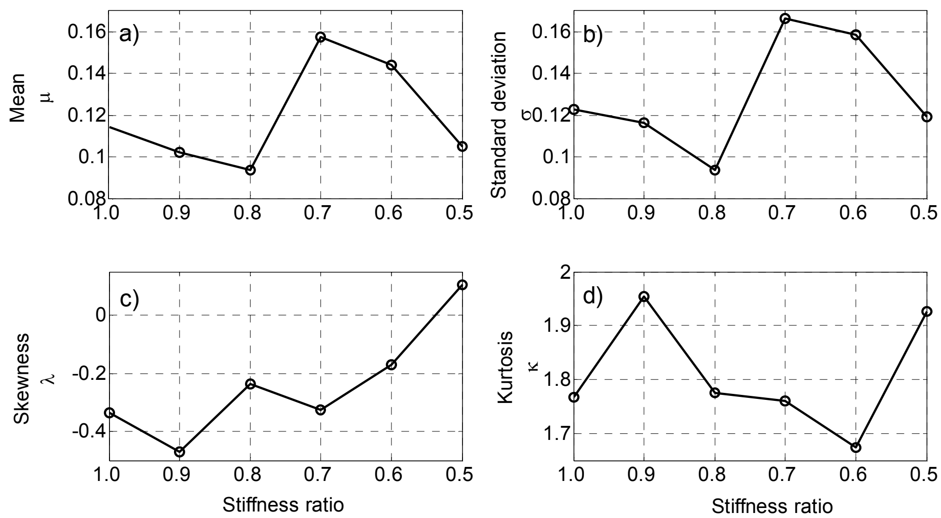

Figure 3.7 Mahalanobis distance to displacement means for system where stiffness of compression and tension are equal: a) mean; b) standard deviation; c) skewness; and d) kurtosis.

A consistent or monotonic relationship can not be established employing these values with changes of the system stiffness for single point measurements, contrary to the potentials observed for multi-point measurements [139]. Consequently, only the lower order cumulants of single-point measurement response are appropriate as faithful descriptors of damage extent.

3.4 Experimental Detection of Sudden Stiffness Changes Due to Damage

Sudden changes in the stiffness of a structure are often indicators of structural damage. Detection of such sudden stiffness change from the vibrations of structures is important for SHM and damage detection. Non-contact measurement of these vibrations is a quick and efficient way for successful detection of sudden stiffness change of a structure. In this part of the chapter, the capability of Laser Doppler Vibrometry to detect sudden stiffness change in a SDOF oscillator within a laboratory environment will be demonstrated.

3.4.1 Background to Experimental Detection of Sudden Stiffness Change

Detecting structural damage is an essential part of SHM. In that regard, reliable and cost effective methods are needed to detect damage in a structure. These methods include non-destructive techniques that can be applied to in-service structures, thereby reducing maintenance costs and improving safety and system performance [10, 27, 140]. Amongst the many approaches in detecting damage in structures, the use of structural vibration data [85, 94, 96, 122] is very popular. Successful detection of a sudden change in vibration data in the presence of noise is a critical component in damage detection. Important examples of these changes within a system are changes in stiffness of vibrating SDOF system and the local disruption of stress and strain fields due to the presence of damage [95, 102, 105]. In order to detect and describe such changes, new methods and analysis techniques have been introduced in the area of SHM. Time-frequency analysis techniques, like wavelet analysis, have been very efficiently used for detection of the presence, location, and calibration of the extent of these changes [2, 81, 84, 117, 141, 142].

The environmental noise and choice of sensors used can considerably affect the accuracy of the damage detection procedure [143]. In the following sections an application of non-contact measurements of vibration by Laser Doppler Vibrometry (LDV) and the importance of wavelet analysis for the successful detection of damage in the presence of Gaussian white noise will be presented. The performance of a 3-D accelerometer and LDV with wavelet analysis on measured data is compared.

3.4.2 Methodology

The dynamic response of a bilinear Single Degree of Freedom (SDOF) system is measured using two wireless instruments, MicroStrain G-Link Wireless Accelerometer Sensor and Polytec RSV-150 Remote Sensing Vibrometer (LDV). LDV employs Laser Doppler Vibrometry for measuring dynamic response, while Accelerometer is mounted on the SDOF system.

3.4.2.1 3D Accelerometer

MicroStrain G-Link Wireless Accelerometer Sensor was used to measure the acceleration of the vibrating SDOF system in Cartesian directions. The accelerometer is a traditional and reliable tool for monitoring structures adopted for laboratory and large scale in-situ measurements [103, 144, 145]. The disadvantage of using this type of sensors is that they have to be attached to the structure at all times during the monitoring, which is not always possible.

3.4.2.2 Laser Doppler Vibrometer

Laser Doppler Vibrometer (LDV) has been successfully employed for a wide range of applications, including lifting of roof tiles in a wind tunnel test [145], vibration mode estimation [146, 147], estimation of acoustic parameters [148], non-destructive diagnostics of fresco paintings [149], estimation of natural frequencies of a rotating plate [150] and damage detection [119]. A Polytec RSV-150 Remote Sensing Vibrometer (Figure 3.8) is used for rapid, accurate, non-contact and long distance measurement of vibrating structures.

Figure 3.8 Polytec RSV-150 Remote Sensing Vibrometer.

The fundamental governing principle of LDV is the Doppler Effect. If a target moves away from a vibrometer of source of frequency f in a straight line with velocity $\vec{v}$ then the target receives a frequency of:

$$f' = \left(\frac{c - \vec{v}.\,\vec{e_t}}{c}\right) f \tag{3.16}$$

where c is the velocity of light in vacuum and $\vec{e_t}$ is the unit vector emanating from the vibrometer to the target and both the vibrometer and the target are considered to be points. The target, now a source of frequency f', reflects the light back and this light is received by the vibrometer with frequency:

$$f'' = \left(\frac{c}{c - \vec{v}.\,\vec{e_r}}\right) f' \tag{3.17}$$

where $\vec{e_r}$ is the unit vector corresponding to the reflecting situation. These two equations can be combined as:

$$f'' = \left(\frac{c - \vec{v}.\,\vec{e_t}}{c - \vec{v}.\,\vec{e_r}}\right) f \tag{3.18}$$

Under the assumption that the velocity of the target is insignificant compared with the velocity of the light, equation 3.18 can be approximated:

$$f'' = \left(1 + \frac{\vec{v}.\,(\vec{e_t} - \vec{e_r})}{c}\right) f \tag{3.19}$$

The change in frequency Δf can then be expressed as:

$$\Delta f = f'' - f = \frac{2v}{\lambda} \tag{3.20}$$

where λ is the wavelength of source laser light emanating from the vibrometer (in this experiment an infra-red source was used) and v is the absolute value of $\vec{v}$ owing to the linearity of motion considered for equation 3.16.

If the direction of velocity of the target and the normal of wave front creates an angle θ:

$$\Delta f = \frac{2\vec{v}.\,\vec{e}}{\lambda} = \frac{2v}{\lambda}cos(\theta) \tag{3.21}$$

where $\vec{e}$ is the instantaneous direction vector between the vibrometer and the target at a given point of time. The measurements are quite precise for an angle θ up to 80^{o}, which is to say that in those circumstances equation 3.20 very successfully replaces equation 3.21 without any loss of accuracy.

3.4.2.3 Experiment Setup

A small scale bilinear SDOF model was tested. The model was made of a SDOF car connected to fixed supports on either side through calibrated springs (Figure 3.9). The SDOF car model was placed on a vibration bench and exposed to the external force in the form of white noise. The main (principal) direction of vibration is following blue array (Figure 3.9) and is in the same line as Channel 1 (CH1) of 3D accelerometer and LDV laser beam direction (see Figure 3.9 and Figure 3.10). Channel 2 (CH2) measures vibration of SDOF system in horizontal plane perpendicular to the principal direction of vibration, while Channel 3 (CH3) measures vibrations in vertical direction (Figure 3.10). The friction between the wheels of the SDOF car and the surface was low. An investigation is carried out in Chapter 5 in support of this statement. The experiment setup is shown in Figure 3.10.

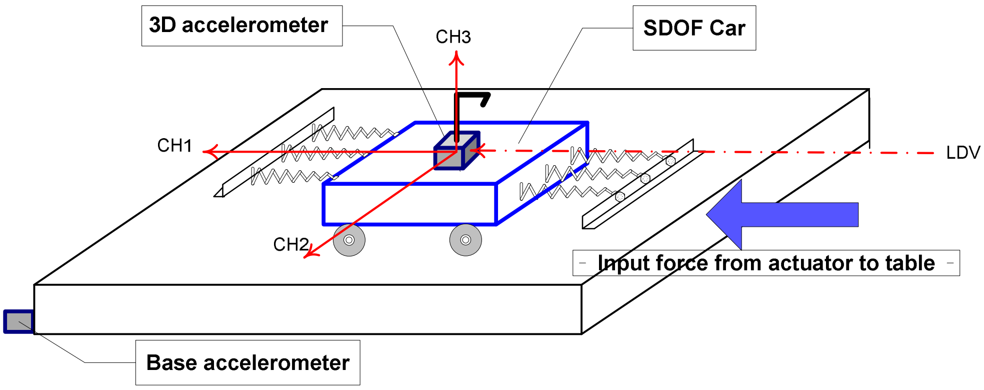

Figure 3.9 SDOF car experiment schematic. The red arrays indicated the Cartesian direction of 3D Accelerometer measurements and dash-dot red array indicate direction of LDV measurements.

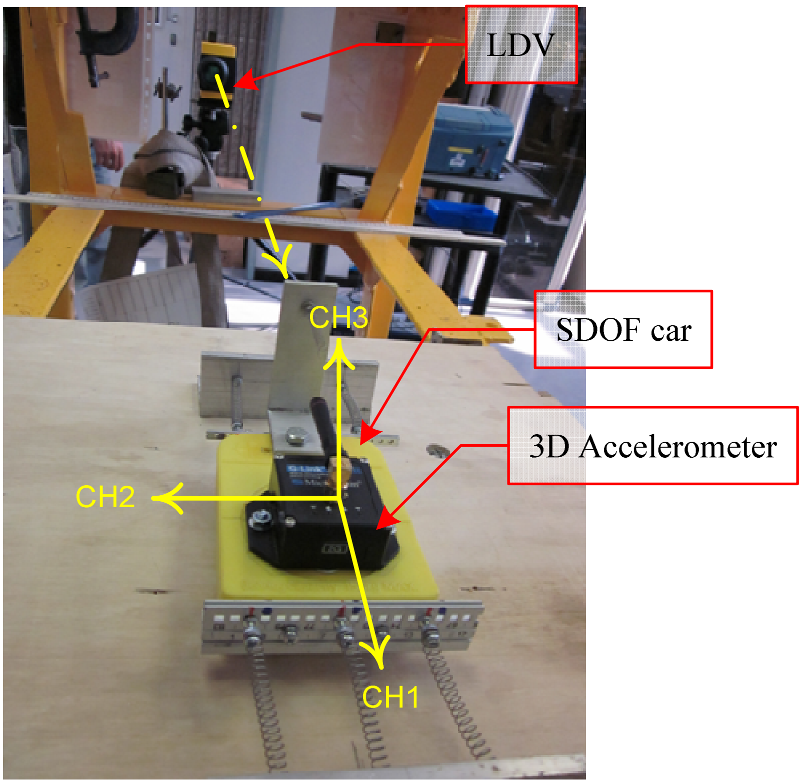

Figure 3.10 Experiment Setup: 1) Single Degree of Freedom (SDOF) Car; 2) MicroStrain G-Link Wireless Accelerometer (yellow arrays indicate Cartesian directions); 3) LDV (Polytec RSV -150 Remote Sensing Vibrometer) the dash-dot array target the point of measurements.

Prior to the experiment, the linear springs were calibrated and the results of this calibration are presented in Figure 3.11.

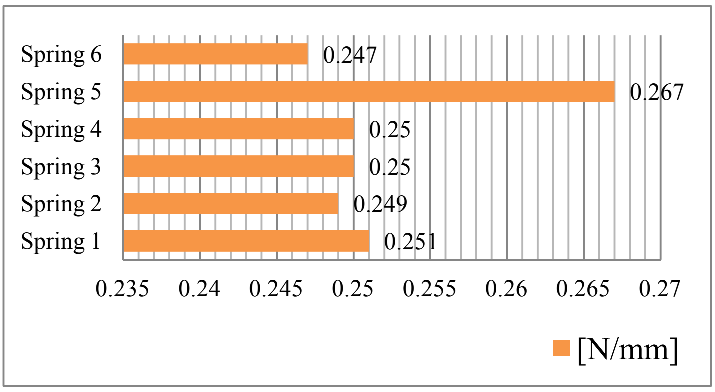

Figure 3.11 Calibration of Spring Stiffness.

3.4.2.4 Equivalent stiffness

The stiffness of the SDOF system was experimentally determined through calibrated linear springs. Calculated equivalent stiffness of the combined springs at the beginning of the experiment was k = 0.378 N/mm. The sudden change of stiffness was simulated by introducing the failure of the middle springs on either side at a certain instant in time during a given period of forced vibration. The first spring got detached after 13 sec (k = 0.303 N/mm) and the second one after 38 sec (k = 0.249 N/mm) from the beginning of measurements.

3.4.2.5 Measurements

The LDV has only two output channels onboard: these are displacement and velocity. In this experiment the voltage is just recorded so the calibration factor needs to be applied manually. A voltage signal, to which a calibration factor is applied, comes out the back. The LDV measurements (obtained as .txt file) keep records of the number of recordings, time (sec), and the voltage ouput from the vibrometer Velocity channel in millivolts (mV). The calibration factor used is 100 mm/s/V for velocity setting. Hence, to get acceleration from the LDV data the calibration factor needs to be applied before differentiation of velocity data. The measurements of the wireless accelerometer recorded (excel file) show number of data recorded and the acceleration in Cartesian directions measured in "g values". In order to get the acceleration in [m/s^2] value recorded data need to be divided by 9.81. The 3D Accelerometer data sample rate is 617 data points per second per channel. This corresponds to 1/617 or a time step of 0.00162075 seconds.

The points on the time axis of responses for the instruments are representative of this sampling. Acceleration responses to sine sweep input are shown in Figure 3.13, where the outputs of the 3D accelerometer are in the Cartesian directions (a-c) and the LDV measurement (d) is measured velocity response. Channel 1 (CH1) of the accelerometer corresponds to the principal direction of vibration. The comparable amplitudes and the cleanness of data for numerically differentiated LDV velocity response indicate the presence of low noise in the data. Consequently, the velocity responses from LDV may be directly exploited to detect the sudden stiffness change in time.

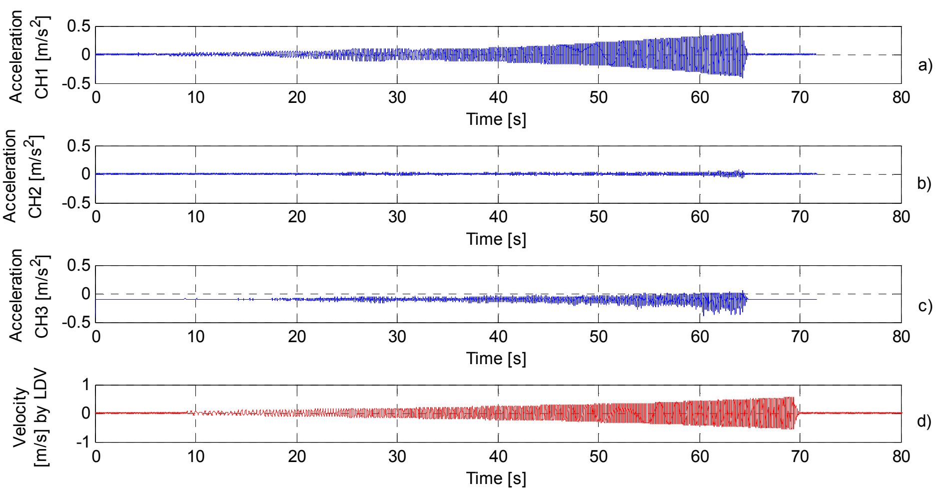

Figure 3.12 Example comparison between accelerometer: a) CH1; b) CH2; and 3) CH3, and d) LDV measurements.

3.4.3 Discussion and Results

3.4.3.1 Time domain response

The time domain response of the SDOF system, including the failure of two (out of six) springs under white noise is shown in Figure 3.13 as recorded by the 3D accelerometer (a-c) and the LDV (d). The times of the failure of the springs are located at 13 sec and 38 sec from the beginning of experiment. It is difficult to identify any prominent peak related to the failures from Figure 3.13.

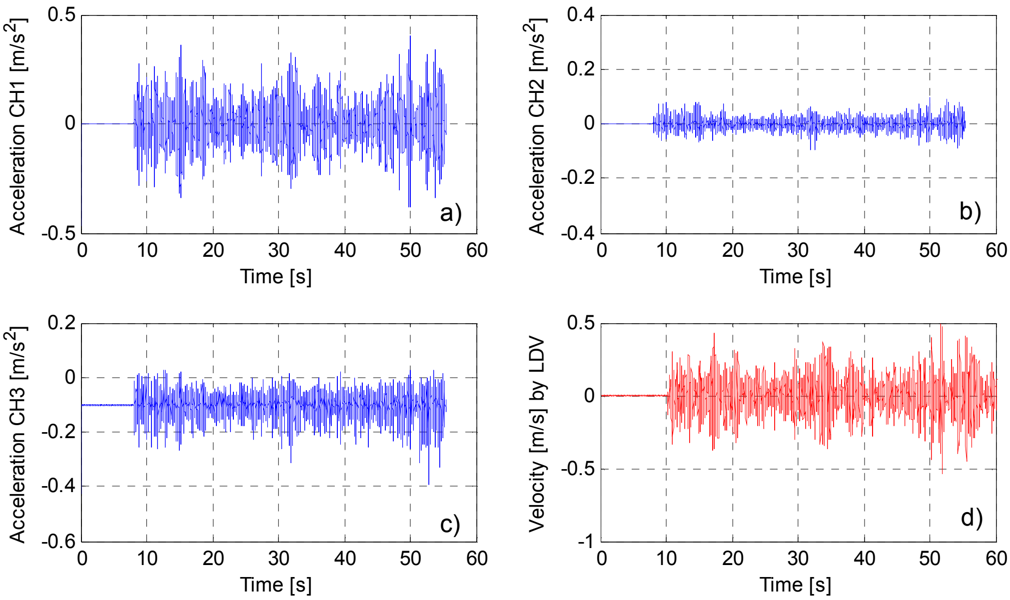

Figure 3.13 Time Domain Response from 3D accelerometer: a) CH1; b) CH2; and 3) CH3, and d) LDV for sudden change of stiffness.

3.4.3.2 Frequency domain response

The time domain responses are converted to the frequency domain through Fourier Transform (Figure 3.14). The frequency domain representation can not detect the sudden change in time due to the averaging effects of Fourier Transform.

The peaks of the frequency domain response are different for the accelerometer and the LDV. This is dependent on the change of a relatively linear system to a strongly bilinear system with some lateral effects for a certain period of time and the return of the system to a relatively linear system, averaged over time. The velocity and acceleration responses cannot necessarily be expected to be proportional under such circumstances. Independent of the difference in the peaks, the inability to detect sudden stiffness change in time through this method remains. A time-frequency domain analysis is attempted next for the detection of the sudden stiffness change.

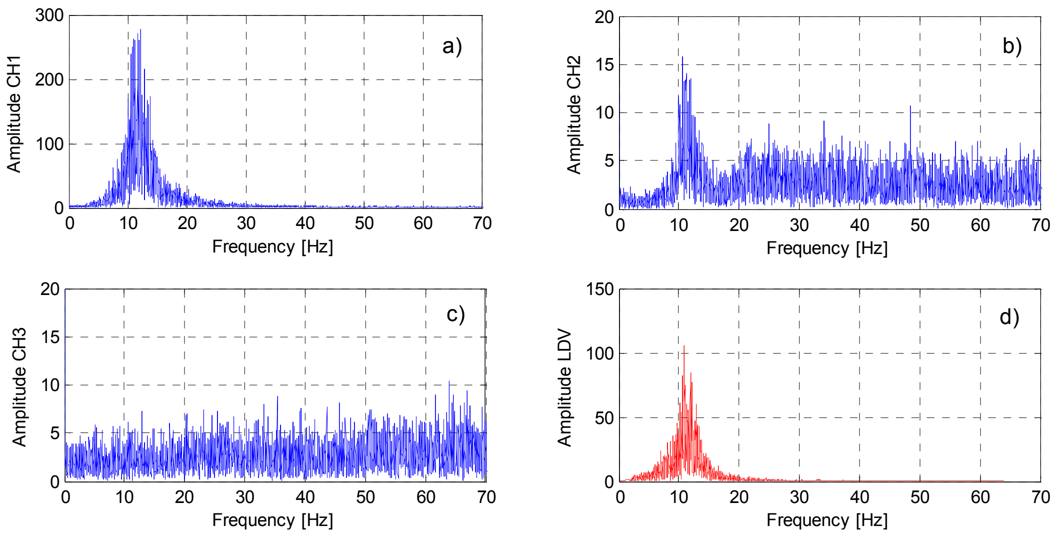

Figure 3.14 Frequency Response from 3D accelerometer: a) CH1; b) CH2; and 3) CH3, and d) LDV for sudden change of stiffness.

3.4.3.3 Continuos Wavelet Transform

Continuous Wavelet Transform (CWT), employing a Coif4 basis function and over scales up to 512 is carried out on the vibration responses detected by LDV and 3D accelerometer. The wavelet transform of 3D accelerometer response can not clearly indicate the occurrence of the damages (Figure 3.15 and 3.16). The response of the dominant non-principal direction of vibration (Channel 2) is of little significance and consequently, noisier masked results of Channel 3 are not presented.

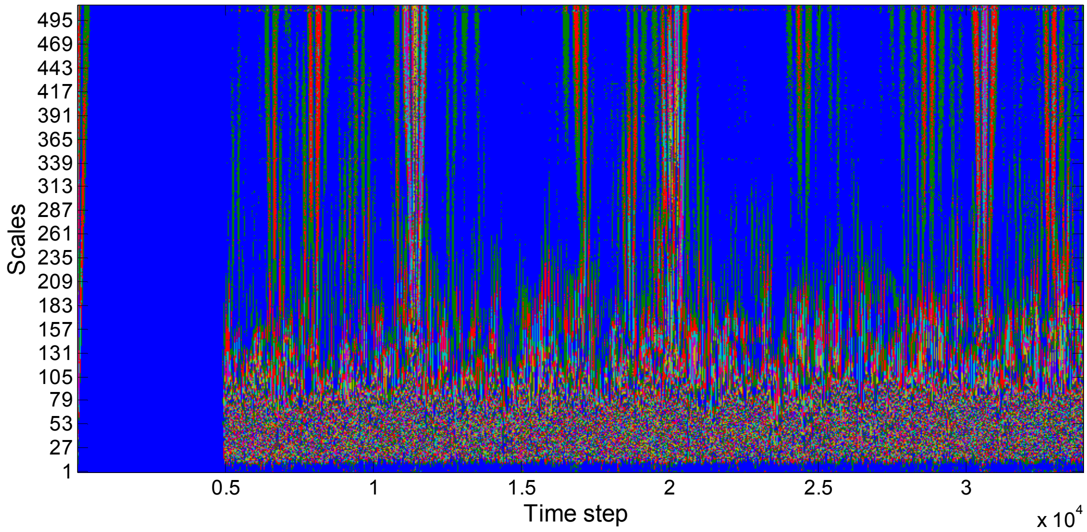

Figure 3.15 Wavelet based analysis on 3D accelerometer data (Channel 1).

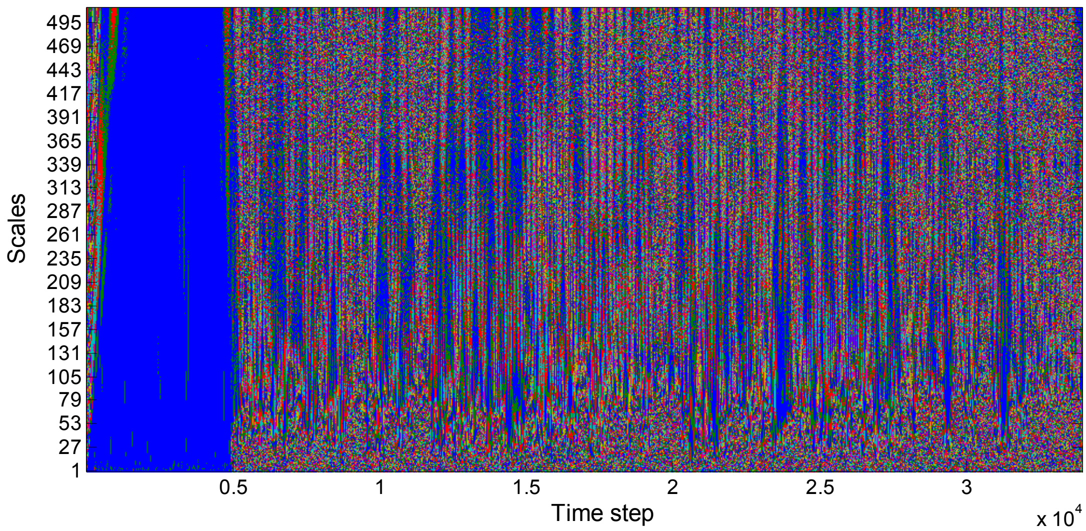

Figure 3.16 Wavelet based analysis on 3D accelerometer data (Channel 2).

Figure 3.17 shows the CWT analysis on LDV output data. Occurrences of damage are clearly determined at the correct time instants as consistent maxima values are observed over all scales. Coif4 wavelet has eight vanishing moments and is efficient in detecting the singularity present in the signal itself. The use of LDV combined with wavelet analysis is found to be advantageous over the use of 3-D accelerometer in the diagnostics of structural damage.

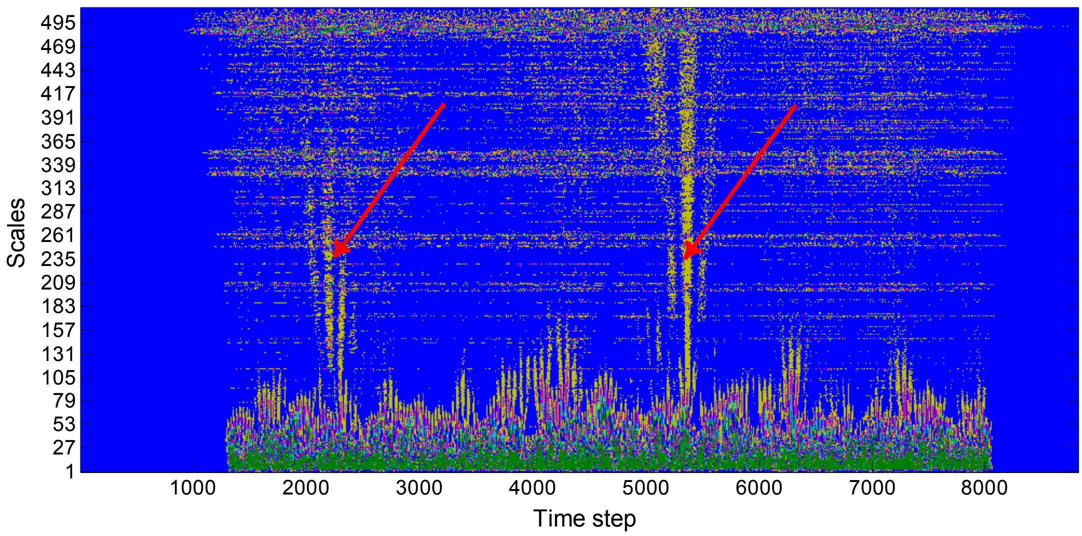

Figure 3.17 Sudden change of stiffness detection using wavelet based analysis on Laser Doppler Vibrometer data.

3.5 Conclusions

In the first part of this chapter the uncertainties in a structural system in the form of surface roughness on a bridge is investigated in order to establish consistent, monotonous and simple to implement damage calibration using bridge-vehicle interaction. The investigation proves that the first and second order cumulants of response are appropriate as consistent and monotonic descriptors of the system characteristics and they are sensitive to change in the stiffness of the system. It is demonstrated that this calibration can be successfully achieved by considering vehicles with uniform speed and with acceleration. However, reasonable acceleration values do not significantly affect damage calibration. Any spatial spectral definition of roughness may be used for this method; the conclusions are not specific to a certain description of surface roughness. Given a spectral broadband definition of surface roughness, consistent and monotonic calibration can be achieved.

The second part of the chapter is experimental detection of sudden stiffness change in structural system. The experiment demonstrates the effectiveness of LDV measurements to for damage detection and its superiority over a traditional accelerometer based approach. Where time or frequency domain detection of sudden stiffness change is not possible for a SDOF bilinear oscillator, the LDV based measurement, in conjunction with wavelet analysis, performs very efficiently in the detection of the presence and the location of damage at each instance. The implementation of the LDV model is easy and the damage diagnostics is quick. This type of remote observation is observed to be particularly suitable for rapid damage detection and health monitoring of structures under a model-free condition or where information related to the structure is not sufficient. LDV technique could be of great importance when monitoring historical structures, strategically important structures, structures such as nuclear and hydro power plants.

Chapter 4

Damage Detection and Calibration from Bridge Vehicle Interaction Employing Surface Roughness

4.1 Introduction

It has been observed previously that, given a spatial spectral definition of roughness, it is possible to compute statistical estimates of response based on single point measurements. Successful demonstration of the concept presented in Chapter 3 for single point measurements opens up possibilities for employing surface roughness for multi-point measurements on a structure, monitored over a considerable period of time, for damage estimation on non-benchmarked situations and in conjunction with higher order cumulants based calibrations. In this chapter we study the effects of road quality and vehicle speed on damage detection on bridges through consideration of bridge-vehicle interaction effects.

A bilinear breathing crack in a damaged Euler Bernoulli beam traversed by a moving oscillator is considered. The Road Surface Roughness (RSR) of the beam is realistically classified as per ISO 8606:1995(E). The stochastic description of the unevenness of the road surface is used as an aid to monitor the health of the structure in its operational condition. Numerical simulations are conducted considering the effects of changing road surface classes from class A (very good) to class E (very poor), effects of changing vehicle speed, location, and extent of damage. The interaction of the moving oscillator with the surface roughness is exploited to define simple, consistent, easy to implement, and robust statistical descriptors to detect and calibrate the existence, location, and extent of damage. The effects of vehicle speed and variable RSR profiles for such detection are investigated and preferable conditions for detection are identified. The proposed method is suitable for experimental analysis where a theoretical model is not available or is not credibly ascertained. The findings in this chapter are important for establishing the expectations from different types of road roughness on a bridge for damage detection using bridge vehicle interaction where the bridge does not need to be closed for monitoring.

4.1.1 Background to Bridge-Vehicle Interaction and Damage Models

Structural Health Monitoring (SHM) addresses the continuous monitoring of a structure in terms of static and dynamic response, including the diagnoses of the onset of anomalous structural behaviour [2]. Non-destructive structural damage detection is becoming an important aspect of integrity assessment for aging, extreme-event affected, or inaccessible structures [3, 5, 6, 132]. In that regard bridge-vehicle interaction damage detection has created considerable interest recently (Chapter 3).

Local damage in beams has been modelled in a number of ways [140]. Narkis [82] has proposed a method for calculation of natural frequencies of a cracked simply supported beam using an equivalent rotational spring.

Sundermeyer and Weaver [137] have exploited the non-linear character of vibrating beam with a breathing crack. The effect of vehicle speed in combination with different grades of surface roughness, location and extent of damage on bridges has never been used as an aid in damage detection. We propose the use of changing road surface roughness in damage detection of beam-like structures through bridge-vehicle interaction and investigate which road quality is appropriate for such detection.

Harris et al. [151] have proposed a method for characterisation of pavement roughness through the analysis of vehicle acceleration. Fryba [103] has shown the effect of RSR on bridge response. Abdel-Rohman and Al-Duaij [95] have investigated the effects of unevenness in the bridge deck on the dynamic response of a single span bridge due to the moving loads.

O'Brien et al. [133] have proposed a Bridge Roughness Index (BRI) which gives insight into the contribution that road roughness makes to dynamics of simply supported bridges. Da Silva [152] has proposed a methodology to evaluate the dynamical effects, displacement, and stress on highway bridge decks due to vehicle crossing on rough pavement surfaces.

There are many interesting numerical and statistical markers and methods available for damage detection [70, 80, 108, 127]. However, up to now all literature considers the inclusion of surface roughness to be a part of making a better model for bridge-vehicle interaction or for assessing the effect surface roughness has on ride quality or the dynamic amplification of the bridge [125, 145, 146].

Jaksic et al. [154] have very recently investigated the potential of using surface roughness for detecting damage, including the analysis of white noise excitation response of a SDOF bilinear oscillator. The white noise represented a broadband excitation, qualitatively similar to the interaction with surface roughness, and the bilinearity attempted to capture a breathing crack. First and second order cumulants of the response of this system were observed to be appropriate markers for detecting changes in system stiffness.

In this chapter we present beam-vehicle interaction based damage detection from multiple point observations in time domain using the interaction with realistic surface roughness testing the effects of range of the vehicle speed. The damage has been modelled as a localized breathing crack and surface roughness has been defined by ISO 8606:1995 [155].

The responses of the first mode of undamaged and damaged beam are observed [120, 132, 135], since they are often easy to detect and are often a good approximation of the actual displacement. The preferable road quality in conjunction with vehicle speed for damage detection process is investigated in considerable detail.

4.2 Bridge Vehicle Interaction

4.2.1 Problem formulation

The schematic of the problem considered is presented in Figure 4.1 where the damaged bridge-vehicle interaction system is represented as a simply supported Euler-Bernoulli beam with a breathing crack traversed by a SDOF oscillator. The beam represents the bridge and the oscillator represents the vehicle. The vehicle is assumed to be moving on the surface without losing contact with it [103].

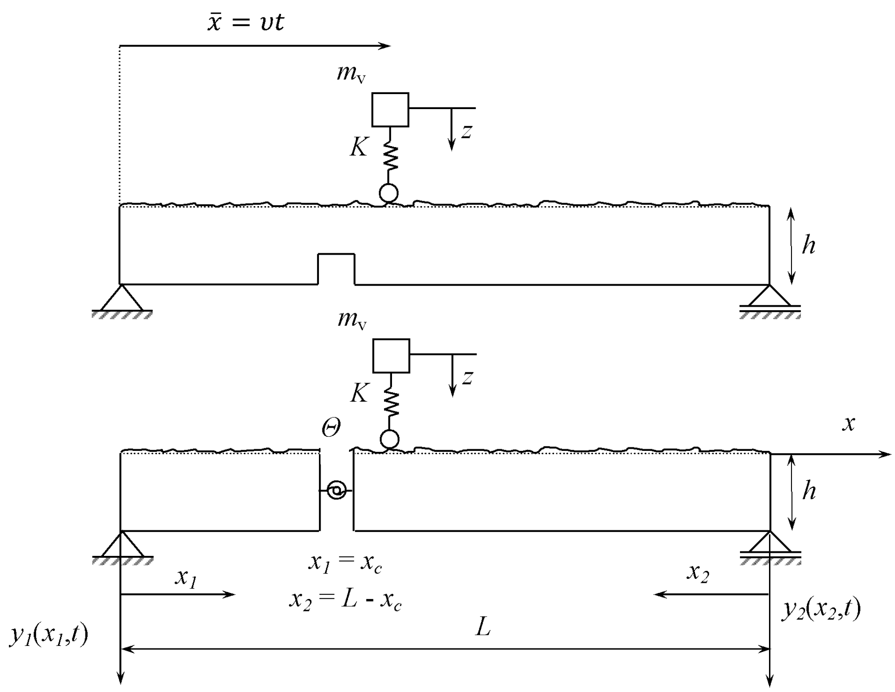

Figure 4.1 Simply supported beam with breathing crack modelled as two beams connected by torsional spring.

The length of the beam is L (m) and the crack is at a distance x_c (m) from the left support. The beam has a constant cross sectional area A (m^2) and a second moment of area I (m^4). The material properties of the beam are the Young's modulus E (N/m^2) and the mass density ρ (kg/m^3). The crack is modelled as a rotational spring [82] when the crack is open.

4.2.2 Equations of motion

The governing equation of motion of cracked beam with mass per unit length $m = \rho A$ (kg/m) and structural damping of the material c, subjected to the weight of the moving load P (N) are coupled through continuity and jump conditions at crack location as:

$$EI\frac{\partial^4 y_i(x,t)}{\partial x^4} + c\frac{\partial y_i(x,t)}{\partial t} + \rho A\frac{\partial^2 y_i(x,t)}{\partial t^2} = P\delta(x - vt); \quad i = 1,2 \tag{4.1}$$

where EI is flexural rigidity (Nm^2); t is the time coordinate with the origin at the instant of the force arriving upon the beam (s); x is the length coordinate with the origin at the simply supported end of each beam (m); $y_i(x,t)$ is the transverse deflection of the i^{th} beam at the point x and time t, measured from the static equilibrium position corresponding to when the beam is loaded under its own weight; δ is the Dirac Delta function [95]; and vt is the position of the vehicle moving with constant speed v from left support (m).The external force P is defined as [95]:

$$P = \{m_V g + K[z - y_i(vt,t) - r(vt)]\}; \quad i = 1,2 \tag{4.2}$$

where m_V is the mass of the vehicle (kg); g is acceleration due to gravity (9.81 m/s^2); K is the stiffness of the vehicle's tires and springs (N/m); z is the vertical displacement of the vehicle with respect to its static equilibrium position (m); and r is the surface roughness (m).

The effects of structural damping are often small and under such circumstances equation (4.1) can be rewritten as:

$$EI\frac{\partial^4 y_i(x,t)}{\partial x^4} + \rho A \frac{\partial^2 y_i(x,t)}{\partial t^2} = \{m_V g + K[z - y_i(\upsilon t,t) - r(\upsilon t)]\}\delta(x - x_i) \qquad i = 1,2 \quad (4.3)$$

with the condition:

$$K[z - y(\upsilon t,t) - r(\upsilon t)] \geq 0 \quad (4.4)$$

The solution of the eigenvalue problem related to this system gives natural frequencies and mode shapes. Two cases, the open and the closed crack states are considered to obtain two sets of natural frequencies and mode shapes for a breathing crack formulation.

4.2.2.1 The open crack eigenvalue problem

When the crack is open, the system consists of two beams connected by a torsional spring, where each continuous segment of the beam can be described by the Euler-Bernoulli partial differential equation of motion (4.3). The eigenvalue problem can then be solved through the method of separation of variables:

$$y_i(x_i,t) = \sum_{j=1}^{n} \phi_j^i(x)\, q_j(t); \quad i = 1,2 \quad (4.5)$$

where ϕ_i^j is the orthogonal mode shape of the i^{th} beam for the j^{th} mode shape and q_j is the time dependent amplitude. By separating temporal and spatial variables, the following ordinary differential equation system is obtained:

$$\phi_j^{i''''}(x) - \frac{\omega_j^2 \rho A}{EI} \phi_j^i(x) = 0 \,; \quad i = 1, 2;\ j = 1\ to\ n \tag{4.6}$$

$$\ddot{q}_j(t) + \omega_j^2 q_j(t) = 0; \quad j = 1\ to\ n \tag{4.7}$$

where ω_j is natural frequency of the beam and the superscripted primes denote differentiation with respect to the spatial coordinate. For free vibrations of the beam, there is no external excitation and consequently there are no displacements or moments at the supports. The corresponding boundary conditions are:

$$x_i = 0 \implies \phi_j^i(0) = 0; \quad \phi_j^{i''}(0) = 0 \,; \quad i = 1, 2;\ j = 1\ to\ n \tag{4.8}$$

Boundary conditions at the crack location x_c must satisfy continuity of displacement, bending moment and shear, leading to:

$$\phi_j^1(x = x_c) = \phi_j^2(x = L - x_c) \tag{4.9}$$

$$\phi_j^{1''}(x = x_c) = \phi_j^{2''}(x = L - x_c) \tag{4.10}$$

$$\phi_j^{1'''}(x = x_c) = -\phi_j^{2'''}(x = L - x_c) \tag{4.11}$$

The slope between the two beam segments can be related to the moment at this section as [137]:

$$\phi_j^{1''}(x_c) + \frac{K_T}{EI}\left[\phi_j^{2'}(x = L - x_c) + \phi_j^{1'}(x = x_c)\right] = 0 \tag{4.12}$$

where K_T is the equivalent rotational spring stiffness as defined by Sundermeyer and Weaver [137] and expressed as a polynomial function of crack depth ratio:

$$K_T = \frac{M}{\theta_c} \tag{4.13}$$

where M is bending moment and θ_c is angle of rotation due to presence of the crack:

$$\theta_c = (72\pi M/Ebh^2)F_1(x_c/h) \tag{4.14}$$

where shape factor for rectangular section width b and height h is:

$$\begin{aligned} F_1(x_c/h) = {} & 19.6(x_c/h)^{10} - 40.69(x_c/h)^9 + 47.04(x_c/h)^8 - 32.99(x_c/h)^7 \\ & + 20.29(x_c/h)^6 - 9.975(x_c/h)^5 + 4.602(x_c/h)^4 - 1.047(x_c/h)^3 \\ & + 0.6294(x_c/h)^2 \end{aligned} \tag{4.15}$$

The solution of the spatial differential equation (4.6) satisfying all eight boundary conditions is thus:

$$0 < \bar{x} < x_c \rightarrow$$

$$\phi = A_0(\sin a\bar{x} + \alpha \sinh a\bar{x}) \tag{4.16}$$

$$x_c < \bar{x} < L \rightarrow$$

$$\phi = A_0\left(\frac{\sin(ax_c)\sin\big(a(L-\bar{x})\big)}{\sin\big(a(L-x_c)\big)} + \alpha\frac{\sinh(ax_c)\sinh\big(a(L-\bar{x})\big)}{\sinh\big(a(L-x_c)\big)}\right) \tag{4.17}$$

where

$$a^4 = \frac{\omega_j^2 \rho A}{EI} \qquad j = 1\ to\ n \tag{4.18}$$

$$\alpha = \frac{\cos ax_c + \dfrac{\sin ax_c}{\tan a(L - x_c)}}{\cosh ax_c + \dfrac{\sinh ax_c}{\tanh a(L - x_c)}} \tag{4.19}$$

and the constant A_0 chosen so that the mode shapes are normalized as:

$$\int_0^{x_c} (\phi_j(\bar{x}))^2 d\bar{x} + \int_{x_c}^{L} (\phi_j(\bar{x}))^2 d\bar{x} = 1 \tag{4.20}$$

where the spatial coordinate $\bar{x}$ is considered from the left hand support and ϕ is the generalised representation of any mode shape as $\{\phi_j^1, \phi_j^2\}$ for any mode, arbitrarily represented as the j^{th} mode here.

The natural frequencies of the beam with the open crack can also be calculated replacing boundary conditions in an assumed solution of mode shape equation (4.6):

$$\phi(x) = A_1 \cos ax + A_2 \sin ax + A_3 \cosh ax + A_4 \sinh ax \tag{4.21}$$

and setting its determinant to zero, or by using equations (4.18) and (4.19) [137]. A comparison of natural frequency results using the approach of Sundermeyer and Weaver [137] was carried out against the approach of Narkis [82] and the results were found to be in agreement.

4.2.2.2 The closed crack eigenvalue problem

When the crack closes, the beam is treated as one continuous Euler-Bernoulli beam and the first mode shape equation is:

$$0 < x < L \;\rightarrow \phi(x) = \sqrt{\frac{2}{L}} sin(ax) \tag{4.22}$$

Since the displacement at the supports equals zero, the equation (4.21) is satisfied when *sin* (*aL*) = 0. Therefore the natural frequencies of the beam when the crack is closed are:

$$\omega_j = j^2\pi^2\sqrt{\frac{EI}{mL^4}}; \quad n = 1, 2, 3, \ldots \tag{4.23}$$

4.2.3 Equation of motion of vehicle

The equation of motion of the vehicle, modelled as a SDOF oscillator with no damping (as shown in Figure 4.1), can be expressed as [95]:

$$m_V\ddot{z} + K[z - r(vt) - y_i(vt, t)] = 0 \quad i = 1,2 \tag{4.24}$$

4.2.4 Surface roughness

The moving vehicle loads are time dependent, because the position of wheel loads changes with time (*t*) and the suspension of the vehicle oscillates (*z*) due to irregularities of the RSR [156]. The randomness of the RSR can be represented through a periodic modulated random process [152, 153, 156, 157]. In the ISO 8606:1995(E) [155] specifications, RSR is related to the vehicle's speed by a formula linking velocity and displacement Power Spectral Density (PSD), where the general form of displacement PSD of RSR in (m^3/cycles) is:

$$S_d(f) = S_d(f_0)\left(\frac{f}{f_0}\right)^{-\alpha} \tag{4.25}$$

where f_0 = 1/2π (cycles/m) is the discontinuity frequency; f is the spatial frequency (cycles/m); $S_d(f_0)$ is roughness coefficient (m^3/cycles); α is an exponent of PSD. In this paper, since this roughness classification is based on constant vehicle speed PSD, $\alpha = 2$. The RSR function $r(\hat{x})$ in its discrete form [153, 156, 157] is:

$$r(\hat{x}) = \sum_{k=1}^{N} \sqrt{4S_d(f_0)\left(\frac{2\pi k}{L_c f_0}\right)^{-2} \frac{2\pi}{L_c}} \cos\left(\frac{2\pi k f_0}{L_c} + \theta_k\right) \tag{4.26}$$

where $\hat{x}$ is the discrete representation of the spatial coordinate. Here L_c is twice the length of the bridge; N is number of data points of successive ordinates of the surface profile; and θ_k is a set of independent random phase angles uniformly distributed between 0 and 2π.

The road classification according to ISO 8606:1995(E) is based on the value of $S_d(f_0)$. Five classes of road surface roughness representing different qualities of the road surface have been observed, defined as A-E from the best to the worst, as shown in Table 4.1. Graphical representation of typical irregular road surface roughness profiles is shown in Figure 4.2.

Table 4.1. The road surface classes (ISO 8606:1995(E)) and corresponding value of roughness coefficient $S_d(f_0)$.

Road class	**A** **Very good**	**B** **Good**	**C** **Average**	**D** **Poor**	**E** **Very poor**
Roughness coefficient $S_d(f_0)$ (m^3/cycle) × 10^{-6}	6	16	64	256	1024

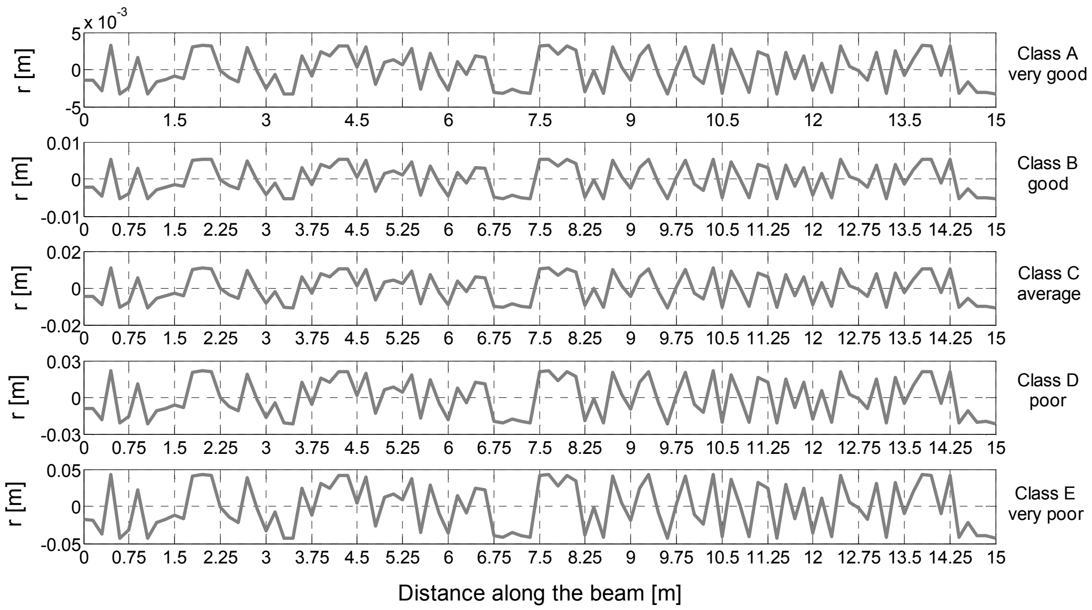

Figure 4.2 Typical road surface profiles.

4.2.5 Damaged Beam – Moving Oscillator Interaction Including Surface Roughness

The bridge vehicle interaction can be defined by a system of second order differential equations coupling the equations of motion of the beam (4.1) and of the vehicle (4.24). For the first mode shape consideration (subscripted 1), equations (4.1) and (4.24) can be written in matrix form as:

$$\begin{bmatrix}1 & 0\\0 & 1\end{bmatrix}\times\begin{Bmatrix}\ddot{q}_1\\\ddot{z}\end{Bmatrix}+\begin{bmatrix}2\xi_1\omega_1 & 0\\0 & 0\end{bmatrix}\times\begin{Bmatrix}\dot{q}_1\\\dot{z}\end{Bmatrix}+\begin{bmatrix}\omega_1^2+\dfrac{K}{\rho A}\phi_1(vt)\phi_1(vt) & \dfrac{K}{\rho A}\phi_1(vt)\\-\omega_V^2\phi_1(vt) & \omega_V^2\end{bmatrix}\times\begin{Bmatrix}q_1\\z\end{Bmatrix}$$
$$=\begin{Bmatrix}\dfrac{m_V g}{\rho A}\phi_1(vt)-\dfrac{K}{\rho A}r(vt)\phi_1(vt)\\\omega_V^2 r(vt)\end{Bmatrix} \tag{4.27}$$

where the natural frequency of the vehicle is $\omega_V^2=\frac{K}{m_V}$; and ξ_j and ξ_V are the damping ratios of the bridge and vehicle, respectively.

The displacements and velocities of the beam and the vehicle are obtained by solving the system of second order differential equations (4.27) using a 4/5th order Runge-Kutta method available in Matlab [158].

4.3 Damage Detection Using Surface Roughness Method

The dynamic response of the beam due to beam-moving oscillator interaction is utilized to detect and calibrate the location and the extent of damage. The data used for the bridge model are, L = 15m; ξ_1 = 2%; $E = 200\times10^9$ N/m^2 and ρ = 7900 kg/m^3. The static deflection of the beam is limited to 0.005 m. The depth (h) of the beam is kept at 1.5 times the width (b) of the beam. Other geometric descriptors like I, A, and m are computed based on this assumption. For the simulations, the selected values are h = 0.4395m; b = 0.293m; I = 0.0021m^4; A = 0.1287m^2. The data used for vehicle are m_v = 3000 kg and K = 3.65e6N/m [157, 159]. Responses of the beam and the vehicle corresponding to changes in x_c at mid-span, quarter-span, and close to the support are considered; Crack Depth Ratio (CDR) ranges from small (0.1) to large (0.45) with 0.05 increment; V_V ranges from slow to fast within 10 to 150 km/h with 10 km/h increment; and RSR changes from very good to very poor.

The proposed detection scheme is illustrated in Figure 4.3 through an example, while the general schematic of the methodology is presented in Figure 4.4. The beam is first divided into a number of equal segments. Many different numbers of segments have been tested, with 20 (0.75m) or 100 (0.15m) segments tested most often. Figure 4.3a shows 20 segments. The first mode shapes of the beam with closed and open crack conditions are computed next. In this example (Figure 4.3b) the crack is located at mid-span (x_c = 0.5L). The first mode shape undergoes only a local change around the crack area resulting in a slope discontinuity. The extent of this change of slope, though difficult to detect, is indicative of the extent of damage, since small cracks have little effect on natural frequencies and mode shapes of beams. Only crack ratios larger than 0.5 result in moderate frequency and large mode shape changes [88]. This ratio range is not useful as structure failure will probably occur before such damage extents are reached. The difference between the damaged and the undamaged mode shapes is found (Figure 4.3c) along with their ordinate values at the middle of each segment. The mode shape difference function ($\Delta\Phi$) has a local maximum and discontinuous slope at the indicated single damage location, although the same will appear in the case of multiple cracks [120]. In the case where cracks are very close to each other, there could be an overlap as these cracks influence each other structurally. In practice, the mode shape difference in the spatial domain may be hard to detect. The first three steps are thus not necessary when an experimental regime is considered. However, an initial benchmarked estimate of the undamaged mode shape and natural frequency should be carried out even under such circumstances. The bridge response (displacement is chosen in this case) obtained by solving equation (4.24) is multiplied with the mode shape difference function ordinate at the middle of each segment ($\Delta\Phi_m$) (Figure 4.3d). The multiplication, $\Delta\Phi_m q(t)$, is not implicit but explicit as in reality the bridge responses are not too difficult to measure using small sensors placed in multiple locations along the structure. The location and the extent of damage is then computed by choosing an appropriate descriptor on the values of $\Delta\Phi_m q(t)$ at multiple locations. The responses at different locations are scaled proportional to the first damaged mode shape with the respect to the maximum value of the mode shape. The involvement of surface roughness ensures that the high frequency components take part in forming the descriptor features apart from the slow moving, vehicular weight driven response. This participation cannot be described without the consideration of surface roughness or by representing the vehicle as a moving point load. Random white noise is cancelled out by considering the passage of many vehicles and the consideration of normalisation. When coloured noise is present in bridge response, the damage might not be identified due to high masking effect. The undamaged mode shape response can be found by considering the estimated values, as mentioned in the previous section. It is observed that the location near the damage is affected in this differential time domain response (Figure 4.3d). The location of the damage(s) could be indicated by using wavelet analysis as shown in Chapter 3 and in numerous papers [10, 55, 84, 142].

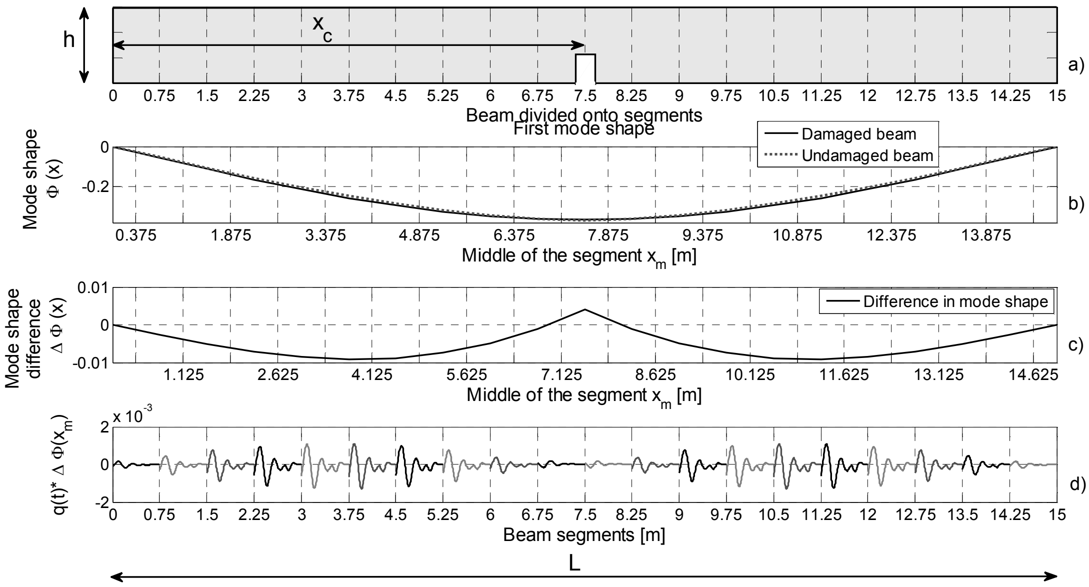

Figure 4.3 Concept employed: a) Simply supported beam, with damage located at the mid-span, divided into equal segments; b) First mode shape of damaged and undamaged beam; c) Difference in mode shapes of undamaged and damaged beam; and d) Difference in mode shape of damaged and undamaged beam at mid location of each segment multiplied with beam response (displacement).

Figure 4.4 indicates the steps to reach the multi-point observation signal $\Delta\Phi_m q(t)$, for which an appropriate descriptor of damage is to be chosen. As discussed, the level of participation for each of these elements in the schematic depends on the available information, degree of experimentation and modeling complexity. When considering such an approach the presence of multiple damages will be accumulated if they are too close, correctly indicating that in effect such close damages behave like a single damage of a modified extent. Although time-frequency techniques like wavelet analysis will be obviously helpful for such detection, there remains the interest in developing simple and consistent descriptors from the output so that computation time is minimized when deployed in real time.

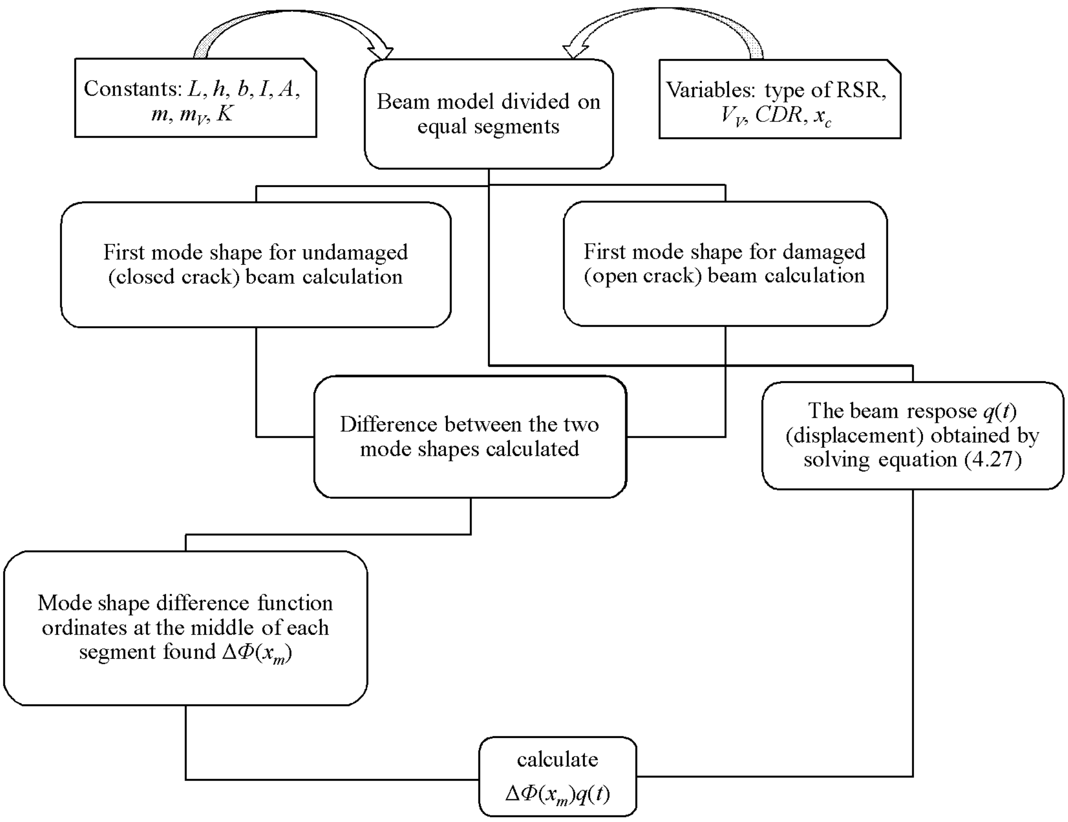

Figure 4. 4 Schematic Diagram of Methodology.

4.4 Choice of Damage Detection and Calibration Markers

Statistical descriptors on $\Delta\Phi_m q(t)$ for each segment of the observed beam and for each combination of variables; x_c, CDR, V_V and RSR were investigated for monotonocity and consistency. The statistical measures considered included mean (μ), standard deviation (σ), skewness (λ), and kurtosis (κ). The choice of mean and standard deviation stemmed out of a recent study [154], presented in Chapter 3. In a separate study [135], the skewness and kurtosis were observed to be markers for beam with an open crack vibrating under white noise and consequently these two parameters were also chosen owing to the similarity of the present problem. The parameters are computed as follows:

$$\mu = \frac{1}{m}\sum_{i=1}^{m} x_i \tag{4.28}$$

$$\sigma = \sqrt{\frac{1}{m}\sum_{i=1}^{m}(x_i - \mu)^2} \tag{4.29}$$

$$\lambda = \frac{\frac{1}{m}\sum_{i=1}^{m}(x_i - \mu)^3}{\left(\sqrt{\frac{1}{m}\sum_{i=1}^{m}(x_i - \mu)^2}\right)^3} \tag{4.30}$$

$$\kappa = \frac{\frac{1}{m}\sum_{i=1}^{m}(x_i - \mu)^4}{\left(\frac{1}{m}\sum_{i=1}^{m}(x_i - \mu)^2\right)^2} \tag{4.31}$$

Additionally, the applicability of a sample Range / Standard deviation of Data (R/S) analysis based Hurst exponent (H) [160] was also investigated in these studies since this statistical measure has been applied before for predicting events or sudden changes [161]. The results of this analysis are shown in Figure 4.5e.

Figure 4.5 shows an example of mean (4.5a), standard deviation (4.5b), kurtosis (4.5c), skewness (4.5d), and Hurst exponent (4.5e) measures of $\Delta\Phi_m q(t)$ calculated for each beam segment, where crack location is at $0.1L$ (1.5m); $0.25L$ (3.75m) and at $0.5L$ (7.5m) from the left support, respectively, the vehicle speed is 80 km/h, CDR is 0.45 and RSR is class C. It is found that the obtained mean (Figure 4.5a) and standard deviation (Figure 4.5b) functions are similar in shape and clearly show the discontinuous slope at the damage location, as per the mode shape difference functions. This finding is consistent with [154] where it has been proven that first and second order cumulants of bilinear and linear system responses are consistent and monotonic descriptors of the system characteristics and are sensitive to system stiffness changes. Due to the similarity of the shapes in mean and standard deviation, a Coefficient of Variation (CoV) based marker will not be efficient; this assumption marker was investigated and CoV marker confirmed not to be consistent. Following the method proposed by Cacciola et.al [135] for beam vibrating under white noise, kurtosis (Figure 4.5c) and skewness (Figure 4.5d) measures were tested but they appear to be insensitive to crack presence. Only for the crack located at mid-span, in the proximity of the crack, does the skewness function suddenly change sign, but this change does not have a consistent trend in case of change of any observed variables. Hurst exponent (Figure 4.5e) is also found to be insensitive to presence of the crack. Therefore μ and σ are chosen as markers for further calibration analysis (Figure 4.6).

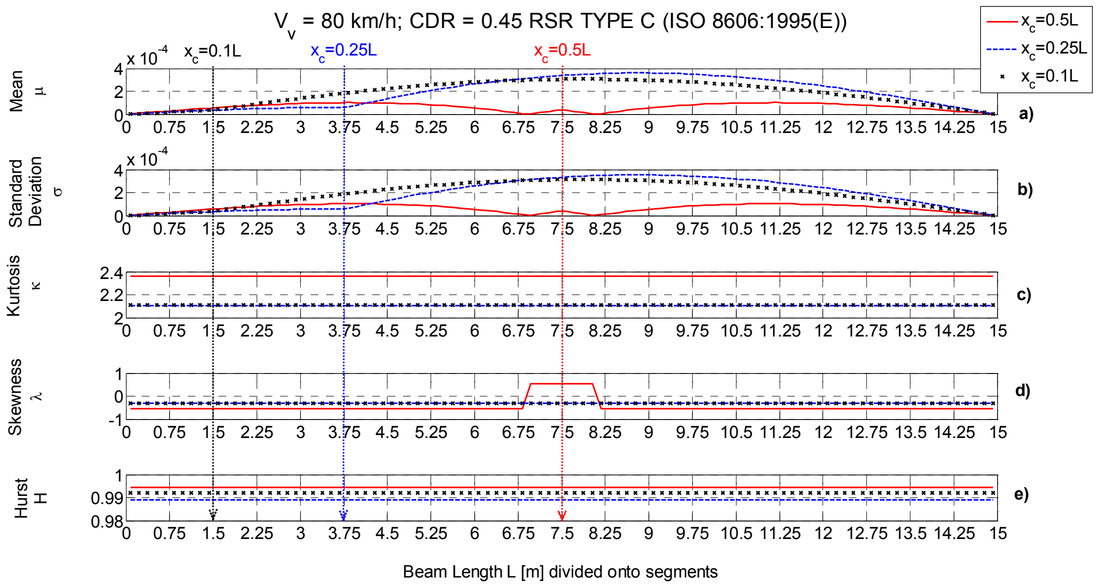

Figure 4.5 Statistic measures observed: a) Mean (μ); b) Standard Deviation (σ); c) Kurtosis (κ); d) Skewness (λ); and e) Hurst (H). Figure shows statistics for crack located at ($x_c = 0.5L$; $0.25L$ and $0.1L$); Speed of the vehicle ($V_V = 80$km/h); Crack Depth Ratio (CDR = 0.45); and Type C Road Surface Roughness (RSR) defined as per ISO 8606:1995(E).

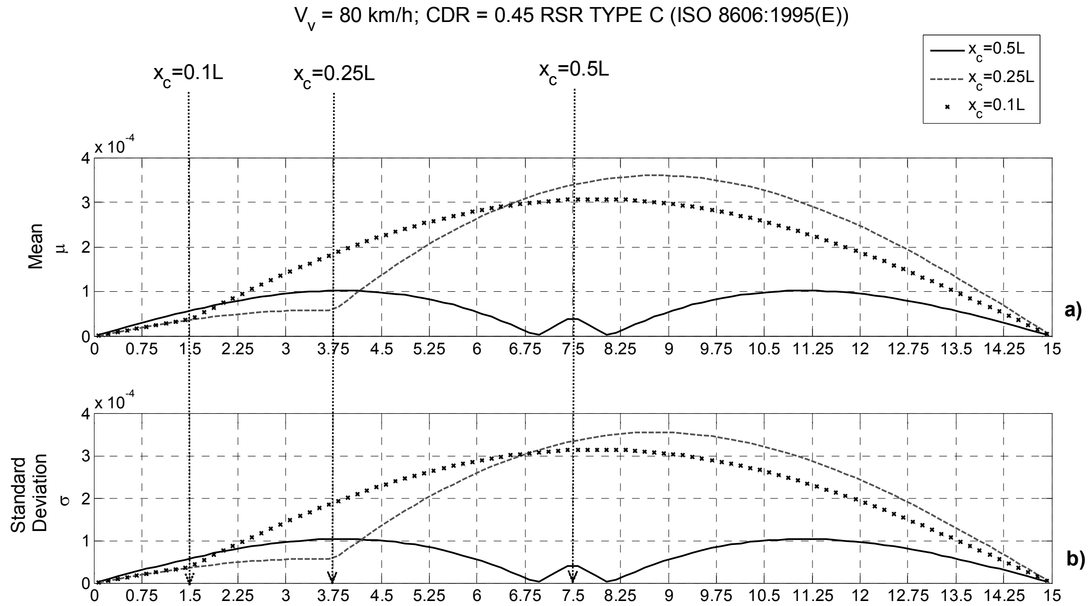

Figure 4.6 Statistics measures adopted: a) Mean (μ) and b) Standard Deviation (σ). Figure shows statistics for crack located at 0.1L (1.5m), 0.25L (3.75m) from the left support and at mid-span 0.5L (7.5m), Speed of the vehicle (V_V = 80km/h), Crack Depth Ratio (CDR = 0.45), and Type C Road Surface Roughness defined as per ISO 8606:1995(E).

4.5 Discussion and Results

4.5.1 Effects of Crack Depth Ratio

Figure 4.7 shows an example of mean and standard deviation functions for the case where the crack is located at quarter-span, RSR is type C, the vehicle is moving with a speed 80km/h, and crack depth ratio increases from 0.1 to 0.45.

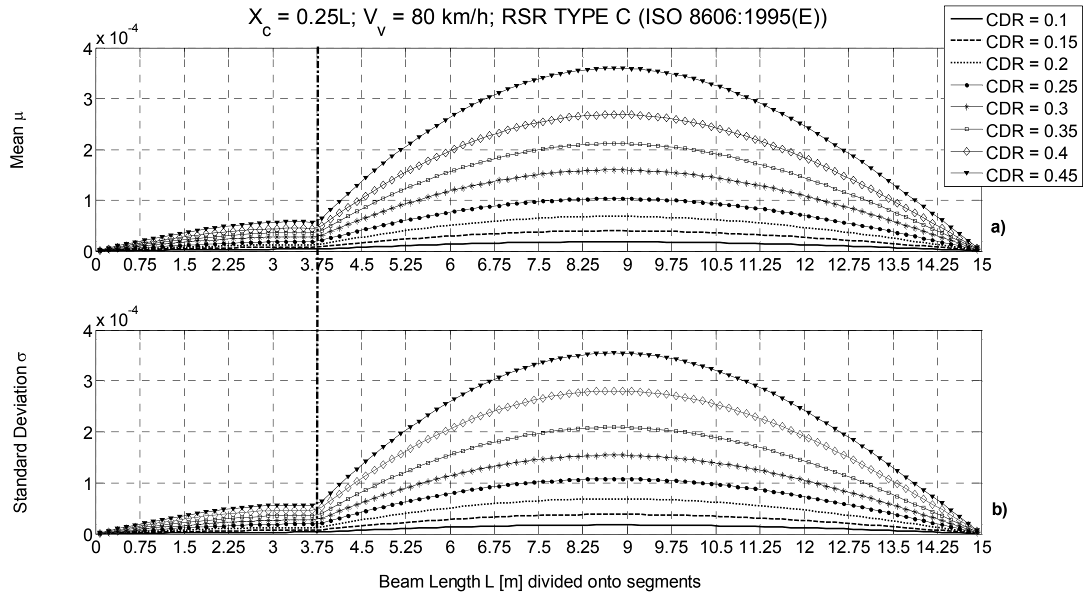

Figure 4.7 Effects of different Crack Depth Ratio (CDR) on: a) Mean (μ) and b) Standard Deviation (σ); for crack located at quarter-span ($x_c = 0.25L$); Speed of the vehicle ($V_V =$ 80km/h); and Type C Road Surface Roughness (RSR) defined as per ISO8606:1995(E).

From this and the similar figures obtained by varying x_c, RSR type and V_V, a number of observations are noted. The markers μ and σ show slope discontinuity at damage location. With increase of CDR the values of statistical parameters (relative to each other) increase and the slope discontinuity of μ and σ at the crack location becomes more obvious. This indicates that the location of crack can be identified by the chosen markers and that consistent calibration is possible. Values of μ and σ at crack locations for all combinations of x_c, RSR type, CDR, and V_V were investigated. More than 1800 cases were observed in order to establish the calibrations of μ and σ at crack locations and variable dependence of the calibrations on variables. The results are shown in Appendix A. Only the most important findings are presented here.

For illustration purposes, Figures 4.8, 4.9, and 4.10 show standard deviation in relation to crack depth ratio and vehicle speed for RSR type C for cases when crack is located at the edge, quarter-span, and mid-span of the beam, respectively.

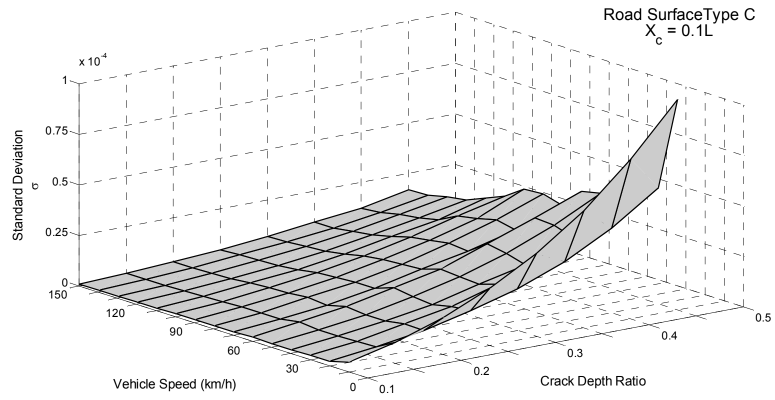

Figure 4.8 Standard deviation at crack location dependence on Crack Depth Ratio and Vehicle speed for Road Surface Roughness Type C for crack located near support.

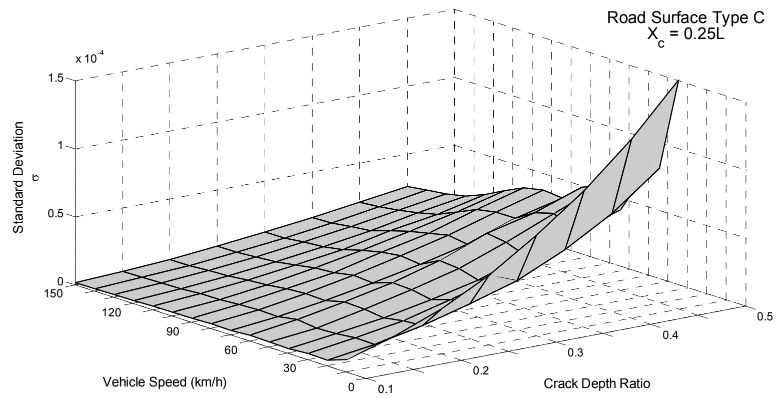

Figure 4.9 Standard deviation at crack location dependence on Crack Depth Ratio and Vehicle speed for Road Surface Roughness Type C for crack located at quarter-span.

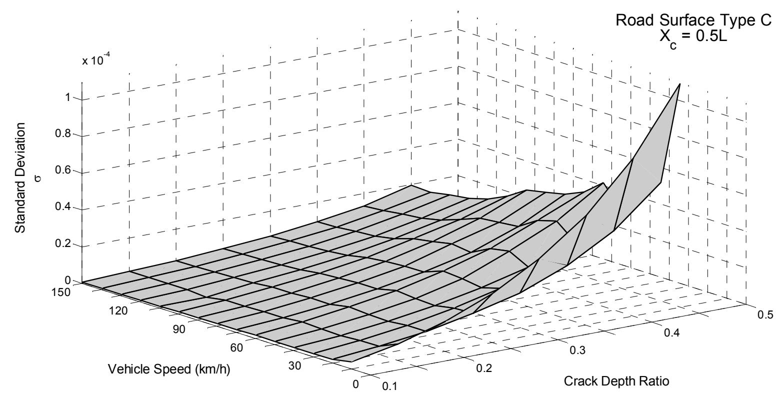

Figure 4.10 Standard deviation at crack location dependence on Crack Depth Ratio and Vehicle speed for Road Surface Roughness Type C for crack located at mid-span.

4.5.1.1 Crack Depth Ratio and Crack Location

Figures 4.11 a) and b) show the relation of μ and σ, respectively with changes in CDR for different positions of the crack along the beam.

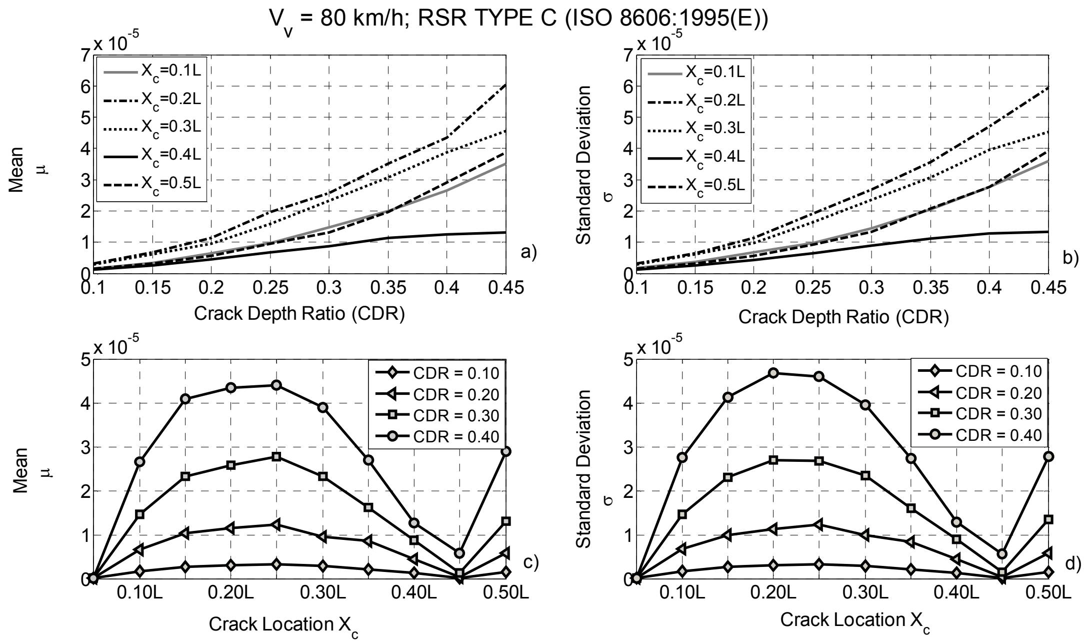

Figure 4.11 a) Mean (μ) and; b) Standard Deviation (STD) variation (at crack location) in function of Crack Depth Ratio (CDR) for different position of crack location (x_c) and; c) Mean; and d) STD in function of x_c for different CDR; while speed of vehicle is constant and type of road is class C as per ISO 8606:1995(E).

In general, calibrations are monotonic (μ and σ increase with CDR) but there is no obvious relation between the curves corresponding to different crack locations. This leads to a conclusion that it is not necessarily true that the edge crack has the smallest values of statistical parameters. Therefore, plotting μ and σ at crack location as a function of crack distance from the left support of the beam for different CDR is more appropriate; this is shown in Figures 4.11 c) and d). It is observed that the values of statistical parameters increase as the position of the crack moves from the support towards the quarter-span (x_c = 0.25L), where it reaches the maximum, and then decrease from quarter-span to 0.4L, to the minimum, before increasing again at mid-span. The reason for this asymmetry in Figure 4.11 c) and d) is that the mode shape difference function has zero values close to the midspan of the observed beam (see Figure 4.3). It is also shown here that more intense cracks are always more responsive in terms of their markers. Since the location of the crack will be identified beforehand, as presented in Figure 4.10, the calibration of the damage extent can always be projected to specific curves.

4.5.1.2 Crack Depth Ratio and Vehicle Speed

Figure 4.12 shows an example of μ and σ functions for the cases of different vehicle speed, ranging from 10km/h to 150km/h with 20km/h step, for the average RSR (type C).

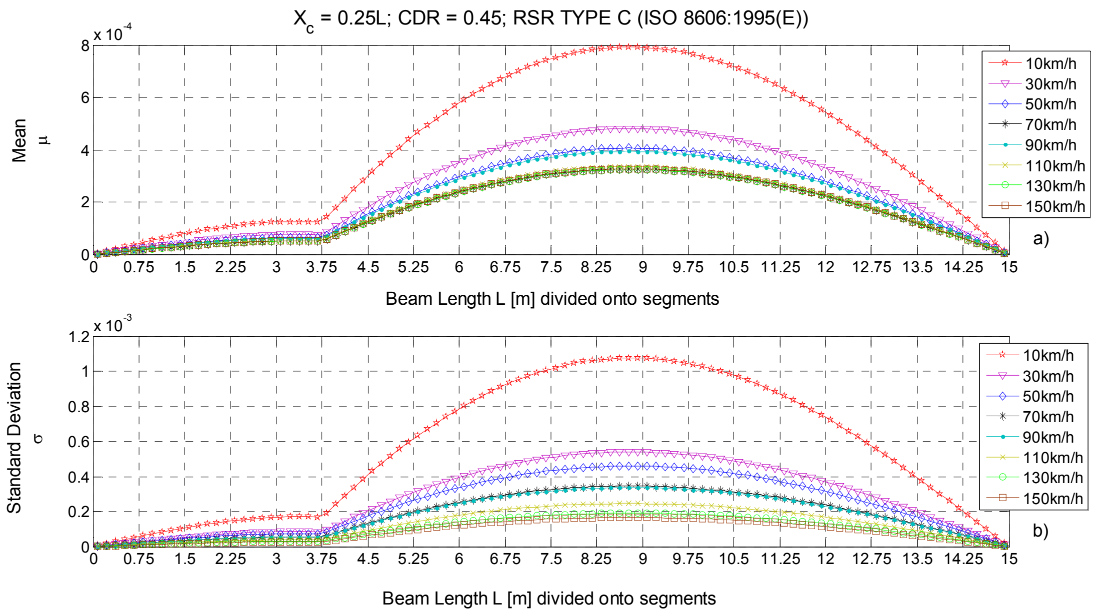

Figure 4.12 a) Mean (μ) and b) Standard Deviation (σ) for crack located at $x_c = 0.25L$ (3.75m), Crack Depth Ratio CDR = 0.45, Type C Road Surface Roughness defined as per ISO 8606:1995(E), and different Vehicle Speed.

In this example the crack is located at quarter-span and CDR is large (0.45). It is observed that in general μ and σ values are higher for low vehicle speeds, in particular 10 km/h, and decrease with vehicle speed. This is more evident in σ plot

(Figure 4.12 b), while in the case of μ there is almost no difference for the vehicle speeds from 50 – 90km/h or 110 – 150 km/h. For this particular example it is shown that μ compared to σ is less sensitive to increasing vehicle speed. The same conclusion is arrived too by observing different combinations of x_c, CDR, and RSR. Therefore the sensitivity of σ marker has been investigated further and compared to the change of these variables.

The relationship between the statistical parameters and CDR in relation to RSR types for three different V_V (50km/h, 100km/h, and 150km/h, representing low, medium, and high vehicle speed, respectively) is shown in Figure 4.13.

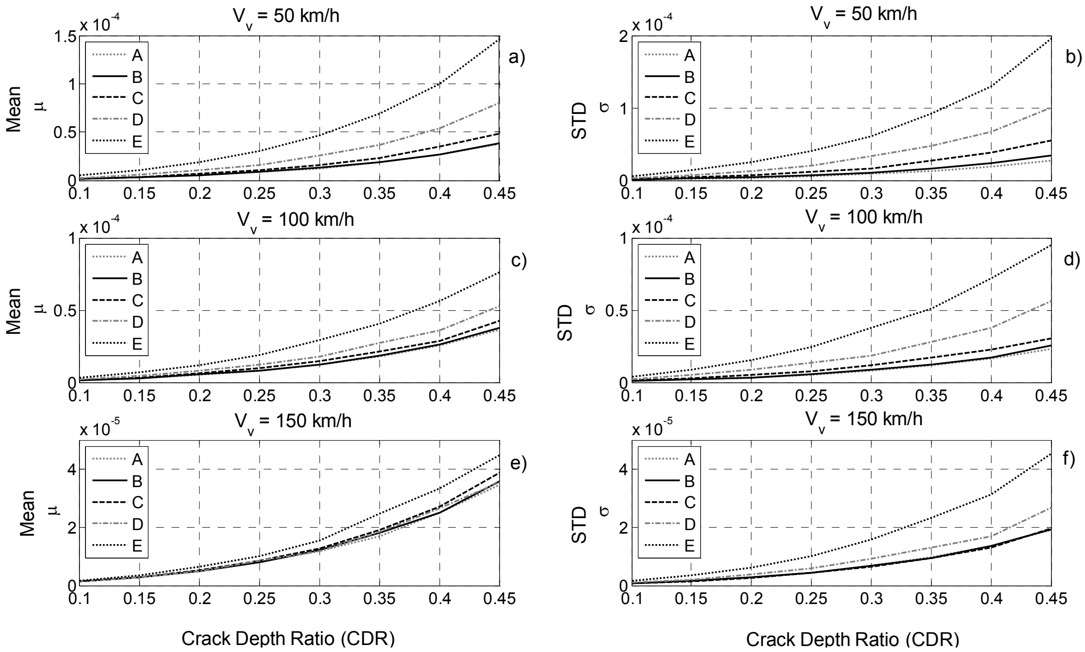

Figure 4.13 Mean (μ) and Standard Deviation (σ) variation for crack located at $x_c = 0.25L$ in function of Crack Depth Ratio (CDR) for different Road Type defined as per ISO 8606:1995(E) analysed for three different Vehicle speed (V_V): Low, Medium and High.

It is observed that the statistical descriptors are larger for lower V_V. This becomes more obvious as CDR increases. For RSR types D and E, the variations of μ and σ are more obvious even for lower vehicle speeds, while for types A, B, and C they are almost the same for the higher speeds of the vehicle. Therefore the consistency of calibration is dependent on the speed and road type. This is more pronounced when the damage extent is higher. The roads with RSR ratings A and B give consistent but less sensitive results, while the roads with RSR rating D and E are less consistent in value but give more sensitive results. Therefore, for calibration purposes it is recommended to use RSR type C as an optimum.

For illustration purposes in Figure 4.14 σ marker of CDR is presented for three different types of road (A, C and E), for crack location at mid span. In general, the relation between μ and σ and CDR for different V_V increases exponentially.

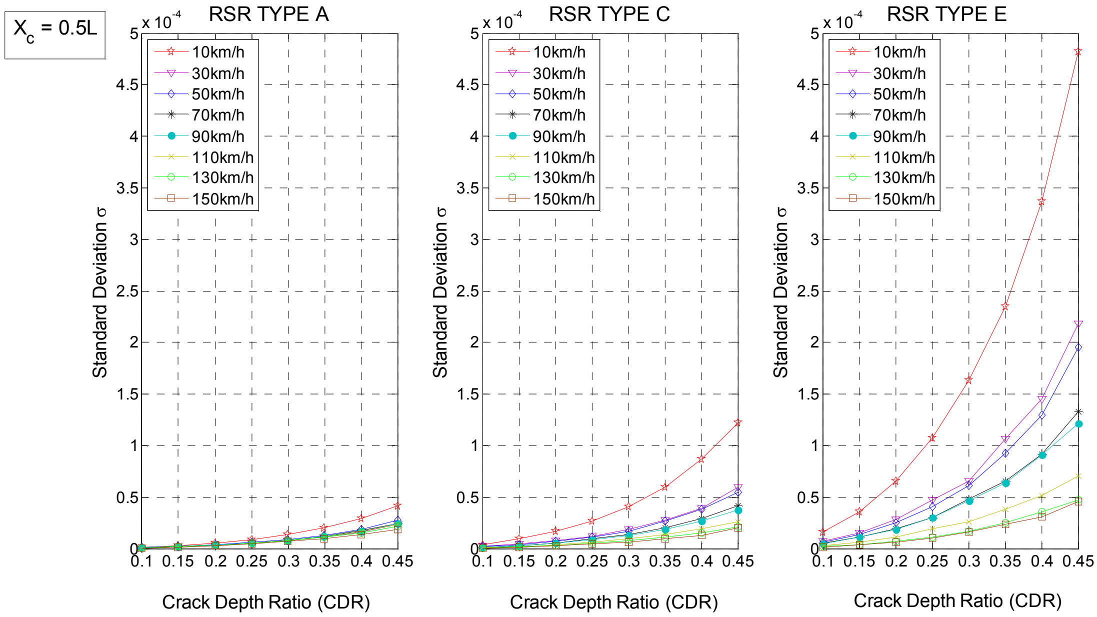

Figure 4.14 Standard Deviation (σ) variation in function of Crack Depth Ratio (CDR) for crack located at mid-span (7.5m), Type A (very good), C (average) and E (very poor) Road Surface Roughness defined as per ISO 8606:1995(E), and different Vehicle Speed.

It is observed that these curves can be separated into four groups depending on V_V: very low speed (10km/h); low speed (20 – 60km/h); medium speed (70 – 100km/h) and high speed (110 – 150km/h), for which variation of μ and σ is very high, high, medium, and low, respectively. This grouping becomes more obvious for higher CDR when RSR is type D and E, while for the RSR type A and B there is very little difference between statistical parameters even for a higher values of CDR for medium and high speeds of the vehicle. The exception is very low V_V for which statistical parameters are observed to be much higher than for other V_V values for all cases of RSR.

In order to determine which road surface is appropriate for calibration, standard deviation of the function of vehicle speed for crack located at mid-span with low, medium and high CDR is plotted in Figure 4.15. The full lines in the figure indicate averaged value of standard deviation for all road types, while grey line bellow and dotted line above represent road types C and D respectively. The asterisks indicate extremes where low values represent road type A and higher values type E. It is concluded that averaged values are very close to values obtained for road types class C and D (the curve is in between these two). Realistically, the average value is too high as standard deviation results for road type class E are way above results obtained for classes A, B, and even C. Hence road type class C is found to be optimal for calibration purposes. In general, calibrations are monotonic (μ and σ increase with CDR) but there is no obvious relation between the curves representing different crack locations.

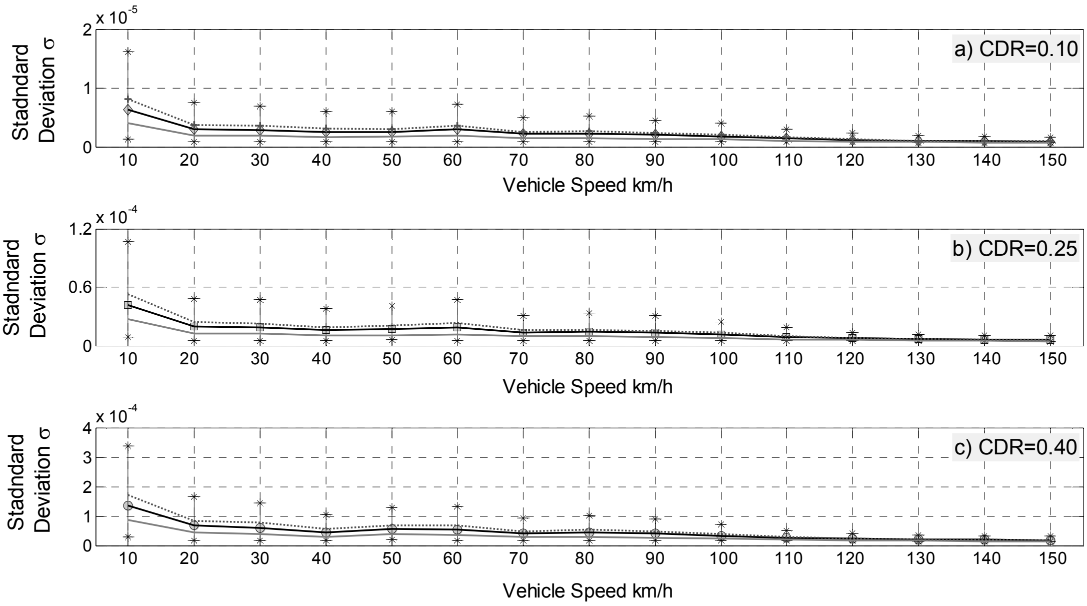

Figure 4.15 Variation of Standard Deviation (σ) in function of Vehicle Speed for crack located at mid-span (7.5m), Crack Depth Ratio a) low (0.1), b) medium (0.25), and c) high (0.4), Road Surface Roughness defined as per ISO 8606:1995(E).

4.5.2 Calibration

Figure 4.16 shows the results of calibration of σ as a function of vehicle speed variation (low, medium, and high) observed for the position of damage close to the support, at quarter-span, and mid-span of the beam. The calibration functions are shown for small (0.1), medium (0.25), and high (0.4) CDR. The dotted grey lines represent a 6th degree polynomial fit which incorporates very low vehicle speeds:

$$\sigma = p_1 V_V^6 + p_2 \times V_V^5 + p_3 \times V_V^4 + p_4 \times V_V^3 + p_5 \times V_V^2 + p_6 \times V_V + p_7 \qquad (4.32)$$

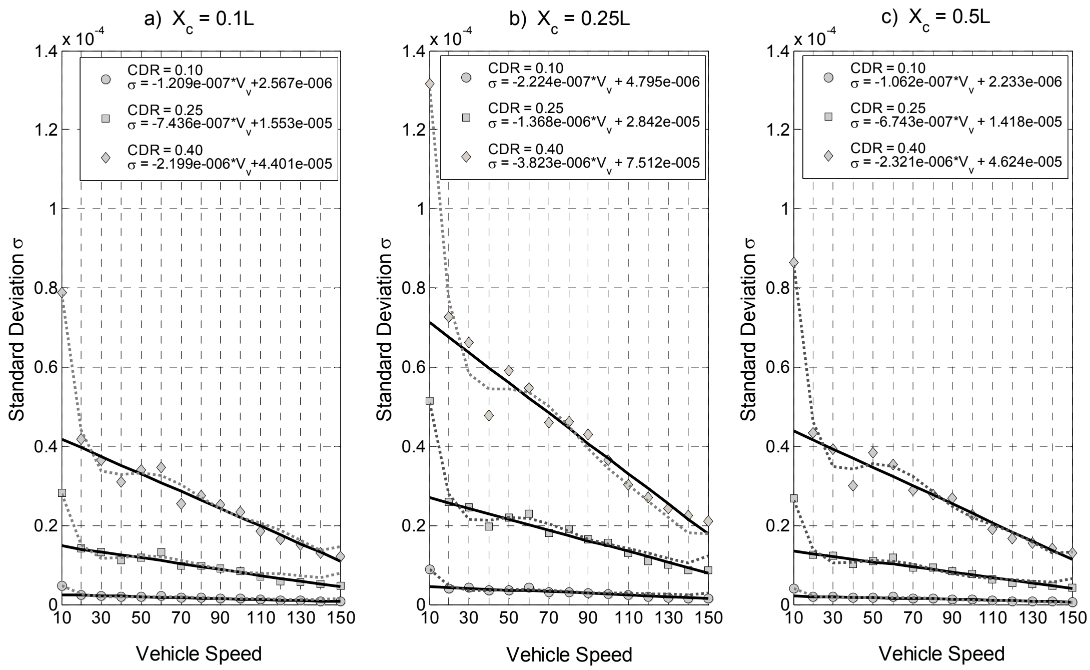

Figure 4.16 Calibration of Standard Deviation (STD) variation in function Vehicle speed (Vv): Low, Medium and High; for three different positions of the damage: a) Edge; b) Quarter-span and c) Mid-span.

For the coefficients with 95% confidence bounds the goodness of fit measure of R^2 is 0.9735 and 0.9865, for the worst and the best fit function, respectively.

A speed of 10km/h shows much higher values of statistical descriptor when compared with other speeds. When the 10km/h value is excluded from the analysis, linear polynomial equations are obtained (represented with the solid line). Corresponding straight line equations coefficients with 95% confidence bounds are shown in Table 4.2. A straight line fit is found to be satisfactory as the goodness the fit (R^2) is close to one in all cases:

$$\sigma = a \times V_V + bc \tag{4.33}$$

Therefore, by knowing the vehicle speed it is possible to determine the CDR using the proposed calibration procedure, but it is hard to determine the location of the crack for low CDR.

Table 4.2 Calibration function for Standard deviation and vehicle speed.

General form of fit is linear polynomial equation $\sigma = a \times V_V + b$

CDR \ **xc**	**0.1L**	**0.25L**	**0.5L**
0.10	a = -1.209e-007 b = 2.567e-006 SSE: 2.209e-013 R^2 = 0.9378	a = -2.224e-007 b = 4.795e-006 SSE: 9.34e-013 R^2 = 0.9234	a = -1.062e-007 b = 2.233e-006 SSE: 1.747e-013 R^2 = 0.9362
0.25	a = -7.436e-007 b = 1.553e-005 SSE: 7.513e-012 R^2 = 0.9436	a = -1.368e-006 b = 2.842e-005 SSE: 2.514e-011 R^2 = 0.9443	a = -6.743e-007 b = 1.418e-005 SSE: 5.505e-012 R^2 = 0.9495
0.40	a = -2.199e-006 b= 4.401e-005 SSE: 5.689e-011 R^2 = 0.9508	a = -3.823e-006 b = 7.512e-005 SSE: 2.346e-010 R^2 = 0.9341	a = -2.321e-006 b = 4.624e-005 SSE: 8.783e-011 R^2 = 0.9331

Figure 4.17 shows a generic fit of damage calibration curve using the detection measures, i.e. the calibration of σ in the function of CDR for three different vehicle speeds (40km/h; 80km/h, and 130km/h representing low, medium and high vehicle speed, respectively), analysed separately for three different positions of the crack.

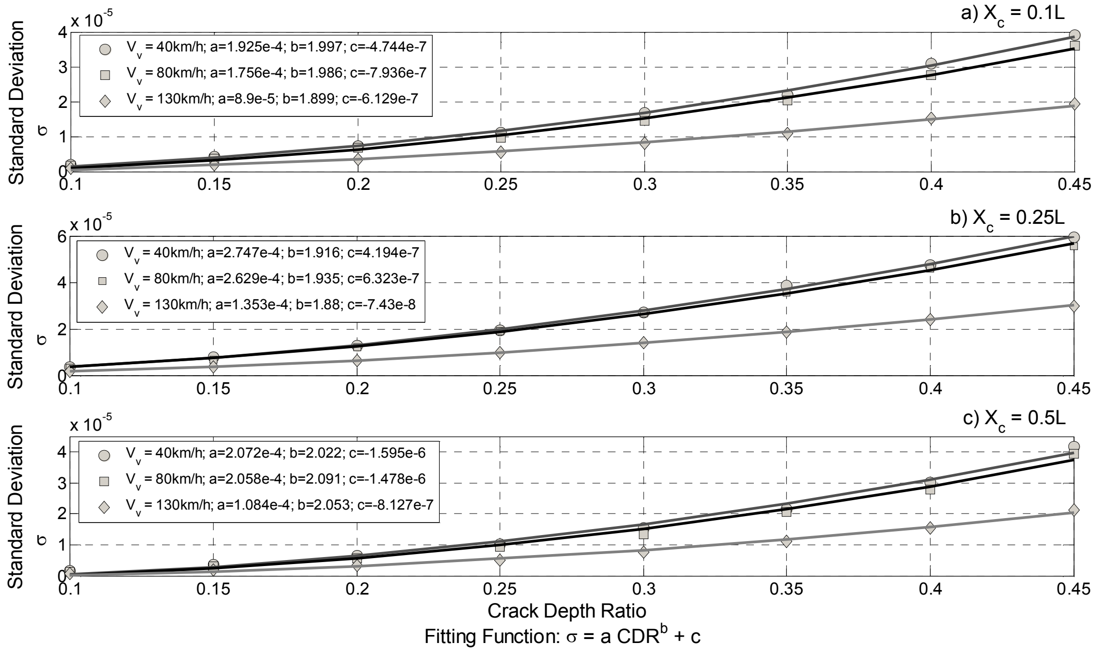

Figure 4.17 Calibration of Standard Deviation (STD) variation in function Crack Depth Ratio (CDR); for Low, Medium and High Vehicle Speed (V_V) and three different positions of the damage: a) Edge; b) Quarter-span and c) Mid-span

The best fit is represented by power law equation:

$$\sigma = a \times CDR^b + c \tag{4.34}$$

Relevant coefficients and indicators of goodness of the fit are given in Table 4.3.

Table 4.3 Calibration function for Standard deviation and CDR.

General form of fit is power equation $\sigma = a \times CDR^b + c$

VV \ xc	0.1L	0.25L	0.5L
low 40km/h	a = 0.0001925 b = 1.997 c = -4.744e-007 SSE: 2.266e-012 R2 = 0.9981	a = 0.0002747 b = 1.916 c = 4.194e-007 SSE: 2.816e-012 R2 = 0.999	a = 0.0002072 b = 2.022 c = -1.595e-006 SSE: 1.211e-011 R2 = 0.9912
medium 80km/h	a = 0.0001756 b = 1.986 c = -7.936e-007 SSE: 2.648e-012 R2 = 0.9974	a = 0.0002629 b = 1.935 c = 6.323e-007 SSE: 2.954e-012 R2 = 0.9988	a = 0.0002058 b = 2.091 c = -1.478e-006 SSE: 1.109e-011 R2 = 0.991
high 130km/h	a = 8.9e-005 b = 1.899 c = -6.129e-007 SSE: 8.243e-013 R2 = 0.9973	a = 0.0001353 b = 1.88 c = -7.43e-008 SSE: 8.575e-014 R2 = 0.9999	a = 0.0001084 b = 2.053 c = -8.127e-007 SSE: 2.524e-012 R2 = 0.993

4.6 Conclusions

Through consideration of bridge-vehicle interaction effects, the bridge deck surface roughness is directly used for damage detection in bridges employing the new methodology, which looks at surface roughness as an aid towards damage detection by focusing only at the high frequency components.

In practice, the response, displacements, and / or velocities (or the first mode shape and its time derivative) can be measured at multiple locations along the bridge relatively close to one another (approx. distance between the locations should not be greater than 0.5m). The undamaged responses may be estimated through computation, e.g. finite element modelling. The responses of the damaged condition measured at different locations are expected to be scaled approximately with respect to the maximum value. This maximum value does not change too much from the undamaged maximum since local damage affects global responses very little. Estimated damaged mode shape values at different locations can be obtained by dividing the time domain responses at each location by the time domain response at the mode shape maximum value. It is also possible to estimate the time domain response at the maximum mode shape value by dividing the response by the normalising value of integral of the squared mode shape. As long as the masking effects from noise and errors are lower than the local disturbance due to damage, the difference in this scaled time domain response will manifest local distortions in the space domain. It is important to note here that the mode shape itself is continuous, the first derivative is discontinuous, while the second and the third derivatives are continuous again to ensure moment and shear transfer. From the discontinuity of the difference of estimated undamaged and damaged state the location of the damage can be found (stage 1 and 2 of damage diagnostics – existence and location of the damage).

Statistical descriptors are computed on a modified time domain response measure for consistent detection of the location and calibration of damage extent. It is shown that mean and standard deviation are consistent and monotonic descriptors of the system characteristics sensitive to crack presence. The first and second order cumulants of response can be efficiently used as damage detection markers, where discontinuity in the slope of the mean and standard deviation curves give the position of damage, with the jump size related to the extent of damage. Once statistical parameters of the system responses have been calculated, damage location found, and traversing vehicle speed measured, the CDR can be obtained using calibration curves shown in Figure 4.17 (stage 3 of damage diagnostics – severity of damage). The proposed methodology eliminates the need for complex analysis and can easily accommodate experimental observations and real time implementation.

When the road quality decreases, the slope discontinuity of mean and standard deviation curves at the crack location become more obvious. This is amplified for poor and very poor grades of road surface roughness.

The consistency of calibration depends on the vehicle speed and road type. This is more pronounced in the case of higher damage. The damage detection and calibration can be divided into low, medium, and high speed zones. Damage calibration on better roads is less uncertain and gives consistent but less sensitive results. Worse roads are less consistent in calibration values but give more sensitive results. Therefore the medium road surface roughness type C is suggested as optimal for calibration purposes.

The study is particularly useful for continuous online bridge health monitoring since the data necessary for analysis can be obtained from the operating condition of the bridge and the structure does not therefore need be closed down.

Chapter 5

Damage Detection Using Delay Vector Variance Method on System Response

5.1 Introduction

The maintenance and monitoring of the structures are critical problems. The changes in stiffness, mass, natural frequency, etc. are often indicators of structural damage. Vibration monitoring is one of the ways to monitor the structure health. The linearity or nonlinearity of the structural system response signals, as indicators of nature of the structure and changes within, has not been examined in the past.

Delay Vector Variance (DVV) method is applied to address the questions:1) are the changes in system parameters reflected onto system response linearity degree, and 2) can a difference in signal nonlinearity be attributed to a difference in system nonlinearity and to what extent? The DVV method is used to analyse responses of one theoretical model – Single Degree of Freedom (SDOF) system, and two experiments – a SDOF oscillator and Wind turbine blade (WTB) – performed in laboratory environment. The dynamic responses of SDOF system and WTB were measured using a MicroStrain G-Link Wireless Accelerometer mounted on the models and a Polytec RSV-150 Remote Sensing Vibrometer. Four strain gauges were attached along the WTB height for monitoring strain at different locations. The forced vibration on the SDOF system and WTB was in the form of harmonic force, sine sweep, and white noise input. The SDOF system moved over three surfaces of different roughness and was subject to stiffness change. The results show that the changes in the damping, stiffness, natural and driving frequency, excitation force and to the extent surface roughness can be successfully detected using the DVV method. The potential of the DVV method is significant as it can be used, in conjunction with non-contact measurements, as a damage diagnostic tool. The method is suitable for health monitoring of structures under a model-free condition or where information related to the structure is not sufficient.

5.1.1 Background to DVV method

In signal analysis there is a need to verify the existence of an underlaying nonlinear process, so that appropriate modelling or filtering techniques can be selected. The response of the system in the form of time series is system output signal. There are many methods for characterizing time series. The most popular technique for detecting the nature or nonlinearity of time series is surrogate data method described by Schreiber, T. and A. Schmitz [162]. The method was originally motivated by statistical hypothesis testing, which presents an indirect way of detecting nonlinearity [163]. The failure to detect nonlinearity may result from an inappropriate choice of test statistic [164] and there are also problems with artefacts occurring in the process of generating surrogate data sets [165]. Many nonparametric analysis techniques have been developed for the detection of nonlinearity in the signal [166]. Gautama et al. [167] introduce the methodology for comparing and testing the degree of nonlinearity between population of signals, rather than limiting analysis to one time series per set. Gautama et al. [168] presented novel test statistic for detecting the determinism and nonlinearity in a time series Delay Vector Variance (DVV) method which, characterises a time series based upon its predictability and compares the results to those obtained for linearised versions of the signal, i.e. surrogate data. The aim of DVV method is to verify whether or not a time series observed is generated by a linear stochastic system [169]. Gautama et al. [169] have investigated nonlinear properties of the EEG signals using two established nonlinear analysis methods, namely third-order autocovariance (C3) [170] and the deviation due to time reversibility (REV) [171], and have introduced a DVV method for better characterizing a time series. They have found that proposed DVV characterization, although not requiring any prior knowledge about the signal, is very robust to the presence of noise, straightforward to interpret and visualise nonlinearity, and exhibits improved performance over other available methods. Comparing traditional test statistic methods such as the third–order autocovariance (C3) method, the δ-ε method [172] and Correlation exponent (COR) [173], Gautama et al. [167, 174], with extensive experimentation and rigorous analysis, have shown DVV to be the method that enables a comprehensive characterization of the time series, allowing for much improved classification of signal models. They have showen that results obtained using DVV are more consistent than those obtained using the other methods [167]; furthermore, DVV method consistently detects nonlinear behaviour for all noise levels [174]. The proposed method is related to the Keplan's δ-ε method [172] and to the false nearest neighbour approach [175, 176], both of which are local prediction techniques, and COR which characterizes reconstructed attractors over different distance scale in phase space [169]. Therefore DVV method is used to analyse theoretically and experimentally achieved mechanical system response for its linearity.

The DVV method has been successfully applied in the past in numerous problems. The method was used to analyse the nature of biomedical signals, such as hand tremor, Electro Encephalogram (EEG) [169], functional Magnetic Resonance Imaging (fMRI) [167, 174], Electrocardiogram (ECG), and Heart Rate Variability (HRV) [174, 177]. Gautama et al. [167] have emphasised that DVV analyses signal, rather than system nonlinearities. However, they have found that a difference in signal nonlinearity can be attributed to a difference in system nonlinearity. For example, when DVV has been applied in diagnostic medicine the aim was to assess the presence or absence of nonlinear behaviour within the signal observed, as the linear or nonlinear nature of the signal conveys information concerning the health condition of the subject [174, 178]. EEG signals are often examined using nonlinearity analysis techniques comparing signals that are recorded during different physiological brain states. Andrzejak et al. [179] state that different analysis results are consequence of either genuine difference in dynamical brain properties or difference in recording parameters. By examining the predictability and the correlation dimension of the time series, they have found the strongest indication of nonlinear deterministic dynamics for epileptic seizures, and no significant indication of nonlinearity for healthy subjects. Gautama et al. [169] have shown that DVV analysis enables a comprehensive characterisation of the dynamical modes of the EEG signals, allowing for an accurate classification of the brain states, i.e. clearly distinguishing between EEG segments recorded in the healthy subject, in epilepsy patients during a seizure-free interval, and during an epileptic seizure, indicating different dynamical properties of brain electrical activity. Jianjun et al. [180] have applied DVV method to analyse vowel ‘a’ signals, used in Traditional Chinese Medicine (TCM) as an important part of diagnostics. According to the TCM, sound, the outward sign of vital activities can reflect the functional activities of human essential internal organs. The results obtained by Jianjun et al. indicate that there exists distinct difference between two groups, healthy persons and patients with deficiency syndrome, of vowel ‘a’ signals, where obtained statistics is found to be helpful in recognizing the persons with deficiency syndrome. The DVV method based on surrogate data as efficient tool for acquiring the information on determinism and nonlinearity of response of mechanical system has been examined by Hongying and Fuliang [164]. They have analysed a diesel engine vibration in different conditions and found that the vibration signals of diesel engine have strong nonlinearity and that nonlinearity is getting stronger as fault becomes worse. Furthermore they have used the Root Mean Square (RMS) deviation of the DVV scatter diagram from bisector line as quantitative analysis of the fault state and concluded that the method could be used to detect faults in diesel engine as well as in other equipment. They have concluded that RMS deviation of the DVV scatter diagram from bisector line is quantitative measure of the degree of fault, i.e. the more severe the fault, the larger the RMS.

5.2 Definitions

5.2.1 System nonlinearity

A linear shift-invariant system, $f(\cdot)$, is defined as one that obeys the superposition and scaling property; namely for $a, b \in \mathcal{R} : f(ax + by) = af(x) + bf(y)$, together with producing identical outputs for a given input at different instants of time. A system which is shift-invariant, but does not possess superposition property is considered nonlinear. The principle of temporal summation for analysing the nonlinearity of a system implies that input and output time series can be measured simultaneously, while in typical real-world settings, this is not favourable or physically possible [167, 174].

5.2.2 Signal nonlinearity

A linear signal, x, is generally defined as the output of a linear shift-invariant system that is given by Gaussian white noise. Any signal that cannot be generated in such a way is generally referred as nonlinear signal [174]. The analysis of the nonlinearity of a signal can often provide information on nature of the underlaying signal production system [167]. However the assessment of nonlinearity within a signal does not necessarily imply that the underlaying signal generation system is nonlinear: the input signal and system (transfer function) nonlinearities are confounded [174]. Therefore care should be taken in the interpretation of the results, e.g. if the input to the system were nonlinear and the system itself linear, the measured signal at the output would be nonlinear [167]. Therefore, no straightforward conclusion can be drawn from the nonlinearity analysis of one signal regarding an underlying system, but this method allows for comparative analysis between different systems, driven by the same input [167].

It is important to know what assumptions of nonlinearity analysis are, especially regarding deterministic chaos, so as not to confuse cause and effect (chaos implies nonlinearity, but not vice versa) [162].

5.3 Surrogate data and DVV method

5.3.1 Surrogate data generation and statistical testing

The surrogate data method is used for assessing the nonlinearity present in the time series. The concept of ‘surrogate data’, used in the context of statistical nonlinearity testing, was introduced by Theiler et al. [163]. A surrogate time series is generated as a realization of the null hypothesis of linearity where the ‘test statistic’ is computed for original time series and is compared to those computed for all generated surrogates, i.e. linearized versions of these data [167, 174]. The null hypothesis is that the original time series is linear. Hence, a time series is nonlinear if the test statistic for the original data is not drawn from the same distribution as the test statistics for the surrogates. When the test statistic computed for original data set is significantly different from that computed for the surrogates, the null hypothesis is rejected, and original time series is hypothesized to be nonlinear [167].

A key issue in surrogate data testing is the definition of an appropriate null hypothesis. There are two main types of null hypothesis: simple and composite. A simple null hypothesis verifies that the data is generated by a specific and known (linear) process, e.g. data are drawn from a Gaussian distribution with zero mean and unit variance. Composite null hypothesis, which is adopted here [163, 167], asserts that the unknown underlying process is a member of a certain family of processes, e.g. data are drawn from a Gaussian distribution [174] (time series is generated by a Gaussian linear stochastic process). Hence, surrogates are constrained to produce autocorrelation functions identical to those of the original time series [167], e.g. by phase randomizing the frequency spectrum of original time series. Schreiber and

Schmitz [181] have proposed a fixed point iteration scheme, i.e. iterative Amplitude Adjusted Fourier Transform (iAAFT) method, which produces a surrogate with identical signal distributions and approximately identical amplitude spectra as the original series, or vice versa [169]. For every original time series, the surrogates are generated using the iAAFT method described by Schreiber and Schmitz [162]. By using iAAFT method, instead of the Amplitude Adjusted Fourier Transform (AAFT) method, the possibility of false rejections of null hypothesis is avoided [167, 181] and computational efficiency is achieved [167]. If the Fourier amplitude spectrum is $\{|S_k|\}$ for original time series, s, and $\{c_k\}$ is sorted version of original time series, at every iteration j, there are two time series, $r^{(j)}$, which has the correct signal distribution, and $s^{(j)}$, which has the correct amplitude spectrum. Then the iterative procedure, starting with $r^{(0)}$, a random permutation of the time samples of the original time series, follows the steps:

1) Compute the phase spectrum of $r^{(j-1)} \rightarrow \{\phi_k\}$
2) $s^{(j)}$ is the inverse transform of $\{|S_k| exp(i\phi_k)\}$
3) $r^{(j)}$ is obtained by rank-ordering $s^{(j)}$ so as to match $\{c_k\}$

These steps are iterated to the point of convergence of the discrepancy between $\{|S_k|\}$ and the amplitude spectrum $r^{(j)}$. Gautama et al. [174] adopt that the convergence is assessed as the point at which the Mean Square Error (MSE) between $\{|S_k|\}$ and the amplitude spectrum of $r^{(j)}$ stops decreasing. Schreiber and Schmitz [162] show that algorithms converge after finite numbers of steps, which in simulations performed by Gautama et al. [174] was typically 50 iterations for time series of 1000 samples, while for the example surrogate for the Lorenz series the method was shown to converge after 25 iterations. In this thesis iAAFT method has been used for generating surrogate time series, since it has been observed that it gives superior results in comparison with other methods [162, 174, 182].

Nonlinearity is assessed here as the absence of linearity. In statistical context, a null hypothesis is asserted that the time series is linear, and it is rejected if the time series does not conform to the properties associated with a linear signal. If the metric of the original time series is significantly different from that of surrogates, the null hypothesis is rejected and the original time series is hypothesised to be nonlinear. For every original time series, we generate N_s = 25 surrogates for the nonlinearity tests. The test statistics for the original, t_0, and for the surrogates, $t_{s,i}$ $(i = 1, \dots, N_s)$ are computed and the series of $\{t_{0,}\ t_{s,i}\}$ is sorted in increasing order, after which the position index or rank r of t_0 is determined. Gautama et al. [167] every original time series use N_s = 99 surrogates to perform nonlinearitry tests, where a right-tailed test (DVV) is rejected if rank r of the original time series exceeds 90, left-tailed test is rejected if it is smaller or equal to 10, and a two-tailed test (C3, REV, and COR) is rejected if rank r is greater than 95, or less or equal to 5. The symmetrical rank r_{symm} is defined [174]:

$$r_{symm}[\%] = \begin{cases} \dfrac{r}{N_s + 1} & for\ right - tailed\ tests \\[2ex] \dfrac{N_s + 2 - r}{N_s + 1} & for\ left - tailed\ tests \\[2ex] \dfrac{\left|\frac{N_s + 1}{2} - r\right|}{\frac{N_s + 1}{2}} & for\ two - tailed\ tests \end{cases} \tag{5.1}$$

For every test statistic, it is important to verify the assumptions on which they are based or the properties they are examining, since these are important issues in the interpretation of analysis results [166, 174]. The DVV method was selected for characterisation of a time series.

5.3.2 Delay Vector Variance (DVV) method

The DVV method is a novel method for detecting the nonlinearity of the time series, which examines the predictability of time series in phase space at different scales, using the method of time delay embedding for representing a time series [168, 169, 174]. DVV analysis is based on surrogate data. It has become fundamental tool for nonlinear time series analysis in many different research fields, such as geophysics and physiology, and can be used with any nonlinear statistic that characterises a time series with single number [162, 168, 169, 183].

The DVV method, as name suggests, is based on time delay embedding representation of a time series $x(n)$, $n = 1, 2, \dots, N$. For a given embedding dimension m, the Delay Vectors (DVs) are denoted as $\mathbf{x}(k) = [x_{k-\tau m}, \dots, x_{k-\tau}]^T$, a vector containing m consecutive time samples and τ denotes time lag (delay). Every DV $\mathbf{x}(k)$ has a corresponding target, namely the following sample, x_k.

A set Ω_k is generated by grouping those DVs that are within a certain distance to $\mathbf{x}(k)$, which is varied in a manner standardised with respect to the distribution of pairwise distance between DVs. In this way, the threshold scales automatically with the embedding dimension m, as well as with dynamical range of the time series at hand, and thus the complete range of pairwise distances is examined. The proposed DVV method, for given embedding parameter m, can be summarised in algorithm [168, 169, 174]:

1) Reconstruct the phase-space and obtain the set of delay vectors (DVs) in phase space

$$\mathbf{x}(k) = [x_{k-\tau m}, \dots, x_{k-\tau}]^T, \quad k = 1, \dots, N - m + 1 \tag{5.2}$$

where N denotes the length of time series.

2) Compute pairwise Euclidian distances between DVs

$$d(i, j) = \|x(i) - x(j)\|, \quad (i \neq j) \tag{5.3}$$

3) Compute the mean μ_d and standard deviation σ_d over all pairwise Euclidian distances between DVs (pragmatic approach to determine 'scaling region' explained in [167])

$$\mu_d = mean\big(d(i, j)\big)_{ij} \tag{5.4}$$

$$\sigma_d = std(d(i,j))_{ij} \tag{5.5}$$

Since the surrogate time series have signal distribution identical to that of the original, the distributions of pairwise distances, and thus, the mean and standard deviation, will be similar [174] (this distribution is approximately Gaussian for high embedding dimensions).

4) The sets $\Omega_k(r_d)$ are generated by grouping those DVs that are within a certain Euclidean distance to $\mathbf{x}(k)$ so that

$$\Omega_k(r_d) = \{\mathbf{x}(i) \mid \|\mathbf{x}(k) - \mathbf{x}(i)\| \leq r_d\} \tag{5.6}$$

i.e. sets that consist of all DVs that lie closer to $\mathbf{x}(k)$ than the certain distance r_d calculated:

$$r_d(n) = \mu_d - n_d\sigma_d + (n-1)\frac{2n_d\sigma_d}{N_{tv}-1}; \quad n = 1, \ldots N_{tv} \tag{5.7}$$

in other words, taken from the interval $[max\{0, \mu_d - n_d\sigma_d\};\ \mu_d + n_d\sigma_d]$, uniformly spaced, where n_d is a parameter controlling the span over which to perform the DVV analysis, usually set to be 3 [183] and N_{tv}, number of target variance, indicates how fine the standardized distance is uniformly spaced.

5) For a given embedding dimension *m*, the main target variance (a measure of unpredictability) σ^{*2} is calculated over all sets $\Omega_k(r_d)$. Namely for every set $\Omega_k(r_d)$, the variance of the corresponding targets $\sigma_k^2(r_d)$ is computed. The average over all sets $\Omega_k(r_d)$ normalised by the variance of the time series, σ_x^2, yields the measure of unpredictability, 'target variance', $\sigma^{*2}(r_d)$:

$$\sigma^{*2}(r_d) = \frac{(1/N)\sum_{k=1}^{N}\sigma_k^2(r_d)}{\sigma_x^2} \tag{5.8}$$

Considering a variance measurement valid, too few points for computing a sample variance yields unreliable estimates of the true variance. Jianjun et al. suggest that the set of $\Omega_k(r_d)$ should contain at least $N_0 = 30$ DVs [180]. A sample of 30 data points for estimating mean or variance is the general rule-of-thumb [167, 169, 174]. In this thesis a variance measurement is valid, if the set $\Omega_k(r_d)$ contains at least 30 DVs.

The basis of the DVV method is that if two DVs of a predictable signal are close to one another in terms of their Euclidean distance, they should have similar targets, i.e. the smaller the Euclidian distance between them, the more similar targets they have. Hence, the presence of strong deterministic component within a signal will result in the smaller target variances for small spans r_d [174, 180]. The minimal target variance $\sigma^{*2}_{min} = min_{r_d}[\sigma^{*2}(r_d)]$ represents the amount of noise present within the time series (the prevalence of the stochastic component) and has upper bound which is unity. The reason for this lies in the fact that all DVs belong to the same set of $\Omega_k(r_d)$ when r_d is sufficiently large. Therefore the variance of the corresponding target of those DVs will be almost equal to that of the original time series. As a result of the standardization of the distance axes the resulting DVV plots are straightforward to interpret.

6) The resulting DVV plots are plotted with the standardised distance r_d on horizontal axis and normalised variance σ^{*2} on vertical axis. At the extreme right, DVV plots smoothly converge to unity, because for maximum spans, all DVs belong to the same set, and the variance of the targets is equal to the variance of the time series. If this is not the case, the span parameter n_d should be increased [168, 169]. If the surrogate time series yield DVV plots similar to that of original time series, it indicates that time series is likely to be linear and vice versa. The example of signal flow within DVV method, i.e. DVV plot is illustrated in Figure 5.1.

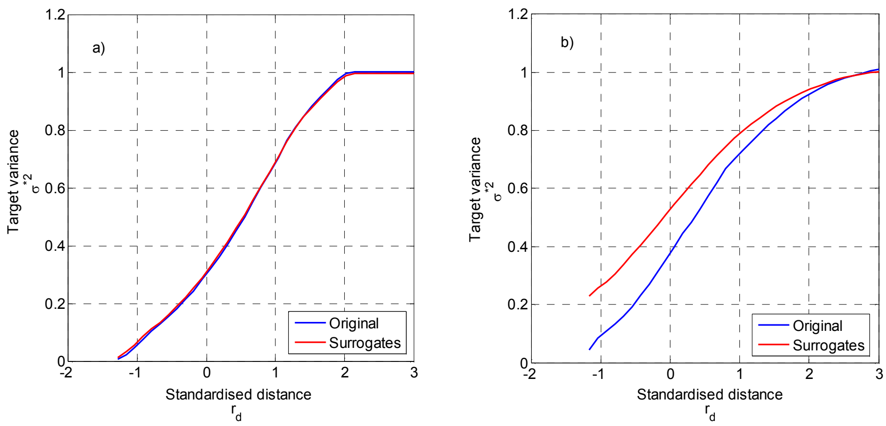

Figure 5.1 DVV plots of SDOF system response a) linear and b) nonlinear / less linear signal.

7) Performing DVV analysis on the original and a number of surrogate time series. DVV scatter diagram can characterise the linear or non linear nature of time series using the optimal embedding dimension of the original time series. If the surrogate time series yield DVV plots similar to the original time series (the DVV scatter diagram coincides with bisector line) than original time series is likely to be linear [168]. Thus the deviation from the bisector line is an indicator of non-linearity of the original time series [168, 174]. As non-linearity increases, the deviation from bisector line grows. The example of DVV scatter plots is given in Figure 5.2.

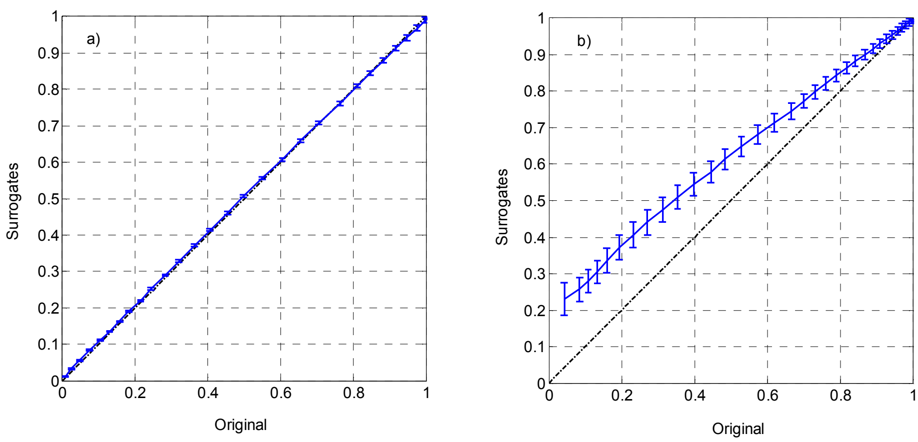

Figure 5.2 DVV scatter plots of SDOF system response a) linear and b) nonlinear / less linear signal.

The deviation from bisector line can be quantified by the root mean squared error (RMSE) between the σ^{*2}'s of the original time series and the σ^{*2}'s averaged over the DVV plots of the surrogate time series (when computing this average, as well as computing RMSE, only the valid variance measurements, e.g. if the set $\Omega_k(r_d)$ contains at least 30 DVs measurements, are taken into account [162]). Thus, a single test statistic t^{DVV} is calculated [169]:

$$t^{DVV} = \sqrt{\langle \left(\sigma^{*2}(r_d) - \frac{\sum_{i=1}^{N_s} \sigma_{s,i}^{*2}(r_d)}{N_s} \right)^2 \rangle_{valid_{r_d}}} \tag{5.9}$$

where $\sigma_{s,i}^{*2}(r_d)$ is the target variance at the span r_d for the i^{th} surrogate, and the average is taken over all spans r_d that are valid in all surrogate and original DVV plots.

Delay Vector Variance toolbox for Matlab and related documentation are available from [184] and are used for this work with little modification of DVV parameters.

5.3.3 Parameters adopted for DVV simulation

5.3.3.1 Embedding dimension m

For correct choice of embedding parameters (which might not be unique), the target variance, σ^{*2}, gives information regarding one of the fundamental properties of a signal, i.e. its predictability [167]. Two extreme cases are white noise, which is entirely unpredictable, and a deterministic signal, which is entirely predictable. Therefore it is very important to determine the embedding dimension and time lag correctly as in combination with the structured signal, similar delay vectors (in terms of their Euclidian distance) have similar targets [172].

The embedding dimension, m determines how many previous time samples are used for examining the local predictability. It is important to choose m sufficiently large, such that the m-dimensional phase space enables for a 'proper' representation of the dynamic system [166, 174]. Hence, the choice of the embedding dimension and the time lag is important for signal nonlinearity analysis [185]. We used and compared three different approaches when adopting the embedding dimension and time lag:

1st Approach (Method 1):

The optimal embedding parameters of the signal were determined using a differential entropy method proposed by Gautama et al. [185]. The main advantage of this method is that based on estimates of the differential entropy ratio of the phase space representation of a sampled time signal and an ensemble of its surrogates the optimal m, and time lag, τ, are simultaneously determined. The entropy ratio method can be summarised:

1) Using the Kozachenko-Leonenko (K-L) estimate of the differential entropy [186]:

$$H(x) = \sum_{j=1}^{N} ln(Nd_j) + ln(2) + C_E \tag{5.10}$$

where N is the number of samples in the data set, d_j is Euclidean distance of jth delay vector to its nearest neighbour, and C_E (≈ 0.5772) is Euler constant.

2) To determine the optimal embedding parameters the ratio between K-L estimates for the time delay embedded versions of the original time series, x, and its surrogates $x_{s,i}$, $i = 1,\dots N_s$ needs to be minimised:

$$I(m,\tau) = \frac{H(x,m,\tau)}{\langle H(x_{s,i},m,\tau)\rangle_i} \tag{5.11}$$

where $\langle - \rangle_i$ denotes the average over i.

3) The Entropy Ratio (ER) is calculated using the expression:

$$R_{ent}(m,\tau) = I(m,\tau)\left(1 + \frac{m\ lnN_{sub}}{N_{sub}}\right) \tag{5.12}$$

N_{sub} is the number of delay vectors, which is kept constant for all values of m and τ under consideration.

If the temporal span of $(m \cdot \tau)$ is too small, the signal variation within the delay vector is mostly governed by noise and either m or τ should be increased. The set of optimal parameters, $\{m_{opt}, \tau_{opt}\}$, yields a phase space representation which best reflects the dynamics of the underlying signal production system and it is expected that this representation has a minimal differential entropy (minimal disorder). The method is explained in detailed by Gautama et al. [185]. The minimum of the plot of the entropy ratio yields the optimal set of embedding parameters. In order to determine the optimum embedding parameters in all simulations Ns = 5 surrogates were generated using iAAFT method and the entropy ratios were evaluated for m = 2, 3, …, 10 and τ = 1, 2, …, 10. Increasing the number of surrogates does not affect the results [185]. The proposed approach is illustrated in Figure 5.3 showing entropy ratio $R_{ent}(m,\tau)$. The minimum of the plot indicated with red circle gives the optimum embedding parameters for the case shown $m_{opt} = 3$; and $\tau_{opt} = 1$.

The ER criterion requires time series to display clear structure in phase space; i.e. for signals with no clear structure, the method will not generate clear minimum, and different approach needs to be adopted [185]. In practice, it is common to have fixed time lag (sampling rate) and to adjust the embedding dimension (length of filter) accordingly.

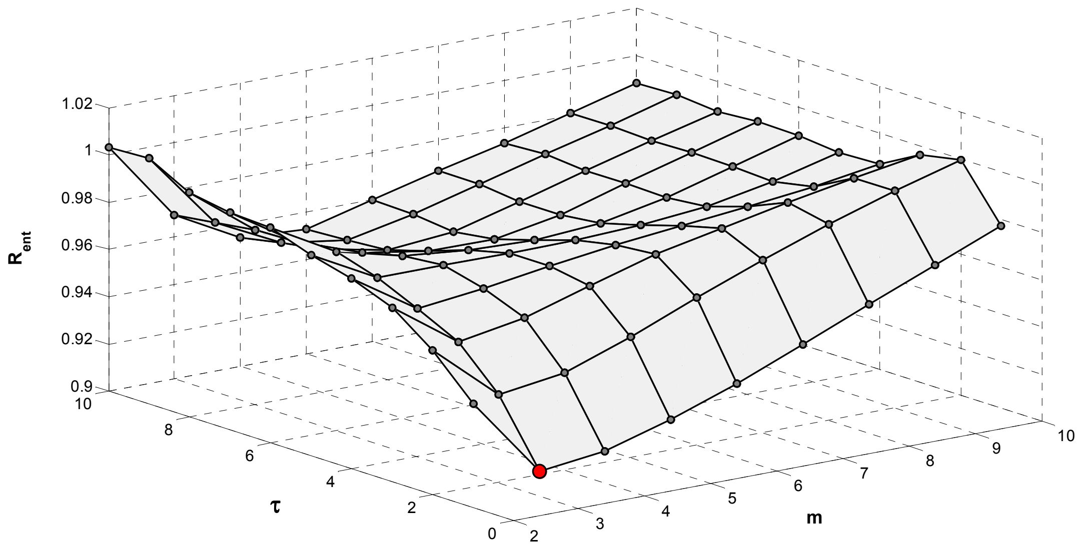

Figure 5.3 Plot of the Entropy Ratio (ER) for harmonically excited SDOF system response signal.

2nd Approach (Method 2):

The optimal embedding dimension can be determined by running a number of DVV analyses for different values of m, and choosing that for which the minimal target variance, σ_{min}^{*2}, is the lowest, i.e which yields the best predictability. In this work we performed this analysis for embedding dimensions ranging from 2 to 25 following Gautama et al. [167] and Gautama et al. [174]. The time lag, τ, for convenience, is set to unity in all simulations as per [167, 169]. This choice of τ is conservative in the context of nonlinearity detection. Assuming the embedding dimension is sufficiently high, a linear time series can be accurately represented using $\tau = 1$, while this is not the case for a nonlinear signal, for which time lag plays an important role in its characterisation [169]. Hence, if the null hypothesis of linearity is rejected, one can assume that the time series is nonlinear. Since the linear part was accurately described for time lag equal to unity the rejection can be attributed to the nonlinear part of the signal. On the other hand, if the null hypothesis is found to hold, the signal is genuinely linear or the phase space is poorly reconstructed using $\tau = 1$, i.e. the signal is actually nonlinear [169]. The example of the method described is shown in Figure 5.4. The dashed line indicates the minimal target variance, σ^{*2}_{min}, and thus the optimal embedding dimension.

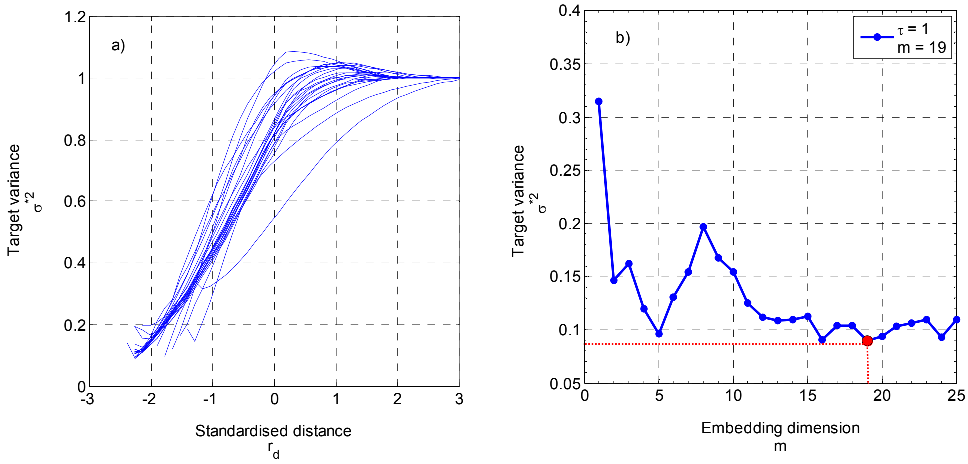

Figure 5.4 Finding the optimal embedding parameter, m: a) DVV plots obtained for m = 2 to 25 and b) Target variance σ^{*2} for response of SDOF undamped system to harmonic excitation as the function of embedding dimension, m.

<u>3rd Approach (Method 3):</u>

However, in the DVV nonlinearity detection context, m is not critical and the optimal embedding dimension of the original time series can be set manually [174]. Gautama et al. [168] report as desirable property for a robust analysis method relative insensitivity of the DVV method to the parameter choice. The embedding dimension was set to 3 and time lag is for convenience set to unity in all the simulations as per Gautama et al. [168]. This convenience does not influence the generality of the results. After observation of DVV plots of available experiments, embedding parameter was set to 3 in this work.

In the following text the methods for determination of embedding parameters, Method 1, 2 and 3, are referred as 1st, 2nd and 3rd approach, respectively.

5.3.3.2 Maximal Span n_d

The maximal span parameter, n_d, determines the range of standardised distances to consider, i.e. it is the parameter controlling the span over which to perform the DVV analysis. Hence, visual inspection of the convergence of DVV plot to unity at the extreme right should be used for setting this parameter, i.e. typically starting at value $n_d = 2$ and increasing it using unit steps until DVV plots converge to unity at extreme right [169]. We adopt $n_d = 3$ in all simulations [174].

5.3.3.3 Number of evaluation points, N_{tv}

The number of standardised distances for which target variances are computed, N_{tv}, has been set to 50.

5.3.3.4 Size of subset Nsub

Number of reference DVs considered, N_{sub}, in all simulations is 200. Reducing the size of subset of DVs to which pair wise Euclidean distances are computed, greatly speeds up DVV analysis [174].

5.3.3.5 Number of surrogates, N_s

For each of the time series we perform a set of DVV based nonlinearity analysis for a range of parameter values using a set of $N_s = 25$ surrogates.

Gautama et al. [174] have analysed the sensitivity of the proposed DVV method to parameter settings for four different time series, of which three were nonlinear. They found that the embedding dimension, m, and the maximal span, n_d, were the only parameters with a noticeable effect with respect to nonlinearity detection. They also concluded that the effects were minor for reasonable parameter values, i.e. $m \in [3, 10]$ and $n_d \geq 1$.

5.4 Reference model – Simple vibration problems

In order to establish benchmark values for linear or nonlinear behaviour of a mechanical system using its response to excitation reference (or template), different diagnostic models have been considered, with SDOF chosen as a reference system. The response signals, for changing reference system parameters (e.g. mass, damping, natural frequency, driving frequency, etc.), are analysed using DVV Method. The reference models, the related time history response, and mathematical solutions are described in Appendix B1. Responses of the reference systems are obtained using Matlab codes [158, 187]. The number of the data analysed in every simulation is approximately 1000.

The results of DVV analysis using three different approaches for choosing embedding parameters for following models separately are shown in Appendix B2. The 'rmse' indicates the root means square error of DVV plots (original vs. surrogate data), while 'RMSE' is quantified deviation from bisector line of DVV scatter plot. The calculated value RMSE is compared for each simulation on few different levels:

- Parameter choice for DVV analysis using three different approaches;
- Variable choice for different systems, and
- Same system, different external excitation (if and when existent).

The following sections, from 5.4.1 to 5.4.13, represent detailed discussion of the DVV analysis results given in Appendix B2 of vibration output of the reference SDOF models presented in Appendix B1. The summary of the findings in relation to the reference model DVV analysis is given in section 5.4.14.

5.4.1. SDOF Undamped Oscillation

The simplest form of vibration - SDOF system without damping or external forcing with three different masses (2, 4 and 12 kg) was observed. Note that the natural frequency decreases with increasing mass. Using three different approaches to determine embedding parameters resulted in slightly different RMSE in the case of low and high system mass. The highest deviation is observed for the mass of the system of 4kg, where RMSE is the highest using 1st and the lowest using the 2nd approach. The calculated RMSE using 2nd and 3rd approach gives similar answers for all masses. In the case of 1st and 2nd approaches there is no visible trend in results while RMSE calculated using 3rd approach shows slight increase when mass of the system increases. Overall, it could be concluded that the RMSE of DVV scatter plot from bisector line of SDOF undamped free oscillator is insensitive to changing the mass of the system and it has an average value of 0.181; 0.156 and 0.174 for 1st, 2nd and 3rd approach respectively.

5.4.2 A Damped SDOF System

The effects of the increasing viscous damping coefficient (ζ = 0.05, 0.2 and 0.5) on underdamped SDOF system was looked at next. As damping ratio increases the response of the system dynamics becomes virtually zero quickly, while RMSE increases in all three approaches. With the 1st approach the increase is almost linear, while with two other approaches it is steeper when damping increases between 0.05 and 0.2 than between 0.2 and 0.5. In general 2nd and 3rd approaches give very similar results, especially for lower dumping ratios than 0.2. RMSE for 2nd approach varies between 0.357 and 0.631, while in the case of 3rd approach it is between 0.347 and 0.682 for damping ratio ζ = 0.05 and 0.5, respectively.

5.4.3 Overdamped SDOF Oscillation

The effects of the decreasing viscous damping coefficient (ζ = 7, 5 and 1) on SDOF system oscillation shows, as expected, that critically damped response returns to equilibrium faster than the others systems. The RMSE in the case of 1st approach does not have clear trend for higher values of damping, but as system damping decreases to ζ = 1, RMSE increases. Again, as in the last case, the results obtained using 2nd and 3rd approaches are very similar, except that for overdamped case RMSE increases as damping decreases. RMSE for 2nd approach varies between 0.330 and 0.646, while in the case of 3rd approach it is between 0.292 and 0.699 for damping ratio ζ = 7 and 1, respectively.

For the damped SDOF system in all three cases, underdamped ($\zeta < 1$), critically damped ($\zeta = 1$), or overdamped ($\zeta > 1$), the initial conditions are assumed to be the same (Appendix B1). The system reaches its equilibrium very fast; as a result DVV plots do not converge to unity at the very right even with increased span parameter n_d [168, 169]. The result is that the response of the system shows nonlinearity. The nonlinearity increases with increasing damping for underdamped case and with decreasing damping for overdamped case, giving the highest value of RMSE for critically damped case. The results of this analysis also show that the measurements of system response obtained close to its equilibrium could highly influence the DVV analysis.

5.4.4 Harmonic Excitation of Undamped SDOF Systems

The effects of an external force on the system are examined here. A harmonic load is imposed on undamped SDOF system and effects of the key parameters which define the response, the natural and driving frequencies, are observed. The initial conditions are kept the same (see Appendix B1).

First the natural frequency is set to 7 Hz, while driving frequency increased taking values 3, 27 and 42 Hz. RMSE values in all approaches have visible trend.

While with increasing driving frequency RMSE decreases when the 1st approach is applied, RMSE increases for 2nd and 3rd approaches. The RMSE values for the later two are very close to each other, for 2nd 0.107, 0.210 and 0.283 and for 3rd approach 0.118, 0.214 and 0.320 for driving frequencies 3, 27 and 42 Hz, respectively.

Similar results are obtained when the driving frequency is set to constant value of 7Hz and natural frequency increased adopting the values: 3, 12 and 26 Hz. The trend of RMSE values is the same as above, i.e. in the case of 1st approach decreasing and 2nd and 3rd increasing. RMSE values in 2nd approach being 0,107 and 0.226 and for 3rd approach 0.118 and 0,204 for natural frequencies 3 and 26 Hz.

Since the response of the system analysed depends on the driving-natural frequency ratio two interesting phenomena, beats and resonance, were investigated next.

To simulate beats, the natural frequency and the driving frequency are arranged so they have close but not equal values (w_n=3, w_{dr}=3.2; w_n=12, w_{dr}=12.2; and w_n=22, w_{dr}=22.2 Hz). This results in a rapid oscillation with slowly varying amplitude, both vary along a sinusoid. The results of DVV analysis of the system response shows that only visible trend in RMSE values is obtained with 3rd approach, i.e. RMSE increases with increasing frequency from 0.137 to 2.217. Also, according to the DVV plots this type of response is less linear than the responses of the same system discussed above.

In the next simulation, for the same SDOF system, the driving and natural frequencies are set equal (w_n=w_{dr}=3; w_n=w_{dr}=12; and w_n=w_{dr}=22 Hz). This results in resonance, i.e. the amplitude of oscillation increases without limit. As in the case of beats, only RMSE calculated using 3rd approach shows the trend, i.e. with increasing frequency it increases from 0.119 to 0.165 for frequencies 3 and 12 Hz, respectively.

Overall, for response of the undamped SDOF system excited with harmonic load with increasing natural frequency, or driving frequency, or both (regardless if it results in the beats or resonance) the results of the DVV analysis show that RMSE obtained using the 3rd approach increases as well. Furthermore, the DVV analysis of the beats shows greater nonlinearity than other cases.

5.4.5 Harmonic Excitation of Damped SDOF Systems

The response of SDOF System excited with the harmonic forcing when the damping ratio ζ was varied and natural and driving frequencies were kept constant was analysed next. It is observed that the transient period of vibration varies inversely with damping ratio and that the damping ratio affects the amplitude of the steady-state vibration, also in an inverse relationship. The value of RMSE calculated using 1st approach does not show distinctive trend, while it increases in the case of 2nd and 3rd approach. As damping increases and RMSE increases, the response amplitude decreases. That is, the amplitude of the response for $\zeta = 0.05$ is almost 2 and RMSE is 0.155 (3rd approach), while that for $\zeta = 0.5$ is less than 1 and RMSE is 0.166 (3rd approach).

Studying the same system: keeping the damping constant while changing the natural frequency (3, 12 and 26 Hz) it is found that amplitude of response decreases while RMSE increases, taking values: 0.138, 0.163 and 0.165 with 3rd and 0.133, 0.161 and 0.208 with 1st approach. It is evident that with the higher frequencies RMSE obtained differs greatly between these two approaches.

5.4.6 Base Excitation of SDOF Systems

The effects of changing the excitation (base) frequency (ω_b = 2, 6 and 12 Hz) on system response while keeping all other parameters constant was looked at first. It is observed that the results obtained using 1st and 3rd approach are very close in the value but do not hold specific trend, while RMSE calculated using 2nd approach increases with base frequency increase. Still, the results obtained with the 3rd approach indicate that the linearity of the signal is almost unaffected by change of base frequency, with average value of RMSE = 0.161.

By increasing input amplitude (y_0 = 3, 7 and 11) and keeping the rest of parameters constant the maximum amplitude of the overall vibration and of the steady-state response both increase. While results of DVV analysis differ slightly between the approaches, they remain almost constant for increase in amplitude. This would mean, again, that increase in amplitude does not affect linearity of the system. The average values of RMSE are 0.1359, 0.1560 and 0.1507 for 1st, 2nd and 3rd approach, respectively.

The changes of damping (ζ = 0.05, 0.1 and 0.3) as in previous cases of increasing damping ratio lead to increase in RMSE value of 1st and 3rd approach, hence nonlinearity of the response signal increases. The values range from 0.136 to 0.156 and from 0.151 to 0.172 for the 1st and the 3rd approach, respectively. The results obtained with the 2nd approach are similar in value with other two, but do not show consistent trend.

5.4.7 SDOF Systems with a Rotating Unbalance

The natural frequency of SDOF system with a rotating unbalance was varied (ω_n = 2, 6 and 12 Hz) while keeping all other parameters constant. The response of the system is analysed using DVV method. The results show that there is no trend in the RMSE obtained with any of approaches proposed, similarly to the previous cases with increased natural frequency. But with the closer look at the results it could be concluded that that RMSE derived using the 1st and the 3rd approach are close in value and almost constant for all natural frequencies considered. Thear average values are 0.162 and 0.168 for the 1st and the3rd approach, respectively.

For the increasing damping of the system (ζ = 0.05, 0.1 and 0.3) DVV analysis gives increasing values of RMSE when applying 2nd and 3rd approach. The results are 0.157, 0.164 and 0.167 for 2nd and 0.170, 0.174 and 0.175 for 3rd approach.

Finally, the variation of vibration with increasing system mass shows that the amplitude of the vibration decreases with increasing mass (1, 3, 6 kg), but there is no reflection on RMSE value calculated for system response. Moreover, the RMSE values are constant, i.e. the response of the system does not change its degree of linearity, when 1st (0.160) and 3rd (0.167) approach is applied.

5.4.8 Step Response of SDOF System

Changing the magnitude of external force of SDOF system shows that the magnitude of the response is directly proportional to the magnitude of the external force. Regarding the DVV analysis, it shows that change in magnitude of system response signal does not influence degree of its linearity. Further more the RMSE values obtained by applying the 2nd and 3rd approach show almost constant values; average being 0.365 and 0.363, respectively.

The step responses of SDOF system when varying the natural frequency causes two changes in the response; the rate of exponential decrease in the response (the effect of damping) is increased; that is, the response stabilizes more quickly and the oscillation frequency decreases, since the natural frequency also dictates the damped frequency. When applying the DVV analysis on system response signal it is evident that RMSE increases with natural frequency (2 to 12 Hz) for all three approaches, from 0.148 to 0.300; 0.163 to 0.366 and from 0.163 to 0.363 for 1st, 2nd and 3rd approach.

The changes in RMSE caused by changing the damping ratio have the same trend as previously for underdamped cases. With increasing damping ratio (ζ = 0.05, 0.1 and 0.3), the amount of time to damp out all vibration decreases, while RMSE increases taking the values 0.300, 0.403 and 0.419 when 1st and 0.373, 0.418 and 0.425 when 3rd approach is applied.

5.4.9 Response of SDOF System to Square Pulse Inputs

A square pulse is a single pulse of constant magnitude and finite duration. To analyse the response of systems to a square wave input, the sensitivity of system response to variation of important parameters (natural frequency, damping and force magnitude) were looked at.

When natural frequency is increased (ω_n = 2, 6 and 12 Hz) the deviation from bisector line of DVV scatter plots decreases in the cases of 2nd and 3rd approach resulting in RMSE values of 0.250, 0.192 and 0.188, and 0.249, 0.190 and 0.188 for the three frequencies, respectively. The results obtained with the two approaches are almost the same and represent the only case, up to now, that RMSE decreases with increasing natural frequency.

On the other hand, when damping coefficient increases (ζ = 0.05, 0.1 and 0.3) the deviation from the bisector line increases, as it was the case with all underdamped cases before. The RMSE varies between 0.143 and 0.325 (0.189 and 0.341) for 2nd (3rd) approach, respectively.

When force magnitude varies (F_o = 3, 7 and 11) the deviation from the bisector line of DVV scatter plots remains unchanged resulting in constant value of RMSE in all three approaches (0.219; 0.191 and 0.188 for 1st; 2nd and 3rd approach).

5.4.10 Response of SDOF System to Ramp Input

The response of SDOF system to ramp input shows that there is no equilibrium position (as for the step and square wave responses) until after the input has levelled off. With increasing initial amplitude (f_o = 3, 7 and 26) and keeping the natural frequency and damping constant the RMSE calculated remains constant, 0.186 and 0.198 for 1st and 3rd approach.

5.4.11 A van der Pol Oscillator

Displacement and velocity of van der Pol oscillator for initial conditions x_0=[1; 0]; $x(0)$=1, $x'(0)$=0, constant e =0.5 and the time interval t_f =30sec shows that the deviation from bisector line obtained from three approaches are very close in the value. For displacement RMSE is 0.167, 0.153 and 0.155; for velocity it is 0.108, 0.122 and 0.114 for 1st, 2nd and 3rd approach, respectively. Note that the velocity related values are lower than those for displacement in all three cases.

5.4.12 Response of SDOF System to Random Vibration

The displacement of SDOF system excited with the random vibration was analysed next. Two cases are looked at: Gaussian distribution and not rigorously Gaussian distribution, where the amplitude is random variable but defined between 0 and 5 ($0 < A \leq 5$). The natural frequency is set to 1, damping ratio is 0.05 and frequency of input force is 3.5. The RMSE for the first case is 0.154, 0.122 and 0.156, for the second case it is 0.156, 0.153 and 0.139 for the 1st, 2nd and 3rd approach, respectively. The results show that the 1st approach is insensitive to change of amplitude, while it increases for 2nd but decreases for 3rd approach.

5.4.13 Randomly-Excited Duffing Oscillator

The numerical solutions for a Duffing oscillator response to a harmonic input $g(x) = -x^2$ when given the input values of $c = 0.05$; $k = 1$; $\varepsilon = 0.01$; and varying A; and ω was analysed using DVV method.

For A=3.7999 and ω =3.7960 the RMSE is found to give almost the same results for displacement and velocity signals when using 1st and 3rd approach. For displacement they are 0.125 for both approaches and for velocity they are 0.132 and 0.136 for 1st and 3rd approach, respectively.

By choosing A=4.4351 and ω =1.7404, the system is in nearly-resonant condition RMSE is same, 0.145 for displacement and velocity when applying 1st approach. For 3rd approach, values are very close: 0.157 for displacement and 0.155 for velocity.

For A=1.0062 and ω =2.0115 the RMSE is found to give almost the same results for displacement and velocity signals when using 1st and 3rd approach, again. For displacement they are 0.151 and 0.158; for velocity they are 0.148 and 0.156 for 1st and 3rd approach, respectively.

The results of DVV analysis of SDOF reference model are shown in Appendix B2 Summary table.

5.4.14 Conclusions

- 3rd approach, keeping m=3 and τ=1, shows the best consistency in interpretation of DVV method results when SDOF parameter changes.

- When changing system mass, RMSE remains constant or almost constant. For undamped free oscillator RMSE is 0.174 and for rotating unbalance it is 0.167 (only negligible increase of RMSE value with system mass is recorded).

- The minimum of the data points needed to perform DVV analysis is 100. This is important when DVV analysing free vibration of underdamped or overdamped systems where system reaches its equilibrium fast since insufficient number of data influence the results.

- For all underdamped systems ($\zeta < 1$) analysed, when damping ratio increases RMSE also increases. Results are shown in Figure 5.5 and Table 5.1. RMSE shows almost the same results for three SDOF systems: exposed to harmonic oscillation, to base excitation, and having rotating unbalance. The curves asymptotically approach RMSE of 0.180 for higher values of damping. However for three other cases: free damped oscillation, step response, and square wave input, this is not the case, i.e. the values are much higher. The reason for these phenomena might be in the fact that the systems reach their equilibrium fast and as a consequence there is no sufficient number of data for DVV analysis. For example, in the case of free vibrations, the response quickly becomes virtually zero; this occurs within ten seconds, even for a damping coefficient as small as 0.05, and the RMSE obtained is the highest recorded.

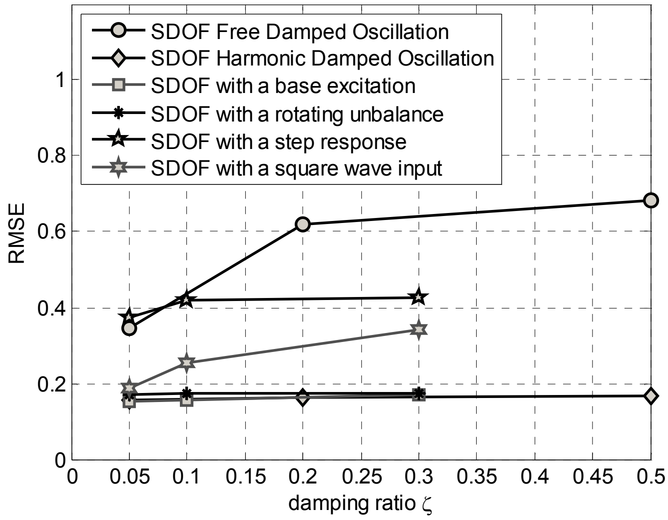

Figure 5.5 RMSE dependency on SDOF damping

- For overdamped ($\zeta > 1$) and critically damped ($\zeta = 1$) system analysed, when damping ratio decreases RMSE increases, reaching the maximum value 0.700 for critically damped system. Note that for underdamped case for $\zeta = 0.5$ RMSE is found to be 0.682. Here as well the system reaches its equilibrium very fast as a result DVV plots do not converge to unity as expected and deviation from bisector line of DVV scatter plot is high.

Table 5.1 RMSE obtained using 3rd approach on dumped SDOF system

SYSTEM	Constants	Damping ratio	RMSE 3rd approach
SDOF Damped Oscillation mx"+cx'+kx=0	natural frequency ω_n=7 initial displacement x_0=3 initial velocity v_0=1 time duration to test t_f=30s	0.05	0.347
		0.20	0.621
		0.50	0.682
SDOF Harmonic Damped Oscillation mx"+cx'+kx=Fcos(ωt)	driving frequency ω_{dr} =3 natural frequency ω_n =3.5 force magnitude per unit mass f_0=6 time duration to test t_f =30s	0.05	0.155
		0.20	0.162
		0.50	0.166
SDOF Base excitation mx"+c(x'-y')+k(x-y)=0 y(t)=Ysin(w_bt)	base amplitude y_0=3 base excitation frequency w_b=6 natural frequency ω_n =4 time duration to test t_f =10s	0.05	0.151
		0.10	0.156
		0.30	0.172
SDOF having a rotating unbalance for zero initial conditions	rotating mass m_o=3 sdof mass m=7 angular velocity of rot mass ω_r =4 natural frequency ω_n =12 time duration to test t_f =10s constant e=0.1	0.05	0.170
		0.10	0.174
		0.30	0.175
SDOF having a step response	system mass m=1 natural frequency ω_n =12 time duration to test t_f =10s force magnitude F_m=5 initial time t_o=2	0.05	0.373
		0.10	0.418
		0.30	0.425
SDOF having a square wave input	system mass m=1 natural frequency ω_n =12 time duration to test t_f =10s force magnitude F_m =7 wave starts at t_o =0 wave stops at t_o =3	0.05	0.189
		0.10	0.254
		0.30	0.341

- When increasing the driving frequency RMSE increases. The results are shown in Figure 5.6. For the case of resonance RMSE has lower, while for beat phenomena higher values in comparison with the case when natural frequency is not close or equal to driving frequency.

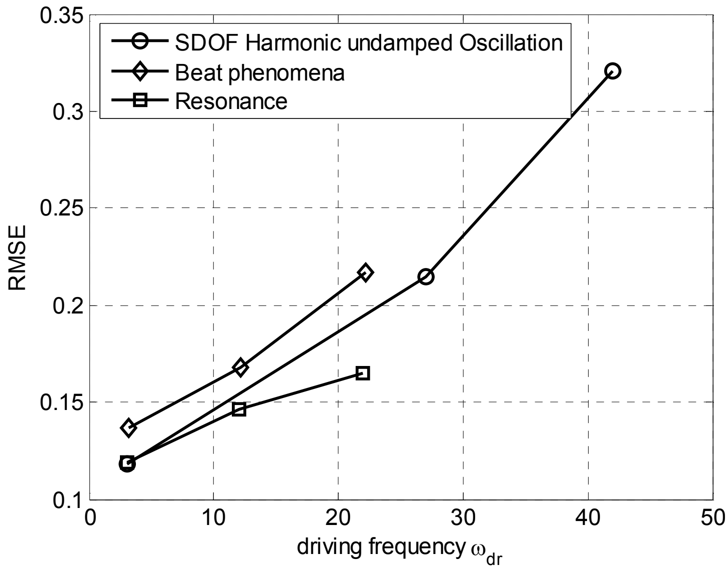

Figure 5.6 RMSE dependency on driving frequency.

- Figure 5.7 shows dependency of RMSE, calculated using 3rd approach, on increasing natural frequency. In all observed cases of SDOF RMSE increases with increased natural frequency, except in the case of a square pulse input, where it has steep decrease from 0.25 for 3 Hz to 0.19 for 6 Hz natural frequency and remains almost constant for higher frequencies. The curve for the case of the step response gives visibly higher values of RMSE in comparison to the other cases observed. This is a result of system fast return to equilibrium as it was the case with some underdamped system observed earlier.

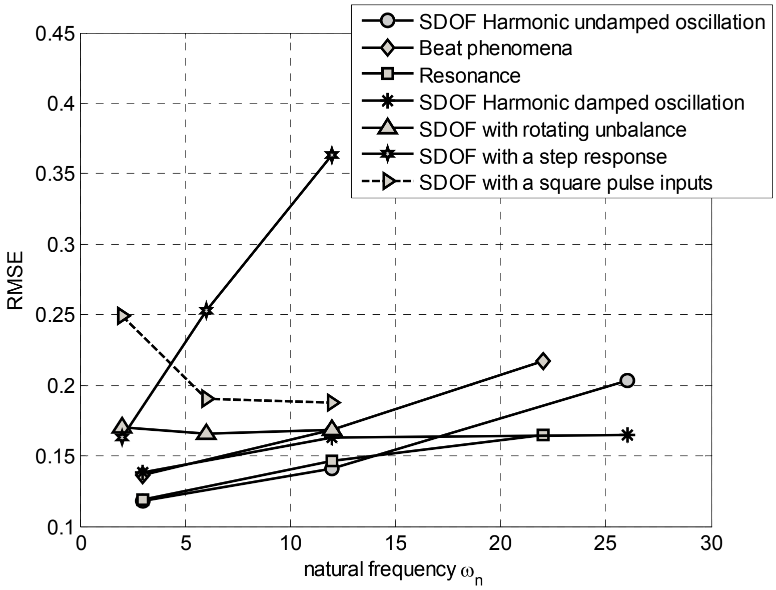

Figure 5.7 RMSE dependency on natural frequency.

- The increase in the base frequency for the SDOF system with base excitation results in almost constant value of RMSE.

- The change in the input force magnitude does not produce change in the RMSE calculated on the system response signal (see Figure 5.8). Note that the SDOF with the step response has the higher value of RMSE than three other cases observed; this is, again, the consequence of 'flat' (equilibrium) part of the system response.

- The linearity or nonlinearity of the system response (signal) could be linked with the type of the system in relative terms. Hence if we have observed the system and have its response in its 'original' form any kind of change to that system will produce the change in its response. By doing the DVV analysis of 'original' and 'new' signal and comparing their RMSE (deviation from bisector line) we could tell if some parameter influencing system response is changed.

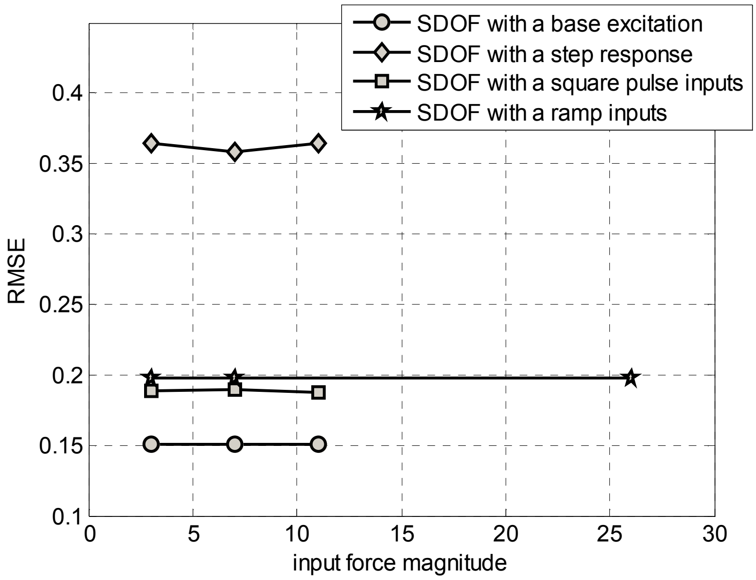

Figure 5.8 RMSE dependency on input force magnitude increase.

5.5 Single Degree of Freedom Car Experiment

The vibration of bilinear system exposed to known input force for a period of time was recorded in laboratory environment (see Chapter 3). The dynamic response of the SDOF system was measured using a Polytec RSV-150 Remote Sensing Vibrometer. This instrument employs Laser Doppler Vibrometry for measuring dynamic response. Additionally, the vibration response of the SDOF system was measured through a MicroStrain G-Link Wireless Accelerometer mounted on the SDOF system. The methodology with details on experiment setup, instrumentation used is given in Chapter 3.

The list of the experiments is given in Table 5.2.

Table 5.2 The list of the SDOF Car experiments performed.

EXPERIMENT	SURFACE	NO of springs	EXTERNAL FORCE			
			2 Hz	2-4-6-8-10 Hz	White Noise	Sine Sweep
EXP 1	wood	2 x 3				
EXP 2	wood	2 x 3				
EXP 3	plastic	2 x 3				
EXP 4	wood	2 x 3				
EXP 5	wood	2 x 3				
EXP 6	plastic	2 x 3				
EXP 7	plastic	2 x 3				
EXP 8	sand paper	2 x 3				
EXP 9	sand paper	2 x 3				
EXP 10	sand paper	2 x 3				
EXP 11	sand paper	2 x 2				
EXP 12	sand paper	2 x 2				
EXP 13 repeated	sand paper	2 x 2				
EXP 14	sand paper	2 x 2				
EXP 15	plastic	2 x 2				
EXP 16	plastic	2 x 2				
EXP 17	plastic	2 x 2				
EXP 18	wood	2 x 2				
EXP 19	wood	2 x 2				
EXP 20	wood	2 x 2				
EXP 21	wood	2 x 3 / 2 x 2				
HF	plastic	2 x 3				

The variables that have been changed between experiments are: the external force, the type of the surface beneath the wheels of the SDOF car, and the stiffness of the SDOF system.

The model was exposed to different external loadings: harmonic loading with increasing frequency (2, 4, 6, 8, and 10 Hz), sine sweep, and white noise. The wheels of SDOF car were moving on three different surfaces: plastic, wood, and sand paper, representing smooth, medium, and rough surface, respectively.

5.5.1 DVV Analysis

The response of the system is simultaneously measured by two instruments; 3D accelerometer and LDV (see Chapter 3). The outputs of the 3D accelerometer are in the Cartesian directions and the LDV measurement is derived through simple numerical differentiation of measured velocity response. Channel 1 of the accelerometer corresponds to the principal direction of vibration identical to LDV response. For all SDOF car experiments recorded responses are shown in Appendix B3.

The plots show all recorded data, i.e. system measurements prior, during, and after excitation. Observing reference model previously, it was concluded that in the 'flat' (equilibrium) part of the system response contributes to noticeable increase in calculated RMSE. Therefore only response of the system data, when it is in between two equilibriums, is used for DVV analysis. This data will be referred to as valid (for DVV analysiss) data further on in the text.

The linear or nonlinear nature of the time series is examined by performing DVV analysis on both the original and number of surrogate time series. Three different approaches to determine embedding parameters for DVV analysis are used and compared. The results of the DVV analysis are shown in Appendix B3.

5.5.1.1 Optimal Parameters

The 1st and the 2nd (see Section 5.3.3.1) approach prove to be difficult to implement on large number of data series, as was the case here. The limitation is imposed by Matlab memory in the case of 1st approach, while in the case of 2nd approach data processing time is long with often unrealistic simulation outcome. Hence, in the cases where data exceed 9000 they need to be windowed. The analysis of system response to white noise shows that parameters calculated using the 1st and the 2nd approach on windowed data applied on all set of data give almost the same RMSE. This was not the case with responses on sine sweep and increasing frequency input. In general the 1st approach yields higher RMSE values than other approaches.

The reason may lay in the nature of response data, i.e. the set of response data has no clear structure, therefore using the 1st approach by applying ER method does not generate clear minimum [185]. When 2nd and 3rd approach is applied on response data, RMSE values are close (or the same) in majority of cases even optimum m, obtained by using 2nd approach, were higher for most analysed examples. This is in agreement with Gautama's et al. [174] findings that the effects with respect to nonlinearity detection are minor for reasonable parameters values, i.e. $m \in [3, 10]$ and $n_d \geq 1$. When comparing the results of all three approaches, the trend tends to be similar between RMSE. Figure 5.9 shows the results of DVV analysis using all three approaches in determination of optimal emending parameters for SDOF car connected with six springs, moving over wooden surface excited by harmonic force.

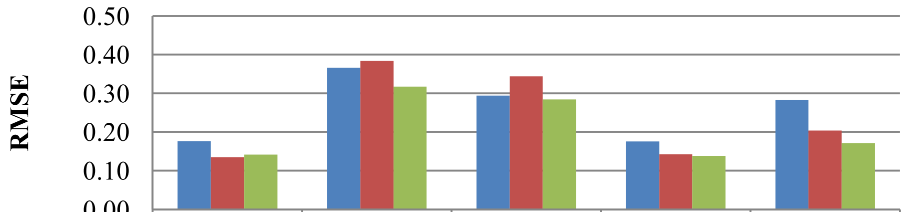

	CH1	CH2	CH3	LDVg	LDV1
Method 1	0.176	0.366	0.294	0.176	0.282
Method 2	0.135	0.384	0.344	0.142	0.204
Method 3	0.142	0.318	0.284	0.139	0.172

Figure 5.9 The example of RMSE obtained when using three methods for calculating embedding parameters.

The complexity and duration of simulation led us to adopt the 3rd approach, as in the case of SDOF template examples. This approach showed to be consistent in application on large set of data. Therefore, only the results obtained by 3rd approach will be discussed.

DVV analysis is performed on all valid measured data, however in most cases the relevant are the data obtained for principal direction of vibrations. In some cases though, data recorded in lateral direction (in horizontal plane and perpendicular to principal direction) are discussed as indicative of some change in the system.

5.5.2 Discussion and Results

5.5.2.1 Surface roughness

Three different surface types beneath the moving vehicle were used in experiments: plastic, wood and sand paper, corresponding to three different surface roughness grades: smooth (good), medium, and rough (poor), respectively. This section investigates the influence of surface roughness on system response while excitation force and system stiffness remain constant.

In the following figures CH1, CH2, and CH3 represent 3D Accelerometer's Cartesian direction measurements recorded by Channel 1, Channel 2, and Channel 3 respectively, while LDVg and LDV1 represent Laser acceleration input and Laser response, respectively.

Figure 5.10 shows RMSE obtained using DVV analysis on response of the system excited by the external force with increasing frequency for three surface types (experiments No. 3, 2, and 10). The results show that RMSE for the measurements in principal direction of vibration, CH1 and LDV1, does not have a trend as surface roughness changes from good to poor. Actually, both analyses give very close values of RMSE for different surfaces, which could indicate that, the friction between the wheels of the SDOF car and the surface is low enough to be neglected. The trend of the results obtained with the two instruments is the same but they differ in the value. RMSE for 3D accelerometer range between 0.128 and 0.142, while for LDV they are between 0.168 and 0.172 for wood and sand paper, respectively. The values of RMSE for LDV data are slightly higher in comparison with 3D Accelerometer data. RMSE calculated for CH2 data (lateral direction to vibration) increases with decrease of surface roughness, the values are about two times higher than for the main direction of vibration, i.e. the system response is less linear than in the main direction and therefore more sensitive to change in surface roughness.

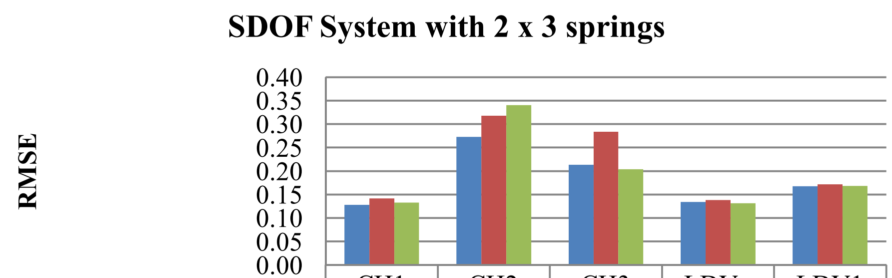

	CH1	CH2	CH3	LDVg	LDV1
plastic 2-4-6-8-10Hz	0.128	0.273	0.213	0.134	0.167
wood 2-4-6-8-10Hz	0.142	0.318	0.284	0.139	0.172
sand paper 2-4-6-8-10Hz	0.133	0.340	0.204	0.132	0.168

Figure 5.10 The effects of surface roughness on SDOF system (k = 0.378 N/mm) exposed to the increasing frequency external force.

Similar situation occurs when the excitation force is a sine sweep (Figure 5.11). The figure shows results for 6th, 4th, and 9th experiment. The RMSE obtained by DVV analysis of accelerometer data and LDV data in the direction of main vibration are very close for all surfaces tested.

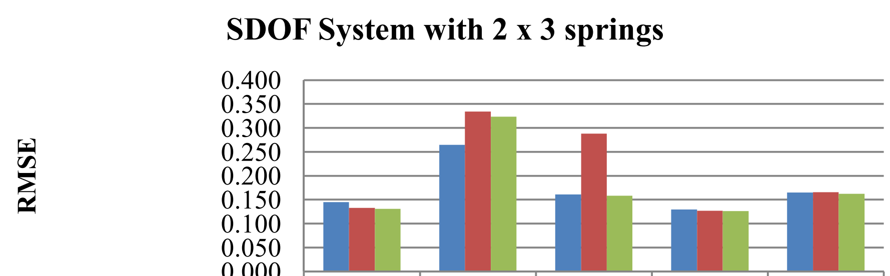

	CH1	CH2	CH3	LDVg	LDV1
plastic Sine Sweep	0.145	0.265	0.161	0.130	0.165
wood Sine Sweep	0.133	0.334	0.288	0.127	0.165
sand paper Sine Sweep	0.131	0.323	0.158	0.126	0.162

Figure 5.11 The effects of surface roughness on SDOF system (k = 0.378 N/mm) exposed to the sine sweep.

Here, the RMSE values for LDV are lower than in the case of harmonic loading and almost constant (approx. 0.165). This could be an indication of LDV sensitivity to load change and needs to be investigated further. The RMSE calculated on CH1 data decrease with road surface change from smooth to rough, ranging from 0.145 to 0.131. RMSE for the CH2 data are about twice higher than for CH1 data.

Figure 5.12 shows RMSE for experiments No. 7, 5, and 8 when SDOF car is exposed to white noise. The RMSE obtained for CH1 data are lower, while for LDV are higher than for two other types of loading. The results for three types of surfaces are similar for both measuring devices in the main direction, for CH1 RMSE is about 0.1 while for LDV it is 0.2. RMSE values for data measured by CH2 increase with decrease of the quality of surface; the values are almost four times greater than in the case of CH1.

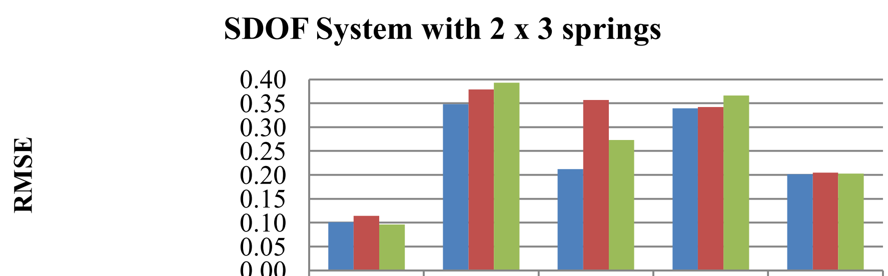

	CH1	CH2	CH3	LDVg	LDV1
plastic White Noise	0.101	0.348	0.212	0.340	0.201
wood White Noise	0.114	0.379	0.357	0.342	0.204
sand paper White Noise	0.096	0.393	0.273	0.366	0.203

Figure 5.12 The effects of surface roughness on SDOF system (k = 0.378 N/mm) exposed to the white noise.

5.5.2.2 System Stiffness and Surface Roughness

Figures 5.10 to 5.12 show the results for SDOF car connected to the supports on each side by three springs. The system stiffness is represented by equivalent stiffness of this springs, which is k = 0.378 N/mm. When two middle springs, one on each side of the car, are removed, the reduced stiffness of the SDOF car is k = 0.249 N/mm. In this subsection SDOF system is observed when moving over different surfaces in the case of reduced stiffness.

Figure 5.13 shows the RMSE for the system excited by external force with increasing frequency (experiments No. 17, 18, and 11). The experiments setup corresponds to experiments shown in Figure 5.10, except for reduced stiffness. The data for the plastic surface recorded by the accelerometer are unknown (lost). The RMSE of available CH1 data are higher while for LDV they are lower for reduced stiffness. The RMSE results are inconclusive, as it seems that CH1 acceleration data are deviated more from bisector line, while LDV data are closer to linear behaviour. This results in higher values of RMSE for CH1 data and lower values for LDV data. By closer inspection of the recorded data and their DVV plots (see Appendix B3) for car experiments 18 and 11, wood and sand paper surface, respectively, evident irregularities are observed. Actually the response output changes amplitude irregularly, having some high and low peaks, which is not the case with response given by experiment 17 (plastic surface). The variation in amplitude leads to higher vales of RMSE of CH1 data and lower for LDV data, than expected. This opens the question: did the change in stiffness combine with surface roughness nature lead to this phenomenon, or this is simply some external influence / force on the system? Hence, the next two cases were looked at with sine sweep and white noise excitation force, respectively.

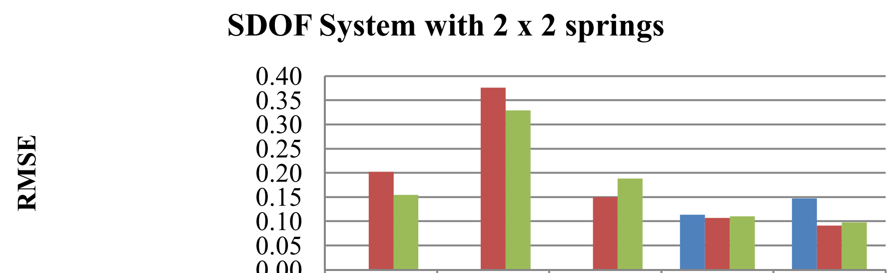

	CH1	CH2	CH3	LDVg	LDV1
plastic 2-4-6-8-10Hz				0.113	0.147
wood 2-4-6-8-10Hz	0.202	0.376	0.150	0.107	0.091
sand paper 2-4-6-8-10Hz	0.155	0.329	0.188	0.110	0.098

Figure 5.13 The effects of surface roughness on SDOF system (k = 0.249 N/mm) exposed to the increasing frequency external force.

Figure 5.14 shows RMSE for sine sweep loading (experiments 16, 20 and 13). The RMSE for principal direction of each instrument is very close in values for all surfaces; for CH1 between 0.14 and 0.15, and for LDV around 0.14. In comparison with the system with higher stiffness, the RMSE values for CH1 data are slightly higher, while for CH2 and LDV data are noticeably lower, especially for wood surface.

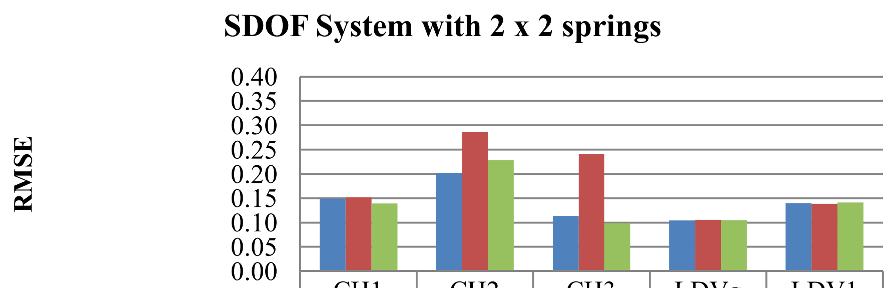

	CH1	CH2	CH3	LDVg	LDV1
plastic Sine Sweep	0.149	0.202	0.114	0.105	0.140
wood Sine Sweep	0.151	0.287	0.242	0.106	0.139
sand paper Sine Sweep	0.139	0.228	0.098	0.105	0.141

Figure 5.14 The effects of surface roughness on SDOF system (k = 0.249 N/mm) exposed to the sine sweep.

The RMSE for system exposed to white noise while moving on different surfaces (experiments 15, 19, and 14) are shown in Figure 5.15. The RMSE produced on recorded data by each instrument is very close in values for all surfaces, as previously observed; for CH1 they are between 0.106 and 0.114, and for LDV are between 0.170 and 0.178. The results of these experiments, in comparison with the ones where the stiffness of the mechanical model was higher, give slightly higher RMSE values for CH1, while they are lower for LDV data.

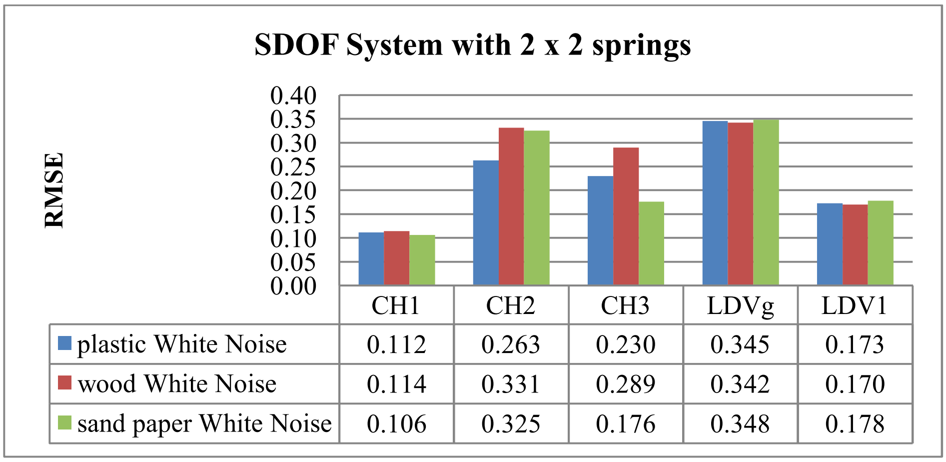

	CH1	CH2	CH3	LDVg	LDV1
plastic White Noise	0.112	0.263	0.230	0.345	0.173
wood White Noise	0.114	0.331	0.289	0.342	0.170
sand paper White Noise	0.106	0.325	0.176	0.348	0.178

Figure 5.15 The effects of surface roughness on SDOF system (k = 0.249 N/mm) exposed to the white noise.

The RMSE values for CH1, CH2, and LDV are summarised in Table 5.3. By closer observation it appears that the RMSE for CH2 and LDV could be indicator of the change in surface roughness. RMSE for CH1 data are insensitive to change in surface roughness. However, in this experiment setup, surface roughness differences are hard to detect using DVV method on recorded data by both instruments. Hence, the surface roughness could be ignored; instead the results produce the idea of the RMSE range for given load and system stiffness.

Table 5.3 The RMSE of 3D Accelerometer and LDV for SDOF system stiffness change.

RMSE		**3D Accelerometer CH1**		**3D Accelerometer CH1**		**Laser Doppler Vibrometer LDV1**	
LOAD	**STIFFNESS (N/mm) SURFACE**	**0.378**	**0.249**	**0.378**	**0.249**	**0.378**	**0.249**
2 – 4 – 6 – 8 – 10 Hz	Plastic	0.128	No data	0.273	No data	0.168	0.147
	Wood	0.142	0.202	0.318	0.376	0.172	0.091
	Sand paper	0.133	0.155	0.340	0.329	0.168	0.098
Sine Sweep	Plastic	0.145	0.149	0.265	0.202	0.165	0.140
	Wood	0.133	0.152	0.334	0.287	0.165	0.139
	Sand paper	0.131	0.139	0.323	0.228	0.162	0.141
White Noise	Plastic	0.102	0.112	0.348	0.263	0.201	0.173
	Wood	0.114	0.114	0.379	0.331	0.205	0.170
	Sand paper	0.096	0.106	0.393	0.325	0.203	0.178

5.5.2.3 Excitation force and system stiffness

The SDOF car was exposed to three different external force types:

1) Harmonic load with increasing frequency 2 – 4 – 6 – 8 – 10 Hz,
2) Sine Sweep (gradually varying the frequency of a sinusoidal signal) with a sweep from 3 to 5 Hz,
3) White Noise.

In this section the influence of change in the type of loading is explored.

Plastic surface

The responses of the SDOF system on the plastic surface, exposed to the three types of loads are analysed. The results are shown in Figure 5.16 and 5.17 for model of the SDOF car with six springs (k = 0.378 N/mm) and four springs (k = 0.249 N/mm), respectively.

Data for the harmonic loading for reduced stiffness are missing. The RMSE for CH1 differ for each case of loading, being greatest for sine sweep, 0.145, and smallest for white noise, 0.101. These values increase to 0.149 for sine sweep and to 0.112 for white noise in case of reduced stiffness. On the other hand, the RMSE calculated on CH2 and LDV recorded data are the highest for white noise loading, i.e. 0.348 and 0.201 for higher stiffness, reducing to 0.263 and 0.173 for lowered stiffness. The RMSE for CH2 for the harmonic and sine sweep loading are very close, 0.273 and 0.265 for higher stiffness. The same observation applies to LDV recorded data, i.e. 0.168 and 0.165 for harmonic and sine sweep loading, respectively, for higher stiffness of the model. While calculated RMSE on CH1 data increase, in the case of CH2 and LDV data it decreases. This decrease of RMSE, for reduced stiffness, in case of CH2 and LDV data is greater than increase in the case of CH1 data.

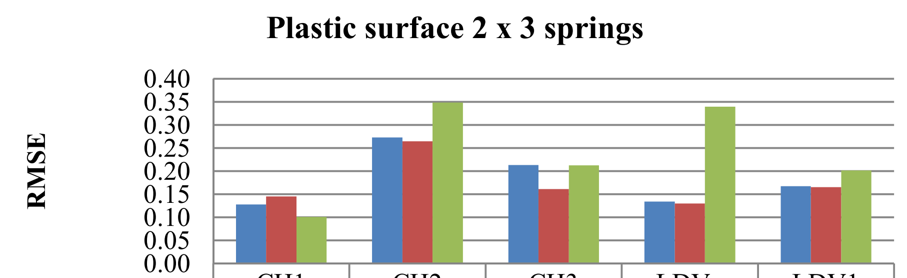

	CH1	CH2	CH3	LDVg	LDV1
2-4-6-8-10Hz	0.128	0.273	0.213	0.134	0.167
Sine sweep	0.145	0.265	0.161	0.130	0.165
White Noise	0.101	0.348	0.212	0.340	0.201

Figure 5.16 The effects of excitation force change on the SDOF system on plastic surface with k = 0.378 N/mm.

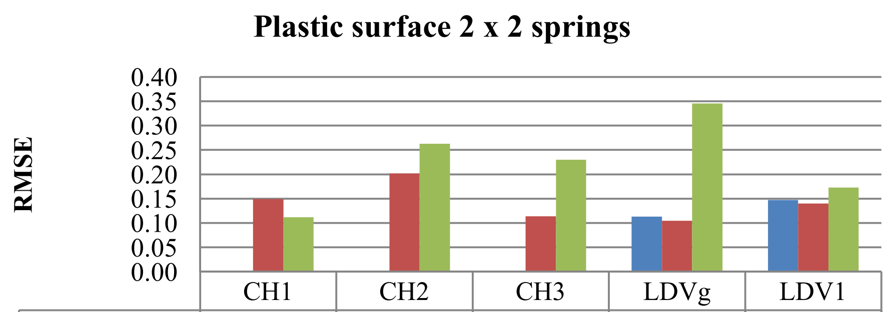

	CH1	CH2	CH3	LDVg	LDV1
2-4-6-8-10Hz				0.113	0.147
Sine sweep	0.149	0.202	0.114	0.105	0.140
White Noise	0.112	0.263	0.230	0.345	0.173

Figure 5.17 The effects of excitation force change on the SDOF system on plastic surface with k = 0.249 N/mm.

Wood surface

Figures 5.18 and 5.19 shows the RMSE results for SDOF system, with higher and lower stiffness, on wood surface exposed to three types of loads.

The results for the system with higher stiffness (see Figure 5.18) show that the effects of change in the input force nature are successfully recorded by LDV and CH2. Here, as for plastic surface, the differences in RMSE for the harmonic and sine sweep loading are small. However the difference in values increases with the change of surface from plastic to wood. The results for CH1 show that calculated RMSE for 2 Hz harmonic and white noise external force differ negligibly. Figure 5.19 demonstrates that 3D Accelerometer and LDV successfully record the change in external force when system stiffness is reduced. The values for CH1 decrease (0.202, 0.152, and 0.114) while for LDV they are increase (0.091, 0.139 and 0.170) with frequency, sine sweep and white noise force, respectively.

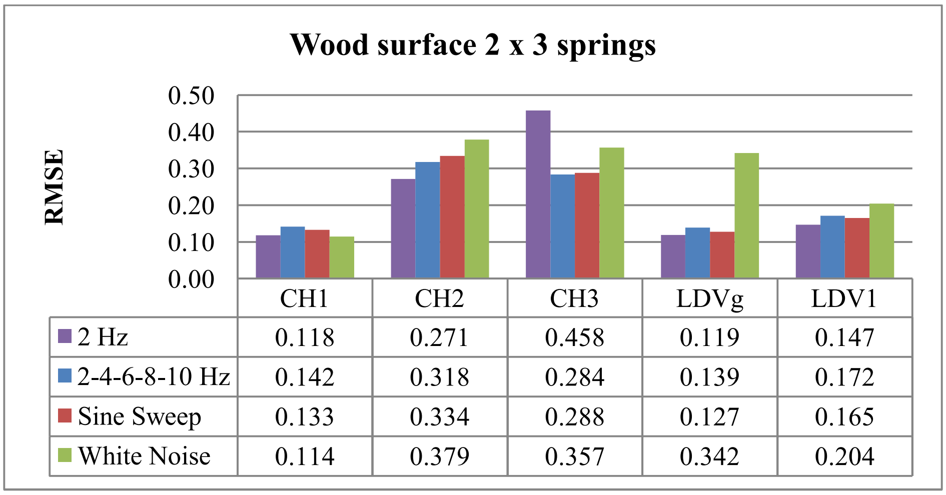

	CH1	CH2	CH3	LDVg	LDV1
2 Hz	0.118	0.271	0.458	0.119	0.147
2-4-6-8-10 Hz	0.142	0.318	0.284	0.139	0.172
Sine Sweep	0.133	0.334	0.288	0.127	0.165
White Noise	0.114	0.379	0.357	0.342	0.204

Figure 5.18 The effects of excitation force change on the SDOF system on wood surface with k = 0.378 N/mm.

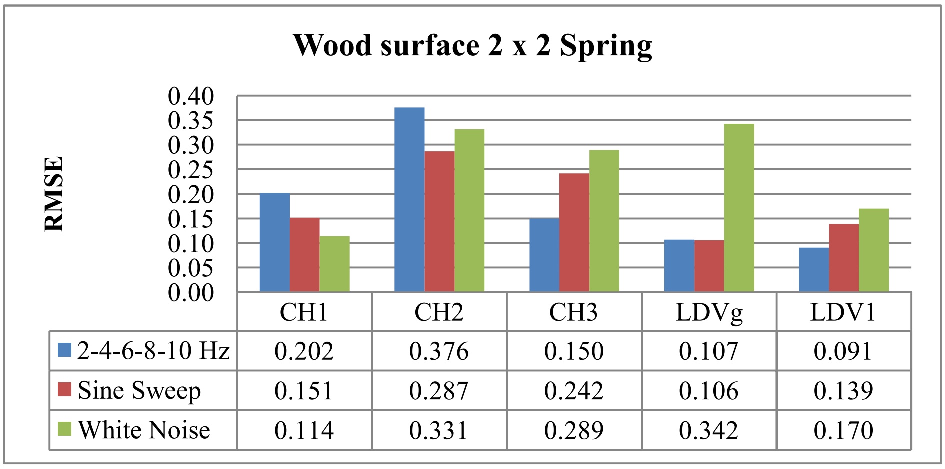

	CH1	CH2	CH3	LDVg	LDV1
2-4-6-8-10 Hz	0.202	0.376	0.150	0.107	0.091
Sine Sweep	0.151	0.287	0.242	0.106	0.139
White Noise	0.114	0.331	0.289	0.342	0.170

Figure 5. 19Figure 1: The effects of excitation force change on the SDOF system on wood surface with k = 0.249 N/mm.

Sand paper surface

Figure 5.20 shows results of three experiments performed on SDOF system moving over sand paper surface exposed to different forces. The RMSE calculated on CH1 data for harmonic and sine sweep force differ negligibly (0.133 vs. 0.131, respectively), while for white noise loading the RMSE is lower, (0.096). The results for CH2 and LDV data also show that the RMSE for harmonic and sine sweep loading are close, but the values are greater than one calculated for CH1 data. On the other hand, the RMSE of the response to white noise is greater, i.e. 0.325 and 0.178 for CH2 and LDV respectively.

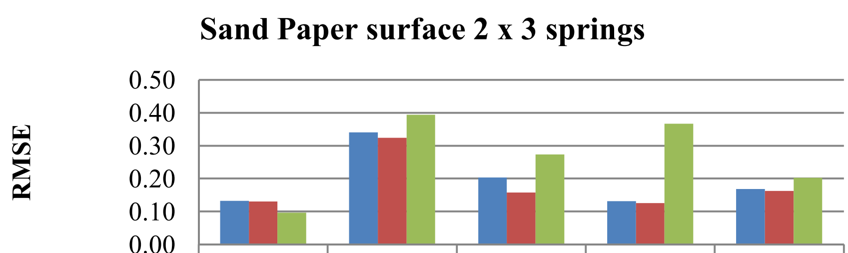

	CH1	CH2	CH3	LDVg	LDV1
2-4-6-8-10Hz	0.133	0.340	0.204	0.132	0.168
Sine Sweep	0.131	0.323	0.158	0.126	0.162
White Noise	0.096	0.393	0.273	0.366	0.203

Figure 5.20 The effects of excitation force change on the SDOF system on sand paper surface with k = 0.378 N/mm.

Results of experiment with reduced stiffness are shown in Figure 5.21. The RMSE for this system are higher for CH1 and lower for CH2 and LDV recorded data in comparison with stiffer system. It is interesting to point out that the trend in RMSE, for loadings applied, for CH1, CH2 and LDV are the same as for the model of the same stiffness moving on wood surface. However values of RMSE for CH1 are lower, while for CH2 and LDV are higher than those for wood surface.

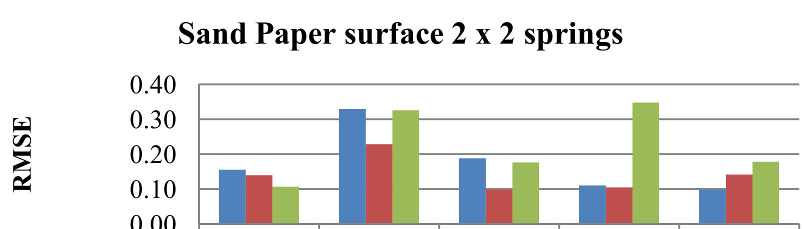

	CH1	CH2	CH3	LDVg	LDV1
2-4-6-8-10Hz	0.155	0.329	0.188	0.110	0.098
Sine Sweep	0.139	0.228	0.098	0.105	0.141
White Noise	0.106	0.325	0.176	0.348	0.178

Figure 5.21 The effects of excitation force change on the SDOF system on sand paper surface with k = 0.249 N/mm.

Table 5.4 summarises the RMSE values for vibration measured in principal direction. The extreme RMSE values in the case of white noise loading, for each of the stiffness, are quite distinctive for measurements of the both instruments. As observed before, harmonic and sine sweep loading give similar results.

Table 5.4 The range of the RMSE values obtained on system response DVV analysed data

		2 – 4 – 6 – 8 – 10 Hz		Sine Sweep		White Noise	
		k = 0.378 N/mm	k = 0.249 N/mm	k = 0.378 N/mm	k = 0.249 N/mm	k = 0.378 N/mm	k = 0.249 N/mm
CH1	min	0.123	0.155*	0.131	0.139	0.096	0.106
	max	0.142	0.202*	0.145	0.152	0.114	0.112
LDV	min	0.168	0.091*	0.165	0.139	0.213	0.170
	max	0.172	0.147	0.162	0.141	0.204	0.178

*Irregularities in measurements observed.

High frequency load

When high frequency load excites the SDOF bilinear car, DVV analysis of the system response signal shows high nonlinearity of collected data (see Appendix B2) in comparison with what was presented for the loads in Table 5.4. The values of RMSE for CH1 and LDV are 0.339 and 0.229, respectively.

Sudden stiffness change

This section explores possibility to detect sudden stiffness change by using DVV method in analysing system response to external force. The sudden change of stiffness was simulated by introducing the failure of a spring at a certain instant in time during a given period of forced vibration. The forced vibration on the SDOF system was in the form of a white noise input. The stiffness of the system at beginning of the experiment was 0.378 N/mm. The first spring got detached after 13 sec, which reduced system stiffness to k = 0.303 N/mm, and the second one after 38 sec, reducing stiffness further to k = 0.249 N/mm.

Figure 5.22 compares RMSE values for response of SDOF car moving over wooden surface, excited with white noise, having different stiffness (experiments 4, 20, and 21 in Table 5.2). The results for CH1 and LDV show the same pattern, i.e. the RMSE values for the system that suffered sudden change of stiffness are lower than for the systems with constant stiffness. The reason for this could be the fact that system goes through change from a relatively linear system to a strongly bilinear system with some lateral effects for a certain period of time and the returns of the system to a relatively linear system, averaged over time. The DVV method can be used to determine occurrence of sudden stiffness change but not the exact time when the change happens.

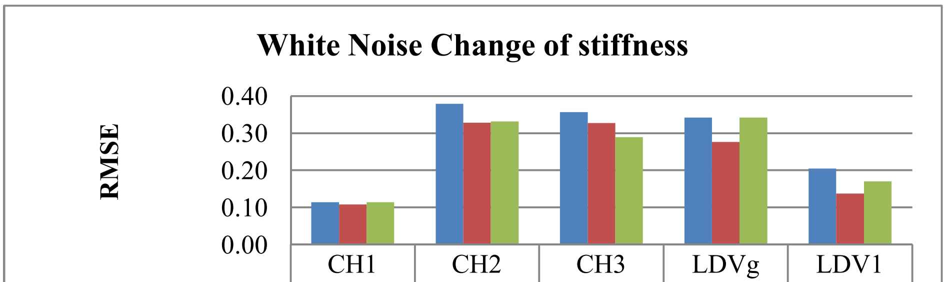

	CH1	CH2	CH3	LDVg	LDV1
wood 2 x 3	0.114	0.379	0.357	0.342	0.204
wood 2 x 3 to 2 x 2	0.108	0.328	0.327	0.276	0.137
wood 2 x 2	0.114	0.331	0.289	0.342	0.170

Figure 5.22 The comparison of SDOF systems with different stiffness.

5.5.3 Single Degree of Freedom Car Experiment: Conclusions

- Only response of the system to excitation measurements should be analysed. Measurements obtained while system is in equilibrium can influence DVV results, i.e. calculated RMSE increases.
- The closer observation of response data is needed prior to their DVV analysis, as irregularities in the response signal can lead to the unexpectedly

higher or lower values of RMSE. These irregularities occur due to sensitivity of 3D accelerometer and LDV to changes in experimental environment, i.e. existence of additional excitation source. Hence, pre-filtering of data in order to perform DVV analysis might be needed.

- 1st and 2nd approaches in determining embedding parameter and time lag prove to have limitations when analysing large sets of data. Therefore, when applying these two methods, the number of data points should be less than 9000 (see 5.5.1.1 Optimal Parameters).

- 3rd approach (embedding parameter m=3 and time lag τ=1) show the best efficiency and consistency in interpretation of DVV method results for observed system.

- The RMSE calculated using measurements data in the main direction of vibration obtained by 3D Accelerometer and Laser Doppler Vibrometer are different in value and often have different trend. The recording parameters within 3D Accelerometer and LDV were fixed; for this reason different results can be attributed to different nature of data collected (acceleration and displacement), but also the sensitivity of instruments to noise.

- The Channel 2 accelerometer data (lateral direction to vibration, horizontal plane) have values multiple times higher than for the main direction of vibration, i.e. the system response is less linear than in the main direction. The DVV analysis of Channel 2 data shows that some changes could be detected observing vibrations in lateral direction.

- The difference in calculated RMSE on DVV analysed response data is hard to detect when surface roughness changes. The surrogate data deviation from bisector line in DVV analysis shows almost same nonlinearity of data for different surfaces. Therefore, for this setup of the experiment, the friction between the wheels of the SDOF car and the surface is low enough to be ignored. However, for the harmonic and white noise load on the SDOF system with higher stiffness it seems that 3D Accelerometer Channel 2 is able to pick up the change in surface roughness. Hence, the nonlinearity of data increases as surface roughness changes from good to poor.

- The switch in the stiffness of the observed system is recorded by both instruments. In the case of 3D Accelerometer CH1 the difference in RMSE is small and increases, while for CH2 and LDV the difference in RMSE is greater and decreases with decrease in system stiffness. Therefore the change in RMSE can be used to identify the change in system stiffness.

- The occurrence of sudden stiffness change in SDOF system can be detected by the DVV method, but not the time or extent of change.

- The difference in the nature of the external force is recorded by both instruments. There are only few exceptions. For example, the difference in RMSE values is negligible for harmonic and sine sweep loading in the case of a plastic surface for response recorded by LDV regardless of the system stiffness. The same is observed for CH1 and LDV data in the case where surface is sand paper, but only for higher stiffness of the studied model. In general calculated RMSE for CH1 are the highest for harmonic load with changing frequency and the lowest for white noise load, while for LDV opposite is the case: the RMSE are the highest for white noise load, and the lowest for harmonic load.

- The difference in loading is best represented in cases when the surface is wood or sand paper while the observed model has lower stiffness. Therefore, the combination of surface roughness and system stiffness could influence the success of DVV model in recognition of the type of excitation force.

- Increase in load frequency results in the response signal extreme non linearity. This phenomenon is successfully recorded by both instruments.

5.6 Wind Turbine Blade Experiment

5.6.1 Methodology and Experiment Set Up

A 1.4 m long Wind Turbine Blade (WTB) employed for the test is made from a polypropylene/glass fibre composite with a weight of 1.7 kg. The instrumentation attachment points are prepared by scoring the surface with 40 grit sandpaper, then cleaned with alcohol. This exposed the glass fibre within the matrix to which a two-part epoxy adhesive readily adhered. The monitoring points are shown in the Figure 5.23.

The strains were monitored at points 1, 2, 3, and 4 at 415mm, 835mm, 1095mm, and 1095mm from the tip of WTB, respectively. The blade was fixed to a shake table using a purpose built clamp at the root to simulate fixing at a nacelle. Base excitations were applied using a uniaxial LDS electrodynamic shaker to which the desired excitation signal was input via an amplifier. The dynamic response of a WTB was measured using two wireless instruments, MicroStrain G-Link Wireless Accelerometer Sensor and Polytec RSV-150 Remote Sensing Vibrometer (see Chapter 3 for details). G-Link, located at 235mm from the blade tip, collected acceleration data in Cartesian coordinates. The Cartesian directions are indicated in Figure 5.23. The accelerometer digital data is passed to the onboard microprocessor, processed with an embedded algorithm, and in turn saved to the 2MB onboard cash memory for later download. The data are recorded at 617 samples/second. LDV focus points varied throughout experiments (Figure 5.23). The list with the description of experiments performed is given in Table 5.5.

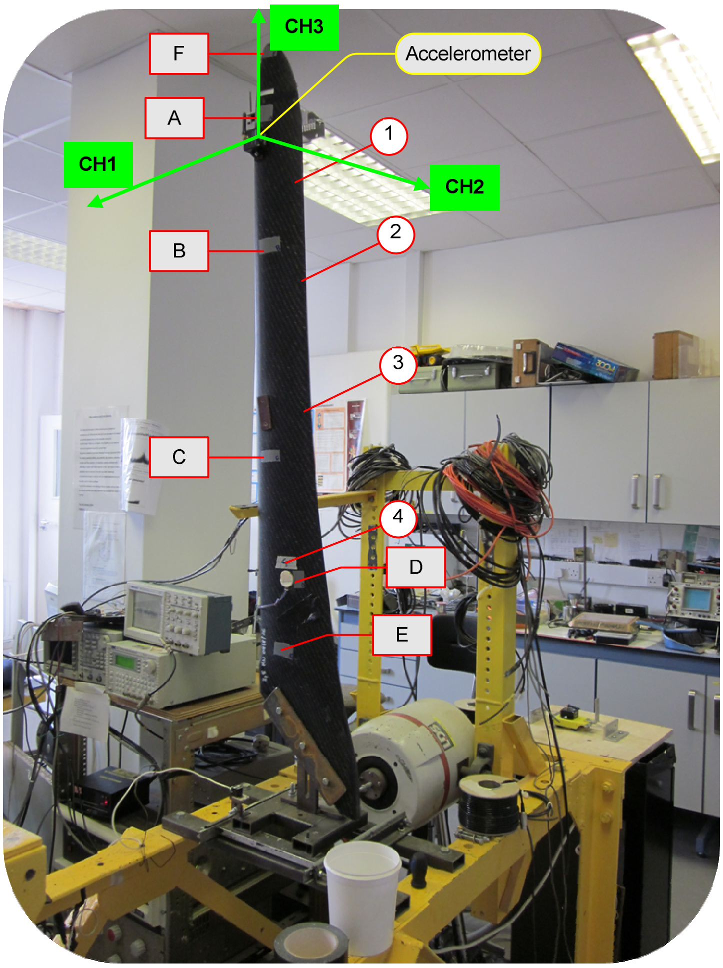

Figure 5.23 Wind Turbine Blade experiment setup. Letters A to F indicate positions of the silver tape used for locating vibrometer targets while numbers 1 to 4 mark locations of strain gauges.

The dynamic response of the WTB to different type of excitation force alongside with WTB strain at four different locations was measured. Three types of excitation force applied are: harmonic resonance, sine sweep, and white noise. The harmonic force is applied so that the frequency increase in following manner: 2.0 – 2.5 – 3.0 – 3.5 – 4.0 – 4.2 – 4.3 – 4.4 – 4.5 – 4.6 – 5.0 – 5.5 – 6.0 – 6.5 – 7.0 Hz. The sine sweep tests, by gradually varying the frequency of a sinusoidal signal, were conducted with a sweep from 3 to 5 Hz.

The experiments were repeated four times, for each type of excitation force, while LDV target changed, focusing on accelerometer and points A, C and E. Prior to the main experiments the instruments were checked and calibrated (initial experiments). The natural frequency of WTB is 4.4Hz.

Table 5.5 The list of the WTB experiments performed.

	No	Location of LDV target	Loading
Initial experiments	1	Angle of incidence 8 degree	Harmonic resonance; frequency 4.38 Hz
	2	Angle of incidence 8 degree	Harmonic resonance; frequency 4.38 Hz
	3	Focus at the accelerometer	Harmonic resonance; frequency 4.38 Hz
	4	Focus at the accelerometer	with knuckles (no base movement) best result
	5	Focus at the accelerometer	Harmonic resonance 4.4 Hz
	6	Focus at the accelerometer	Harmonic resonance 2.0 Hz, 2.5 Hz, 3.0 Hz, 3.5 Hz, 4.0 Hz, 4.2 Hz, 4.3 Hz, 4.4 Hz, 4.5 Hz, 4.6 Hz, 5.0 Hz, 5.5 Hz, 6.0 Hz, 6.5 Hz, 7.0 Hz
	7	Focus at the accelerometer	Sine sweep 2.0 Hz, 6.0 Hz 60 sec
	8	Focus at the accelerometer	White Noise
	9	Focus at top, point A	White noise 4.365 Hz at the peak
	10	Focus at top, point A	Sine Sweep 2.0 Hz, 6.0 Hz 60 sec
	11	Focus at top, point A	Harmonic resonance 2.0 Hz, 2.5 Hz, 3.0 Hz, 3.5 Hz, 4.0 Hz, 4.2 Hz, 4.3 Hz, 4.4 Hz, 4.5 Hz, 4.6 Hz, 5.0 Hz, 5.5 Hz, 6.0 Hz, 6.5 Hz, 7.0 Hz
	12	Focus at mid, point C	Harmonic resonance 2.0 Hz, 2.5 Hz, 3.0 Hz, 3.5 Hz, 4.0 Hz, 4.2 Hz, 4.3 Hz, 4.4 Hz, 4.5 Hz, 4.6 Hz, 5.0 Hz, 5.5 Hz, 6.0 Hz, 6.5 Hz, 7.0 Hz
	13	Focus at mid, point C	Sine Sweep 2.0 Hz, 6.0 Hz 60 sec
	14	Focus at mid, point C	White noise 4.336 Hz at the peak (next 23Hz)
	15	Focus at bottom, point E	White noise 4.336 Hz at the peak (next 23Hz)
	16	Focus at bottom, point E	Sine Sweep 2.0 Hz, 6.0 Hz 60 sec
	17	Focus at bottom, point E	Harmonic resonance 2.0 Hz, 2.5 Hz, 3.0 Hz, 3.5 Hz, 4.0 Hz, 4.2 Hz, 4.3 Hz, 4.4 Hz, 4.5 Hz, 4.6 Hz, 5.0 Hz, 5.5 Hz, 6.0 Hz, 6.5 Hz, 7.0 Hz

5.6.2 DVV Analysis

The example of acceleration responses to external excitation applied, in this case harmonic force are shown in Figure 5.24 – 5.26 for 3D accelerometer, LDV and, strain gauges, respectively. The recorded responses for all WTB experiments are shown in Appendix B3.

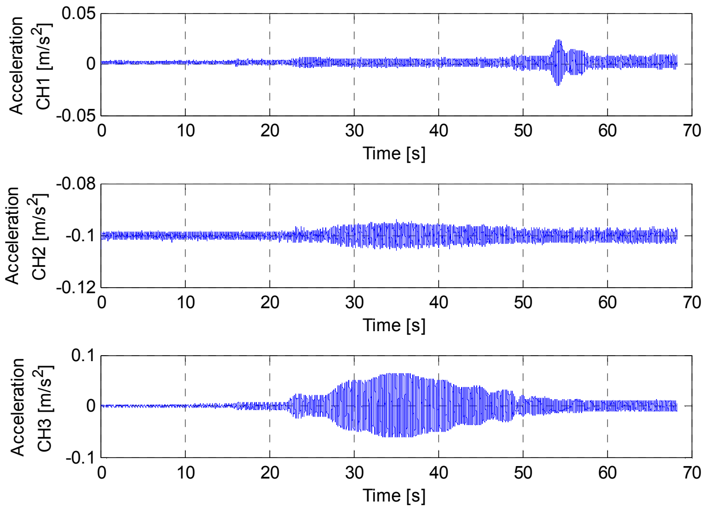

Figure 5.24 An example of 3D accelerometer measurements for system excited by harmonic force.

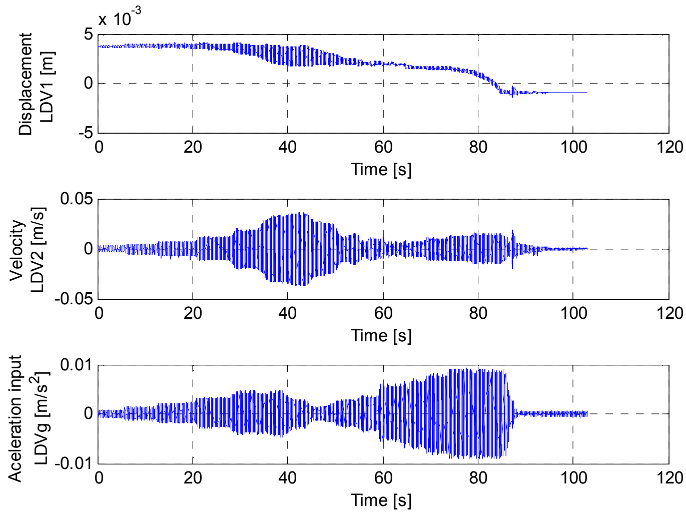

Figure 5.25 An example of LDV (focusing strain gauge 4) measurements for system excited by harmonic force.

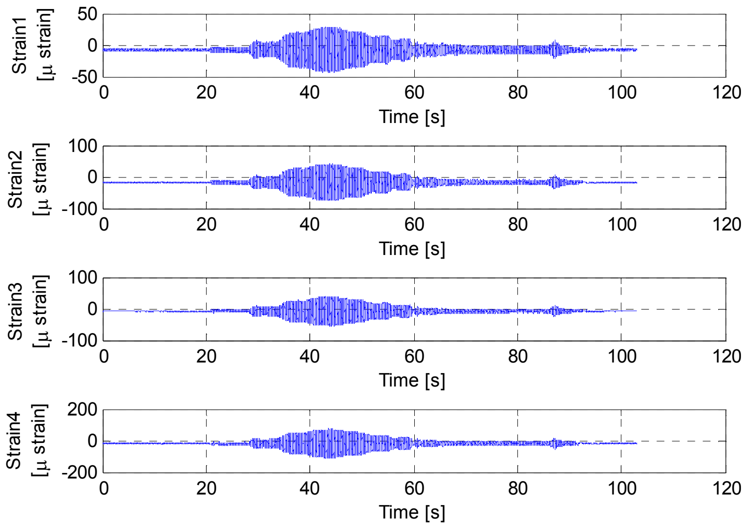

Figure 5.26 An example of strain gauge measurements at four different locations along WTB excited by harmonic force.

The plots show all recorded data, i.e. system measurements prior, during and after excitation. Only measurements in between two equilibriums are used for DVV analysis, as it was done for the SDOF car experiment.

DVV is performed on recorded data in order to examine and compare their linearity or nonlinearity. The results of DVV analysis, employing three different approaches when determining embedding parameter, are shown in Appendix B4.

5.6.2.1 Optimal Parameters

The sets of recorded data were in most cases too long to be analysed by the 1^{st} approach as a whole. Matlab memory puts restriction on analysis of such large set of data. The attempt to find optimal embedding parameter using the 1^{st} approach was done by sectioning response signal. The obtained embedding parameters prove to give visibly different values of RMSE of response signal section and the whole signal when DVV is analysed. The difference in RMSE increases when embedding parameter is greater than 5 and time lag greater than 1. The example of sectioning valid measured data is given in Appendix B4, Example 6A – C. It is observed that

RMSE changes are representative of changes within the signal but can not be used to compare two or more different responses of the system. The method proves to be time consuming and unreliable for the large sets of data. Namely it is hard to observe the time series structure in phase space as a whole, and therefore impossible to determine its clear minimum in order to find adequate parameters, m and τ, to represent the response signal. Similar applies when implementing 2nd approach, i.e. long set of response data are taking too long to be processed and obtained values of embedding parameter are in the most cases out of reasonable range $m \in [3, 10]$, Gautama et al. [174]. When comparing the results obtained by analysis of one set of data by all three methods, the trend tends to be similar, i.e. the values of RMSE for the measured in general data keep their relative relationship. By closer inspection of the results obtained by 2nd and 3rd approach the calculated RMSE are similar or even identical when embedding parameter chosen is less than 10. Therefore it is quite adequate to use the 3rd approach, where for convenience time lag was set to unity, while embedding parameter was set to 3. The results of DVV analysis obtained when using 3rd approach are discussed here while the results obtained when analysing data using all three approaches are given in Appendix B4.

DVV analysis is performed on all valid measured data.

5.6.3 Results and Discussion

The results shown are for 3D accelerometer, Laser Doppler Vibrometer and strain gauges. The abbreviations appearing in further text and in the figures below are indicating results related to measurements:

- CH1 – acceleration measured in the main direction of vibration,
- CH2 – acceleration measured laterally to the main direction of vibration (horizontal plane),
- CH3 – acceleration measured laterally to the main direction of vibration (vertical plane),
- LDVg –Laser acceleration input,
- LDV1 – displacement recorded by LDV,

- LDV2 – velocity generated by LDV,
- Strain 1 – strain gauge measurement at 415mm (top strain gauge),
- Strain 2 – strain gauge measurement at 835mm,
- Strain 3 – strain gauge measurement at 1095mm, and
- Strain 4 – strain gauge measurement at 1095mm (bottom strain gauge)

5.6.3.1 Initial Experiments

Initial experiments are group of experiments (No 1 to 5 in Table 5.5) carried out in order to set up the LDV equipment. The results of DVV analysis, RMSE of deviation from bisector line, are shown in Figure 5.27.

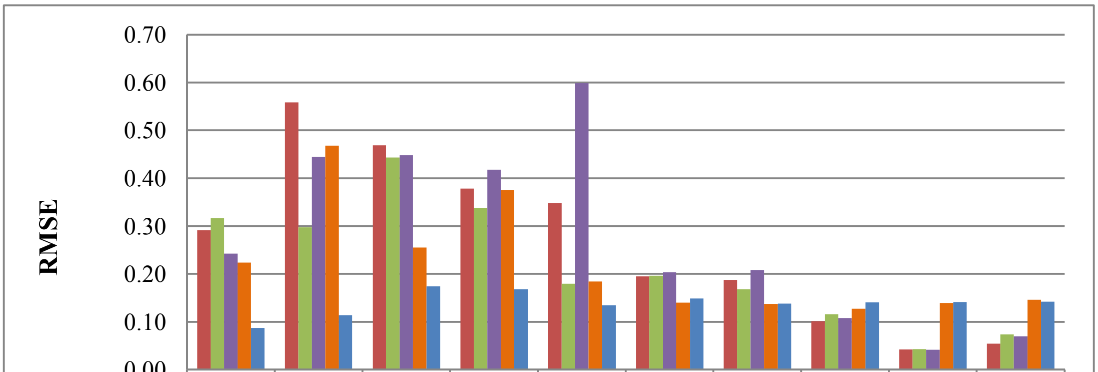

	CH1	CH2	CH3	LDVg	LDV1	LDV2	Strain 1	Strain 2	Strain 3	Strain 4
Initial exp. 1	0.292	0.558	0.469	0.378	0.348	0.195	0.188	0.101	0.042	0.054
Initial exp. 2	0.317	0.297	0.444	0.338	0.179	0.196	0.168	0.116	0.043	0.074
Initial exp. 3	0.243	0.445	0.448	0.418	0.598	0.204	0.208	0.108	0.041	0.070
Initial exp. 4	0.224	0.468	0.255	0.375	0.184	0.140	0.138	0.127	0.139	0.146
Initial exp. 5	0.087	0.114	0.174	0.168	0.134	0.149	0.138	0.141	0.142	0.142

Figure 5.27 Initial Wind Turbine Blade experiments.

Experiments 1 and 2 are the same; the system is moved from equilibrium position by harmonic force with 4.38Hz frequency. The angle of incidence of LDV is 8 degrees. The results for 3D accelerometer show that responses monitored by CH1 and CH3 give close values of RMSE for two experiments. The same is observed for LDVg, LDV2, and strain gauges measurements. The same appear to be the case when analysing data of strain gauges. The abnormality within LDV1 raw data (experiment 2) is reflected onto calculated RMSE for these two measurements.

In experiment 3 the focus of the LDV is 3D accelerometer located at the top of the WTB.The system is excited by harmonic force frequency 4.38 Hz. The RMSE in the case of CH1 decreases noticeably; the reason for this is the length of available valid data. LDV1 shows large increase in RMSE as there are irregularities in the response signal recorded, while RMSE calculated on LDV2 are close in values for all three measurements. This shows that DVV method (RMSE) is sensitive to any abnormalities that occur in the recorded signal. Strain gauges give results similar to the ones obtained in the first two experiments.

Experiment 4 represents results of the measurement when there is no base (shaker) excitation, as in previous tests, but the WTB is excited by impact force (knock). The results are close to the experiment 3 in the case of CH1 and CH2, while noticeable lower for CH3 data. LDV1 result is comparable with 2^{nd} experiment, but for LDV2 decreases in comparison with previous experiments. There is also noticeable change in RMSE values calculated for data collected by strain gauges. While in the previous experiments RMSE for data collected with the strain gauges had the same trend, in this experiment the results are almost constant (see Figure 5.28).

In Experiment 5, the WTB is excited by harmonic resonance force with frequency 4.4 Hz. The values of RMSE calculated for all recorded responses of accelerometer and LDV1 decrease significantly when compared with previous experiments. In previous experiments the damping of the vibration contributed to the higher values of RMSE, which is in agreement with what was observed earlier for reference model. On the other hand, RMSE calculated for data collected by strain gauges are almost constant, e.g. show the same degree of nonlinearity (see Figure 5.28).

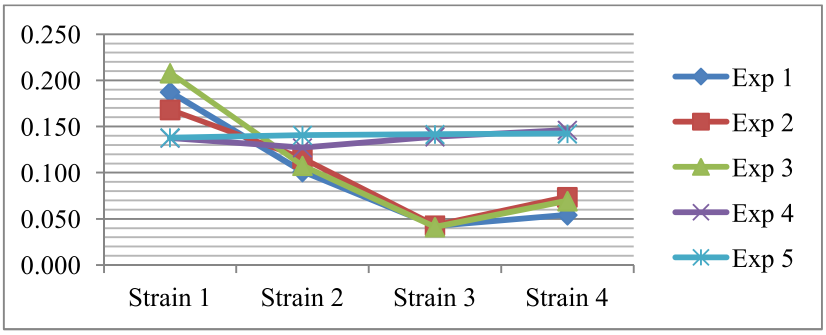

Figure 5.28 The measure of linearity of strain gauges recorded signals.

5.6.3.2 Focus of LDV

Focus at Accelerometer

The results of DVV analysis, in the form of calculated RMSE on response data, for WTB exposed to different loads when focus of the LDV is the accelerometer are shown in Figure 5.29. The RMSE for CH1 and CH3 of accelerometer are showing maximum values for sine sweep (0.318 and 0.272) and minimum values for white noise (0.069 and 0.092). The RMSE obtained on LDV1 data show the same trend, maximum is 0.171 for sine sweep and minimum 0.127 for white noise. The values for LDV2 are the highest for white noise and lowest for harmonic. The strain gauges measurements linearity will be discussed later in the text.

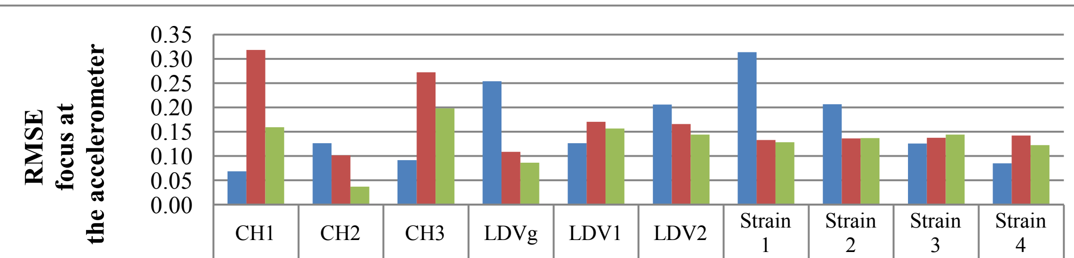

	CH1	CH2	CH3	LDVg	LDV1	LDV2	Strain 1	Strain 2	Strain 3	Strain 4
White Noise	0.069	0.126	0.092	0.254	0.127	0.206	0.313	0.206	0.126	0.085
Sine Sweep	0.318	0.102	0.272	0.109	0.171	0.166	0.133	0.136	0.137	0.142
Harmonic resonance	0.160	0.037	0.198	0.086	0.157	0.144	0.128	0.137	0.144	0.123

Figure 5. 29 Comparison of WTB results when exposed to different forces (LDV focused at the accelerometer).

Focus at WTB Top

Figure 5.30 shows RMSE results of DVV analysis on response data collected by the instruments when system is exposed to different forces, when LDV target WTB top. The RMSE of CH1 and CH3 data show the same trend as in previous experiments, with the maximum value for sine sweep (0.261 and 0.3) and minimum value for white noise (0.07 and 0.095). LDV1 and LDV2 results keep the same trend as in Figure 5.30. LDV1 shows more nonlinearity for sine sweep loading response than for the other two types of excitation. RMSE for LDV2 shows more nonlinearity of the response signal when system is excited with white noise than with the other type of loading.

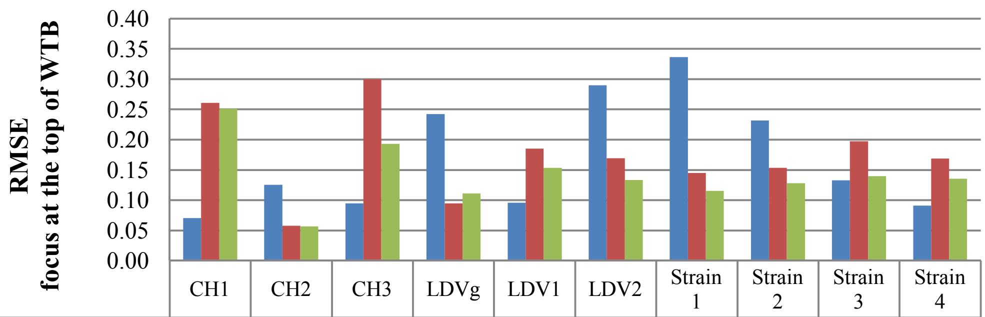

	CH1	CH2	CH3	LDVg	LDV1	LDV2	Strain 1	Strain 2	Strain 3	Strain 4
White Noise	0.070	0.126	0.095	0.242	0.096	0.290	0.336	0.232	0.133	0.091
Sine Sweep	0.261	0.058	0.300	0.095	0.185	0.170	0.145	0.153	0.198	0.169
Harmonic resonance	0.251	0.057	0.193	0.111	0.153	0.133	0.115	0.128	0.140	0.135

Figure 5.30 Comparison of WTB results when exposed to different forces (LDV focused at the top of WTB).

Focus at WTB Middle Section

The RMSE results of DVV analysis on response data when WTB is exposed to different loads, with LDV focused on its mid section are shown in Figure 5.31. Here, as in previous examples, the relative pattern of the response nonlinearity is kept. Still there is visible discrepancy in RMSE of acceleration data when system is exposed to harmonic force in comparison with previous calculation. This is due to length of recorded data, i.e. total response is not recorded. The irregularity in LDV recorded data when WTB is exposed to sine sweep is reflected in calculated RMSE values, resulting in much greater nonlinearity of the signal from what was observed in previous examples.

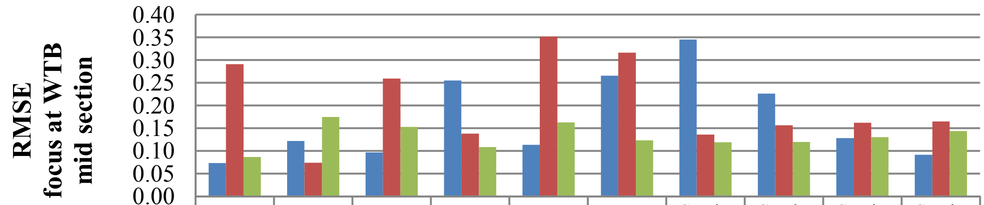

	CH1	CH2	CH3	LDVg	LDV1	LDV2	Strain 1	Strain 2	Strain 3	Strain 4
White Noise	0.073	0.122	0.096	0.255	0.113	0.266	0.345	0.226	0.128	0.091
Sine Sweep	0.291	0.074	0.259	0.138	0.351	0.316	0.136	0.156	0.162	0.164
Harmonic resonance	0.087	0.175	0.152	0.108	0.162	0.123	0.119	0.119	0.130	0.143

Figure 5.31 Comparison of WTB results when exposed to different forces (LDV focused at the WTB mid section).

Focus at WTB Base

Figure 5.32 shows the results of RMSE calculated on DVV analysed responses of WTB excited by different forces, while LDV focuses at the base (point E see Figure 5.23). The trend of nonlinearities represented by RMSE is the same to the Figure 5.30 except that the nonlinearity of the signals recorded by all instruments decreases.

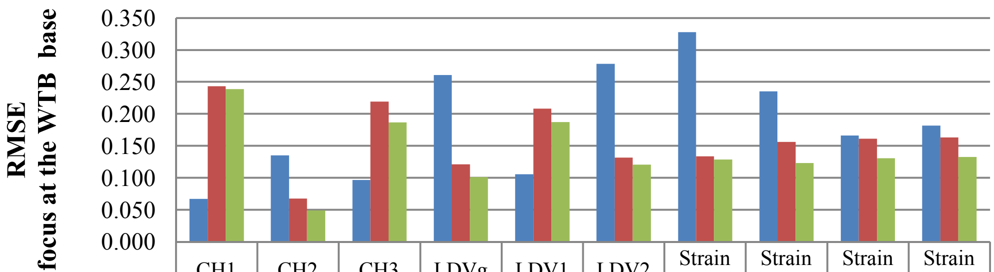

	CH1	CH2	CH3	LDVg	LDV1	LDV2	Strain 1	Strain 2	Strain 3	Strain 4
White Noise	0.067	0.135	0.096	0.261	0.106	0.278	0.328	0.235	0.166	0.181
Sine Sweep	0.243	0.067	0.219	0.121	0.208	0.132	0.134	0.156	0.161	0.163
Harmonic resonance	0.239	0.049	0.187	0.101	0.187	0.121	0.128	0.123	0.130	0.132

Figure 5.32 Comparison of WTB results when exposed to different forces (LDV focused at the WTB base).

In general, displacement data show the highs nonlinearity when system is exposed to sine sweep and the smallest nonlinearity for white noise loading, regardless of the LDV focus target (Figure 5.33). The velocity shows the greatest nonlinearity when WTB is excited by white noise, and thee smallest for harmonic loading (Figure 5.34).

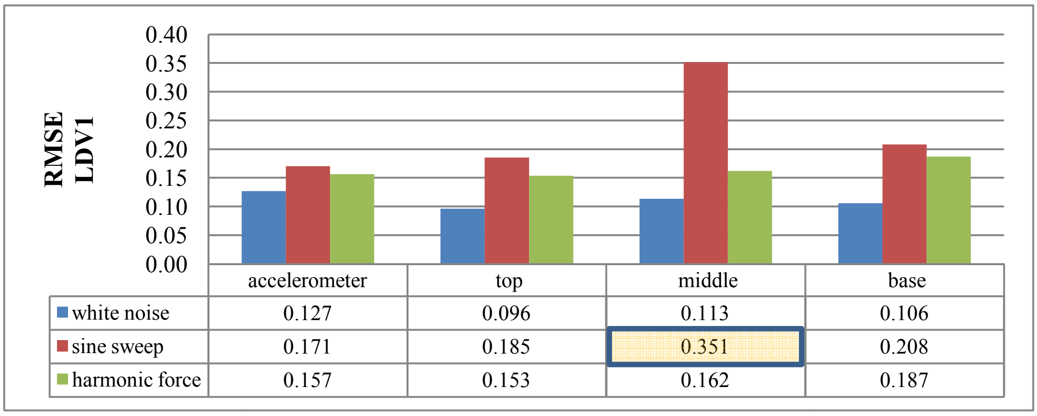

	accelerometer	top	middle	base
white noise	0.127	0.096	0.113	0.106
sine sweep	0.171	0.185	0.351	0.208
harmonic force	0.157	0.153	0.162	0.187

Figure 5.33 RMSE of DVV analysed displacement data at different LDV focus points.

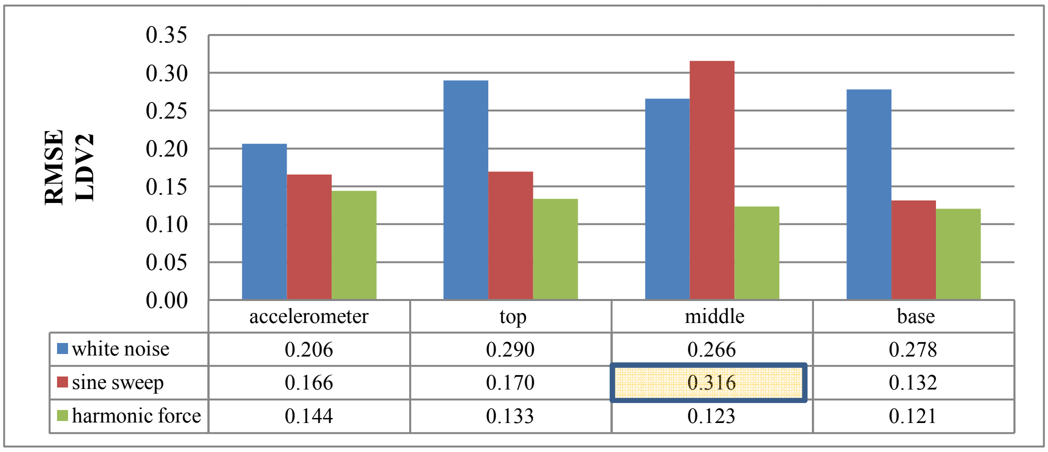

	accelerometer	top	middle	base
white noise	0.206	0.290	0.266	0.278
sine sweep	0.166	0.170	0.316	0.132
harmonic force	0.144	0.133	0.123	0.121

Figure 5.34 RMSE of DVV analysed velocity data at different LDV focus points.

The acceleration data recorded are descriptors of responses to the given loading only at one location, i.e. the location of the accelerometer at the top of WTB. Therefore the range of RMSE for acceleration measured when system is exposed to different forces as well as the range and trend of RMSE of strain data along WTB is investigated next.

5.6.3.3 Excitation Force

Harmonic resonance

Figure 5.35 shows RMSE values obtained as result of DVV analysis when WTB was exposed to harmonic force. The RMSE of acceleration data obtained when LDV focus point was WTB mid section are invalid, as observed earlier. The range of RMSE for CH1 data is wide, from 0.160 to 0.251. On the other hand the nonlinearity of response signal recorded by CH2 and CH3 is about the same for all measurements, where CH3 measurements show greater nonlinearity. LDV measurements show increase in nonlinearity of displacement and decrease in nonlinearity of velocity signal from top to bottom of WTB. The RMSE maximum are 0.187 and 0.144, while minimum are 0.153 and 0.121 for LDV1 and LDV2, respectively. The results for measured strain at four different locations do show the tendency of recorded signal to exhibit greater nonlinearity closer to the base, but can not be held a rule.

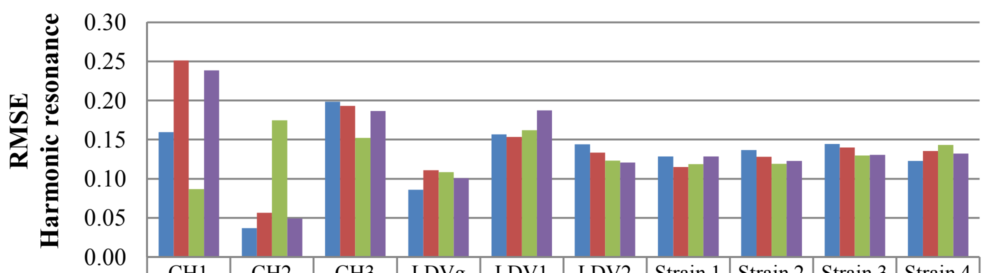

	CH1	CH2	CH3	LDVg	LDV1	LDV2	Strain 1	Strain 2	Strain 3	Strain 4
accelerometer	0.160	0.037	0.198	0.086	0.157	0.144	0.128	0.137	0.144	0.123
WTB top	0.251	0.057	0.193	0.111	0.153	0.133	0.115	0.128	0.140	0.135
WTB mid section	0.087	0.175	0.152	0.108	0.162	0.123	0.119	0.119	0.130	0.143
WTB base	0.239	0.049	0.187	0.101	0.187	0.121	0.128	0.123	0.130	0.132

Figure 5.35 The effects of harmonic force on linearity of response measurements.

Sine Sweep

The results of DVV analysis, RMSE values, obtained on sine sweep response data recorded by the instruments are presented in Figure 5.36. The RMSE values are greater for this type of loading than for harmonic loading in the case of acceleration measurements. This would mean that the measured acceleration signal shows more nonlinearity in the case of sine sweep loading. The RMSE maximum are 0.318, 0.102 and 0.3, while minimum are 0.243, 0.058 and 0.219 for CH1, CH2 and CH3, respectively. LDV measurements show greater nonlinearity than when system is exposed to harmonic loading, with increasing trend in case of displacement and decreasing trend in case of velocity measurements. The RMSE ranges from 0.171 to 0.208 and from 0.132 to 0.170, for LDV1 and LDV2, respectively. The RMSE values calculated on strain data are in general higher that for previous loading observed.

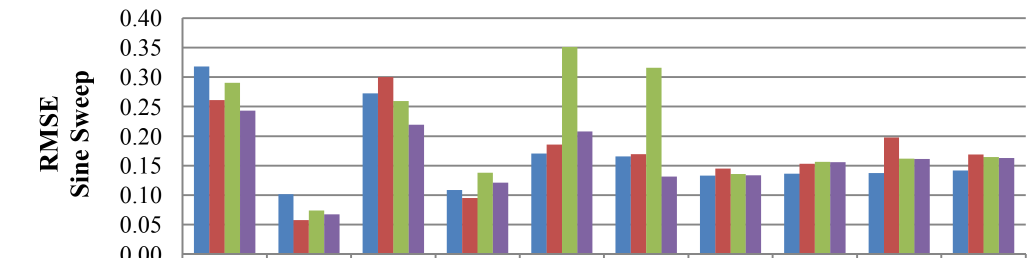

	CH1	CH2	CH3	LDVg	LDV1	LDV2	Strain 1	Strain 2	Strain 3	Strain 4
accelerometer	0.318	0.102	0.272	0.109	0.171	0.166	0.133	0.136	0.137	0.142
WTB top	0.261	0.058	0.300	0.095	0.185	0.170	0.145	0.153	0.198	0.169
WTB mid section	0.291	0.074	0.259	0.138	0.351	0.316	0.136	0.156	0.162	0.164
WTB base	0.243	0.067	0.219	0.121	0.208	0.132	0.134	0.156	0.161	0.163

Figure 5.36 The effects of sine sweep force on linearity of response measurements.

White Noise

Figure 5.37 shows the results of DVV analysis of WTB recorded responses when excitation force is white noise. The results for acceleration data, CH1 and CH3, show less nonlinearity than for the other types of loadings observed, more over the RMSE is almost constant between the measurements. The DVV analysis of LDV measurements shows greater nonlinearity for velocity than for displacement data.

The results show that measured displacement is more linear, while velocity is less linear when comparing with the results obtained for harmonic and sine sweep loading measurements.

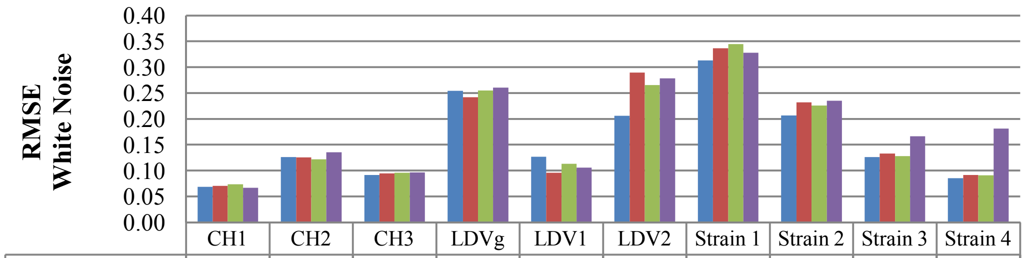

	CH1	CH2	CH3	LDVg	LDV1	LDV2	Strain 1	Strain 2	Strain 3	Strain 4
accelerometer	0.069	0.126	0.092	0.254	0.127	0.206	0.313	0.206	0.126	0.085
WTB top	0.070	0.126	0.095	0.242	0.096	0.290	0.336	0.232	0.133	0.091
WTB mid section	0.073	0.122	0.096	0.255	0.113	0.266	0.345	0.226	0.128	0.091
WTB base	0.067	0.135	0.096	0.261	0.106	0.278	0.328	0.235	0.166	0.181

Figure 5.37 The effects of white noise force on linearity of response measurements.

5.6.3.4 The Instruments

WTB responses to the external excitation were measured by different instruments: 3D Accelerometer, LDV and strain gauges. DVV analysis results for measurements performed by each instrument are presented in this section.

<u>3D Accelerometer</u>

3D Accelerometer recorded the acceleration in three different directions (CH1, CH2 and CH3) of the top (free end) of WTB. Figure 5.38 shows DVV results on data recorded by the three channels. The results summarise all three types of loading applied. The responses obtained for WTB exposed to harmonic loading in experiment 12 (see point 3 at X – axis) were not recorded in full length, therefore the outcome of DVV analysis can not be used for results comparison. The data recorded by CH1 and CH3 show the highest nonlinearity of the signal when WTB is exposed to sine sweep and the lowest when exposed to white noise. Sine sweep loading produces less nonlinearity than white noise for acceleration measured by CH2. The extreme RMSE values from DVV analysis of the 3D Accelerometer recorded data are given in Table 5.6.

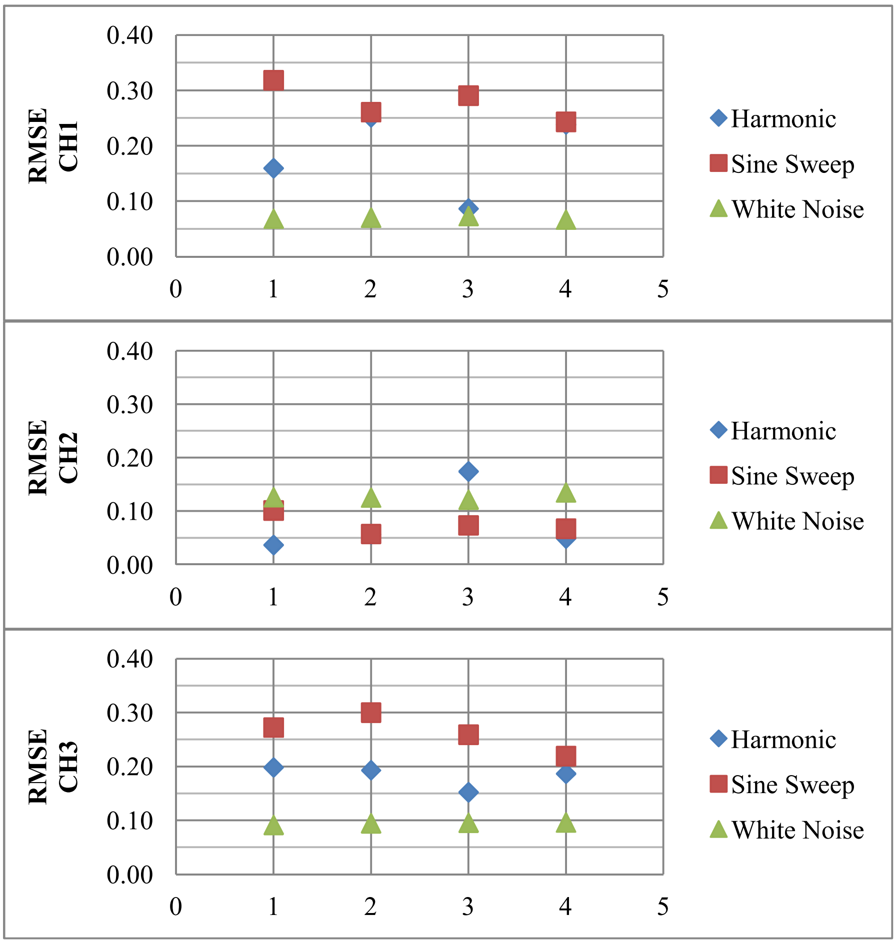

Figure 5.38 Comparison of DVV analysis results (RMSE) for 3D Accelerometer measurements.

Table 5.6 The extreme RMSE values for DVV analysed 3D Accelerometer data.

Load	CH1		CH2		CH3	
	min	max	min	max	min	max
Harmonic	0.160	0.251	0.037	0.057	0.187	0.198
Sine sweep	0.243	0.318	0.058	0.102	0.219	0.300
White noise	0.067	0.073	0.122	0.135	0.092	0.096

LDV

The LDV recorded measurements of displacement, LDV1, and velocity, LDV2, at four different locations for WTB exposed to three different excitation forces. Figure 5.39 shows the results of DVV analysis of the LDV data. The responses obtained for the WTB exposed to sine sweep when LDV focus point is in its mid section encounter some irregularities (see Figure 5.39, point 3 at X – axis). These results are not considered in the discussion. The displacement measurements show the highest nonlinearity for sine sweep load, and the lowest for white noise. In the case of velocity, white noise produces the highest nonlinearity and harmonic loading the smallest. The nonlinearity of the displacement data slightly increases, while the nonlinearity of velocity data slightly decreases in the case when excitation is harmonic for the WTB top to base measurements. The extreme RMSE values of the LDV recorded data are given in Table 5.7.

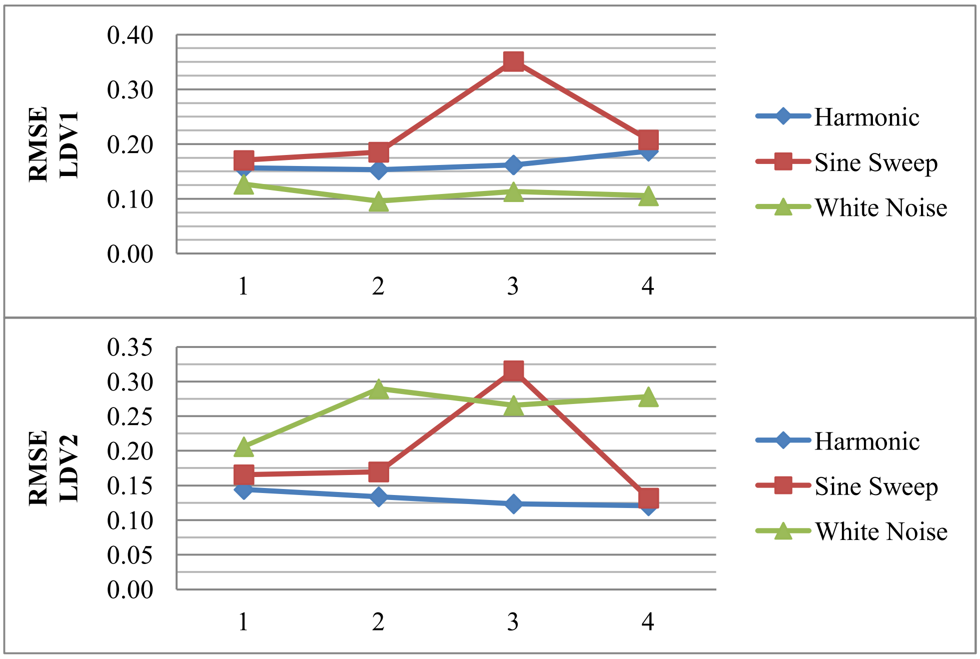

Figure 5.39 Comparison of DVV analysis results (RMSE) for LDV measurements.

Table 5.7 The extreme RMSE values for DVV analysed LDV data.

Load	LDV1		LDV2	
	min	max	min	max
Harmonic	0.153	0.187	0.121	0.144
Sine sweep	0.171	0.208	0.132	0.170
White noise	0.096	0.127	0.206	0.290

Strain gauge

Figure 5.40 shows RMSE results of the DVV analysis of strain gauges recorded data at four different locations for different loadings. The experiments were repeated four times for each load. The nonlinearity of the strain data varies very little at observed points between experiments for all loads. The exceptions are two measurements, Strain 3 for sine sweep and Strain 4 for white noise load, where the RMSE values are high for irregularities in obtaining some of the surrogates. In the case of white noise excitation the nonlinearity of measurements decreases from WTB top to its base.

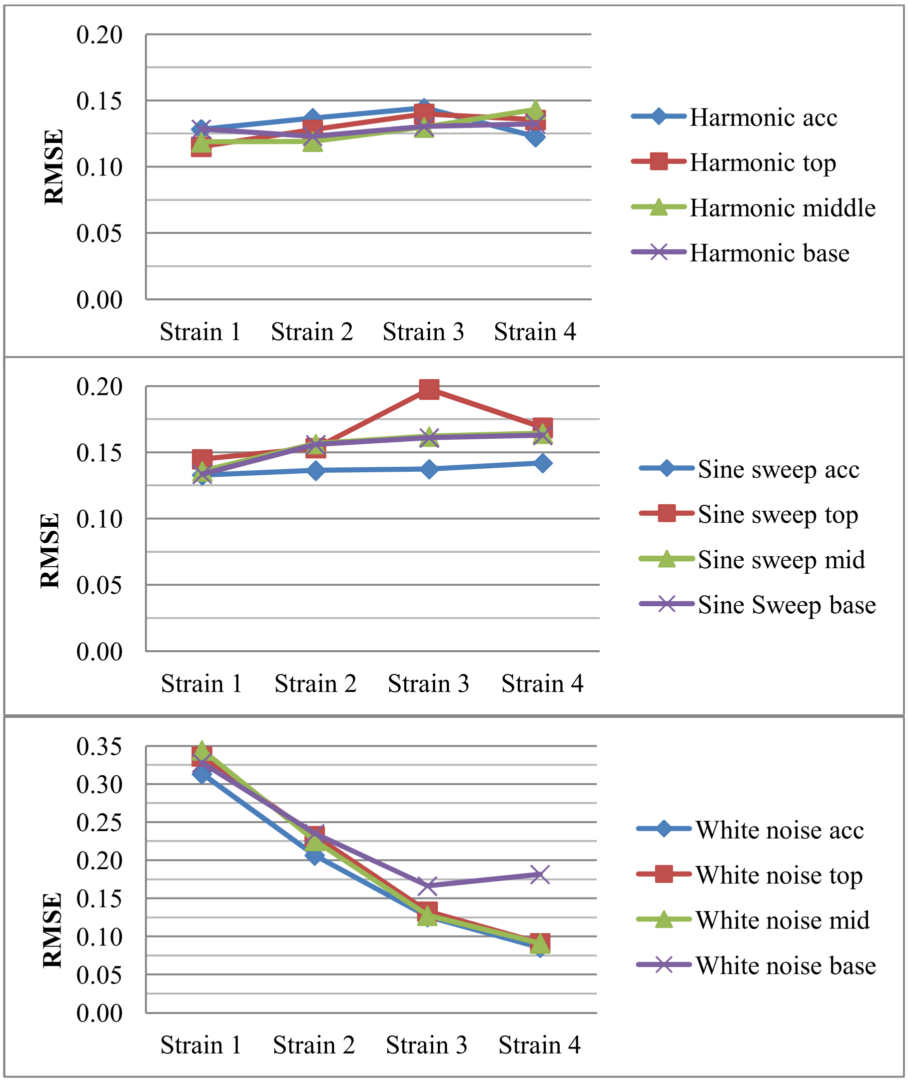

Figure 5.40 Comparison of DVV analysis results (RMSE) for strain gauges measurements.

5.6.4 Wind Turbine Blade Experiment: Conclusions

- Only response of the system to excitation measurements should be used for DVV analysis. Measurements recorded while the system is in equilibrium can influence DVV results.

- 1st and 2nd approaches for determining embedding parameter and time lag have limitations when analysing large sets of data.

- 3rd approach (the embedding parameter m=3 and time lag τ=1) shows the best efficiency and consistency in interpretation of DVV method results for the observed system.
- The method is sensitive to rapid/unexpected change in the recorded signal. The results of DVV analysis are dependant on length of data recorded.
- The acceleration data recorded by CH1 and CH3 show the highest nonlinearity of the signal when WTB is exposed to sine sweep and the lowest nonlinearity when WTB is exposed to white noise.
- Sine sweep loading produces less nonlinearity than white noise for acceleration measured by CH2.
- The sine sweep loading causes the greatest nonlinearity in acceleration measurements in comparison with harmonic and white noise loading.
- The displacement measurements show the greatest nonlinearity for sine sweep and the lowest nonlinearity for white noise loading, regardless of the LDV focus point.
- The velocity measurements show the highest nonlinearity for white noise and the lowest for harmonic loading, regardless of the LDV focus point.
- The nonlinearity of the strain data varies very little at observed points between experiments in all load cases. This shows the stability of the instruments' measurements. In the case of white noise the nonlinearity of measurements decreases from WTB top to its base. From the results, range of RMSE, it is possible to detect difference in the external force.

5.7 Conclusions

The DVV method has been applied to analyse the response signals of one theoretical and two experimental models. The first goal was to establish the best method of choosing the embedding parameters for DVV analysis. The methods considered were differential entropy method, the minimal target variance method, and manually setting embedding dimensions. It has been found that manually setting embedding parameter, $m = 3$ and time lag $\tau = 1$, gives the best results in all observed cases. The DVV method proves to be sensitive to length of available data, as well as to existence of any rapid (unexpected) change in recorded data. In the examples where the observed system reaches equilibrium fast there is not sufficient number of data for DVV analysis. Outcome of DVV analysis on the response signal is represented by a single number, RMSE, which quantifies deviation from bisector line of DVV scatter plot. Hence, RMSE is used to determine the degree of linearity/nonlinearity of response signal.

The DVV analysis of the SDOF theoretical model exposed to different types of oscillations has shown that the RMSE is sensitive to some system parameters and insensitive to the others. The former group includes damping ratio, driving frequency, and natural frequency; the latter group includes mass, base frequency, and input force magnitude.

The SDOF car experiments show that the DVV method can be used in detection of change in the system stiffness as well as change in the nature of excitation force. The change of the system stiffness is successfully recorded by 3D accelerometer and LDV. The occurrence of sudden stiffness change in SDOF system can be detected by the DVV method, but not the exact time or extent of change. Determination of time and extent of change require the assistance of another method, e.g. the continuous wavelet transform analysis. The change of the surface roughness is difficult to detect by measurements in main direction of vibration. Still the change in surface roughness is recorded by accelerometer in lateral direction to the movement of the SDOF car. The difference in the nature of the external force is recorded by both instruments. The difference in loading is best represented in cases when the surface is wood or sand paper, while the observed model has lower stiffness. Therefore, the combination of surface roughness and system stiffness could influence the success of the DVV model in recognition of the type of excitation force. Increase in load frequency results in the extreme nonlinearity of response signal; this phenomenon is successfully recorded by both instruments.

In WTB experiments the three different instruments have been used to monitor responses of the system to vibration: 3D accelerometer, LDV, and strain gauges. All three instruments successfully record the changes in loading, but with different sensitivities. For example, 3D accelerometer data recorded by CH1 and CH3 show the highest nonlinearity of the signal when WTB is exposed to sine sweep and the lowest nonlinearity when exposed to white noise. On the other hand, the sine sweep loading produces less nonlinearity than white noise for acceleration measured by CH2. The displacement shows the greatest nonlinearity for sine sweep and the lowest nonlinearity for white noise loading, while the velocity exhibits the highest nonlinearity for white noise and the lowest for harmonic loading, regardless of the LDV focus point. For the same load, the nonlinearity of the strain data varies very little at observed points; this indicates the stability of strain gauges measurements.

The results demonstrate the effectiveness of the DVV method in detecting the changes within the system. DVV also allows for comparative analysis between different systems driven by the same input. However, no straightforward conclusion can be drawn from the nonlinearity analysis of the output signal regarding an underlying system linearity or nonlinearity.

DVV method proves to be the useful tool for recording the changes within the mechanical system signal due to changes in the system parameters. Many of these changes are indicators of potential structural damage, e.g. change in stiffness, frequency, strain field, etc. The detection of such changes from the vibration of the structure is important for Structural Health Monitoring. The implementation of the DVV method is easy and cost effective. This type of structural vibration response analysis, in conjunction with non-contact measurements of these vibrations, is a quick and efficient way for successful monitoring of the structures.

For the future experiments it is recommended to set up manually embedding parameter m while keeping time lag $\tau = 1$. Also, the white noise as excitation force should be avoided. The duration of experiments should be longer than 200 and less than 9000 data points. In the case of longer than 9000 data records, the data should be windowed.

Chapter 6

DVV Analysis of Large Structural Systems

6.1 Introduction

The implementation of the DVV method on the responses of the theoretical SDOF systems and laboratory experiments on SDOF car and wind turbine blade is presented in Chapter 5. The method is successful in diagnosis of several system characteristics changes, such as variation in damping ratio, driving frequency, natural frequency, system stiffness, and change in the nature of the excitation force. The findings of the previous chapter are important for SHM since many of these system vibration data changes can be the indicators of the potential damage of the structural system under observation.

In this chapter the DVV method is employed to analyse the recorded responses of real structures from a SHM point of view. The objective of this chapter is to establish the ability of DVV method to recognise different events in real structures using in-situ structural measurement tools. This chapter is also an application of the DVV method on Bridge-Vehicle interaction based detection structural systems, which is the focus of the thesis.

The first observed structure is an impact damaged prestressed concrete bridge. DVV is employed to analyse the bridge responses, monitored during the rehabilitation works incorporating a network of strain gauges located in and around the damaged region, with objective to establish sensitivity of DVV analysis to different events taking place during repairs. The works were part of an emergency rehabilitation following the impact of a low-loader carrying an excavator, passing underneath the bridge, to the soffit of the bridge [188].

The second structure studied is a single-span composite railway bridge. It carries one ballasted truck. The bridge is light and flexible and vibrates easily when a train passes [189]. A measuring system is installed to measure strains and acceleration at different points of the steel beams and the concrete slab. Here, the response of the bridge to passage of nine trains of different characteristics is analysed using DVV method.

6.2 An impact damaged prestressed bridge

DVV method is used to analyse pseudo-dynamic measurements of a damaged bridge structure during rehabilitation through continuous monitoring. The case is interesting as DVV is used for the first time to analyse the time series which are product of varied natural and human activities imposed on a large structure over significant period of time. The product of DVV analysis of recorded data and its surrogates, i.e. RMSE, are compared with respect to specific events during the rehabilitation, as well as with the data collection locations.

The full-scale experiment on this bridge is not the part of this thesis. Hence, the following sections of this chapter describing the bridge, details of damage, bridge monitoring instrumentation, and the rehabilitation process are based on relevant literature [188, 190, 191] and are included here for better understanding of changes that structure is going through and overall completeness.

6.2.1 Details of Damage

The two-span continuous slab-girder bridge consisting of six precast prestressed U8 type simply supported concrete beams connected by a continuity diaphragm was damaged by impact force to its soffit [191]. The beams are 27.35 m in span. The edge of the outer beam was damaged in a benign fashion although one of the tendons in the lower row snapped. A rapid assessment calculation proved that the beam was well within the safe zone under stability and serviceability conditions with the exclusion of the tendon [188]. On the other hand, an internal beam was more significantly damaged in which the tendons remained intact but the concrete was crushed from the impact. An unknown redistribution of stresses took place following the impact. The damaged region has been inspected by a three-dimensional laser scan visualisation, impact echo testing, and a hammer tapping survey near the location of the main damage. These surveys indicated that the true damage extended beyond the visually superficial regions. Figure 6.1 presents the close-up photographs of damaged beams [190].

Figure 6.1 Damaged region of outer beam (left) and inner beam (right) [190].

There was no structural cracking in the prestressed concrete beams following the damage in an unloaded state or due to the passage of vehicles. This qualitatively supports the fact that the concrete was probably within a linear and compressive zone. Although it was difficult to estimate the existing stresses within the beam, calculations on extreme hypothetical situations revealed that the beams had significant windows of operation on the compressive and the tensile side from its unloaded state while remaining within the linear elastic zone [188].

6.2.2 Instrumentation

Nineteen strain gauges (SG) are installed at five preselected monitoring points. The schematic details of the arrangement of the multichannel SG and monitoring point (MP) locations is provided in Figure 6.2.

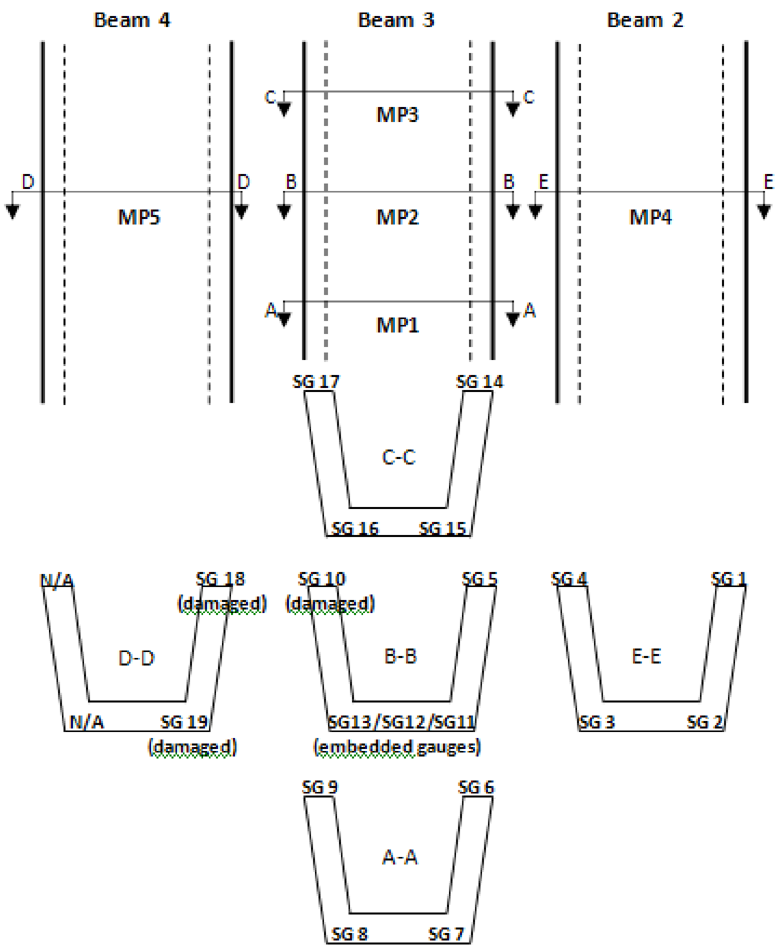

Figure 6.2 Arrangement of multichannel strain gauge network [188].

The monitoring points are strategically chosen so that the interaction of the damaged and undamaged beams, including the behaviour of gauges at, near, and away from the damage, can be probed [188]. There are three monitoring points at the centre (MP2, MP4, and MP5) and at the two ends of the damage (MP1 and MP3), at the centre of the two undamaged beams, and the two sides of the damaged beams. Gauges are installed at the top and at the bottom of the soffit so that the deformations at these two levels could be observed simultaneously. Three gauges at MP 2, the centre of damaged location, are embedded to the tendons and zeroed at a later period than the remaining gauges.

The sampling rate was kept at 1 min and the data were logged in microstrain units. The low sampling frequency is related to the practical implementation of measurements at large scale. Pakrashi et al. [191] explains further that the choice is guided by the sampling resolution, robustness against physical activities, exposure to environmental and mechanical conditions, and accuracy of collected data. A higher sampling frequency usually corresponds to small gauges that are easily affected by small electrical, mechanical, and environmental fluctuations and lead to a lower quality of data with associated noise and fluctuations that are very difficult to estimate. Also, due to the small size of the gauges and the rough surface of large structures, the connection with the large structure is not very good from an implementation perspective. Additionally, these gauges with higher sampling frequency (1Hz) are not very robust against activities carried out, and the probability of losing the operational capability of significant number of gauges is unusually high. Although the vibrating wire SG used for the study has low sampling rate, it provides reliable measurements and good resistance against activities with a low rate of sensor defect during monitoring periods. The connection with the structure is also good. Consequently, these types of gauges were considered to be better for large-scale monitoring than the ones with a higher sampling frequency [191].

The embedded SG were Geokon vibrating wire embedment gauge model 4200 while the rest of the gauges were Geokon vibrating wire SG model 4000. These gauges were chosen based on their high durability, range of operation, resolution, and operational temperature range [188]. The tolerance level and stability of readings of the gauges were ensured.

6.2.3 Rehabilitation Process

The rehabilitation was carried out by preloading the bridge to either side of the damaged region in order to release some of the high prestressing compressive force in the soffit of the beam. Preloading consisted of placing 20 t bales of concrete blocks either side of the damaged region. These were staged in three applications to a total of 120 t. Hydrodemolition and removal of damaged concrete was carried out next, after which rapid-hardening and high-strength repair material was applied to the damaged region. The repair material chosen was a fibre reinforced spray mortar. It was designed to have a 28 day compressive strength of 70 MPa and was able to take greater tensile force than standard concrete. The preloads were removed from the top of the bridge after the hardening of repair material, i.e. after the repair material had gained adequate strength. The removal of preload was expected to reintroduce some amount of lost prestress in the repaired zone [191].

6.2.3.1 Monitoring

The gauges (excluding embedded gauges) were simultaneously zeroed and readings were automatically logged for all of the gauges every minute. Prior to the rehabilitation stage, the structure was monitored under relatively inactive conditions, during which the main action on the structure was thermal, due to the diurnal temperature variation. The structure was also monitored for some time after the rehabilitation during which some strength gain and strain redistributions were expected to occur along with thermal effects. Some of the gauges were damaged during the rehabilitation process at different times [191]. Embedded SG (SG11, SG12, and SG13) were directly attached to the tendons before the hydrodemolition process and were zeroed at a later time than the other gauges. Consequently, a direct comparison of the embedded gauges with the other gauges is not necessarily appropriate at all times [190]. These gauges are important since they are located at the centre of the damage and are the only gauges that are sheltered from thermal effects and are in direct contact with the hardening repair material.

The monitoring of repair can be divided into seven periods:

1. the installation of the gauges
2. the application of preload
3. concrete removal employing hydrodemolition
4. full loading application and all concrete removed
5. application of repair material, shrinkage, and hardening with embedment of gauges SG11, SG12, and SG13
6. removal of load
7. further strength gain.

The SG remained for a further four days to allow any further strength gain to be examined.

6.2.4 Results of DVV Analysis

The results of DVV analysis, i.e. DVV plots and DVV scatter plots, of the recorded strain data during rehabilitation are shown in Appendix C1. The parameters chosen for DVV analysis are kept the same as for the SDOF car and WTB experiments described in Chapter 5. Hence embedding dimension m = 3, time lag τ = 1, maximal span parameter n_d = 3, the number of standardised distances for which target variances are computed N_{tv} = 50, number of surrogates considered $N_S = 25$, and number of reference DVs considered N_{sub} = 200 (or 100 where small data sets are available). The results of DVV analysis, i.e. the deviation from bisector line of scatter plot quantified by the root mean squared error, will be referred to as RMSE.

6.2.4.1 Thermal Period

Thermal period (relatively inactive time between the installation of the gauges and the application of load) is a stage before any rehabilitation works, where fluctuations due to the diurnal cycle can be observed [188]. SG's readings during this period at each observed cross section (MP), are shown in Figure 6.3.

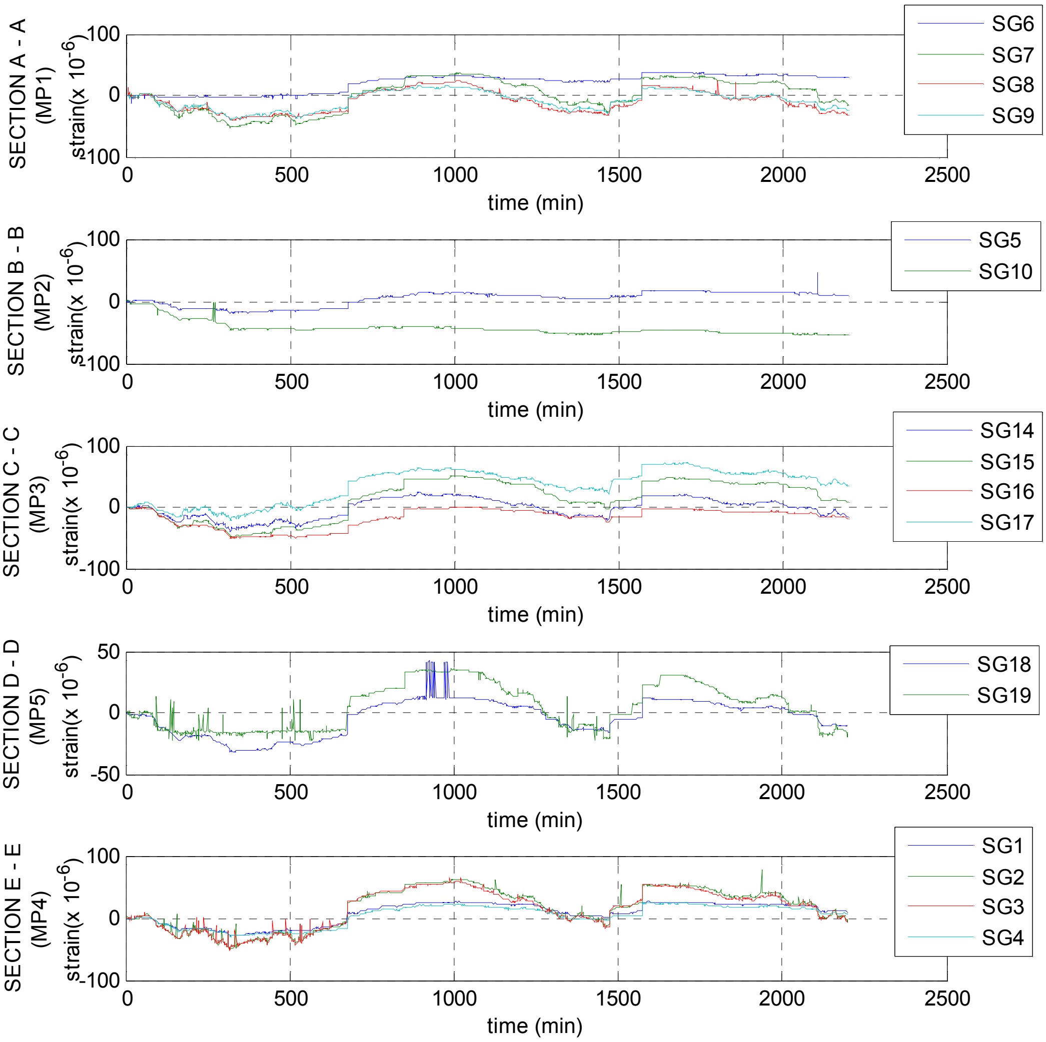

Figure 6.3 Change in strain of the top and soffit gauges over the thermal period.

The tensile forces are induced due to the expansion on warming up throughout the day leading to a positive increase in strain. On the other hand, cooler temperatures at night cause compressive action represented by a negative strain change. The exception in SG 10 could not be directly explained but is suspected to be related to partial damage of the gauge during installation [188].

The results of DVV analysis are shown in Figure 6.4. The maximum RMSE is 0.281 for SG10. The possible reason for the highest nonlinearity of strain recorded is malfunctioning of SG10. Still, the highest RMSE of 0.241, 0.212, and 0.212 are obtained for top strain gauges SG18, SG5, and SG6, respectively. However, the higher nonlinearity of SG18 signal seems to be the result of a series of unusual events, i.e. unexpected peaks within the signal (see Figure 6.3). The minimum value of RMSE is 0.159 for the top strain gauges SG9 and SG14. The dominant trend of the undamaged beams is that the top gauges show the higher nonlinearity of the signal than the corresponding bottom gauges (MP4 and MP5). Furthermore, the degree of the signal nonlinearity of the section E – E (MP4) is almost the same for the top and the same for the bottom gauges, as it would be expected since the amplitude of the strain measurements of SG's are almost the same (see Figure 6.3). The DVV results for the sections of affected beam do not hold this pattern. With exclusion of SG6 and SG7, the nonlinearity of the signal seems to be about the same or greater value for the bottom strain.

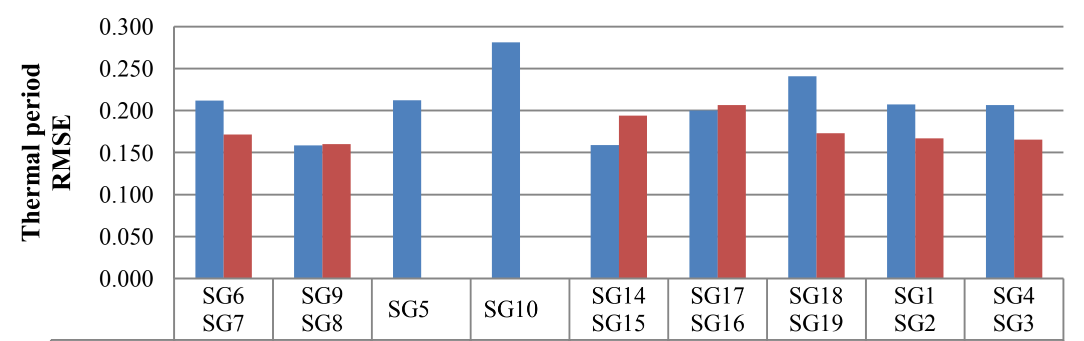

	SG6 SG7	SG9 SG8	SG5	SG10	SG14 SG15	SG17 SG16	SG18 SG19	SG1 SG2	SG4 SG3
Top SG	0.212	0.159	0.212	0.281	0.159	0.200	0.241	0.207	0.206
Soffit SG	0.171	0.160			0.194	0.207	0.173	0.167	0.165

Figure 6.4 DVV analysis results of strain gauges measurements obtained during thermal period.

6.2.4.2 Preloading Period

The preloading consisted of placing concrete bales staged in three main applications. The application of preloading essentially reduces an increase of compressive stress at the soffit [190]. The preloading will cause tension in the bottom of the beams releasing prestressing force and will cause compression at the top of the beam. This allowed for the hydrodemolition to be carried out in a safer manner. The preload also introduces a prestrain at and around the damaged zone. At the centre of damage, the bottom embedded gauges are expected to undergo tension and the top gauges compression [188].

Figure 6.5 shows the change in strain over the loading period at each observed cross section (MP). SG 10 is identified as damaged, however it does react albeit insensitively to events during the bridge rehabilitation [190].

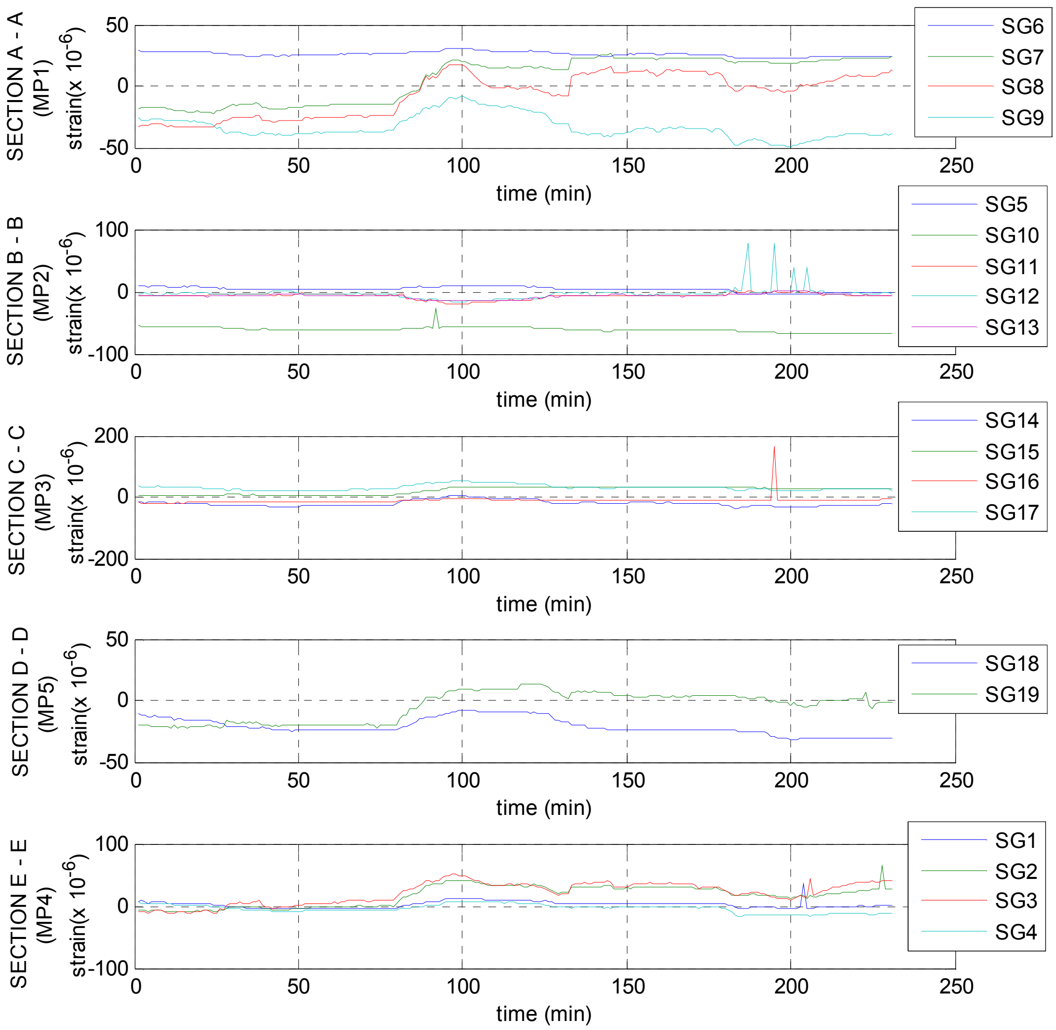

Figure 6.5 Change in strain of the top and soffit gauges over the preloading period.

Figure 6.6 shows the results of DVV analysis of recorded strain for preloading period. The preloading period is very short which resulted in reduced number of reference DV's considered when DVV analysed. Therefore the comparison of DVV numerical results between the repairing stages would not be appropriate. The largest degree of nonlinearity of the signal is recorded by SG 16. The reason for this could be the sudden jump in strain data (which are predominantly negative) to positive values of high amplitude. Similar appears to be the case with SG12, with second highest degree of nonlinearity of data. Around the same period, with little delay, the similar, but smaller, jump appears in records of SG1, SG2, and SG3 and does not result in comparably high RMSE. There is still the same relationship between degrees of nonlinearities in section E-E, that is greater nonlinearity in top SG than in the bottom. All other sections are affected, and degree of nonlinearity of top and bottom SG reversed or noticeably changed in value. In general, for this period time series have lower degree of nonlinearity than for the thermal period. Harkin [190] and Pakrashi et al. [188] point out the appearance of bumps in strain data due to the redistribution of stress affecting already fractured concrete. Here, even with the limited number of data for DVV analysis, it seems that the method was capable to detect this change.

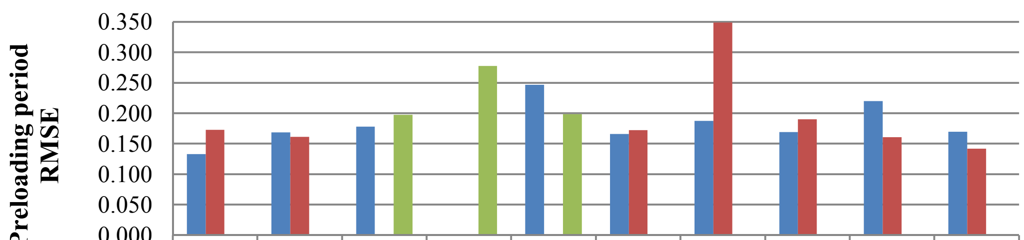

	SG6 SG7	SG9 SG8	SG5 SG11	SG12	SG10 SG13	SG14 SG15	SG17 SG16	SG18 SG19	SG1 SG2	SG4 SG3
Top SG	0.133	0.169	0.178		0.247	0.166	0.187	0.169	0.220	0.170
Soffit SG	0.173	0.161				0.172	0.349	0.190	0.161	0.142
Embedded SG			0.197	0.278	0.198					

Figure 6.6 DVV analysis results of strain gauges measurements obtained during preloading period.

6.2.4.3 Hydrodemolition Period

The recorded strain data are expected to reflect disturbance due to the hydrodemolition activity. However, at the centre of damage (Figure 6.7) it is noted that the embedded gauges (SG 11, SG 12 and SG 13) show little reaction. This is to be expected as these gauges are attached to the tendons rather than the concrete, which is suffering the bulk of the disturbance from the hydrodemolition. The lack of reaction also supports the efficiency of the hydrodemolition process as it takes the concrete away while affecting the tendons minimally [188]. Regarding the top and soffit of the beams, it would be anticipated that the gauges along the soffit would experience more disturbance as they are located closer to the region of removal. The soffit gauges do indeed show greater disturbance than those at the top of the beams. The sharp jumps or noise in readings can be explained by the nature of the disturbance and for most gauges the disturbance is momentary. The gauge SG 18 was damaged in this period and went off the typical scale of the strain gauges [188, 190]. The disturbance that the beams have undergone during the hydrodemolition period is clearly evident from the agitated strain gauge readings.

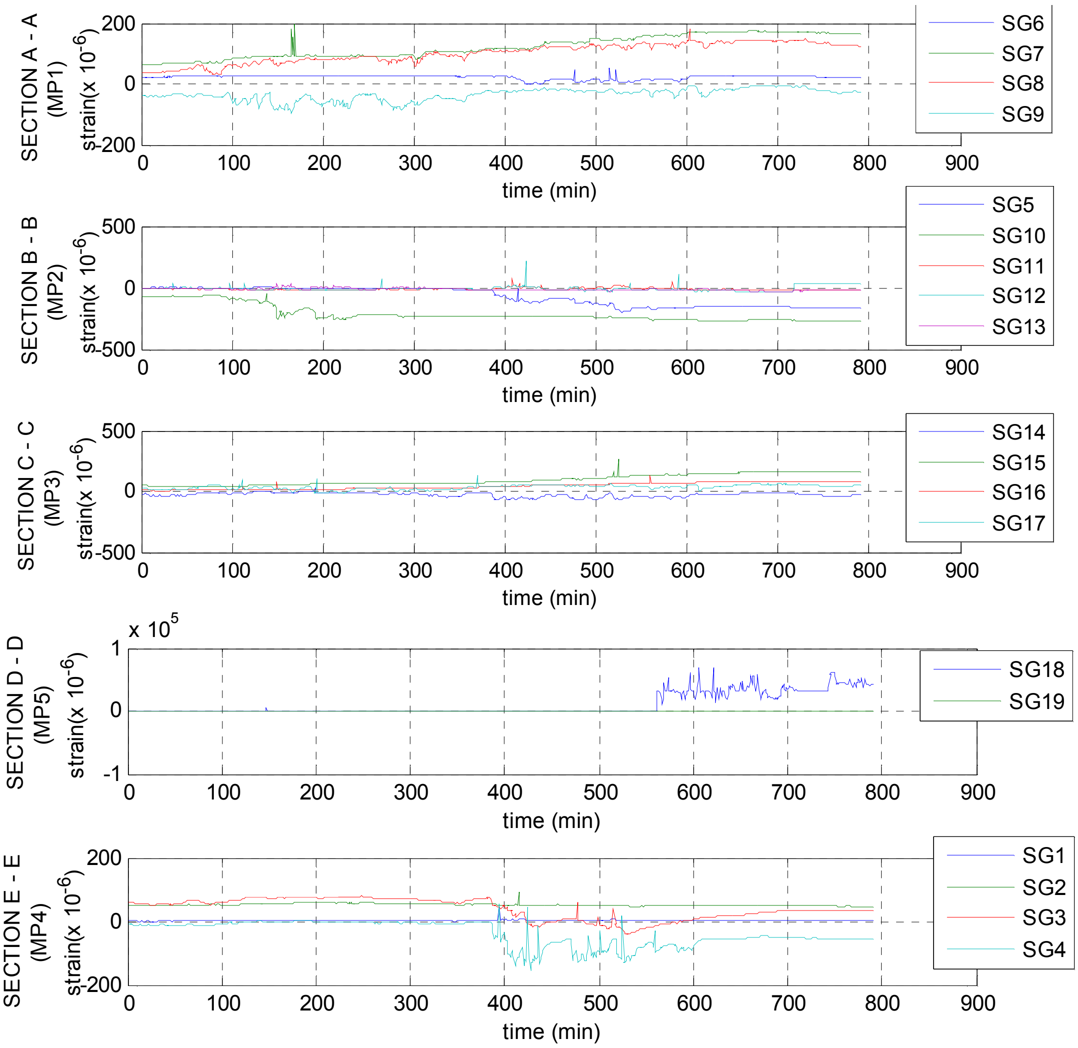

Figure 6.7 Change in strain of the top and soffit gauges over the hydrodemolition period.

Figure 6.8 shows the results of DVV analysis of strain records during hydrodemolition period. The degree of nonlinearity of the strain recorded by the embedded gauges (SG 11, SG 12 and SG 13) is noticeably reduced during this period. This proves the fact from above that the gauges are not recording the strain of the concrete but that of the tendons. The highest degree of nonlinearity show strain data of two top gauges (SG5 and SG10) of the damaged section, which supports the fact that the strain readings changed noticeably due to hydrodemolition. SG18 also shows high nonlinearity but this is the consequence of malfunctioning due to SG damage. In general, RMSE is greater for the soffit than for the top gauges, which is in agreement with observations that the soffit gauges do show greater disturbance than those at the top. However, SG1 and SG2 do not follow this pattern. The reason may be the location of the gauges, undamaged beam at far side from damage (Figure 6.2).

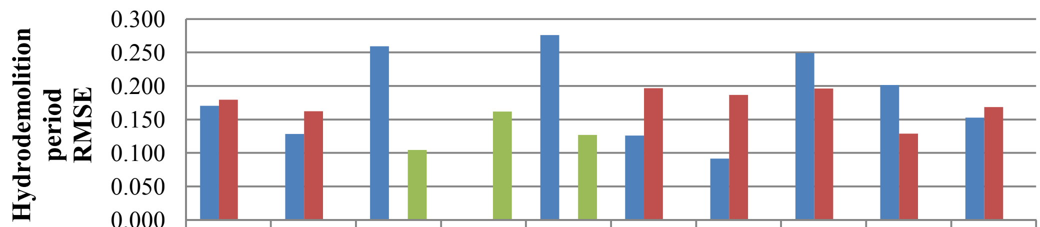

	SG6 SG7	SG9 SG8	SG5 SG11	SG12	SG10 SG13	SG14 SG15	SG17 SG16	SG18 SG19	SG1 SG2	SG4 SG3
Top SG	0.171	0.128	0.259		0.276	0.126	0.092	0.249	0.201	0.153
Soffit SG	0.179	0.162				0.197	0.186	0.196	0.129	0.169
Embedded SG			0.104	0.162	0.127					

Figure 6.8 DVV analysis results of strain gauges measurements obtained during hydrodemolition period.

6.2.4.4 Full loading application

This is the period just before the application of the repair material, after competition of hydrodemolition and application of total loading. The recordings of the SG's are shown in Figure 6.9. During this period there is no significant disturbance in the data. However, the damaged gauge SG18 is off the typical scale of the strain gauges. Also, the readings of SG11 and SG15 show disturbance in the signal for shot periods of time.

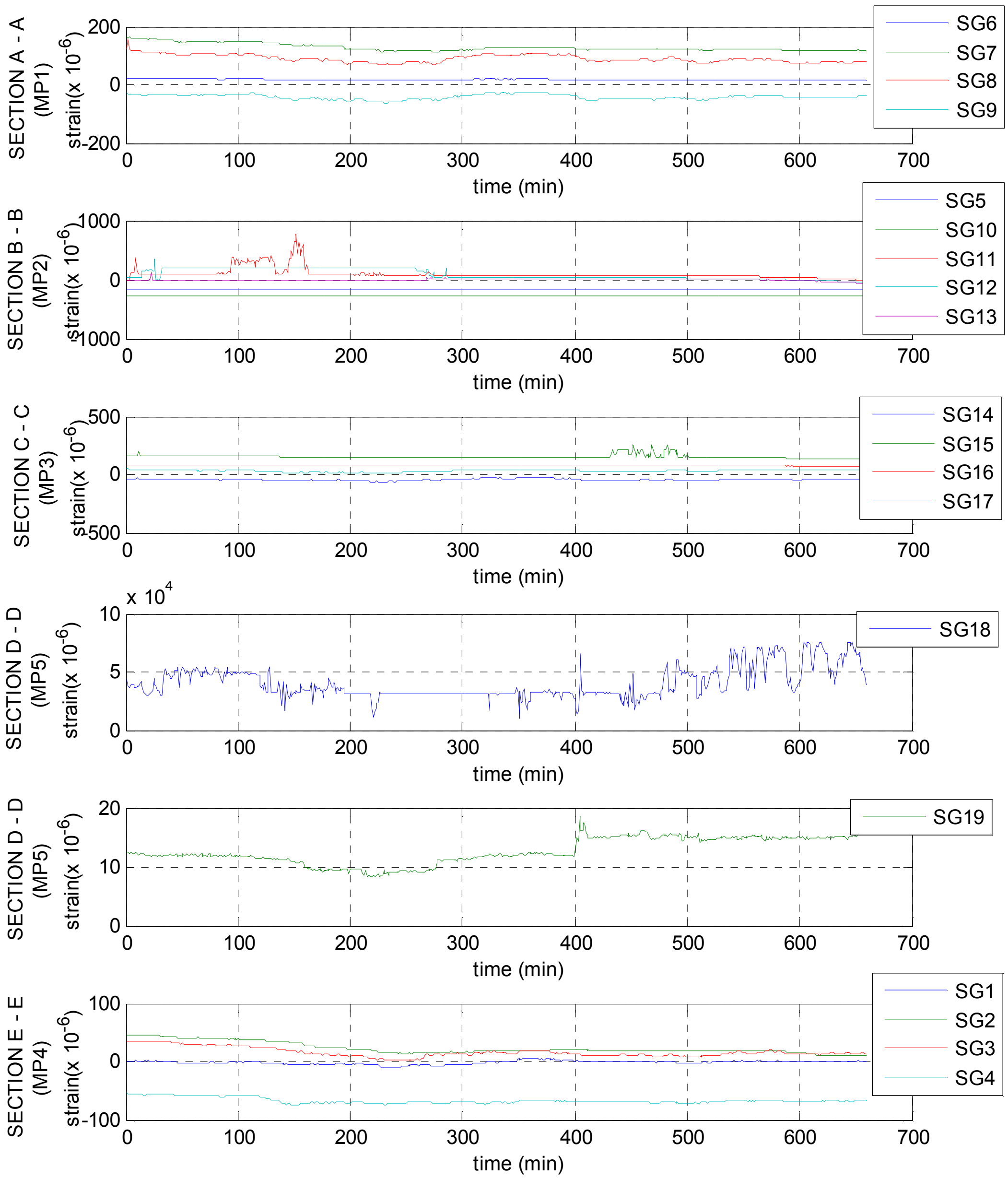

Figure 6.9 Change in strain of the top and soffit gauges over the full load application period.

Figure 6.10 shows DVV analysis results. The degree of nonlinearity of the strain recorded by the embedded gauges is higher than during hydrodemolition period. Moreover, the embedded SG11 data show the highest degree of nonlinearity of all recorded strains, which is due to the irregularities of the signal (the signal went off the scale for short period of time). In general, the soffit strain data show greater nonlinearity than the top data, with the exception of SG3 of section E-E.

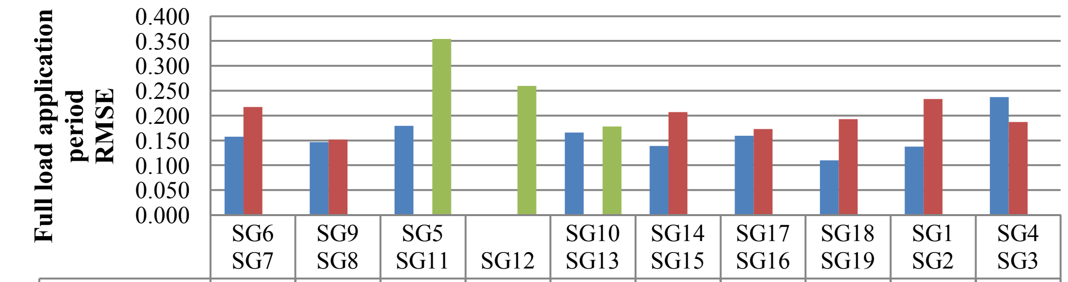

	SG6 SG7	SG9 SG8	SG5 SG11	SG12	SG10 SG13	SG14 SG15	SG17 SG16	SG18 SG19	SG1 SG2	SG4 SG3
Top SG	0.157	0.146	0.179		0.166	0.139	0.160	0.110	0.138	0.237
Soffit SG	0.218	0.151				0.207	0.173	0.193	0.233	0.187
Embedded SG			0.354	0.259	0.178					

Figure 6.10 DVV analysis results of strain gauges measurements obtained during full load application period.

6.2.4.5 Shrinkage Period

The recordings of SG for the period of application of repair material, shrinkage, and initial hardening with embedment of gauges SG11, SG12, and SG13 is shown in Figure 6.11. This time zone is shortly called shrinkage period. At the centre of damage it is expected that the embedded gauges will be significantly affected by the force due to the shrinkage of the repair material.

The embedded gauges show an increase in strain due to the tensile force of the repair material shrinking. The top gauges at MP2 show little change in strain as there is no action occurring at this location other than the secondary action from the repair material shrinkage. In general, the top gauges show little change in strain. The gauges located on the soffit of the beams show an increase in tension due to the shrinkage of the repair material. The centrally located gauges (SG11, SG12, and SG13) show the highest changes due to their position within the repair material. Note that SG 15 recorded an unexpected increase in tension.

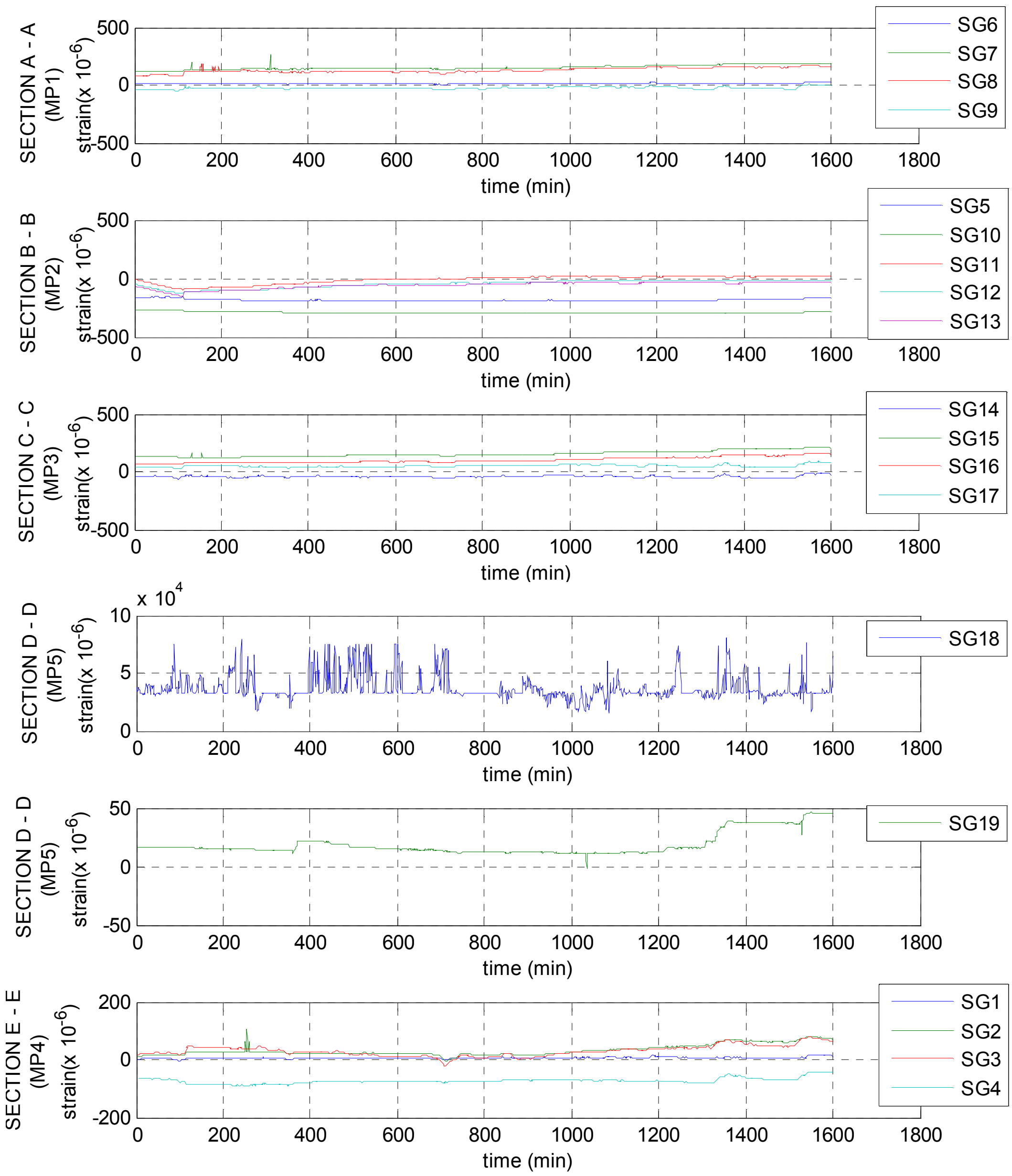

Figure 6. 11 Change in strain of the top and soffit gauges over the shrinkage period.

The results of DVV analysis for shrinkage period are shown in Figure 6.12. The overall observation is that the strain at the top shows greater nonlinearity degree than the strain measured at the soffit of the beam, with exception of SG14. Also, the strain measured in the damaged section B-B (MP2) shows greater nonlinearity than the strain measured at the other sections at the corresponding locations. This could be due to the increase in tensile force due to shrinkage of concrete. The recordings of the SG18 and SG19 give the extreme values of RMSE; the reason could be the damage of the gauges.

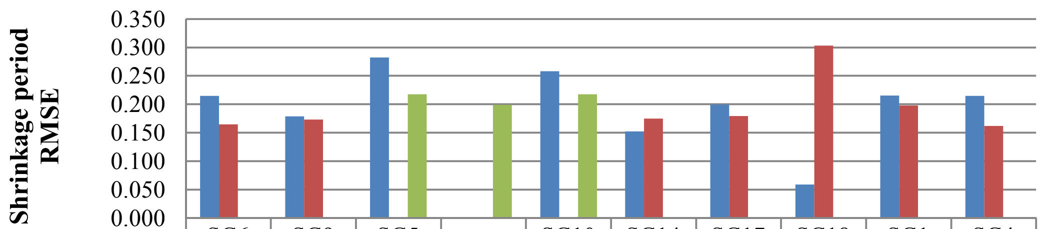

	SG6 SG7	SG9 SG8	SG5 SG11	SG12	SG10 SG13	SG14 SG15	SG17 SG16	SG18 SG19	SG1 SG2	SG4 SG3
Top SG	0.215	0.179	0.282		0.258	0.152	0.199	0.059	0.215	0.215
Soffit SG	0.165	0.173				0.175	0.179	0.303	0.198	0.162
Embedded SG			0.218	0.199	0.217					

Figure 6.12 DVV analysis results of strain gauges measurements obtained during shrinkage period.

6.2.4.6 Unloading Period

Unloading is performed in three stages in order to remove the full load of 120t. It would be anticipated that these stages are clearly visible as stepped changes in strain. The strain recordings are shown in Figure 6.13.

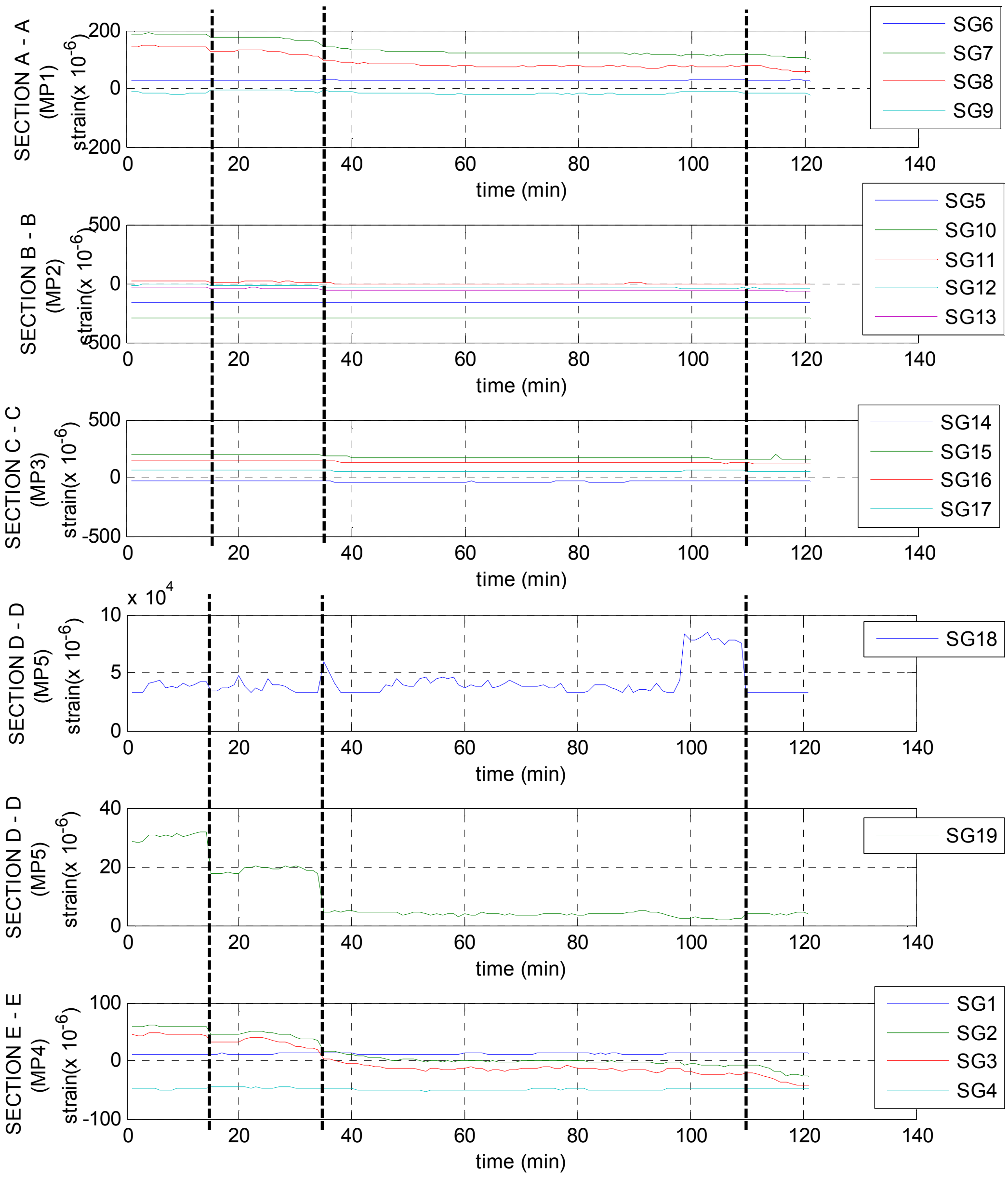

Figure 6.13 Change in strain of the top and soffit gauges over the unloading period.

The top gauges show very little change over the period as a minor decrease in compression is experienced. The strain records of gauges along the soffit show decrease of the strain representing a significant reduction in tensile force along the soffit of the beams. This is due to the beams adjusting to an intended compression state typical of a prestressed bridge [190]. The dash-dot black vertical lines in Figure 6.13 indicate the three time steps where there are sudden decreases in stress; this would be indicative of the three stages where the load was removed from the deck. The unloading stages are clearly identified in the bottom gauges. The approximate level of change of strain in the soffit at the location of the centre of damage for each set of removal has been observed to be approximately 20 microstrains [188].

The results of DVV analysis of recorded strain for unloading period are shown in Figure 6.14. The unloading period is very short which resulted in reduced number of reference DV's considered (N_{sub} = 100) when DVV analysed. Therefore the comparison of DVV numerical results between the repairing stages would not be appropriate. Overall RMSE for the top gauges readings decrease for this period and are smaller in comparison with bottom gauges. The values of RMSE between the gauges vary from 0.1 to 0.15. Similar trend of DVV results is consequence of the minor changes in compression. On the other hand, the nonlinearity degree of soffit strain is noticeably greater than of top strain measured, as the soffit strain decrease.

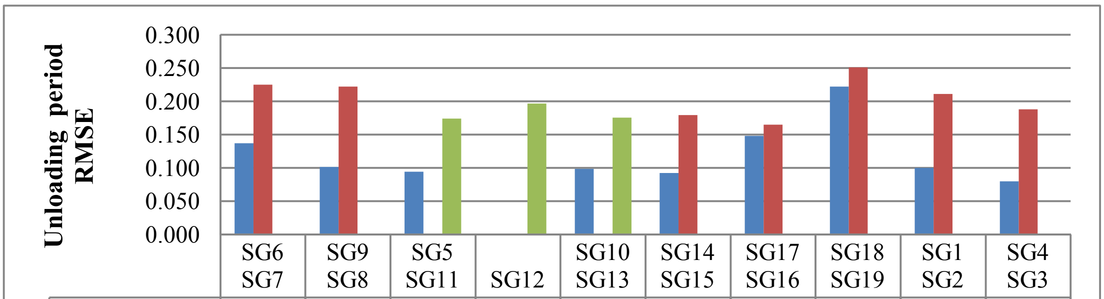

	SG6 SG7	SG9 SG8	SG5 SG11	SG12	SG10 SG13	SG14 SG15	SG17 SG16	SG18 SG19	SG1 SG2	SG4 SG3
Top SG	0.137	0.101	0.094		0.098	0.092	0.148	0.222	0.100	0.080
Soffit SG	0.225	0.222				0.179	0.165	0.251	0.211	0.188
Embedded SG			0.174	0.197	0.175					

Figure 6.14 DVV analysis results of strain gauges measurements obtained during unloading period.

6.2.4.7 Further strength gain

The further strength gain period covers more than four days of strain gauge readings following the removal of load. Very little evidence is present of shrinkage effects except in the first few hours (Figure 6.15). From this time on diurnal temperature effects dominate the strain changes, as no other action is occurring on the bridge. There is a strong response to the thermal changes with few exceptions. Two of these poorly responsive gauges (SG 5 and SG 10) are located as external gauges on the top of the damaged region. The soffit gauges show a strong response to the thermal changes as well. However, the embedded gauges (SG 11, SG 12, and SG 13) are within the hardened repair material and are therefore shielded from the temperature effects; consequently, the diurnal variations are not observed. SG18 and SG19 were damaged at this stage.

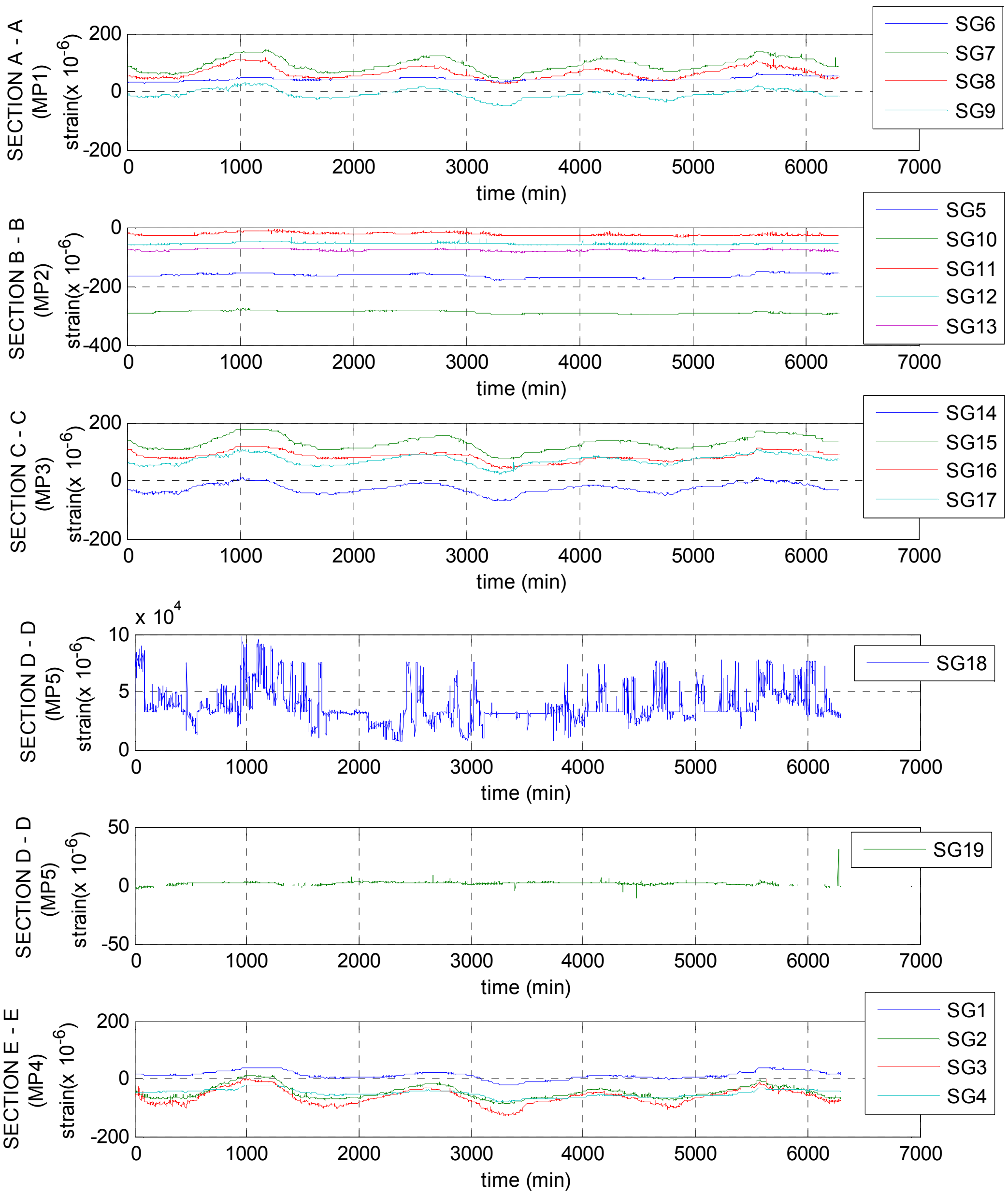

Figure 6.15 Change in strain of the top and soffit gauges over the further strength period.

The results of DVV analysis of recorded strain for further strength gain are shown in Figure 6.16. The observed period is the longest during which the strain measured got stabile readings. Overall RMSE for the top and bottom gauges readings are very close, with few exceptions. The exceptions are embedded gauges SG11 and SG13, which have measurements that show more linear behaviour than measurements of the other gauges; the reason may be that they are not affected by temperature effects. Also, SG18 and SG19 DVV analysed measurements are unreasonably low, this could be the consequence of gauges malfunctioning.

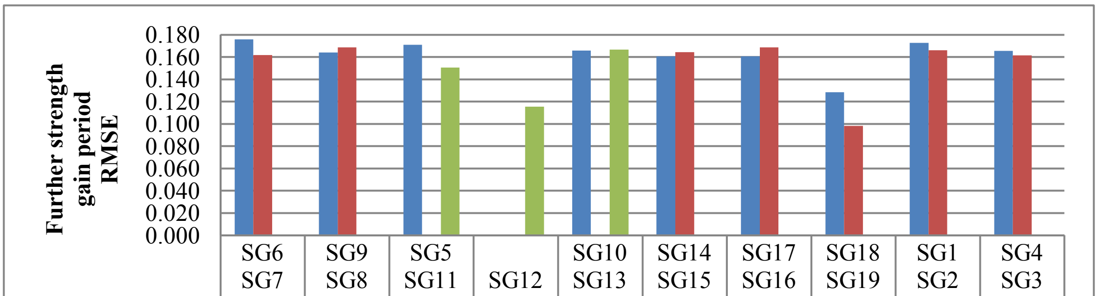

	SG6 SG7	SG9 SG8	SG5 SG11	SG12	SG10 SG13	SG14 SG15	SG17 SG16	SG18 SG19	SG1 SG2	SG4 SG3
Top SG	0.176	0.164	0.171		0.166	0.161	0.161	0.129	0.173	0.165
Soffit SG	0.162	0.169				0.164	0.169	0.098	0.166	0.161
Embedded SG			0.151	0.115	0.167					

Figure 6.16 DVV analysis results of strain gauges measurements obtained during further strength period.

6.2.4.8 Correlation of Top Gauges

The Figure 6.17 shows the variation of RMSE for top gauges. It is reported that SG10 and SG18 are malfunctioning [188, 190], therefore the results of DVV analysis on strain measured by them will not be discussed. However, the malfunctioning of these gauges is notable from DVV analysis results, i.e. RMSE is either extremely high or extremely low in comparison with mainstream results. The largest deviation in the strain nonlinearity (ΔRMSE = 0.168) is recorded during hydrodemolition stage. This is expected as this is the period of great disturbance. During shrinkage period the deviation of DVV results between top gauges is less than during hydrodemolition period (ΔRMSE = 0.130). However, it is noticeably high since the disturbances of small scale, due to the secondary action of shrinkage, are successfully recorded by DVV analysis of the strain measured. The smallest RMSE deviation is recorded during the final stage (ΔRMSE = 0.015) which proves the fact there is no more shrinkage effect on the beams but just diurnal temperature effects. The top strain measured during the last stage for all the beams is approximately of the same degree of nonlinearity ($RMSE_{avg}$ = 0.168).

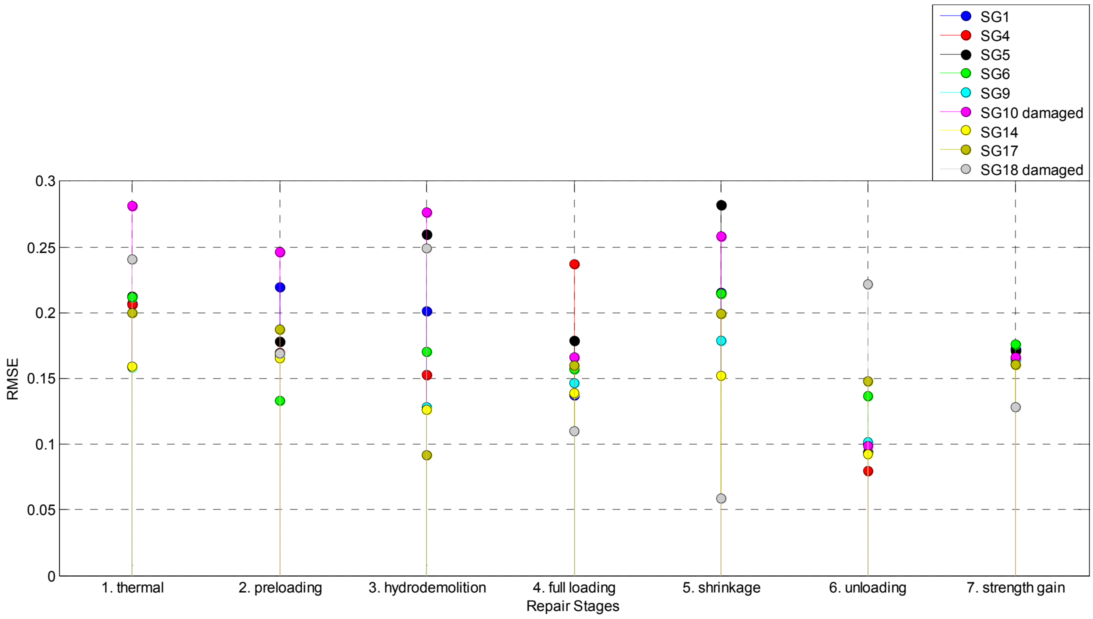

Figure 6.17 Variation of DVV analysis results on strain measured by top strain gauges.

6.2.4.9 Correlation of Soffit Gauges

Figure 6.18 shows the variation of RMSE for soffit gauges. SG19 did not perform well ever since full load application period, but definitely failed during the last stage. Hence the DVV analysis results for SG19 even presented here will not be encountered for the last three repair stages. High deviations in the strain nonlinearity, 0.206 and 0.203, are recorded during preloading and full loading application, respectively. The high nonlinearity in the strain is due to the high tension and section adjustment to the full loading. The difference in the soffit strain nonlinearity is also high during the hydrodemolition stage (0.092) as the embedded gauges had a little reaction in comparison to the rest of the soffit SGs. For all other stages, i.e. thermal, shrinkage, unloading, and full strength gain period, the difference in the soffit strain nonlinearity is small. This is the evidence that the readings of the SG are stable.

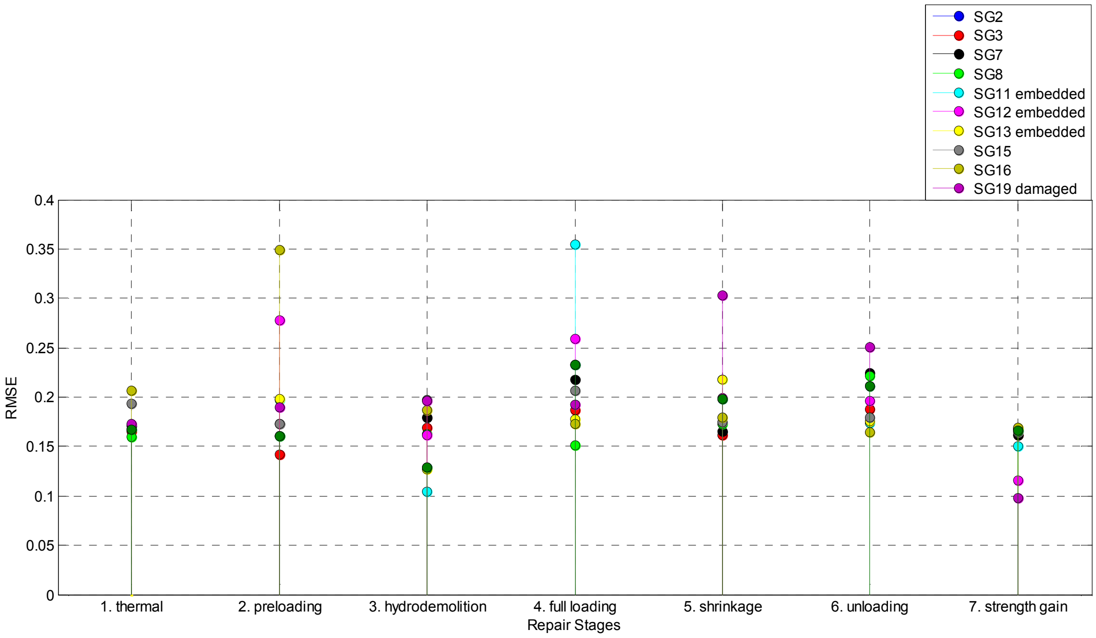

Figure 6.18 Variation of DVV analysis results on strain measured by top strain gauges.

6.2.4.10 Comparisons of the Beams

In order to test performance of DVV analysis on pseudostatic data the relationships between the damaged beam and the undamaged beams on either side is analysed. Figure 6.19 shows a plot comparing the RMSE of three beams for each repairing stage. 'Beam 3' is the damaged beam while 'Beam 2' and 'Beam 4' are undamaged beams on either side of it (see Figure 6.2), represented by SG5, SG1, and SG18 respectively. The bridge is expected to be within the linear zone of response with good relationships between the beams [188]. From the Figure 6.19 it is evident that 'Beam 2' and 'Beam 3' strain is of the same nonlinearity pattern. The nonlinearity degree of the strain of damaged beam is approximately proportionally greater for hydrodemolition, full loading, and shrinkage period, while it is almost the same for thermal, unloading, and further strength gain periods. This is in agreement with the expected behaviour during the bridge repair, as described in previous sections. The disagreement in RMSE pattern appears during the preloading period where the nonlinearity degree of SG1 measurements is higher; this is due to the unexpected peaks within the signal (see Figure 6.5). The DVV scatter plots show that strain signal recorded by SG1 and SG5 become linear during the last stage.

The DVV results for 'Beam 4', represented by SG18, show good agreement with damaged beam, SG5, for the first three stages of repair; however the mailfunctioning of the SG18 was reported during the second stage. The reason for this is that the signal during the second stage went off the scale, but it was still 'regular'. Also the observation period was short while the data noisy for DVV analysis [174]. Otherwise the disagreement in RMSE pattern of SG18 with SG5 and SG1 is indicator of malfunctioning.

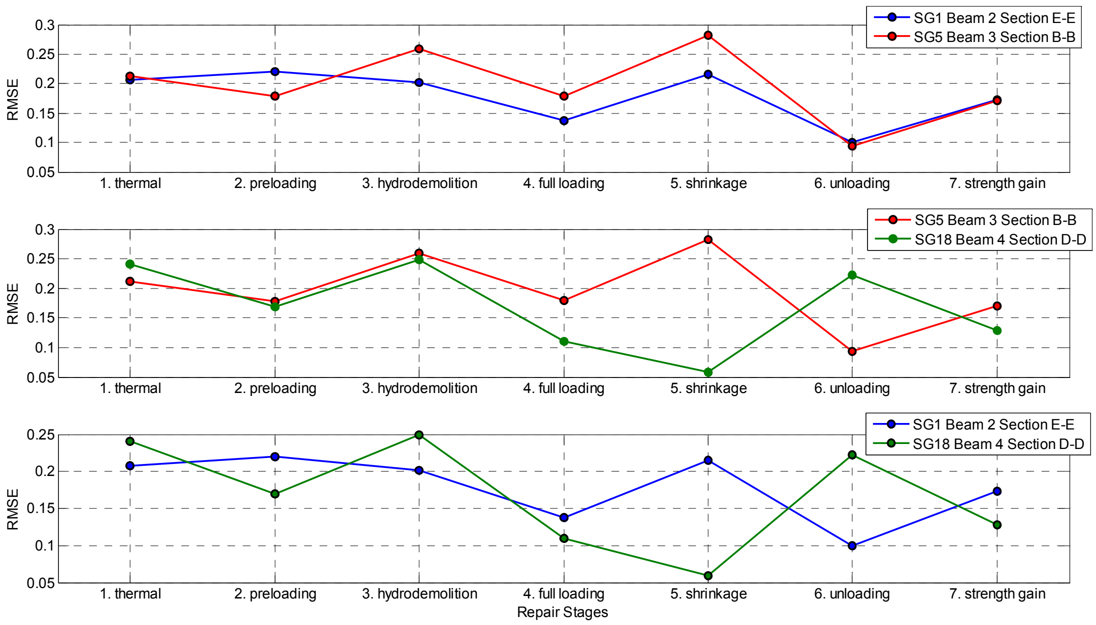

Figure 6. 19 Comparisons of DVV analysis of damaged and undamaged beams.

6.3 Single Span Steel-Concrete Composite Bridge

DVV method is used to analyse dynamic response of a composite bridge structure traversed by trains with continuous monitoring of different characteristics.

As in previous example, DVV is used for the first time to analyse the time series which are product imposed train loadings on a large bridge structure over period of time. The product of DVV analysis of recorded data and its surrogates, i.e. RMSE, are compared with respect to the type of the train crossing and location of dynamic measurements.

The real scale experiment on this bridge is not the part of this thesis. The experimental site and *in situ* measurements are part of research conducted by Division of Structural Design and Bridges, Department of Civil and Architectural Engineering, Royal Institute of Technology (KTH), Stockholm, Sweden. Hence, the following sections of this chapter describing the bridge, the bridge monitoring instrumentation, and the details of the trains used in the experiment are based on relevant literature [189, 192-194] and are included here for completeness.

6.3.1 Description of the Bridge

Skidträsk Bridge, located in the North of Sweden, is a single span steel-concrete composite bridge caring a single ballasted track and spaning 36m (Figure 6.20).

Figure 6.20 Photograph of Skidträsk Bridge [189].

The bridge is simply supported with respect to vertical bending moments. The rails are supported by concrete sleepers, separated by a regular distance of 65cm. The sleepers lie on a layer of ballast of approximately 50cm and this lies on a layer of sub-ballast, also of depth 50cm. The rock particles in the ballast layer have a diameter around 5cm and the particles in the sub-ballast layer have a diameter of around 10cm. The ballast layers are on a reinforced concrete slab, which transfers the load from the tracks to two steel beams. The width of the concrete slab is 6.7m and it varies in height between 30 and 40 cm. The steel beams also have a variable cross section (Figure 6.20). The cross section of the bridge is shown in Figure 6.21.

6.3.1.1 Material and Structural Properties of the Bridge

The material properties for the observed bridge are summarised in Table 6.1. The table includes Young's Modulus, Poisson's Ratio and the density of the steel, concrete, ballast, and the concrete and ballast combined i.e. when the mass of the ballast is added to the concrete deck. In the case of the combined section of concrete and ballast, the stiffness is not altered but the mass is increased [193].

Table 6.1 Material properties of the bridge [189].

Material	Young's Modulus (GPa)	Poisson's Ratio ν	Density ρ (kg/m^3)
Concrete	32	0.2	2500
Steel	210	0.3	7850
Ballast	-	-	2000
Concrete with additional mass of Ballast	32	0.2	5700

The recommended lower bound estimate of damping in EN 1991-2 [195] for this bridge type is 0.5%. However, the previous studies [189, 193, 196] of this bridge show that the damping ratio obtained from measurements is 1.5%.

6.3.2 Traffic Loading on the Bridge

The bridge is used by freight trains and passenger trains. The details of the trains used in the experiment are given in the Table 6.2 (N. A. Nolan, personal communication, 19.08.2013).

Table 6.2 Train Characteristics

Train		**1**	**2**	**3**	**4**	**5**	**6**	**7**	**8**	**9**
No. Locomotives		2	2	2	2	3	2	2	2	2
No. Wagons		0	0	36	0	36	28	0	27	0
Loaded				No		Yes	Yes		Yes	
Max. acc.	*(m/s^2)*	-0.65	1.22	2.3	-0.42	2.4	-3.4	5	-1.3	1.6
Max. speed	*(m/s)*	23	50	33	17	33	27	33	18	42
	(km/hr)	82.8	180	118.8	61.2	118.8	97.2	118.8	64.8	151.2
No.Bogies		4	4	76	4	78	60	4	58	4
Distance bogie-locomotive	*(m)*	20	20	7.7	20	7.7	7.7	7.7	7.7	20
Distance bogie-wagon	*(m)*	0	0	8.6	0	8.6	8.6	0	8.6	0
Distance loco-bogie	*(m)*	6.5	6.5	6.28	6.5	6.28	6.28	6.28	6.28	6.5
Distance wagon-bogie	*(m)*	0	0	5.38	0	5.38	5.38	0	5.38	0
Distance loc & wag bogie	*(m)*	0	0	5.83	0	5.83	5.83	0	5.83	0
Distance axles (loco)	*(m)*			2.7		2.7	2.7	2.7	2.7	
Distance axles (wag)	*(m)*			1.8		1.8	1.8	1.8	1.8	
Locomotive length	*(m)*			10.4		10.4	10.4		10.4	
Wagon length	*(m)*	0		10.4		10.4	10.4		10.4	
Load on bogie (loco)	*(N/axle)*					1.95E+05	1.95E+05		1.95E+05	
	(N/bogie)	9.00E+05	9.00E+05	1.00E+06	9.00E+05	3.90E+05	3.90E+05	3.90E+05	3.90E+05	9.00E+05
Load on bogie (wagon)	*(N/axle)*					2.25E+05	2.25E+05		2.25E+05	
	(N/bogie)					4.50E+05	4.50E+05		4.50E+05	

The Swedish Steel Arrow train (shadowed blue in Table 6.2), which is a common iron ore freight train in Sweden, is a particularly frequent loading on the bridge [192]. The Steel Arrow (SA) usually comprises 2 power cars or locomotives and 26 wagons, with a total length of 388m. Both the locomotives and wagons are 10.4m long and have two bogies. The bogies on the locomotive are 7.7m apart and 8.6m apart on the wagons. The distance between the axles on the bogies is 2.7m on the locomotives and 1.8m on the wagons. The axles for the locomotives and wagons are loaded by 19.5 tons and 25 tons respectively [189].

The trains listed in Table 6.2 can be generally divided in two groups according to their characteristics; group A (Train 1, 2, 4 and 9) and group B (Train 3, 5, 6, 7, 8). There are two different characteristics among the train model of group A; maximum acceleration and maximal speed. On the other hand group B trains have more differences among themselves (i.e. the number of locomotives and wagons, the maximal acceleration and speed, the number of bogies, and loading). Special case is Train 7 with just few common characteristics with group B trains.

6.3.4 Instrumentation

The bridge was monitored by the Division of Structural Engineering & Bridges, KTH Royal Institute of Technology, Stockholm. Details of the system can be found in Loireaux 2008 [189]. In summary, permanent and temporary monitoring systems are installed consisting of 6 and 10 sensors, respectively. Figure 6.21 shows the locations of the permanent and temporary sensors (N. A. Nolan, personal communication, 20.07.2013).

The permanent system consisted of:

- 4 strain gauges situated on the east beam, at midpoint and quarter-point, on the upper and the bottom flanges (CH1 to CH4),
- 3 Si-flex SF1500S accelerometers for vertical deck accelerations were installed: two of them are on the east beam at midpoint and quarter-point (CH5 and CH7); and the third, on the west beam at midpoint (CH6),

- 2 strain transducers (B-WIM sensors) on the concrete slab at midpoint and quarter-point (CH9 & CH11), to measure transversal strain,
- A temperature gauge (CH8).

The temporary system consisted of four accelerometers installed around the mid-span of the bridge (midpoint of the central sleeper (T-1), end point of the central sleeper (T-2), in the rail placed at the level of the central sleeper (T-3) and in the ballast between two sleepers (T-4)). Two optical laser sensors were also installed on the rail to measure the speed of the train. The signals from the optical laser sensors allowed the determination of the number of wagons of the train and the distance between two axles, and this then allowed the calculation of train speed and the determination of train type by the distance between axles, bogies and wagons. The distance between the two optical sensors was 26.05 meters [189].

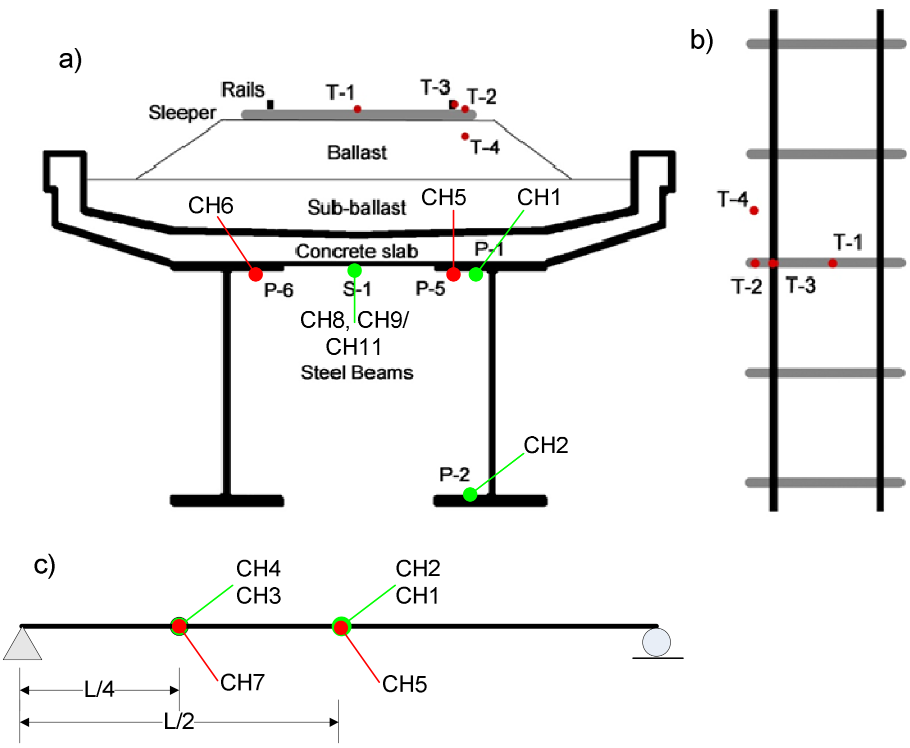

Figure 6.21 a) Section of the bridge, b) part of the track at midspan, and c) schematic representation of the bridge span with location of the sensors (accelerometers in red and strain gauges in green).

During the first day, the sampling rate was 150 Hz and a Bessel (anti-aliasing) filter was applied with a filter cut-off frequency of 20 Hz. During the rest of the year in which the system was in use, the sampling rate was increased to 600 Hz and the filter cut-off frequency of the anti-aliasing filter to 75 Hz [189].

6.3.5 Measurements and Data Filtering

The list of measurements used for DVV analysis is given in Table 6.3.

Table 6.3 The list of measurements used in DVV analysis.

<table>
<tr><th>Data measured</th><th colspan="4">STRAIN</th><th colspan="3">ACCELERATION</th><th colspan="2">TRANSVERSAL STRAIN</th></tr>
<tr><th>Measurement point</th><td>CH1</td><td>CH2</td><td>CH3</td><td>CH4</td><td>CH5</td><td>CH6</td><td>CH7</td><td>CH9</td><td>CH11</td></tr>
<tr><th rowspan="2">Location</th><td colspan="2">East beam L/2</td><td colspan="2">East beam L/4</td><td>East beam L/2</td><td>West beam L/2</td><td>East beam L/4</td><td rowspan="2">Slab L/2</td><td rowspan="2">Slab L/4</td></tr>
<tr><td>Upper flange</td><td>Lower flange</td><td>Upper flange</td><td>Lower flange</td><td colspan="3">Upper flange</td></tr>
</table>

The examples of strain and acceleration responses to train passage are shown in Figure 6.22 – 6.24 for beams and slab. The recorded bridge responses to all train types crossing are shown in Appendix C2.

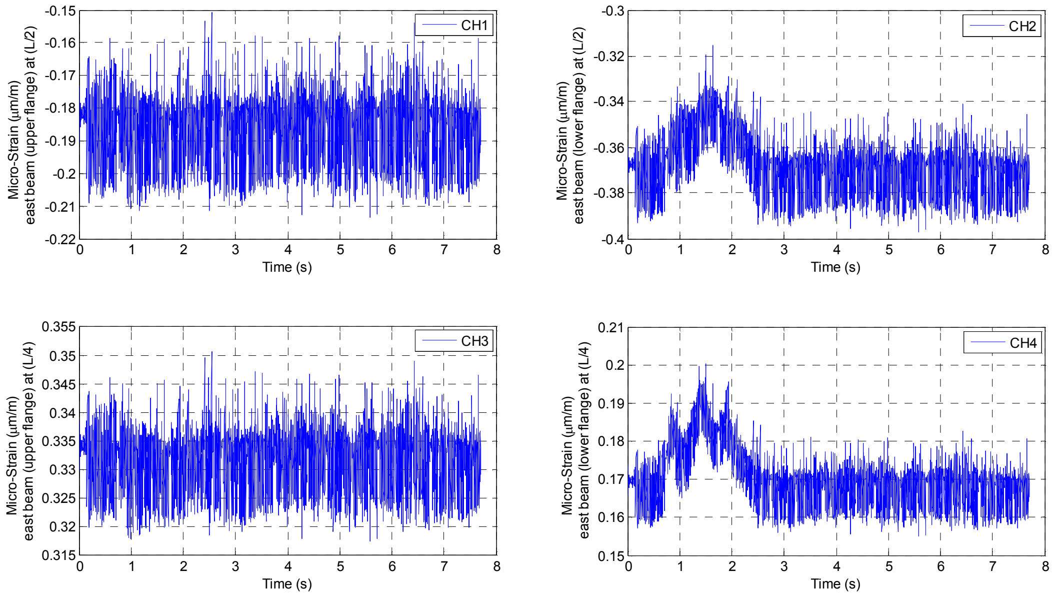

Figure 6.22 Strain of the east beam measured at top and bottom flange at the mid- and quarter-span for the Train 2.

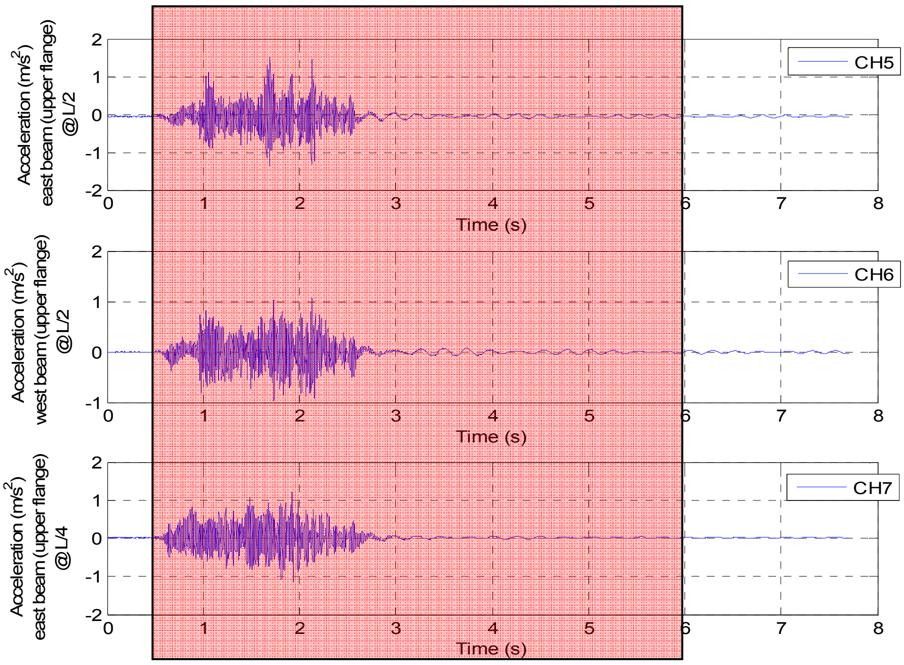

Figure 6.23 Acceleration measured at the upper flange of the east and west beam for the Train 2 (red rectangle indicates the region of valid data for DVV analysis).

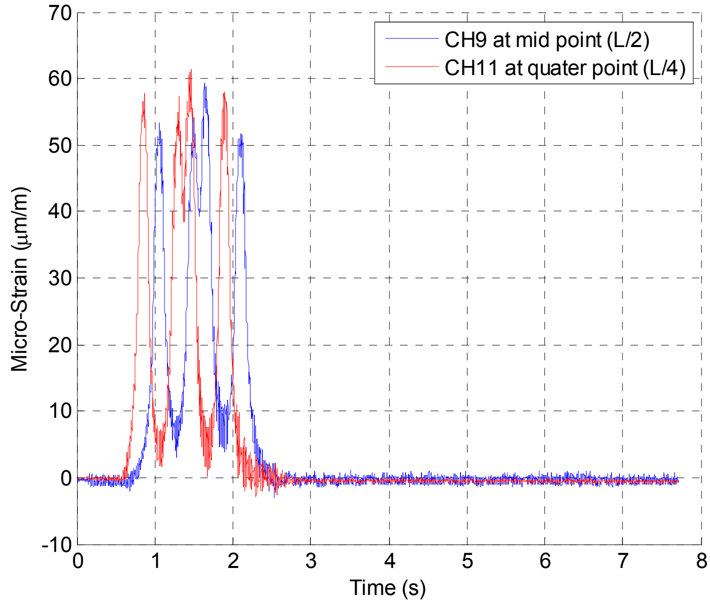

Figure 6.24 Transversal strain measured at mid- and quarter-span of the slab for the Train 2.

There are two stages in filtering data. In the first stage only the responses of the bridge due to passage of the train are included, i.e. the acceleration of the bridge recorded prior to the train passage and after the bridge reaches its equilibrium position (saturation of vibration) is excluded. In the second stage the data that went off the scale for no apparent reason are excluded. These data are categorised as bad data. The duration of the periods of bad data are very small (usually it is only one bad point), but their contribution in the signal nonlinearity analysis can be significant. The data that was filtered prior to DVV analysis are:

Train 4 – CH3

Train 5 – CH3, CH5-7

Train 6 – CH1-4

Train 9 – CH3-4

6.3.6 Results of DVV Analysis

The results of DVV analysis, i.e. DVV plots and DVV scatter plots, of the acceleration and strain recorded in bridge due to train traffic loading (Table 6.1) are shown in Appendix C2. The parameters chosen for DVV analysis are kept the same as in section 6.2.4. The results of DVV analysis, i.e. the deviation from bisector line of scatter plot quantified by the root mean squared error, will be referred to as RMSE.

6.3.6.1 Strain measured in the Beams

The results of DVV analysis of the strain measured in the east beam at top (TF) and bottom (BF) flange at the mid- (L/2) and quarter- (L/4) span for all trains are shown in Figure 6.25. The nonlinearity of the top flange strain is greater than that of the bottom flange in all cases observed.

The RMSE calculated for the top flange at midspan is generally greater than for the quarter span, which is expected as the magnitude of strain is greater at midspan. This is in agreement with the Chapter 5 observations. However, the variation in nonlinearity between mid- and quarter-span is small for each train model observed. For all cases observed, the RMSE for the top flange ranges from 0.340 to 0.407 and 0.333 to 0.402, for mid- and quarter- span, respectively. There is noticeable trend in the strain linearity for Train 1, 2, 3, 4 and 9 crossing, where top flange at midspan has maximum and bottom flange quarter span has minim RMSE. However, there is no correlation between train characteristics and nonlinearity of top flange strain.

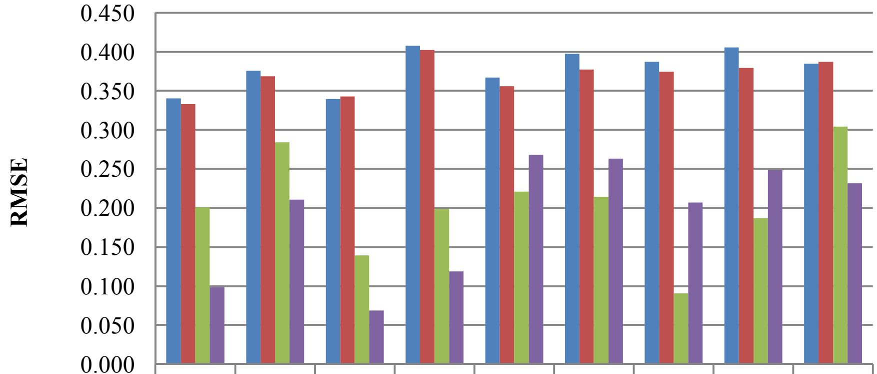

	1	2	3	4	5	6	7	8	9
CH1 (TF L/2)	0.340	0.376	0.340	0.407	0.367	0.397	0.387	0.406	0.385
CH3 (TF L/4)	0.333	0.369	0.343	0.402	0.356	0.377	0.374	0.379	0.387
CH2 (BF L/2)	0.201	0.284	0.139	0.199	0.221	0.215	0.091	0.187	0.304
CH4 (BF L/4)	0.099	0.211	0.069	0.119	0.268	0.263	0.207	0.248	0.232

Figure 6.25 DVV analysis results of strain gauges measurements for East beam.

The nonlinearity of the strain measured at the bottom flange is noticeably lower than at top flange. However, the trend between RMSE of strain measured at the mid- and quarter-span is inconclusive for some cases (i.e. Train 5, 6, 7, and 8). Also, the variation of RMSE between measurements at mid- and quarter-span is noticeably greater. For the trains of group A the nonlinearity of the strain at the midspan is greater than at quarter span, which is in agreement with findings for top flange. On the other hand, the RMSE obtained for the beam strain of group B the degree of nonlinearity of the strain measured at quarter- is greater than at mid-span. The reason for this could be the characteristics of the train. One possibility is that this phenomenon is driven by the loadings, e.g. Train 3 has no loading and nonlinearity of the strain at midspan is greater than at quarter span. However, the group B trains have many differences and the nonlinearity can not be linked to the specific one. The other possibility is that the choice of DVV parameters is such that DVV scatter plot is crossing the bisector line (see appendix C2) giving the lower RMSE values. Even with this adjustment of DVV parameters, the relationship between degree of nonlinearity of strain at bottom flange and train characteristics is hard to establish.

6.3.6.2 Acceleration of the Beams

The results of DVV analysis of Beam acceleration are shown in Figure 6.26. The RMSE has larger nonlinearity at mid span and lower nonlinearity at quarter-span, for the responses of the bridge to the crossing of Train 1, 2, 3 and 9. The nonlinearity degree is about the same (apx. 0.2) for the Trains 5, 6, and 7 for three measurement locations. The highest nonlinearity of the response signal is recorded for Train 8, between 0.371 and 0.39. Again there is many variables involved and it is hard to connect the degree of the acceleration nonlinearity to any particular one of them.

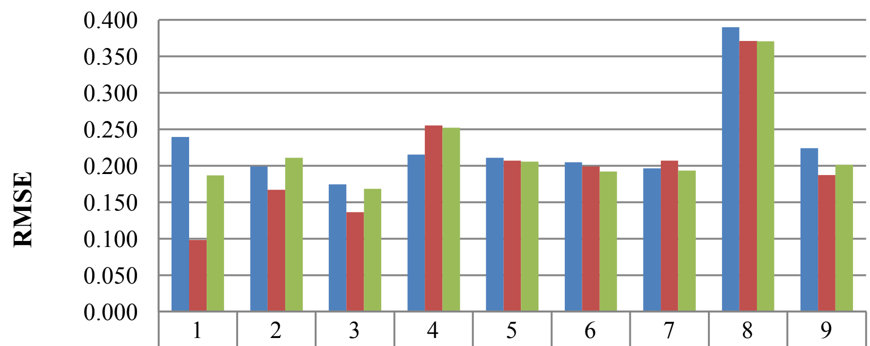

	1	2	3	4	5	6	7	8	9
CH5 (EB L/2)	0.239	0.199	0.175	0.216	0.211	0.205	0.196	0.390	0.224
CH7 (EB L/4)	0.098	0.167	0.137	0.255	0.207	0.199	0.207	0.371	0.187
CH6 (WB L/2)	0.187	0.211	0.169	0.252	0.206	0.192	0.193	0.371	0.202

Figure 6.26 DVV analysis results of accelerometer measurements for East and West beam.

6.3.6.3 Strain of Concrete Slab

Figure 6.27 shows the results of DVV analysis for the strain measured in the slab at mid- and quarter-span. The degree of nonlinearity of strain at these two locations is about the same (or slightly higher for midspan) for the train crossing. For the crossing of the group A trains the maximum nonlinearity is for Train 2 and minimum for Train 4, which appears to be linked to the train crossing speed. For higher speeds of the train the degree of nonlinearity decreases, i.e. Train 4 with speed 61.2km/h, Train 1 speed 82.8km/h, Train 9 speed 151.2km/h, and Train 2 speed

180km/h (see Figure 6.27 for RMSE). The RMSE obtained for the group B train crossing the bridge has the same relationship to the speed of train. However, the level of nonlinearity is visibly lower, from 0.201 to 0.203. This is the proof that the train speed is not the only contributor to the nonlinearity. The observation and comparison of the train characteristics leads to conclusion that the loading of the train or/and number of the wagons are the factors that can reduce the nonlinearity of slab transversal strain. Also the RMSE for the bridge response to the unloaded Train 7 is higher than for Train 3 or 5, yet these three trains have the same speed.

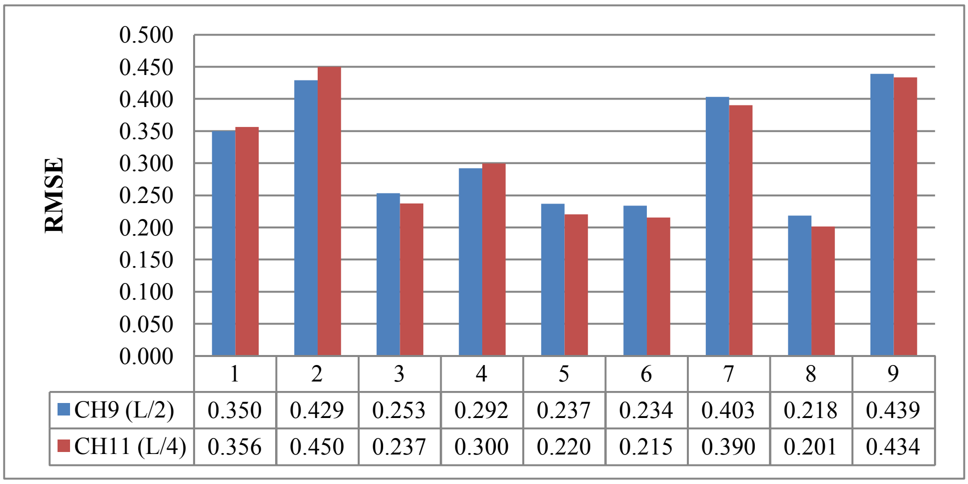

	1	2	3	4	5	6	7	8	9
CH9 (L/2)	0.350	0.429	0.253	0.292	0.237	0.234	0.403	0.218	0.439
CH11 (L/4)	0.356	0.450	0.237	0.300	0.220	0.215	0.390	0.201	0.434

Figure 6.27 DVV analysis results of strain transducers measurements for concrete slab.

6.4 Conclusions

DVV method is employed to characterize the behaviour of two bridge systems through analysis of their response.

The DVV method applied on strain data measured during the seven stages of a bridge repair shows that:

- The low and uneven sampling rate, due to fundamentally different activities during the rehabilitation process, lead to re-evaluation of DVV parameters and therefore it is hard to compare the numerical results between different stages.

- The results should be compared relatively to each other (with close observation of DVV and DVV scatter plots).
- The number of data varies between repairing stages, therefore comparison of DVV numerical results between stages is inadequate.
- For specific stage, the sudden and gradual changes in the bridge's behaviour can be identified.
- The strain gauges malfunctioning can be detected to the certain extent.

Upon analysis of the damaged and undamaged beams, processing of the original strain data has been seen to be beneficial for indicating both sudden and gradual changes. DVV showed promising results in detecting the rehabilitation activities. The closer observations of DVV plots showed linear behaviour of the strain measured after rehabilitation process.

DVV method employed to analyse the behaviour of single span composite bridge in use showed that:

- The degree of nonlinearity of the bridge response does not depend only on bridge structural characteristics but on the vehicle crossing, i.e. on the interaction between the two.
- There are many vehicle characteristics that contribute to the nonlinearity of the structure responses.
- There is link between the speed of the vehicle and degree of nonlinearity of slab transversal strain, where if speed increases the nonlinearity decreases.
- The other influential factor for the degree of nonlinearity of the slab strain response is the weight of the moving vehicle.

It is very difficult to compare two observed systems, prestressed concrete bridge and composite steel bridge, from the structural point of view. It is even harder to compare the responses of these two systems. However the pseudo static data analysed after the repairs reveal that the degree of nonlinearity of the strain measured becomes stable (approx. 0.166), while DVV plots indicate linear behaviour of the bridge response. For dynamic loading of the composite bridge the degree of nonlinearity varies between locations and responses measured. However it is generally higher for the same types of measurements and this high nonlinearity is reflected onto DVV plots.

The DVV method in combination with online structure monitoring (by any of the devices observed) can be used for the fast and inexpensive structure assessment. The initial values of RMSE should be calculated for the when structure is unloaded and for the expected loading on the structure. These values would be used as bench mark.

Overall, the method proves to be practical for fast assessment of real structures through analysis of its responses and could be used for SHM diagnostics.

Chapter 7

Discussions and Conclusions

7.1 Introduction

The focus of the thesis is structural health monitoring based on bridge-vehicle interaction approach. Different methodologies of structural damage detection techniques are proposed and critically investigated from different aspects. Damage detection employing bridge-vehicle interaction is considered from theoretical, experimental, and full scale operational structure viewpoints. The outcomes of the thesis can be used by engineers, infrastructure owners, and investors in developing infrastructure monitoring and maintenance strategies in order to secure safety and serviceability of the structures.

7.2 Summary of Research

The beginning of the research deals with system characterization, i.e. type and degree of non-linearity of the system, as well as with characterization of damping of the system. In the next stage the uncertainties in the structural system, in the form of surface roughness and sudden stiffness change, are investigated, both theoretically and experimentally, using bridge vehicle interaction. Investigation into the presence of noise in the signal and related masking effects is conducted. Different statistical parameters are tested and new robust SHM markers along with calibration curves are established for estimation of damage extent. The new surface roughness method for first three levels of damage diagnostics is proposed and tested in detail. In the final stage a novel signal processing technique, employed for the first time for characterization of the system through system response, is tested on theoretical and experimental models, as well as on real structures. In the process different structure response measurement techniques are compared.

The findings can be useful for planning maintenance and rehabilitation strategies of damaged bridges.

7.3 Detailed Results

The contributions of the thesis are listed in detail in this section.

A new simple, consistent, and robust statistical descriptors to calibrate damping ratios in linear and non-linear systems are established taking in consideration different sampling rates and measurement noise. It is found that the kurtosis measure tends to characterize damage, while skewness measure is important for characterizing the type and degree of non-linearity of the system. The general approach and findings are immediately applicable under model-free conditions for frequency responses that typically contain a single significant global extremum within the analysis window. With slight modification of windowing, the approach is also readily applicable for responses with multiple significant extrema. The findings are general and lead to investigation of new markers from the specific system perspective.

The possibility of using surface roughness for detecting the damage in bilinear SDOF system is established. The white noise represents a broadband excitation, qualitatively similar to the interaction with surface roughness and the bilinearity attempts to capture a breathing crack. First and second order cumulants of the response of this system are observed to be appropriate markers for detecting changes in system stiffness.

The effectiveness of LDV measurements for damage detection and its superiority over traditional accelerometer based approach is demonstrated. Thus, where time or frequency domain detection of sudden stiffness change for a SDOF bilinear oscillator is not possible, the LDV based measurements combined with wavelet analysis represent efficient method for detection of presence and location of damage.

The new damage detection using surface roughness method is proposed through consideration of bridge-vehicle interaction effects. The method employs the RSR of the beam, realistically classified as per ISO 8606:1995(E), as an aid to monitor the health of the structure in its operational condition. New simple, consistent, easy to implement, and robust statistical descriptors to detect and calibrate the existence, location, and extent of damage considering the effects of vehicle speed and variable RSR profiles are established. The appropriate calibration curves are obtained. It is found that first and second order cumulants of response can be used as damage detection markers. The discontinuities in the mean and standard deviation curves give position of the damage and the jump size is related to the extent of damage. The damage calibration is found to depend on vehicle speed and road type. When the road quality decreases the slope discontinuity of mean and standard deviation at crack location becomes more obvious. Furthermore, the damage calibration on better roads is less uncertain and gives consistent but less sensitive results, while worse roads are less consistent in calibration values but give more sensitive results. Therefore, it is found that the medium road surface roughness (type C) is optimal for calibration purposes. The study is particularly useful for continuous online bridge health monitoring.

The effectiveness of the DVV method in detecting the changes within the system is demonstrated. The responses of theoretical model and two experiments (SDOF car and WTB) are analysed by DVV method and it is found that there is good correlation between certain system parameters and degree of nonlinearity of observed system response. The results of DVV analysis on SDOF theoretical model showed that the parameter that determines degree of linearity/nonlinearity of response signal (RMSE) is sensitive to change in damping ratio, driving frequency, and natural frequency, but insensitive to mass, base frequency, and input force magnitude change. The SDOF car experiments show that the DVV method can be used to detect system stiffness change and nature of excitation force. On the other hand, the method proves inappropriate for detection of exact time and extent of damage in the case of sudden stiffness change. When contrasting DVV analysis on the responses obtained by 3D Accelerometer and LDV it is found that both instruments can successfully record stiffness change and the change in nature of excitation force, but not the change of surface roughness. In the WTB experiment the DVV method applied on responses obtained by 3D accelerometer, LDV, and strain gauges proves to be successful in detecting different type of loading. However, the comparison between the instruments measurements' is not possible as the DVV results do not have the same / similar trend for the same type of loading. No straightforward conclusion regarding the underlying system can be drawn from the nonlinearity analysis of a signal, but the DVV method allows for comparative analysis between different systems driven by the same input.

The application of DVV method on full scale structures response data is found to be quick and easy. It is found that sudden and gradual changes in the bridge behaviour can be identified. The malfunctioning of strain gauges can be identified to an extent, and further observation and comparison of the instrument recordings is needed. The DVV shows promising results for the bridge that went trough rehabilitation process after being damaged, i.e. it is possible to detect the rehabilitation activities. However, the number of data varies between repairing stages, therefore comparison of DVV numerical results between the stages is inadequate. Closer observations of DVV plots show linear behaviour of the pseudo-static data after rehabilitation process, i.e. the degree of nonlinearity of the strain measured becomes stable (approx. 0.166). The analysis of the composite single span bridge responses to the passage of the different train types shows that the degree of nonlinearity of the bridge response does not depend only on bridge structural characteristics but on the vehicle crossing, i.e. on the interaction between the two. Moreover, there are many vehicle characteristics that contribute to the nonlinearity of the structure response, e.g. vehicle speed, weight, length etc. However, there is correlation between the speed of the vehicle and degree of nonlinearity of slab transversal strain, i.e. if speed increases the nonlinearity decreases. Generally the degree of nonlinearity of the composite bridge dynamic loading varies between locations and responses measured. However, it is higher for the same types of measurements than for the pseudo-static data and this high nonlinearity is reflected onto DVV plots. Overall, the method proves to be practical for fast assessment of real structures through analysis of the responses and could be used for SHM diagnostics.

7.4 Limitations of the Developed Work

The successful damage detection using bridge vehicle interaction depends on presence of noise. The noise is seen to play a central role because of masking effects since the damage and the noise both possess similar characteristics in terms of singularities or sudden change in the neighbourhood of the location of damage. Thus, the effects of damage still need to be considerably greater than the effects of noise. This issue is addressed in Chapter 4, where random white noise is cancelled out by considering the passage of many vehicles and the consideration of normalisation. However, when coloured noise is present in bridge response, the damage might not be identified due to high masking effect. In this case the location of the damage(s) could be indicated by using wavelet analysis as shown in Chapter 3 and in numerous papers. Accurate continuous measurement of the spatial data poses practical difficulties in identifying damage using the damaged deflected shape or strain through wavelets. Although modern devices based on Lasers (see Chapter 3 and 5) or Fibre Optic Cables are reliable in recording continuous measurements in small laboratory based experiments, their use is limited by availability and high cost. Applications on full scale structures are yet to be developed as well.

Study of the system response trough DVV method shows that there are limitations to the DVV application. Fundamentally, the method is sensitive to the choice of parameters and the frequency of measurements. The computational time increases with the quantity of data and due to the applied software limitations, in some cases, the adjustment of DVV parameters or windowing of data is needed. It is demonstrated that while the DVV method can be used for the valuation of output signal degree of nonlinearity, it can not be used for characterization of an underlying system linearity or nonlinearity. Moreover, DVV can not register the change in system mass, frequency, input force magnitude, and time and extent of sudden stiffness change. The numerical results of DVV analysis can not be compared if the numbers of data points vary or if the nature of output signal measured is different.

7.5 Recommendations for Further Research

The results of the present work open up many directions in which further research can develop.

The new developed method for damage detection using surface roughness should be tested for new materials (e.g. concrete) or different cross-section geometries. Also, the method could be used as the basis for designing software which would be fed with the geometry and material characteristics of the bridge to perform the first three steps in damage diagnostics.

Another challenging and ambitious task in terms of theory would be further testing and evaluation of surface roughness method for damage detection for the variability of the bridge or/and vehicle weights, variability of vehicle tire pressures, two axles crossing, and multiple vehicles moving in the same and opposite directions.

The proposed bridge-vehicle model could be expanded to the case of multiple cracks and identification methodology extended to deal with multi-site damage cases.

It would be interesting to develop a model that captures coupling between longitudinal, torsional, and transverse vibrations and to investigate the use of coupling effects for damage diagnostics. Furthermore, the DVV method could be used for characterization of system responses, contribution of each type of vibration, and for evaluation of the coupling effects on damage.

The DVV method can be explored further on the full scale bridges. Ideally the chosen structure would be remotely monitored during the same time intervals by LDV for no traffic and controlled traffic situation. In this way the contribution of diurnal and nocturnal temperatures to the structure response could be evaluated. By evaluation response of the bridge under controlled traffic situation it would be possible to compare responses and set benchmarks for different types and numbers of vehicles. The information collected can be used later on for remote monitoring of the observed structure.

References

1. Znidaric, A., V. Pakrashi, E. O'Brien, and A. O'Connor, *A Review of Road Structure data in Six European Countries.* Proceedings of the ICE - Urban Design and Planning,, 2011. 164(4): p. 225-232.
2. Moyo, P. and J.M.W. Brownjohn, *Detection of Anomalous Structural Behaviours using Wavelet Analysis.* Mechanical Systems and Signal Processing 2002. 16(2-3): p. 429-445.
3. Kisa, M., *Free vibration analysis of a cantilever composite beam with multiple cracks.* Composites Science and Technology, 2004. 64(9): p. 1391–1402.
4. O'Brien, E., A. Znidaric, K. Brady, A. Gonzalez, and A. O'Connor, *Procedures for the Assessment of Highway Structures.* ICE Transport Journal, 2005. 158(TR1): p. 17-25.
5. Rucka, M. and K. Wilde, *Crack identification using wavelets on experimental static deflection profiles.* Engineering Structures, 2006. 28(2): p. 279–288.
6. Farrar, C.R. and K. Worden, *An introduction to structural health monitoring.* Philosofical Transactions of the Royal Society A: Mathematical, Phisical and Engineering Sciences, 2007. 365: p. 303-315.
7. Doebling, S.W., C.R. Farrar, and M.B. Prime, *A Summary Review of Vibration-Based Damage Identification Methods.* The Shock and Vibration Digest, 1998. 30(2): p. 91-105.
8. Doebling, S.W., C.R. Farrar, M.B. Prime, and D.W. Shevitz, *Damage Identification and Health Monitoring of Structural and Mechanical Systems from Changes in Their Vibration Characteristics: A Literature Review*, N. LABORATORY, Alamos, and f.t.U.S.D.o.E. . Editors. 1996, Los Alamos National Laboratory is operated by the University of California for the United States Department of Energy under contract W-7405-ENG-36. p. 136.

9. Patsias, S. and W.J. Staszewskiy, *Damage detection using optical measurements and wavelets.* Structural Health Monitoring, 2002. 1(1): p. 5-22.

10. Pakrashi, V., *Damage Detection using Wavelet based techniques and structural vibration control*, in *Departemnt of Civil Engineering*. 2006, University of Dublin, Trinity College: Dublin. p. 198.

11. Pakrashi, V., A. O'Connor, and B. Basu, *A Bridge–Vehicle Interaction Based Experimental Investigation of Damage Evolution.* Structural Health Monitoring, 2010. 9(4): p. 285 - 296.

12. Askeland, D.R., *The Science and Engineering of Materials*. 1994, Boston: PWS Publishing Co.

13. Owston, C.N., *Eddy current methods for the examination of carbon fibre reinforced epoxy resins.* Materials Evaluation, 1976. 34: p. 237-244.

14. Hung, Y.Y., *Shearography: A novel and practical approach for nondestructive inspection.* Journal of Nondestructive Evaluation, 1989. 8(2): p. 55-67.

15. Hung, Y.Y., *Shearography for non-destructive evaluation of composite structures.* Optics and Lasers in Engineering, 1996. 24(2–3): p. 161-182.

16. Gros, X.E., K. Takahashi, and M.-A.D. Smet. *On the efficiency of current NDT methods for impact damage detection and quantification in thermoplastic toughened CFRP materials*. in International Conference on Advanced Materials (NDT session). 1998. Hurghada, Egypt.

17. Stewart, M. and D. Rosowsky, *Structural Safety and Serviceability of Concrete Bridges Subject to Corrosion.* Journal of Infrastructure Systems, 1998. 4(4): p. 146-155.

18. Micic, T.V., M.K. Chryssanthopoulos, and M.J. Baker, *Reliability analysis for highway bridge deck assessment.* Structural Safety, 1995. 17(3): p. 135-150.

19. Huang, Y., T. Adams, and J. Pincheira, *Analysis of Life-Cycle Maintenance Strategies for Concrete Bridge Decks.* Journal of Bridge Engineering, 2004. 9(3): p. 250-258.

20. Rafiq, M.I., M.K. Chryssanthopoulos, and T. Onoufriou, *Performance updating of concrete bridges using proactive health monitoring methods.* Reliability Engineering & System Safety, 2004. 86(3): p. 247-256.

21. Enright, M. and D. Frangopol, *Service-Life Prediction of Deteriorating Concrete Bridges.* Journal of Structural Engineering, 1998. 124(3): p. 309-317.

22. Akgül, F. and D. Frangopol, *Lifetime Performance Analysis of Existing Reinforced Concrete Bridges. II: Application.* Journal of Infrastructure Systems, 2005. 11(2): p. 129-141.

23. Enright, M.P. and D.M. Frangopol, *Time Variant System Reliability Prediction*, in *8th ASCE Specialty Conference on Probabilistic Mechanics and Structural Reliability*. 2000: University of Notre Dame, Indiana, USA.

24. Akgül, F. and D. Frangopol, *Bridge Rating and Reliability Correlation: Comprehensive Study for Different Bridge Types.* Journal of Structural Engineering, 2004. 130(7): p. 1063-1074.

25. Kong, J. and D. Frangopol, *Life-Cycle Reliability-Based Maintenance Cost Optimization of Deteriorating Structures with Emphasis on Bridges.* Journal of Structural Engineering, 2003. 129(6): p. 818-828.

26. Rytter, A., *Vibration Based Inspection of Civil Engineering Structures*. 1993, Aalborg University, Denmark.

27. Carneiro, S.H.S., *Model-Based Vibration Diagnostic of Cracked Beams in the Time Domain*, in *Engineering Mechanics, Faculty of the Virginia Polytechnic Institute and State University*. 2000, Virginia State University: Blacksburg, Virginia.

28. Lifshitz, J.M. and A. Rotem, *Determination of Reinforcement Unbonding of Composites by a Vibration Technique.* Journal of Composite Materials, 1969. 3(3): p. 412-423.

29. Salawu, O.S., *Detection of structural damage through changes in frequency: a review.* Engineering Structures, 1997. 19(9): p. 718-723.

30. Adams, R.D., P. Cawley, C.J. Pye, and B.J. Stone, *A Vibration Technique for Non-Destructively Assessing the Integrity of Structures.* Journal of Mechanical Engineering Science, 1978. 20(2): p. 93-100.

31. Cawley, P. and R.D. Adams, *The location of defects in structures from measurements of natural frequencies.* The Journal of Strain Analysis for Engineering Design, 1979. 14(2): p. 49-57.

32. Stubbs, N. and R. Osegueda, *Global non-destructive damage evaluation in solids.* Modal Analysis: The International Journal of Analytical and Experimental Modal Analysis, 1990. 5(2): p. 67–79.

33. Armon, D., Y. Ben-Haim, and S. Braun, *Crack detection in beams by rankordering of eigenfrequency shifts.* Mechanical Systems and Signal Processing, 1994. 8(1): p. 81-91.

34. Friswell, M., J. Penny, and D. Wilson, *Using vibration data and statistical measures to locate damage in structures.* Modal Analysis: The International Journal of Analytical and Experimental Modal Analysis, 1994. 9(4): p. 239-254.

35. Luo, H. and S. Hanagud, *Dynamic Learning Rate Neural Network Training and Composite Structural Damage Detection.* AIAA Journal, 1997. 35(9): p. 1522-1527.

36. Mahmoud, M.A. and M.A. Abu Kiefa, *Neural network solution of the inverse vibration problem.* NDT & E International, 1999. 32(2): p. 91-99.

37. Friswell, M.I., J.E.T. Penny, and S.D. Garvey, *A combined genetic and eigensensitivity algorithm for the location of damage in structures.* Computers & Structures, 1998. 69(5): p. 547-556.

38. Wang, X.D. and G.L. Huang, *Identification of embedded cracks using back propagating elastic waves.* Inverse Problems, 2004. 20(5): p. 1393–1409.

39. Yin, H.P., *An average inverse power ratio method for the damping estimation from a frequency response function.* Mechanical Systems and Signal Processing, 2010. 24(3): p. 617-622.

40. West, W.M. *Illustration of the use of modal assurance criterion to detect structural changes in an Orbiter test specimen*. in Airforce Conference on Aircraft Structural Integrity. 1984. NASA Johnson Space Center; Houston, TX, United States.

41. Pastor, M., M. Binda, and T. Harcharik, *Modal Assurance Criterion.* Procedia Engineering, 2012. 48: p. 543-548.

42. Yuen, M.M.F., *A numerical study of the eigenparameters of a damaged cantilever.* Journal of Sound and Vibration, 1985. 103(3): p. 301-310.

43. Rizos, P.F., N. Aspragathos, and A.D. Dimarogonas, *Identification of crack location and magnitude in a cantilever beam from the vibration modes.* Journal of Sound and Vibration, 1990. 138(3): p. 381-388.

44. Pandey, A.K., M. Biswas, and M.M. Samman, *Damage detection from changes in curvature mode shapes.* Journal of Sound and Vibration, 1991. 145(2): p. 321-332.

45. Chance, J., G.R. Tomlinson, and K. Worden. *A Simplified Approach to the Numerical and Experimental Modelling of the Dynamics of a Cracked Beam*. in IMAC XII - 12th International Modal Analysis Conference. 1994.

46. Swamidas, A.S.J. and Y. Chen, *Monitoring crack growth through change of modal parameters.* Journal of Sound and Vibration, 1995. 186(2): p. 325-343.

47. Chen, Y. and A.S.J. Swamidas, *Modal Updating for Crack Detection in Plated T-joints*, in *15th, International modal analysis conference*. 1997, Society for Experimental Mechanics Inc.

48. Yam, L.Y., T.P. Leung, D.B. Li, and K.Z. Xue, *Theoretical and experimental study of modal strain analysis.* Journal of Sound and Vibration, 1996. 191(2): p. 251-260.

49. Ratcliffe, C.P., *Damage detection using a modified laplacian operator on modeshape data.* Journal of Sound and Vibration, 1997. 204(3): p. 505-517.

50. Stubbs, N. and J.-T. Kim, *Damage localization in structures without baseline modal parameters.* AIAA Journal, 1996. 34(8): p. 1644-1649.

51. Cornwell, P., S.W. Doebling, and C.R. Farrar, *Application of the strain energy damage detection method to plate-like structures.* Journal of Sound and Vibration, 1999. 224(2): p. 359-374.

52. Yoo, S.H., H.K. Kwak, and B.S. Kim. *Detection and location of a crack in a plate using modal analysis*. in Proceedings of International Modal Analysis Conference (IMAC-XVII). 1999.

53. Kam, T.Y. and T.Y. Lee, *Crack size identification using an expanded mode method.* International Journal of Solids and Structures, 1994. 31(7): p. 925-940.

54. Kim, H.M. and T.J. Bartkowicz, *A Two-Step Structural Damage Detection Approach With Limited Instrumentation.* Journal of Vibration and Acoustics, 1997. 119(2): p. 258-264.

55. Okafor, A.C. and A. Dutta, *Structural damage detection in beams by wavelet transforms.* Smart Materials and Structures, 2000. 9(6): p. 906–917.

56. Swamidas, A.S.J. and S. Cheng, *Detection of Fatigue Crack Initiation and Crack Growth in Tubular T-joints Using Modal Analysis* in *IMAC XV - 15th International Modal Analysis Conference*. 1997.

57. Perchard, D.R. and A.S.J. Swamidas, *Crack Detection in Slender Cantilever Plates Using Modal Analysis* in *IMAC XII - 12th International Modal Analysis Conference*. 1994. p. 1769-1777.

58. Fritzen, C.P., D. Jennewein, and T. Kiefer, *Damage detection based on model updating methods.* Mechanical Systems and Signal Processing, 1998. 12(1): p. 163-186.

59. Lopes, V., G. Park, H.H. Cudney, and D.J. Inman, *Impedance-Based Structural Health Monitoring with Artificial Neural Networks.* Journal of Intelligent Material Systems and Structures, 2000. 11(3): p. 206-214.

60. Sampaio, R.P.C., N.M.M. Maia, and J.M.M. Silva, *More Insight Into Some Frequency-response-function Methods for Damage Detection*, in *IMAC-XVIII: A Conference on Structural Dynamics*. 2000. p. 681.

61. Mannan, M.A. and M.H. Richardson, *Detection and Location of Structural Cracks using FRF Measurements*, in *8th international Modal Analysis Conference*. 1990. p. 652-657.

62. Hyoung, K.I.M. and T. Bartkowicz, *Damage detection and health monitoring of large space structures*, in *34th Structures, Structural Dynamics and Materials Conference*. 1993, American Institute of Aeronautics and Astronautics.

63. Pandey, A.K. and M. Biswas, *Experimental verification of flexibility difference method for locating damage in structures.* Journal of Sound and Vibration, 1995. 184(2): p. 311-328.

64. Zimmerman, D.C. and M. Kaouk, *Structural damage detection using a minimum rank update theory.* Journal of vibration and acoustics, 1994. 116(2): p. 222-231.

65. Zimmerman, D.C., M. Kaouk, and T. Simmermacher, *On the Role of Engineering Insight and Judgement Structural Damage Detection*, in *IMAC XIII - 13th International Modal Analysis Conference*. 1995. p. 414-420.

66. Smith, S.W., D.C. Zimmerman, T.J. Bartkowicz, and H.M. Kim, *Experiments for Damage Location in a Damped Structure* in *IMAC XV - 15th International Modal Analysis Conference*. 1997. p. 1096-1102.

67. Lopez, F.P. and D.C. Zimmerman, *Evaluation of reduced models for damage localization using subspace recognition* S.o.P.-O.I. Engineers, Editor. 2000: Bellingham, WA. p. 1200-1206.

68. Abdalla, M., K. Grigoriadis, and D. Zimmerman, *An Optimal Hybrid Expansion—Reduction Damage Detection Method.* Journal of Vibration and Control, 2003. 9(8): p. 983-995.

69. Qian, G.L., S.N. Gu, and J.S. Jiang, *The dynamic behaviour and crack detection of a beam with a crack.* Journal of Sound and Vibration, 1990. 138(2): p. 233-243.

70. Ostachowicz, W.M. and M. Krawczuk, *Analysis of the effect of cracks on the natural frequencies of a cantilever beam.* Journal of Sound and Vibration, 1991. 150(2): p. 191-201.

71. Banks, H.T., D.J. Inman, D.J. Leo, and Y. Wang, *An experimentally validated damage detection theory in smart structures.* Journal of Sound and Vibration, 1996. 191(5): p. 859-880.

72. Masri, S., M. Nakamura, A. Chassiakos, and T. Caughey, *Neural network approach to detection of changes in structural parameters.* Journal of Engineering Mechanics, 1996. 122(4): p. 350-360.

73. Seibold, S. and K. Weinert, *A time domain method for the localization of cracks in rotors.* Journal of Sound and Vibration, 1996. 195(1): p. 57-73.

74. Cattarius, J. and D.J. Inman, *Time domain analysis for damage detection in smart structures.* Mechanical Systems and Signal Processing, 1997. 11(3): p. 409-423.

75. Garcia, G.V. and R. Osegueda. *Combining Damage Index Method and ARMA Method to Improve Damage Detection*. in 2000 IMAC XVIII - 18th International Modal Analysis Conference. 2000. San Antonio.

76. Sohn, H., C.R. Farrar, N.F. Hunter, and K. Worden, *Structural Health Monitoring using Statistical Pattern Recognition Techniques.* ASME Journal of Dynamic Systems, Measurement and Control 2001. 123(4): p. 706-717.

77. Bao, C., H. Hao, and Z.-X. Li, *Integrated ARMA model method for damage detection of subsea pipeline system.* Engineering Structures, 2013. 48(0): p. 176-192.

78. Trendafilova, I., *Vibration-based damage detection in structures using time series analysis.* Proceedings of the Institution of Mechanical Engineers, Part C: Journal of Mechanical Engineering Science, 2006. 220(3): p. 261-272.

79. Bovsunovsky, A.P. and V.V. Matveev, *Analytical approach to the determination of dynamic characteristics of a beam with a closing crack.* Journal of Sound and Vibration, 2000. 235(3): p. 415-434.

80. Cerri, M.N. and F. Vestroni, *Detection of Damage in Beams Subjected to Diffused Cracking.* Journal of Sound and Vibration, 2000. 234(2): p. 259-276.

81. Gentile, A. and A. Messina, *On the continuous wavelet transforms applied to discrete vibrational data for detecting open cracks in damaged beams.* International Journal of Solids and Structures, 2003. 40(2): p. 295–315.

82. Narkis, Y., *Identification of crack Location in vibrating simply supported beams.* Journal of sound and Vibrations, 1994. 172(4): p. Pages 549-558

83. Tian, J., Z. Li, and X. Su, *Crack detection in beams by wavelet analysis of transient flexural waves.* Journal of Sound and Vibration, 2003. 261(4): p. 715-727.

84. Chang, C.-C. and L.-W. Chen, *Vibration damage detection of a Timoshenko beam by spatial wavelet based approach* Applied Acoustics, 2003. 64(12): p. 1217-1240

85. Bilello, C. and L.A. Bergman, *Vibration of damaged beams under a moving mass: Theory and experimental validation.* Journal of Sound and Vibration, 2004. 274(3-5): p. 567–582.

86. Hadjileontiadis, L.J., E. Douka, and A. Trochidis, *Crack detection in beams using kurtosis.* Computers & Structures, 2005. 83(12–13): p. 909-919.

87. Christides, S. and A.D.S. Barr, *One-dimensional theory of cracked Bernoulli-Euler beams.* International Journal of Mechanical Sciences, 1984. 26(11–12): p. 639-648.

88. Shen, M.-H.H. and C. Pierre, *Natural modes of Bernoulli-Euler beams with symmetric cracks.* Journal of Sound and Vibration 1990. 138(1): p. 115-134.

89. Shen, M.H.H. and C. Pierre, *Free Vibrations of Beams With a Single-Edge Crack.* Journal of Sound and Vibration, 1994. 170(2): p. 237-259.

90. Hu, H., *Variational Principles of Theory of Elasticity With Applications (Psychic Studies)*. 1984: Gordon and Breach.

91. Washizu, K., *Variational Methods in Elasticity and Plasticity, 2nd Edition*. 1975: Pergamon Press.

92. Friswell, M.I. and J.E.T. Penny. *Is Damage Location Using Vibration Measurements Practical?* in EUROMECH 365 International Workshop: DAMAS 97, Structural Damage Assessment using Advanced Signal Processing Procedures. 1997. Sheffield, UK.

93. Delgado, R.M. and R.C.S.M. dos Santos, *Modelling of a railway bridge–vehicle interaction on high speed tracks.* Computers and Structures, 1997. 63(3): p. 511-523

94. Omenzetter, P., J.M.W. Brownjohn, and P. Moyo, *Identification of Unusual Events in Multi-Channel Bridge Monitoring Data.* Mechanical Systems and Signal Processing 2004. 18(2): p. 409-430.

95. Abdel-Rohman, M. and J. Al-Duaij, *Dynamic response of hinged-hinged single span bridges with uneven deck.* Computers & Structures, 1996. 59(2): p. 291-299.

96. Lee, J.W., J.D. Kim, C.B. Yun, J.H. Yi, and J.M. Shim, *Health monitoring method for bridges under ordinary traffic loadings.* Journal of Sound and Vibration, 2002. 257(2): p. 247–264.

97. Law, S.S. and X.Q. Zhu, *Dynamic behaviour of damaged concrete bridge structures under moving vehicular loads.* Engineering Structures, 2004. 26(9): p. 1279–1293.

98. Bu, J.Q., S.S. Law, and X.Q. Zhu, *Innovative bridge condition assessment from dynamic response of a passing vehicle.* ASCE Journal of Engineering Mechanics, 2006. 132(12): p. 1372–1379.

99. Pesterev, A.V. and L.A. Bergman, *Vibration of elastic continuum carrying accelerating oscillator.* ASCE Journal of Engineering Mechanics, 1997. 123(8): p. 886-889.

100. Majumder, L. and C.S. Manohar, *A timedomain approach for damage detection in beam structures using vibration data with a moving oscillator as an excitation source.* . Journal of Sound and Vibration, 2003. 268: p. 699–716.

101. Bilello, C., A.L. Bergman, and D. Kuchma, *Experimental investigation of a small-scale bridge model under a moving mass.* ASCE Journal of Structural Engineering, 2004. 130(5): p. 799–804.

102. Zhu, X.Q. and S.S. Law, *Damage detection in simply supported concrete bridge structures under moving vehicular loads.* ASME Journal of Vibration and Acoustics, 2007. 129(1): p. 58-65.

103. Fryba, L., *Vibration of Solids and Structures under Moving Loads*. 3rd edition ed, ed. c.-e.T.T.L. Publishing house of Academy of Sciences of the Czech Republic. Vol. 1. 1999, Prague, London: Publishing house of Academy of Sciences of the Czech Republic, Thomas Telford Ltd. 494.

104. Yazdi, M., S.J. Addin, and S. Irani. *Transverse vibration of double cracked beam using assumed mode method*. in Recent Advances in Space Technologies, 2009. RAST '09. 4th International Conference. 2009.

105. Clough, R.W. and J. Penzien, *Dynamics of Structures*. second edition ed, ed. B.J. Clark. 1993, Singapore: McGraw-Hill Book Co.

106. Lamarque, C.H., S. Pernot, and A. Cuer, *Damping Identification in Multi-Degree-of-Freedom Systems via a Wavelet-Logarithmic Decrement – Part 1:Theory.* Journal of Sound and Vibration, 2000. 235(3): p. 361-374.

107. Prandina, M., J.E. Mottershead, and E. Bonisoli, *An assessment of damping identification methods.* Journal of Sound and Vibration, 2009. 323(3–5): p. 662-676.

108. Yin, H.P., D. Duhamel, and P. Argoul, *Natural frequencies and damping estimation using wavelet transform of a frequency response function.* Journal of Sound and Vibration, 2004. 271(3–5): p. 999-1014.

109. Phani, S.A. and J. Woodhouse, *Viscous Damping Identification in Linear Vibration.* Journal of Sound and Vibration, 2007. 303(3-5): p. 475-500.

110. Challa, V.R., M.G. Prasad, and F.T. Fisher, *A coupled piezoelectric–electromagnetic energy harvesting technique for achieving increased power output through damping matching.* Smart Materials and Structures, 2009. 18(9): p. 095029 (1-11).

111. Mann, B.P. and N.D. Sims, *Energy harvesting from the non-linear oscillations of magnetic levitation.* Journal of Sound and Vibration, 2009. 319(1-2): p. 515–530.

112. Ali, S.F., M.I. Friswell, and S. Adhikari, *Piezoelectric Energy Harvesting with Parametric Uncertainty.* Smart Materials and Structures, 2010. 19(10): p. 105010 (1-9).

113. Carrella, A., *Passive Vibration Isolators With High-Static-Low-Dynamic-Stiffness*, in *Faculty of Engineering, Science and Mathematics; Institute of Sound and Vibration Research*. 2008, University of Southamton: Southampton. p. 226.

114. Ravindra, B. and A.K. Mallik, *Role of Nonlinear Dissipation in Soft Duffing Oscillators.* Physical Review E, 1994. 49(6): p. 4950-4954.

115. Cross, E.J. and K. Worden, *Approximation of the Duffing oscillator frequency response function using the FPK equation.* Journal of Sound and Vibration, 2011. 330(4): p. 743-756.

116. Hadjileontiadis, L.J. and E. Douka, *Kurtosis analysis for crack detection in thin isotropic rectangular plates.* Engineering Structures, 2007. 29(9): p. 2353-2364.

117. Pakrashi, V., B. Basu, and A. O' Connor, *Structural damage detection and calibration using a wavelet-kurtosis technique.* Engineering Structures, 2007. 29(9): p. 2097-2108

118. Song, M.-K., H.-C. Noh, and C.-K. Choi, *A new three-dimensional finite element analysis model of high-speed train–bridge interactions.* Engineering Structures, 2003. 25(13): p. 1611-1626.

119. Khan, A.Z., A.B. Stanbridge, and D.J. Ewins, *Detecting damage in vibrating structures with a scanning LDV.* Optics and Lasers in Engineering, 2000. 32(6): p. 583–592.

120. Poudel, U.P., G. Fu, and J. Ye, *Structural damage detection using digital video imaging technique and wavelet transformation.* Journal of Sound and Vibration, 2005. 286(4-5): p. 869–895.

121. Taha, M.M.R., A. Noureldin, J.L. Lucero, and T.J. Baca, *Wavelet transform for structural health monitoring: A compendium of uses and features.* Structural Health Monitoring, 2006. 5(3): p. 267–295.

122. Chati, M., R. Rand, and S. Mukherjee, *Modal analysis of a cracked beam.* Journal of Sound and Vibration, 1997. 207(2): p. 249–270.

123. Dado, M.H., *A comprehensive crack identification algorithm for beams under different end conditions.* Applied Acoustics, 1997. 51(4): p. 381–398.

124. Lakshmi, N.K., *Sensitivity analysis of local/global modal parameters for identification of crack in a beam.* Journal of Sound and Vibration, 1999. 228(5): p. 977–994.

125. Masoud, S., M.A. Jarrah, and M. Al-Mamoory, *Effect of crack depth on the natural frequency of a prestressed fixed-fixed beam.* Journal of Sound and Vibration, 1998. 214(2): p. 201–212.

126. Tomasel, F.G. and P.A.A. Laura, *Assessing the healing of mechanical structures through changes in their vibrational characteristics as detected by fiber optic bragg gratings.* Journal of Sound and Vibration, 2002. 253(523–527).

127. Yang, X.F., A.S.J. Swamidas, and R. Seshadri, *Crack identification in vibrating beams using the energy method.* . Journal of Sound and Vibration, 2001. 244(2): p. 339–357.

128. Moniz, L., J. Nichols, S. Trickey, M. Seaver, D. Pecora, and L.M. Pecora, *Using chaotic forcing to detect damage in a structure.* Chaos, 2005. 15: p. 1-10.

129. Moniz, M., J.M. Nichols, C.J. Nichols, M. Seaver, S.T. Trickey, M.D. Todd, L.M. Pecora, and L.M. Virgin, *A multivariate, attractor-based approach to structural health monitoring.* Journal of Sound and Vibration, 2005. 283(1-2): p. 295–310.

130. Nichols, J.M., M.D. Todd, and M. Seaver, *Use of Chaotic excitation and attractor property analysis in structural health monitoring.* Physical Review E, 2003. 67(016209): p. 1-8.

131. Nichols, J.M., S.T. Trickey, M.D. Todd, and L.N. Virgin, *Structural health monitoring through chaotic interrogation.* Meccanica, 2003. 38(2): p. 239–250.

132. Pakrashi, V., B. Basu, and A.O. Connor, *A Statistical Measure for Wavelet Based Singularity Detection.* Journal of Vibration and Acoustics, 2009. 131(4): p. 041015 (6 pages)

133. O'Brien, E., Y. Li , and A. Gonzalez, *Bridge roughness index as an indicator of bridge dynamic amplification.* Compurers & Structures, 2006. Volume 84(12): p. 759–769.

134. Peng, Z.K., Z.Q. Lang, S.A. Billings, and Y. Lu, *Analysis of bilinear oscillators under harmonic loading using nonlinear output frequency response functions.* International Journal of Mechanical Sciences, 2007. 49(2007): p. 1213–1225.

135. Cacciola, P., N. Impollonia, and G. Muscolino, *Crack detection and location in a damaged beam vibrating under white noise.* Computers and Structures, 2003. 81: p. 1773–1782.

136. Douka, E., K.A. Zacharias, L.J. Hadjileontiadis, and A. Trochidis, *Non-linear Vibration Technique for Crack Detection in Beam Structures Using Frequency Mixing.* Acta Acustica united with Acustica, 2010. 96 (5): p. 977-980.

137. Sundermeyer, J.N. and R.L. Weaver, *On Crack Identification and Characterization in a beam by non-linear vibration analysis.* Journal of Sound and Vibration, 1994. 183(5): p. 857-871.

138. Figueiredo, E., C.R. Farrar, K. Worden, and J. Figueiras (2010) *Machine Learning Algorithms to Damage Detection under Operational and Environmental Variability*. Structural Health Monitoring DOI: 10.1177/1475921710388971

139. Jaksic, V. and V. Pakrashi, *A Robust Skewness-Kurtosis Descriptor for Damping Calibration from Frequency Response.* Journal of Aerospace Engineering, 2012. 1(1): p. 140.

140. Friswell, M.I. and J.E.T. Penny, *Crack Modeling for Structural Health Monitoring.* Structural Health Monitoring, 2002. 1(2): p. 139 - 148.

141. Hou, Z., M. Noori, and R.S. Amand, *Wavelet-Based Approach for Structural Damage Detection.* Journal of Engineering Mechanics, 2000. 126 (7): p. 677-684.

142. Loutridis, S., E. Doukab, and A. Trochidis, *Crack identification in double-cracked beams using wavelet analysis* Journal of Sound and Vibration, 2004. 277(4-5): p. 1025-1039

143. Douka, E., S. Loutridis, and A. Trochidis, *Crack identification in beams using wavelet analysis.* International Journal of Solids and Structures, 2003. 40(13–14): p. 3557-3569.

144. Ghaffar, A.M.A. and R.H. Scanlan, *Ambient Vibration Studies of Golden Gate Bridge: II. Pier Tower Structure.* Journal of Engineering Mechanics, 1985. 111(4): p. 483-500.

145. Okamoto, S., R. Nanba, K. Shibao, M. Satou, and Y. Shibao, *Research on Vibration and Scattering of Roof Tiles by Wind Tunnel Test.* Journal of Environment and Engineering, 2007. 2(2): p. 237-246.

146. Vanlanduit, S., B. Cauberghe, P. Guillaume, and P. Verboven, *Automatic Vibration Mode Tracking using a Scanning Laser Doppler Vibrometer.* Optics and Lasers in Engineering, 2004. 42: p. 315-326.

147. Siringoringo, D.M. and Y. Fujino, *Noncontact Operational Modal Analysis of Structural Members by Laser Doppler Vibrometer.* Computer-Aided Civil and Infrastructure Engineering 2009. 24(4): p. 249-265.

148. Vuye, C., S. Vanlanduit, and P. Guillaume, *Accurate Estimate of Normal Incidence Absorption Coefficient with Confidence Intervals using a Scanning Laser Doppler Vibrometer.* Optics and Lasers in Engineering 2009. 47(6): p. 644-650.

149. Castellini, P., N. Paone, and E.P. Tomasini, *The Laser Doppler Vibrometer as an Instrument for Nonintrusive Diagnostic of Works of Art: Application to Fresco Paintings.* Optics and Lasers in Engineering, 1996. 25(4-5): p. 227-246.

150. Senatore, A., *Measurement of the Natural Frequencies of a Uniform Rod Loaded with Centrifugal Forces using a Laser Doppler Vibrometer.* Measurement Techniques 2006. 49(1): p. 43-48.

151. Harris, N.K., A. Gonzalez, E.J. Obrien, and P. McGetrick, *Characterisation of pavement profile heights using accelerometer readings and a combinatorial optimisation technique.* Journal of Sound and Vibration, 2010. 329(5): p. 497-508.

152. da Silva, J.G.S., *Dynamical performance of highway bridge decks with irregular pavement surface.* Computers & Structures, 2004. 82(11-12): p. 871-881

153. Law, S.S. and X.Q. Zhu, *Bridge dynamic responses due to road surface roughness and braking of vehicle.* Journal of Sound and Vibration, 2005. 282(3-5): p. 805-830

154. Jaksic, V., V. Pakrashi, and A. O'Connor. *Employing Surface Roughness for Bridge-Vehicle Interaction based damage detection*. in ASME 2011 International Mechanical Engineering Congress and Exposition (IMECE 2011) 2011. Denver, Colorado, USA: ASME.

155. ISO, in *ISO 8606:1995(E). Mechanical vibration - road surface profiles-reporting of measured data*. 1995, International Organization for Standardization.

156. Wu, S.Q. and S.S. Law, *Vehicle axle load identification on bridge deck with irregular road surface profile.* Engineering Structures, 2011. 33(2): p. 591-601

157. Henchi, K., M. Fafard, M. Talbot, and G. Dhatt, *An Efficient Algorthm for Dynamic Analysis of Bridges under Moving Vehicles Using a Coupled Modal and Physical Components Aproach.* Journal of Sound and Vibration, 1998. 212(4): p. 663-683

158. *MATLAB*. 2004; Available from: http://www.mathworks.co.uk/products/matlab/.

159. Law, S.S., J.Q. Bub, X.Q. Zhua, and S.L. Chana, *Vehicle axle loads identification using finite element method.* Engineering Structures, 2004. 26(8): p. 1143-1153

160. Qian, B. and K. Rasheed. *Hurst exponent and financial market predictability*. in IASTED conference on Financial Engineering and Applications (FEA 2004). 2004. Cambridge, Massachusetts, USA: International Association of Science and Technology for Development (IASTED).

161. Morales, R., T. Di Matteo, R. Gramatica, and T. Aste, *Dynamical generalized Hurst exponent as a tool to monitor unstable periods in financial time series.* Physica A: Statistical Mechanics and its Applications, 2012. 391(11): p. 3180-3189.

162. Schreiber, T. and A. Schmitz, *Surrogate time series.* Physica D: Nonlinear Phenomena, 2000. 142(3–4): p. 346-382.

163. Theiler, J., S. Eubank, A. Longtin, B. Galdrikian, and J. Doyne Farmer, *Testing for nonlinearity in time series: the method of surrogate data.* Physica D: Nonlinear Phenomena, 1992. 58(1–4): p. 77-94.

164. Hongying, H. and Y. Fuliang. *Diesel Engine Fault Information Acquisition Based on Delay Vector Variance Method*. in Knowledge Acquisition and Modeling, 2009. KAM '09. Second International Symposium on. 2009.

165. Rapp, P.E., A.M. Albano, I.D. Zimmerman, and M.A. Jiménez-Montaño, *Phase-randomized surrogates can produce spurious identifications of non-random structure.* Physics Letters A, 1994. 192(1): p. 27-33.

166. Hegger, R., H. Kantz, and T. Schreiber, *Practical implementation of nonlinear time series methods: The TISEAN package.* Chaos, 1999. 9(2): p. 413-433.

167. Gautama, T., D.P. Mandic, and M.M.V. Hulle, *Signal Nonlinearity in fMRI: A Comparison Between BOLD and MION.* IEEE Transactions on Medical Imagining, 2003. 22(5): p. 636 - 644.

168. Gautama, T., D.P. Mandic, and M.M.V. Hulle, *The delay vector variance method for detecting determinism and nonlinearity in time series.* Physica D: Nonlinear Phenomena, 2004. 190(3-4): p. 167–176.

169. Gautama, T., D.P. Mandic, and M.M.V. Hulle, *Indications of nonlinear structures in brain electrical activity.* Physical Review E, 2003. 67(4): p. 046204 (5).

170. LeCaillec, J.-M. and R. Garello, *Comparison of statistical indices using third order statistics for nonlinearity detection.* Signal Processing, 2004. 84(3): p. 499-525.

171. Schreiber, T. and A. Schmitz, *Discrimination power of measures for nonlinearity in a time series.* Physical Review E, 1997. 55(5): p. 5443-5447.

172. Kaplan, D.T., *Exceptional events as evidence for determinism.* Physica D: Nonlinear Phenomena, 1994. 73(1–2): p. 38-48.

173. Grassberger, P. and I. Procaccia, *Measuring the strangeness of strange attractors.* Physica D: Nonlinear Phenomena, 1983. 9(1–2): p. 189-208.

174. Gautama, T., M.M.V. Hulle, and D.P. Mandic, *On the characterisation of the deterministic/stochastic and linear/nonlinear nature of time series*, in *DPM-04-05*. 2004, Imperial College London. p. 30.

175. Casdagli, M., *Chaos and Deterministic versus Stochastic Non-Linear Modelling.* Journal of the Royal Statistical Society. Series B (Methodological), 1992. 54(2): p. 303-328.

176. Kennel, M.B., R. Brown, and H.D.I. Abarbanel, *Determining embedding dimension for phase-space reconstruction using a geometrical construction.* Physical Review A, 1992. 45(6): p. 3403-3411.

177. Kuntamalla, S. and R.G.L. Reddy, *The Effect of Aging on Nonlinearity and Stochastic Nature of Heart Rate Variability Signal Computed using Delay*

Vector Variance Method. International Journal of Computer Applications 2011. 14(5): p. 40-44.

178. Schreiber, T., *Interdisciplinary Application of Nonlinear Time Series Methods.* Physics Reports, 1999. 308: p. 1-64.

179. Andrzejak, R.G., K. Lehnertz, F. Mormann, C. Rieke, P. David, and C.E. Elger, *Indications of nonlinear deterministic and finite-dimensional structures in time series of brain electrical activity: dependence on recording region and brain state.* Physical Review E, 2001. 64: p. (6 Pt 1):061907.

180. Jianjun, Y., W. Haijun, X. Chunming, W. Yiqin, L. Fufeng, G. Rui, and M. Tiancai. *Nonlinear Analysis in TCM Acoustic Diagnosis Using Delay Vector Variance*. in Bioinformatics and Biomedical Engineering, 2008. ICBBE 2008. The 2nd International Conference on. 2008.

181. Schreiber, T. and A. Schmitz, *Improved Surrogate Data for Nonlinearity Tests.* Physical Review Letters, 1996. 77(4): p. 635-638.

182. Kugiumtzis, D., *Test your surrogate data before you test for nonlinearity.* Physical Review E, 1999. 60(3): p. 2808-2816.

183. Zi-li, X., W. Yi-yang, Z. Ji-liu, and H. Pei-yu, *Detecting the Nonlinear Determinism of a Room Acoustic System Using Surrogates.* Journal of Sichuan University (Engineering Science Edition) 2007. 39(5): p. 155-158.

184. Mandic, D.P. *Delay Vector Variance MATLAB Toolbox*. 2010; Available from: http://www.commsp.ee.ic.ac.uk/~mandic/dvv.htm.

185. Gautama, T., D.P. Mandic, and M.M. Van Hulle. *A differential entropy based method for determining the optimal embedding parameters of a signal*. in Acoustics, Speech, and Signal Processing, 2003. Proceedings. (ICASSP '03). 2003 IEEE International Conference on. 2003.

186. Beirlant, J., E.J. Dudewicz, L. Gyorfi, and E.C.v.d. Meulen, *Nonparametric entropy estimation: An overview.* International Journal of Mathematical and Statistical Sciences, 1997. 6: p. 17-39.

187. Kuchnicki, S., *Simple Vibration Problems with MATLAB (and Some Help from MAPLE); This document is companion to the text: Mechanical Vibration: Analysis, Uncertainties and Control, by Haym Benaroya and Mark Nagurka, CRC Press 2010*. 2009. p. 165.

188. Pakrashi, V., J. Harkin, J. Kelly, A. Farrell, and S. Nanukuttan, *Monitoring and repair of an impact damaged prestressed bridge.* ICE - Bridge Engineering, 2012. 166(Issue BE1): p. 16-29.

189. Lorieux, L., *Analysis of train-induced vibrations on a single-span composite bridge*, in *Department of Civil and Architectural Engineering, Division of Structural Design and Bridges*. 2008, Royal Institute of Technology (KTH): Stockholm, Sweden.

190. Harkin, J., *Structural Health Monitoring During the Rehabilitation of an Impact Damage Prestressed Concrete Bridge*, in *School of Planning, Architecture and Civil Engineering*. 2010, Queen's University: Belfast. p. 198.

191. Pakrashi, V., J. Kelly, J. Harkin, and A. Farrell, *Hurst exponent footprints from activities on a large structural system.* Physica A: Statistical Mechanics and its Applications, 2013. 392(8): p. 1803-1817.

192. Martino, D., *Train-Bridge Interaction on Freight Railway Lines*, in *Department of Civil and Architectural Engineering, Division of Structural Design and Bridges*. 2011, Royal Institute of Technology (KTH): Stockholm, Sweden.

193. Tang, D., *Dynamic response of a composite railway bridge to passing trains - Comparison of FEM simulations and measurements*, in *Department of Civil and Architectural Engineering, Division of Structural Design and Bridges*. 2012, Royal Institute of Technology (KTH): Stockholm, Sweden.

194. Ülker-Kaustell, M. and R. Karoumi, *Application of the continuous wavelet transform on the free vibrations of a steel–concrete composite railway bridge.* Engineering Structures, 2011. 33(3): p. 911-919.

195. EuropeanStandard, *Eurocode 1: Actions on structures* - in *Part 2: Traffic loads on bridges EN 1991-2:2003/AC:2010*. 2003: EU.

196. Battini, J.-M. and M. Ülker-Kaustell, *A simple finite element to consider the non-linear influence of the ballast on vibrations of railway bridges.* Engineering Structures, 2011. 33(9): p. 2597-2602.

197. Akhtar, I., O.A. Marzouk, and A.H. Nayfeh, *A van der Pol--Duffing Oscillator Model of Hydrodynamic Forces on Canonical Structures.* Journal of Computational and Nonlinear Dynamics, 2009. 4(4): p. 041006.

198. Barrón-Meza, M.A., *Vibration Analysis Of a Self-Excited Elastic Beam.* Journal of applied research and technology, 2010. 8: p. 227-238.

199. Ikeda, T. and S. Murakami, *Autoparametric resonances in a structure/fluid interaction system carrying a cylindrical liquid tank.* Journal of Sound and Vibration, 2005. 285: p. 517–546.

Appendices

APPENDIX A

Calibration Markers for Damage Detection from Bridge Vehicle Interaction Employing Surface Roughness

Table A.1 Mean of $\Delta\Phi_m q(t)$ calculated for each beam segment where crack location is at 0.1L (1.5m) from the left support, the vehicle speed ranging from 10 to 150km/h with 10km/h step, CDR is ranging from 0.1 to 0.45 with 0.05 step, and RSR is class A (ISO 8606:1995(E)).

A		CDR							
xc=0.1·L		0.10	0.15	0.20	0.25	0.30	0.35	0.40	0.45
V_V (km/h)	10	1.59E-06	3.46E-06	6.05E-06	9.52E-06	1.38E-05	1.91E-05	2.52E-05	3.24E-05
	20	1.35E-06	2.98E-06	5.14E-06	8.12E-06	1.19E-05	1.66E-05	2.24E-05	2.90E-05
	30	1.37E-06	3.00E-06	5.31E-06	7.99E-06	1.18E-05	1.70E-05	2.38E-05	2.96E-05
	40	1.40E-06	3.19E-06	5.40E-06	8.47E-06	1.23E-05	1.70E-05	2.32E-05	2.98E-05
	50	1.55E-06	3.34E-06	5.77E-06	9.13E-06	1.30E-05	1.87E-05	2.41E-05	3.07E-05
	60	1.50E-06	3.38E-06	6.09E-06	8.84E-06	1.32E-05	1.82E-05	2.48E-05	3.13E-05
	70	1.47E-06	3.24E-06	5.56E-06	8.57E-06	1.28E-05	1.75E-05	2.39E-05	3.20E-05
	80	1.56E-06	3.46E-06	5.84E-06	9.12E-06	1.34E-05	1.86E-05	2.54E-05	3.17E-05
	90	1.57E-06	3.30E-06	5.66E-06	9.28E-06	1.33E-05	1.76E-05	2.45E-05	3.17E-05
	100	1.53E-06	3.24E-06	5.46E-06	8.56E-06	1.25E-05	1.77E-05	2.40E-05	3.03E-05
	110	1.48E-06	3.16E-06	5.38E-06	8.72E-06	1.23E-05	1.70E-05	2.26E-05	3.02E-05
	120	1.43E-06	3.20E-06	5.64E-06	8.53E-06	1.26E-05	1.75E-05	2.38E-05	2.93E-05
	130	1.36E-06	3.07E-06	5.54E-06	8.47E-06	1.23E-05	1.72E-05	2.29E-05	2.94E-05
	140	1.39E-06	3.22E-06	5.49E-06	8.16E-06	1.19E-05	1.73E-05	2.21E-05	2.84E-05
	150	1.48E-06	3.18E-06	5.58E-06	8.62E-06	1.26E-05	1.71E-05	2.32E-05	2.99E-05

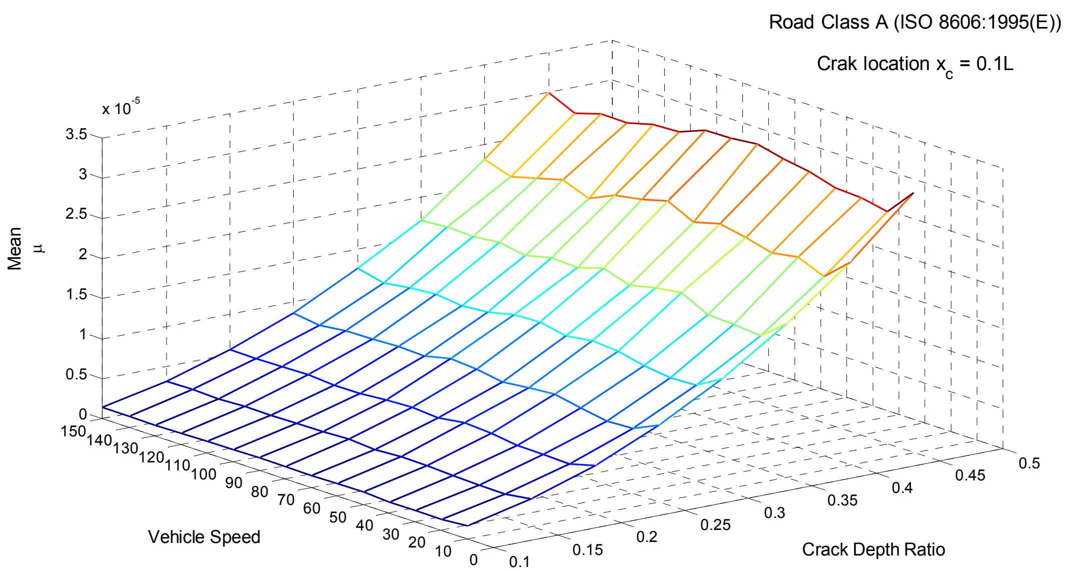

Figure A.1 Mean of $\Delta\Phi_m q(t)$ dependence on Crack Depth Ratio and Vehicle speed for Road Surface Roughness Type A for crack located near support.

Table A.2Mean of $\Delta\Phi_m q(t)$ calculated for each beam segment where crack location is at 0.25*L* (3.75m) from the left support, the vehicle speed ranging from 10 to 150km/h with 10km/h step, CDR is ranging from 0.1 to 0.45 with 0.05 step, and RSR is class A (ISO 8606:1995(E)).

A		CDR							
xc=0.25·L		0.10	0.15	0.20	0.25	0.30	0.35	0.40	0.45
V_V (km/h)	10	2.99E-06	6.53E-06	1.13E-05	1.73E-05	2.42E-05	3.30E-05	4.15E-05	5.36E-05
	20	2.55E-06	5.62E-06	9.88E-06	1.48E-05	2.16E-05	2.88E-05	3.74E-05	4.82E-05
	30	2.56E-06	5.62E-06	9.73E-06	1.45E-05	2.11E-05	2.88E-05	3.66E-05	4.78E-05
	40	2.69E-06	5.77E-06	9.89E-06	1.56E-05	2.21E-05	2.96E-05	3.67E-05	4.68E-05
	50	2.93E-06	6.37E-06	1.11E-05	1.65E-05	2.32E-05	3.19E-05	4.12E-05	5.01E-05
	60	2.89E-06	6.43E-06	1.10E-05	1.59E-05	2.37E-05	3.15E-05	4.10E-05	5.12E-05
	70	2.89E-06	5.82E-06	1.04E-05	1.61E-05	2.26E-05	2.81E-05	3.86E-05	4.86E-05
	80	2.97E-06	6.06E-06	1.11E-05	1.65E-05	2.38E-05	3.29E-05	4.18E-05	5.24E-05
	90	2.94E-06	5.89E-06	1.08E-05	1.71E-05	2.30E-05	3.07E-05	4.16E-05	4.83E-05
	100	2.74E-06	5.90E-06	1.03E-05	1.66E-05	2.27E-05	3.17E-05	3.92E-05	5.01E-05
	110	2.67E-06	5.94E-06	9.98E-06	1.55E-05	2.21E-05	2.87E-05	3.74E-05	4.63E-05
	120	2.71E-06	5.99E-06	1.05E-05	1.53E-05	2.33E-05	2.98E-05	3.78E-05	4.85E-05
	130	2.67E-06	5.72E-06	1.01E-05	1.49E-05	2.21E-05	2.88E-05	3.59E-05	4.68E-05
	140	2.60E-06	5.51E-06	9.87E-06	1.48E-05	2.16E-05	2.87E-05	3.64E-05	4.51E-05
	150	2.76E-06	5.95E-06	1.04E-05	1.57E-05	2.25E-05	2.96E-05	3.86E-05	4.88E-05

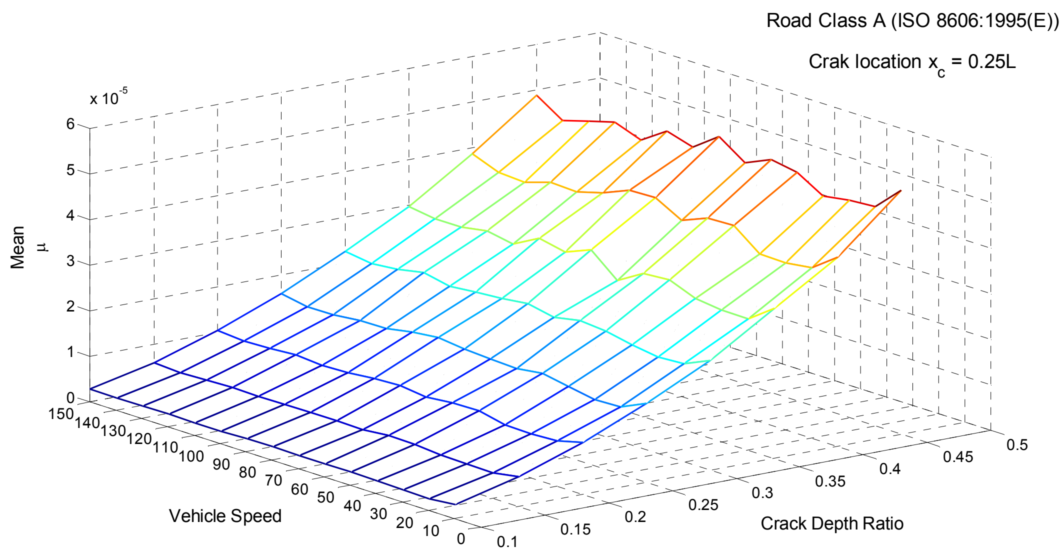

Figure A.2 Mean of $\Delta\Phi_m q(t)$ dependence on Crack Depth Ratio and Vehicle speed for Road Surface Roughness Type A for crack located at quarter-span.

Table A.3 Mean of $\Delta\Phi_m q(t)$ calculated for each beam segment where crack location is at 0.5L (7.5m), the vehicle speed ranging from 10 to 150km/h with 10km/h step, CDR is ranging from 0.1 to 0.45 with 0.05 step, and RSR is class A (ISO 8606:1995(E)).

A		**CDR**							
xc=0.5·L		**0.10**	**0.15**	**0.20**	**0.25**	**0.30**	**0.35**	**0.40**	**0.45**
V_V (km/h)	**10**	1.73E-06	3.81E-06	6.91E-06	1.13E-05	1.73E-05	2.54E-05	3.61E-05	5.08E-05
	20	1.22E-06	2.75E-06	4.94E-06	8.12E-06	1.16E-05	1.83E-05	2.65E-05	3.80E-05
	30	1.14E-06	2.59E-06	4.59E-06	7.73E-06	1.15E-05	1.71E-05	2.58E-05	3.76E-05
	40	1.26E-06	2.78E-06	5.31E-06	8.33E-06	1.22E-05	1.78E-05	2.58E-05	3.67E-05
	50	1.28E-06	2.89E-06	4.96E-06	8.38E-06	1.32E-05	1.82E-05	2.63E-05	3.86E-05
	60	1.46E-06	3.16E-06	5.97E-06	9.49E-06	1.42E-05	2.10E-05	2.93E-05	4.06E-05
	70	1.33E-06	3.03E-06	5.07E-06	8.79E-06	1.26E-05	1.67E-05	2.75E-05	4.04E-05
	80	1.41E-06	3.18E-06	5.70E-06	9.05E-06	1.34E-05	1.92E-05	2.81E-05	3.92E-05
	90	1.38E-06	3.14E-06	5.57E-06	8.80E-06	1.37E-05	1.92E-05	2.80E-05	4.00E-05
	100	1.32E-06	2.88E-06	5.51E-06	8.26E-06	1.24E-05	1.86E-05	2.60E-05	3.75E-05
	110	1.31E-06	2.91E-06	5.20E-06	8.09E-06	1.30E-05	1.83E-05	2.51E-05	3.66E-05
	120	1.26E-06	2.73E-06	5.07E-06	7.68E-06	1.22E-05	1.78E-05	2.55E-05	3.72E-05
	130	1.28E-06	2.82E-06	5.28E-06	8.35E-06	1.25E-05	1.77E-05	2.62E-05	3.72E-05
	140	1.23E-06	2.82E-06	4.95E-06	7.99E-06	1.22E-05	1.75E-05	2.65E-05	3.65E-05
	150	1.24E-06	2.73E-06	5.00E-06	8.03E-06	1.21E-05	1.82E-05	2.51E-05	3.58E-05

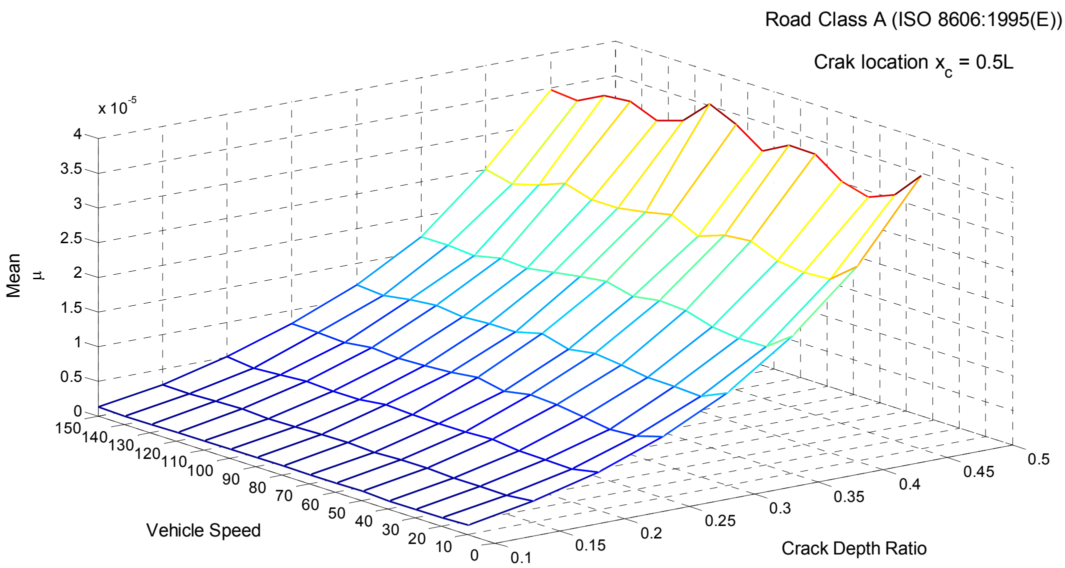

Figure A.3 Mean of $\Delta\Phi_m q(t)$ dependence on Crack Depth Ratio and Vehicle speed for Road Surface Roughness Type A for crack located at mid-span.

Table A.4 Mean of $\Delta\Phi_m q(t)$ calculated for each beam segment where crack location is at 0.1L (1.5m) from the left support, the vehicle speed ranging from 10 to 150km/h with 10km/h step, CDR is ranging from 0.1 to 0.45 with 0.05 step, and RSR is class B (ISO 8606:1995(E)).

B		CDR							
xc=0.1·L		0.10	0.15	0.20	0.25	0.30	0.35	0.40	0.45
V_V (km/h)	10	2.01E-06	4.35E-06	7.63E-06	1.20E-05	1.75E-05	2.43E-05	3.27E-05	4.27E-05
	20	1.39E-06	3.09E-06	5.37E-06	8.52E-06	1.27E-05	1.73E-05	2.44E-05	3.24E-05
	30	1.37E-06	3.04E-06	5.10E-06	8.10E-06	1.23E-05	1.80E-05	2.34E-05	3.16E-05
	40	1.49E-06	3.11E-06	5.53E-06	9.14E-06	1.36E-05	1.84E-05	2.37E-05	3.19E-05
	50	1.49E-06	3.27E-06	5.69E-06	9.06E-06	1.30E-05	1.83E-05	2.51E-05	3.20E-05
	60	1.71E-06	3.84E-06	6.27E-06	1.04E-05	1.44E-05	2.07E-05	2.62E-05	3.50E-05
	70	1.56E-06	3.34E-06	5.79E-06	9.74E-06	1.32E-05	1.76E-05	2.34E-05	2.94E-05
	80	1.67E-06	3.58E-06	6.28E-06	9.85E-06	1.40E-05	1.91E-05	2.61E-05	3.27E-05
	90	1.57E-06	3.50E-06	6.32E-06	9.85E-06	1.39E-05	2.06E-05	2.58E-05	3.41E-05
	100	1.48E-06	3.28E-06	5.82E-06	9.34E-06	1.31E-05	1.73E-05	2.45E-05	3.28E-05
	110	1.53E-06	3.27E-06	5.67E-06	8.91E-06	1.29E-05	1.82E-05	2.42E-05	3.08E-05
	120	1.40E-06	3.00E-06	5.66E-06	8.54E-06	1.27E-05	1.73E-05	2.27E-05	2.95E-05
	130	1.47E-06	3.26E-06	5.71E-06	8.85E-06	1.27E-05	1.78E-05	2.43E-05	3.04E-05
	140	1.43E-06	3.21E-06	5.49E-06	8.83E-06	1.27E-05	1.73E-05	2.28E-05	2.97E-05
	150	1.45E-06	3.20E-06	5.67E-06	8.49E-06	1.28E-05	1.74E-05	2.33E-05	3.08E-05

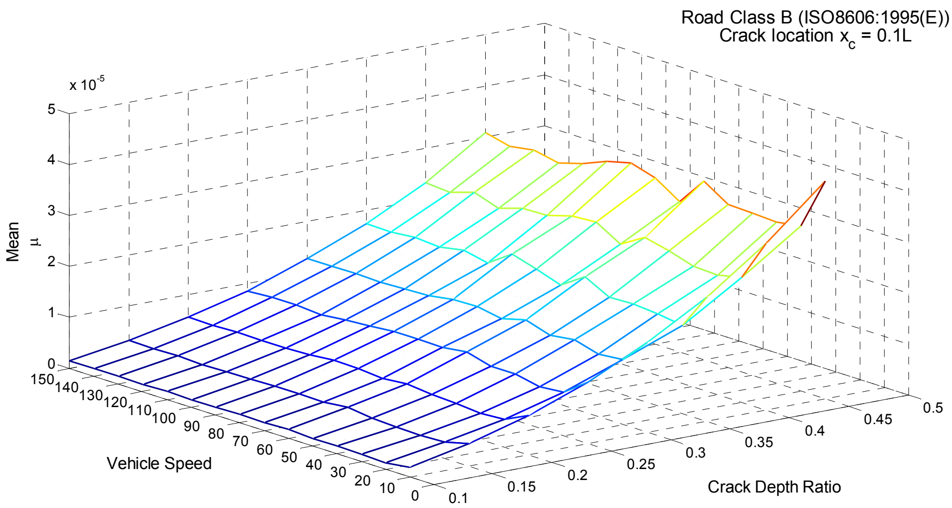

Figure A.4 Mean of $\Delta\Phi_m q(t)$ dependence on Crack Depth Ratio and Vehicle speed for Road Surface Roughness Type B for crack located near support.

Table A.5 Mean of $\Delta\Phi_m q(t)$ calculated for each beam segment where crack location is at 0.25L (3.75m) from the left support, the vehicle speed ranging from 10 to 150km/h with 10km/h step, CDR is ranging from 0.1 to 0.45 with 0.05 step, and RSR is class B (ISO 8606:1995(E)).

B		**CDR**							
x_c=**0.25·*L***		**0.10**	**0.15**	**0.20**	**0.25**	**0.30**	**0.35**	**0.40**	**0.45**
V_V (km/h)	**10**	3.79E-06	8.20E-06	1.41E-05	2.18E-05	3.09E-05	4.17E-05	5.35E-05	6.97E-05
	20	2.65E-06	5.83E-06	1.02E-05	1.60E-05	2.37E-05	3.10E-05	4.33E-05	5.49E-05
	30	2.63E-06	5.45E-06	8.99E-06	1.54E-05	2.24E-05	3.10E-05	4.20E-05	5.34E-05
	40	2.75E-06	6.09E-06	1.07E-05	1.59E-05	2.31E-05	3.09E-05	3.88E-05	4.70E-05
	50	2.76E-06	6.17E-06	1.10E-05	1.61E-05	2.35E-05	3.30E-05	4.14E-05	5.21E-05
	60	3.37E-06	6.88E-06	1.22E-05	1.89E-05	2.59E-05	3.44E-05	4.62E-05	5.66E-05
	70	2.76E-06	6.62E-06	1.09E-05	1.71E-05	2.33E-05	2.87E-05	3.85E-05	5.14E-05
	80	3.17E-06	6.35E-06	1.14E-05	1.79E-05	2.55E-05	3.35E-05	4.22E-05	5.16E-05
	90	3.19E-06	6.64E-06	1.13E-05	1.80E-05	2.47E-05	3.29E-05	4.30E-05	5.35E-05
	100	2.78E-06	6.36E-06	1.06E-05	1.70E-05	2.33E-05	2.99E-05	3.96E-05	5.23E-05
	110	2.88E-06	6.18E-06	1.09E-05	1.58E-05	2.31E-05	3.11E-05	4.00E-05	4.66E-05
	120	2.82E-06	6.03E-06	9.99E-06	1.54E-05	2.19E-05	2.91E-05	3.84E-05	4.54E-05
	130	2.77E-06	6.43E-06	1.06E-05	1.64E-05	2.28E-05	3.08E-05	3.87E-05	4.95E-05
	140	2.70E-06	5.99E-06	1.03E-05	1.57E-05	2.21E-05	3.12E-05	3.91E-05	4.65E-05
	150	2.70E-06	5.94E-06	1.02E-05	1.53E-05	2.17E-05	2.97E-05	3.84E-05	4.85E-05

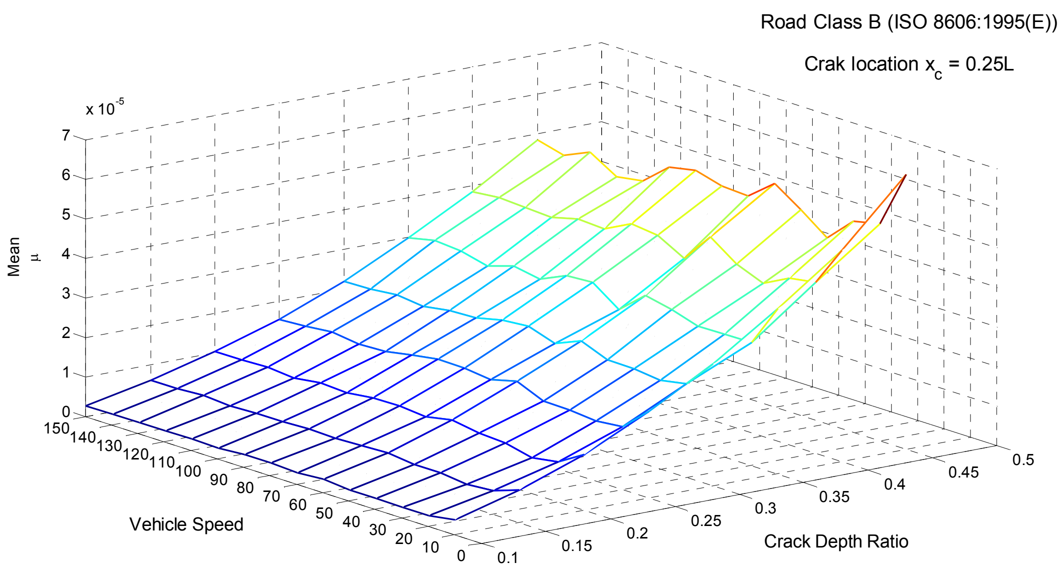

Figure A.5 Mean of ΔΦmq(t) dependence on Crack Depth Ratio and Vehicle speed for Road Surface Roughness Type B for crack located at quarter-span.

Table A.6 Mean of $\Delta\Phi_m q(t)$ calculated for each beam segment where crack location is at 0.5L (7.5m), the vehicle speed ranging from 10 to 150km/h with 10km/h step, CDR is ranging from 0.1 to 0.45 with 0.05 step, and RSR is class B (ISO 8606:1995(E)).

B		**CDR**							
x_c=0.5·L		**0.10**	**0.15**	**0.20**	**0.25**	**0.30**	**0.35**	**0.40**	**0.45**
V_V (km/h)	**10**	1.73E-06	3.81E-06	6.91E-06	1.13E-05	1.73E-05	2.54E-05	3.61E-05	5.08E-05
	20	1.22E-06	2.75E-06	4.94E-06	8.12E-06	1.16E-05	1.83E-05	2.65E-05	3.80E-05
	30	1.14E-06	2.59E-06	4.59E-06	7.73E-06	1.15E-05	1.71E-05	2.58E-05	3.76E-05
	40	1.26E-06	2.78E-06	5.31E-06	8.33E-06	1.22E-05	1.78E-05	2.58E-05	3.67E-05
	50	1.28E-06	2.89E-06	4.96E-06	8.38E-06	1.32E-05	1.82E-05	2.63E-05	3.86E-05
	60	1.46E-06	3.16E-06	5.97E-06	9.49E-06	1.42E-05	2.10E-05	2.93E-05	4.06E-05
	70	1.33E-06	3.03E-06	5.07E-06	8.79E-06	1.26E-05	1.67E-05	2.75E-05	4.04E-05
	80	1.41E-06	3.18E-06	5.70E-06	9.05E-06	1.34E-05	1.92E-05	2.81E-05	3.92E-05
	90	1.38E-06	3.14E-06	5.57E-06	8.80E-06	1.37E-05	1.92E-05	2.80E-05	4.00E-05
	100	1.32E-06	2.88E-06	5.51E-06	8.26E-06	1.24E-05	1.86E-05	2.60E-05	3.75E-05
	110	1.31E-06	2.91E-06	5.20E-06	8.09E-06	1.30E-05	1.83E-05	2.51E-05	3.66E-05
	120	1.26E-06	2.73E-06	5.07E-06	7.68E-06	1.22E-05	1.78E-05	2.55E-05	3.72E-05
	130	1.28E-06	2.82E-06	5.28E-06	8.35E-06	1.25E-05	1.77E-05	2.62E-05	3.72E-05
	140	1.23E-06	2.82E-06	4.95E-06	7.99E-06	1.22E-05	1.75E-05	2.65E-05	3.65E-05
	150	1.24E-06	2.73E-06	5.00E-06	8.03E-06	1.21E-05	1.82E-05	2.51E-05	3.58E-05

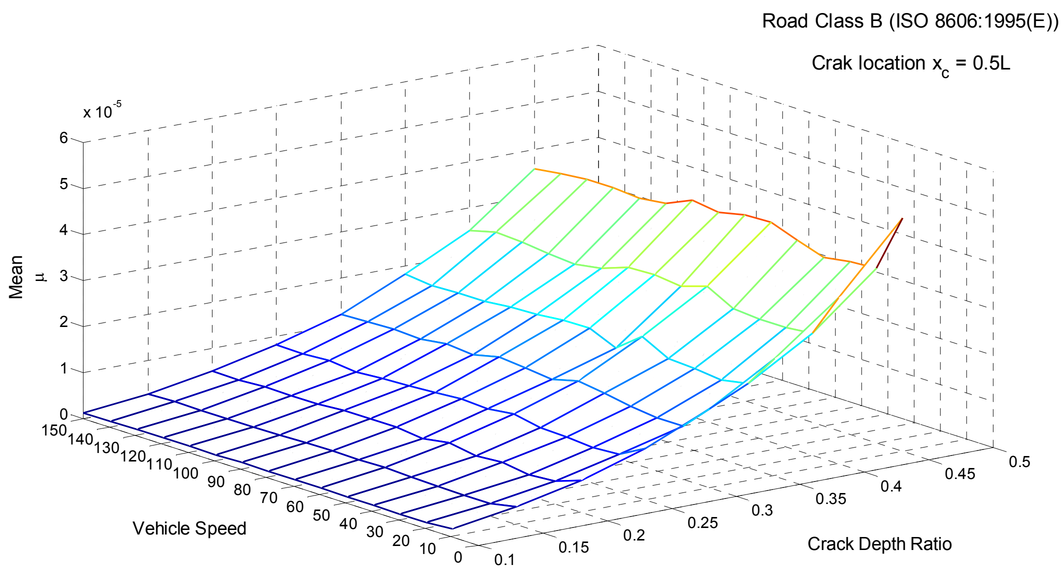

Figure A.6 Mean of $\Delta\Phi_m q(t)$ dependence on Crack Depth Ratio and Vehicle speed for Road Surface Roughness Type B for crack located at mid-span.

Table A.7 Mean of $\Delta\Phi_m q(t)$ calculated for each beam segment where crack location is at $0.1L$ (1.5m) from the left support, the vehicle speed ranging from 10 to 150km/h with 10km/h step, CDR is ranging from 0.1 to 0.45 with 0.05 step, and RSR is class C (ISO 8606:1995(E)).

C		**CDR**							
x_c=0.1·L		**0.10**	**0.15**	**0.20**	**0.25**	**0.30**	**0.35**	**0.40**	**0.45**
V_V (km/h)	**10**	3.61E-06	7.75E-06	1.37E-05	2.12E-05	3.06E-05	4.30E-05	5.87E-05	7.60E-05
	20	1.83E-06	4.13E-06	6.95E-06	1.09E-05	1.65E-05	2.38E-05	3.35E-05	4.56E-05
	30	1.79E-06	4.04E-06	7.23E-06	1.08E-05	1.66E-05	2.42E-05	3.26E-05	4.69E-05
	40	1.90E-06	4.41E-06	7.50E-06	1.18E-05	1.68E-05	2.39E-05	3.25E-05	4.20E-05
	50	1.87E-06	4.07E-06	7.07E-06	1.12E-05	1.62E-05	2.31E-05	3.06E-05	4.20E-05
	60	1.95E-06	4.69E-06	8.11E-06	1.23E-05	1.77E-05	2.49E-05	3.20E-05	4.09E-05
	70	1.65E-06	3.43E-06	5.82E-06	9.35E-06	1.46E-05	1.88E-05	2.37E-05	3.11E-05
	80	1.63E-06	3.43E-06	6.54E-06	9.83E-06	1.47E-05	1.99E-05	2.67E-05	3.51E-05
	90	1.72E-06	3.90E-06	6.86E-06	1.02E-05	1.54E-05	2.13E-05	2.82E-05	3.94E-05
	100	1.83E-06	3.95E-06	6.66E-06	1.07E-05	1.48E-05	2.17E-05	2.81E-05	3.75E-05
	110	1.67E-06	3.47E-06	6.30E-06	1.00E-05	1.51E-05	2.02E-05	2.74E-05	3.49E-05
	120	1.57E-06	3.48E-06	5.85E-06	9.15E-06	1.31E-05	1.91E-05	2.53E-05	3.33E-05
	130	1.46E-06	3.22E-06	5.66E-06	8.79E-06	1.28E-05	1.74E-05	2.36E-05	3.03E-05
	140	1.50E-06	3.32E-06	5.77E-06	8.97E-06	1.33E-05	1.85E-05	2.44E-05	3.26E-05
	150	1.57E-06	3.42E-06	6.09E-06	9.29E-06	1.33E-05	1.89E-05	2.52E-05	3.20E-05

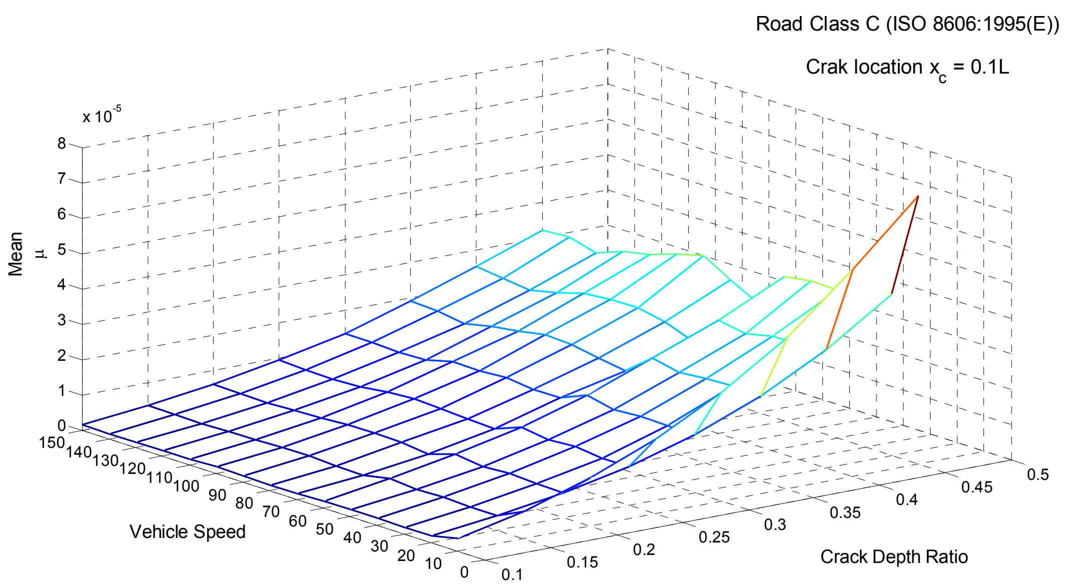

Figure A.7 Mean of $\Delta\Phi_m q(t)$ dependence on Crack Depth Ratio and Vehicle speed for Road Surface Roughness Type C for crack located near support.

Table A.8 Mean of $\Delta\Phi_m q(t)$ calculated for each beam segment where crack location is at 0.25L (3.75m) from the left support, the vehicle speed ranging from 10 to 150km/h with 10km/h step, CDR is ranging from 0.1 to 0.45 with 0.05 step, and RSR is class C (ISO 8606:1995(E)).

C		CDR							
x_c=0.25·L		0.10	0.15	0.20	0.25	0.30	0.35	0.40	0.45
V_V (km/h)	10	6.78E-06	1.47E-05	2.50E-05	3.84E-05	5.49E-05	7.41E-05	9.67E-05	1.24E-04
	20	3.38E-06	7.19E-06	1.30E-05	2.08E-05	2.90E-05	4.34E-05	5.83E-05	8.05E-05
	30	3.44E-06	7.57E-06	1.30E-05	2.06E-05	2.98E-05	4.39E-05	5.83E-05	7.54E-05
	40	3.71E-06	8.10E-06	1.38E-05	2.13E-05	2.90E-05	3.97E-05	5.10E-05	6.20E-05
	50	3.56E-06	7.49E-06	1.34E-05	2.07E-05	2.99E-05	4.10E-05	5.39E-05	6.37E-05
	60	3.86E-06	8.66E-06	1.48E-05	2.21E-05	3.01E-05	4.46E-05	5.12E-05	6.39E-05
	70	3.08E-06	6.58E-06	1.21E-05	1.76E-05	2.33E-05	3.18E-05	4.17E-05	5.12E-05
	80	3.23E-06	7.16E-06	1.22E-05	1.82E-05	2.77E-05	3.59E-05	4.40E-05	5.64E-05
	90	3.28E-06	6.78E-06	1.26E-05	1.92E-05	2.82E-05	3.83E-05	4.80E-05	6.17E-05
	100	3.48E-06	6.90E-06	1.21E-05	2.00E-05	2.77E-05	3.83E-05	4.68E-05	5.82E-05
	110	3.16E-06	7.25E-06	1.19E-05	1.72E-05	2.49E-05	3.43E-05	4.26E-05	5.27E-05
	120	3.11E-06	6.42E-06	1.09E-05	1.71E-05	2.40E-05	3.04E-05	4.16E-05	4.92E-05
	130	2.70E-06	5.98E-06	1.03E-05	1.59E-05	2.34E-05	3.14E-05	3.94E-05	5.07E-05
	140	2.88E-06	6.24E-06	1.08E-05	1.64E-05	2.36E-05	3.09E-05	4.05E-05	5.06E-05
	150	2.98E-06	6.41E-06	1.12E-05	1.67E-05	2.38E-05	3.18E-05	4.02E-05	5.12E-05

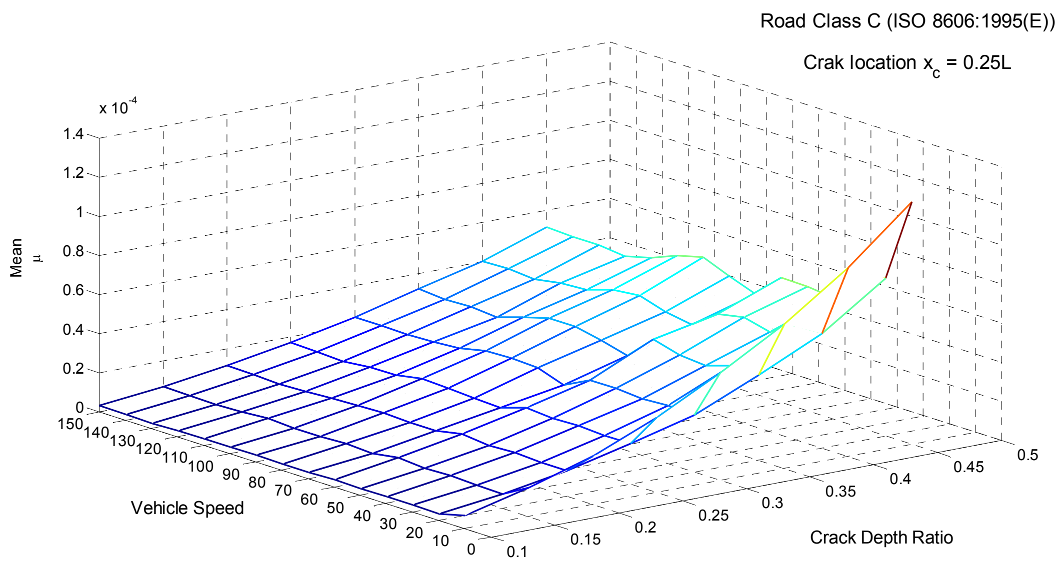

Figure A.8 Mean of ΔΦmq(t) dependence on Crack Depth Ratio and Vehicle speed for Road Surface Roughness Type C for crack located at quarter-span.

Table A.9 Mean of $\Delta\Phi_m q(t)$ calculated for each beam segment where crack location is at 0.5L (7.5m), the vehicle speed ranging from 10 to 150km/h with 10km/h step, CDR is ranging from 0.1 to 0.45 with 0.05 step, and RSR is class C (ISO 8606:1995(E)).

C		**CDR**							
x_c=0.5·L		**0.10**	**0.15**	**0.20**	**0.25**	**0.30**	**0.35**	**0.40**	**0.45**
V_V (km/h)	**10**	3.10E-06	6.92E-06	1.24E-05	2.01E-05	3.05E-05	4.43E-05	6.30E-05	8.95E-05
	20	1.55E-06	3.49E-06	6.14E-06	9.89E-06	1.53E-05	2.34E-05	3.58E-05	5.37E-05
	30	1.57E-06	3.43E-06	6.00E-06	1.02E-05	1.55E-05	2.48E-05	3.46E-05	5.37E-05
	40	1.74E-06	3.77E-06	6.86E-06	1.05E-05	1.61E-05	2.27E-05	3.27E-05	4.59E-05
	50	1.61E-06	3.53E-06	6.38E-06	9.98E-06	1.60E-05	2.34E-05	3.52E-05	4.84E-05
	60	1.84E-06	3.97E-06	6.79E-06	1.14E-05	1.71E-05	2.39E-05	3.50E-05	4.71E-05
	70	1.43E-06	3.10E-06	5.38E-06	8.81E-06	1.32E-05	1.82E-05	2.79E-05	4.03E-05
	80	1.42E-06	3.24E-06	5.69E-06	9.42E-06	1.30E-05	1.98E-05	2.90E-05	3.87E-05
	90	1.41E-06	3.19E-06	5.71E-06	9.64E-06	1.46E-05	2.06E-05	3.03E-05	4.45E-05
	100	1.52E-06	3.42E-06	6.08E-06	1.01E-05	1.45E-05	2.16E-05	2.89E-05	4.23E-05
	110	1.38E-06	1.38E-06	5.46E-06	9.11E-06	1.32E-05	1.92E-05	2.67E-05	3.74E-05
	120	1.35E-06	2.95E-06	5.26E-06	8.77E-06	1.32E-05	1.86E-05	2.74E-05	3.77E-05
	130	1.27E-06	2.80E-06	5.03E-06	8.06E-06	1.23E-05	1.93E-05	2.64E-05	3.91E-05
	140	1.28E-06	2.94E-06	5.18E-06	8.09E-06	1.26E-05	1.87E-05	2.61E-05	3.82E-05
	150	1.37E-06	2.96E-06	5.23E-06	8.61E-06	1.28E-05	1.89E-05	2.72E-05	3.88E-05

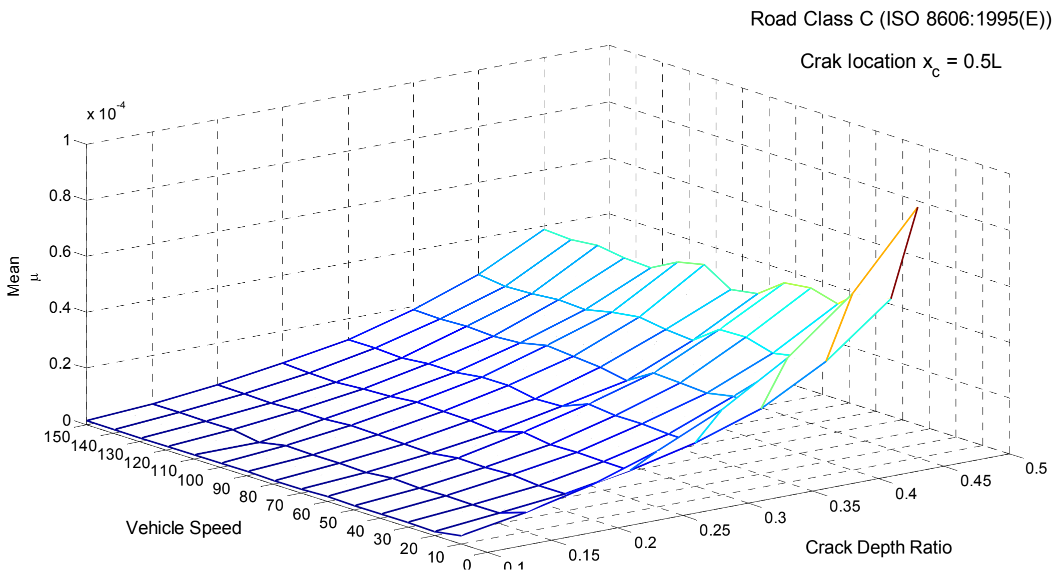

Figure A.9 Mean of $\Delta\Phi_m q(t)$ dependence on Crack Depth Ratio and Vehicle speed for Road Surface Roughness Type C for crack located at mid-span.

Table A.10 Mean of $\Delta\Phi_m q(t)$ calculated for each beam segment where crack location is at 0.1L (1.5m) from the left support, the vehicle speed ranging from 10 to 150km/h with 10km/h step, CDR is ranging from 0.1 to 0.45 with 0.05 step, and RSR is class D (ISO 8606:1995(E)).

D		**CDR**							
x_c=0.1·L		**0.10**	**0.15**	**0.20**	**0.25**	**0.30**	**0.35**	**0.40**	**0.45**
V_V (km/h)	**10**	6.74E-06	1.48E-05	2.58E-05	4.07E-05	5.86E-05	8.24E-05	1.09E-04	1.51E-04
	20	2.95E-06	6.58E-06	1.18E-05	1.81E-05	2.75E-05	4.07E-05	5.78E-05	8.03E-05
	30	2.93E-06	6.59E-06	1.17E-05	1.84E-05	2.70E-05	3.87E-05	5.26E-05	7.71E-05
	40	3.06E-06	6.82E-06	1.22E-05	1.83E-05	2.61E-05	3.63E-05	4.94E-05	6.36E-05
	50	2.84E-06	6.02E-06	1.12E-05	1.70E-05	2.63E-05	3.59E-05	5.03E-05	6.67E-05
	60	3.55E-06	7.48E-06	1.29E-05	2.08E-05	2.95E-05	4.18E-05	5.06E-05	7.09E-05
	70	2.42E-06	5.22E-06	9.23E-06	1.45E-05	1.98E-05	2.86E-05	3.76E-05	4.59E-05
	80	2.43E-06	5.73E-06	1.02E-05	1.55E-05	2.40E-05	3.31E-05	4.32E-05	5.82E-05
	90	2.53E-06	5.70E-06	9.46E-06	1.49E-05	2.16E-05	3.11E-05	4.20E-05	5.34E-05
	100	2.19E-06	4.78E-06	8.79E-06	1.31E-05	1.87E-05	2.66E-05	3.52E-05	4.57E-05
	110	1.93E-06	4.41E-06	6.99E-06	1.20E-05	1.57E-05	2.27E-05	2.96E-05	4.01E-05
	120	1.72E-06	3.76E-06	6.39E-06	9.43E-06	1.39E-05	1.96E-05	2.62E-05	3.42E-05
	130	1.54E-06	3.45E-06	6.06E-06	9.55E-06	1.41E-05	1.95E-05	2.50E-05	3.32E-05
	140	1.58E-06	3.26E-06	6.24E-06	9.51E-06	1.32E-05	1.90E-05	2.44E-05	3.19E-05
	150	1.49E-06	3.23E-06	5.58E-06	8.90E-06	1.32E-05	1.76E-05	2.30E-05	3.28E-05

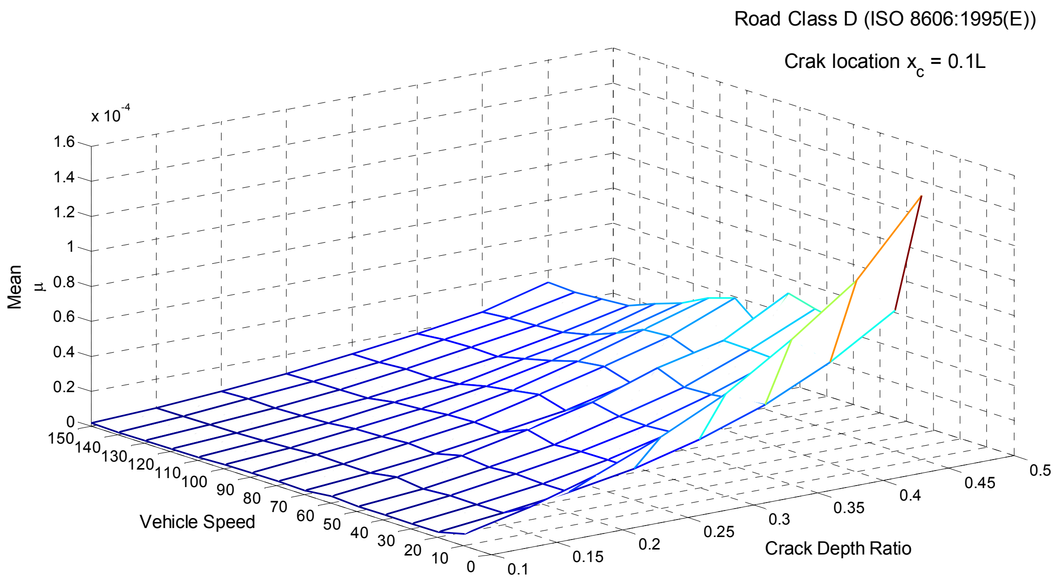

Figure A.10 Mean of $\Delta\Phi_m q(t)$ dependence on Crack Depth Ratio and Vehicle speed for Road Surface Roughness Type D for crack located near support.

Table A.11 Mean of $\Delta\Phi_m q(t)$ calculated for each beam segment where crack location is at 0.25L (3.75m) from the left support, the vehicle speed ranging from 10 to 150km/h with 10km/h step, CDR is ranging from 0.1 to 0.45 with 0.05 step, and RSR is class D (ISO 8606:1995(E)).

D		**CDR**							
xc=0.25·L		**0.10**	**0.15**	**0.20**	**0.25**	**0.30**	**0.35**	**0.40**	**0.45**
V_V (km/h)	10	1.29E-05	2.74E-05	4.80E-05	7.20E-05	1.05E-04	1.40E-04	1.85E-04	2.42E-04
	20	5.75E-06	1.27E-05	2.18E-05	3.56E-05	5.26E-05	7.66E-05	1.01E-04	1.43E-04
	30	5.95E-06	1.21E-05	2.13E-05	3.23E-05	5.22E-05	6.87E-05	9.18E-05	1.19E-04
	40	5.85E-06	1.29E-05	2.17E-05	3.28E-05	4.30E-05	5.74E-05	7.71E-05	9.08E-05
	50	5.21E-06	1.21E-05	2.08E-05	3.32E-05	4.79E-05	6.41E-05	8.19E-05	1.09E-04
	60	6.40E-06	1.37E-05	2.40E-05	3.94E-05	5.58E-05	7.08E-05	9.26E-05	1.08E-04
	70	4.36E-06	9.25E-06	1.65E-05	2.67E-05	3.71E-05	4.57E-05	5.93E-05	7.05E-05
	80	4.92E-06	1.04E-05	1.85E-05	2.79E-05	3.87E-05	5.47E-05	6.98E-05	8.54E-05
	90	4.68E-06	1.01E-05	1.89E-05	2.76E-05	3.80E-05	5.41E-05	6.49E-05	8.27E-05
	100	4.32E-06	9.55E-06	1.52E-05	2.30E-05	3.09E-05	4.24E-05	5.78E-05	6.76E-05
	110	3.60E-06	7.15E-06	1.27E-05	2.08E-05	2.91E-05	3.82E-05	4.78E-05	5.71E-05
	120	3.13E-06	6.99E-06	1.23E-05	1.81E-05	2.44E-05	3.29E-05	4.23E-05	5.27E-05
	130	2.85E-06	6.49E-06	1.18E-05	1.73E-05	2.30E-05	3.31E-05	3.99E-05	5.02E-05
	140	2.80E-06	6.16E-06	1.14E-05	1.70E-05	2.36E-05	3.18E-05	4.11E-05	5.17E-05
	150	2.94E-06	6.12E-06	1.03E-05	1.66E-05	2.36E-05	3.01E-05	3.93E-05	4.98E-05

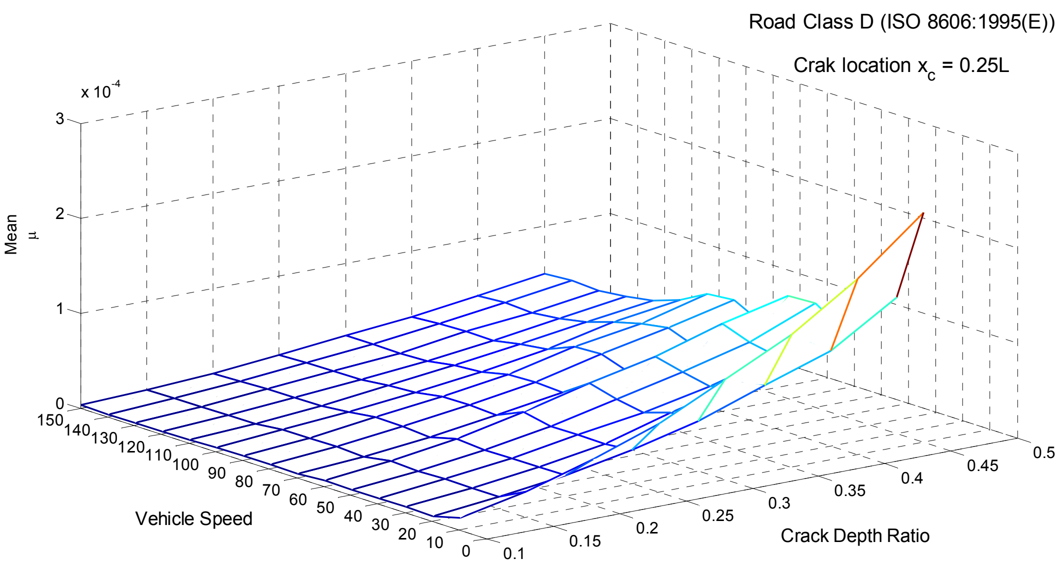

Figure A.11 Mean of $\Delta\Phi_m q(t)$ dependence on Crack Depth Ratio and Vehicle speed for Road Surface Roughness Type D for crack located at quarter-span.

Table A.12 Mean of $\Delta\Phi_m q(t)$ calculated for each beam segment where crack location is at 0.5L (7.5m), the vehicle speed ranging from 10 to 150km/h with 10km/h step, CDR is ranging from 0.1 to 0.45 with 0.05 step, and RSR is class D (ISO 8606:1995(E)).

D		**CDR**							
x_c=0.5·L		**0.10**	**0.15**	**0.20**	**0.25**	**0.30**	**0.35**	**0.40**	**0.45**
V_V (km/h)	**10**	5.93E-06	1.30E-05	2.40E-05	3.86E-05	5.92E-05	8.64E-05	1.22E-04	1.73E-04
	20	2.56E-06	5.72E-06	1.01E-05	1.69E-05	2.64E-05	4.08E-05	5.90E-05	9.30E-05
	30	2.52E-06	5.89E-06	1.06E-05	1.62E-05	2.47E-05	3.98E-05	5.79E-05	8.22E-05
	40	2.62E-06	5.87E-06	1.04E-05	1.59E-05	2.46E-05	3.53E-05	4.80E-05	6.65E-05
	50	2.36E-06	5.58E-06	1.01E-05	1.62E-05	2.55E-05	3.69E-05	5.36E-05	8.01E-05
	60	2.87E-06	6.60E-06	1.20E-05	1.89E-05	2.87E-05	4.06E-05	5.85E-05	7.93E-05
	70	2.01E-06	4.28E-06	7.91E-06	1.25E-05	1.83E-05	2.68E-05	3.74E-05	5.53E-05
	80	2.18E-06	4.51E-06	8.60E-06	1.36E-05	2.19E-05	2.85E-05	4.36E-05	6.31E-05
	90	2.09E-06	4.86E-06	8.68E-06	1.36E-05	2.15E-05	2.73E-05	4.20E-05	6.00E-05
	100	1.82E-06	4.47E-06	8.05E-06	1.26E-05	1.79E-05	2.74E-05	3.57E-05	5.30E-05
	110	1.72E-06	3.79E-06	6.49E-06	1.09E-05	1.55E-05	2.16E-05	3.09E-05	4.59E-05
	120	1.47E-06	3.28E-06	5.67E-06	9.14E-06	1.32E-05	2.09E-05	2.76E-05	4.18E-05
	130	1.34E-06	3.06E-06	5.48E-06	8.63E-06	1.33E-05	1.94E-05	2.45E-05	3.80E-05
	140	1.34E-06	2.91E-06	5.37E-06	8.69E-06	1.32E-05	1.93E-05	2.69E-05	3.69E-05
	150	1.31E-06	2.92E-06	5.04E-06	8.52E-06	1.19E-05	1.84E-05	2.64E-05	3.54E-05

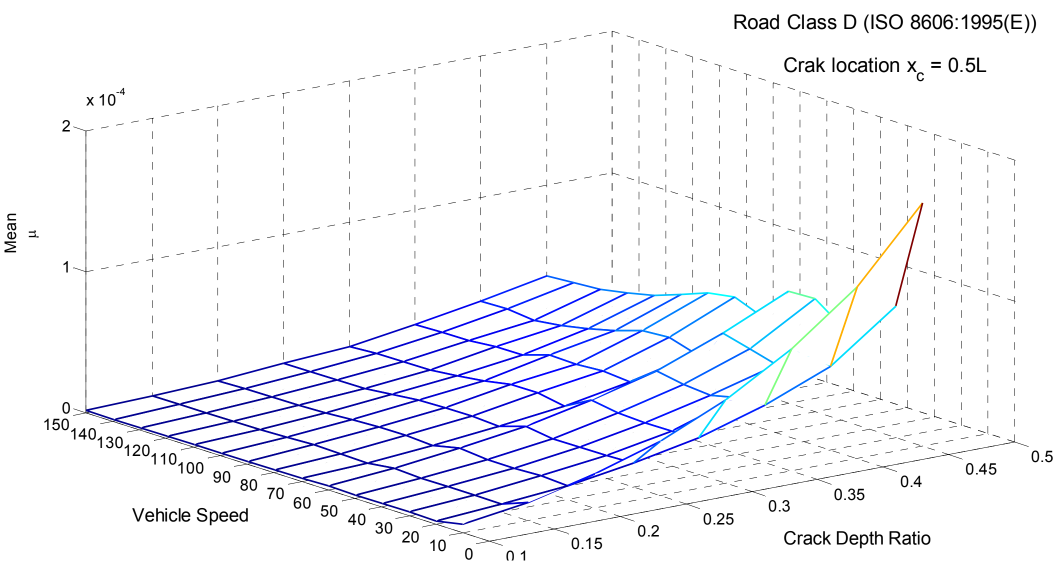

Figure A.12 Mean of $\Delta\Phi_m q(t)$ dependence on Crack Depth Ratio and Vehicle speed for Road Surface Roughness Type D for crack located at mid-span.

Table A.13 Mean of $\Delta\Phi_m q(t)$ calculated for each beam segment where crack location is at $0.1L$ (1.5m) from the left support, the vehicle speed ranging from 10 to 150km/h with 10km/h step, CDR is ranging from 0.1 to 0.45 with 0.05 step, and RSR is class E (ISO 8606:1995(E)).

E		**CDR**							
x_c=0.1·L		**0.10**	**0.15**	**0.20**	**0.25**	**0.30**	**0.35**	**0.40**	**0.45**
V_V (km/h)	**10**	1.33E-05	2.92E-05	5.03E-05	7.86E-05	1.16E-04	1.61E-04	2.19E-04	2.99E-04
	20	5.65E-06	1.21E-05	2.19E-05	3.51E-05	5.31E-05	7.60E-05	1.05E-04	1.54E-04
	30	5.86E-06	1.26E-05	2.08E-05	3.48E-05	5.21E-05	7.09E-05	9.80E-05	1.34E-04
	40	5.58E-06	1.20E-05	2.16E-05	3.28E-05	4.89E-05	6.90E-05	8.03E-05	1.10E-04
	50	5.24E-06	1.13E-05	2.09E-05	3.31E-05	4.77E-05	6.60E-05	8.99E-05	1.32E-04
	60	6.00E-06	1.32E-05	2.43E-05	3.81E-05	5.46E-05	7.58E-05	9.82E-05	1.36E-04
	70	4.36E-06	9.75E-06	1.77E-05	2.51E-05	3.55E-05	5.08E-05	6.82E-05	8.54E-05
	80	4.61E-06	9.23E-06	1.64E-05	2.74E-05	3.86E-05	5.70E-05	8.49E-05	9.59E-05
	90	4.45E-06	9.15E-06	1.68E-05	2.46E-05	3.93E-05	5.29E-05	7.26E-05	8.67E-05
	100	3.53E-06	7.59E-06	1.38E-05	2.19E-05	3.03E-05	4.43E-05	5.86E-05	7.34E-05
	110	2.61E-06	5.99E-06	1.03E-05	1.73E-05	2.38E-05	3.21E-05	4.49E-05	5.38E-05
	120	2.28E-06	5.01E-06	9.03E-06	1.36E-05	1.99E-05	2.65E-05	3.79E-05	4.80E-05
	130	2.08E-06	4.65E-06	7.99E-06	1.26E-05	1.77E-05	2.46E-05	3.17E-05	4.37E-05
	140	1.89E-06	4.06E-06	7.67E-06	1.19E-05	1.79E-05	2.26E-05	3.33E-05	4.29E-05
	150	1.87E-06	4.41E-06	7.45E-06	1.11E-05	1.67E-05	2.24E-05	2.95E-05	3.84E-05

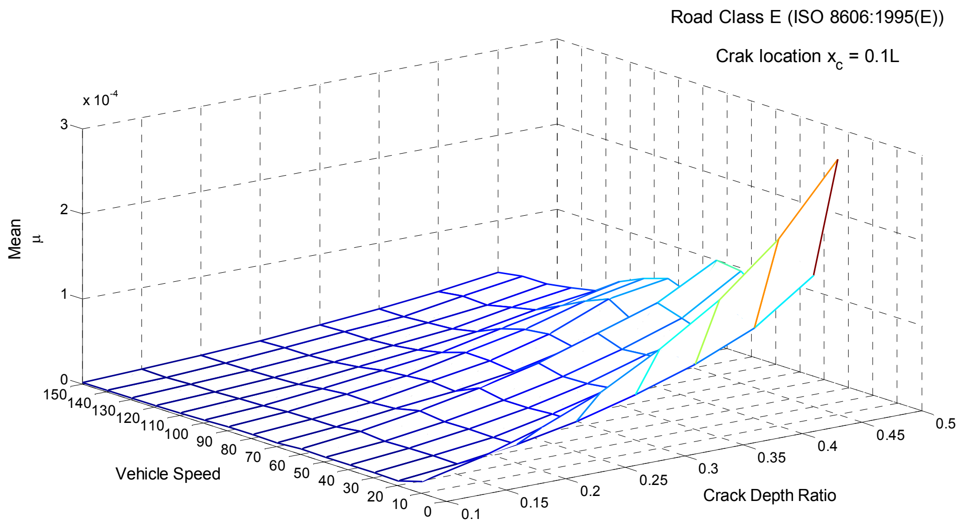

Figure A.13 Mean of $\Delta\Phi_m q(t)$ dependence on Crack Depth Ratio and Vehicle speed for Road Surface Roughness Type E for crack located near support.

Table A.14 Mean of $\Delta\Phi_m q(t)$ calculated for each beam segment where crack location is at 0.25L (3.75m) from the left support, the vehicle speed ranging from 10 to 150km/h with 10km/h step, CDR is ranging from 0.1 to 0.45 with 0.05 step, and RSR is class E (ISO 8606:1995(E)).

E		**CDR**							
x_c**=0.25·L**		**0.10**	**0.15**	**0.20**	**0.25**	**0.30**	**0.35**	**0.40**	**0.45**
V_V (km/h)	**10**	2.51E-05	5.49E-05	9.36E-05	1.43E-04	2.05E-04	2.78E-04	3.70E-04	4.79E-04
	20	1.05E-05	2.42E-05	4.04E-05	6.69E-05	1.05E-04	1.39E-04	2.00E-04	2.75E-04
	30	1.17E-05	2.35E-05	4.30E-05	6.61E-05	8.60E-05	1.21E-04	1.74E-04	2.26E-04
	40	1.05E-05	2.30E-05	3.83E-05	5.80E-05	8.12E-05	1.13E-04	1.30E-04	1.68E-04
	50	1.02E-05	2.32E-05	3.95E-05	6.40E-05	9.08E-05	1.16E-04	1.64E-04	2.02E-04
	60	1.25E-05	2.59E-05	4.71E-05	6.71E-05	9.41E-05	1.24E-04	1.57E-04	1.89E-04
	70	8.05E-06	1.80E-05	3.03E-05	4.59E-05	6.14E-05	8.67E-05	1.10E-04	1.49E-04
	80	8.72E-06	1.87E-05	3.31E-05	5.22E-05	7.37E-05	9.67E-05	1.26E-04	1.66E-04
	90	8.22E-06	1.80E-05	3.09E-05	4.83E-05	6.90E-05	8.62E-05	1.18E-04	1.51E-04
	100	6.73E-06	1.46E-05	2.55E-05	3.88E-05	5.39E-05	7.45E-05	9.59E-05	1.10E-04
	110	4.96E-06	1.11E-05	1.92E-05	3.07E-05	4.22E-05	5.43E-05	7.11E-05	7.94E-05
	120	4.56E-06	9.78E-06	1.66E-05	2.47E-05	3.50E-05	4.70E-05	5.89E-05	6.99E-05
	130	4.11E-06	8.79E-06	1.54E-05	2.34E-05	3.19E-05	4.25E-05	5.61E-05	6.54E-05
	140	3.63E-06	7.93E-06	1.42E-05	2.11E-05	2.87E-05	4.00E-05	5.33E-05	6.35E-05
	150	3.48E-06	7.68E-06	1.40E-05	2.03E-05	2.89E-05	3.85E-05	4.95E-05	6.13E-05

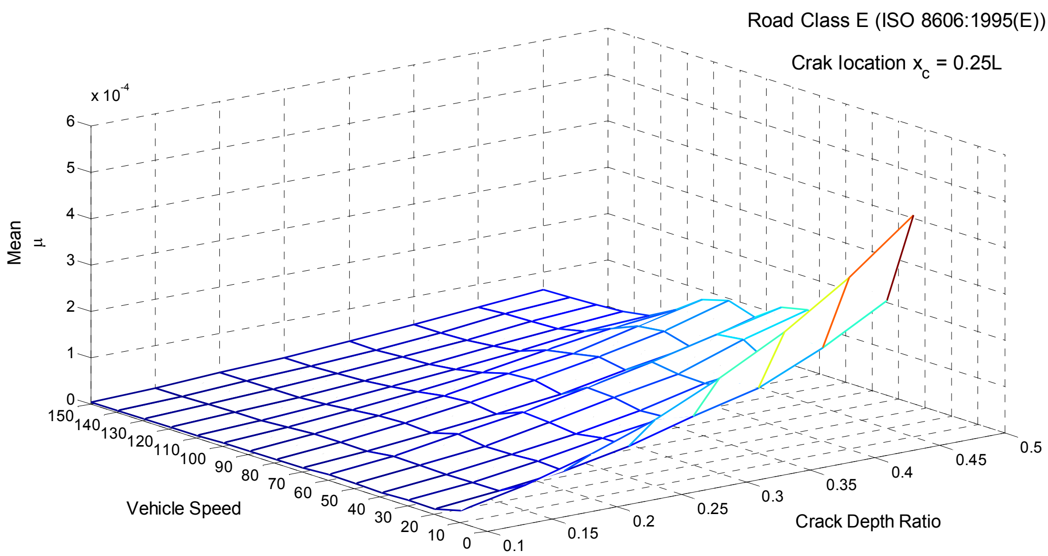

Figure A.14 Mean of $\Delta\Phi_m q(t)$ dependence on Crack Depth Ratio and Vehicle speed for Road Surface Roughness Type E for crack located at quarter-span.

Table A.15 Mean of $\Delta\Phi_m q(t)$ calculated for each beam segment where crack location is at 0.5L (7.5m), the vehicle speed ranging from 10 to 150km/h with 10km/h step, CDR is ranging from 0.1 to 0.45 with 0.05 step, and RSR is class E (ISO 8606:1995(E)).

E		**CDR**							
x_c=0.5·L		**0.10**	**0.15**	**0.20**	**0.25**	**0.30**	**0.35**	**0.40**	**0.45**
V_V (km/h)	**10**	1.17E-05	2.58E-05	4.66E-05	7.62E-05	1.16E-04	1.66E-04	2.37E-04	3.40E-04
	20	4.87E-06	1.07E-05	1.91E-05	3.22E-05	5.10E-05	7.82E-05	1.17E-04	1.77E-04
	30	4.78E-06	1.08E-05	1.95E-05	3.22E-05	4.44E-05	7.23E-05	9.93E-05	1.52E-04
	40	4.76E-06	1.10E-05	1.86E-05	3.02E-05	4.12E-05	6.03E-05	7.91E-05	1.22E-04
	50	4.57E-06	1.05E-05	1.89E-05	3.05E-05	4.63E-05	6.93E-05	1.00E-04	1.46E-04
	60	5.35E-06	1.11E-05	2.18E-05	3.49E-05	5.31E-05	7.36E-05	9.77E-05	1.40E-04
	70	3.76E-06	8.04E-06	1.41E-05	2.17E-05	3.47E-05	4.64E-05	6.37E-05	9.67E-05
	80	4.06E-06	8.56E-06	1.63E-05	2.58E-05	3.87E-05	5.94E-05	7.86E-05	1.18E-04
	90	3.42E-06	8.41E-06	1.38E-05	2.38E-05	3.59E-05	4.85E-05	7.13E-05	9.35E-05
	100	3.08E-06	6.76E-06	1.20E-05	1.89E-05	2.94E-05	4.04E-05	5.62E-05	7.64E-05
	110	2.41E-06	5.13E-06	8.99E-06	1.50E-05	2.21E-05	3.07E-05	4.34E-05	5.83E-05
	120	2.11E-06	4.31E-06	7.87E-06	1.25E-05	1.85E-05	2.60E-05	3.60E-05	4.97E-05
	130	1.79E-06	4.19E-06	7.23E-06	1.08E-05	1.73E-05	2.61E-05	3.67E-05	4.97E-05
	140	1.79E-06	3.87E-06	6.46E-06	1.02E-05	1.59E-05	2.41E-05	3.32E-05	4.84E-05
	150	1.58E-06	3.53E-06	6.33E-06	9.89E-06	1.55E-05	2.47E-05	3.35E-05	4.48E-05

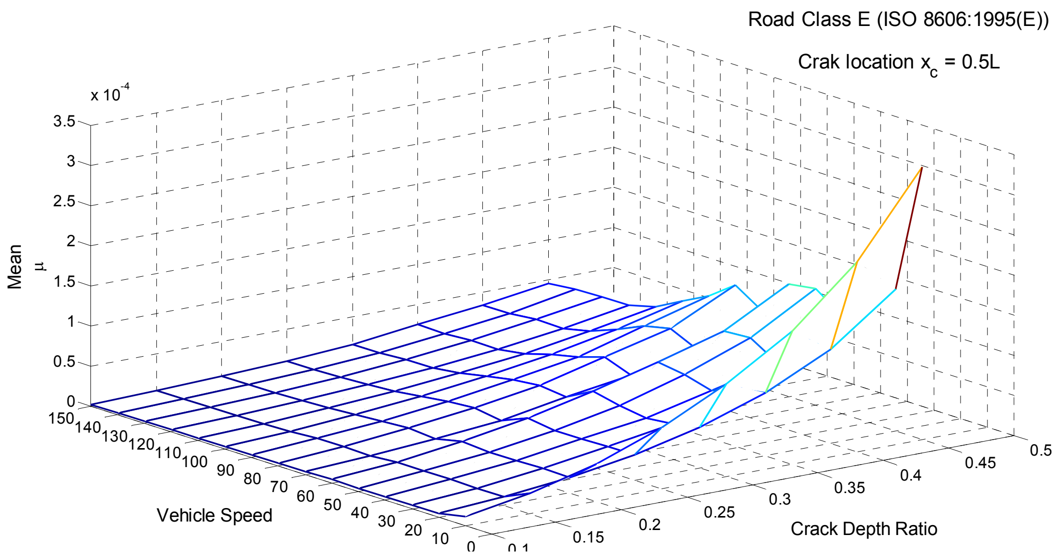

Figure A.15 Mean of $\Delta\Phi_m q(t)$ dependence on Crack Depth Ratio and Vehicle speed for Road Surface Roughness Type E for crack located at mid-span.

Table A.16 STD of $\Delta\Phi_m q(t)$ calculated for each beam segment where crack location is at 0.1L (1.5m) from the left support, the vehicle speed ranging from 10 to 150km/h with 10km/h step, CDR is ranging from 0.1 to 0.45 with 0.05 step, and RSR is class A (ISO 8606:1995(E)).

A		**CDR**							
x_c=0.1·L		**0.10**	**0.15**	**0.20**	**0.25**	**0.30**	**0.35**	**0.40**	**0.45**
V_V (km/h)	**10**	1.58E-06	3.43E-06	6.04E-06	9.51E-06	1.39E-05	1.95E-05	2.62E-05	3.48E-05
	20	8.94E-07	2.05E-06	3.56E-06	5.65E-06	8.21E-06	1.17E-05	1.64E-05	2.11E-05
	30	9.98E-07	2.06E-06	3.57E-06	5.57E-06	8.14E-06	1.18E-05	1.57E-05	2.03E-05
	40	9.00E-07	1.97E-06	3.52E-06	5.38E-06	8.02E-06	1.05E-05	1.43E-05	1.86E-05
	50	1.03E-06	2.19E-06	3.83E-06	5.91E-06	8.73E-06	1.26E-05	1.63E-05	2.15E-05
	60	8.96E-07	2.14E-06	3.59E-06	5.61E-06	7.89E-06	1.11E-05	1.53E-05	1.88E-05
	70	9.16E-07	2.06E-06	3.42E-06	5.33E-06	8.29E-06	1.09E-05	1.47E-05	1.95E-05
	80	9.74E-07	2.17E-06	3.68E-06	6.09E-06	8.41E-06	1.14E-05	1.52E-05	2.03E-05
	90	9.63E-07	2.03E-06	3.77E-06	5.56E-06	8.24E-06	1.08E-05	1.48E-05	1.96E-05
	100	8.99E-07	2.02E-06	3.57E-06	5.47E-06	8.34E-06	1.12E-05	1.50E-05	1.90E-05
	110	9.24E-07	1.98E-06	3.43E-06	5.49E-06	7.82E-06	1.13E-05	1.49E-05	1.91E-05
	120	8.68E-07	1.90E-06	3.50E-06	5.16E-06	7.87E-06	1.10E-05	1.46E-05	1.84E-05
	130	9.31E-07	1.93E-06	3.42E-06	5.29E-06	7.72E-06	1.07E-05	1.45E-05	1.90E-05
	140	8.68E-07	1.89E-06	3.26E-06	5.27E-06	7.35E-06	1.00E-05	1.36E-05	1.82E-05
	150	7.77E-07	1.71E-06	3.05E-06	4.71E-06	6.91E-06	9.53E-06	1.21E-05	1.65E-05

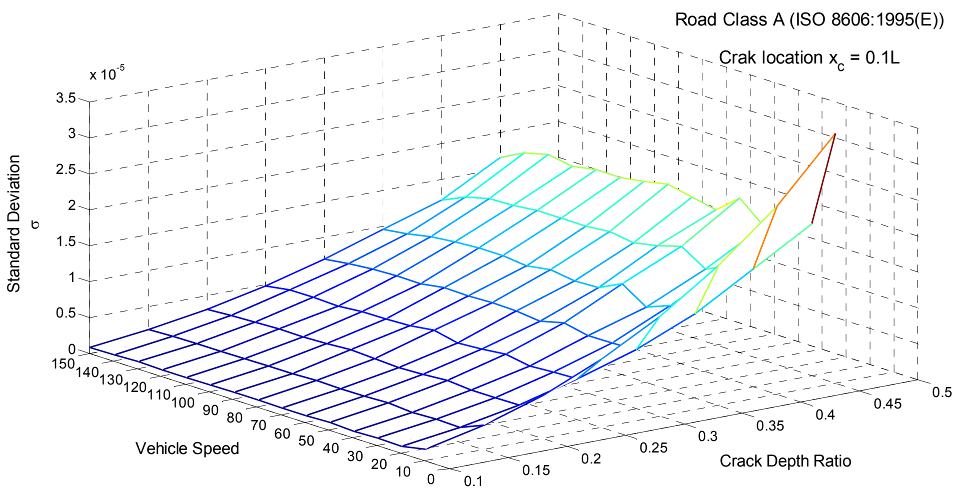

Figure A.16 STD of $\Delta\Phi_m q(t)$ dependence on Crack Depth Ratio and Vehicle speed for Road Surface Roughness Type A for crack located near support.

Table A.17 STD of $\Delta\Phi_m q(t)$ calculated for each beam segment where crack location is at 0.25L (3.75m) from the left support, the vehicle speed ranging from 10 to 150km/h with 10km/h step, CDR is ranging from 0.1 to 0.45 with 0.05 step, and RSR is class A (ISO 8606:1995(E)).

A		CDR							
x_c=0.25·L		0.10	0.15	0.20	0.25	0.30	0.35	0.40	0.45
V_V (km/h)	10	3.00E-06	6.44E-06	1.12E-05	1.73E-05	2.47E-05	3.39E-05	4.36E-05	5.60E-05
	20	1.79E-06	3.84E-06	6.62E-06	1.04E-05	1.54E-05	2.09E-05	2.77E-05	3.62E-05
	30	1.79E-06	3.94E-06	6.74E-06	1.02E-05	1.47E-05	1.98E-05	2.44E-05	3.25E-05
	40	1.74E-06	3.77E-06	6.38E-06	9.87E-06	1.41E-05	1.80E-05	2.35E-05	2.88E-05
	50	1.84E-06	4.00E-06	7.21E-06	1.11E-05	1.57E-05	2.13E-05	2.81E-05	3.50E-05
	60	1.69E-06	3.94E-06	6.65E-06	1.01E-05	1.47E-05	1.90E-05	2.33E-05	2.94E-05
	70	1.73E-06	3.74E-06	6.57E-06	1.00E-05	1.45E-05	1.99E-05	2.64E-05	3.13E-05
	80	1.88E-06	3.91E-06	6.78E-06	1.03E-05	1.55E-05	2.08E-05	2.61E-05	3.31E-05
	90	1.82E-06	3.91E-06	6.55E-06	1.08E-05	1.51E-05	2.07E-05	2.49E-05	3.05E-05
	100	1.85E-06	3.96E-06	6.68E-06	9.75E-06	1.39E-05	2.01E-05	2.45E-05	3.08E-05
	110	1.72E-06	3.76E-06	6.41E-06	9.89E-06	1.41E-05	1.99E-05	2.52E-05	3.14E-05
	120	1.67E-06	3.71E-06	6.56E-06	9.65E-06	1.40E-05	1.85E-05	2.55E-05	3.01E-05
	130	1.71E-06	3.75E-06	6.44E-06	9.46E-06	1.41E-05	1.85E-05	2.29E-05	2.85E-05
	140	1.63E-06	3.50E-06	6.09E-06	9.30E-06	1.32E-05	1.79E-05	2.29E-05	2.89E-05
	150	1.49E-06	3.18E-06	5.54E-06	8.28E-06	1.19E-05	1.63E-05	2.07E-05	2.53E-05

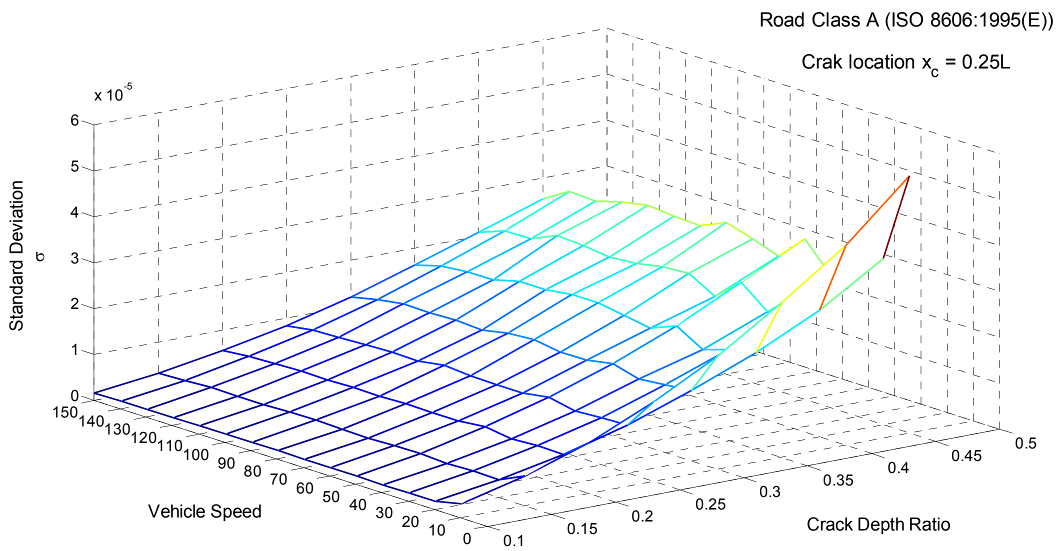

Figure A.17 STD of $\Delta\Phi_m q(t)$ dependence on Crack Depth Ratio and Vehicle speed for Road Surface Roughness Type A for crack located at quarter-span.

Table A.18 STD of $\Delta\Phi_m q(t)$ calculated for each beam segment where crack location is at 0.5L (7.5m), the vehicle speed ranging from 10 to 150km/h with 10km/h step, CDR is ranging from 0.1 to 0.45 with 0.05 step, and RSR is class A (ISO 8606:1995(E)).

A		**CDR**							
x_c=0.5·L		**0.10**	**0.15**	**0.20**	**0.25**	**0.30**	**0.35**	**0.40**	**0.45**
V_V (km/h)	**10**	1.36E-06	3.02E-06	5.48E-06	8.88E-06	1.37E-05	2.04E-05	2.93E-05	4.17E-05
	20	8.09E-07	1.79E-06	3.21E-06	5.24E-06	8.12E-06	1.20E-05	1.73E-05	2.54E-05
	30	7.86E-07	1.81E-06	3.22E-06	4.94E-06	7.84E-06	1.11E-05	1.61E-05	2.34E-05
	40	7.87E-07	1.75E-06	3.23E-06	5.15E-06	7.64E-06	1.11E-05	1.62E-05	2.35E-05
	50	8.66E-07	1.84E-06	3.42E-06	5.91E-06	8.95E-06	1.25E-05	1.83E-05	2.77E-05
	60	8.05E-07	1.73E-06	3.16E-06	5.17E-06	7.65E-06	1.16E-05	1.58E-05	2.22E-05
	70	7.97E-07	1.75E-06	3.11E-06	5.14E-06	7.73E-06	1.18E-05	1.74E-05	2.44E-05
	80	8.58E-07	1.95E-06	3.40E-06	5.29E-06	8.26E-06	1.22E-05	1.79E-05	2.40E-05
	90	8.36E-07	1.79E-06	3.36E-06	5.31E-06	8.21E-06	1.21E-05	1.70E-05	2.46E-05
	100	8.20E-07	1.85E-06	3.27E-06	5.10E-06	7.88E-06	1.19E-05	1.64E-05	2.31E-05
	110	8.03E-07	1.76E-06	3.09E-06	4.97E-06	7.64E-06	1.10E-05	1.66E-05	2.33E-05
	120	7.72E-07	1.72E-06	3.17E-06	5.15E-06	7.56E-06	1.12E-05	1.61E-05	2.29E-05
	130	7.60E-07	1.71E-06	3.10E-06	4.99E-06	7.46E-06	1.09E-05	1.54E-05	2.19E-05
	140	7.49E-07	1.66E-06	2.95E-06	4.85E-06	7.22E-06	1.04E-05	1.53E-05	2.12E-05
	150	6.60E-07	1.53E-06	2.69E-06	4.34E-06	6.73E-06	9.65E-06	1.37E-05	1.89E-05

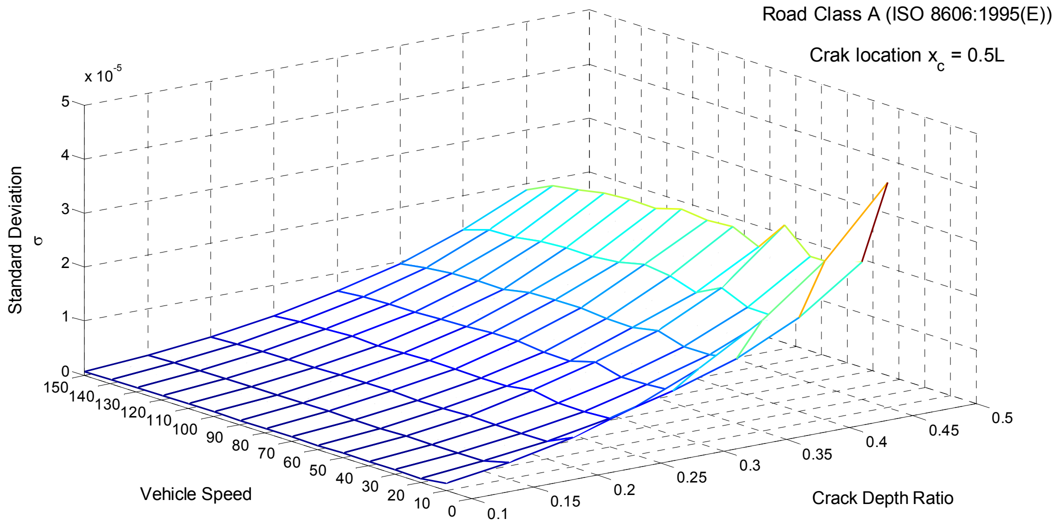

Figure A.18 STD of $\Delta\Phi_m q(t)$ dependence on Crack Depth Ratio and Vehicle speed for Road Surface Roughness Type A for crack located at mid-span.

Table A.19 STD of $\Delta\Phi_m q(t)$ calculated for each beam segment where crack location is at 0.1L (1.5m) from the left support, the vehicle speed ranging from 10 to 150km/h with 10km/h step, CDR is ranging from 0.1 to 0.45 with 0.05 step, and RSR is class B (ISO 8606:1995(E)).

B		**CDR**							
x_c=0.1·L		**0.10**	**0.15**	**0.20**	**0.25**	**0.30**	**0.35**	**0.40**	**0.45**
V_V (km/h)	**10**	2.44E-06	5.25E-06	9.25E-06	1.46E-05	2.14E-05	2.98E-05	4.04E-05	5.36E-05
	20	1.26E-06	2.76E-06	4.87E-06	7.55E-06	1.14E-05	1.64E-05	2.28E-05	3.08E-05
	30	1.32E-06	2.87E-06	4.87E-06	7.30E-06	1.11E-05	1.66E-05	2.10E-05	2.76E-05
	40	1.11E-06	2.47E-06	4.35E-06	6.69E-06	9.92E-06	1.40E-05	1.81E-05	2.29E-05
	50	1.27E-06	2.74E-06	4.80E-06	7.88E-06	1.08E-05	1.61E-05	2.13E-05	2.77E-05
	60	1.26E-06	2.71E-06	4.74E-06	7.36E-06	1.03E-05	1.41E-05	1.87E-05	2.53E-05
	70	1.12E-06	2.53E-06	4.22E-06	7.16E-06	9.85E-06	1.29E-05	1.77E-05	2.20E-05
	80	1.15E-06	2.40E-06	4.39E-06	6.86E-06	9.68E-06	1.36E-05	1.86E-05	2.43E-05
	90	1.02E-06	2.32E-06	4.23E-06	6.56E-06	8.94E-06	1.32E-05	1.67E-05	2.23E-05
	100	1.07E-06	2.24E-06	3.91E-06	6.27E-06	9.08E-06	1.22E-05	1.67E-05	2.19E-05
	110	9.57E-07	2.00E-06	3.63E-06	5.79E-06	8.20E-06	1.14E-05	1.50E-05	2.02E-05
	120	9.74E-07	2.04E-06	3.54E-06	5.65E-06	7.86E-06	1.10E-05	1.47E-05	1.94E-05
	130	8.96E-07	1.87E-06	3.43E-06	5.05E-06	7.78E-06	1.04E-05	1.39E-05	1.73E-05
	140	8.38E-07	1.80E-06	3.27E-06	5.02E-06	7.18E-06	9.77E-06	1.28E-05	1.72E-05
	150	7.75E-07	1.74E-06	3.01E-06	4.80E-06	6.97E-06	9.42E-06	1.26E-05	1.59E-05

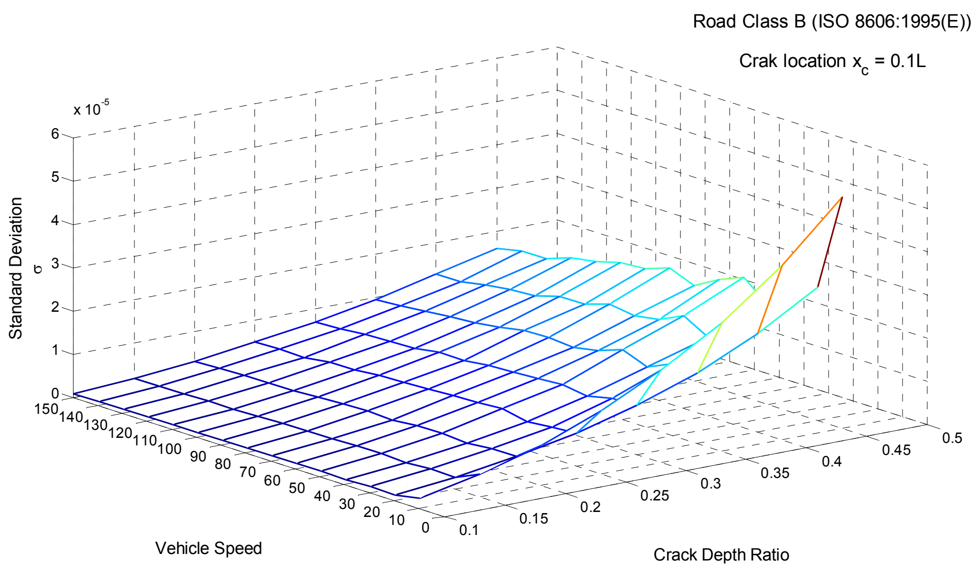

Figure A.19 STD of $\Delta\Phi_m q(t)$ dependence on Crack Depth Ratio and Vehicle speed for Road Surface Roughness Type B for crack located near support.

Table A.20 STD of $\Delta\Phi_m q(t)$ calculated for each beam segment where crack location is at 0.25L (3.75m) from the left support, the vehicle speed ranging from 10 to 150km/h with 10km/h step, CDR is ranging from 0.1 to 0.45 with 0.05 step, and RSR is class B (ISO 8606:1995(E)).

B		**CDR**							
x_c=**0.25·*L***		**0.10**	**0.15**	**0.20**	**0.25**	**0.30**	**0.35**	**0.40**	**0.45**
V_V (km/h)	**10**	4.58E-06	9.93E-06	1.71E-05	2.65E-05	3.80E-05	5.18E-05	6.72E-05	8.65E-05
	20	2.34E-06	5.24E-06	8.95E-06	1.43E-05	2.15E-05	2.89E-05	4.15E-05	5.20E-05
	30	2.38E-06	5.11E-06	8.77E-06	1.43E-05	2.03E-05	2.71E-05	3.74E-05	4.63E-05
	40	2.12E-06	4.66E-06	7.89E-06	1.17E-05	1.76E-05	2.27E-05	2.84E-05	3.47E-05
	50	2.33E-06	5.33E-06	9.35E-06	1.35E-05	1.97E-05	2.77E-05	3.68E-05	4.61E-05
	60	2.38E-06	4.95E-06	8.55E-06	1.36E-05	1.88E-05	2.47E-05	3.11E-05	3.68E-05
	70	2.07E-06	4.92E-06	8.12E-06	1.23E-05	1.78E-05	2.30E-05	2.88E-05	3.91E-05
	80	2.25E-06	4.37E-06	7.88E-06	1.25E-05	1.86E-05	2.35E-05	3.10E-05	3.78E-05
	90	2.07E-06	4.25E-06	7.33E-06	1.18E-05	1.61E-05	2.16E-05	2.93E-05	3.55E-05
	100	1.94E-06	4.35E-06	7.34E-06	1.17E-05	1.59E-05	1.94E-05	2.83E-05	3.43E-05
	110	1.86E-06	3.92E-06	6.81E-06	1.04E-05	1.45E-05	2.04E-05	2.59E-05	3.15E-05
	120	1.71E-06	3.85E-06	6.60E-06	1.02E-05	1.42E-05	1.92E-05	2.51E-05	2.93E-05
	130	1.64E-06	3.59E-06	6.13E-06	9.20E-06	1.33E-05	1.74E-05	2.27E-05	2.89E-05
	140	1.58E-06	3.41E-06	5.81E-06	8.92E-06	1.28E-05	1.68E-05	2.19E-05	2.76E-05
	150	1.52E-06	3.21E-06	5.75E-06	8.69E-06	1.25E-05	1.64E-05	2.11E-05	2.53E-05

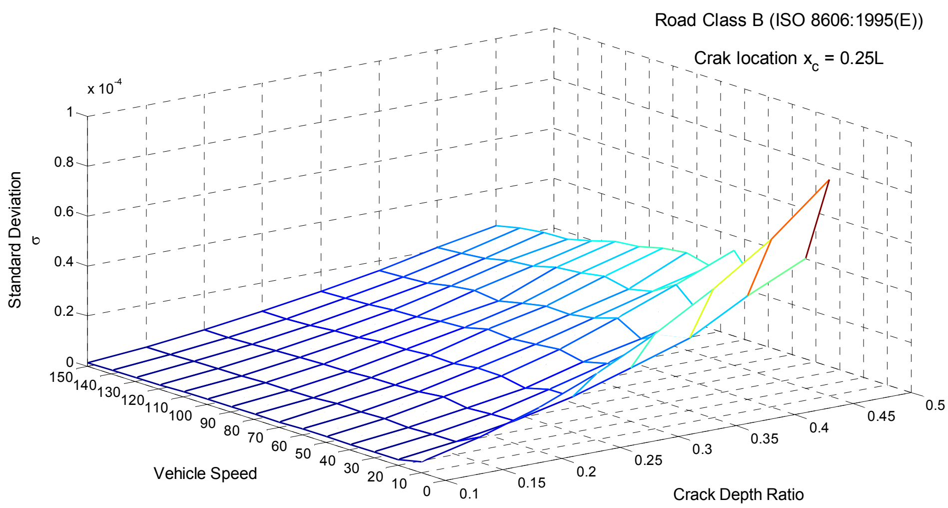

Figure A.20 STD of $\Delta\Phi_m q(t)$ dependence on Crack Depth Ratio and Vehicle speed for Road Surface Roughness Type B for crack located at quarter-span.

Table A.21 STD of $\Delta\Phi_m q(t)$ calculated for each beam segment where crack location is at 0.5L (7.5m), the vehicle speed ranging from 10 to 150km/h with 10km/h step, CDR is ranging from 0.1 to 0.45 with 0.05 step, and RSR is class B (ISO 8606:1995(E)).

B		**CDR**							
x_c=0.5·L		**0.10**	**0.15**	**0.20**	**0.25**	**0.30**	**0.35**	**0.40**	**0.45**
V_V (km/h)	**10**	2.09E-06	4.59E-06	8.39E-06	1.38E-05	2.14E-05	3.12E-05	4.49E-05	6.33E-05
	20	1.07E-06	2.44E-06	4.31E-06	7.22E-06	1.06E-05	1.67E-05	2.47E-05	3.59E-05
	30	1.06E-06	2.53E-06	4.17E-06	6.92E-06	1.05E-05	1.54E-05	2.23E-05	3.25E-05
	40	9.64E-07	2.11E-06	3.83E-06	6.26E-06	9.09E-06	1.34E-05	1.93E-05	2.72E-05
	50	1.07E-06	2.43E-06	4.34E-06	6.98E-06	1.06E-05	1.60E-05	2.30E-05	3.48E-05
	60	1.05E-06	2.24E-06	4.04E-06	6.74E-06	9.92E-06	1.39E-05	2.02E-05	2.61E-05
	70	9.68E-07	2.26E-06	3.77E-06	6.37E-06	9.54E-06	1.36E-05	2.03E-05	2.97E-05
	80	1.02E-06	2.14E-06	3.99E-06	6.46E-06	9.73E-06	1.34E-05	2.04E-05	2.81E-05
	90	9.05E-07	2.05E-06	3.63E-06	5.72E-06	8.79E-06	1.23E-05	1.79E-05	2.54E-05
	100	9.11E-07	2.03E-06	3.59E-06	5.80E-06	8.51E-06	1.22E-05	1.71E-05	2.53E-05
	110	8.05E-07	1.82E-06	3.35E-06	5.20E-06	8.22E-06	1.19E-05	1.66E-05	2.35E-05
	120	7.93E-07	1.78E-06	3.32E-06	5.15E-06	7.77E-06	1.12E-05	1.60E-05	2.30E-05
	130	7.37E-07	1.63E-06	2.91E-06	4.78E-06	7.19E-06	1.03E-05	1.50E-05	2.12E-05
	140	7.18E-07	1.61E-06	2.81E-06	4.63E-06	6.91E-06	1.02E-05	1.42E-05	2.04E-05
	150	6.86E-07	1.56E-06	2.70E-06	4.44E-06	6.72E-06	9.55E-06	1.36E-05	1.94E-05

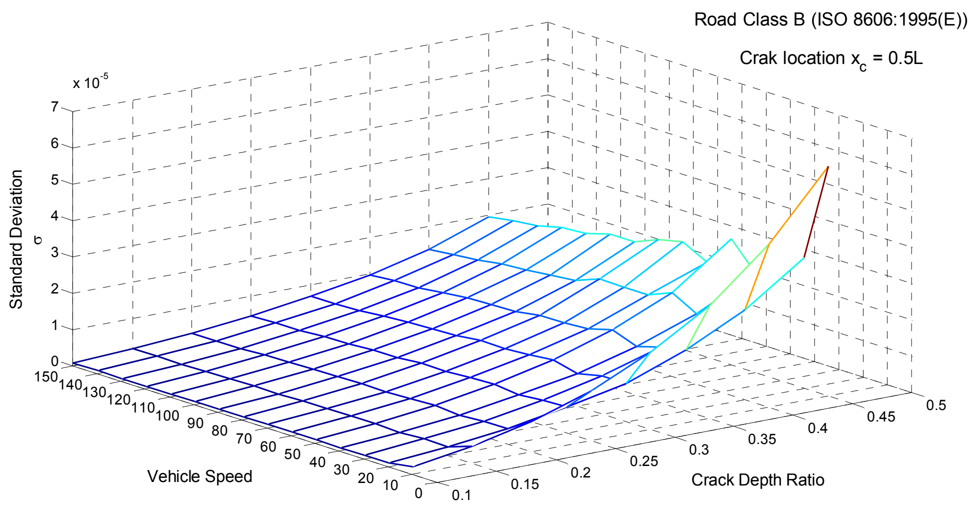

Figure A.21STD of $\Delta\Phi_m q(t)$ dependence on Crack Depth Ratio and Vehicle speed for Road Surface Roughness Type B for crack located at mid-span.

Table A.22 STD of $\Delta\Phi_m q(t)$ calculated for each beam segment where crack location is at 0.1L (1.5m) from the left support, the vehicle speed ranging from 10 to 150km/h with 10km/h step, CDR is ranging from 0.1 to 0.45 with 0.05 step, and RSR is class C (ISO 8606:1995(E)).

C		CDR							
x_c=0.1·L		**0.10**	**0.15**	**0.20**	**0.25**	**0.30**	**0.35**	**0.40**	**0.45**
V_V (km/h)	**10**	4.77E-06	1.03E-05	1.82E-05	2.82E-05	4.13E-05	5.78E-05	7.90E-05	1.04E-04
	20	2.34E-06	5.07E-06	8.70E-06	1.41E-05	2.06E-05	2.94E-05	4.17E-05	5.74E-05
	30	2.19E-06	4.77E-06	9.11E-06	1.31E-05	2.00E-05	2.77E-05	3.65E-05	5.20E-05
	40	1.87E-06	4.27E-06	7.29E-06	1.12E-05	1.67E-05	2.20E-05	3.09E-05	3.91E-05
	50	1.88E-06	4.27E-06	7.39E-06	1.18E-05	1.72E-05	2.45E-05	3.40E-05	4.56E-05
	60	2.19E-06	5.16E-06	8.60E-06	1.32E-05	1.82E-05	2.62E-05	3.46E-05	4.34E-05
	70	1.64E-06	3.56E-06	6.12E-06	9.88E-06	1.50E-05	1.97E-05	2.56E-05	3.33E-05
	80	1.66E-06	3.59E-06	6.68E-06	9.72E-06	1.45E-05	2.05E-05	2.76E-05	3.60E-05
	90	1.59E-06	3.47E-06	5.93E-06	9.18E-06	1.38E-05	1.88E-05	2.51E-05	3.54E-05
	100	1.43E-06	3.09E-06	5.61E-06	8.41E-06	1.25E-05	1.73E-05	2.33E-05	2.88E-05
	110	1.18E-06	2.61E-06	4.73E-06	7.06E-06	1.03E-05	1.44E-05	1.85E-05	2.49E-05
	120	9.99E-07	2.25E-06	3.90E-06	5.93E-06	8.79E-06	1.23E-05	1.64E-05	2.08E-05
	130	9.75E-07	1.98E-06	3.44E-06	5.54E-06	8.13E-06	1.10E-05	1.52E-05	1.93E-05
	140	8.47E-07	1.84E-06	3.13E-06	5.13E-06	7.11E-06	9.53E-06	1.30E-05	1.72E-05
	150	7.71E-07	1.67E-06	2.93E-06	4.67E-06	6.83E-06	9.33E-06	1.20E-05	1.67E-05

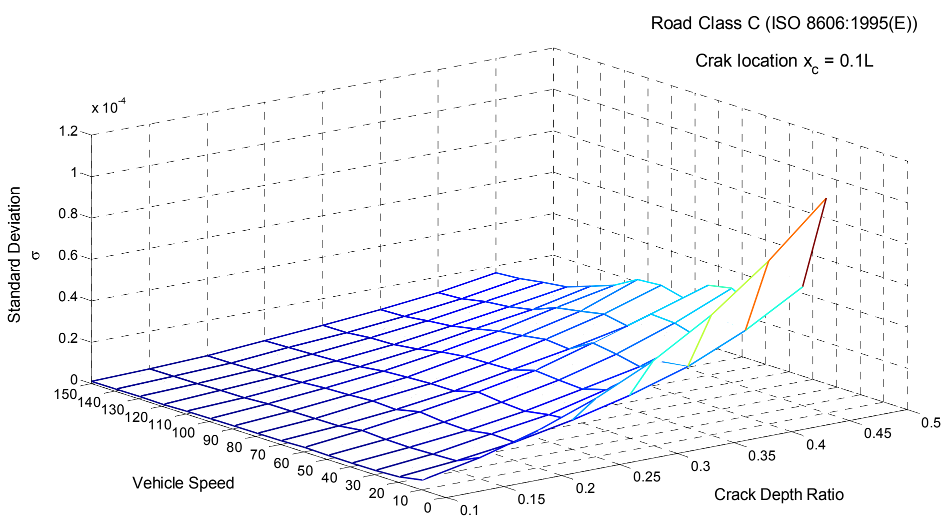

Figure A.22 STD of $\Delta\Phi_m q(t)$ dependence on Crack Depth Ratio and Vehicle speed for Road Surface Roughness Type C for crack located near support.

Table A.23 STD of $\Delta\Phi_m q(t)$ calculated for each beam segment where crack location is at 0.25L (3.75m) from the left support, the vehicle speed ranging from 10 to 150km/h with 10km/h step, CDR is ranging from 0.1 to 0.45 with 0.05 step, and RSR is class C (ISO 8606:1995(E)).

C		**CDR**							
x_c**=0.25·*L***		**0.10**	**0.15**	**0.20**	**0.25**	**0.30**	**0.35**	**0.40**	**0.45**
V_V (km/h)	**10**	8.97E-06	1.94E-05	3.33E-05	5.15E-05	7.41E-05	1.00E-04	1.32E-04	1.69E-04
	20	4.12E-06	8.97E-06	1.65E-05	2.58E-05	3.62E-05	5.25E-05	7.27E-05	9.91E-05
	30	4.21E-06	9.29E-06	1.53E-05	2.45E-05	3.44E-05	4.87E-05	6.61E-05	8.46E-05
	40	3.47E-06	7.97E-06	1.28E-05	1.96E-05	2.73E-05	3.86E-05	4.77E-05	5.95E-05
	50	3.63E-06	7.50E-06	1.46E-05	2.21E-05	3.13E-05	4.40E-05	5.90E-05	7.21E-05
	60	4.19E-06	9.20E-06	1.53E-05	2.29E-05	3.25E-05	4.62E-05	5.47E-05	6.66E-05
	70	3.11E-06	6.49E-06	1.18E-05	1.82E-05	2.53E-05	3.34E-05	4.60E-05	5.40E-05
	80	3.17E-06	6.90E-06	1.23E-05	1.90E-05	2.68E-05	3.55E-05	4.61E-05	5.56E-05
	90	2.95E-06	6.21E-06	1.15E-05	1.64E-05	2.51E-05	3.22E-05	4.30E-05	5.27E-05
	100	2.72E-06	5.61E-06	9.69E-06	1.55E-05	2.16E-05	2.90E-05	3.66E-05	4.56E-05
	110	2.37E-06	5.16E-06	8.45E-06	1.30E-05	1.79E-05	2.51E-05	3.03E-05	3.84E-05
	120	1.93E-06	4.13E-06	7.00E-06	1.10E-05	1.54E-05	2.04E-05	2.70E-05	3.28E-05
	130	1.74E-06	3.61E-06	6.43E-06	9.92E-06	1.41E-05	1.88E-05	2.42E-05	2.99E-05
	140	1.61E-06	3.45E-06	5.69E-06	8.61E-06	1.26E-05	1.69E-05	2.23E-05	2.78E-05
	150	1.45E-06	3.17E-06	5.20E-06	8.68E-06	1.21E-05	1.62E-05	2.11E-05	2.61E-05

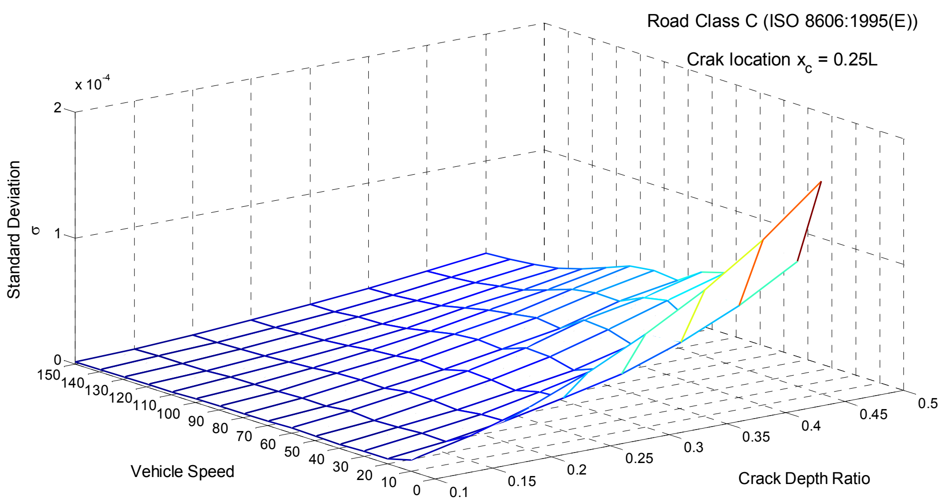

Figure A.23 STD of $\Delta\Phi_m q(t)$ dependence on Crack Depth Ratio and Vehicle speed for Road Surface Roughness Type C for crack located at quarter-span.

Table A.24 STD of $\Delta\Phi_m q(t)$ calculated for each beam segment where crack location is at 0.5L (7.5m), the vehicle speed ranging from 10 to 150km/h with 10km/h step, CDR is ranging from 0.1 to 0.45 with 0.05 step, and RSR is class C (ISO 8606:1995(E)).

C		CDR							
x_c=0.5·L		**0.10**	**0.15**	**0.20**	**0.25**	**0.30**	**0.35**	**0.40**	**0.45**
V_V (km/h)	**10**	4.09E-06	9.13E-06	1.64E-05	2.68E-05	4.11E-05	6.00E-05	8.64E-05	1.22E-04
	20	1.93E-06	4.36E-06	7.71E-06	1.25E-05	1.91E-05	2.93E-05	4.35E-05	6.51E-05
	30	1.93E-06	4.18E-06	7.48E-06	1.22E-05	1.83E-05	2.77E-05	3.92E-05	5.94E-05
	40	1.66E-06	3.61E-06	6.47E-06	1.03E-05	1.53E-05	2.16E-05	3.00E-05	4.18E-05
	50	1.67E-06	3.84E-06	6.87E-06	1.09E-05	1.67E-05	2.71E-05	3.84E-05	5.48E-05
	60	1.94E-06	4.17E-06	7.63E-06	1.18E-05	1.75E-05	2.51E-05	3.54E-05	4.63E-05
	70	1.42E-06	3.22E-06	5.49E-06	9.26E-06	1.36E-05	1.98E-05	2.90E-05	4.18E-05
	80	1.41E-06	3.17E-06	5.73E-06	9.28E-06	1.34E-05	2.08E-05	2.77E-05	3.93E-05
	90	1.34E-06	2.91E-06	5.25E-06	8.41E-06	1.29E-05	1.86E-05	2.69E-05	3.73E-05
	100	1.22E-06	2.66E-06	4.98E-06	7.66E-06	1.15E-05	1.72E-05	2.27E-05	3.05E-05
	110	1.02E-06	1.02E-06	4.10E-06	6.26E-06	9.51E-06	1.37E-05	1.90E-05	2.55E-05
	120	8.74E-07	1.90E-06	3.39E-06	5.50E-06	8.40E-06	1.15E-05	1.66E-05	2.25E-05
	130	8.04E-07	1.75E-06	3.20E-06	5.08E-06	7.65E-06	1.10E-05	1.55E-05	2.11E-05
	140	7.38E-07	1.55E-06	2.86E-06	4.80E-06	7.09E-06	9.73E-06	1.41E-05	1.93E-05
	150	6.57E-07	1.47E-06	2.61E-06	4.30E-06	6.56E-06	9.29E-06	1.31E-05	1.98E-05

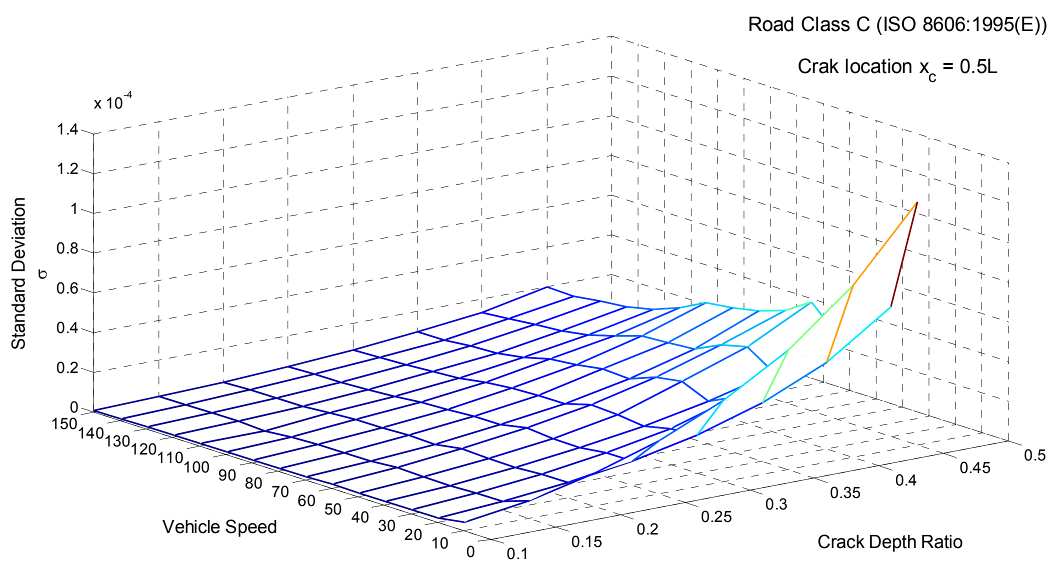

Figure A.24 STD of $\Delta\Phi_m q(t)$ dependence on Crack Depth Ratio and Vehicle speed for Road Surface Roughness Type C for crack located at mid-span.

Table A.25 STD of $\Delta\Phi_m q(t)$ calculated for each beam segment where crack location is at 0.1L (1.5m) from the left support, the vehicle speed ranging from 10 to 150km/h with 10km/h step, CDR is ranging from 0.1 to 0.45 with 0.05 step, and RSR is class D (ISO 8606:1995(E)).

D		**CDR**							
x_c**=0.1·*L***		**0.10**	**0.15**	**0.20**	**0.25**	**0.30**	**0.35**	**0.40**	**0.45**
V_V (km/h)	**10**	9.23E-06	2.03E-05	3.56E-05	5.63E-05	8.15E-05	1.15E-04	1.54E-04	2.09E-04
	20	4.44E-06	9.75E-06	1.72E-05	2.63E-05	3.92E-05	5.68E-05	7.97E-05	1.10E-04
	30	4.10E-06	9.02E-06	1.67E-05	2.55E-05	3.77E-05	5.36E-05	7.05E-05	9.96E-05
	40	3.63E-06	7.81E-06	1.41E-05	2.15E-05	3.10E-05	4.29E-05	5.69E-05	7.56E-05
	50	3.48E-06	7.61E-06	1.38E-05	2.19E-05	3.27E-05	4.52E-05	6.39E-05	8.67E-05
	60	4.32E-06	9.43E-06	1.60E-05	2.66E-05	3.63E-05	5.15E-05	6.34E-05	8.50E-05
	70	3.01E-06	6.51E-06	1.12E-05	1.75E-05	2.58E-05	3.69E-05	4.78E-05	6.27E-05
	80	2.95E-06	6.98E-06	1.23E-05	1.89E-05	2.82E-05	3.91E-05	5.14E-05	6.87E-05
	90	2.93E-06	6.52E-06	1.09E-05	1.70E-05	2.40E-05	3.43E-05	4.68E-05	6.20E-05
	100	2.38E-06	5.24E-06	9.00E-06	1.43E-05	2.12E-05	2.85E-05	3.80E-05	4.88E-05
	110	1.92E-06	4.17E-06	6.85E-06	1.09E-05	1.59E-05	2.18E-05	2.87E-05	3.72E-05
	120	1.54E-06	3.49E-06	5.62E-06	8.61E-06	1.28E-05	1.80E-05	2.29E-05	3.04E-05
	130	1.24E-06	2.69E-06	4.65E-06	7.45E-06	1.06E-05	1.49E-05	1.89E-05	2.57E-05
	140	1.18E-06	2.56E-06	4.20E-06	6.56E-06	9.94E-06	1.36E-05	1.81E-05	2.42E-05
	150	1.07E-06	2.46E-06	4.14E-06	6.62E-06	9.77E-06	1.38E-05	1.82E-05	2.36E-05

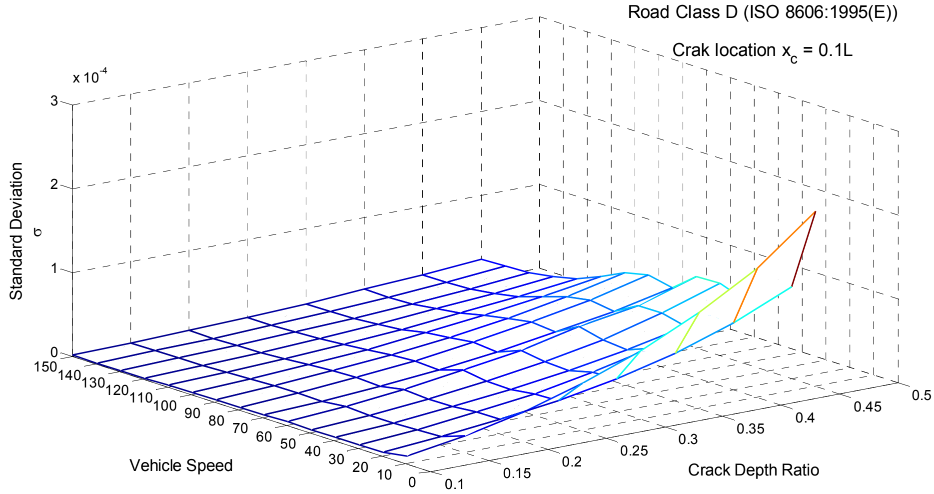

Figure A.25 STD of $\Delta\Phi_m q(t)$ dependence on Crack Depth Ratio and Vehicle speed for Road Surface Roughness Type D for crack located near support.

Table A.26 STD of $\Delta\Phi_m q(t)$ calculated for each beam segment where crack location is at 0.25L (3.75m) from the left support, the vehicle speed ranging from 10 to 150km/h with 10km/h step, CDR is ranging from 0.1 to 0.45 with 0.05 step, and RSR is class D (ISO 8606:1995(E)).

D		**CDR**							
x_c=0.25·L		**0.10**	**0.15**	**0.20**	**0.25**	**0.30**	**0.35**	**0.40**	**0.45**
V_V (km/h)	**10**	1.76E-05	3.80E-05	6.61E-05	1.01E-04	1.47E-04	1.96E-04	2.60E-04	3.35E-04
	20	8.49E-06	1.86E-05	3.17E-05	5.07E-05	7.34E-05	1.04E-04	1.39E-04	1.97E-04
	30	8.22E-06	1.69E-05	2.98E-05	4.56E-05	7.23E-05	9.21E-05	1.22E-04	1.57E-04
	40	6.88E-06	1.51E-05	2.52E-05	3.70E-05	5.06E-05	6.80E-05	8.99E-05	1.10E-04
	50	6.56E-06	1.51E-05	2.59E-05	4.21E-05	5.98E-05	8.26E-05	1.04E-04	1.42E-04
	60	8.17E-06	1.71E-05	3.03E-05	4.77E-05	6.72E-05	8.64E-05	1.09E-04	1.27E-04
	70	5.53E-06	1.20E-05	2.14E-05	3.30E-05	4.66E-05	6.06E-05	7.90E-05	9.36E-05
	80	5.84E-06	1.25E-05	2.27E-05	3.36E-05	4.67E-05	6.72E-05	8.47E-05	1.03E-04
	90	5.49E-06	1.15E-05	2.11E-05	3.17E-05	4.36E-05	5.89E-05	7.24E-05	9.45E-05
	100	4.73E-06	9.93E-06	1.69E-05	2.43E-05	3.49E-05	4.81E-05	6.25E-05	7.24E-05
	110	3.59E-06	7.20E-06	1.27E-05	2.00E-05	2.85E-05	3.59E-05	4.70E-05	5.78E-05
	120	2.83E-06	5.96E-06	1.03E-05	1.56E-05	2.21E-05	3.00E-05	3.70E-05	4.65E-05
	130	2.42E-06	4.96E-06	8.71E-06	1.28E-05	1.88E-05	2.50E-05	3.11E-05	3.85E-05
	140	2.15E-06	4.65E-06	7.76E-06	1.24E-05	1.70E-05	2.28E-05	2.98E-05	3.72E-05
	150	2.10E-06	4.44E-06	7.78E-06	1.19E-05	1.67E-05	2.29E-05	3.01E-05	3.81E-05

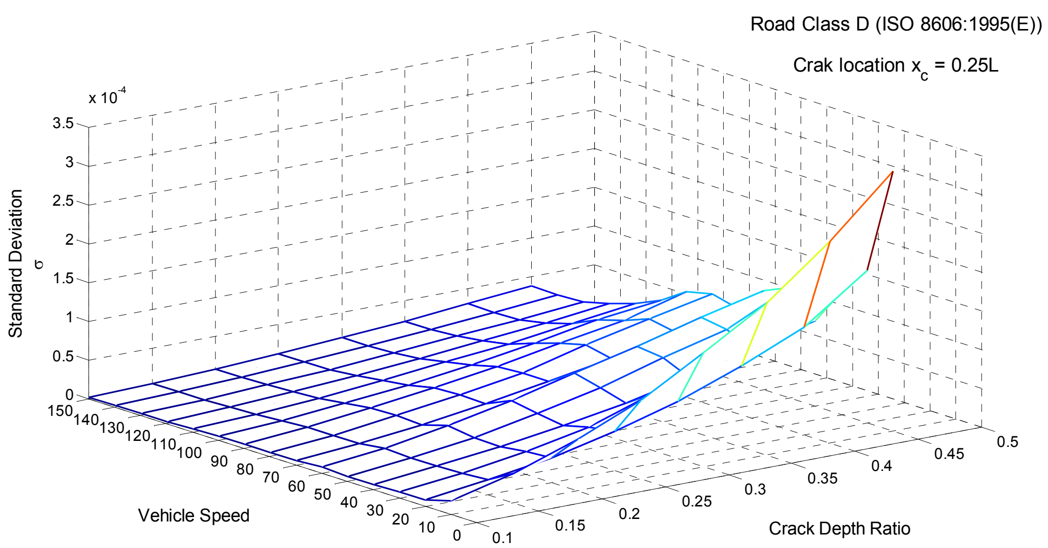

Figure A.26 STD of $\Delta\Phi_m q(t)$ dependence on Crack Depth Ratio and Vehicle speed for Road Surface Roughness Type D for crack located at quarter-span.

Table A.27 STD of $\Delta\Phi_m q(t)$ calculated for each beam segment where crack location is at 0.5L (7.5m), the vehicle speed ranging from 10 to 150km/h with 10km/h step, CDR is ranging from 0.1 to 0.45 with 0.05 step, and RSR is class D (ISO 8606:1995(E)).

D		CDR							
x_c=0.5·L		0.10	0.15	0.20	0.25	0.30	0.35	0.40	0.45
V_V (km/h)	10	8.11E-06	1.79E-05	3.30E-05	5.31E-05	8.19E-05	1.20E-04	1.71E-04	2.43E-04
	20	3.76E-06	8.53E-06	1.49E-05	2.44E-05	3.76E-05	5.67E-05	8.26E-05	1.27E-04
	30	3.56E-06	8.19E-06	1.44E-05	2.25E-05	3.47E-05	5.35E-05	7.72E-05	1.09E-04
	40	3.06E-06	6.86E-06	1.21E-05	1.84E-05	2.81E-05	4.12E-05	5.71E-05	7.68E-05
	50	2.97E-06	6.82E-06	1.28E-05	2.03E-05	3.29E-05	4.75E-05	6.74E-05	1.01E-04
	60	3.53E-06	8.13E-06	1.46E-05	2.33E-05	3.42E-05	4.89E-05	6.70E-05	9.47E-05
	70	2.55E-06	5.65E-06	9.81E-06	1.60E-05	2.40E-05	3.43E-05	4.81E-05	7.04E-05
	80	2.63E-06	5.51E-06	1.03E-05	1.59E-05	2.61E-05	3.51E-05	5.19E-05	7.41E-05
	90	2.42E-06	5.42E-06	1.00E-05	1.51E-05	2.39E-05	3.15E-05	4.77E-05	6.56E-05
	100	2.10E-06	4.84E-06	8.44E-06	1.33E-05	1.87E-05	2.81E-05	3.75E-05	5.61E-05
	110	1.63E-06	3.42E-06	6.08E-06	9.77E-06	1.48E-05	2.09E-05	2.99E-05	4.04E-05
	120	1.25E-06	2.79E-06	4.88E-06	7.92E-06	1.16E-05	1.69E-05	2.27E-05	3.29E-05
	130	1.06E-06	2.27E-06	4.26E-06	6.78E-06	9.89E-06	1.42E-05	2.03E-05	2.78E-05
	140	9.74E-07	2.16E-06	3.81E-06	6.07E-06	9.00E-06	1.35E-05	1.93E-05	2.60E-05
	150	9.38E-07	2.07E-06	3.70E-06	5.96E-06	9.07E-06	1.31E-05	1.69E-05	2.69E-05

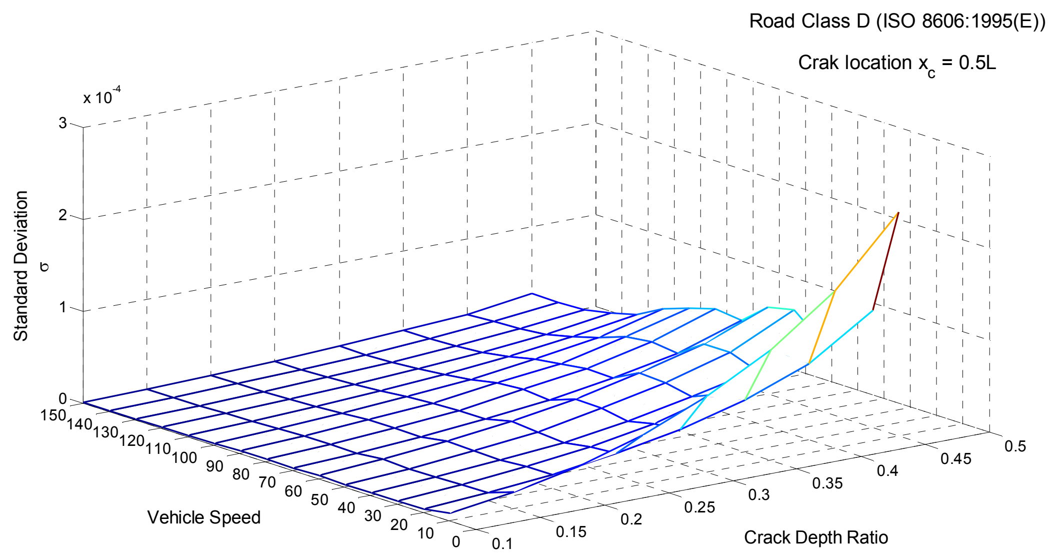

Figure A.27 STD of $\Delta\Phi_m q(t)$ dependence on Crack Depth Ratio and Vehicle speed for Road Surface Roughness Type D for crack located at mid-span.

Table A.28 STD of $\Delta\Phi_m q(t)$ calculated for each beam segment where crack location is at 0.1L (1.5m) from the left support, the vehicle speed ranging from 10 to 150km/h with 10km/h step, CDR is ranging from 0.1 to 0.45 with 0.05 step, and RSR is class E (ISO 8606:1995(E)).

E		**CDR**							
x_c**=0.1·*L***		**0.10**	**0.15**	**0.20**	**0.25**	**0.30**	**0.35**	**0.40**	**0.45**
V_V (km/h)	**10**	1.85E-05	4.07E-05	7.05E-05	1.11E-04	1.63E-04	2.28E-04	3.08E-04	4.18E-04
	20	8.79E-06	1.86E-05	3.37E-05	5.33E-05	7.89E-05	1.12E-04	1.54E-04	2.18E-04
	30	8.30E-06	1.82E-05	3.01E-05	5.03E-05	7.62E-05	1.04E-04	1.38E-04	1.89E-04
	40	7.16E-06	1.52E-05	2.78E-05	4.17E-05	6.36E-05	8.83E-05	1.03E-04	1.40E-04
	50	6.96E-06	1.49E-05	2.72E-05	4.38E-05	6.30E-05	8.66E-05	1.19E-04	1.73E-04
	60	8.25E-06	1.80E-05	3.29E-05	5.10E-05	7.29E-05	1.01E-04	1.30E-04	1.76E-04
	70	5.88E-06	1.33E-05	2.40E-05	3.42E-05	4.98E-05	7.09E-05	9.50E-05	1.21E-04
	80	6.05E-06	1.24E-05	2.19E-05	3.61E-05	5.14E-05	7.46E-05	1.07E-04	1.25E-04
	90	5.53E-06	1.19E-05	2.16E-05	3.24E-05	5.02E-05	6.83E-05	9.22E-05	1.13E-04
	100	4.69E-06	9.94E-06	1.74E-05	2.79E-05	3.91E-05	5.56E-05	7.40E-05	9.43E-05
	110	3.21E-06	7.29E-06	1.34E-05	2.09E-05	3.07E-05	4.02E-05	5.37E-05	6.66E-05
	120	2.64E-06	5.59E-06	1.02E-05	1.50E-05	2.25E-05	2.97E-05	4.23E-05	5.20E-05
	130	2.11E-06	4.72E-06	8.25E-06	1.28E-05	1.95E-05	2.55E-05	3.45E-05	4.43E-05
	140	1.94E-06	4.17E-06	7.55E-06	1.17E-05	1.70E-05	2.40E-05	3.15E-05	4.16E-05
	150	1.85E-06	4.18E-06	7.06E-06	1.15E-05	1.69E-05	2.32E-05	3.12E-05	3.85E-05

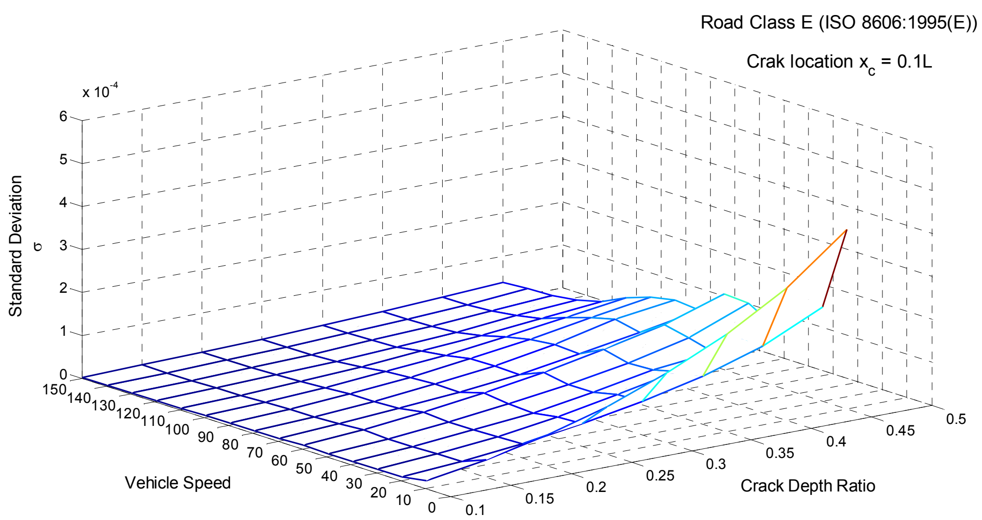

Figure A.28 STD of $\Delta\Phi_m q(t)$ dependence on Crack Depth Ratio and Vehicle speed for Road Surface Roughness Type E for crack located near support.

Table A.29 STD of $\Delta\Phi_m q(t)$ calculated for each beam segment where crack location is at 0.25L (3.75m) from the left support, the vehicle speed ranging from 10 to 150km/h with 10km/h step, CDR is ranging from 0.1 to 0.45 with 0.05 step, and RSR is class E (ISO 8606:1995(E)).

E		**CDR**							
x_c**=0.25·*L***		**0.10**	**0.15**	**0.20**	**0.25**	**0.30**	**0.35**	**0.40**	**0.45**
V_V	**10**	3.49E-05	7.64E-05	1.31E-04	2.02E-04	2.89E-04	3.94E-04	5.22E-04	6.67E-04
	20	1.62E-05	3.74E-05	6.15E-05	1.00E-04	1.52E-04	2.01E-04	2.84E-04	3.92E-04
	30	1.65E-05	3.38E-05	6.30E-05	9.50E-05	1.26E-04	1.77E-04	2.48E-04	3.23E-04
	40	1.32E-05	2.88E-05	5.03E-05	7.14E-05	1.04E-04	1.41E-04	1.66E-04	2.15E-04
	50	1.32E-05	3.02E-05	5.15E-05	8.40E-05	1.21E-04	1.53E-04	2.13E-04	2.70E-04
	60	1.66E-05	3.54E-05	6.33E-05	9.11E-05	1.26E-04	1.65E-04	2.06E-04	2.48E-04
	70	1.10E-05	2.44E-05	4.16E-05	6.30E-05	8.58E-05	1.21E-04	1.55E-04	2.05E-04
	80	1.12E-05	2.42E-05	4.40E-05	6.76E-05	9.53E-05	1.28E-04	1.60E-04	2.11E-04
	90	1.06E-05	2.27E-05	3.87E-05	6.21E-05	8.55E-05	1.13E-04	1.51E-04	1.92E-04
	100	8.80E-06	1.89E-05	3.30E-05	5.01E-05	7.18E-05	9.72E-05	1.20E-04	1.46E-04
	110	6.18E-06	1.38E-05	2.31E-05	3.68E-05	5.11E-05	6.74E-05	8.88E-05	9.70E-05
	120	4.96E-06	1.02E-05	1.83E-05	2.90E-05	3.85E-05	5.03E-05	6.57E-05	7.91E-05
	130	3.99E-06	8.57E-06	1.49E-05	2.33E-05	3.26E-05	4.28E-05	5.63E-05	6.90E-05
	140	3.65E-06	7.59E-06	1.39E-05	2.14E-05	2.91E-05	3.88E-05	5.22E-05	6.53E-05
	150	3.51E-06	7.69E-06	1.31E-05	2.02E-05	2.90E-05	3.83E-05	4.92E-05	6.32E-05

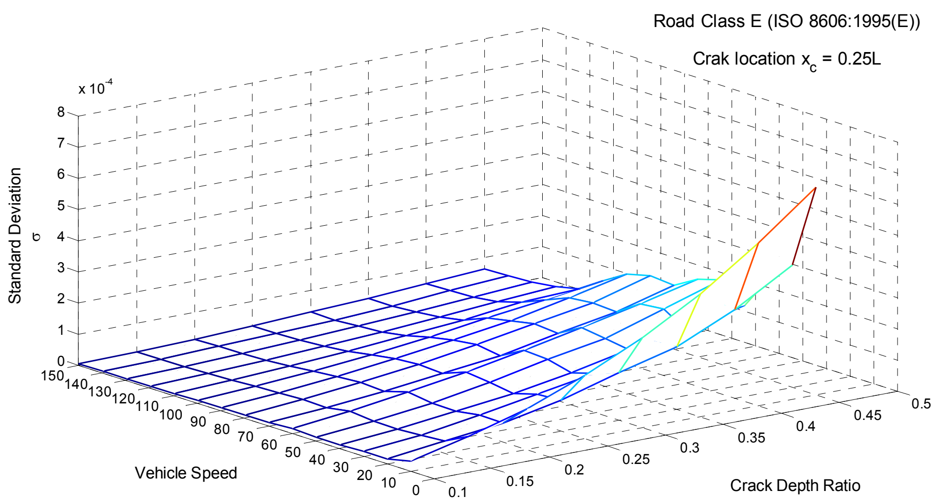

Figure A.29 STD of $\Delta\Phi_m q(t)$ dependence on Crack Depth Ratio and Vehicle speed for Road Surface Roughness Type E for crack located at quarter-span.

Table A.30 STD of $\Delta\Phi_m q(t)$ calculated for each beam segment where crack location is at 0.5L (7.5m), the vehicle speed ranging from 10 to 150km/h with 10km/h step, CDR is ranging from 0.1 to 0.45 with 0.05 step, and RSR is class E (ISO 8606:1995(E)).

E		CDR							
x_c=0.5·L		0.10	0.15	0.20	0.25	0.30	0.35	0.40	0.45
V_V (km/h)	10	1.61E-05	3.59E-05	6.51E-05	1.07E-04	1.64E-04	2.35E-04	3.37E-04	4.82E-04
	20	7.53E-06	1.62E-05	2.92E-05	4.83E-05	7.59E-05	1.13E-04	1.67E-04	2.50E-04
	30	6.83E-06	1.54E-05	2.84E-05	4.70E-05	6.57E-05	1.06E-04	1.45E-04	2.18E-04
	40	6.04E-06	1.39E-05	2.37E-05	3.81E-05	5.30E-05	7.87E-05	1.03E-04	1.57E-04
	50	5.95E-06	1.38E-05	2.49E-05	4.09E-05	6.11E-05	9.23E-05	1.30E-04	1.95E-04
	60	7.26E-06	1.50E-05	2.88E-05	4.67E-05	7.06E-05	9.75E-05	1.32E-04	1.84E-04
	70	4.98E-06	1.09E-05	1.95E-05	3.03E-05	4.79E-05	6.57E-05	9.14E-05	1.33E-04
	80	5.22E-06	1.13E-05	2.11E-05	3.32E-05	5.02E-05	7.31E-05	1.01E-04	1.47E-04
	90	4.50E-06	1.09E-05	1.84E-05	3.04E-05	4.64E-05	6.41E-05	9.06E-05	1.21E-04
	100	4.00E-06	8.59E-06	1.55E-05	2.45E-05	3.77E-05	5.10E-05	7.22E-05	9.51E-05
	110	3.00E-06	6.17E-06	1.13E-05	1.89E-05	2.57E-05	3.83E-05	5.11E-05	7.04E-05
	120	2.28E-06	4.76E-06	8.84E-06	1.37E-05	2.01E-05	2.87E-05	4.08E-05	5.20E-05
	130	1.83E-06	3.99E-06	7.24E-06	1.14E-05	1.68E-05	2.53E-05	3.61E-05	4.77E-05
	140	1.69E-06	3.61E-06	6.59E-06	1.03E-05	1.58E-05	2.32E-05	3.16E-05	4.58E-05
	150	1.60E-06	3.54E-06	6.19E-06	1.01E-05	1.57E-05	2.33E-05	3.11E-05	4.54E-05

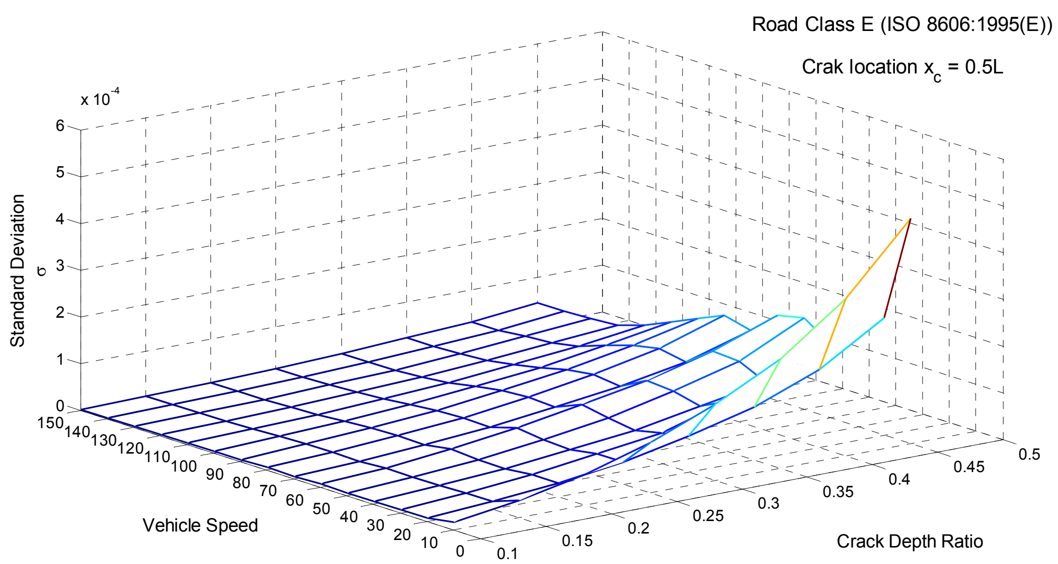

Figure A.30 STD of $\Delta\Phi_m q(t)$ dependence on Crack Depth Ratio and Vehicle speed for Road Surface Roughness Type E for crack located at mid-span.

APPENDIX B1

Reference Model and Simple Vibration Problems

B1.1 SDOF Undamped Oscillation

The simplest form of vibration that we can study is the single degree of freedom system without damping or external forcing. A sample of such a system is shown in Figure B1.1.

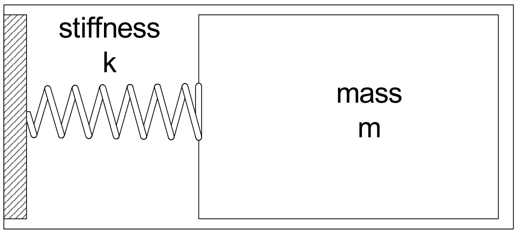

Figure B1.1 Typical SDOF free oscillator.

The mechanical system equation of motion is:

$$m\ddot{x} + kx = 0 \qquad (B1.1)$$

where m is mass, k is stiffness and x is displacement. In general, we would have the forcing function F (t) on the right-hand side but it is assumed zero for this analysis. Dividing through by m and introducing parameter $\omega_n = \sqrt{\frac{k}{m}}$ the solution is obtained:

$$x(t) = Asin(\omega_n t + \phi) \qquad (B1.2)$$

where A is amplitude, ω_n is natural frequency, t is period and ϕ is phase angle. In the terms of physical parameters of the system:

$$x(t) = \frac{\sqrt{\omega_n^2 x_0^2 + \dot{x}_0^2}}{\omega_n} cos\,(\omega_n t - tan^{-1}\frac{\dot{x}_0}{\omega_n x_0}) \qquad (B1.3)$$

From equation (B1.3), the complete response of an undamped, unforced, one degree of freedom oscillator depends on three physical parameters: ω_n, x_0 and $\dot{x}_0$ (e.g. the natural frequency, initial velocity, and initial displacement, respectively). It is also evident that the phase angle and maximum amplitude are also functions of the natural frequency.

From the definition of the natural frequency, we see that it is inversely proportional to $\sqrt{m}$, and is directly proportional to $\sqrt{k}$. Variation of mass or stiffness, then, will cause a variation in the frequency of vibration. Therefore we looked at case of varying mass. The initial conditions adopted are: velocity is $\dot{x}_0$ = 1, and the initial displacement x_0= 3.

B.1.1.1 SDOF Undamped Oscillation – varying mass

Figure B1.2 shows the variation of the vibrational characteristics for an increasing mass (m = 2, 4 and 12 kg) while stiffness remains constant (k = 8 N/m).

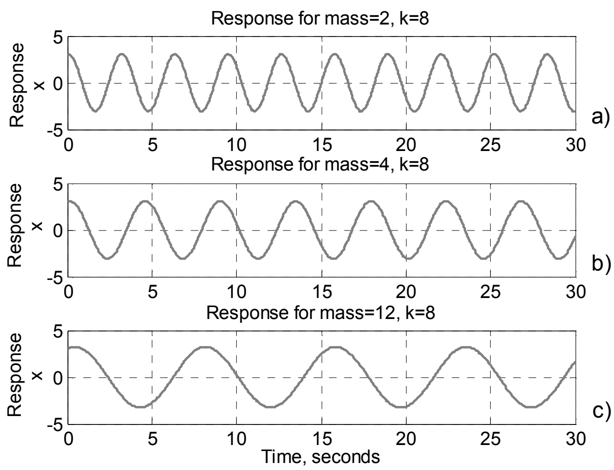

Figure B1.2 Responses of SDOF undamped system for different masses.

The frequency decreases with increasing mass; hence it would increases with increasing stiffness, as expected. Also, the maximum amplitude decreases with increasing mass, due to the corresponding reduction in natural frequency. As a result, the phase shift diminishes, with the peak of oscillation becoming nearer to $t = 0$. The maximum displacement would occur at $t = 0$ if the initial velocity were zero. For this case, the parameter A (see equation B1.2) reduces to x_0, and the phase angle becomes 0º.

B1.2 A Damped SDOF System

The equation of motion for a damped single degree of freedom oscillator shown in Figure B1.3 can be written:

$$m\ddot{x} + c\dot{x} + kx = 0 \qquad (B1.4)$$

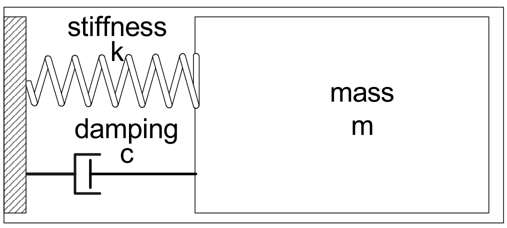

Figure B1.3 Typical damped SDOF oscillator.

If we divide through by m, we introduce the dimensionless parameters ω and ζ:

$$\ddot{x} + 2\zeta\omega_n\dot{x} + \omega_n^2 x = 0 \qquad (B1.5)$$

where ω_n represents the undamped natural frequency, and ζ is the viscous damping ratio. For the purposes of this example, it is assumed the underdamped case ($\zeta < 1$). The solution to this equation is:

$$x(t) = Ae^{-\zeta\omega_n t} sin\,(\omega_d t + \phi) \qquad (B1.6)$$

where $\omega_d = \omega_n\sqrt{1-\zeta^2}$ is damped natural frequency. The equation B1.6 can be written in the function of the parameters ω_n and ζ:

$$x(t) = \sqrt{\frac{(v_0 + \zeta\omega_n x_0)^2 + \left(x_0\omega_n\sqrt{1-\zeta^2}\right)^2}{\left(\omega_n\sqrt{1-\zeta^2}\right)^2}}\, e^{(-\zeta\omega_n t)} sin\left[\left(\omega_n\sqrt{1-\zeta^2}\right)t + tan^{-1}\left(\frac{x_0\omega_n\sqrt{1-\zeta^2}}{v_0 + \zeta\omega_n x_0}\right)\right] \qquad (B1.7)$$

The response of the system therefore only depends on four quantities: x_0, v_0, ω_n and ζ (e.g. the initial displacement, initial velocity, natural frequency, and, viscous damping coefficient, respectively). The only difference to the undamped case is existence of viscous damping coefficient. The effects of the increasing viscous damping coefficient (ζ = 0.05, 0.2 and 0.5) on the system response are shown in Figure B1.4. The initial conditions adopted are: velocity is $v_0 = 1$, and the initial displacement $x_0 = 3$ while natural frequency is set to $\omega_n = 7$.

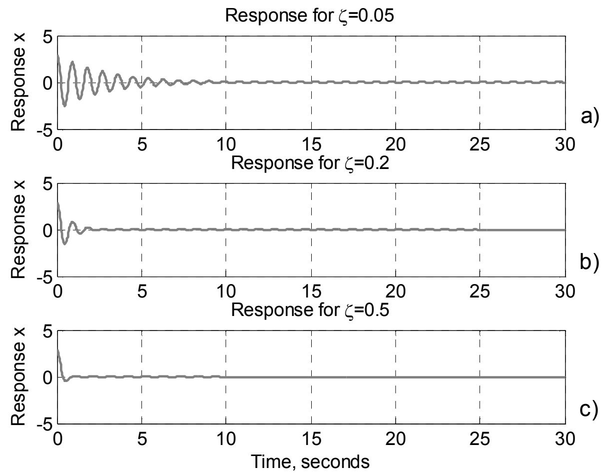

Figure B1.4 Responses of SDOF damped system for different damping values.

Note how quickly the response becomes virtually zero; this occurs within ten seconds, even for a damping coefficient as small as 0.05. The Matlab code used in this analysis only works for the underdamped case since the term $\omega_d = \omega_n\sqrt{1-\zeta^2}$ is in the denominator of the response equation which would lead to division by zero for $\zeta = 1$, and when $\zeta > 1$ will give an imaginary damped natural frequency.

B1.3 Overdamped SDOF Oscillation

The equation B1.5 represents equation of motion of a damped single degree of freedom oscillator. Assume a solution of the form $Ae^{\lambda t}$ substitute it into equation B1.5, and obtain the quadratic formula defining possible values for λ:

$$\lambda = -\zeta\omega_n \pm \omega_n\sqrt{\zeta^2 - 1} \qquad (B1.8)$$

Since it was assumed that $\zeta > 1$ the quantity inside the radical is always greater than zero. Therefore, the solution of the equation of motion is:

$$x(t) = e^{-\zeta\omega_n t}\left(a_1 e^{\omega_n t\sqrt{\zeta^2-1}} + a_2 e^{-\omega_n t\sqrt{\zeta^2-1}}\right) \qquad (B1.9)$$

If initial displacement is x_0 and initial velocity is v_0, the constants a_1 and a_2 become

$$a_1 = \frac{-v_0 + \left(-\zeta + \sqrt{\zeta^2-1}\right)\omega_n x_0}{2\omega_n\sqrt{\zeta^2-1}} \qquad (B1.10)$$

$$a_2 = \frac{v_0 + \left(\zeta + \sqrt{\zeta^2-1}\right)\omega_n x_0}{2\omega_n\sqrt{\zeta^2-1}} \qquad (B1.11)$$

Equation B1.9 is a decaying exponential and the system will simply return to its initial position instead of oscillating about the equilibrium. This is shown in Figure B1.5. Note that if ζ = 1, a singularity exists in the constants; a second independent solution must be found; from ordinary differential equations, we can find response of such system

$$x(t) = (a_1 + a_2 t)e^{-\omega_n t} \qquad (B1.12)$$

Where $a_1 = x_0$ and $a_2 = v_0 + \omega_n x_0$.

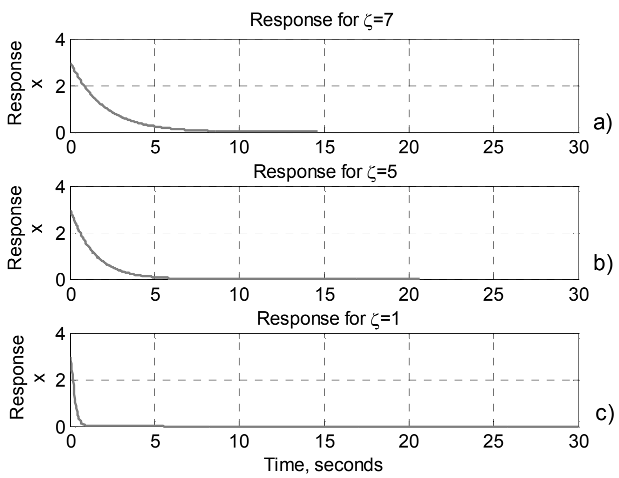

Figure B1.5 Response of three overdamped system for decreasing damping.

Figure B1.5 was generated for ω_n = 7; x_0 = 3; and υ_0 = 1. The critically damped response returns to equilibrium faster than the others. For the plots in the figure, the motion with critical damping is stopped after about two seconds, while the others do not reach equilibrium until more than eight seconds. This is the distinguishing characteristic of the critically damped case. Also the motion of the masses is, as expected, purely exponential; there is no oscillation, only a decay of the response to equilibrium.

B1.4 Harmonic Excitation of Undamped SDOF Systems

The effects of an external force on the system are examined next. The simplest form of external force, harmonic load, is adopted and system under consideration is shown in Figure B1.6.

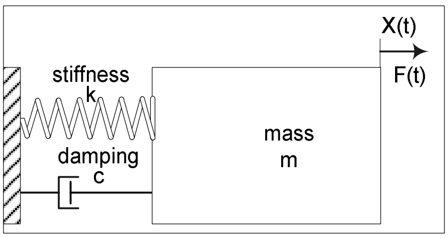

Figure B1.6 SDOF system subject to external force.

The assumed form of external force is:

$$F(t) = F_o cos\omega t \qquad (B1.13)$$

where ω is driving frequency. When there is no damping, Newton’s Second Law gives us the equation of motion:

$$m\ddot{x} + kx = F_o cos\omega t \qquad (B1.14)$$

$$\ddot{x} + \omega_n^2 x = f_o cos\omega t \qquad (B1.15)$$

where $f_o = F_o/m$. The solution for response $x(t)$ is:

$$x(t) = A_1 sin\omega_n t + A_2 cos\omega_n t + \frac{f_o}{\omega_n^2 - \omega^2} cos\omega t \qquad (B1.16)$$

where constants are: $A_1 = \frac{v_0}{\omega_n}$ and $A_2 = \frac{f_o}{\omega_n^2 - \omega^2}$. The key parameters which define the response are the natural and driving frequencies, or more precisely, their ratio ω/ω_n. Figure B1.7 shows the effect of varying driving frequency ω (in the figure indicated as ω_{dr}) for a given natural frequency. Figure B1.8 the same for various natural frequencies ω_n. The figures are generated using initial displacement, amplitude and force magnitude per unit mass: $v_0 = 0$ $x_0 = 0$; and $f_0 = 6$, respectively. Making the initial conditions zero allows us to better see the effects of varying frequencies.

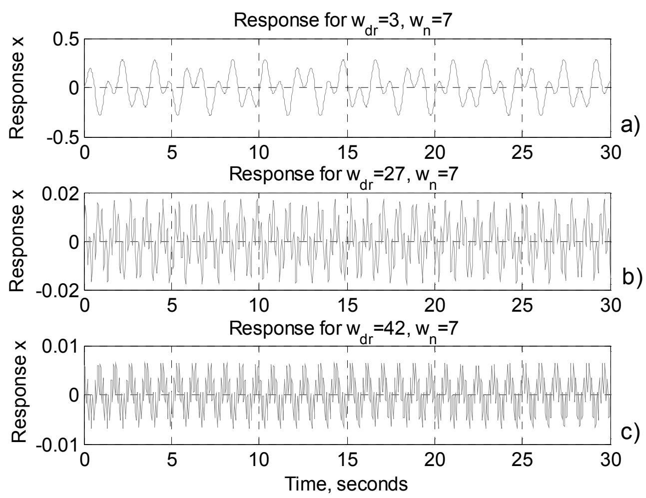

Figure B1.7 SDOF undamped system response to harmonic load for increasing driving and set natural frequencies.

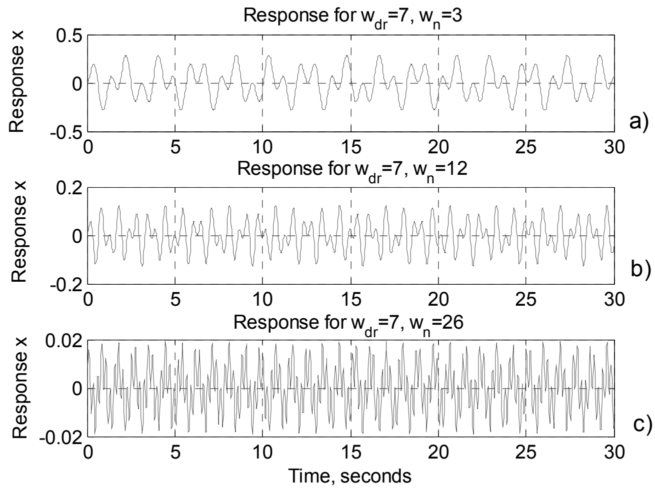

Figure B1.8 SDOF undamped system response to harmonic load for set driving and increased natural frequencies.

The fact that two of the three constants in the expression for x(t), equation B1.16, involve the difference between the frequencies gives rise to two interesting phenomena: beats and resonance. Beats occur when the natural frequency and the driving frequency are close but not equal. The result is then a rapid oscillation with slowly varying amplitude, as shown in Figure B1.9. The rapid oscillation and the slow change of the amplitude both vary along a sinusoid.

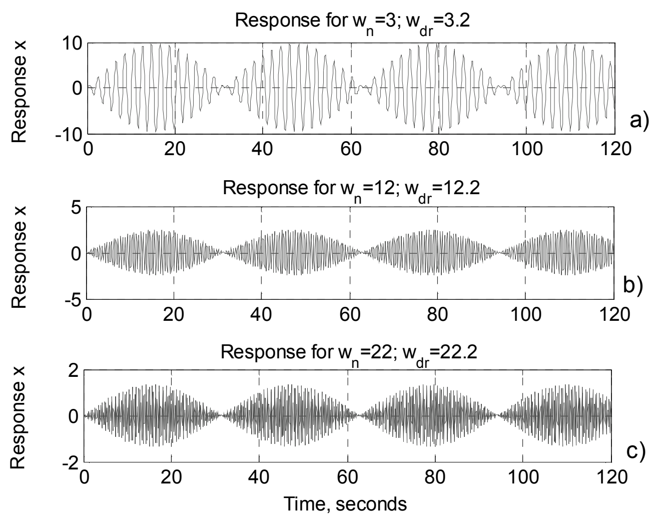

Figure B1.9 SDOF undamped system response to harmonic load – Beating phenomenon.

When the driving and natural frequencies are equal, $\omega_{dr} = \omega_n$ resonance is the result. The third term in Equation B1.16 is not valid as a particular solution of the governing equation of motion. Instead, the particular solution is:

$$x_p(t) = \frac{f_o}{2\omega_n} t sin\omega_n t \qquad (B1.17)$$

In this case the amplitude of oscillation will increase without limit. In a real system, the stiffness element has a certain yield point which will be met and exceeded by a resonant vibration. Figure B1.10 shows resonant vibration.

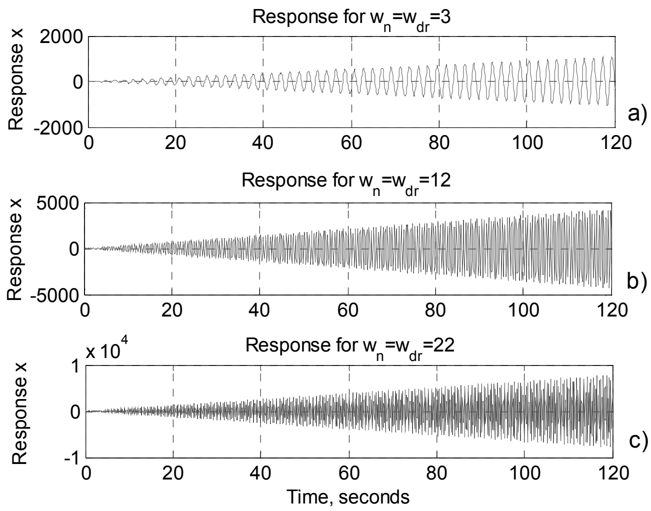

Figure B1.10 SDOF undamped system response to harmonic load – Resonance phenomenon.

B1.5 Harmonic Excitation of Damped SDOF Systems

The equation of motion of damped SDOF System excited with the harmonic forcing can be written:

$$m\ddot{x} + c\dot{x} + kx = Fcos\omega t \qquad (B1.18)$$

$$\zeta = c/2m\omega_n \tag{B1.19}$$

$$\ddot{x} + 2\zeta\omega_n\dot{x} + \omega_n^2 x = f cos\omega t \tag{B1.20}$$

where $f = F/m$. The homogeneous solution to equation B1.20 is of the form:

$$x_h(t) = Ae^{-\zeta\omega t} sin(\omega_d t + \theta) \tag{B1.21}$$

$$\omega_d = \omega_n\sqrt{1-\zeta^2} \tag{B1.22}$$

Constants A and θ depend on initial conditions. The particular solution to the external force is:

$$x_p(t) = A_0 cos(\omega t - \phi) \tag{B1.23}$$

where the constants are:

$$A_0 = \frac{f}{\sqrt{(\omega_n^2 - \omega^2)^2 + (2\zeta\omega_n\omega)^2}} \tag{B1.24}$$

$$\phi = tan^{-1}\frac{2\zeta\omega_n\omega}{\omega_n^2 - \omega^2} \tag{B1.25}$$

The complete solution:

$$x(t) = x_h(t) + x_p(t) \tag{B1.26}$$

is used to evaluate constants, A and θ. These constants are found for zero initial conditions. The damping causes the response of the system to differ slightly, as shown in Figure B1.11 and Figure B1.12.

In Figure B1.11, the damping ratio ζ was varied, which shows that the transient period of vibration varies inversely with damping ratio. The length of the transient period varies from about 4.5 seconds for $\zeta = 0.05$ to about 1.5 seconds for $\zeta = 0.5$; showing that, in many cases, the transient response can be ignored due to its short time period. However, for some cases, the transient period may be much longer or may have very large amplitude, so it is always important to examine the transient effects of a system before neglecting them. It is also noticeable that the damping ratio affects the amplitude of the steady-state vibration, also in an inverse relationship. That is, the amplitude of the response for $\zeta = 0.05$ is almost 2, while that for $\zeta = 0.5$ is less than 1.

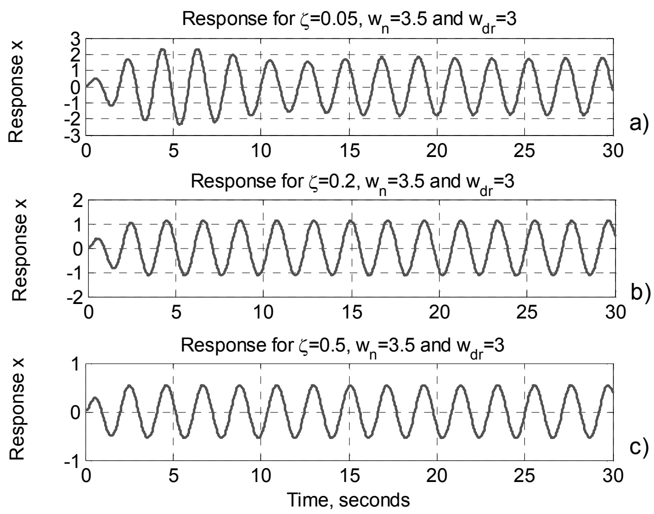

Figure B1.11 Responses of damped SDOF system to harmonic loading for different damping values.

Figure B1.12 shows the effects of changing the natural frequency. For the two frequencies that are near the driving frequency, the transient period is quite long, almost 10 seconds. However, for the large natural frequency, the transient period is less than 4 seconds, which shows that the length of the transient period also depends on the natural frequency. In the damped system, resonance also takes on a different meaning (for $\omega = \omega_n$ the amplitude does not become infinite) the introduction of damping introduces a term that keeps the denominator of the steady-state amplitude from becoming zero. However, at this point, the phase angle becomes 90º. For a damped system, this condition defines resonance; since it is also at this point that the denominator of the amplitude is a minimum (i.e. the amplitude will be maximized when the denominator is minimized and both terms are never negative, so the minimum will occur when the two frequencies are equal; making the first term of the denominator zero). Also, as the driving frequency increases greatly, the amplitude nears zero.

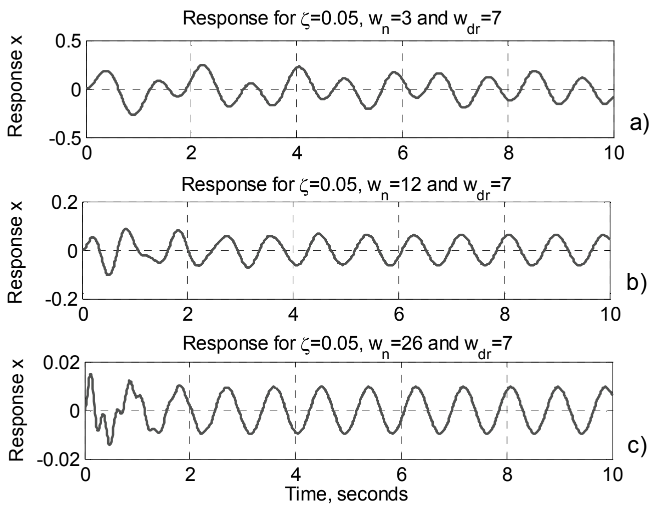

Figure B1.12 Responses of damped SDOF system to harmonic loading for different natural frequencies.

B1.6 Base Excitation of SDOF Systems

The equation of the motion for the system with base excitation shown in Figure B1.13 is:

$$m\ddot{x} + c(\dot{x} - \dot{y}) + k(x - y) = 0 \qquad (B1.27)$$

where the base motion is $y(t)$ and the response of the mass by $x(t)$. Using assumed form for the motion:

$$y(t) = Ysin(\omega_b t) \qquad (B1.28)$$

we can substitute for y and its derivative, resulting in:

$$m\ddot{x} + c\dot{x} + kx = cY\omega_b cos(\omega_b t) + kYsin(\omega_b t) \qquad (B1.29)$$

which when divided through by the mass, yields:

$$\ddot{x} + 2\zeta\omega\dot{x} + \omega^2 x = 2\zeta\omega\omega_b Ycos(\omega_b t) + \omega^2 Ysin(\omega_b t) \qquad (B1.30)$$

The homogeneous solution is of the form:

$$x_h(t) = Ae^{-\zeta\omega t}\, sin(\omega_d t + \theta) \qquad (B1.31)$$

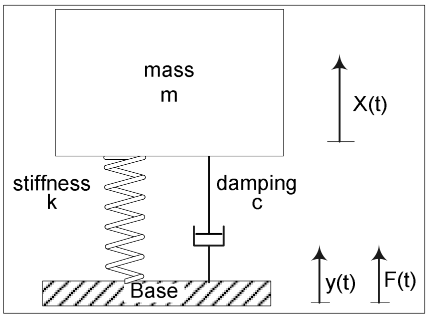

Figure B1.13 SDOF system subject to base excitation.

The expression for each part of the particular solution is similar to that for the general sinusoidal forcing function; the sine term produces a sine solution, and the cosine term produces a cosine solution. If we find these solutions and combine their sum into a single sinusoid, we obtain:

$$x_p(t) = A_0\, cos(\omega_b t - \phi_1 - \phi_2) \qquad (B1.32)$$

Constants are:

$$A_0 = \omega Y \sqrt{\frac{\omega^2 + (2\zeta\omega_b)^2}{(\omega^2 - \omega_b^2)^2 + (2\zeta\omega\omega_b)^2}} \tag{B1.33}$$

$$\phi_1 = tan^{-1}\frac{2\zeta\omega_b\omega}{\omega^2 - \omega_b^2} \tag{B1.34}$$

$$\phi_2 = tan^{-1}\frac{\omega}{2\zeta\omega_b} \tag{B1.35}$$

Thus, the complete solution is the sum of the homogeneous and particular solutions, or:

$$x(t) = Ae^{-\zeta\omega t}sin(\omega_d t + \theta) + A_0 cos(\omega_b t - \phi_1 - \phi_2) \tag{B1.36}$$

From equation B1.36 one can notice that the particular solution represents the steady-state response, while the homogeneous solution is the transient response, since the particular solution is independent of the initial displacement and velocity. After solving equation for initial velocity and displacement (which are not necessarily equal to zero), it was found that both are dependent upon the initial velocity and displacement. However, the expression for the constants A and θ is, in general, very difficult to solve therefore the initial velocity and displacement were both assumed to be zero.

Figure B1.14 shows the effects of changing the excitation (base) frequency while holding all other parameters constant. In the steady state, from about three seconds forward, the frequency of vibration increases with the base frequency. This is expected, since the base excitation portion dominates the steady state. Figure B1.14 (c) where ω_b =12, in the transient portion, the response has the shape of a sum of two sinusoids; these are, of course, the transient and steady-state functions. Since the base excitation is of such high frequency, this graph shows best what is happening between the transient and steady responses. Note that, if a line was drawn through the upper or lower peaks of the motion, the result would be a curve similar to that shown by a damped free response (section B1.2. A Damped SDOF System). The midpoint of the oscillation caused by the steady response becomes exponentially closer to zero with increasing time, as the transient response diminishes.

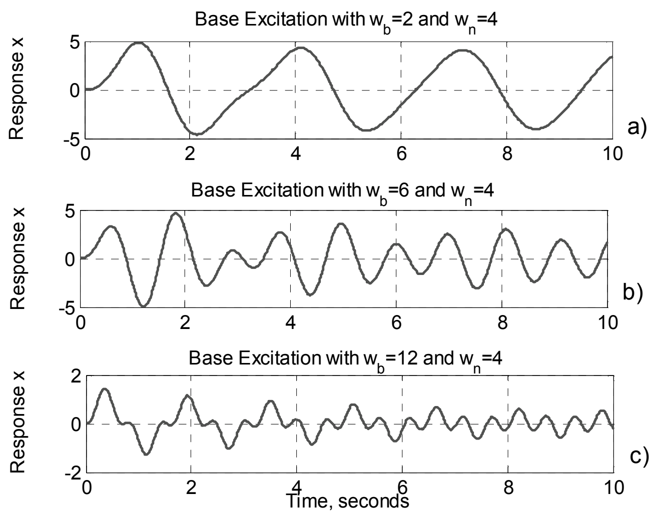

Figure B1.14 Responses of a base-excited SDOF system for different excitation frequencies.

Figure B1.15 shows plots for three different vibration amplitudes. The differences caused by changing the amplitude is what would be expected; the maximum amplitude of the overall vibration and of the steady-state response both increase with increasing input amplitude.

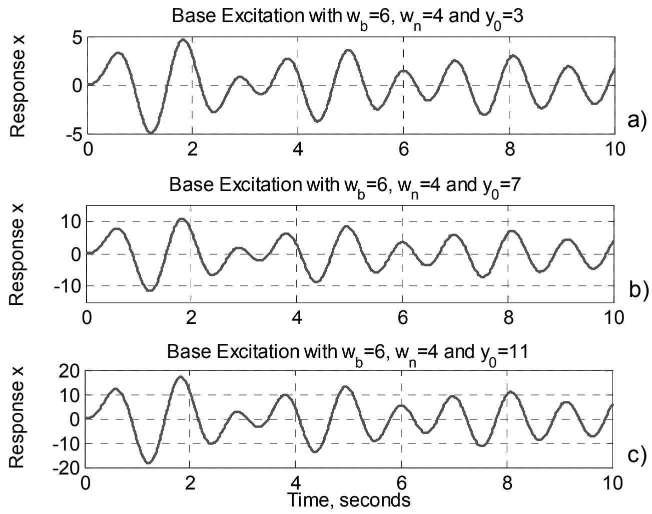

Figure B1.15 Responses of a base-excited SDOF system for different base excitation magnitudes.

The plots in figure B1.16 for various damping ratios show two effects of changing the damping ratio. First, the change in damping ratio causes the length of the transient period to vary; an increase in ζ causes the transient period to decrease, as the plots show. Also, the change in damping ratio causes a change in the frequency of the transient vibration. Again, an increase in ζ causes a decrease in the damped natural frequency. Because the plots also include the base excitation (steady-state) terms, whose frequency has not changed, the decrease is not entirely evident from just looking at the plots. The initial displacements are zero for all plots, as are the initial velocities.

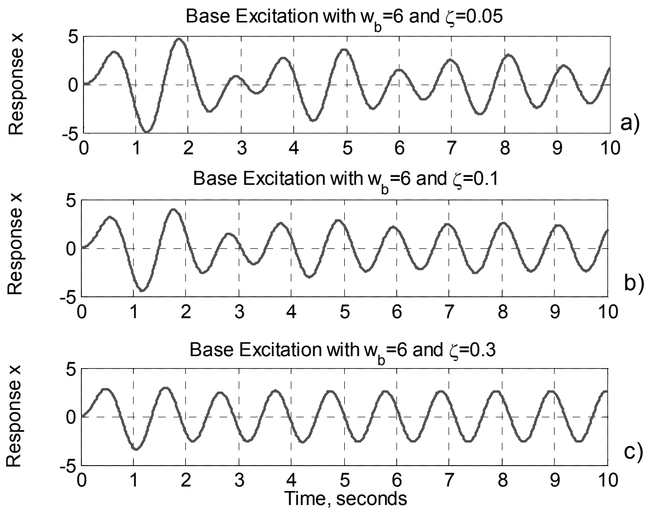

Figure B1.16 Responses of a base-excited SDOF system for different damping ratios.

B1.7 SDOF Systems with a Rotating Unbalance

A SDOF System with rotating unbalance and assumed coordinates is shown in Figure B1.17. It is assumed that the guides are frictionless. The radius e is measured from the center of the mass m. To write the equation of motion, we need an expression for the motion of the rotating unbalance in terms of displacement x. If the mass rotates with a constant angular velocity ω_r then parametrically the circle it defines can be described as:

$$x(t) = e \sin \omega_r t \quad (B1.37)$$

$$y(t) = e \cos \omega_r t \quad (B1.38)$$

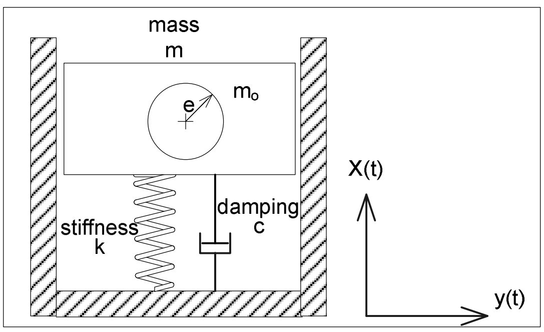

Figure B1.17 SDOF System with Rotating Unbalance.

With the coordinate x being vertical, the position coordinate of the rotating unbalance is defined as $x + sin\omega_r t$ and the acceleration is the second derivative of this expression with respect to time. The acceleration of the mass without the unbalance is $\ddot{x}$; adding in the effects of the stiffness and damper the equation of motion is:

$$(m - m_o)\ddot{x} + m_o \frac{d^2}{dt^2}(x + e\ sin\omega_r t) = -kx - c\dot{x} \qquad (B1.39)$$

$$(m - m_o)\ddot{x} + m_o(\ddot{x} + e\omega_r^2\ sin\omega_r t) = -kx - c\dot{x} \qquad (B1.40)$$

Collecting x and its derivatives, moving the sine term to the other side of the expression, and dividing by the system mass, the equation of motion can be written in form:

$$\ddot{x} + 2\zeta\omega_n\dot{x} + \omega_n^2 x = m_o e\omega_r^2 sin\omega_r t \qquad (B1.41)$$

This is identical to the harmonic forcing function case (section B1.5 Harmonic Excitation of Damped SDOF Systems) except that the force is in the form of a sine rather than a cosine. For that reason, the particular solution is of the form:

$$x_p(t) = A_1\ sin(\omega_r t - \phi) \qquad (B1.42)$$

If the ratio of rotating and natural frequency is $r = \omega_r/\omega_n$ the constants are:

$$A_1 = \frac{m_o e}{m}\frac{r^2}{\sqrt{(1 - r^2)^2 + (2\zeta r)^2}} \qquad (B1.43)$$

$$\phi = tan^{-1}\frac{2\zeta r}{1 - r^2} \qquad (B1.44)$$

The homogenous solution for this expression is:

$$x_h(t) = Ae^{-\zeta\omega_n t}\,sin(\omega_d t + \theta) \qquad (B1.45)$$

constants A and θ are determined from the initial conditions. The final solution is:

$$x(t) = x_p(t) + x_h(t) = A_1\,sin(\omega_r t - \phi) + Ae^{-\zeta\omega_n t}\,sin(\omega_d t + \theta) \qquad (B1.46)$$

For modelling purposes the initial conditions were assumed to be zero and, unless otherwise specified, m = 7; m_o = 3; and e = 0,1. The solution to this is not reproduced here, due to the complexity of the expression; the solution for A and θ depend on the solution to a quadratic equation. In following figures effects of different varying parameters on the system were explored.

For Figure B1.18, the natural frequency was varied while holding all other parameters constant. In the case when ω_n is not a multiple of ω_r the motion is the sum of two sinusoids (Figure B1.18 (a)). For the highest natural frequency tested, the oscillation occurs along a single sinusoid. This is because the natural frequency of the system is too high to be excited by the relatively slow rotation frequencies. The first two plots, (a) and (b), have natural frequencies small enough to be excited by the slow rotation of the eccentric mass.

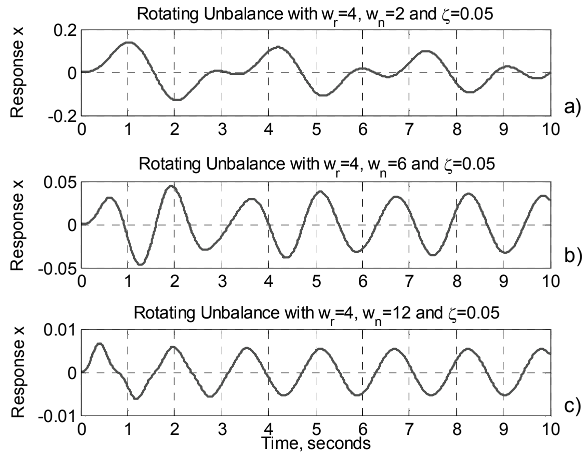

Figure B1.18 Responses of a SDOF system with different natural frequencies to a rotating unbalance.

In Figure B1.19, the system damping is varied. The result is that the transient portion (the portion with the curve that looks like the sum of sinusoids) becomes smaller, to the point where it disappears at $\zeta = 0.3$. A difference in the magnitude of oscillation, as would be predicted from the expression we have derived for the parameter A_1 is not present because the frequency ratio we are testing is in the range where oscillation magnitude shows little variation with damping ratio. This consideration is important in the design of machinery; if the machine can be designed to have a much higher natural frequency than the oscillating mass, then the level of damping can be made low without increasing the amplitude past acceptable levels.

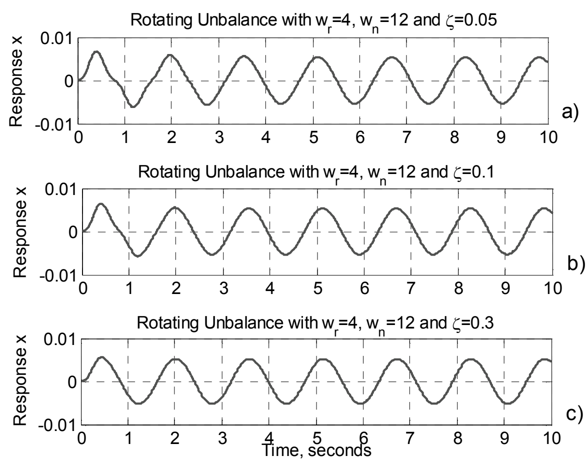

Figure B1.19 Responses of a SDOF system with varying damping ratio to a rotating unbalance.

Figure B1.20 shows the variation of vibration with increasing system mass. The amplitude of the vibration decreases with increasing mass which is due to the dependence of A_1 on the mass ratio, i.e. as m_o/m decreases, so does the amplitude of vibration.

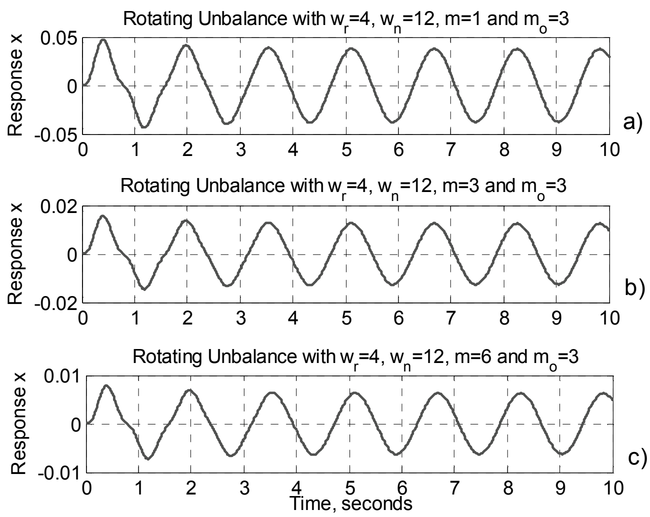

Figure B1.20 Responses of a SDOF system with varying system mass to a rotating unbalance.

B1.8 Step Response of SDOF System

The force is assumed to be applied instantaneously, but it is sustained out to infinity. If a force of this sort is plotted versus time, the force looks like a step up. The behaviour of the system under this type of load is considered the step response of the SDOF system. It is assumed that the system is underdamped ($\zeta < 1$) and will have zero initial conditions. The equation of motion of the system is:

$$\ddot{x} + 2\zeta\omega_n\dot{x} + \omega_n^2 x = F(t)/m \qquad (B1.47)$$

where

$$F(t) = \begin{cases} 0 & if \ \ 0 < t < t_o \\ F_o & if \ \ \ \ \ \ \ t \geq t_o \end{cases} \qquad (B1.48)$$

In order to solve the differential equation, the convolution integral was used:

$$x(t) = \int_0^t F(\tau) g(t-\tau)\, d\tau \qquad (B1.49)$$

The convolution integral is derived by treating the force as an infinite series of impulse forces; hence the infinite series can be treated as the integral given above. The impulse response can be expressed:

$$x(t) = \frac{F_o}{m\omega_d} e^{-\zeta\omega_n t} sin\omega_d t = F_o g(t) \qquad (B1.50)$$

Where

$$g(t) = \frac{1}{m\omega_d} e^{-\zeta\omega_n t} sin\omega_d t \qquad (B1.51)$$

Therefore,

$$x(t) = \frac{1}{m\omega_d} e^{-\zeta\omega_n t} \int_0^t F(\tau) e^{\zeta\omega_n \tau} sin\omega_d (t-\tau) d\tau \qquad (B1.52)$$

Substituting F(t) into (A1.8f):

$$x(t) = \frac{1}{m\omega_d} e^{-\zeta\omega_n t} \left\{ \int_0^{t_o} F(0) e^{\zeta\omega_n \tau} sin\omega_d(t-\tau) d\tau + \int_{t_o}^{t} F_o e^{\zeta\omega_n \tau} sin\omega_d(t-\tau) d\tau \right\} \qquad (B1.53)$$

The first term inside the brackets is zero, hence, for t < t_o, the response of the system is zero. To find the response for all other times, the second integral needs to be evaluated (by parts):

$$x(t) = \frac{F_o}{k}\left\{1 - \frac{1}{\sqrt{1-\zeta^2}} e^{-\zeta\omega_n(t-t_o)} cos[\omega_d(t-t_o) - \phi]\right\} \; for \; t \geq t_o \qquad (B1.54)$$

$$\phi = tan^{-1}\frac{\zeta}{\sqrt{1-\zeta^2}} \qquad (B1.55)$$

This equation (B1.54) is only valid for the time after the force is applied; the response is zero before application of the force.

Figure B1.21 shows the variation of the response with the force magnitude. The only difference that result from changing the magnitude of the external force is that the magnitude of the response changes. That is, the magnitude of the response is directly proportional to the magnitude of the external force. The magnitude of the external force also causes a second difference, i.e. when the oscillatory motion begins, it is not centered around zero. Instead, the mass oscillates around a displacement greater than zero. The value of this center point is also dependent on the magnitude of the external force (see first term in equation B1.53).

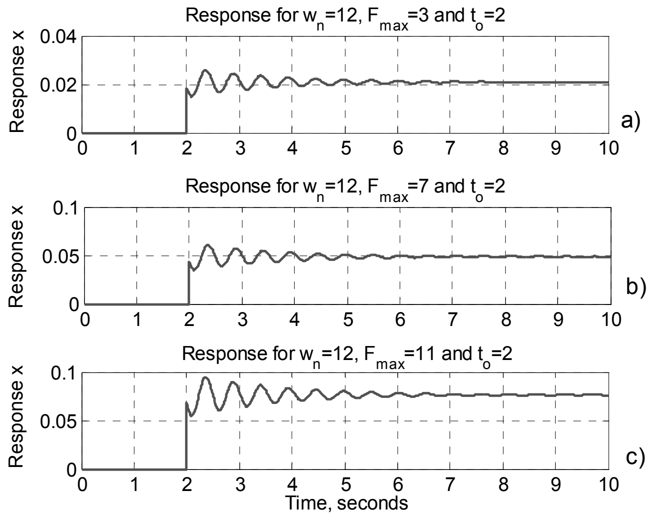

Figure B1.21 Step response of SDOF system to different step magnitudes.

Figure B1.22 shows the step responses of SDOF system when vary the natural frequency. This causes two changes in the response. First, the rate of exponential decrease in the response (the effect of damping) is increased; that is, the response stabilizes more quickly. Second, the oscillation frequency decreases, since the natural frequency also dictates the damped frequency.

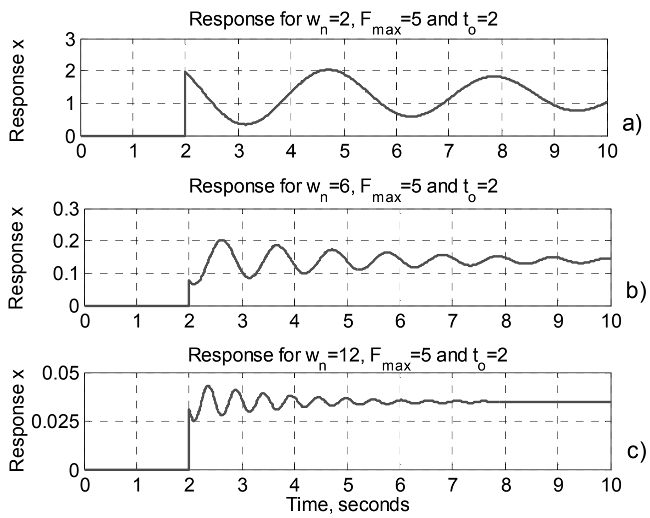

Figure B1.22 Step response of SDOF system having different natural frequencies.

Figure B1.23 shows the changes caused by changing the damping ratio. With increasing damping ratio, the amount of time to damp out all vibration decreases. For the third ratio tested, ζ = 0.3, the damping is sufficient to allow no oscillation around the new center point (x = 1.5). A second result, which is not immediately evident from the figure but follows from the mathematics, is that the phase angle changes with the damping ratio (ϕ is a function of only ζ).

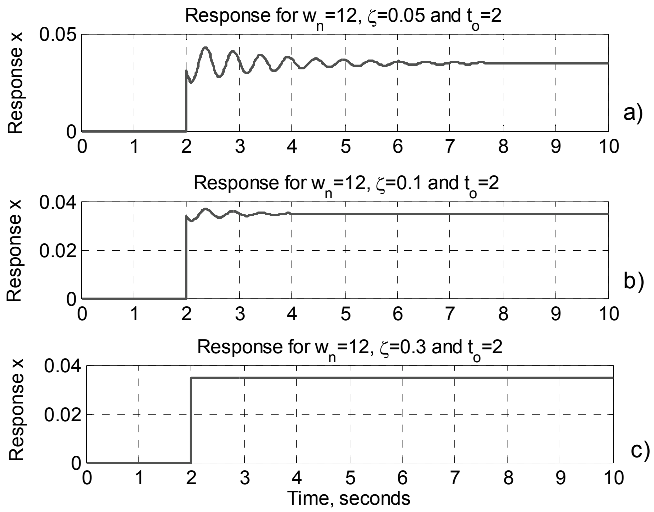

Figure B1.23 Step response of SDOF system to different levels of damping.

B1.9 Response of SDOF System to Square Pulse Inputs

A square pulse is a single pulse of constant magnitude and finite duration. To analyse the response of systems to a square wave input, the square wave is treated as the sum of two equal and opposite step inputs applied at different times. The time interval between applications of the step inputs is the duration of the square wave. If the magnitude of the square wave is F_o, and its duration is t_1 seconds, to simulate the wave using step inputs, we begin with a step input of magnitude F_o from time $t = 0$; and add to it at time t_1 a step input of magnitude $-F_o$. By superposition, the total response is the sum of the response of the system to each step input.

As per section B1.8 the response of a single degree of freedom system to a step input of magnitude F_m applied at time t_o is:

$$x(t) = \frac{F_m}{k}\left\{1 - \frac{1}{\sqrt{1-\zeta^2}} e^{-\zeta\omega_n(t-t_o)} cos[\omega_d(t-t_o) - \phi]\right\} \; for\ t \geq t_o \qquad (B1.56)$$

where

$$\phi = tan^{-1}\frac{\zeta}{\sqrt{1-\zeta^2}} \qquad (B1.57)$$

Considering the two step inputs separately and denoting the response of the system to the input at time $t = 0$ as $x_1(t)$ and the response to the input at time $t = t_1$ as $x_2(t)$:

$$x_1(t) = \frac{F_o}{k}\left\{1 - \frac{1}{\sqrt{1-\zeta^2}} e^{-\zeta\omega t} cos[\omega_d t - \phi]\right\} \; for\ t \geq 0 \qquad (B1.58)$$

$$x_2(t) = -\frac{F_o}{k}\left\{1 - \frac{1}{\sqrt{1-\zeta^2}} e^{-\zeta\omega(t-t_1)} cos[\omega_d(t-t_1) - \phi]\right\} \; for\ t \geq t_1 \qquad (B1.59)$$

The total response is:

$$x(t) = \frac{F_o}{k}\left\{1 - \frac{1}{\sqrt{1-\zeta^2}} e^{-\zeta\omega_n t} cos[\omega_d t - \phi]\right\} \; for\ 0 \leq t < t_1 \qquad (B1.60)$$

$$x(t) = \frac{F_o e^{-\zeta\omega_n t}}{k\sqrt{1-\zeta^2}}\left\{e^{\zeta\omega_n t_1} cos[\omega_d(t-t_1) - \phi] - cos(\omega_d t - \phi)\right\} for\ t \geq t_1 \qquad (B1.61)$$

For the time interval after period t_1, the response no longer includes a (1-) term; the addition of the two responses has removed this term entirely. This term caused the oscillation to be about a new equilibrium (i.e., $x = F_o/k$). Now, since the term has disappeared, the oscillation is centered around zero.

The movement of the center point of the oscillation is best shown in Figure B1.24. This figure shows response of the system for three different values of F_o. The oscillation begins about a center point at $x = F_o/k$; when the square wave ends, or, when the equal and opposite step is added, the center point returns to zero. If assumed that the magnitude of the second step (F_1) is not equal to that of the first, the center point of the oscillation after adding the second step input would be at $x = (F_o - F_1)/k$. From Figure B1.24 is also evident that the change in F_o causes the magnitude of the oscillations to increase, as expected from Equation B1.61.

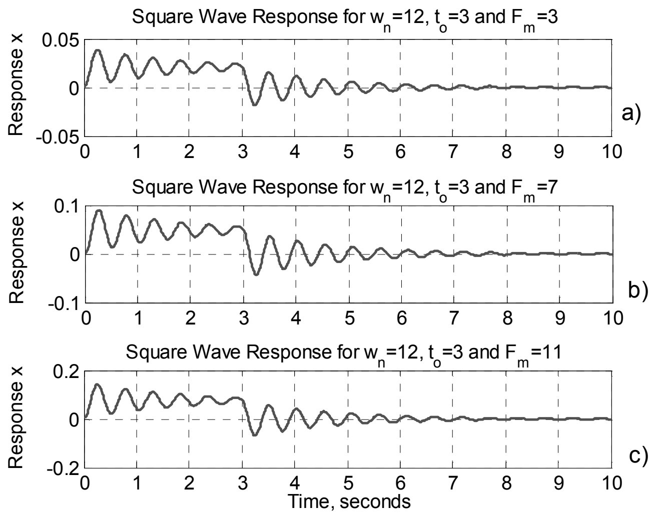

Figure B1.24 Response of SDOF systems to square pulse inputs for different force magnitudes.

Figure B1.25 demonstrates the effects of changing the natural frequency. A transition point occurs when the second step input is added. The sudden shift in vibration characteristics is expected, since we have a piecewise expression for $x(t)$. But while the transition becomes more abrupt as the natural frequency increases, it is never discontinuous. Since the motion of the mass remains continuous, we can infer that the approach is correct; if we had obtained a discontinuity in the motion, we would know the expression is incorrect. This is because a discontinuous expression would imply that the mass moved from one point to another nonadjacent point without passing through the points in between, which is a physically impossible situation.

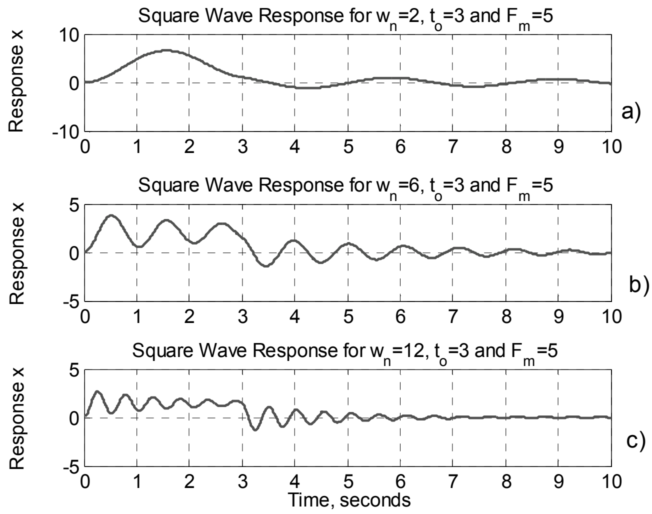

Figure B1.25 Response of SDOF systems to square pulse inputs for different natural frequencies.

Figure B1.26 shows the response behaviour for three different damping ratios. The high damping ratio ($\zeta = 0.3$) causes all of the vibration to be damped out quickly, so that the mass is practically at rest when the second step input is applied. Again, we see that the transient period decreases with increasing damping ratio.

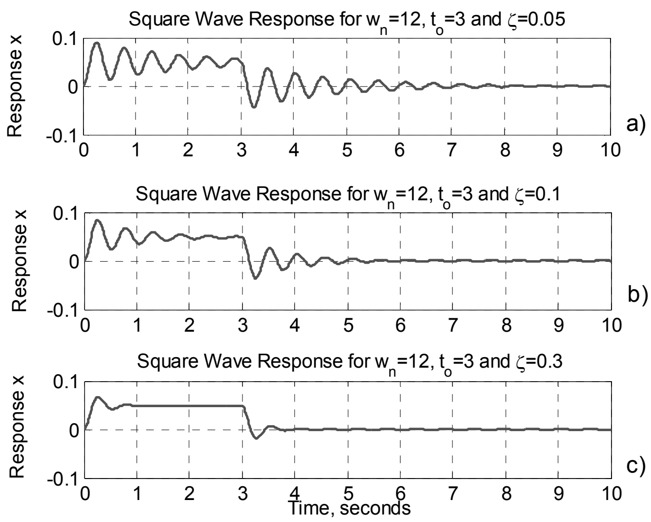

Figure B1.26 Response of SDOF systems to square pulse inputs for different damping ratio.

B1.10 Response of SDOF System to Ramp Input

To examine the response of a SDOF system to ramp input, we must again apply the convolution integral. Assuming that the load is increased uniformly at a rate of *fo* per second and reaches its maximum at time t_d, the expression for the external force is:

$$F(t) = \begin{cases} f_o t & for \;\; 0 \leq t < t_d \\ f_o t_d & for \qquad t \geq t_d \end{cases} \qquad (B1.62)$$

Substituting the expression for *F*(*t*) into the convolution integral yields:

$$x(t) = \begin{cases} \dfrac{f_o}{m\omega_d} e^{-\zeta\omega_n t} \displaystyle\int_0^{t_o} \tau e^{\zeta\omega_n\tau} sin\omega_d(t-\tau)d\tau & for \;\; 0 \leq t < t_d \\ \dfrac{f_o}{m\omega_d} e^{-\zeta\omega_n t} \left\{ \displaystyle\int_0^{t_d} \tau e^{\zeta\omega_n\tau} sin\omega_d(t-\tau)d\tau + t_d \int_{t_d}^{t} e^{\zeta\omega_n\tau} sin\omega_d(t-\tau)d\tau \right\} & for \; t \geq t_d \end{cases} \qquad (B1.63)$$

In its evaluated form:

$$x(t) = \frac{f_o}{m\omega_d} e^{-\zeta\omega_n t} \left(\frac{1}{(\zeta^2\omega_n^2 + \omega_d^2)^2} \right) \{ \omega_d e^{\zeta\omega_n t} [t\zeta^2\omega_n^2 + t\omega_d^2 - 2\zeta\omega_n] + 2\zeta\omega_n\omega_d cos(\omega_d t) + (\zeta^2\omega_n^2 - \omega_d^2) sin(\omega_d t) \}; \; for \; 0 \leq t < t_d \qquad (B1.64)$$

$$x(t) = \frac{f_o}{m\omega_d} e^{-\zeta\omega_n t} \left(\frac{1}{(\zeta^2\omega_n^2 + \omega_d^2)^2} \right) \{ \omega_d e^{\zeta\omega_n t} [t\zeta^2\omega_n^2 + t\omega_d^2 - 2\zeta\omega_n] + 2\zeta\omega_n\omega_d cos(\omega_d t) + (\zeta^2\omega_n^2 - \omega_d^2) sin(\omega_d t) \} + \frac{f_o t_d}{k} - \frac{f_o t_d}{k\sqrt{1-\zeta^2}} e^{-\zeta\omega_n (t-t_d)} cos(\omega_d (t-t_d) - \phi); \; for \;\; t \geq t_d \qquad (B1.65)$$

The solution of this expression shows that there is no equilibrium position (as for the step and square wave responses) until after the input has levelled off. This is because the constant that creates the new center point is the result of an integration that does not start at zero, and no such integration exists in this solution until after time t_d.

From Figure B1.27 can be concluded that the transition to the new equilibrium of vibration is discontinuous (as in the step and square wave responses). It seems that the response is nonexistent for the first few seconds, until the load is fully applied, and then begins oscillating, as in the step response. It appears that the ramp response and step response of a single degree of freedom system are similar.

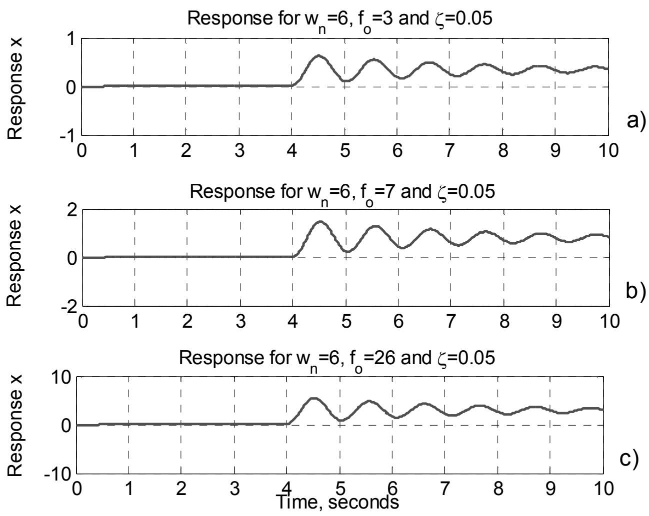

Figure B1.27 Response of SDOF system to Ramp input for different rates of loading.

However, if the response during the transient loading period (Figure B1.28) is observed it can be seen that this is not the case. Actually is quite evident that the system is oscillating during this period, around a constantly increasing equilibrium. That is, if a line was drawn through the identical point on each period of the sinusoid, the result would be a line of positive slope. This shows that the ramp response is different than the step response; the ramp response has less deflection at the point in time that the full load is applied than the step response.

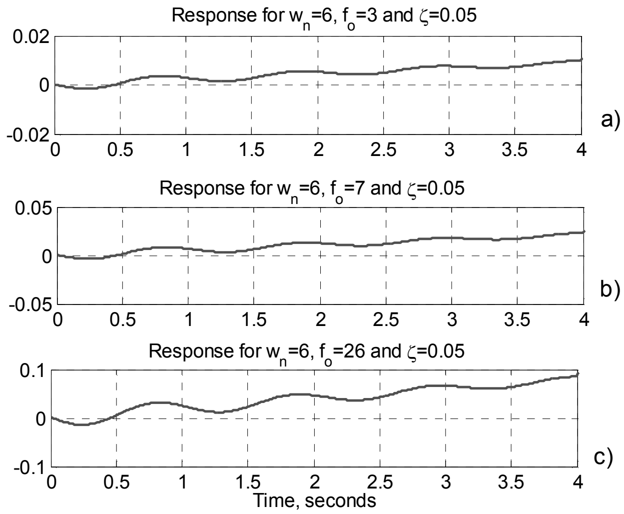

Figure B1.28 Response of SDOF system to Ramp input for different rates of loading – focusing on first few seconds of oscillation, showing that system oscillate during the transient period.

B1.11 Modeling a van der Pol Oscillator

The real-world vibratory systems such as the oscillatory motion of a structure surrounded by a fluid (e.g. structures include the support pylons of offshore oil platforms and antennae attached to the exterior surfaces of aircraft) are looked at next. These structures exhibit vibratory motion due to the creation of vortices in the fluid by viscous interaction between the structure and the particles comprising the fluid. The van der Pol equation can be applied as a model for the motion of such a structure:

$$\ddot{x} + e(x^2 - 1)\dot{x} + x = 0, e > 0 \qquad (B1.66)$$

This equation, given the positive parameter e exhibits the usual form of damping when $|x| < 1$. When $|x| > 1$ the term multiplying first derivative of x will become negative. If equation B1.66 is solved for $\ddot{x}$ then, the damping term would add energy to the system, instead of removing it. This negative damping approximates some of the phenomena observed in such fluid-structure interactions, and so is an attractive (and necessary) feature of the model.

In order to solve the problem the equation B1.66 need to be integrated analytically over a particular time interval [187]. The only parameters to use here are the parameter *e*, the initial conditions and the time step.

Figure B1.29 and Figure B1.30 shows results for e =0.5, initial conditions x_0=[1; 0]; $x(0)=1$, $x'(0)=0$ and the time interval t_f=30sec. Figure B1.29 shows a simple comparison of displacement and velocity versus time representing oscillatory behaviour. Figure B1.30 represents phase diagram (these diagrams are often used in studies of nonlinear and chaotic systems, since they can clearly show the effects of initial conditions on the response). The key feature of Figure B1.30 is the closed loop.

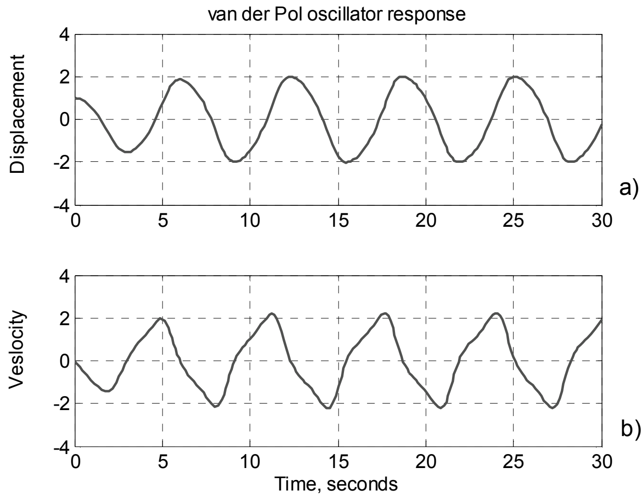

Figure B1.29 Displacement and velocity vs. time for the van der Pol oscillator.

The initial location is denoted by a circle and the final state by a triangle. The closed loop means that the van der Pol system eventually settled down into oscillatory behaviour. It can be proved that a closed loop in phase space corresponds to an oscillating response by considering the function $x = sin\ (t)$. If this (obviously oscillating) function is assumed displacement, then the velocity is described by $y = cos\ (t)$. Plotting this result in phase space, circle is obtained as these functions $x\ (t)$

and y (t) are parametric equations for a circle. The van der Pol oscillator's loop is not precisely circular, so it is not periodic in the same regular way as the sine or cosine function. However, it will repeat the same sets of positions and velocities.

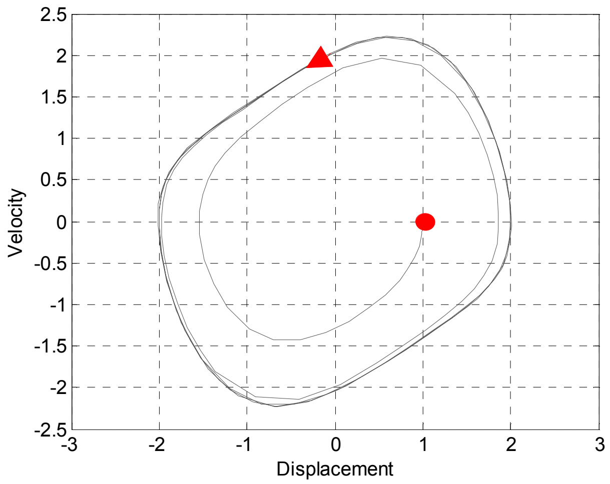

Figure B1.30 Velocity vs. Displacement for van der Pol oscillator.

If different initial conditions are considered the motion will settle into the same limit cycle. Thus, the limit cycle is determined by the parameter e; and not by the initial conditions. This limit cycle behaviour is similar to a phenomenon seen in the vibration of structures in a moving fluid; thus, several investigators have used the van der Pol equation to describe these systems [197-199].

B1.12 Response of SDOF System to Random Vibration

Assuming random forcing input as a sinusoidal forcing input of the form:

$$F(t) = Acos(\omega t + \varphi) \qquad (B1.67)$$

The vast majority of the energy input to the system comes at one particular frequency. For this case, we could then (as a first approximation) treat the forcing frequency as deterministic, and use a random distribution for the amplitude. The uniform and Gaussian distributions are built into Matlab through the rand and randn commands, respectively. If this is applied to damped SDOF system defined by equation:

$$\ddot{x} + 2\zeta\omega_n\dot{x} + \omega_n^2 x = F(t) \tag{B1.68}$$

where $F\ (t)$ defined above having random amplitude $A(t)$. It will be convenient to solve for the steady-state response only, neglecting the transient response, which also eliminates the need to specify initial conditions. The analytical solutions can be found the same way as in section B1.5, or the numerical integration routines can be used.

First differential equation at the time $t = t_0$ is solved, and than substitute into the relation the values of the forcing and the forced response at that time, to solve for the initial position and velocity required to match the forced response. As in section A1.5 the complete solution is:

$$x(t) = x_h(t) + x_p(t) \tag{B1.69}$$

$$x_h(t) = A_h e^{-\zeta\omega t} sin(\omega_d t + \theta) \tag{B1.70}$$

$$x_p(t) = A_0(t) cos(\omega t - \phi) \tag{B1.71}$$

where the constants are:

$$A_0 = \frac{A(t)}{\sqrt{(\omega_n^2 - \omega^2) + (2\zeta\omega_n\omega)^2}} \tag{B1.72}$$

$$\phi = tan^{-1}\frac{2\zeta\omega_n\omega}{\omega_n^2 - \omega^2} \tag{B1.73}$$

The next is to specify the initial conditions $x(t_0)$ and $\dot{x}(t_0)$ so that we can have $A_h = 0$, i.e. eliminating transient response. Using the initial value of the force amplitude, specifying $x(t_0) = x_p(t_0)$ and $\dot{x}(t_0) = \dot{x_p}(t_0)$, or

$$x(t_0) = A_0(t_0)cos(\omega t_0 - \phi) \qquad (B1.74)$$

$$\dot{x}(t_0) = -\omega A_0(t_0)sin(\omega t_0 - \phi) \qquad (B1.75)$$

the coding using Matlab is simplified [187].

Figure B1.31 represents displacement versus time of SDOF system exposed to random vibration. The oscillation remains periodic even with the random forcing amplitude, albeit with an irregular amplitude.

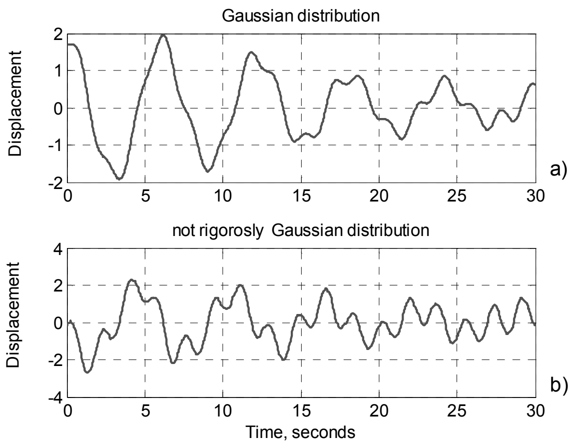

Figure B1.31 Response of SDOF system to Random Vibration

In the top figure it is assumed Gaussian distribution and A is random variable, while the bottom figure represents displacement of the system when the distribution is not rigorously Gaussian as the amplitude is defined between 0 and 5 ($0 < A \leq 5$). In this example natural frequency is set to 1, damping ratio is 0.05 and frequency of input force is 3.5.

B1.13 Randomly-Excited Duffing Oscillator

A nonlinear oscillator is excited with a random forcing. For SDOF system Duffing equation can be written in the form:

$$\ddot{x} + c\dot{x} + kx + \varepsilon g(x) = A\cos\omega t \qquad (B1.76)$$

where the parameters c and k are assumed to be positive, and $|\varepsilon| \ll 1$ (i.e. ε is not restricted to solely positive nor negative values). This equation allows us to choose the parameter ε and the function $g\,(x)$ to model nearly-linear springs, for example. Also, this equation retains some attractive quasi-linear qualities. For example if $A = 0$ and $c = 0$ a roughly oscillatory motion for small amplitudes x would be expected; if further introduce a small damping coefficient c; these small-amplitude oscillations would reduce to zero. Further, function g (x) can be manipulated so that the sign of the parameter ε determines the character of the stiffness element being modelled. For the case where $\varepsilon < 0$ the restoring force will be smaller in extension, and arrive at a soft spring. Conversely, if $\varepsilon > 0$ the spring gains stiffness in extension over the purely linear case, and is called a hard spring.

Also it could be set parameter $\varepsilon > 0$ and select $g(x) = -x^2$, a net restoring force would then be $kx + \varepsilon\, g(x)$ that is negative for $x < 0$ and positive for $x > 0$. In other words, the spring will be soft in extension but hard in compression, meaning that the center of oscillation (equilibrium point) will be shifted slightly away from zero, where the magnitude of the shift depends on the relative values of k and ε.

For the modelling purposes Duffing oscillator response to a harmonic input was looked at. The differential equation solver suite inside Matlab [158] to calculate a numerical solution to a Duffing equation, given the input values of $c = 0.05$; $k = 1$; $\varepsilon = 0.01$; A; and ω. The function used is $g(x) = -x^2$. A random forcing frequency [0, 2] and amplitude [0, 5], which will remain constant for the duration of the oscillation is specified next.

The results for a few default runs are plotted below, along with the random frequency and amplitude used. In Figure B1.33 a random forcing frequency is very close to the system's natural frequency. Hence, we see a nearly-resonant condition in this undamped oscillator. The phase diagram in the same figure corresponds to this run. The response traces out arcs in the phase plane that are circular, but by no means closed.

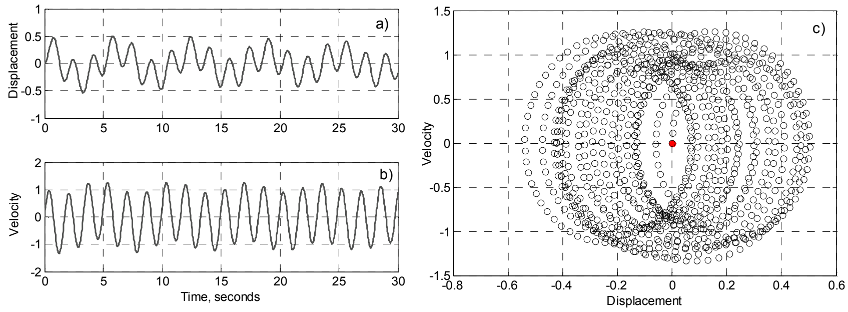

Figure B1.32 Response of the Duffing oscillator to amplitude A = 3.7999 and forcing frequency ω = 3.7960.

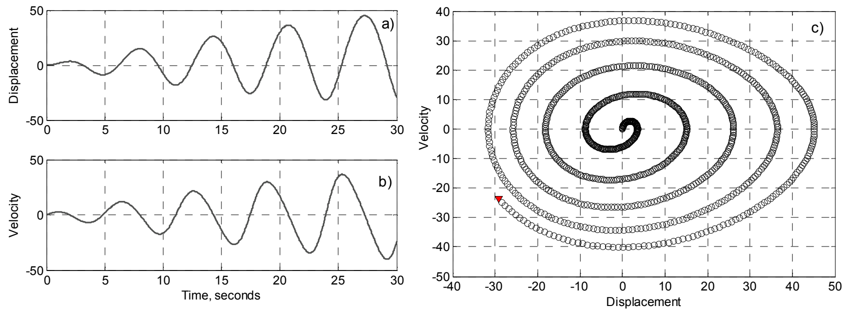

Figure B1.33 Response of the Duffing oscillator to amplitude A = 4.4531 and forcing frequency ω = 1.7404.

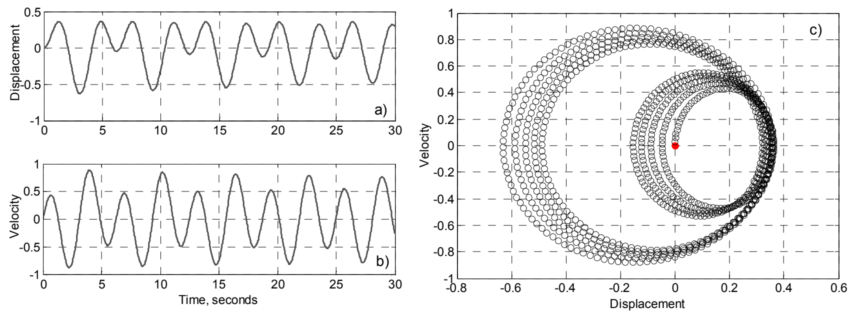

Figure B1.34 Response of the Duffing oscillator to amplitude A = 1.0062 and forcing frequency ω = 2.0115.

APPENDIX B2

Delay Vector Variance Method Results for Reference Model

	B	C	D	E	F	G	H	I	J	K	L	M	N	O	P	Q
1	SYSTEM	DETAILS	VARIABLES		METHOD 1				METHOD 2				METHOD 3			
2					best m	best τ	rmse	RMSE	calc m	τ	rmse	RMSE	calc m	τ	rmse	RMSE
3	SDOF UNDAMPED OSCILATION VARYING MASS	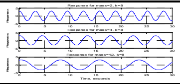	stiffness k=8; initial displacement x0=3; initial velocity v0=1; time duration to test tf=30s;	m=2	5	10	0.0726	0.1672	5	1	0.0109	0.1637	3	1	0.0073	0.1714
4				m=4	4	10	0.0452	0.2237	9	1	0.0755	0.1476	3	1	0.0279	0.1729
5				m=12	2	7	0.0132	0.1510	11	1	0.0405	0.1580	3	1	0.0058	0.1764
6	DAMPED SDOF SYSTEM OSCLATION FOR VARYING DAMPING VALUES (only for underdamped case xi<1)	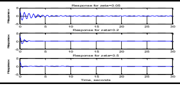	natural frequency wn=7; initial displacement x0=3; initial velocity v0=1; time duration to test tf=30s;	ζ=0.05	10	10	0.6891	0.4716	11	1	0.1921	0.3570	3	1	0.0268	0.3465
7				ζ=0.2	10	9	0.8662	0.5372	23	1	0.3338	0.6046	3	1	0.0967	0.6207
8				ζ=0.5	2	9	1.0195	0.5799	21	1	0.2961	0.6309	3	1	0.1076	0.6818
9	OVERDAMPED SDOF SYSTEM OSCILATION FOR VARYING DAMPING VALUES (only for overdamped case xi>1)!!!	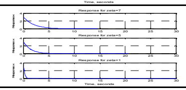	natural frequency wn=7; initial displacement x0=3; initial velocity v0=1; time duration to test tf=30s;	ζ=7	5	10	0.6491	0.4364	18	1	0.2885	0.3296	3	1	0.0486	0.2918
10				ζ=5	2	1	0.0313	0.4253	24	1	0.4093	0.4717	3	1	0.0742	0.4349
11				ζ=1	3	10	0.8726	0.5464	22	1	0.2759	0.6457	3	1	0.0927	0.6995
12	HARMONIC EXCITATION OF UNDAMPED SDOF SYSTEMS effect of varying driving frequency w for a given natural frequency wn	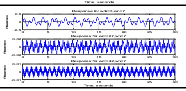	natural frequency wn=7; initial displacement x0=0; initial velocity v0=0; force magnitude per unit mass f0=6; time duration to test tf=30s;	wdr=3	4	10	0.2300	0.3334	5	1	0.0061	0.1073	3	1	0.0028	0.1185
13				wdr=27	6	8	0.0365	0.2433	19	1	0.0238	0.2103	3	1	0.0108	0.2143
14				wdr=42	5	10	0.0682	0.2271	10	1	0.0606	0.2832	3	1	0.0736	0.3205
15	HARMONIC EXCITATION OF UNDAMPED SDOF SYSTEMS effect of varying natural frequency wn for a given driving frequency w	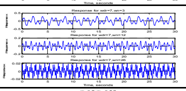	driving frequency wdr=7; initial displacement x0=0; initial velocity v0=0; force magnitude per unit mass f0=6; time duration to test tf=30s;	wn=3	4	10	0.2300	0.3334	4	1	0.0042	0.1071	3	1	0.0034	0.1176
16				wn=12	5	7	0.0627	0.2938	3	1	0.1336	0.1416	3	1	0.1283	0.1406
17				wn=26	6	9	0.0617	0.2581	17	1	0.0388	0.2256	3	1	0.0170	0.2037
18	HARMONIC EXCITATION OF UNDAMPED SDOF SYSTEMS BEAT Phenomenon natural and driving frequencies are close but not equal	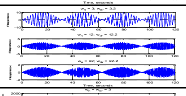	initial displacement x0=0; initial velocity v0=0; force magnitude per unit mass f0=6; time duration to test tf=120s;	wn=3; wdr=3.2;	3	1	0.1314	0.1759	3	1	0.0046	0.1369	3	1	0.0037	0.1366
19				wn=12; wdr=12.2;	6	10	0.1740	0.2360	2	1	0.0068	0.1337	3	1	0.0094	0.1682
20				wn=22; wdr=22.2;	3	6	0.0150	0.1044	3	1	0.1248	0.2167	3	1	0.1260	0.2172
21	HARMONIC EXCITATION OF UNDAMPED SDOF SYSTEMS RESONANCE natural and driving frequencies are equal	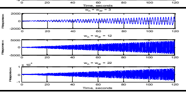	initial displacement x0=0; initial velocity v0=0; force magnitude per unit mass f0=6; time duration to test tf=120s	wn=wdr=3;	4	9	0.1462	0.1205	7	1	0.0165	0.1439	3	1	0.0096	0.1190
22				wn=wdr=12;	7	10	0.0613	0.1334	3	1	0.0027	0.1461	3	1	0.0035	0.1462
23				wn=wdr=22;	4	6	0.0194	0.1176	6	1	0.0044	0.1199	3	1	0.0041	0.1646
24	HARMONIC EXCITATION OF DAMPED SDOF SYSTEMS (VARYING DAMPING VALUES)	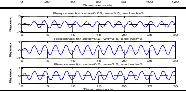	driving frequency wdr =3; natural frequency wn=3.5; force magnitude per unit mass f0=6; time duration to test tf=30s;	ζ=0.05	5	10	0.1243	0.2020	4	1	0.0039	0.1476	3	1	0.0052	0.1550
25				ζ=0.2	7	10	0.0550	0.1791	3	1	0.0030	0.1617	3	1	0.0048	0.1620
26				ζ=0.5	6	10	0.2053	0.2243	4	1	0.0044	0.1615	3	1	0.0082	0.1659
27	HARMONIC EXCITATION OF DAMPED SDOF SYSTEMS VARYING NATURAL FREQUENCY	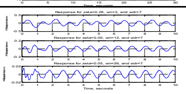	driving frequency wdr =7; damping ratio ζ=0.05; force magnitude per unit mass f0=6; time duration to test tf=30s;	wn=3	4	1	0.0403	0.1326	1	1	0.0110	0.1507	3	1	0.0312	0.1383
28				wn=12	3	1	0.0029	0.1613	6	1	0.0075	0.1496	3	1	0.0059	0.1625
29				wn=26	4	10	0.2174	0.2077	4	1	0.0034	0.1604	3	1	0.0054	0.1648
30	BASE EXCITATION OF SDOF SYSTEMS VARYING EXCITATION FREQUENCY	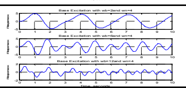	base excitation magnitude yo=3; damping ratio ζ=0.05; natural frequency wn=4 time duration to test tf=10s;	wb=2	4	1	0.0125	0.1600	19	1	0.0159	0.1489	3	1	0.0053	0.1651
31				wb=6	4	1	0.0415	0.1359	1	1	0.0029	0.1548	3	1	0.0043	0.1509
32				wb=12	3	1	0.0049	0.1604	1	1	0.0074	0.1765	3	1	0.0101	0.1661
33	BASE EXCITATION OF SDOF SYSTEMS VARYING BASE EXCITATION MAGNITUDE	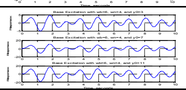	base excitation frequency wb=6; damping ratio ζ=0.05; natural frequency wn=4 time duration to test tf=10s;	y0=3	4	1	0.0415	0.1359	1	1	0.0050	0.1567	3	1	0.0018	0.1509
34				y0=7	4	1	0.0415	0.1359	1	1	0.0051	0.1571	3	1	0.0018	0.1502
35				y0=11	4	1	0.0405	0.1359	1	1	0.0072	0.1543	3	1	0.0028	0.1509
36	BASE EXCITATION OF SDOF SYSTEMS VARYING DAMPING RATIO	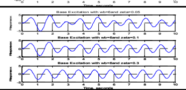	base amplitude y0=3; base excitation frequency wb=6; natural frequency wn=4 time duration to test tf=10s;	ζ=0.05	4	1	0.0415	0.1359	1	1	0.0050	0.1567	3	1	0.0021	0.1511
37				ζ=0.1	4	1	0.0412	0.1399	10	1	0.0061	0.1266	3	1	0.0023	0.1561
38				ζ=0.3	4	1	0.0371	0.1557	7	1	0.0050	0.1576	3	1	0.0062	0.1717
39	SDOF SYSTEM WITH A ROTATING UNBALANCE VARYING NATURAL FREQUENCY	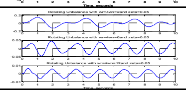	rotating mass mo=3; sdof mass m=7; angular velocity of rot mass wr=4; damping ratio ζ=0.05; time duration to test tf=10s; constant e=0.1	wn=2	3	1	0.0079	0.1642	1	1	0.0057	0.1695	3	1	0.0036	0.1702
40				wn=6	4	1	0.0224	0.1575	12	1	0.0151	0.1450	3	1	0.0042	0.1661
41				wn=12	4	1	0.0064	0.1654	6	1	0.0047	0.1624	3	1	0.0051	0.1681
42	SDOF SYSTEM WITH A ROTATING UNBALANCE VARYING DAMPING	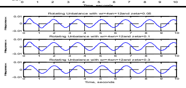	rotating mass mo=3; sdof mass m=7; angular velocity of rot mass wr=4; natural fequency wn=12; time duration to test tf=10s; constant e=0.1	ζ=0.05	4	1	0.0064	0.1654	9	1	0.0076	0.1568	3	1	0.0097	0.1695
43				ζ=0.1	4	1	0.0207	0.1642	8	1	0.0104	0.1636	3	1	0.0049	0.1737
44				ζ=0.3	4	2	0.0531	0.1506	8	1	0.0068	0.1665	3	1	0.0083	0.1746
45	SDOF SYSTEM WITH A ROTATING UNBALANCE VARYING MASS	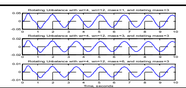	rotating mass mo=3; damping ratio ζ=0.05; angular velocity of rot mass wr=4; natural fequency wn=12; time duration to test tf=10s; constant e=0.1	m=1	4	1	0.0152	0.1595	7	1	0.0056	0.1582	3	1	0.0043	0.1673
46				m=3	4	1	0.0202	0.1595	8	1	0.0089	0.1607	3	1	0.0026	0.1674
47				m=6	4	1	0.0202	0.1595	7	1	0.0058	0.1599	3	1	0.0026	0.1678
48	SDOF-STEP RESPONSE VARYING FORCE MAGNITUDE	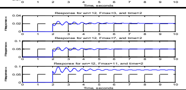	initial time to=2; damping ratio ζ=0.05; natural fequency wn=12; time duration to test tf=10s; system mass m=1;	Fm=3	3	1	0.1690	0.3004	1	1	0.0256	0.3678	3	1	0.0364	0.3647
49				Fm=7	3	1	0.1690	0.3004	1	1	0.0585	0.3636	3	1	0.0296	0.3588
50				Fm=11	3	1	0.0364	0.3533	1	1	0.0265	0.3645	3	1	0.0592	0.3647
51	SDOF-STEP RESPONSE VARYING NATURAL FREQUENCY	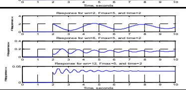	system mass m=1; damping ratio ζ=0.05; natural fequency wn=12; time duration to test tf=10s; force magnitude Fm=5; initial time to=2;	wn=2	3	1	0.0488	0.1475	2	1	0.0110	0.1628	3	1	0.0105	0.1626
52				wn=6	3	1	0.0865	0.2209	1	1	0.0193	0.2567	3	1	0.0168	0.2534
53				wn=12	3	1	0.1690	0.3004	1	1	0.0317	0.3662	3	1	0.0489	0.3632
54	SDOF-STEP RESPONSE VARYING DAMPING RATIO	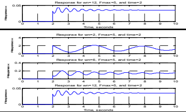	system mass m=1; natural fequency wn=12; time duration to test tf=10s; force magnitude Fm=5; initial time to=2;	ζ=0.05	3	1	0.1690	0.3004	1	1	0.0347	0.3757	3	1	0.0833	0.3732
55				ζ=0.1	2	1	0.0353	0.4032	19	1	0.0881	0.3670	3	1	0.1318	0.4179
56				ζ=0.3	2	1	0.0512	0.4191	6	1	0.1731	0.4233	3	1	0.0320	0.4253
57	SDOF SQUARE PULSE INPUTS VARYING NATURAL FREQUENCY	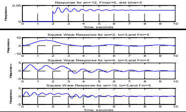	system mass m=1; damping ratio ζ=0.05; time duration to test tf=10s; force magnitude Fm=5; wave starts at to=0; wave stops at to=3;	wn=2	4	1	0.0311	0.2394	3	1	0.0134	0.2502	3	1	0.017315	0.2490
58				wn=6	6	10	0.2304	0.1718	1	1	0.0086	0.1917	3	1	0.005819	0.1903
59				wn=12	9	10	0.4009	0.2187	4	1	0.0179	0.1875	3	1	0.010036	0.1876
60	SDOF SQUARE PULSE INPUTS VARYING DAMPING RATIO	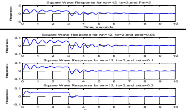	system mass m=1; natural frequency wn=12; time duration to test tf=10s; force magnitude Fm=7; wave starts at to=0; wave stops at to=3;	ζ=0.05	9	10	0.4009	0.2187	19	1	0.0359	0.1428	3	1	0.0095	0.1886
61				ζ=0.1	10	10	0.4237	0.2176	3	1	0.0247	0.2544	3	1	0.0236	0.2544
62				ζ=0.3	5	5	0.1207	0.2798	10	1	0.0270	0.3248	3	1	0.0085	0.3409
63	SDOF SQUARE PULSE INPUTS VARYING FORCE MAGNITUDE	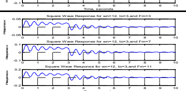	system mass m=1; natural frequency wn=12; time duration to test tf=10s; damping ratio ζ=0.05; wave starts at to=0; wave stops at to=3;	Fm=3	9	10	0.4009	0.2187	5	1	0.0051	0.1798	3	1	0.0074	0.1882
64				Fm=7	9	10	0.4009	0.2187	3	1	0.0053	0.1906	3	1	0.0052	0.1892
65				Fm=11	9	10	0.4009	0.2187	3	1	0.0130	0.1908	3	1	0.0096	0.1880
66	SDOF RAMP INPUT VARYING RATE OF LOADING	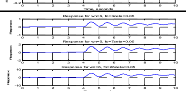	system mass m=1; natural frequency wn=6; k=wn^2; wd=wn*sqrt(1-zeta^2); damping ratio ζ=0.05; force starts at to=0; force levels at at te=4;	fo=3	5	1	0.0442	0.1861	11	1	0.0183	0.1864	3	1	0.0101	0.1982
67				fo=7	5	1	0.0442	0.1861	4	1	0.0107	0.1978	3	1	0.0062	0.1977
68				fo=26	5	1	0.0442	0.1861	6	1	0.0069	0.1932	3	1	0.0073	0.1980
69	VAN DER POL OSCILLATOR	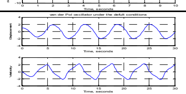	e =0.5; initial conditions x0=[1; 0]; x(0)=1, x'(0)=0 time interval tf=30;	disp	2	1	0.0063	0.1667	3	1	0.0078	0.1534	3	1	0.0113	0.1554
70				vel	2	1	0.1088	0.1082	1	1	0.0804	0.1218	3	1	0.1344	0.1136
71																
72																

	B	C	D	E	F	G	H	I	J	K	L	M	N	O	P	Q
73	SYSTEM	DETAILS	VARIABLES		METHOD 1				METHOD 2				METHOD 3			
74					best m	best τ	rmse	RMSE	calc m	τ	rmse	RMSE	calc m	τ	rmse	RMSE
75	SDOF RANDOM VIBRATION	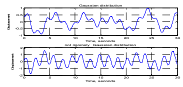	A is a random variable; distflag should be zero for uniform, and 1 for Gaussian distribution	case 1	4	1	0.0084	0.1541	18	1	0.0418	0.1220	3	1	0.0070	0.1556
76			A=[0 to 5] for the uniform distribution, and as a distribution with mean of 2.5 for the Gaussian (won't be rigorously Gaussian).	case 2	2	1	0.0015	0.1560	1	1	0.0224	0.1534	3	1	0.0366	0.1391
77	SDOF RANDOMLY EXCITED DUFFING OSCILLATOR	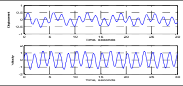	tspan=[0 30]; xinit=[0 0]'; e=0.01; c=0.05; k=1; A=3.7999; w=3.7960; chosen to prevent resonance	dis	3	1	0.0523	0.1252	1	1	0.0187	0.1435	3	1	0.0545	0.1252
78				vel	4	1	0.0910	0.1316	10	1	0.1201	0.1712	3	1	0.0703	0.1365
79	SDOF RANDOMLY EXCITED DUFFING OSCILLATOR	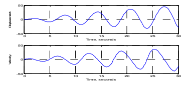	tspan=[0 30]; xinit=[0 0]'; e=0.01; c=0.05; k=1; A=4.4351; w=1.7404; chosen to prevent resonance	dis	6	1	0.0332	0.1452	16	1	0.0106	0.1342	3	1	0.0090	0.1573
80				vel	5	1	0.0266	0.1450	20	1	0.0965	0.1187	3	1	0.0269	0.1548
81	SDOF RANDOMLY EXCITED DUFFING OSCILLATOR	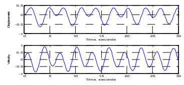	tspan=[0 30]; xinit=[0 0]'; e=0.01; c=0.05; k=1; A=1.0062; w=2.0115; chosen to prevent resonance	dis	4	1	0.0376	0.1507	1	1	0.0153	0.1656	3	1	0.0379	0.1579
82				vel	3	1	0.0245	0.1484	10	1	0.0079	0.1318	3	1	0.0035	0.1560

	SYSTEM	DETAILS	VARIABLES		METHOD 1				METHOD 2				METHOD 3			
				mass:	best **m**	best **τ**	rmse	RMSE	calc **m**	**τ**	rmse	RMSE	set **m**	set **τ**	rmse	RMSE
1	SDOF UNDAMPED OSCILATION VARYING MASS	SDOF Undamped Oscillation mx"+kx=0; x(t) = Asin(ωnt + φ)	stiffness k=8; initial displacement x0=3; initial velocity v0=1; time duration to test tf=30s;	m=2	5	10	0.0726	0.1672	5	1	0.0109	0.1637	3	1	0.0073	0.1714
				m=4	4	10	0.0452	0.2237	9	1	0.0755	0.1476	3	1	0.0279	0.1729
				m=12	2	7	0.0132	0.1510	11	1	0.0405	0.1580	3	1	0.0058	0.1764

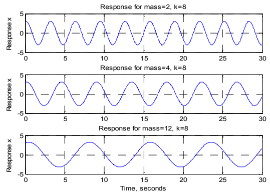

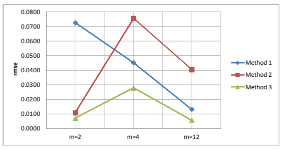

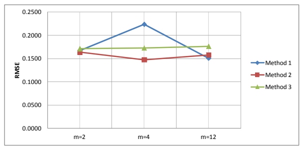

m=2 m=4 m=12

METHOD 1

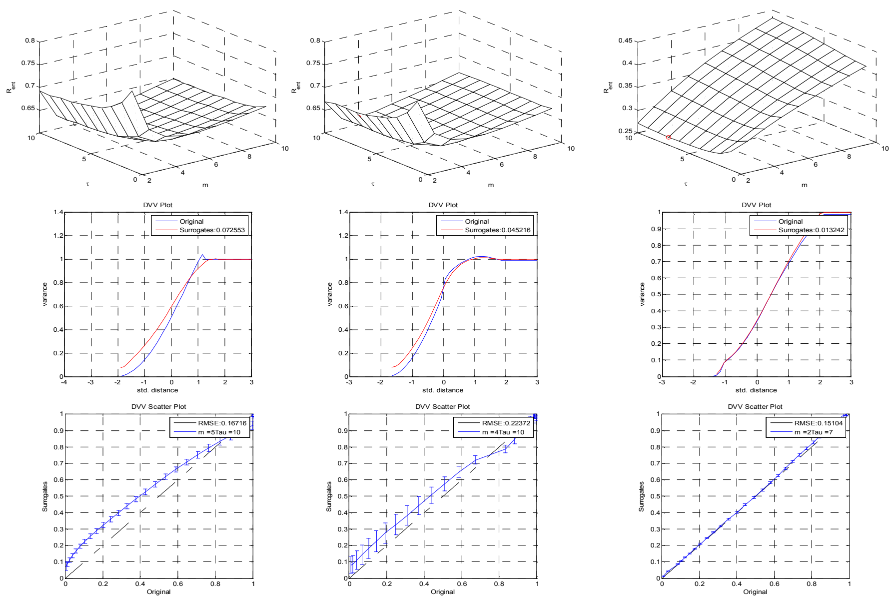

m=2 m=4 m=12

METHOD 2

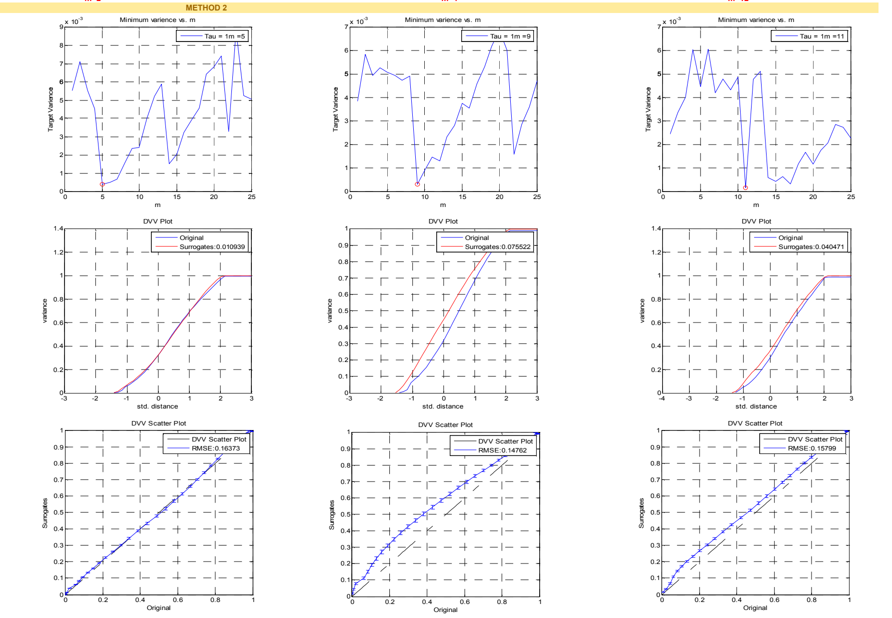

m=2 m=4 m=12

METHOD 3

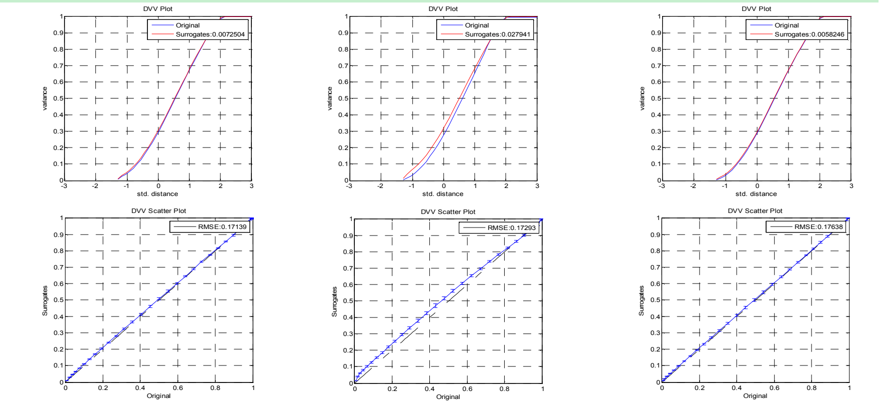

	SYSTEM	DETAILS	VARIABLES		METHOD 1				METHOD 2				METHOD 3			
				mass:	best **m**	best **τ**	rmse	RMSE	calc **m**	**τ**	rmse	RMSE	set **m**	set **τ**	rmse	RMSE
2	DAMPED SDOF SYSTEM OSCILATION FOR VARYING DAMPING VALUES (only for underdamped case xi<1)	SDOF Damped Oscillation mx''+cx'+kx=0	natural frequency wn=7; initial displacement x0=3; initial velocity v0=1; time duration to test tf=30s;	ζ=0.05	10	10	0.6891	0.4716	11	1	0.1921	0.3570	3	1	0.0268	0.3465
				ζ=0.2	10	9	0.8662	0.5372	23	1	0.3338	0.6046	3	1	0.0967	0.6207
				ζ=0.5	2	9	1.0195	0.5799	21	1	0.2961	0.6309	3	1	0.1076	0.6818

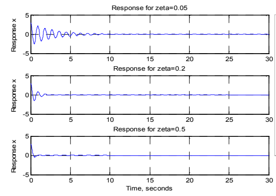

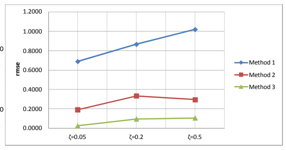

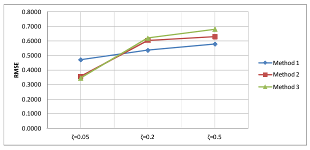

ζ=0.05 ζ=0.2 ζ=0.5

METHOD 1

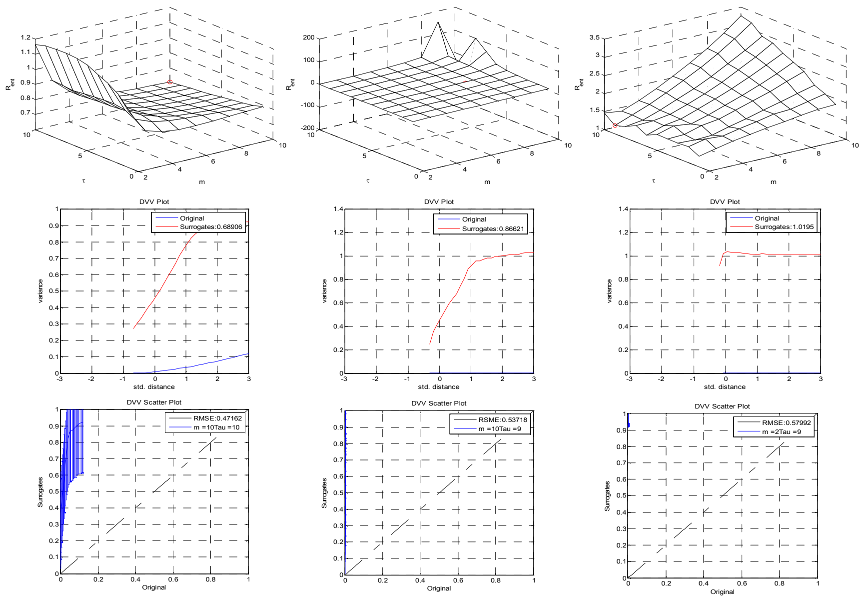

ζ=0.05 ζ=0.2 ζ=0.5

METHOD 2

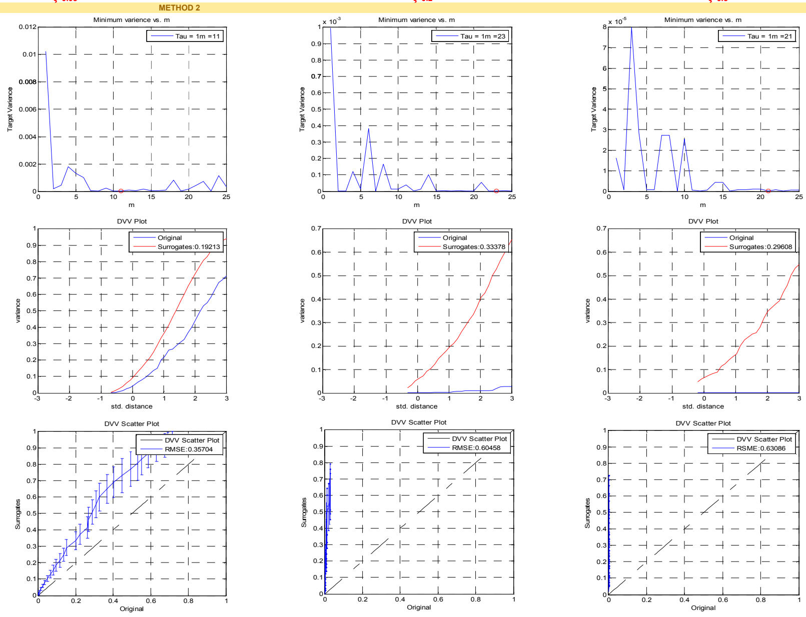

ζ=0.05 ζ=0.2 ζ=0.5

METHOD 3

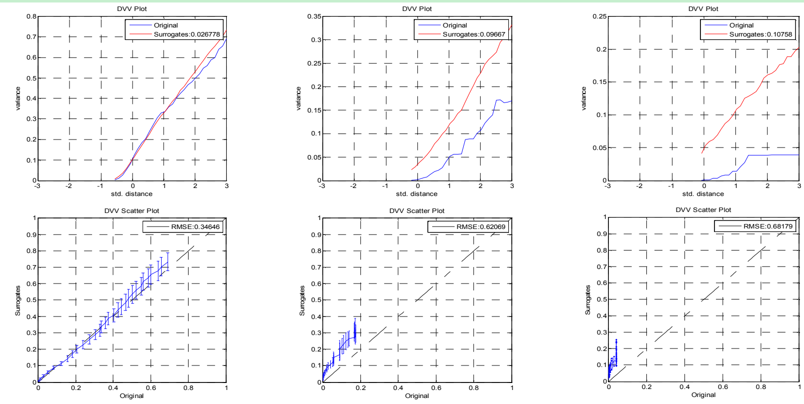

	SYSTEM	DETAILS	VARIABLES		METHOD 1				METHOD 2				METHOD 3			
				mass:	best m	best τ	rmse	RMSE	calc m	τ	rmse	RMSE	set m	set τ	rmse	RMSE
3	OVERDAMPED SDOF SYSTEM OSCILATION FOR VARYING DAMPING VALUES (only for overdamped case xi>1)!!!	SDOF Damped Oscillation x''+2ζwnx'+wn²x=0;	natural frequency wn=7; initial displacement x0=3; initial velocity v0=1; time duration to test tf=30s;	ζ=7	5	10	0.6491	0.4364	18	1	0.2885	0.3296	3	1	0.0486	0.2918
				ζ=5	2	1	0.0313	0.4253	24	1	0.4093	0.4717	3	1	0.0742	0.4349
				ζ=1	3	10	0.8726	0.5464	22	1	0.2759	0.6457	3	1	0.0927	0.6995

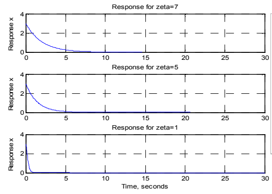

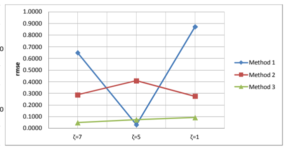

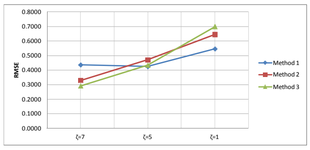

ζ=7 ζ=5 ζ=1

METHOD 1

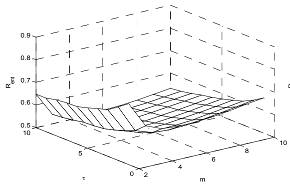
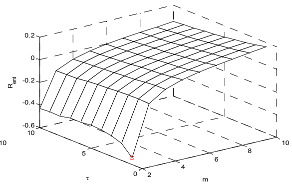
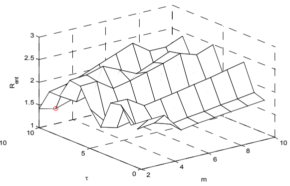
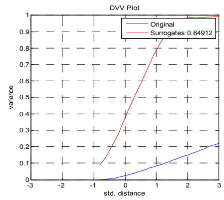

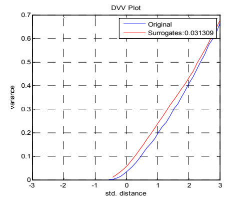

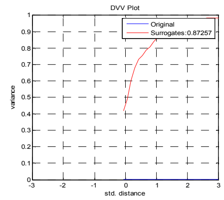

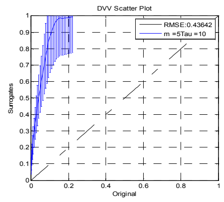

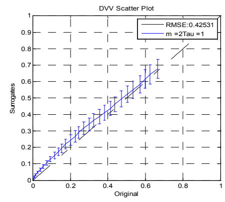

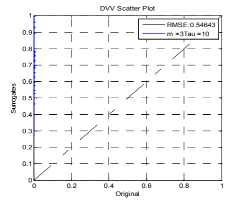

ζ=7 ζ=5 ζ=1

METHOD 2

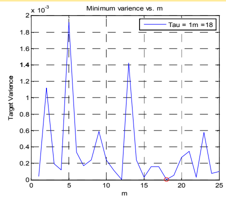

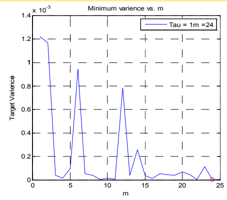

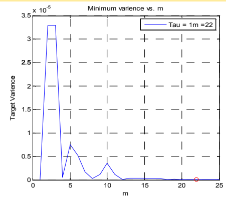

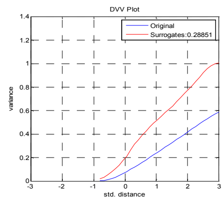

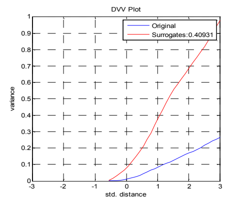

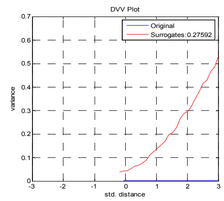

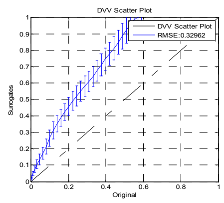

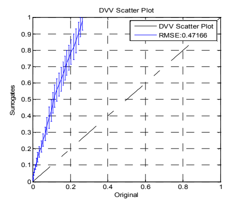

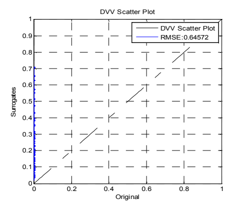

ζ=7 ζ=5 ζ=1

METHOD 3

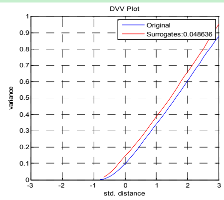

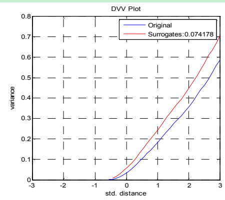

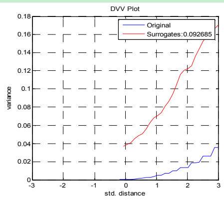

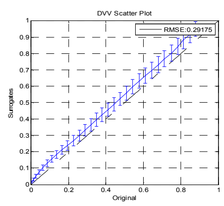

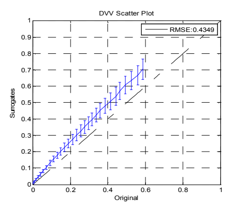

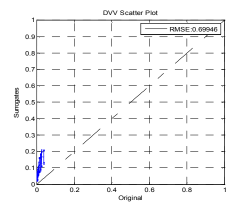

	m-file	SYSTEM	DETAILS	VARIABLES		METHOD 1				METHOD 2				METHOD 3			
					mass:	best **m**	best **τ**	rsme	RSME	calc **m**	**τ**	rsme	RSME	set **m**	set **τ**	rsme	RSME
4	OFhar_undamp_vary	4-1 HARMONIC EXCITATION OF UNDAMPED SDOF SYSTEMS effect of varying driving frequency w for a given natural frequency wn	SDOF Harmonic Undamped Oscillation mx''+kx=Focoswt;	natural frequency wn=7; initial displacement x0=0; initial velocity v0=0; force magnitude per unit mass f0=6;	wdr=3	4	10	0.2300	0.3334	5	1	0.0061	0.1073	3	1	0.0028	0.1185
					wdr=27	6	8	0.0365	0.2433	19	1	0.0238	0.2103	3	1	0.0108	0.2143
					wdr=42	5	10	0.0682	0.2271	10	1	0.0606	0.2832	3	1	0.0736	0.3205

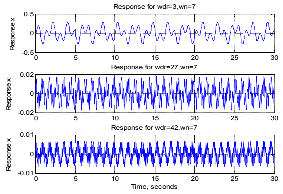

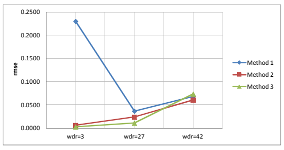

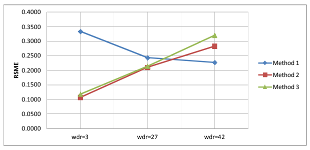

wdr=3 wdr=27 wdr=42

METHOD 1

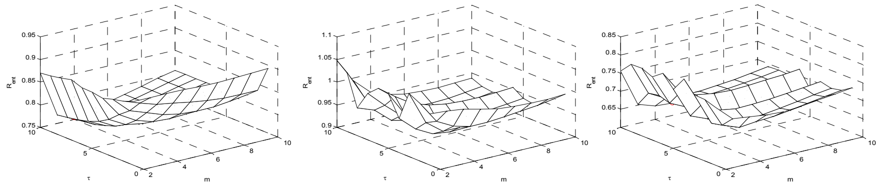

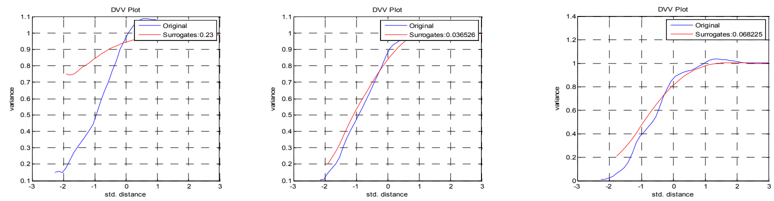

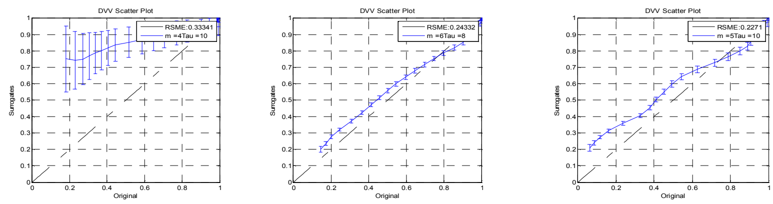

wdr=3 wdr=27 wdr=42

METHOD 2

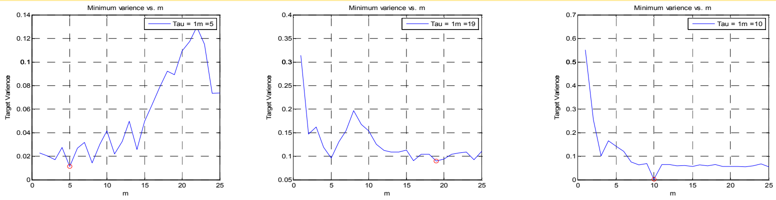

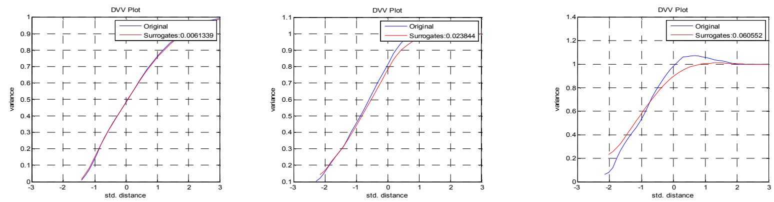

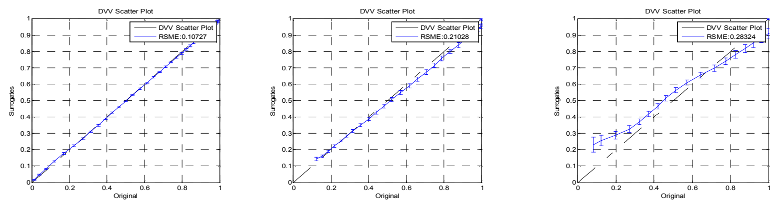

wdr=3 wdr=27 wdr=42

METHOD 3

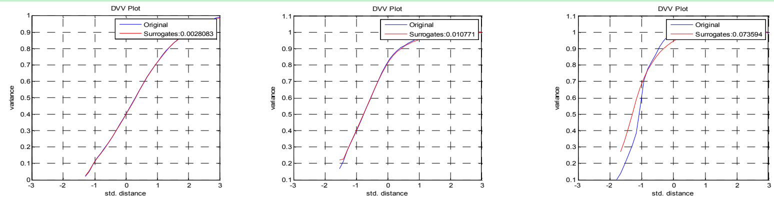

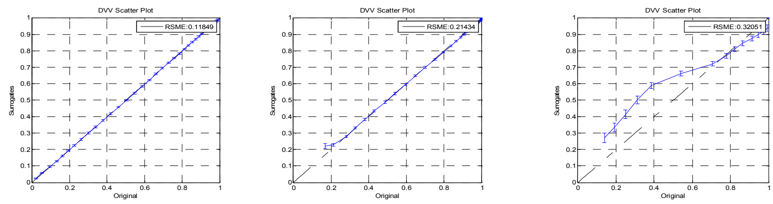

	SYSTEM	DETAILS	VARIABLES		METHOD 1				METHOD 2				METHOD 3			
				mass:	best m	best τ	rmse	RMSE	calc m	τ	rmse	RMSE	set m	set τ	rmse	RMSE
5	HARMONIC EXCITATION OF UNDAMPED SDOF SYSTEMS effect of varying natural frequency wn for a given driving frequency w	SDOF Harmonic Undamped Oscillation mx"+kx=Focoswt ;	driving frequency wdr=7; initial displacement x0=0; initial velocity v0=0; force magnitude per unit mass f0=6; time duration to test tf=30s;	wn=3	4	10	0.2300	0.3334	4	1	0.0042	0.1071	3	1	0.0034	0.1176
				wn=12	5	7	0.0627	0.2938	3	1	0.1336	0.1416	3	1	0.1283	0.1406
				wn=26	6	9	0.0617	0.2581	17	1	0.0388	0.2256	3	1	0.0170	0.2037

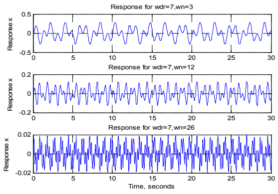

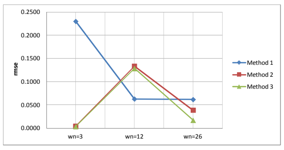

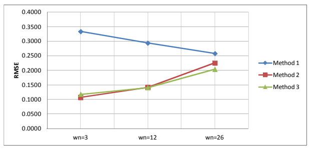

wn=3 wn=12 wn=26

METHOD 1

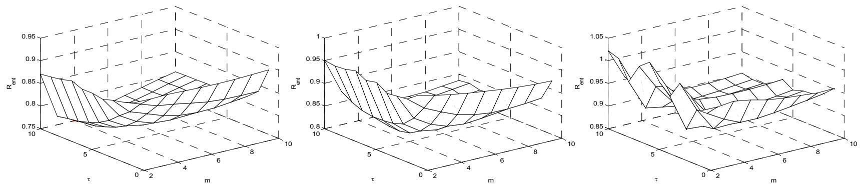

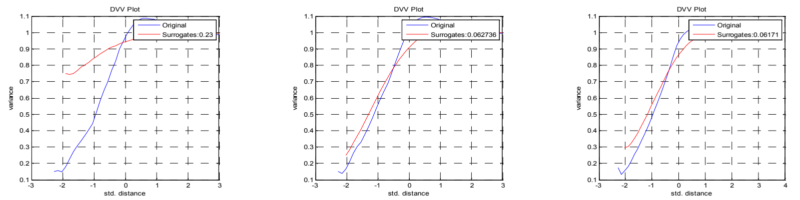

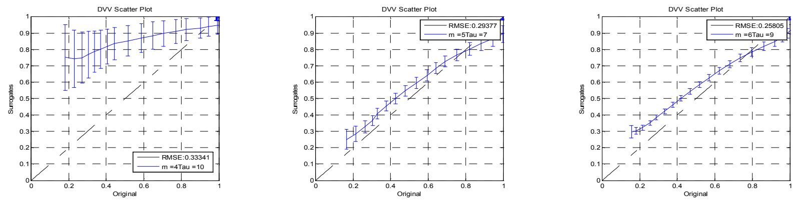

wn=3 wn=12 wn=26

METHOD 2

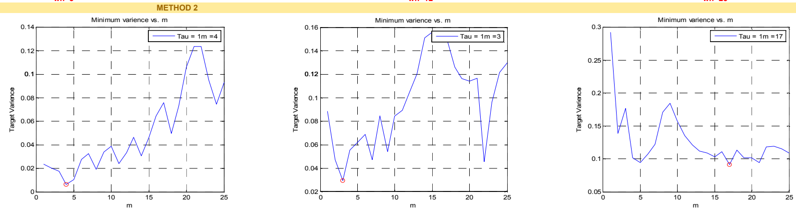

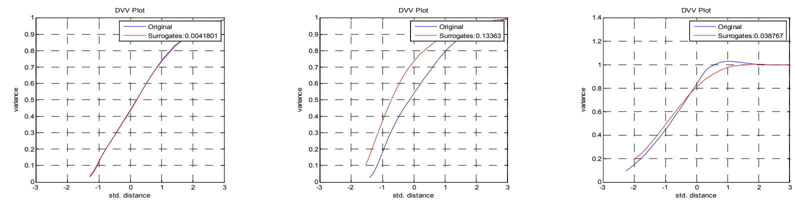

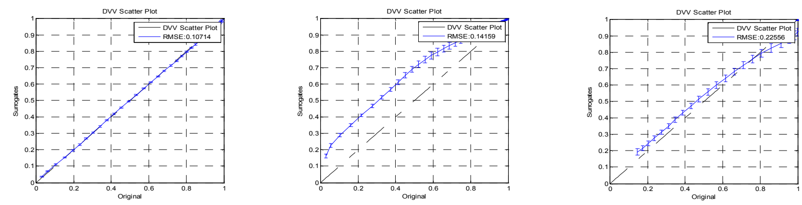

wn=3 wn=12 wn=26

METHOD 3

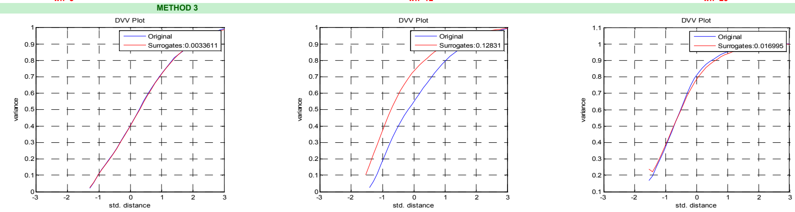

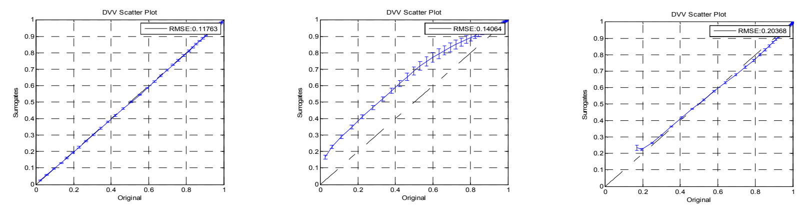

	SYSTEM	DETAILS	VARIABLES		METHOD 1				METHOD 2				METHOD 3			
				mass:	best m	best τ	rmse	RMSE	calc m	τ	rmse	RMSE	set m	set τ	rmse	RMSE
6	HARMONIC EXCITATION OF UNDAMPED SDOF SYSTEMS BEAT Phenomenon natural and driving frequencies are close but not equal	SDOF Harmonic Undamped Oscillation mx''+kx=Focoswt;	initial displacement x0=0; initial velocity v0=0; force magnitude per unit mass f0=6; time duration to test tf=120s;	wn=3; wdr=3.2;	3	1	0.1314	0.1759	3	1	0.0046	0.1369	3	1	0.0037	0.1366
				wn=12; wdr=12.	6	10	0.1740	0.2360	2	1	0.0068	0.1337	3	1	0.0094	0.1682
				wn=22; wdr=22.	3	6	0.0150	0.1044	3	1	0.1248	0.2167	3	1	0.1260	0.2172

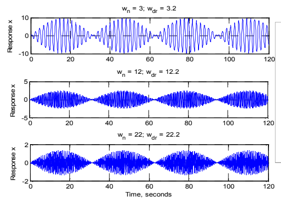
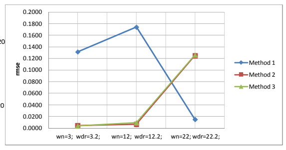
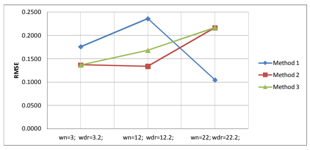

wn=3; wdr=3.2; wn=12; wdr=12.2; wn=22; wdr=22.2;

METHOD 1

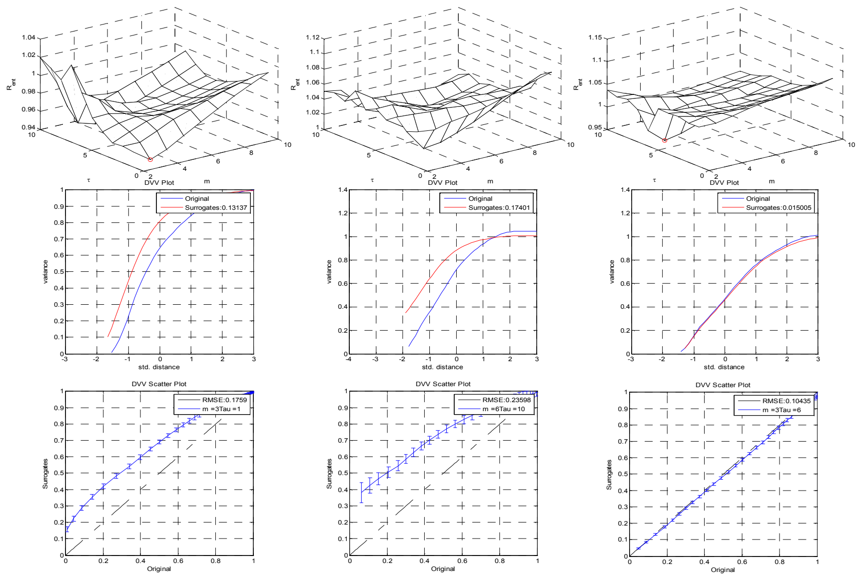

wn=3; wdr=3.2; wn=12; wdr=12.2; wn=22; wdr=22.2;

METHOD 2

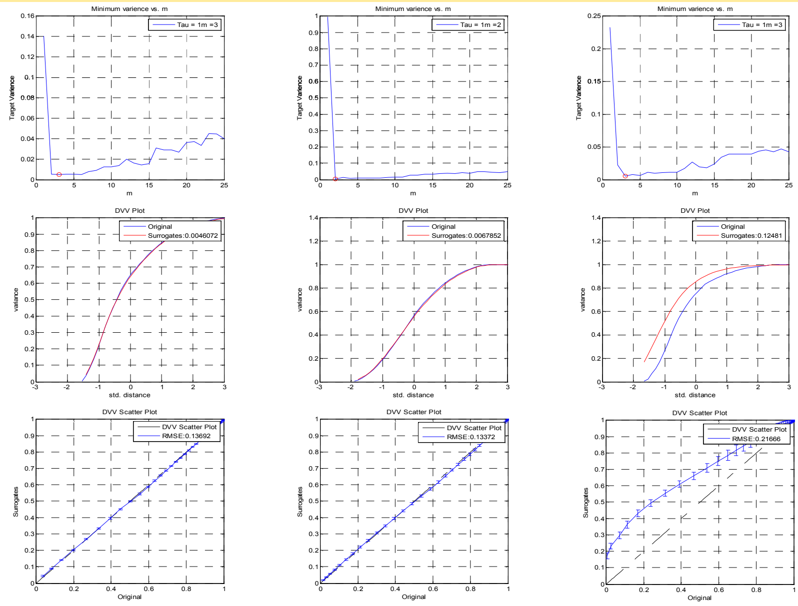

wn=3; wdr=3.2; wn=12; wdr=12.2; wn=22; wdr=22.2;

METHOD 3

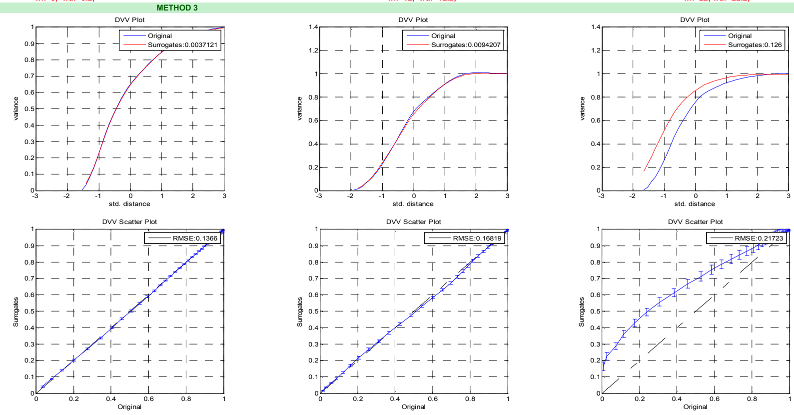

	SYSTEM	DETAILS	VARIABLES		METHOD 1				METHOD 2				METHOD 3			
				wn=wdr=	best **m**	best **τ**	rmse	RMSE	calc **m**	**τ**	rmse	RMSE	set **m**	set **τ**	rmse	RMSE
7	HARMONIC EXCITATION OF UNDAMPED SDOF SYSTEMS RESONANCE natural and driving frequencies are equal	SDOF Harmonic Undamped Oscillation mx"+kx=Focoswt	initial displacement x0=0; initial velocity v0=0; force magnitude per unit mass f0=6; time duration to test tf=120s	wn=wdr	4	9	0.1462	0.1205	7	1	0.0165	0.1439	3	1	0.0096	0.1190
				wn=wdr	7	10	0.0613	0.1334	3	1	0.0027	0.1461	3	1	0.0035	0.1462
				wn=wdr	4	6	0.0194	0.1176	6	1	0.0044	0.1199	3	1	0.0041	0.1646

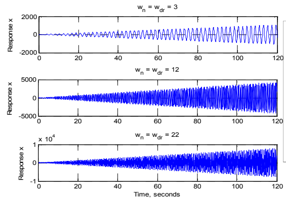

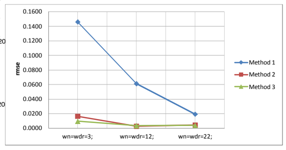

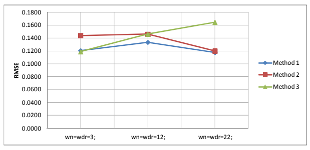

wn=wdr=3; wn=wdr=12; wn=wdr=22;

METHOD 1

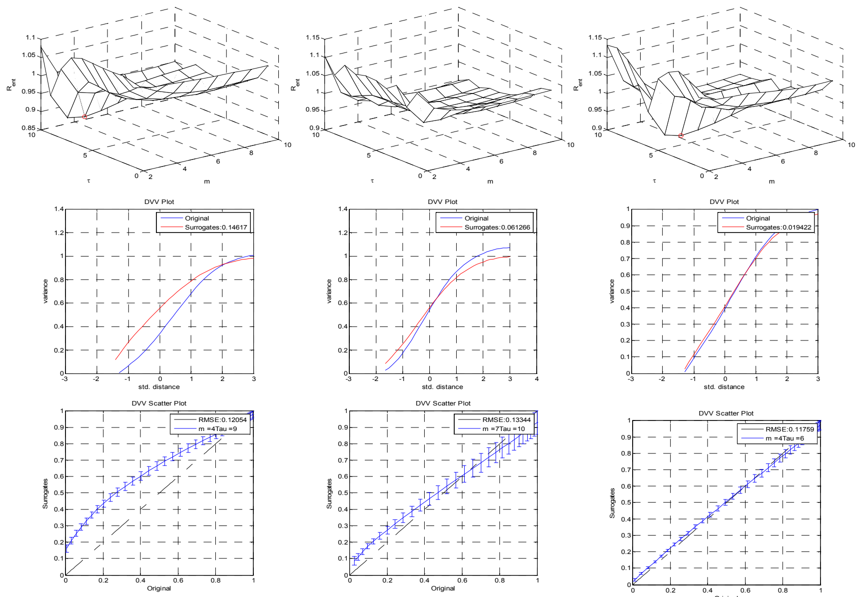

wn=wdr=3; wn=wdr=12; wn=wdr=22;

METHOD 2

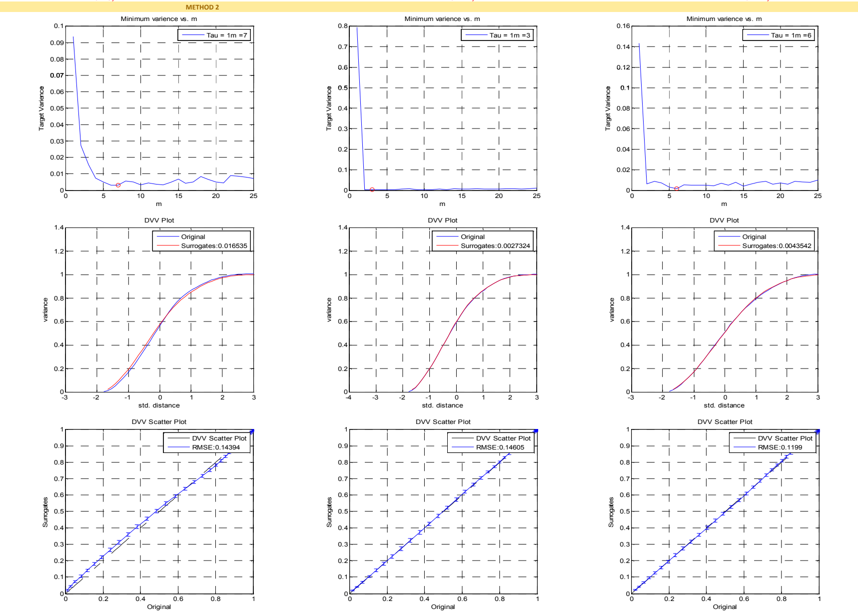

wn=wdr=3; wn=wdr=12; wn=wdr=22;

METHOD 3

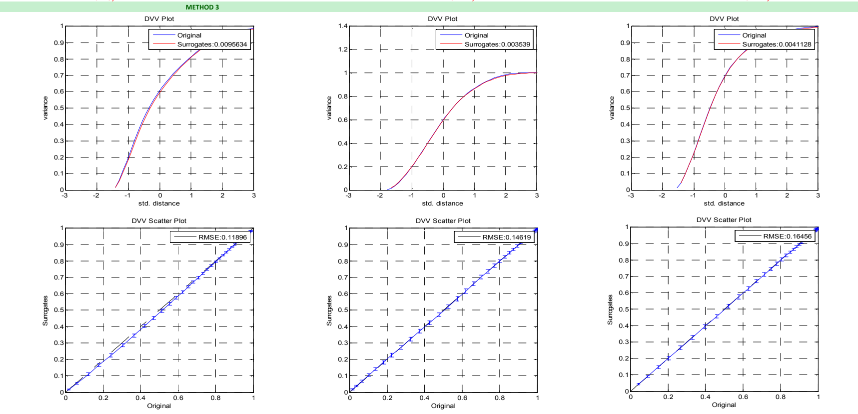

	SYSTEM	DETAILS	VARIABLES		METHOD 1				METHOD 2				METHOD 3			
				wn=wdr=	best **m**	best **τ**	rmse	RMSE	calc **m**	**τ**	rmse	RMSE	set **m**	set **τ**	rmse	RMSE
8	HARMONIC EXCITATION OF DAMPED SDOF SYSTEMS (VARYING DAMPING VALUES)	SDOF Harmonic Damped Oscillation mx''+cx'+kx=Fcos(wt)	driving frequency wdr =3; natural frequency wn=3.5; force magnitude per unit mass f0=6; time duration to test tf=30s;	ζ=0.05	5	10	0.1243	0.2020	4	1	0.0039	0.1476	3	1	0.0052	0.1550
				ζ=0.2	7	10	0.0550	0.1791	3	1	0.0030	0.1617	3	1	0.0048	0.1620
				ζ=0.5	6	10	0.2053	0.2243	4	1	0.0044	0.1615	3	1	0.0082	0.1659

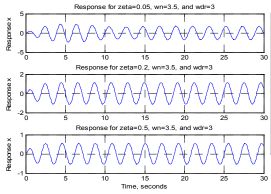

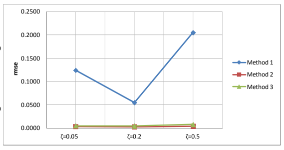

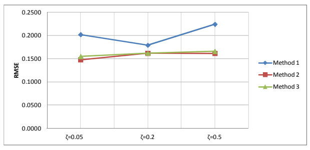

ζ=0.05 ζ=0.2 ζ=0.5

METHOD 1

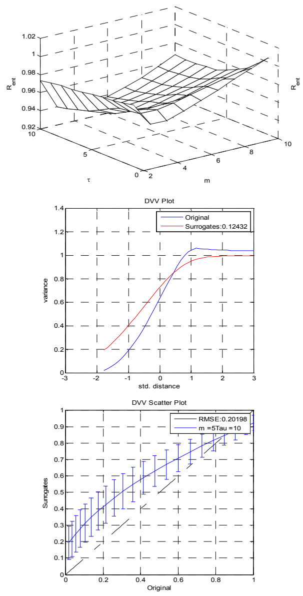

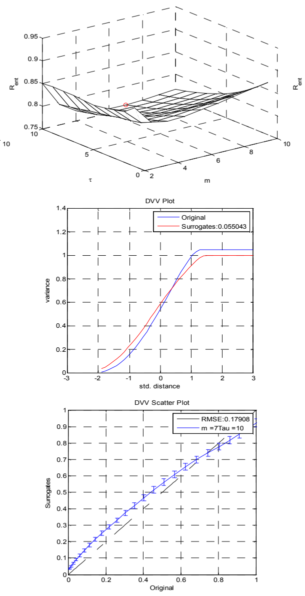

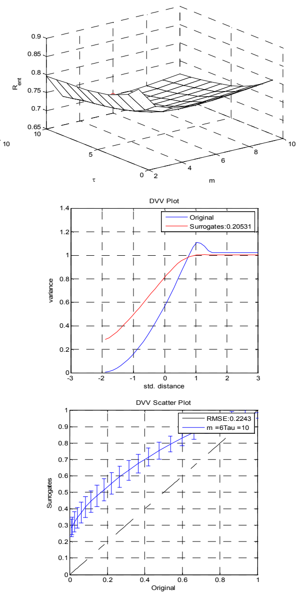

ζ=0.05 ζ=0.2 ζ=0.5

METHOD 2

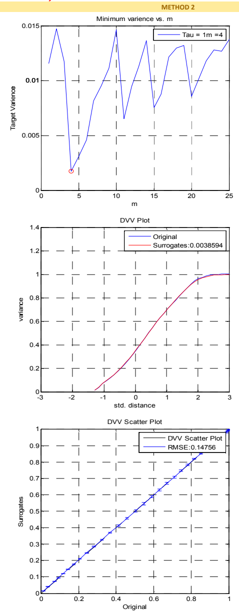

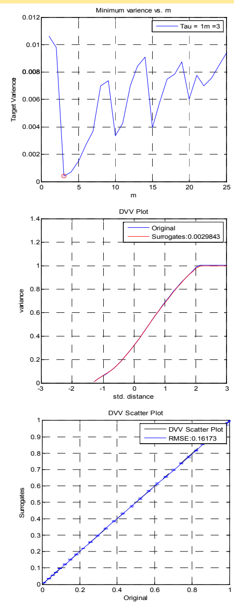

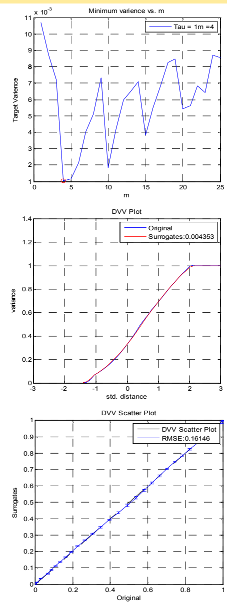

ζ=0.05 ζ=0.2 ζ=0.5

METHOD 3

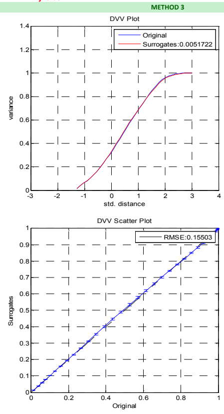

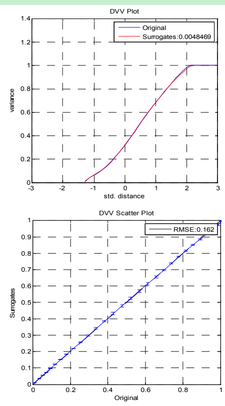

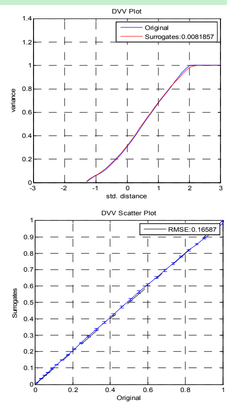

	SYSTEM	DETAILS	VARIABLES		METHOD 1				METHOD 2				METHOD 3			
					best m	best τ	rmse	RMSE	calc m	τ	rmse	RMSE	set m	set τ	rmse	RMSE
9	HARMONIC EXCITATION OF DAMPED SDOF SYSTEMS VARYNG NATURAL FREQUENCY	SDOF Harmonic Damped Oscillation mx''+cx'+kx=Fcos(wt)	driving frequency wdr =7; damping ratio ζ=0.05; force magnitude per unit mass f0=6; time duration to test tf=30s;	wn=3	4	1	0.0403	0.1326	1	1	0.0110	0.1507	3	1	0.0312	0.1383
				wn=12	3	1	0.0029	0.1613	6	1	0.0075	0.1496	3	1	0.0059	0.1625
				wn=26	4	10	0.2174	0.2077	4	1	0.0034	0.1604	3	1	0.0054	0.1648

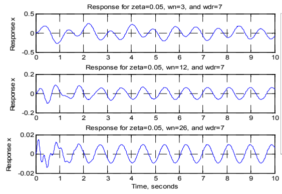

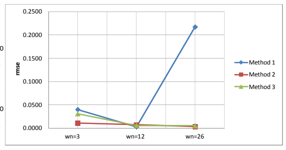

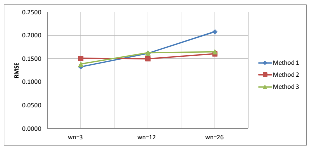

wn=3 wn=12 wn=26

METHOD 1

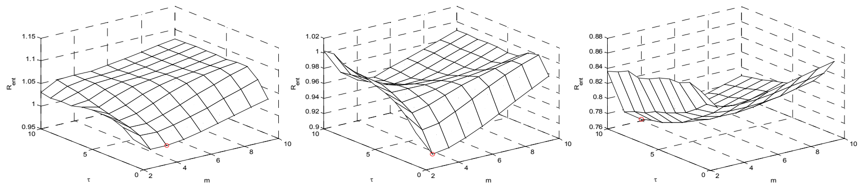

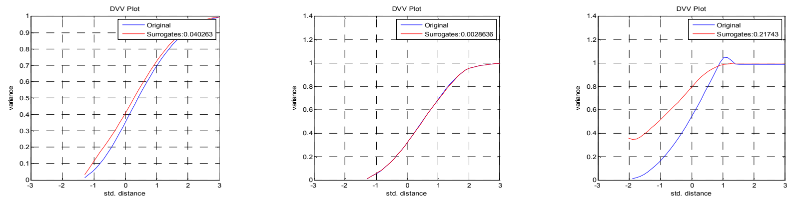

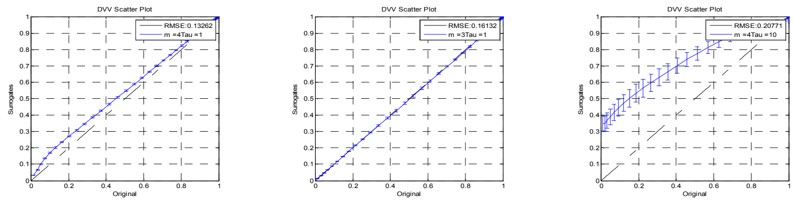

wn=3 wn=12 wn=26

METHOD 2

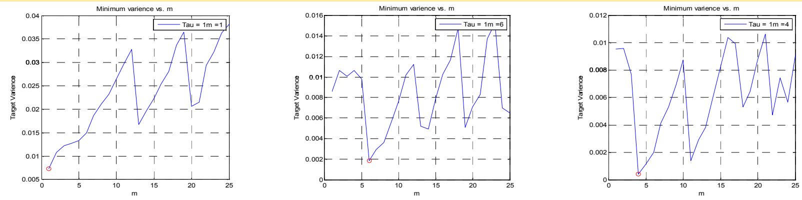

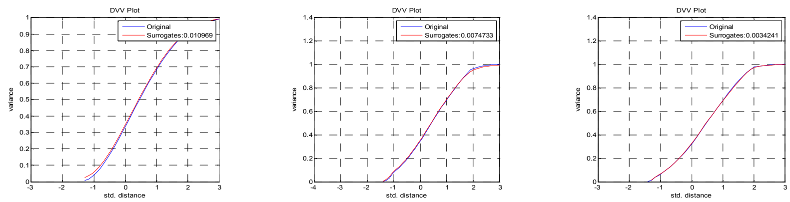

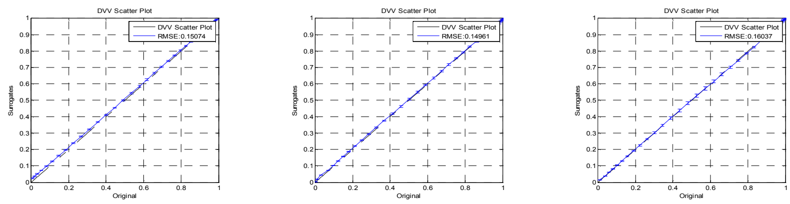

wn=3 wn=12 wn=26

METHOD 3

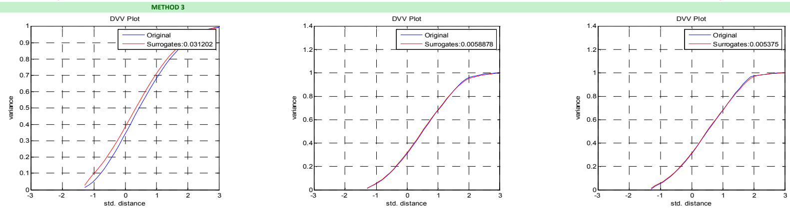

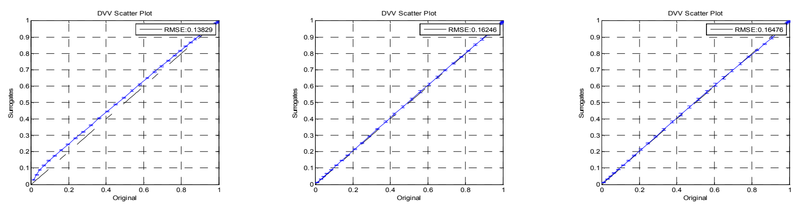

	SYSTEM	DETAILS	VARIABLES		METHOD 1				METHOD 2				METHOD 3			
				base freq	best m	best τ	rmse	RMSE	calc m	τ	rmse	RMSE	set m	set τ	rmse	RMSE
10	BASE EXCITATION OF SDOF SYSTEMS VARYING EXCITATION FREQUENCY	SDOF Base excitation mx''+c(x'-y')+k(x-y)=0; y(t)=Ysin(wbt)	base excitation magnitude yo=3; damping ratio ζ=0.05; natural frequency wn=4 time duration to test tf=10s;	wb=2	4	1	0.0125	0.1600	19	1	0.0159	0.1489	3	1	0.0053	0.1651
				wb=6	4	1	0.0415	0.1359	1	1	0.0029	0.1548	3	1	0.0043	0.1509
				wb=12	3	1	0.0049	0.1604	1	1	0.0074	0.1765	3	1	0.0101	0.1661

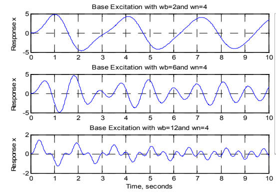

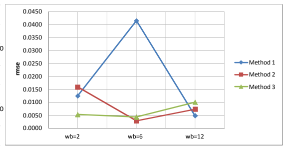

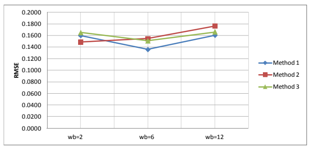

wb=2 wb=6 wb=12

METHOD 1

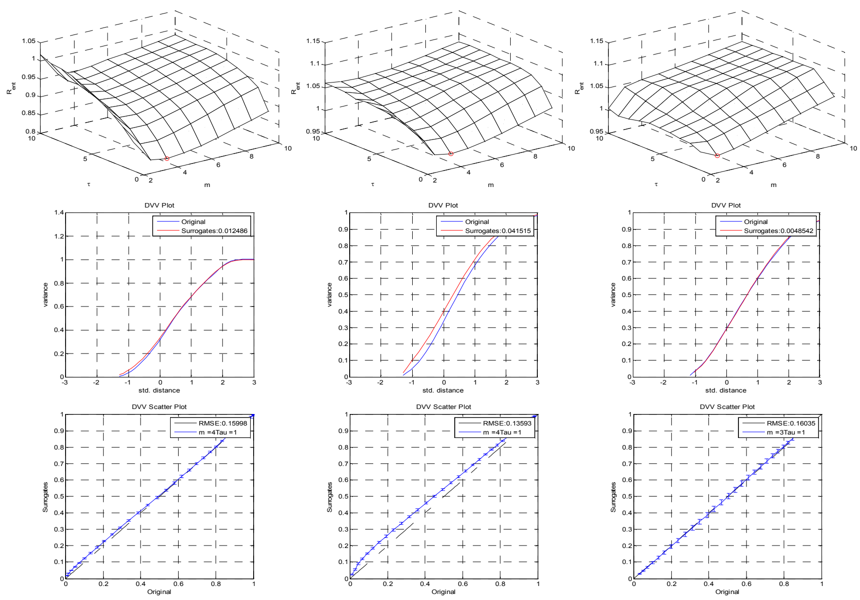

wb=2 wb=6 wb=12

METHOD 2

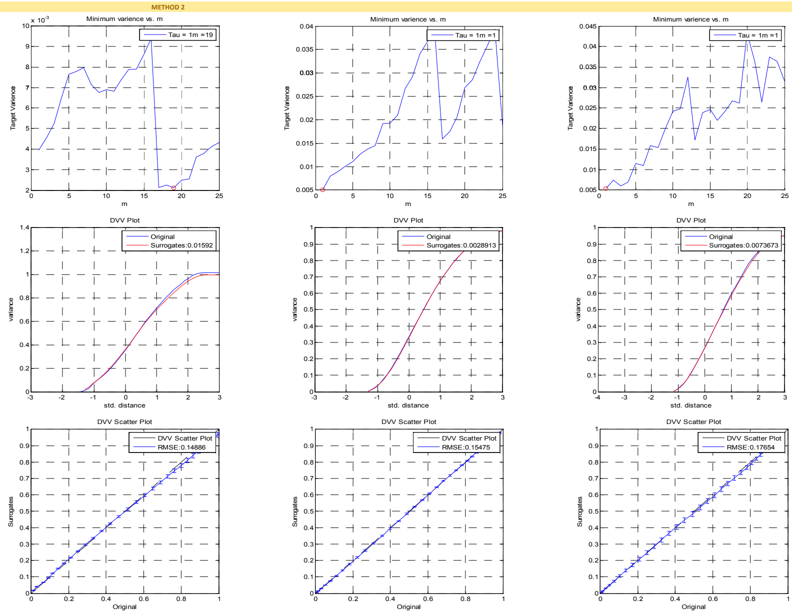

wb=2 wb=6 wb=12

METHOD 3

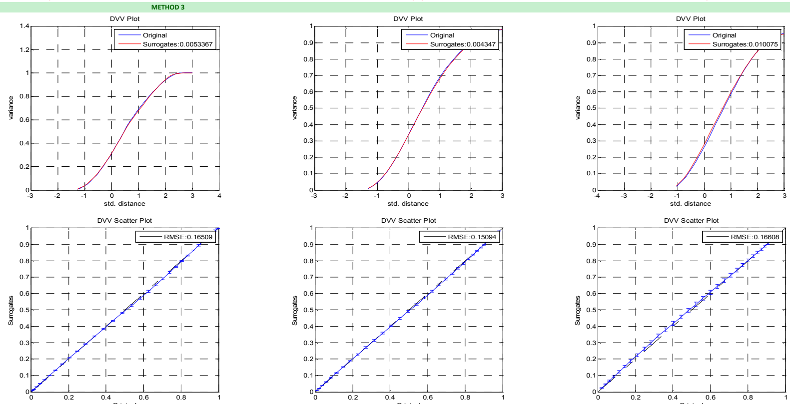

	SYSTEM	DETAILS	VARIABLES		METHOD 1				METHOD 2				METHOD 3			
				baseamplitu	best m	best τ	rmse	RMSE	calc m	τ	rmse	RMSE	set m	set τ	rmse	RMSE
11	BASE EXCITATION OF SDOF SYSTEMS VARYING BASE EXCITATION MAGNITUDE	SDOF Base excitation mx''+c(x'-y')+k(x-y)=0; y(t)=Ysin(wbt)	base excitation frequency wb=6; damping ratio ζ=0.05; natural frequency wn=4 time duration to test tf=10s;	y0=3	4	1	0.0415	0.1359	1	1	0.0050	0.1567	3	1	0.0018	0.1509
				y0=7	4	1	0.0415	0.1359	1	1	0.0051	0.1571	3	1	0.0018	0.1502
				y0=11	4	1	0.0405	0.1359	1	1	0.0072	0.1543	3	1	0.0028	0.1509

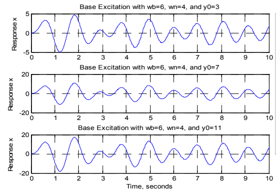

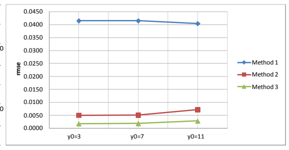

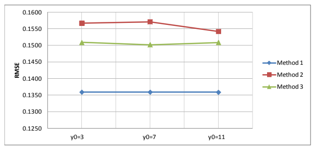

y0=3 y0=7 y0=11

METHOD 1

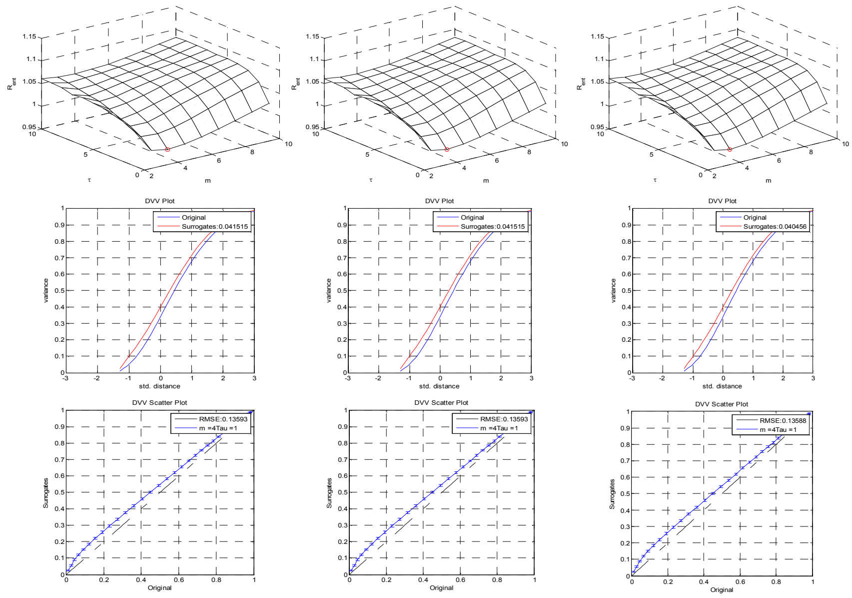

y0=3 y0=7 y0=11

METHOD 2

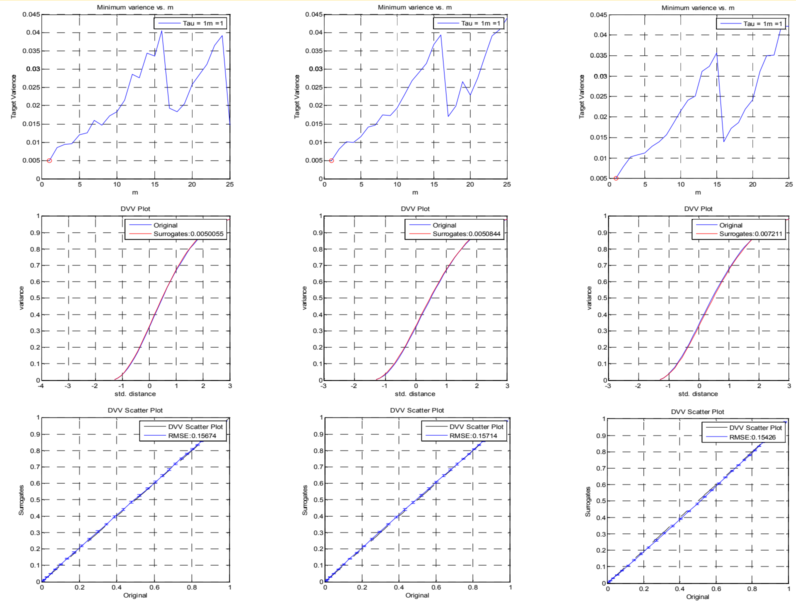

y0=3 y0=7 y0=11

METHOD 3

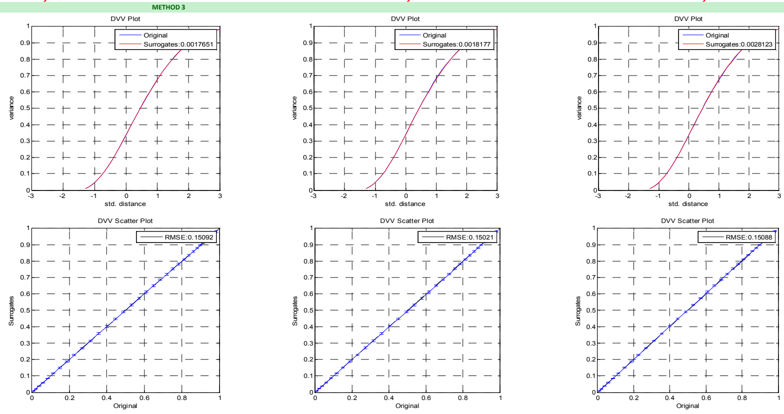

	SYSTEM	DETAILS	VARIABLES		METHOD 1				METHOD 2				METHOD 3			
				damping rat	best m	best τ	rmse	RMSE	calc m	τ	rmse	RMSE	set m	set τ	rmse	RMSE
12	BASE EXCITATION OF SDOF SYSTEMS VARYING DAMPING RATIO	SDOF Base excitation mx''+c(x'-y')+k(x-y)=0; y(t)=Ysin(wbt)	base amplitude y0=3; base excitation frequency wb=6; natural frequency wn=4 time duration to test tf=10s;	ζ=0.05	4	1	0.0415	0.1359	1	1	0.0050	0.1567	3	1	0.0021	0.1511
				ζ=0.1	4	1	0.0412	0.1399	10	1	0.0061	0.1266	3	1	0.0023	0.1561
				ζ=0.3	4	1	0.0371	0.1557	7	1	0.0050	0.1576	3	1	0.0062	0.1717

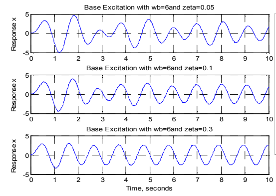

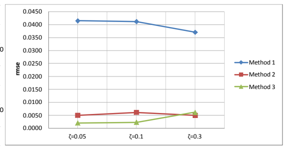

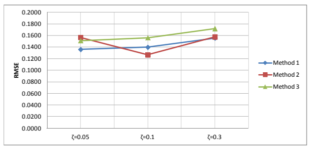

ζ=0.05 ζ=0.1 ζ=0.3

METHOD 1

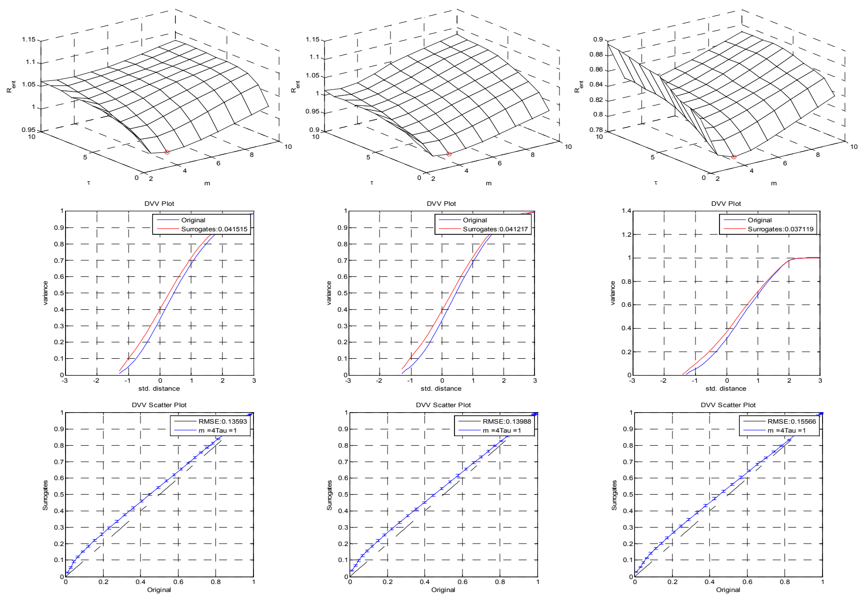

ζ=0.05 ζ=0.1 ζ=0.3

METHOD 2

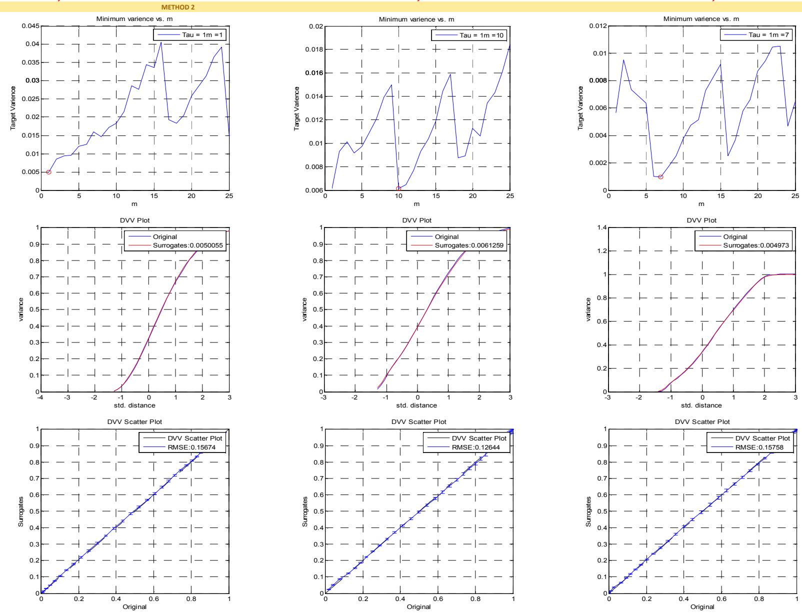

ζ=0.05 ζ=0.1 ζ=0.3

METHOD 3

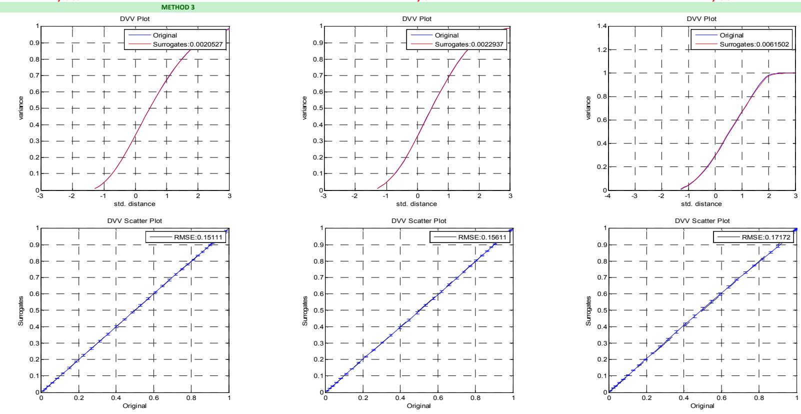

	SYSTEM	DETAILS	VARIABLES		METHOD 1				METHOD 2				METHOD 3			
				natural freq	best m	best τ	rmse	RMSE	calc m	τ	rmse	RMSE	set m	set τ	rmse	RMSE
13	SDOF SYSTEM WITH A ROTATING UNBALANCE VARYING NATURAL FREQUENCY	SDOF having a rotating unbalance for zero initial conditions	rotating mass mo=3; sdof mass m=7; angular velocity of rot mass wr=4; damping ratio ζ=0.05; time duration to test tf=10s; constant e=0.1	wn=2	3	1	0.0079	0.1642	1	1	0.0057	0.1695	3	1	0.0036	0.1702
				wn=6	4	1	0.0224	0.1575	12	1	0.0151	0.1450	3	1	0.0042	0.1661
				wn=12	4	1	0.0064	0.1654	6	1	0.0047	0.1624	3	1	0.0051	0.1681

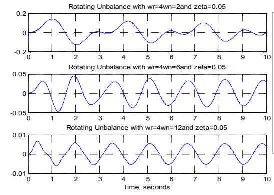

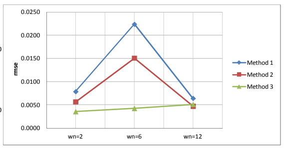

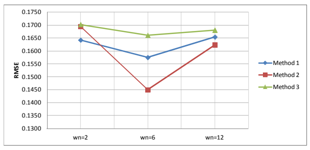

wn=2 wn=6 wn=12

METHOD 1

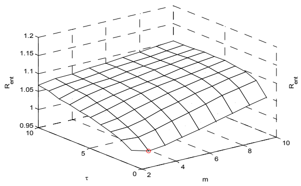
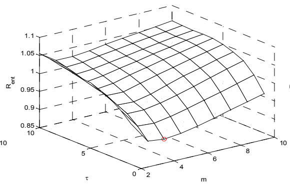
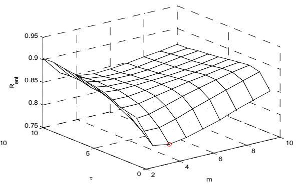

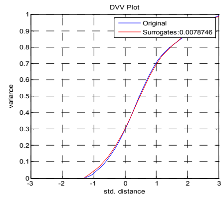

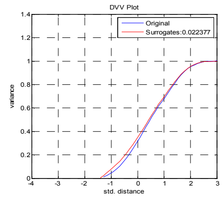

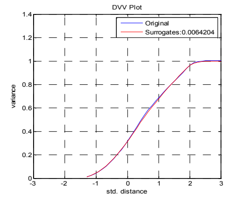

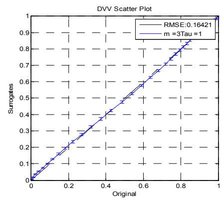

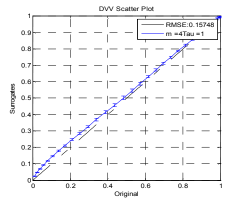

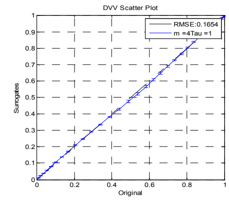

wn=2 wn=6 wn=12

METHOD 2

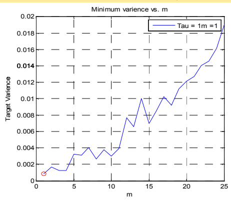

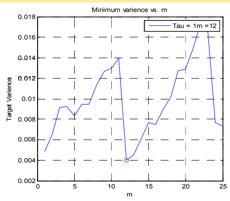

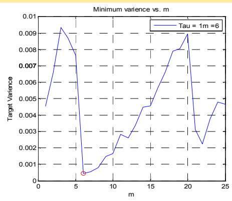

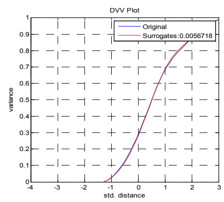

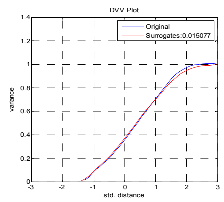

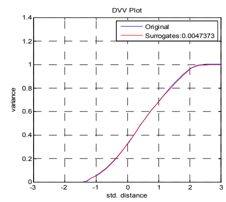

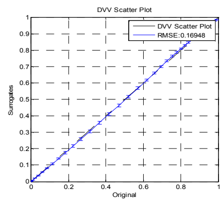

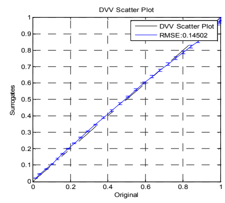

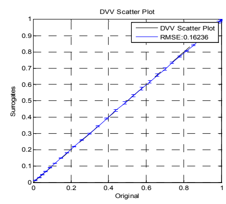

wn=2 wn=6 wn=12

METHOD 3

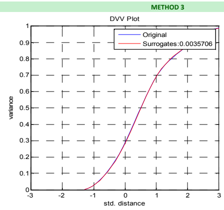

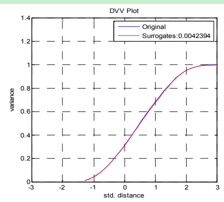

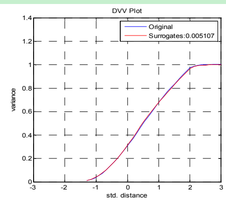

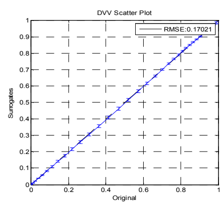

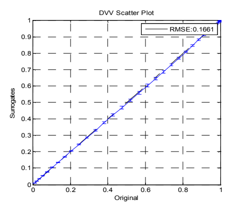

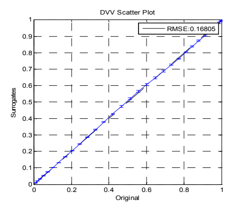

	SYSTEM	DETAILS	VARIABLES		METHOD 1				METHOD 2				METHOD 3			
				damping rat	best m	best τ	rmse	RMSE	calc m	τ	rmse	RMSE	set m	set τ	rmse	RMSE
14	SDOF SYSTEM WITH A ROTATING UNBALANCE VARYING DAMPING	SDOF having a rotating unbalance for zero initial conditions	rotating mass mo=3; sdof mass m=7; angular velocity of rot mass wr=4; natural fequency wn=12; time duration to test tf=10s; constant e=0.1	ζ=0.05	4	1	0.0064	0.1654	9	1	0.0076	0.1568	3	1	0.0097	0.1695
				ζ=0.1	4	1	0.0207	0.1642	8	1	0.0104	0.1636	3	1	0.0049	0.1737
				ζ=0.3	4	2	0.0531	0.1506	8	1	0.0068	0.1665	3	1	0.0083	0.1746

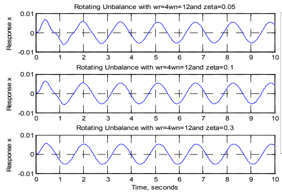

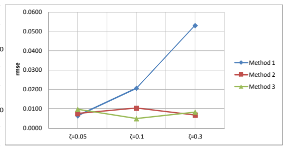

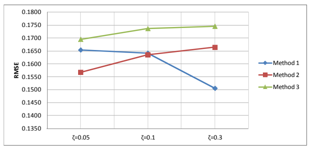

ζ=0.05 ζ=0.1 ζ=0.3

METHOD 1

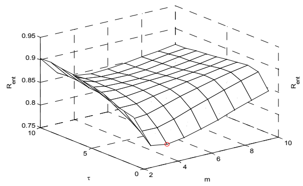
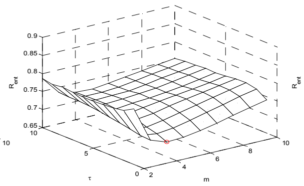
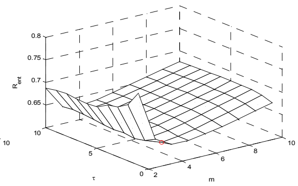

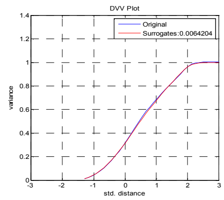

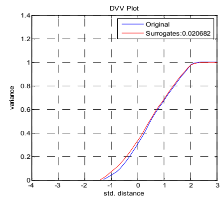

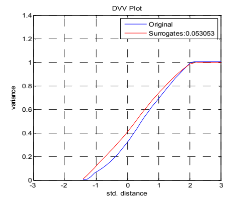

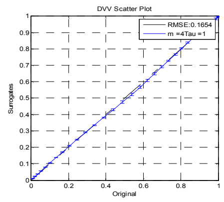

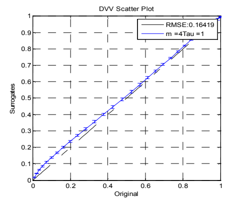

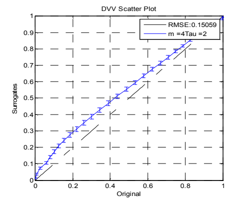

ζ=0.05 ζ=0.1 ζ=0.3

METHOD 2

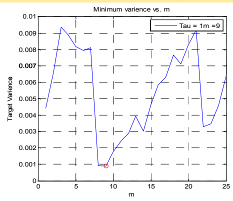

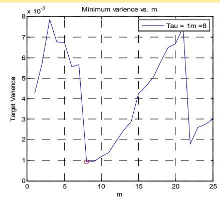

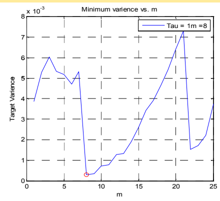

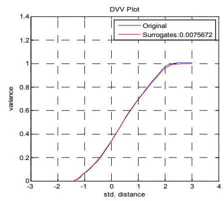

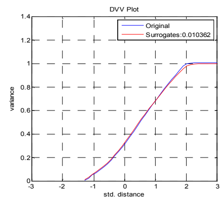

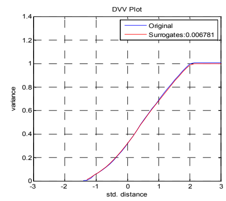

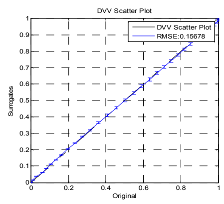

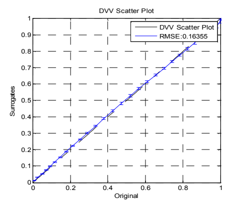

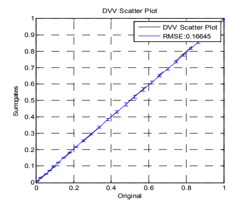

ζ=0.05 ζ=0.1 ζ=0.3

METHOD 3

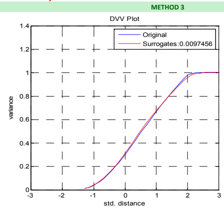

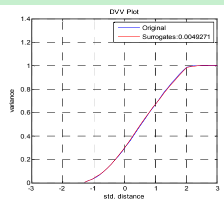

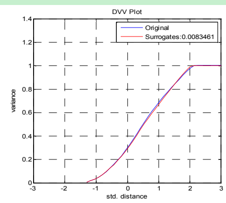

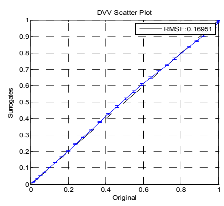

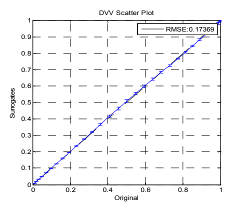

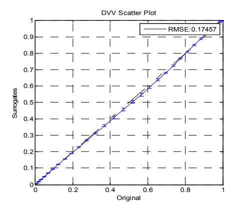

	SYSTEM	DETAILS	VARIABLES		METHOD 1				METHOD 2				METHOD 3			
				mass	best m	best τ	rmse	RMSE	calc m	τ	rmse	RMSE	set m	set τ	rmse	RMSE
15	SDOF SYSTEM WITH A ROTATING UNBALANCE VARYING MASS	SDOF having a rotating unbalance for zero initial conditions	rotating mass mo=3; damping ratio ζ=0.05; angular velocity of rot mass wr=4; natural fequency wn=12; time duration to test tf=10s; constant e=0.1	m=1	4	1	0.0152	0.1595	7	1	0.0056	0.1582	3	1	0.0043	0.1673
				m=3	4	1	0.0202	0.1595	8	1	0.0089	0.1607	3	1	0.0026	0.1674
				m=6	4	1	0.0202	0.1595	7	1	0.0058	0.1599	3	1	0.0026	0.1678

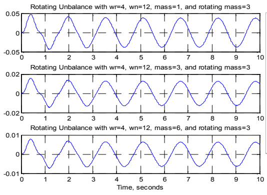

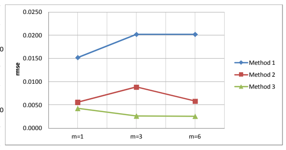

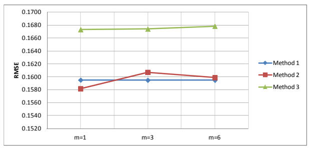

m=1 m=3 m=6

METHOD 1

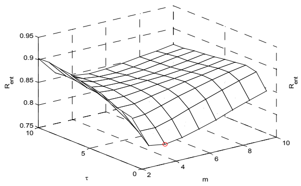
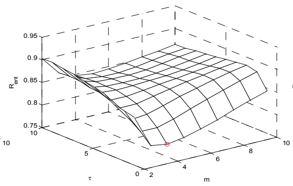
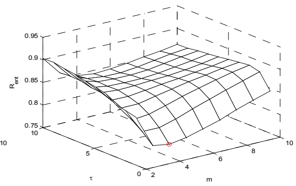

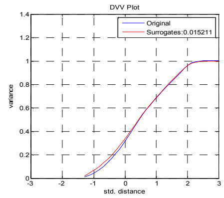

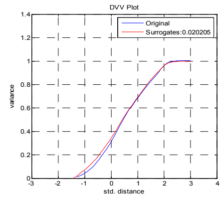

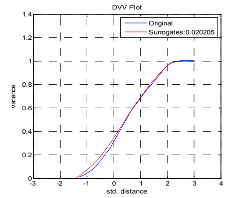

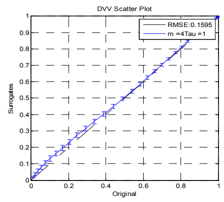

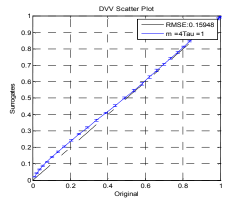

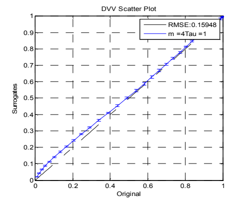

m=1 m=3 m=6

METHOD 2

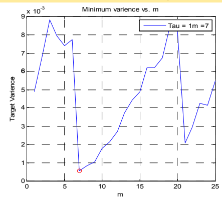

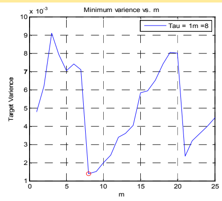

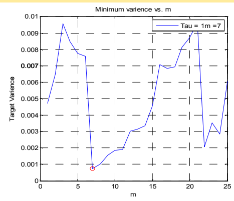

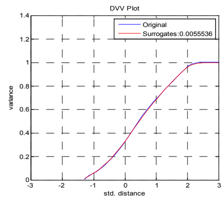

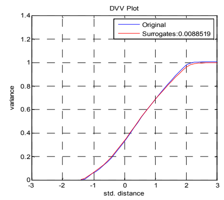

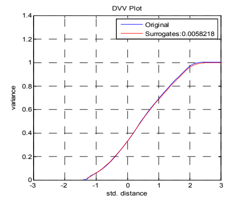

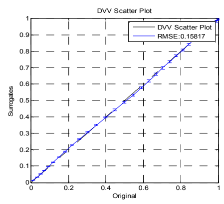

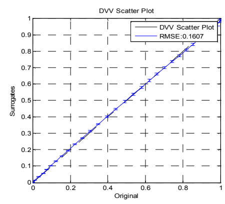

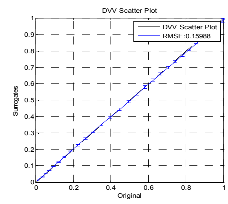

m=1 m=3 m=6

METHOD 3

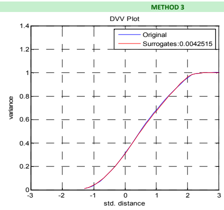

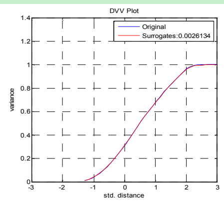

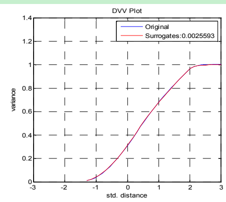

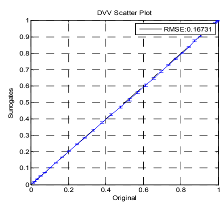

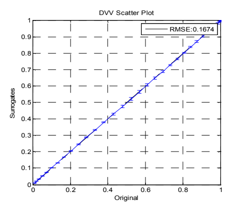

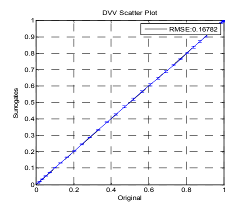

	SYSTEM	DETAILS	VARIABLES		METHOD 1				METHOD 2				METHOD 3			
				force mag	best m	best τ	rmse	RMSE	calc m	τ	rmse	RMSE	set m	set τ	rmse	RMSE
16	SDOF-STEP RESPONSE VARYING FORCE MAGNITUDE	SDOF with step response	initial time to=2; damping ratio ζ=0.05; natural fequency wn=12; time duration to test tf=10s; system mass m=1;	Fm=3	3	1	0.1690	0.3004	1	1	0.0256	0.3678	3	1	0.0364	0.3647
				Fm=7	3	1	0.1690	0.3004	1	1	0.0585	0.3636	3	1	0.0296	0.3588
				Fm=11	3	1	0.0364	0.3533	1	1	0.0265	0.3645	3	1	0.0592	0.3647

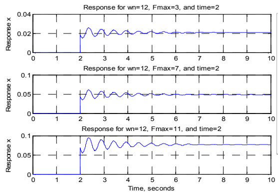

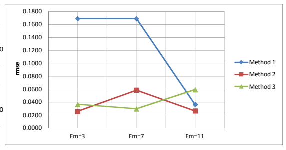

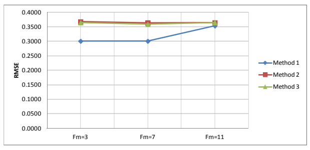

Fm=3 Fm=7 Fm=11

METHOD 1

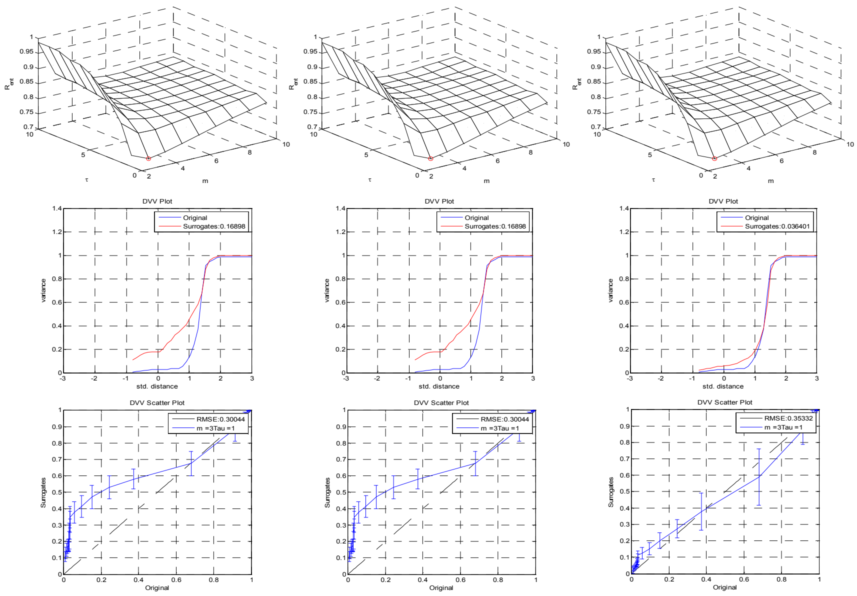

Fm=3 Fm=7 Fm=11

METHOD 2

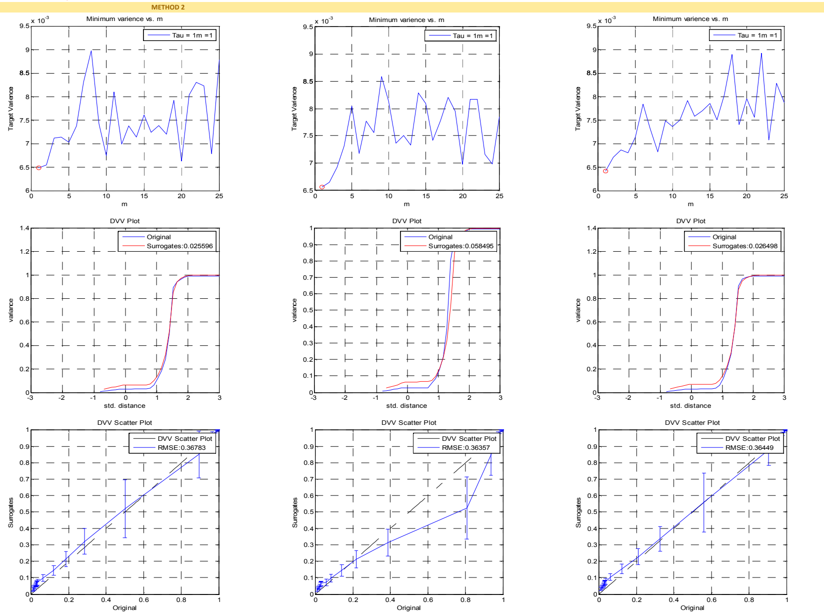

Fm=3 Fm=7 Fm=11

METHOD 3

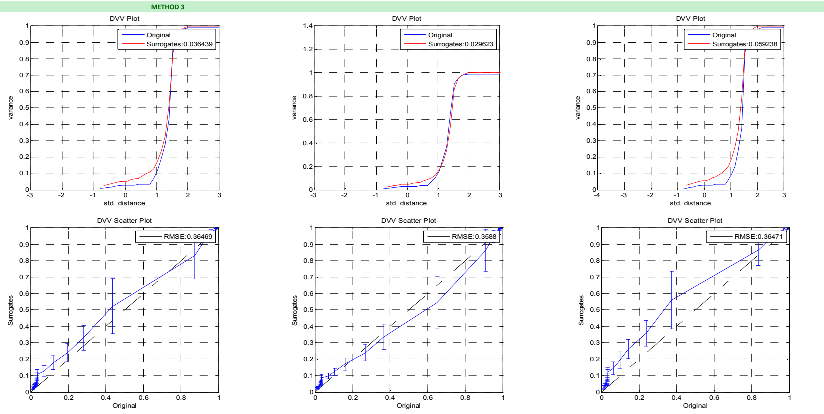

	SYSTEM	DETAILS	VARIABLES		METHOD 1				METHOD 2				METHOD 3			
				nat frequen	best m	best τ	rmse	RMSE	calc m	τ	rmse	RMSE	set m	set τ	rmse	RMSE
17	SDOF-STEP RESPONSE VARYING NATURAL FREQUENCY	SDOF having a step response	system mass m=1; damping ratio ζ=0.05; natural fequency wn=12; time duration to test tf=10s; force magnitude Fm=5; initial time to=2;	wn=2	3	1	0.0488	0.1475	2	1	0.0110	0.1628	3	1	0.0105	0.1626
				wn=6	3	1	0.0865	0.2209	1	1	0.0193	0.2567	3	1	0.0168	0.2534
				wn=12	3	1	0.1690	0.3004	1	1	0.0317	0.3662	3	1	0.0489	0.3632

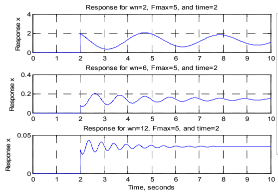

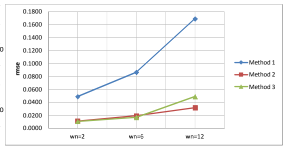

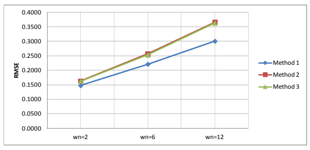

wn=2 wn=6 wn=12

METHOD 1

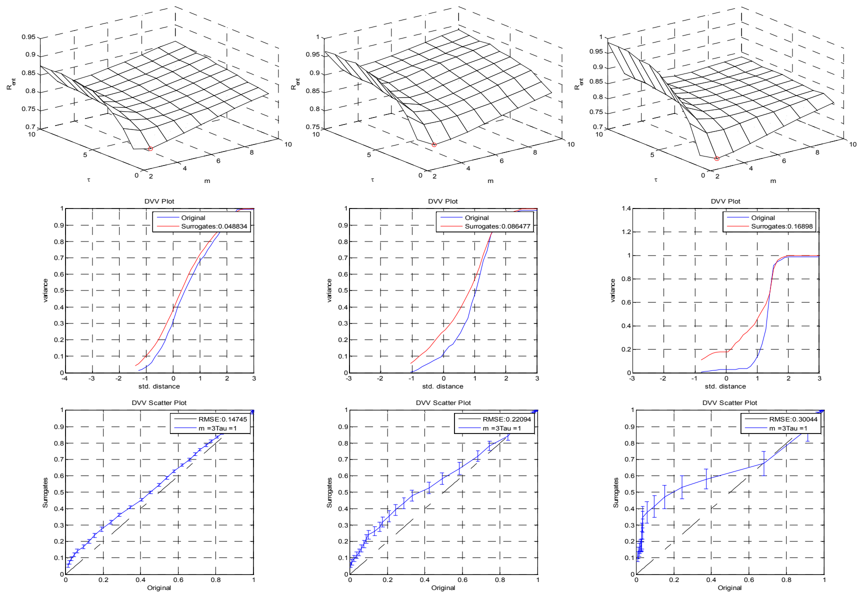

wn=2 wn=6 wn=12

METHOD 2

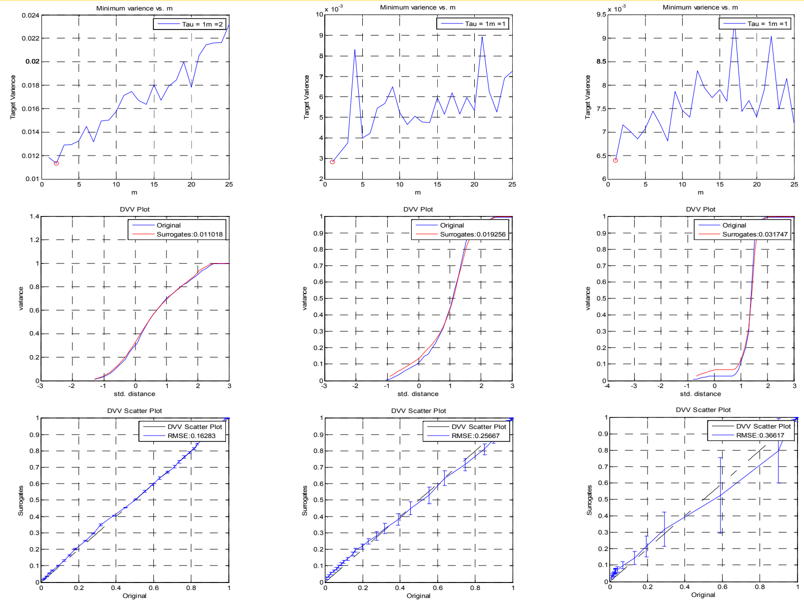

wn=2 wn=6 wn=12

METHOD 3

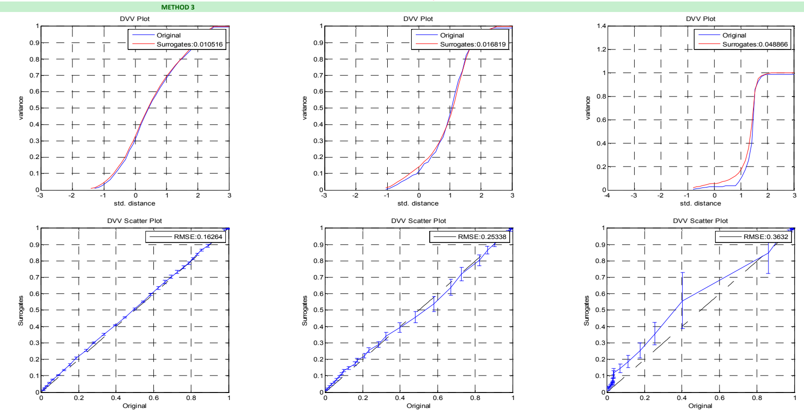

	SYSTEM	DETAILS	VARIABLES		METHOD 1				METHOD 2				METHOD 3			
				damping rat	best m	best τ	rmse	RMSE	calc m	τ	rmse	RMSE	set m	set τ	rmse	RMSE
18	SDOF-STEP RESPONSE VARYING DAMPING RATIO	SDOF having a step response	system mass m=1; natural fequency wn=12; time duration to test tf=10s; force magnitude Fm=5; initial time to=2;	ζ=0.05	3	1	0.1690	0.3004	1	1	0.0347	0.3757	3	1	0.0833	0.3732
				ζ=0.1	2	1	0.0353	0.4032	19	1	0.0881	0.3670	3	1	0.1318	0.4179
				ζ=0.3	2	1	0.0512	0.4191	6	1	0.1731	0.4233	3	1	0.0320	0.4253

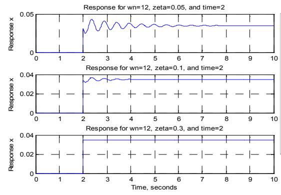

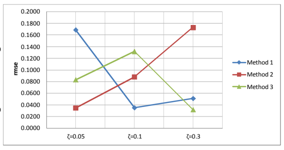

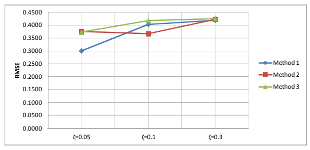

ζ=0.05 ζ=0.1 ζ=0.3

METHOD 1

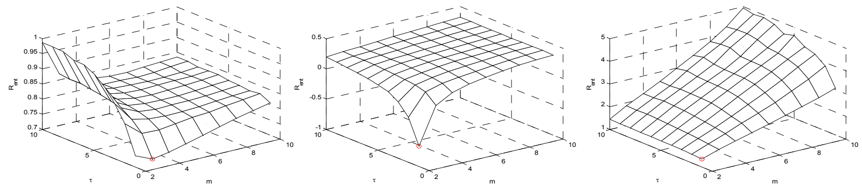

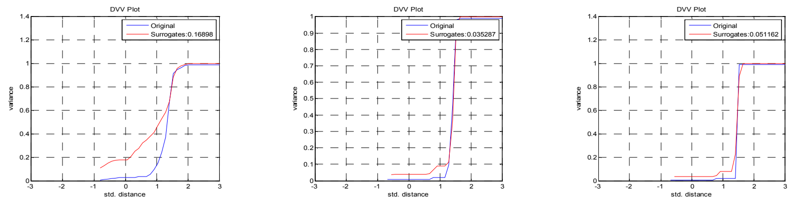

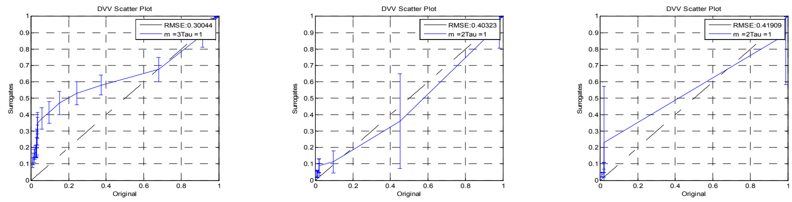

ζ=0.05 ζ=0.1 ζ=0.3

METHOD 2

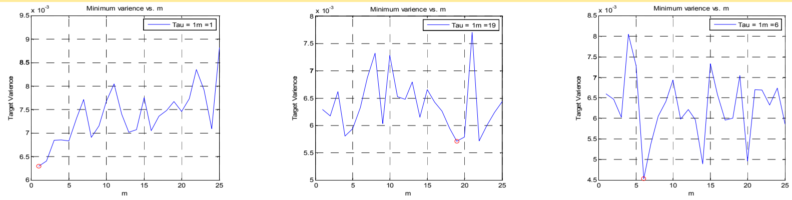

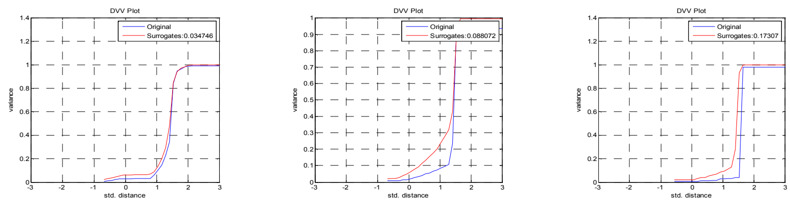

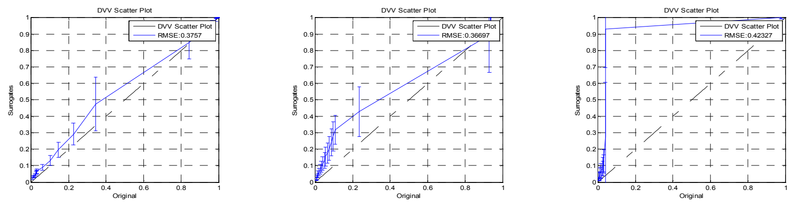

ζ=0.05 ζ=0.1 ζ=0.3

METHOD 3

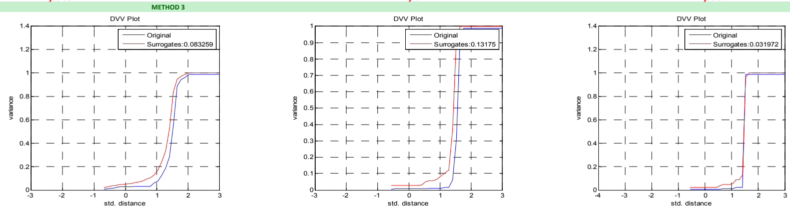

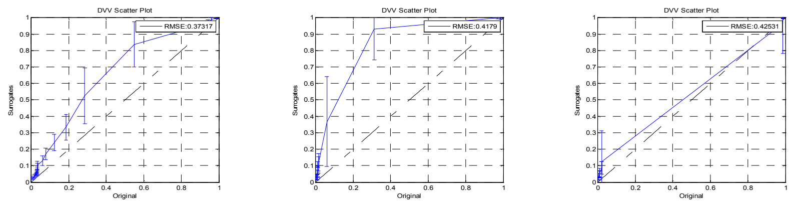

	SYSTEM	DETAILS	VARIABLES		METHOD 1				METHOD 2				METHOD 3			
				nat.freq.	best m	best τ	rmse	RMSE	calc m	τ	rmse	RMSE	set m	set τ	rmse	RMSE
19	SDOF SQUARE PULSE INPUTS VARYING NATURAL FREQUENCY	SDOF having a square wave input	system mass m=1; damping ratio ζ=0.05; time duration to test tf=10s; force magnitude Fm=5; wave starts at to=0; wave stops at to=3;	wn=2	4	1	0.0311	0.2394	3	1	0.0134	0.2502	3	1	0.0173	0.2490
				wn=6	6	10	0.2304	0.1718	1	1	0.0086	0.1917	3	1	0.0058	0.1903
				wn=12	9	10	0.4009	0.2187	4	1	0.0179	0.1875	3	1	0.0100	0.1876

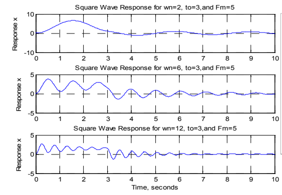

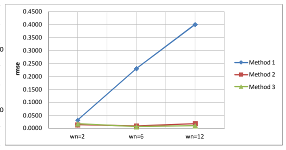

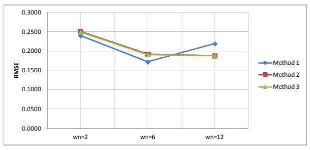

wn=2 wn=6 wn=12

METHOD 1

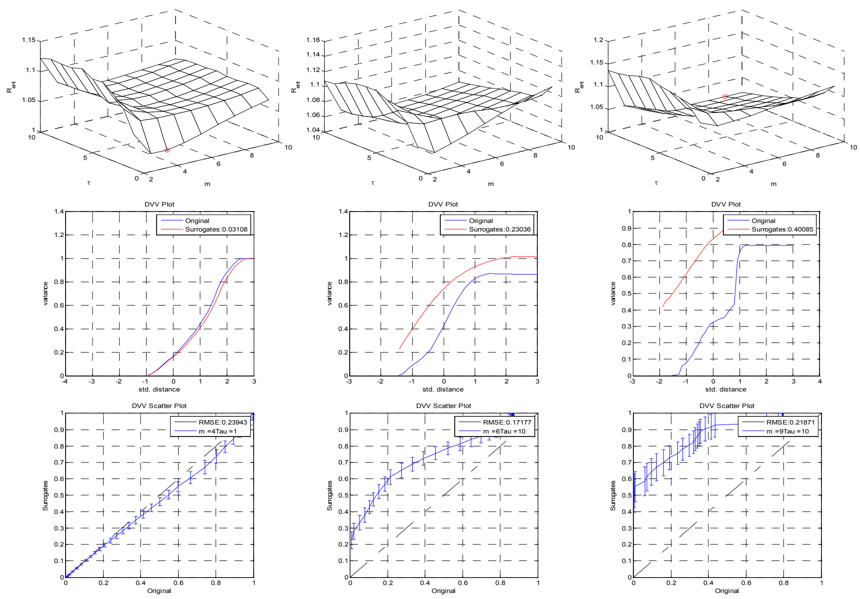

wn=2 wn=6 wn=12

METHOD 2

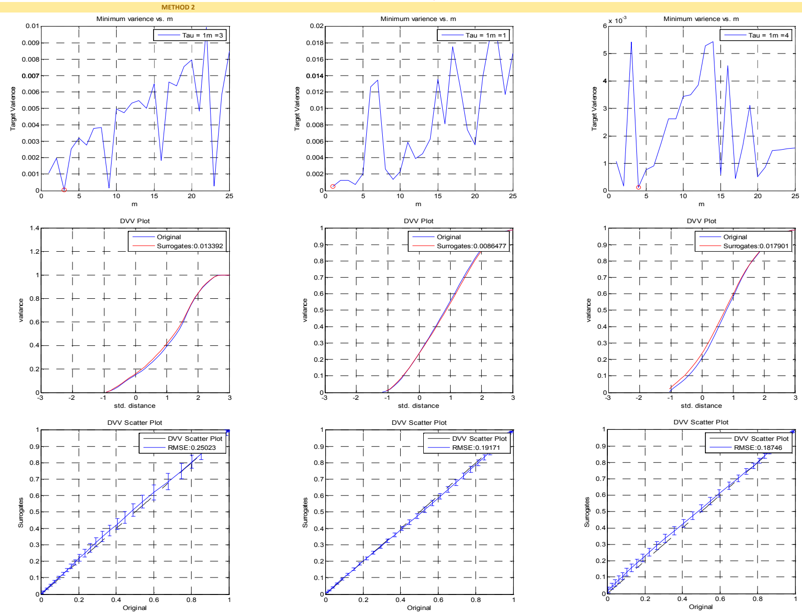

wn=2 wn=6 wn=12

METHOD 3

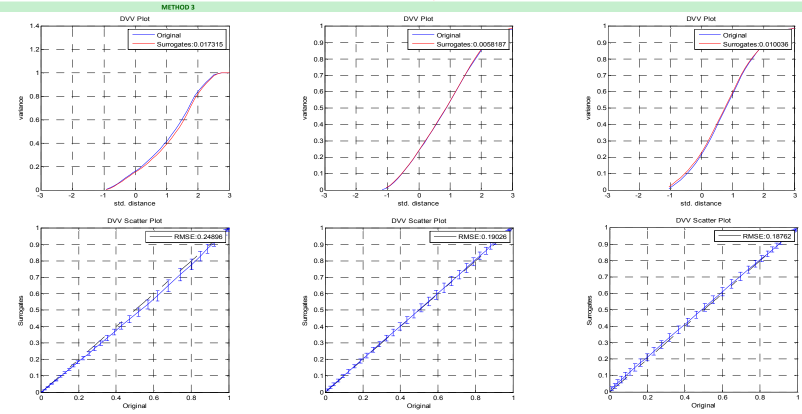

	SYSTEM	DETAILS	VARIABLES		METHOD 1				METHOD 2				METHOD 3			
				damping rat	best m	best τ	rmse	RMSE	calc m	τ	rmse	RMSE	set m	set τ	rmse	RMSE
20	SDOF SQUARE PULSE INPUTS VARYING DAMPING RATIO	SDOF having a square wave input	system mass m=1; natural frequency wn=12; time duration to test tf=10s; force magnitude Fm=7; wave starts at to=0; wave stops at to=3;	ζ=0.05	9	10	0.4009	0.2187	19	1	0.0359	0.1428	3	1	0.0095	0.1886
				ζ=0.1	10	10	0.4237	0.2176	3	1	0.0247	0.2544	3	1	0.0236	0.2544
				ζ=0.3	5	5	0.1207	0.2798	10	1	0.0270	0.3248	3	1	0.0085	0.3409

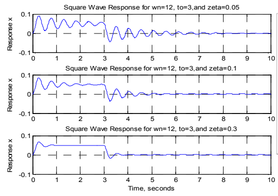

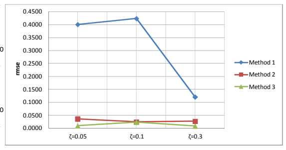

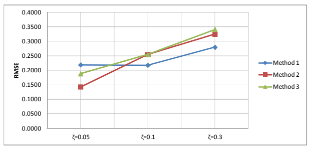

ζ=0.05 ζ=0.1 ζ=0.3

METHOD 1

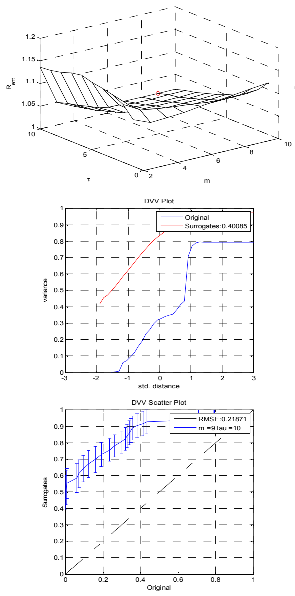

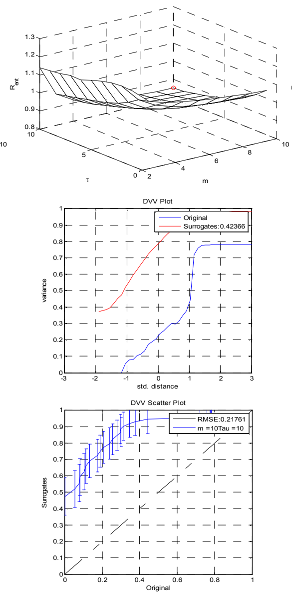

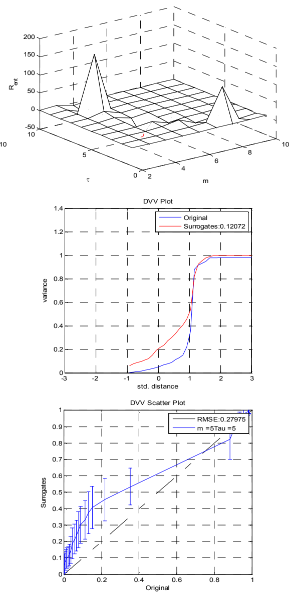

ζ=0.05 ζ=0.1 ζ=0.3

METHOD 2

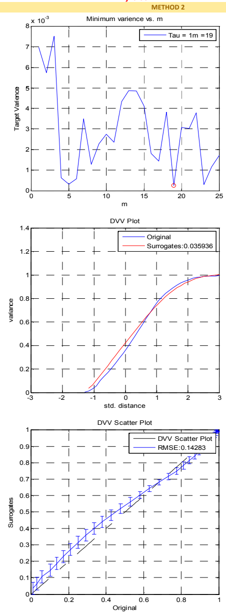

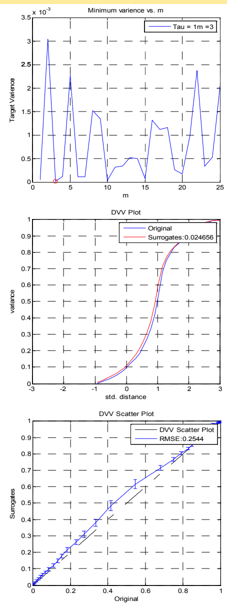

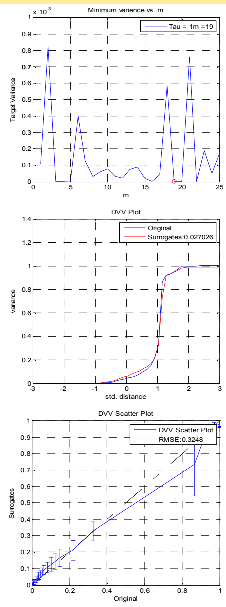

ζ=0.05 ζ=0.1 ζ=0.3

METHOD 3

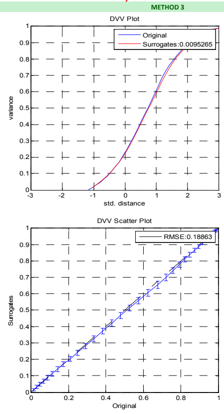

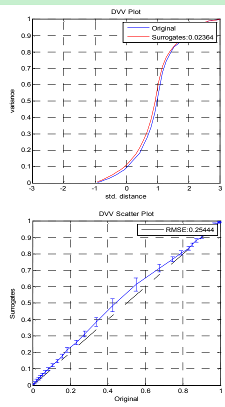

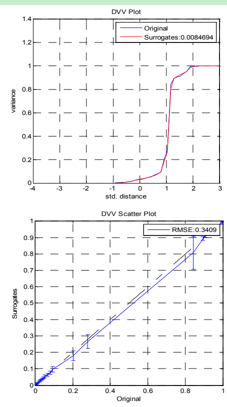

	SYSTEM	DETAILS	VARIABLES		METHOD 1				METHOD 2				METHOD 3			
				force magnitu	best m	best τ	rmse	RMSE	calc m	τ	rmse	RMSE	set m	set τ	rmse	RMSE
21	SDOF SQUARE PULSE INPUTS VARYING FORCE MAGNITUDE	SDOF having a square wave input	system mass m=1; natural frequency wn=12; time duration to test tf=10s; damping ratio ζ=0.05; wave starts at to=0; wave stops at to=3;	Fm=3	9	10	0.4009	0.2187	5	1	0.0051	0.1798	3	1	0.0074	0.1882
				Fm=7	9	10	0.4009	0.2187	3	1	0.0053	0.1906	3	1	0.0052	0.1892
				Fm=11	9	10	0.4009	0.2187	3	1	0.0130	0.1908	3	1	0.0096	0.1880

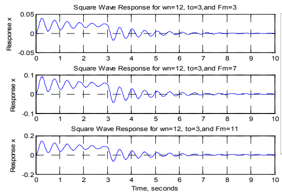

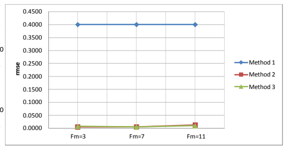

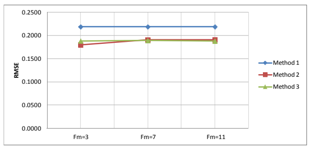

Fm=3 Fm=7 Fm=11

METHOD 1

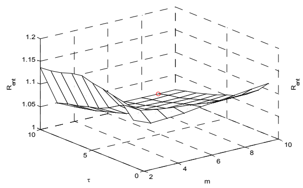
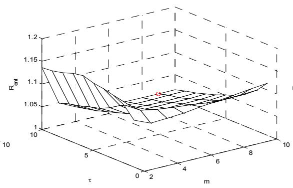
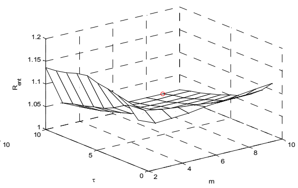

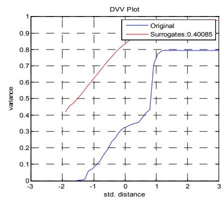

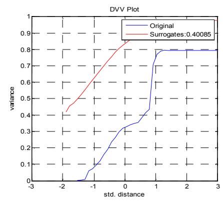

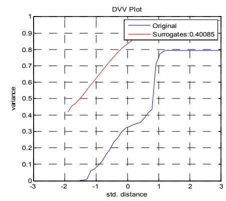

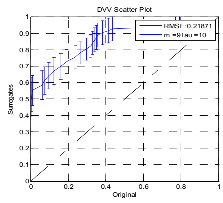

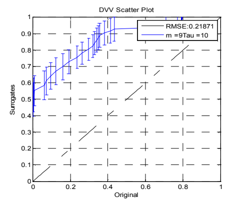

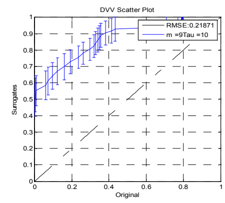

Fm=3 Fm=7 Fm=11

METHOD 2

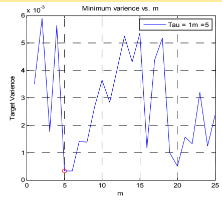

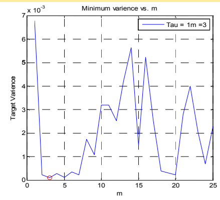

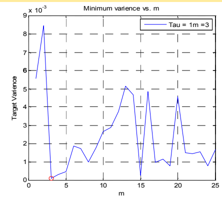

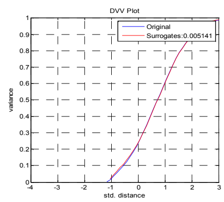

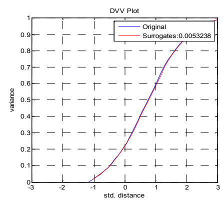

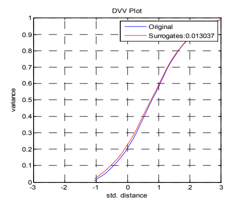

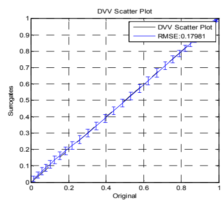

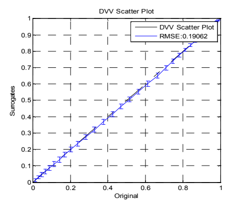

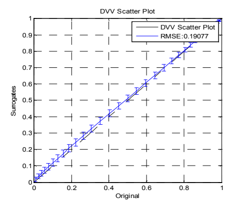

Fm=3 Fm=7 Fm=11

METHOD 3

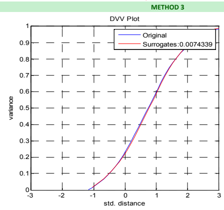

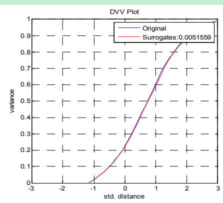

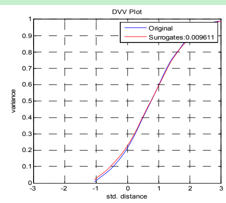

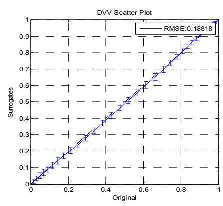

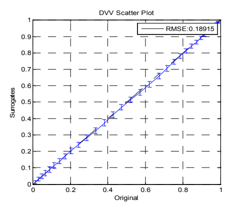

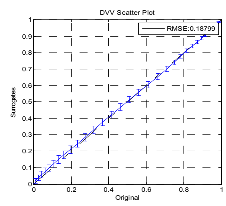

	SYSTEM	DETAILS	VARIABLES	force magnitu	METHOD 1 best m	METHOD 1 best τ	METHOD 1 rmse	METHOD 1 RMSE	METHOD 2 calc m	METHOD 2 τ	METHOD 2 rmse	METHOD 2 RMSE	METHOD 3 set m	METHOD 3 set τ	METHOD 3 rmse	METHOD 3 RMSE
22	SDOF RAMP INPUT VARYING RATE OF LOADING	SDOF having a ramp response external force F(t)=fo*t levels off at F=fo*te until infnity	system mass m=1; natural frequency wn=6; k=wn^2; wd=wn*sqrt(1-zeta^2); damping ratio ζ=0.05; force starts at to=0; force levels at at te=4;	fo=3	5	1	0.0442	0.1861	11	1	0.0183	0.1864	3	1	0.0101	0.1982
				fo=7	5	1	0.0442	0.1861	4	1	0.0107	0.1978	3	1	0.0062	0.1977
				fo=26	5	1	0.0442	0.1861	6	1	0.0069	0.1932	3	1	0.0073	0.1980

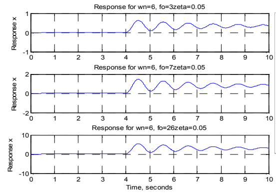

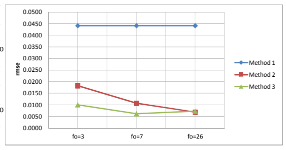

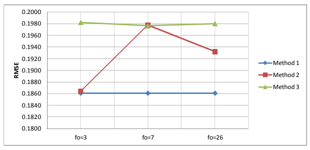

fo=3 fo=7 fo=26

METHOD 1

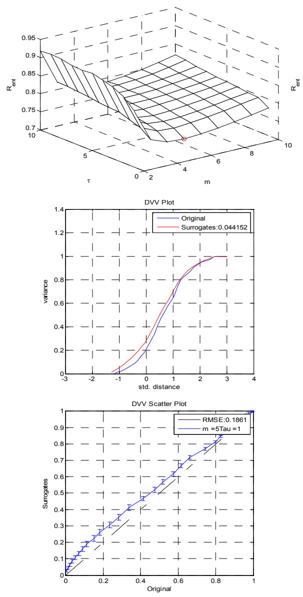

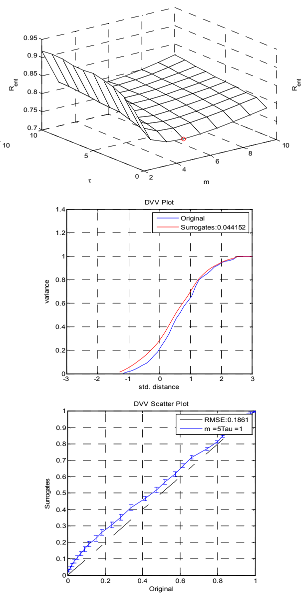

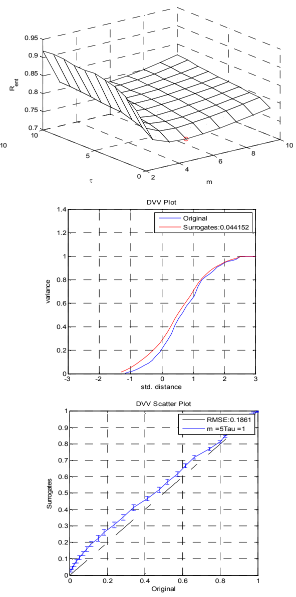

fo=3 fo=7 fo=26

METHOD 2

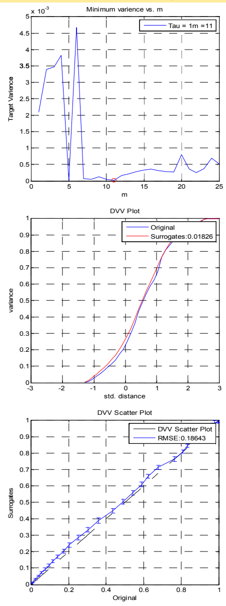

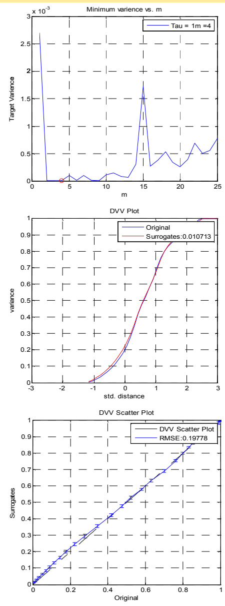

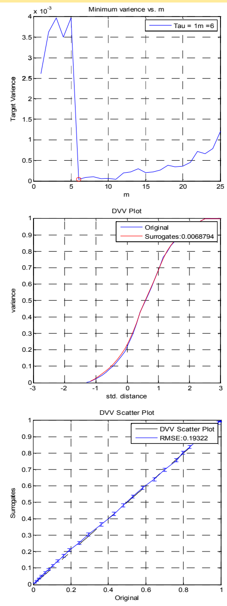

fo=3 fo=7 fo=26

METHOD 3

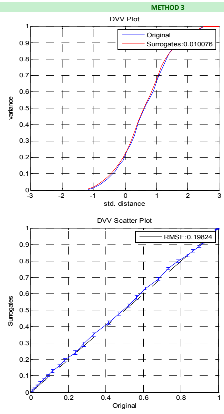

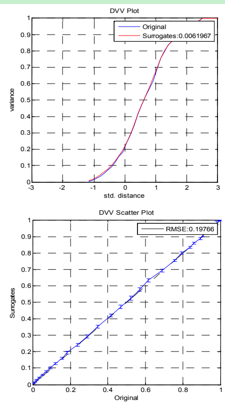

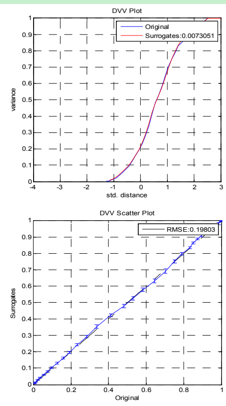

	SYSTEM	DETAILS	VARIABLES		METHOD 1				METHOD 2				METHOD 3			
				signal	best m	best τ	rmse	RMSE	calc m	τ	rmse	RMSE	set m	set τ	rmse	RMSE
23	VAN DER POL OSCILLATOR	van der Pol oscillator expression, x''+e(x^2-1)x'+x=0	e =0.5; initial conditions x0=[1; 0]; x(0)=1, x'(0)=0 time interval tf=30;	disp	2	1	0.0063	0.1667	3	1	0.0078	0.1534	3	1	0.0113	0.1554
				vel	2	1	0.1088	0.1082	1	1	0.0804	0.1218	3	1	0.1344	0.1136

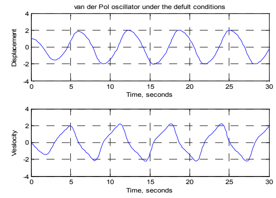

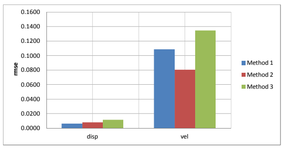

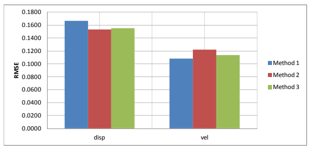

disp vel

METHOD 1

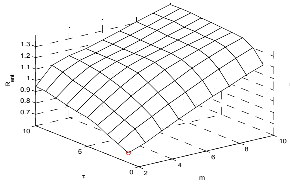

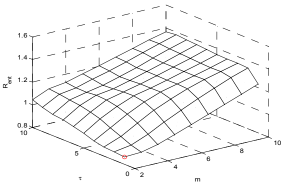

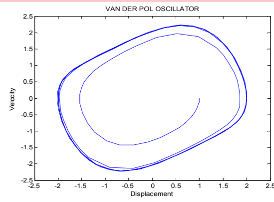

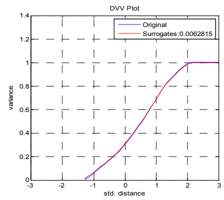

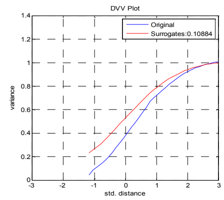

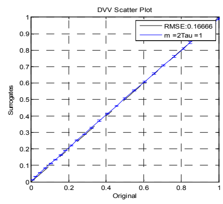

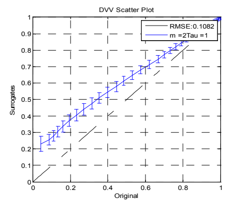

disp vel

METHOD 2

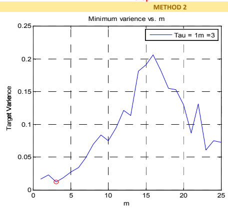

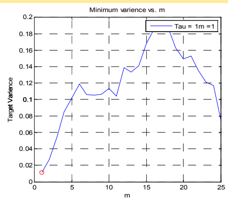

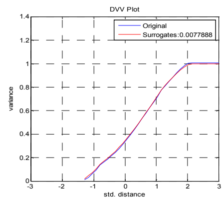

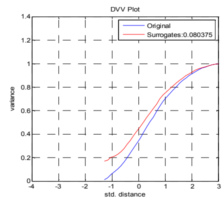

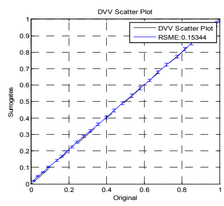

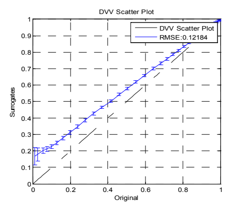

disp vel

METHOD 3

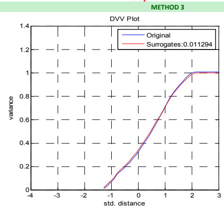

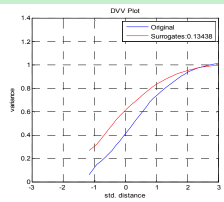

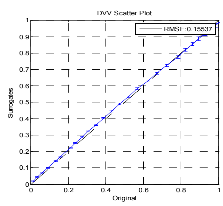

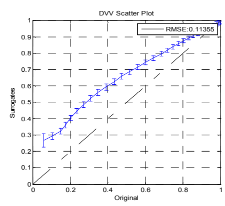

	SYSTEM	DETAILS	VARIABLES		METHOD 1				METHOD 2				METHOD 3			
				case	best m	best τ	rmse	RMSE	calc m	τ	rmse	RMSE	set m	set τ	rmse	RMSE
24	SDOF RANDOM VIBRATION	input: F(t)=Acos(omega*t+phi),	A is a random variable; distflag should be zero for uniform, and 1 for Gaussian distribution	case 1	4	1	0.0084	0.1541	18	1	0.0418	0.1220	3	1	0.0070	0.1556
			A=[0 to 5] for the uniform distribution, and as a distribution with mean of 2.5 for the Gaussian (won't be rigorously Gaussian).	case 2	2	1	0.0015	0.1560	1	1	0.0224	0.1534	3	1	0.0366	0.1391

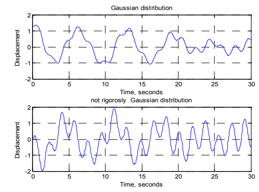

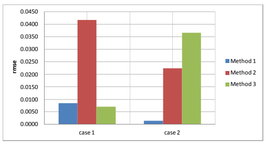

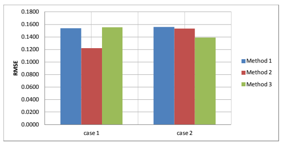

case 1 case 2

METHOD 1

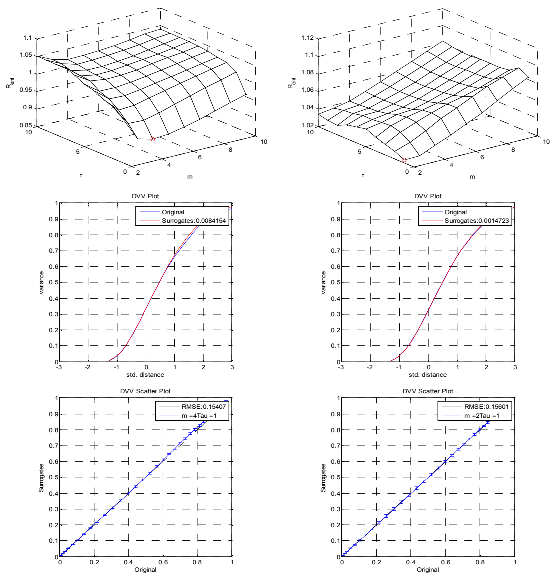

case 1 case 2

METHOD 2

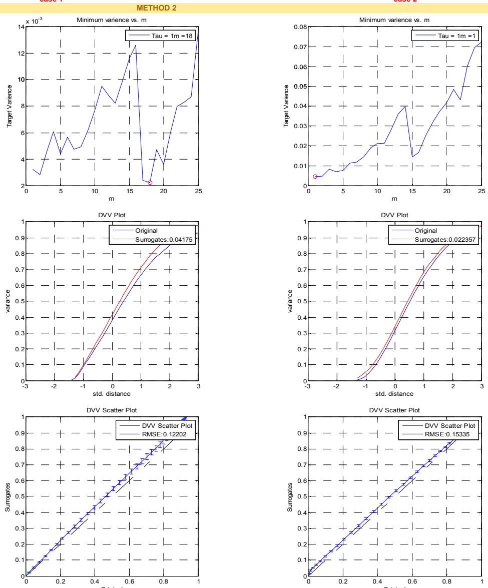

case 1 case 2

METHOD 3

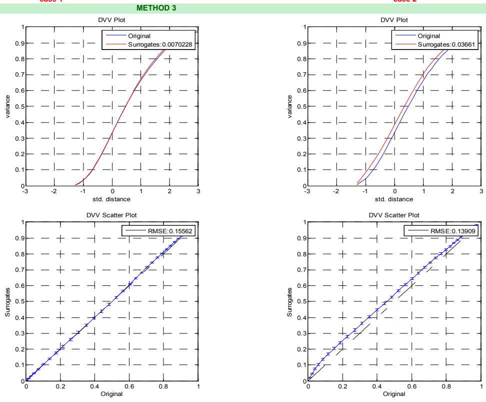

	SYSTEM	DETAILS	VARIABLES	case	METHOD 1 best m	METHOD 1 best τ	METHOD 1 rmse	METHOD 1 RMSE	METHOD 2 calc m	METHOD 2 τ	METHOD 2 rmse	METHOD 2 RMSE	METHOD 3 set m	METHOD 3 set τ	METHOD 3 rmse	METHOD 3 RMSE
25	SDOF RANDOMLY EXCITED DUFFING OSCILLATOR	Duffing oscillator	tspan=[0 30]; xinit=[0 0]'; e=0.01; c=0.05; k=1; A=3.7999; w=3.7960; chosen to prevent resonance	dis	3	1	0.0523	0.1252	1	1	0.0187	0.1435	3	1	0.0545	0.1252
				vel	4	1	0.0910	0.1316	10	1	0.1201	0.1712	3	1	0.0703	0.1365

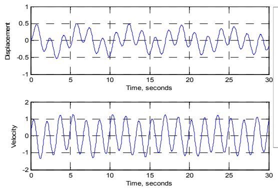

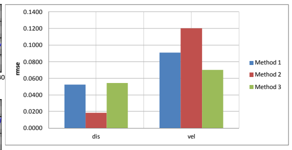

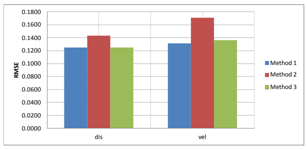

dis vel

METHOD 1

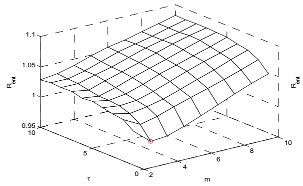

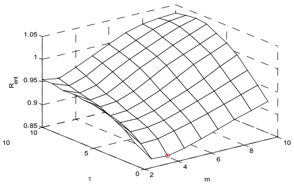

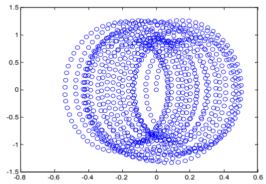

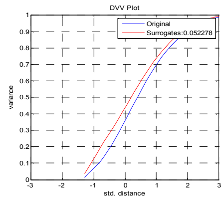

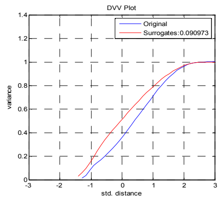

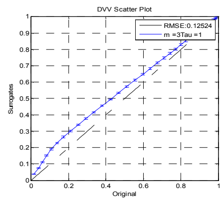

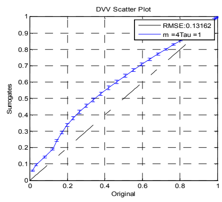

dis vel

METHOD 2

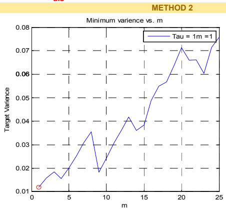

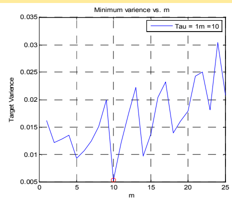

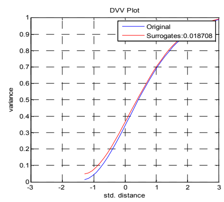

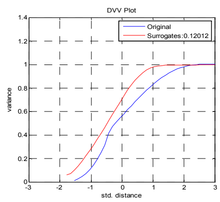

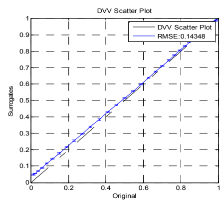

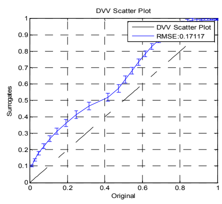

dis vel

METHOD 3

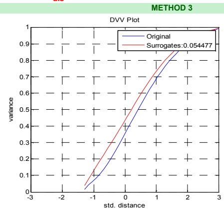

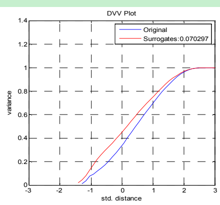

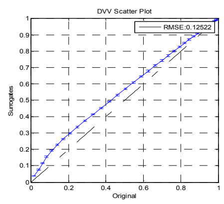

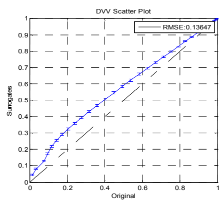

	SYSTEM	DETAILS	VARIABLES		METHOD 1				METHOD 2				METHOD 3			
				case	best m	best τ	rmse	RMSE	calc m	τ	rmse	RMSE	set m	set τ	rmse	RMSE
26	SDOF RANDOMLY EXCITED DUFFING OSCILLATOR	Duffing oscillator	tspan=[0 30]; xinit=[0 0]'; e=0.01; c=0.05; k=1; A=4.4351; w=1.7404; chosen to prevent resonance	dis	6	1	0.0332	0.1452	16	1	0.0106	0.1342	3	1	0.0090	0.1573
				vel	5	1	0.0266	0.1450	20	1	0.0965	0.1187	3	1	0.0269	0.1548

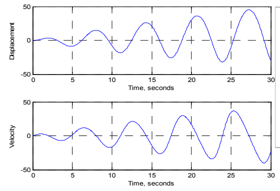

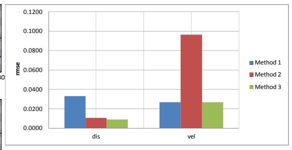

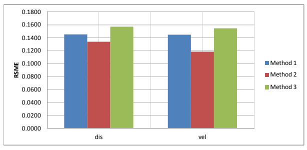

dis
METHOD 1
vel

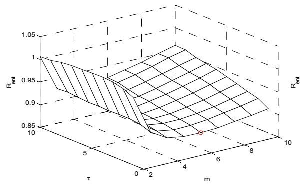

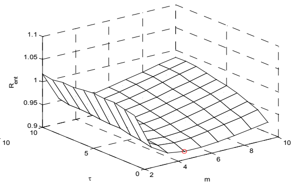

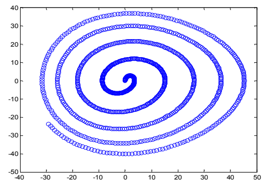

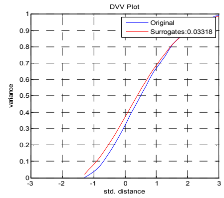

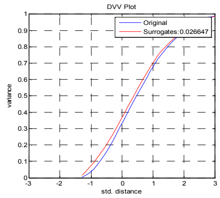

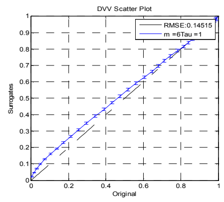

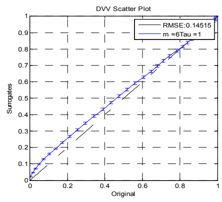

dis
METHOD 2
vel

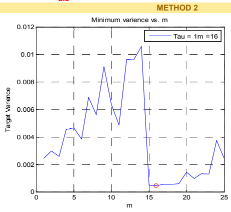

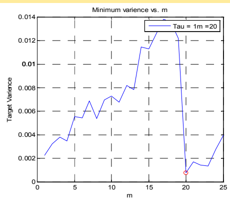

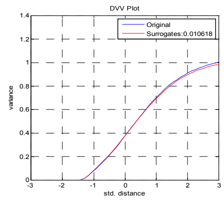

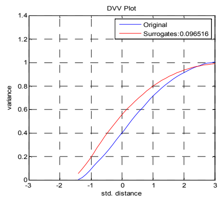

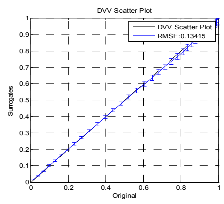

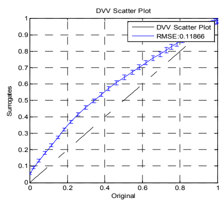

dis
METHOD 3
vel

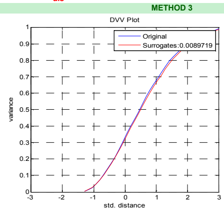

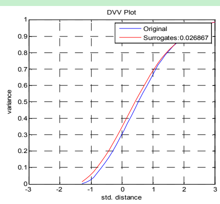

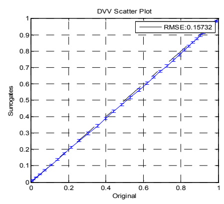

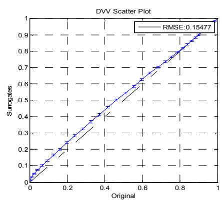

	SYSTEM	DETAILS	VARIABLES	case	METHOD 1 best m	METHOD 1 best τ	METHOD 1 rmse	METHOD 1 RMSE	METHOD 2 calc m	METHOD 2 τ	METHOD 2 rmse	METHOD 2 RMSE	METHOD 3 set m	METHOD 3 set τ	METHOD 3 rmse	METHOD 3 RMSE
27	SDOF RANDOMLY EXCITED DUFFING OSCILLATOR	Duffing oscillator	tspan=[0 30]; xinit=[0 0]'; e=0.01; c=0.05; k=1; A=1.0062; w=2.0115; chosen to prevent resonance	dis	4	1	0.0376	0.1507	1	1	0.0153	0.1656	3	1	0.0379	0.1579
				vel	3	1	0.0245	0.1484	10	1	0.0079	0.1318	3	1	0.0035	0.1560

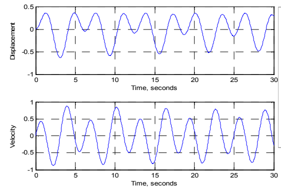

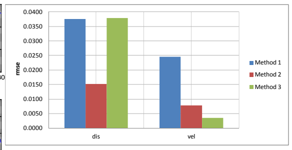

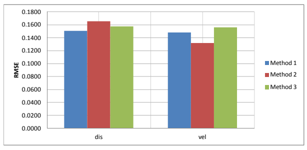

dis | vel

METHOD 1

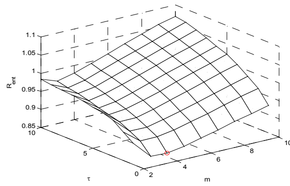

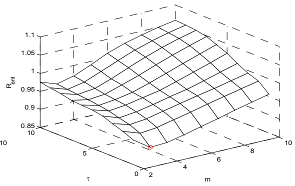

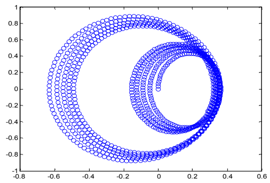

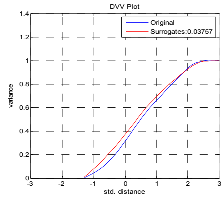

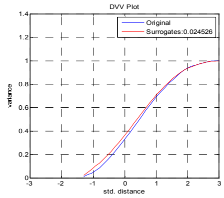

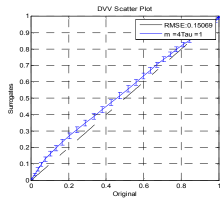

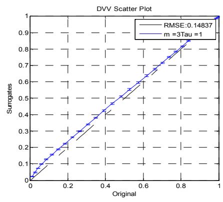

dis | vel

METHOD 2

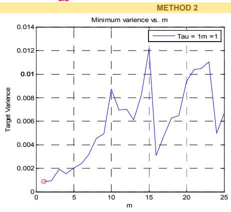

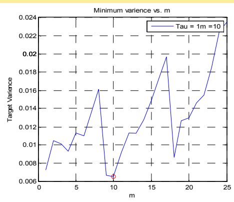

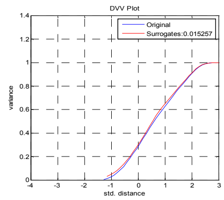

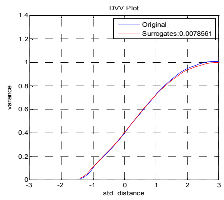

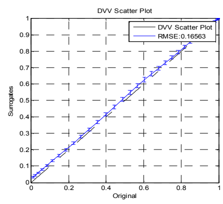

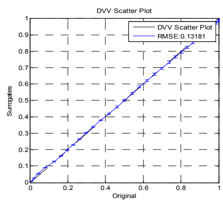

dis | vel

METHOD 3

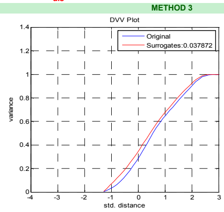

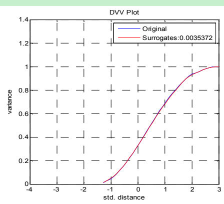

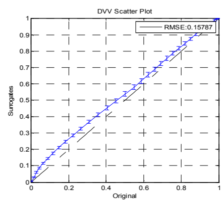

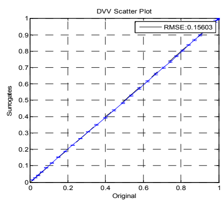

APPENDIX B3

Delay Vector Variance Method SDOF Car Experiment Results

	SYSTEM	VARIABLES		METHOD 1				METHOD 2				METHOD 3			
				best m	best τ	rsme	RSME	calc m	τ	rsme	RSME	calc m	τ	rsme	RSME
1	SDOF CAR attached to fixed supports by 6 calibrated springs (3 on each side)	surface wood; number of springs 2 x 3; loading harmonic 2Hz	CH1	5	10	0.3538	0.3800	19	1	0.1669	0.1712	3	1	0.0760	0.1182
			CH2	2	3	0.2853	0.3461	9	1	0.2991	0.3017	3	1	0.2429	0.2713
			CH3	2	4	0.0071	0.4538	21	1	0.0375	0.5017	3	1	0.0088	0.4579
			LDVg	5	1	0.0861	0.1384	6	1	0.0097	0.1256	3	1	0.0763	0.1186
			LDV1	3	10	0.0562	0.1599	20	1	0.0519	0.1932	3	1	0.0073	0.1467
2	SDOF CAR attached to fixed supports by 6 calibrated springs (3 on each side)	surface wood; number of springs 2 x 3; loading harmonic 2-4-6-8-10 Hz	CH1	5	9	0.2918	0.1763	17	1	0.1821	0.1349	3	1	0.1537	0.1416
			CH2	10	1	0.4714	0.3659	15	1	0.5078	0.3839	3	1	0.3069	0.3176
			CH3	9	1	0.4371	0.2938	24	1	0.5226	0.3441	3	1	0.2395	0.2839
			LDVg	8	5	0.2085	0.1758	5	1	0.0277	0.1421	3	1	0.0303	0.1386
			LDV1	6	5	0.4141	0.2822	21	1	0.3169	0.2037	3	1	0.2106	0.1716
3	SDOF CAR attached to fixed supports by 6 calibrated springs (3 on each side)	surface plastic (smooth) number of springs 2 x 3; loading harmonic 2-4-6-8-10 Hz	CH1	4	10	0.2571	0.1755	11	1	0.1748	0.1235	3	1	0.2326	0.1279
			CH2	10	1	0.4215	0.2985	14	1	0.4728	0.3259	3	1	0.2326	0.2729
			CH3	10	1	0.3278	0.2016	19	1	0.4009	0.2342	3	1	0.1274	0.2131
			LDVg	9	5	0.2006	0.1526	15	1	0.0743	0.1285	3	1	0.0336	0.1340
			LDV1	6	5	0.4473	0.3014	5	1	0.2631	0.1786	3	1	0.1406	0.1675
4	SDOF CAR attached to fixed supports by 6 calibrated springs (3 on each side)	surface wood number of springs 2 x 3; loading Sine Sweep	CH1	4	10	0.3245	0.1879	25	1	0.2112	0.1329	3	1	0.1167	0.1327
			CH2	10	2	0.4291	0.3725	22	1	0.4903	0.3679	3	1	0.2855	0.3344
			CH3	9	1	0.4660	0.2979	13	1	0.4939	0.3062	3	1	0.2418	0.2878
			LDVg	10	3	0.3765	0.2964	17	1	0.0839	0.1140	3	1	0.0320	0.1272
			LDV1	9	4	0.3671	0.2911	11	1	0.2483	0.1759	3	1	0.1722	0.1654
5	SDOF CAR attached to fixed supports by 6 calibrated springs (3 on each side)	surface wood number of springs 2 x 3; loading White Noise	CH1	7	1	0.1448	0.1130	9	1	0.1392	0.1295	3	1	0.1344	0.1141
			CH2	6	1	0.2556	0.3944	14	1	0.3764	0.3937	3	1	0.1444	0.3790
			CH3	7	1	0.3480	0.3566	10	1	0.3926	0.3682	3	1	0.1853	0.3566
			LDVg	6	1	0.0703	0.2926	10	1	0.1983	0.4177	3	1	0.2496	0.3423
			LDV1	3	1	0.0052	0.1550	3	1	0.1789	0.2018	3	1	0.1805	0.2045
6	SDOF CAR attached to fixed supports by 6 calibrated springs (3 on each side)	surface plastic (smooth) number of springs 2 x 3; loading Sine Sweep	CH1	4	10	0.2964	0.1693	23	1	0.1757	0.1291	3	1	0.1165	0.1448
			CH2	10	2	0.3993	0.3150	16	1	0.3979	0.2878	3	1	0.2521	0.2645
			CH3	10	1	0.3018	0.1605	14	1	0.2986	0.1663	3	1	0.1607	0.1612
			LDVg	10	6	0.2407	0.2245	6	1	0.0417	0.1360	3	1	0.0289	0.1296
			LDV1	8	10	0.4237	0.3596	6	1	0.2396	0.1734	3	1	0.1724	0.1652
7	SDOF CAR attached to fixed supports by 6 calibrated springs (3 on each side)	surface plastic (smooth) number of springs 2 x 3; loading White Noise	CH1	6	1	0.1415	0.1096	13	1	0.1231	0.1480	3	1	0.1145	0.1007
			CH2	6	1	0.3002	0.3599	14	1	0.3477	0.3946	3	1	0.1855	0.3481
			CH3	7	1	0.2142	0.1943	14	1	0.2655	0.2077	3	1	0.0841	0.2121
			LDVg	6	1	0.2506	0.3666	4	1	0.2516	0.3528	3	1	0.2431	0.3397
			LDV1	2	3	0.2555	0.2630	3	1	0.1849	0.2014	3	1	0.1942	0.2013
8	SDOF CAR attached to fixed supports by 6 calibrated springs (3 on each side)	surface sand paper (rough) number of springs 2 x 3; loading White Noise	CH1	6	1	0.1395	0.1110	5	1	0.1363	0.1030	3	1	0.1236	0.0964
			CH2	3	8	0.0632	0.4353	12	1	0.3188	0.4012	3	1	0.1377	0.3934
			CH3	4	4	0.0432	0.3464	7	1	0.1167	0.2232	3	1	0.0657	0.2730
			LDVg	6	1	0.1901	0.4007	9	1	0.1931	0.4276	3	1	0.1886	0.3663
			LDV1	5	1	0.1922	0.1463	17	1	0.2249	0.2143	3	1	0.1933	0.2026
9	SDOF CAR attached to fixed supports by 6 calibrated springs (3 on each side)	surface sand paper (rough) number of springs 2 x 3; loading Sine Sweep	CH1	5	9	0.2844	0.1682	4	1	0.1280	0.1360	3	1	0.1015	0.1308
			CH2	10	1	0.4205	0.3643	7	1	0.3815	0.3498	3	1	0.2444	0.3234
			CH3	10	1	0.3147	0.1674	18	1	0.3119	0.1823	3	1	0.1763	0.1581
			LDVg	10	3	0.1551	0.1549	15	1	0.0677	0.1084	3	1	0.0391	0.1260
			LDV1	9	4	0.3675	0.2888	22	1	0.2944	0.2135	3	1	0.1745	0.1623
10	SDOF CAR attached to fixed supports by 6 calibrated springs (3 on each side)	surface sand paper (rough) number of springs 2 x 3; loading harmonic 2-4-6-8-10 Hz	CH1	3	9	0.2816	0.1670	14	1	0.1980	0.1349	3	1	0.1458	0.1328
			CH2	8	1	0.3732	0.3401	11	1	0.4204	0.3552	3	1	0.2067	0.3402
			CH3	8	1	0.3422	0.1905	12	1	0.3237	0.2037	3	1	0.1902	0.2038
			LDVg	8	5	0.2355	0.1912	11	1	0.0542	0.1181	3	1	0.0303	0.1316
			LDV1	6	5	0.2460	0.1848	12	1	0.2924	0.1828	3	1	0.2012	0.1681
11	SDOF CAR attached to fixed supports by 4 calibrated springs (2 on each side)	surface sand paper (rough) Middle spring taken out number of springs 2 x2; loading harmonic 2-4-6-8-10 Hz	CH1	4	10	0.3958	0.2010	10	1	0.2735	0.1514	3	1	0.2079	0.1548
			CH2	10	1	0.6419	0.3674	20	1	0.6193	0.3486	3	1	0.5733	0.3291
			CH3	10	1	0.2980	0.1626	19	1	0.2564	0.1484	3	1	0.3044	0.1883
			LDVg	8	6	0.2343	0.1855	14	1	0.0675	0.1175	3	1	0.0235	0.1102
			LDV1	7	5	0.2680	0.1687	14	1	0.1438	0.1134	3	1	0.0710	0.0978
12	SDOF CAR attached to fixed supports by 4 calibrated springs (2 on each side)	surface sand paper (rough) Middle spring taken out number of springs 2 x2; loading Sine Sweep	CH1	4	10	0.2691	0.1546	9	1	0.1486	0.1102	3	1	0.1325	0.1415
			CH2	10	3	0.5232	0.2775	15	1	0.5250	0.2838	3	1	0.4094	0.2149
			CH3	10	1	0.3269	0.1693	14	1	0.3390	0.1803	3	1	0.1057	0.1350
			LDVg	8	3	0.1022	0.1263	8	1	0.0302	0.1164	3	1	0.0276	0.1029
			LDV1	7	7	0.1367	0.1063	24	1	0.0805	0.1195	3	1	0.0141	0.0981
13	SDOF CAR attached to fixed supports by 4 calibrated springs (2 on each side) REPEATED EXPERIMENT NO.12	surface sand paper (rough) Middle spring taken out number of springs 2 x2; loading Sine Sweep	CH1	4	10	0.2932	0.1736	19	1	0.1795	0.1250	3	1	0.1026	0.1393
			CH2	10	3	0.4319	0.3034	13	1	0.4338	0.2673	3	1	0.2973	0.2284
			CH3	9	1	0.2023	0.1111	15	1	0.2177	0.1216	3	1	0.1123	0.0981
			LDVg	8	3	0.1056	0.1260	20	1	0.0875	0.1072	3	1	0.0357	0.1047
			LDV1	7	5	0.1701	0.1632	12	1	0.2371	0.1559	3	1	0.1701	0.1410
14	SDOF CAR attached to fixed supports by 4 calibrated springs (2 on each side)	surface sand paper (rough) Middle spring taken out number of springs 2 x2; loading White Noise	CH1	6	1	0.1597	0.1052	21	1	0.1710	0.1335	3	1	0.1340	0.1064
			CH2	5	1	0.3213	0.3289	14	1	0.4115	0.3509	3	1	0.2359	0.3252
			CH3	3	6	0.0762	0.2905	25	1	0.1015	0.1225	3	1	0.0583	0.1759
			LDVg	6	1	0.0144	0.2840	4	1	0.1934	0.3564	3	1	0.2385	0.3479
			LDV1	4	1	0.2109	0.1760	8	1	0.2282	0.1448	3	1	0.1994	0.1780
15	SDOF CAR attached to fixed supports by 4 calibrated springs (2 on each side)	surface plastic (smooth) Middle spring taken out number of springs 2 x2; loading White Noise	CH1	4	1	0.1428	0.1078	7	1	0.1520	0.1053	3	1	0.1312	0.1118
			CH2	4	5	0.1913	0.3615	19	1	0.3416	0.2899	3	1	0.1730	0.2628
			CH3	8	1	0.2986	0.3386	10	1	0.2631	0.2176	3	1	0.1307	0.2297
			LDVg	6	1	0.0212	0.2731	9	1	0.1961	0.4149	3	1	0.2533	0.3451
			LDV1	2	1	0.1941	0.1550	11	1	0.2138	0.1470	3	1	0.1862	0.1727
16	SDOF CAR attached to fixed supports by 4 calibrated springs (2 on each side)	surface plastic (smooth) Middle spring taken out number of springs 2 x2; loading Sine Sweep	CH1	5	9	0.2767	0.1552	17	1	0.1652	0.1195	3	1	0.0990	0.1493
			CH2	10	2	0.3390	0.2481	13	1	0.3118	0.2162	3	1	0.2198	0.2020
			CH3	10	1	0.3098	0.1654	18	1	0.3506	0.1856	3	1	0.1513	0.1137
			LDVg	8	3	0.0936	0.1236	19	1	0.0688	0.1058	3	1	0.0306	0.1046
			LDV1	8	5	0.1726	0.1714	21	1	0.2837	0.1924	3	1	0.1688	0.1401

	SYSTEM	VARIABLES		METHOD 1				METHOD 2				METHOD 3			
				best m	best τ	rsme	RSME	calc m	τ	rsme	RSME	calc m	τ	rsme	RSME
17	SDOF CAR attached to fixed supports by 4 calibrated springs (2 on each side)	surface plastic (smooth) Middle spring taken out number of springs 2 x2; loading harmonic 2-4-6-8-10 Hz	CH1						~~1~~			~~3~~	~~1~~		
			CH2						~~1~~			~~3~~	~~1~~		
			CH3						~~1~~			~~3~~	~~1~~		
			LDVg	8	7	0.4169	0.2947	9	1	0.0295	0.1135	3	1	0.0213	0.1132
			LDV1	6	6	0.3819	0.2660	11	1	0.2797	0.1535	3	1	0.2075	0.1473
18	SDOF CAR attached to fixed supports by 4 calibrated springs (2 on each side)	surface wood Middle spring taken out number of springs 2 x2; loading harmonic 2-4-6-8-10 Hz	CH1	4	10	0.3734	0.1949	2	1	0.2415	0.1973	3	1	0.2609	0.2021
			CH2	9	1	0.6737	0.3737	25	1	0.7082	0.3989	3	1	0.6603	0.3757
			CH3	5	2	0.3453	0.1859	8	1	0.2877	0.1577	3	1	0.2672	0.1497
			LDVg	9	7	0.4325	0.3138	17	1	0.0782	0.1186	3	1	0.0362	0.1067
			LDV1	7	5	0.2536	0.1535	3	1	0.0788	0.0906	3	1	0.0824	0.0909
19	SDOF CAR attached to fixed supports by 4 calibrated springs (2 on each side)	surface wood Middle spring taken out number of springs 2 x2; loading White Noise	CH1	6	2	0.1763	0.1301	10	1	0.1571	0.1116	3	1	0.1344	0.1141
			CH2	4	1	0.2821	0.3305	22	1	0.4097	0.3801	3	1	0.2458	0.3314
			CH3	4	1	0.2183	0.2895	24	1	0.4016	0.3327	3	1	0.1942	0.2893
			LDVg	6	1	0.2554	0.3742	3	1	0.2775	0.3400	3	1	0.2496	0.3423
			LDV1	2	4	0.2657	0.2551	9	1	0.2023	0.1411	3	1	0.1988	0.1703
20	SDOF CAR attached to fixed supports by 4 calibrated springs (2 on each side)	surface wood Middle spring taken out number of springs 2 x2; loading Sine Sweep	CH1	5	10	0.2834	0.1563	10	1	0.1620	0.1213	3	1	0.1279	0.1515
			CH2	10	1	0.4544	0.3182	12	1	0.4903	0.3278	3	1	0.3329	0.2866
			CH3	4	1	0.3403	0.2314	25	1	0.5086	0.2976	3	1	0.2175	0.2418
			LDVg	9	3	0.1069	0.1251	17	1	0.0593	0.1081	3	1	0.0348	0.1059
			LDV1	8	5	0.1804	0.1634	14	1	0.2493	0.1649	3	1	0.1649	0.1388
21	SDOF CAR attached to fixed supports by 6 / 4 calibrated springs; Two middle springs are glued, detached at 13 sec / 38sec	surface wood Two middle springs are glued, detached at 13 sec / 38sec number of springs 2x3 / 2 x2; loading White Noise	CH1	6	1	0.1562	0.1031	6	1	0.1554	0.1043	3	1	0.1335	0.1079
			CH2	4	4	0.2074	0.3631	19	1	0.3613	0.3404	3	1	0.1947	0.3281
			CH3	3	1	0.1947	0.3281	14	1	0.3901	0.3646	3	1	0.2148	0.3271
			LDVg	6	1	0.1677	0.3935	10	1	0.0412	0.3492	3	1	0.0193	0.2759
			LDV1	2	8	0.0519	0.2460	20	1	0.0448	0.1007	3	1	0.0050	0.1372
HF	SDOF CAR attached to fixed supports by 4 calibrated springs	surface plastic (smooth) number of springs 2 x 3; loading High Frequency	CH1	2	8	0.1395	0.3746	24	1	0.3550	0.3235	3	1	0.2382	0.3390
			CH2	2	4	0.0564	0.4120	22	1	0.4344	0.3732	3	1	0.1624	0.3904
			CH3	2	2	0.0888	0.3616	20	1	0.4163	0.3340	3	1	0.1799	0.3568
			LDVg	5	1	0.3344	0.3091	22	1	0.4547	0.3248	3	1	0.2707	0.2848
			LDV1	2	2	0.0344	0.1209	13	1	0.2846	0.2393	3	1	0.2800	0.2289

EXPERIMENT	SYSTEM CHARACTERISTCS	VARIABLES		METHOD 1				METHOD 2				METHOD 3			
				best m	best τ	rsme	RSME	calc m	τ	rsme	RSME	set m	set τ	rsme	RSME
1	SDOF CAR attached to fixed supports by 6 calibrated springs (3 on each side)	surface wood; number of springs 2 x 3; loading harmonic 2Hz	CH1	5	10	0.354	0.380	19	1	0.167	0.171	3	1	0.076	0.118
			CH2	2	3	0.285	0.346	9	1	0.299	0.302	3	1	0.243	0.271
			CH3	2	4	0.007	0.454	21	1	0.038	0.502	3	1	0.009	0.458
			LDVg	5	1	0.086	0.138	6	1	0.010	0.126	3	1	0.076	0.119
			LDV1	3	10	0.056	0.160	20	1	0.052	0.193	3	1	0.007	0.147

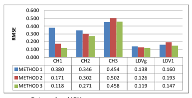

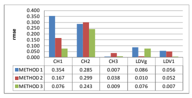

Data recorded 3D Accelerometer

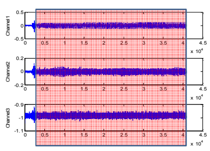

Data analysed 3D Accelerometer

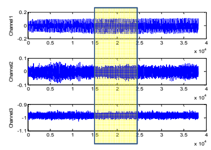

Data recorded LDV

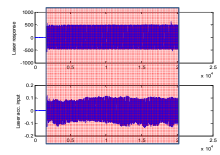

Data analysed LDV

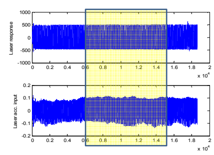

CH1 CH2 CH3 LDVg LDV1

METHOD 1

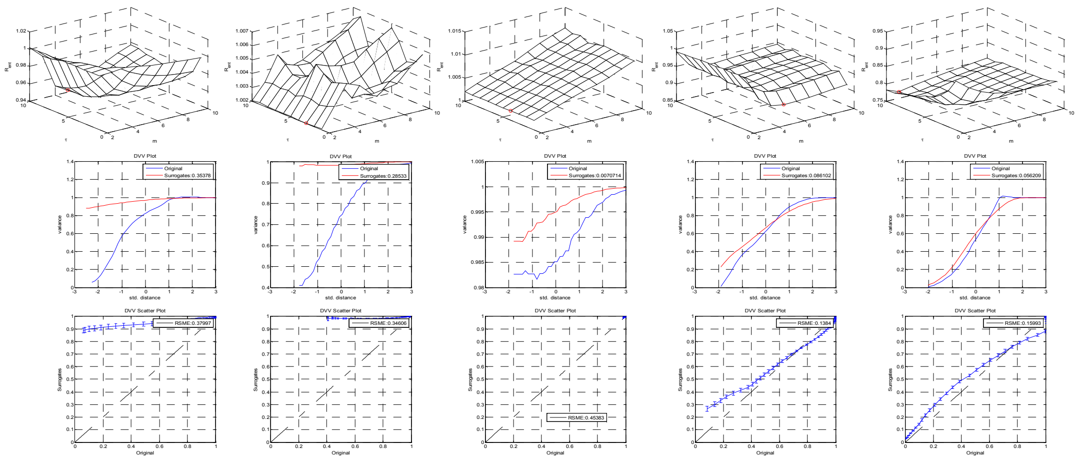

CH1 CH2 CH3 LDVg LDV1

METHOD 2

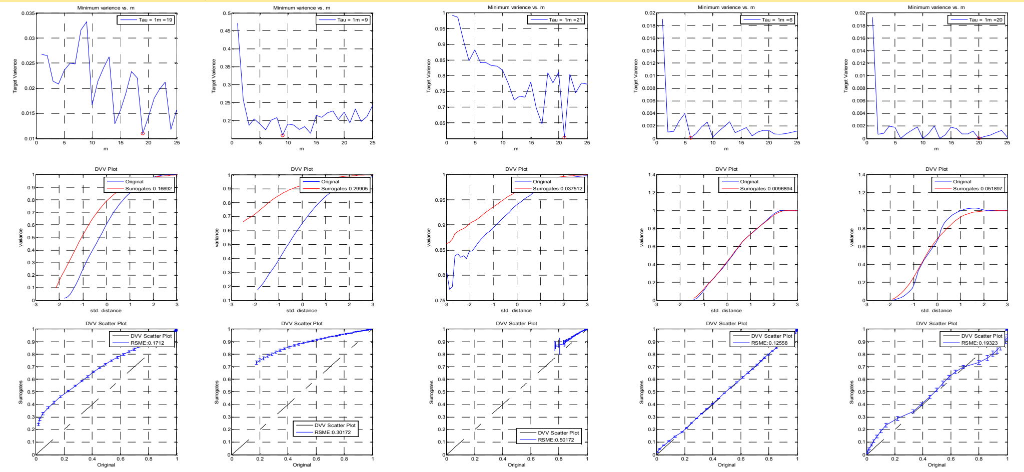

CH1 CH2 CH3 LDVg LDV1

METHOD 3

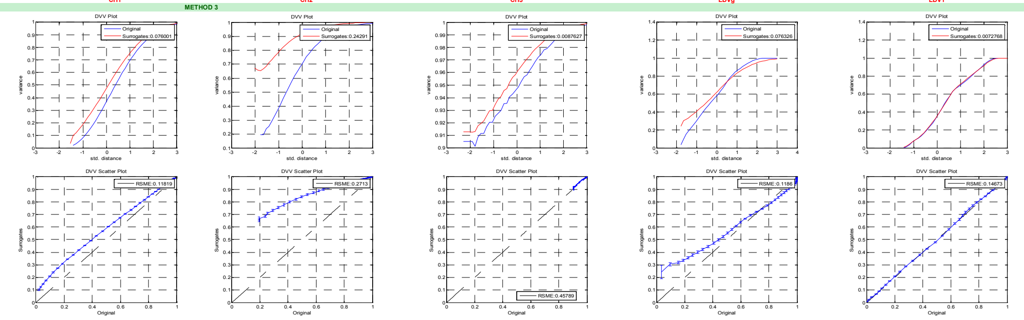

EXPERIMENT	SYSTEM CHARACTERISTCS	VARIABLES		METHOD 1				METHOD 2				METHOD 3			
				best m	best τ	rsme	RSME	calc m	τ	rsme	RSME	set m	set τ	rsme	RSME
2	SDOF CAR attached to fixed supports by 6 calibrated springs (3 on each side)	surface wood; number of springs 2 x 3; loading harmonic 2-4-6-8-10 Hz	CH1	5	9	0.292	0.176	17	1	0.182	0.135	3	1	0.154	0.142
			CH2	10	1	0.471	0.366	15	1	0.508	0.384	3	1	0.307	0.318
			CH3	9	1	0.437	0.294	24	1	0.523	0.344	3	1	0.239	0.284
			LDVg	8	5	0.208	0.176	5	1	0.028	0.142	3	1	0.030	0.139
			LDV1	6	5	0.414	0.282	21	1	0.317	0.204	3	1	0.211	0.172

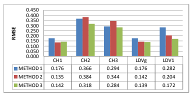

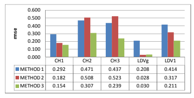

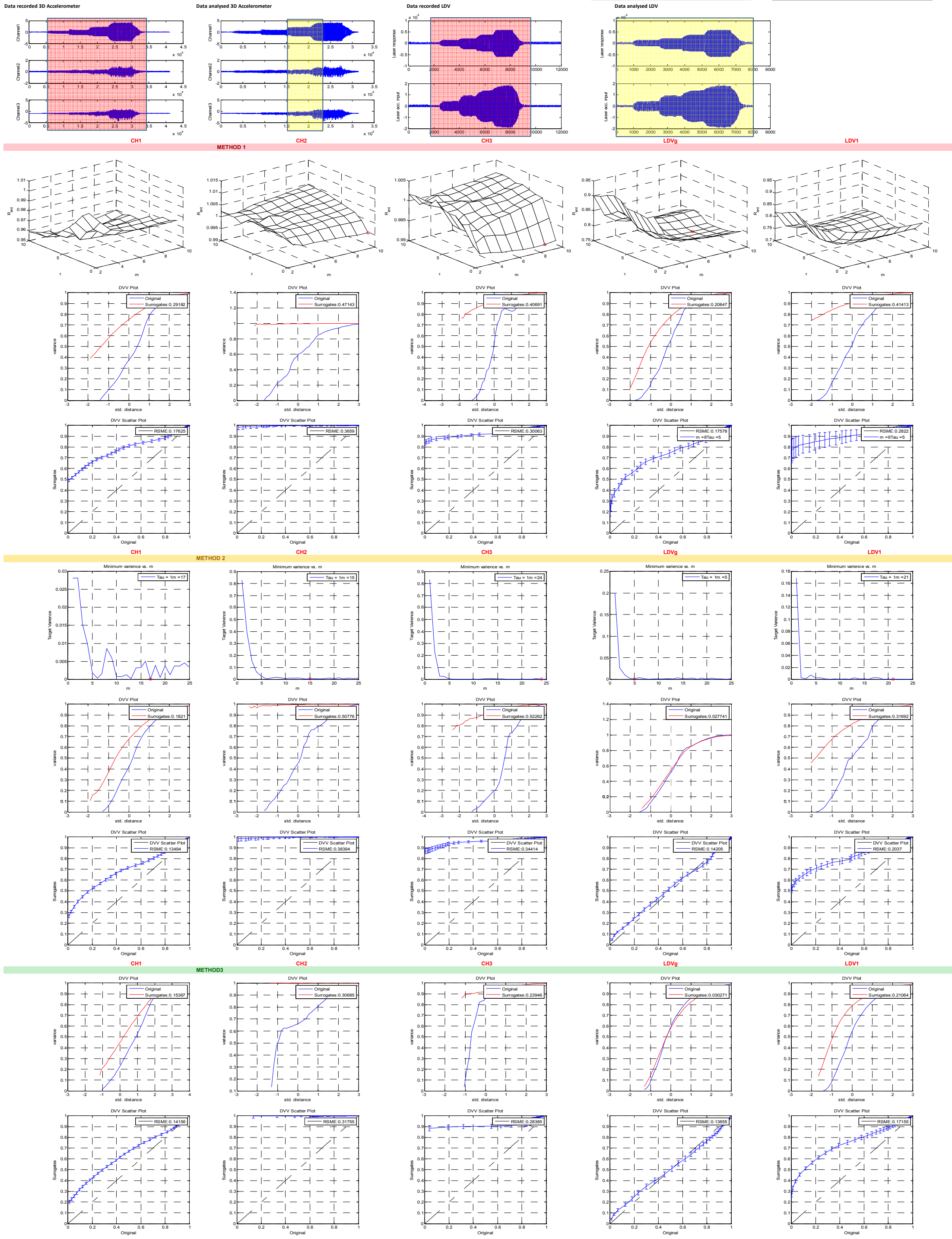

EXPERIMENT	SYSTEM CHARACTERISTCS	VARIABLES		METHOD 1				METHOD 2				METHOD 3			
				best m	best τ	rsme	RSME	calc m	τ	rsme	RSME	set m	set τ	rsme	RSME
3	SDOF CAR attached to fixed supports by 6 calibrated springs (3 on each side)	surface plastic (smooth) number of springs 2 x 3; loading harmonic 2-4-6-8-10 Hz	CH1	4	10	0.257	0.175	11	1	0.175	0.123	3	1	0.233	0.128
			CH2	10	1	0.421	0.299	14	1	0.473	0.326	3	1	0.233	0.273
			CH3	10	1	0.328	0.202	19	1	0.401	0.234	3	1	0.127	0.213
			LDVg	9	5	0.201	0.153	15	1	0.074	0.129	3	1	0.034	0.134
			LDV1	6	5	0.447	0.301	5	1	0.263	0.179	3	1	0.141	0.167

* results from EXP3_A-C

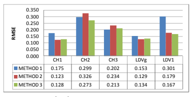

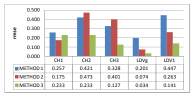

Data recorded 3D Accelerometer | Data analysed 3D Accelerometer | Data recorded LDV | Data analysed LDV

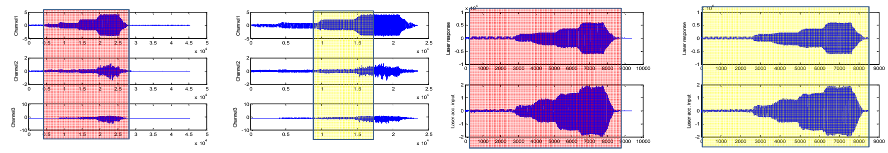

CH1 CH2 CH3 LDVg LDV1

METHOD 1

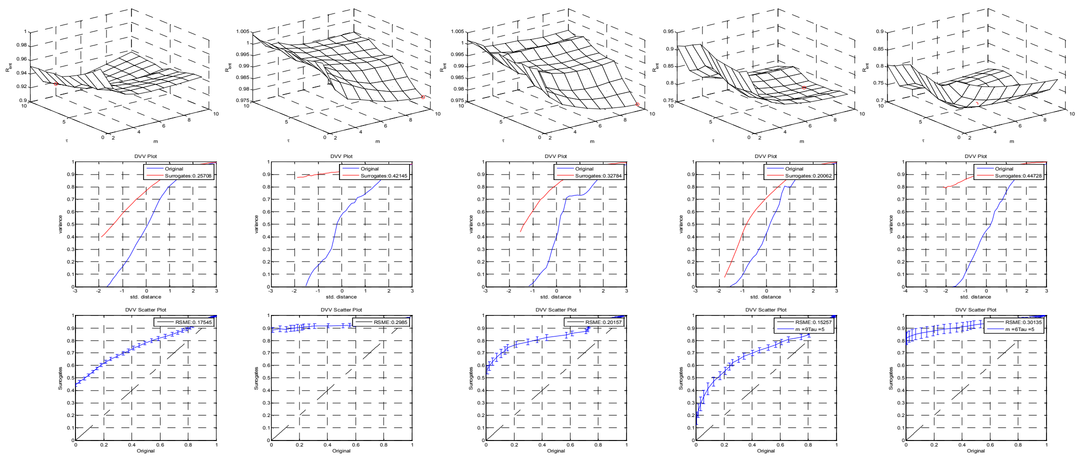

CH1 CH2 CH3 LDVg LDV1

METHOD 2

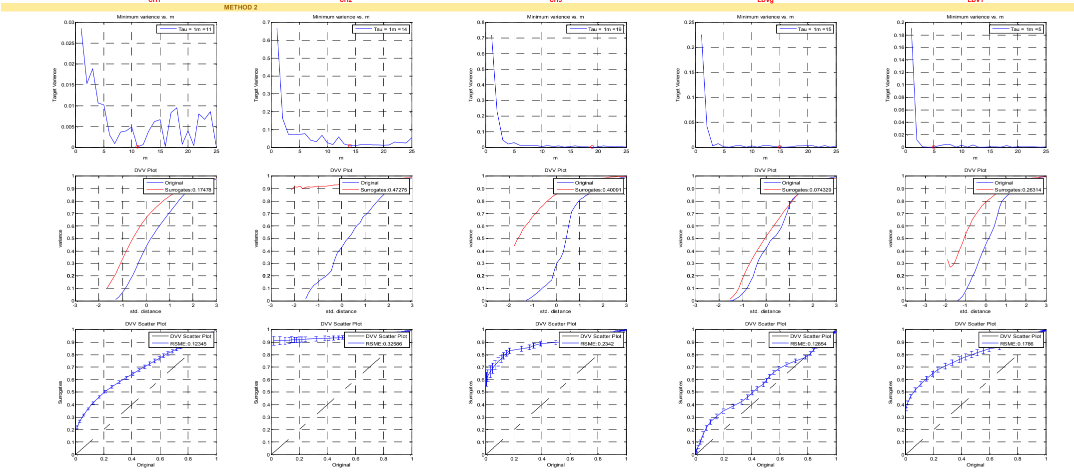

CH1 CH2 CH3 LDVg LDV1

METHOD 3

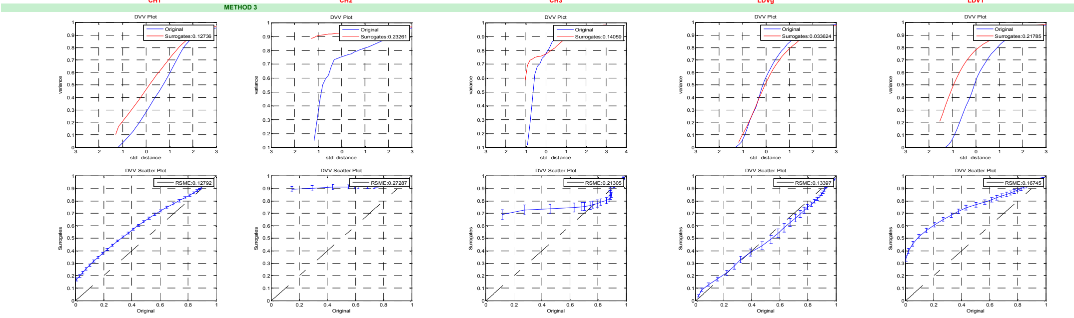

EXPERIMENT	SYSTEM CHARACTERISTCS	VARIABLES		METHOD 1				METHOD 2				METHOD 3			
				best m	best τ	rsme	RSME	calc m	τ	rsme	RSME	set m	set τ	rsme	RSME
4	SDOF CAR attached to fixed supports by 6 calibrated springs (3 on each side)	surface wood number of springs 2 x 3; loading Sine Sweep	CH1	4	10	0.325	0.188	25	1	0.211	0.133	3	1	0.117	0.133
			CH2	10	2	0.429	0.373	22	1	0.490	0.368	3	1	0.286	0.334
			CH3	9	1	0.466	0.298	13	1	0.494	0.306	3	1	0.242	0.288
			LDVg	10	3	0.376	0.296	17	1	0.084	0.114	3	1	0.032	0.127
			LDV1	9	4	0.367	0.291	11	1	0.248	0.176	3	1	0.172	0.165

* results from EXP4_A-E

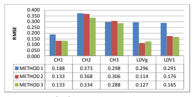

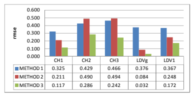

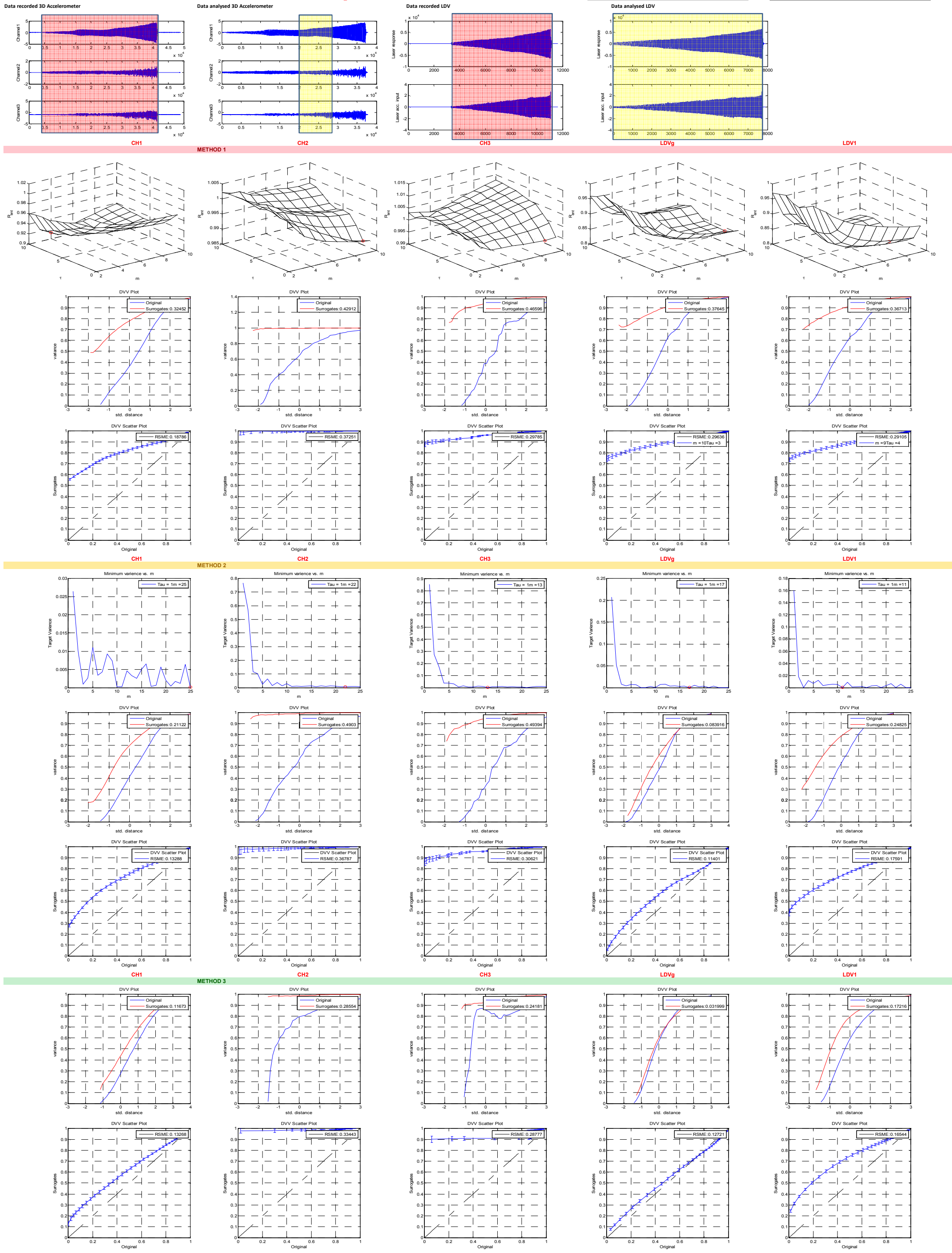

EXPERIMENT	SYSTEM CHARACTERISTCS	VARIABLES		METHOD 1				METHOD 2				METHOD 3			
				best **m**	best **τ**	rsme	RSME	calc **m**	**τ**	rsme	RSME	set **m**	set **τ**	rsme	RSME
5	SDOF CAR attached to fixed supports by 6 calibrated springs (3 on each side)	surface wood number of springs 2 x 3; loading White Noise	CH1	7	1	0.145	0.113	9	1	0.139	0.129	3	1	0.122	0.097
			CH2	6	1	0.256	0.394	14	1	0.376	0.394	3	1	0.144	0.379
			CH3	7	1	0.348	0.357	10	1	0.393	0.368	3	1	0.185	0.357
			LDVg	6	1	0.070	0.293	10	1	0.198	0.418	3	1	0.232	0.347
			LDV1	3	1	0.005	0.155	3	1	0.179	0.202	3	1	0.180	0.204

* results from EXP5_A

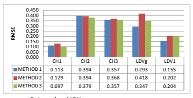

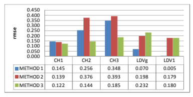

Data recorded 3D Accelerometer

Data analysed 3D Accelerometer

Data recorded LDV

Data analysed LDV

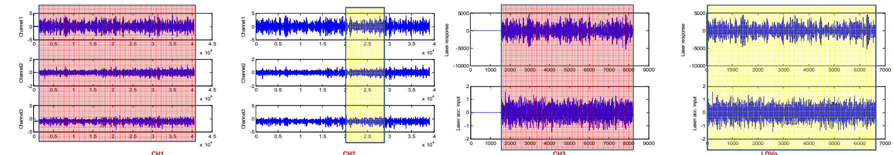

CH1 CH2 CH3 LDVg LDV1

METHOD 1

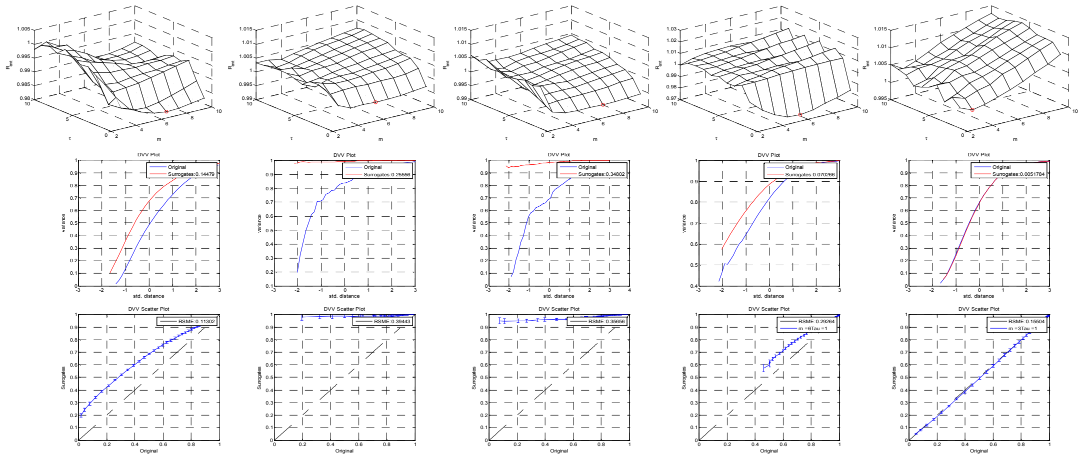

CH1 CH2 CH3 LDVg LDV1

METHOD 2

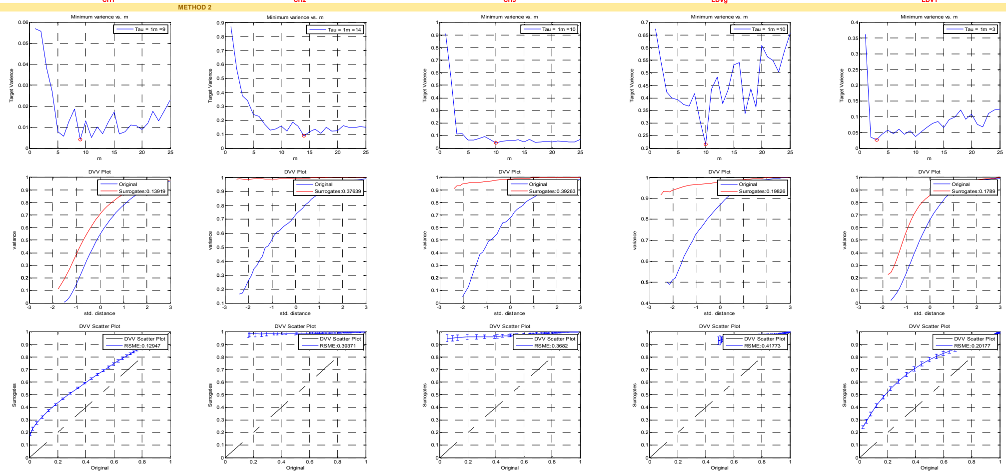

CH1 CH2 CH3 LDVg LDV1

METHOD 3

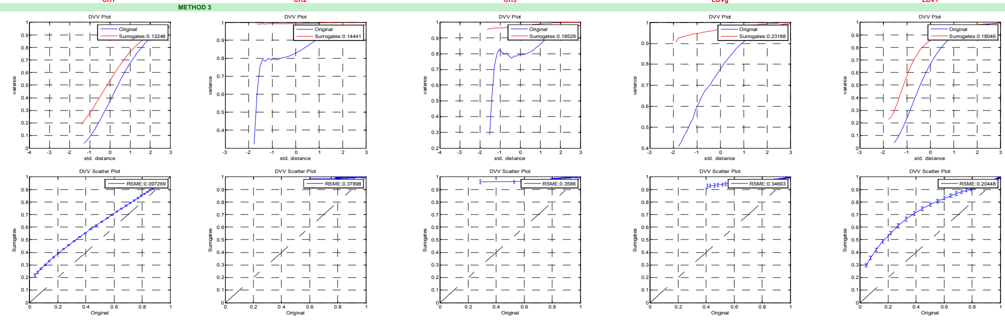

EXPERIMENT	SYSTEM CHARACTERISTCS	VARIABLES		METHOD 1				METHOD 2				METHOD 3			
				best m	best τ	rsme	RSME	calc m	τ	rsme	RSME	set m	set τ	rsme	RSME
6	SDOF CAR attached to fixed supports by 6 calibrated springs (3 on each side)	surface plastic (smooth) number of springs 2 x 3; loading Sine Sweep	CH1	4	10	0.296	0.169	23	1	0.176	0.129	3	1	0.117	0.145
			CH2	10	2	0.399	0.315	16	1	0.398	0.288	3	1	0.252	0.265
			CH3	10	1	0.302	0.160	14	1	0.299	0.166	3	1	0.161	0.161
			LDVg	10	6	0.241	0.224	6	1	0.042	0.136	3	1	0.029	0.130
			LDV1	8	10	0.424	0.360	6	1	0.240	0.173	3	1	0.172	0.165

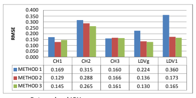

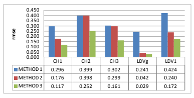

Data recorded 3D Accelerometer **Data analysed 3D Accelerometer** **Data recorded LDV** **Data analysed LDV**

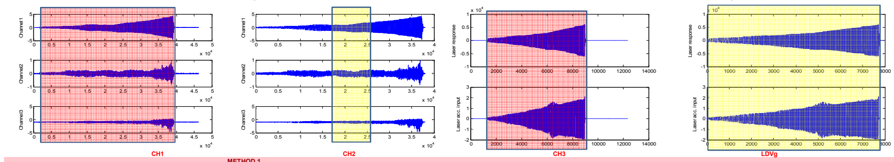

CH1 CH2 CH3 LDVg LDV1

METHOD 1

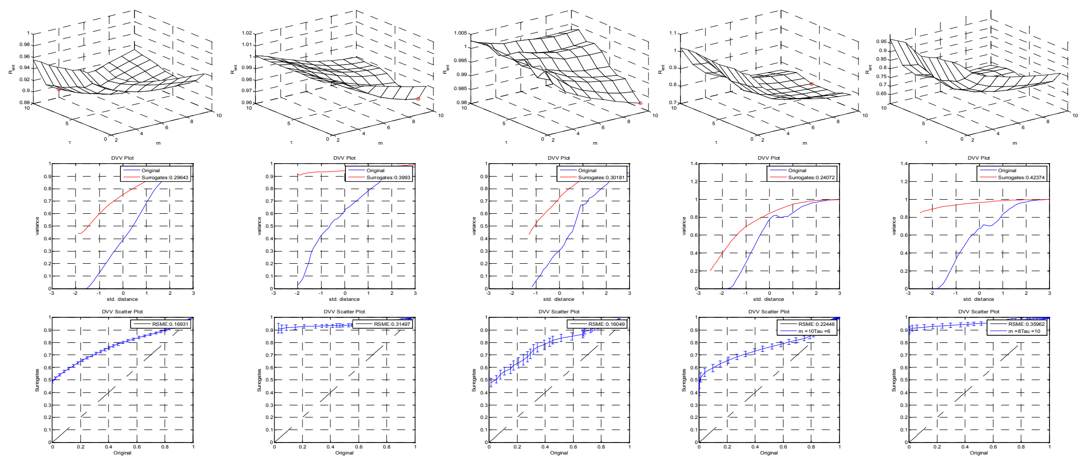

CH1 CH2 CH3 LDVg LDV1

METHOD 2

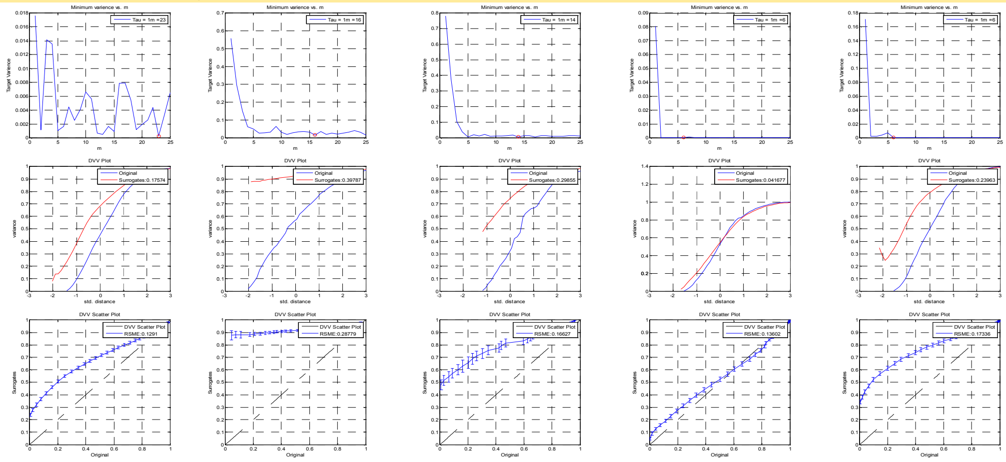

CH1 CH2 CH3 LDVg LDV1

METHOD 3

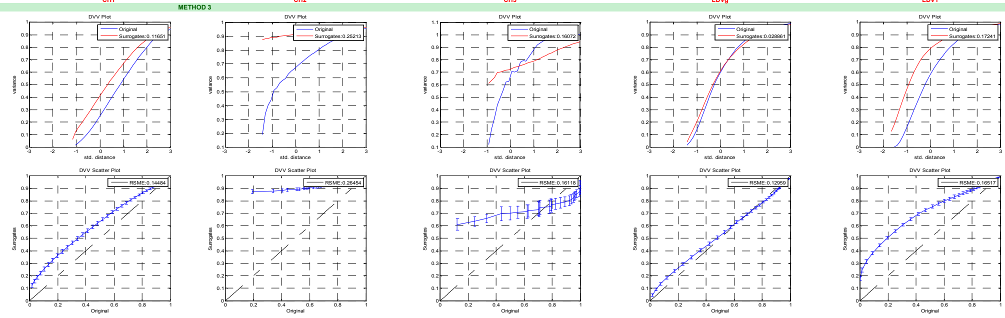

EXPERIMENT	SYSTEM CHARACTERISTCS	VARIABLES		METHOD 1				METHOD 2				METHOD 3			
				best m	best τ	rsme	RSME	calc m	τ	rsme	RSME	set m	set τ	rsme	RSME
7	SDOF CAR attached to fixed supports by 6 calibrated springs (3 on each side)	surface plastic (smooth) number of springs 2 x 3; loading White Noise	CH1	6	1	0.142	0.110	13	1	0.123	0.148	3	1	0.115	0.101
			CH2	6	1	0.300	0.360	14	1	0.348	0.395	3	1	0.185	0.348
			CH3	7	1	0.214	0.194	14	1	0.266	0.208	3	1	0.084	0.212
			LDVg	6	1	0.251	0.367	4	1	0.252	0.353	3	1	0.243	0.340
			LDV1	2	3	0.256	0.263	3	1	0.185	0.201	3	1	0.194	0.201

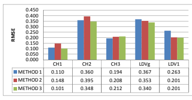

	CH1	CH2	CH3	LDVg	LDV1
METHOD 1	0.110	0.360	0.194	0.367	0.263
METHOD 2	0.148	0.395	0.208	0.353	0.201
METHOD 3	0.101	0.348	0.212	0.340	0.201

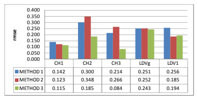

	CH1	CH2	CH3	LDVg	LDV1
METHOD 1	0.142	0.300	0.214	0.251	0.256
METHOD 2	0.123	0.348	0.266	0.252	0.185
METHOD 3	0.115	0.185	0.084	0.243	0.194

Data recorded 3D Accelerometer

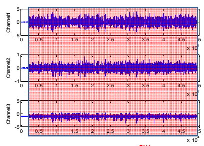

Data analysed 3D Accelerometer

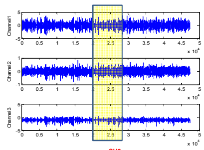

Data recorded LDV

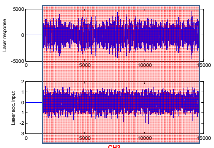

Data analysed LDV

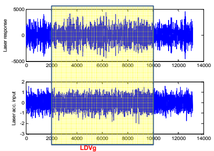

CH1 CH2 CH3 LDVg LDV1

METHOD 1

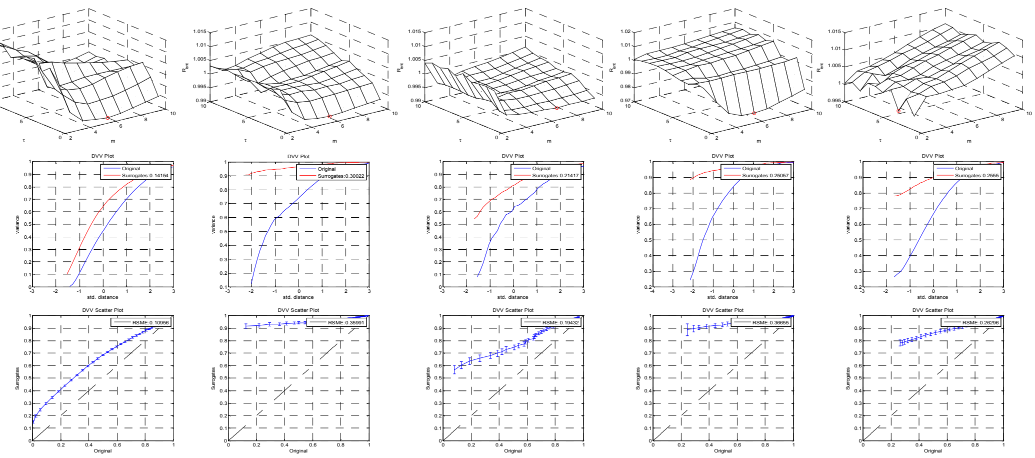

CH1 CH2 CH3 LDVg LDV1

METHOD 2

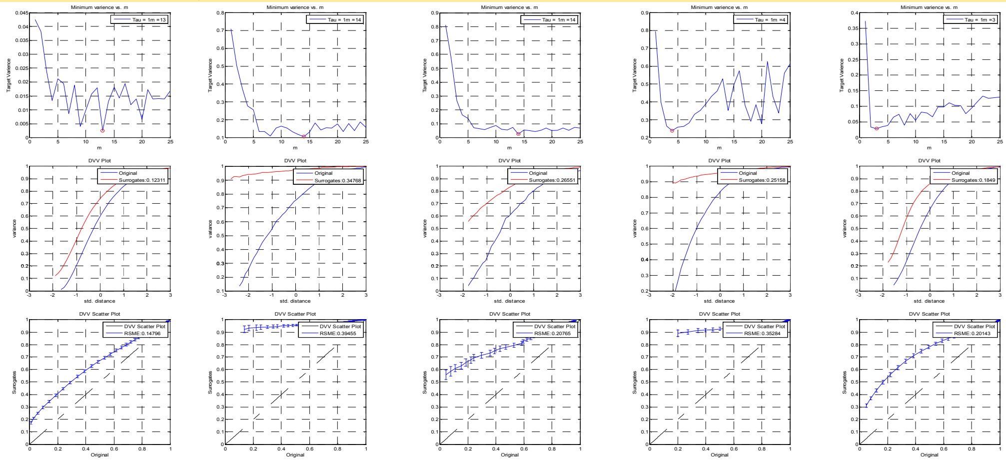

CH1 CH2 CH3 LDVg LDV1

METHOD 3

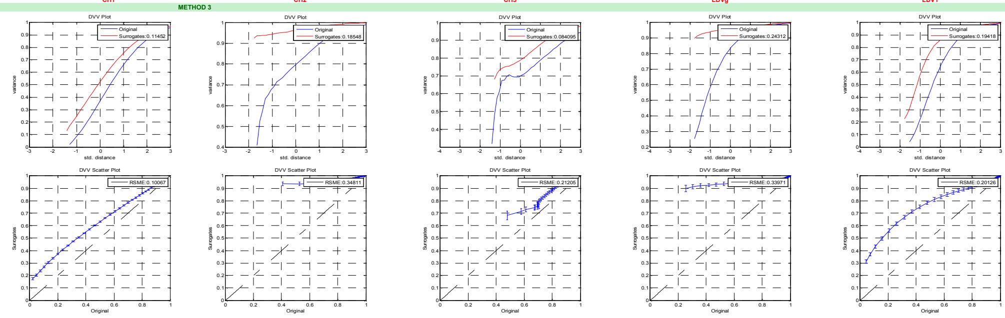

EXPERIMENT	SYSTEM CHARACTERISTCS	VARIABLES		METHOD 1				METHOD 2				METHOD 3			
				best **m**	best **τ**	rsme	RSME	calc **m**	**τ**	rsme	RSME	set **m**	set **τ**	rsme	RSME
8	SDOF CAR attached to fixed supports by 6 calibrated springs (3 on each side)	surface sand paper (rough) number of springs 2 x 3; loading White Noise	CH1	6	1	0.1395	0.1110	5	1	0.1363	0.1030	3	1	0.1236	0.0964
			CH2	3	8	0.0632	0.4353	12	1	0.3188	0.4012	3	1	0.1377	0.3934
			CH3	4	4	0.0432	0.3464	7	1	0.1167	0.2232	3	1	0.0657	0.2730
			LDVg	6	1	0.1901	0.4007	9	1	0.1931	0.4276	3	1	0.1886	0.3663
			LDV1	5	1	0.1922	0.1463	17	1	0.2249	0.2143	3	1	0.1933	0.2026

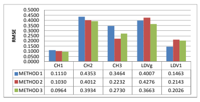

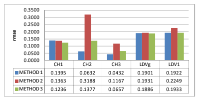

Data recorded 3D Accelerometer **Data analysed 3D Accelerometer** **Data recorded LDV** **Data analysed LDV**

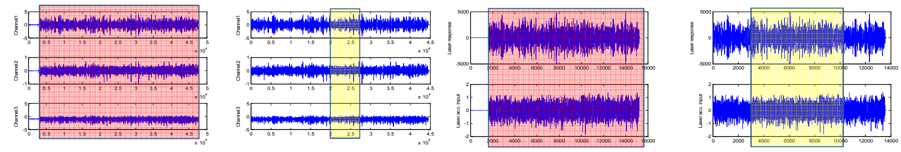

CH1 CH2 CH3 LDVg LDV1

METHOD 1

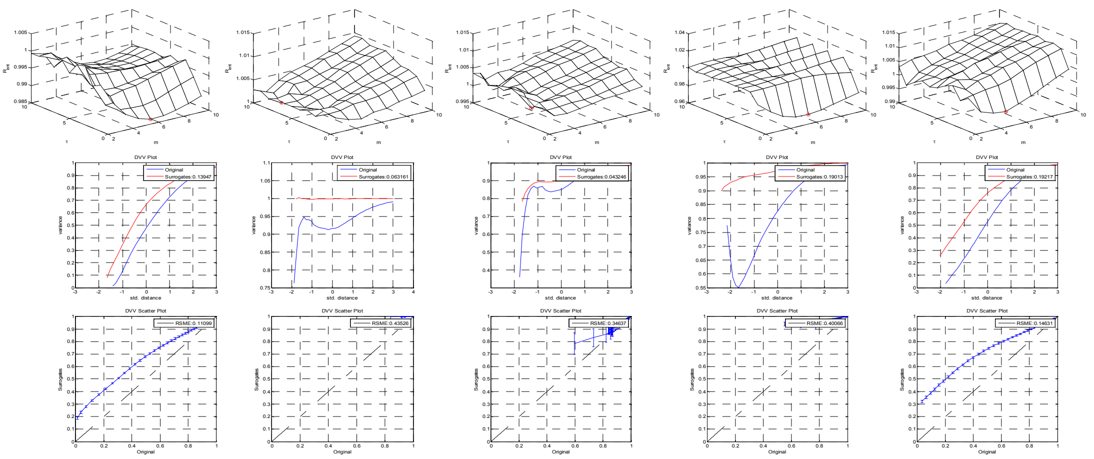

CH1 CH2 CH3 LDVg LDV1

METHOD 2

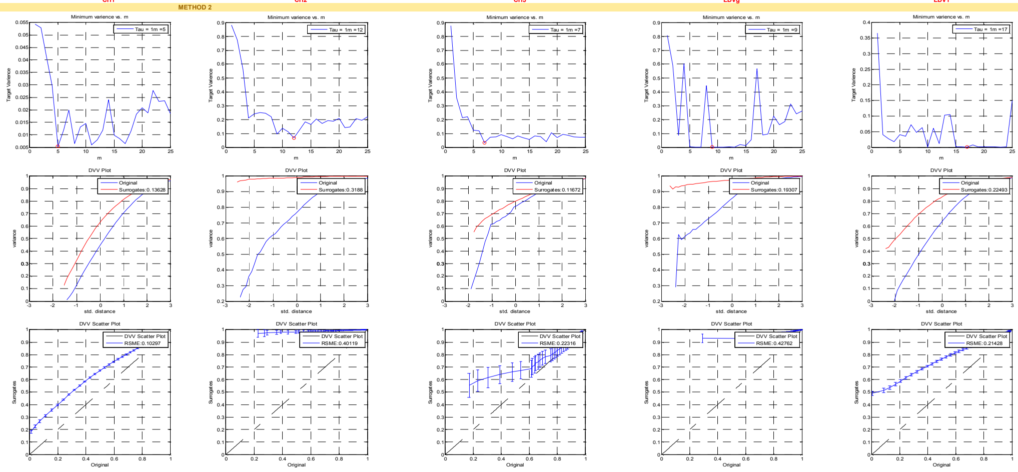

CH1 CH2 CH3 LDVg LDV1

METHOD 3

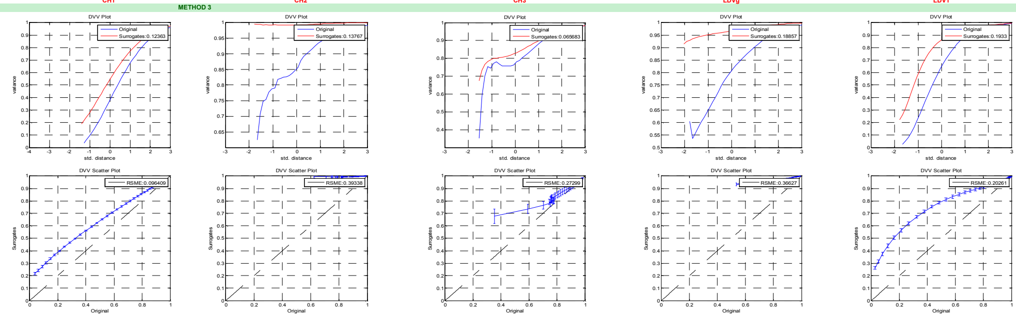

EXPERIMENT	SYSTEM CHARACTERISTCS	VARIABLES		METHOD 1				METHOD 2				METHOD 3			
				best m	best τ	rsme	RSME	calc m	τ	rsme	RSME	set m	set τ	rsme	RSME
9	SDOF CAR attached to fixed supports by 6 calibrated springs (3 on each side)	surface sand paper (rough) number of springs 2 x 3; loading Sine Sweep	CH1	5	9	0.2844	0.1682	4	1	0.1280	0.1360	3	1	0.1015	0.1308
			CH2	10	1	0.4205	0.3643	7	1	0.3815	0.3498	3	1	0.2444	0.3234
			CH3	10	1	0.3147	0.1674	18	1	0.3119	0.1823	3	1	0.1763	0.1581
			LDVg	10	3	0.1551	0.1549	15	1	0.0677	0.1084	3	1	0.0391	0.1260
			LDV1	9	4	0.3675	0.2888	22	1	0.2944	0.2135	3	1	0.1745	0.1623

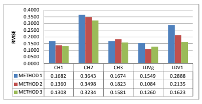

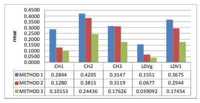

Data recorded 3D Accelerometer

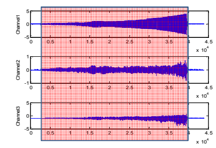

Data analysed 3D Accelerometer

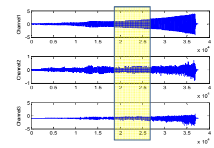

Data recorded LDV

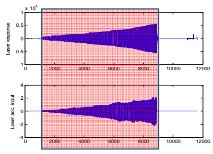

Data analysed LDV

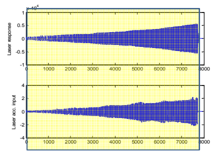

CH1 CH2 CH3 LDVg LDV1

METHOD 1

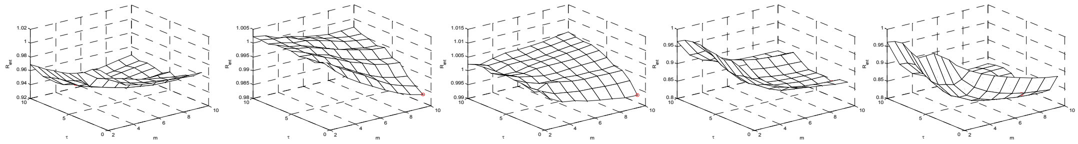

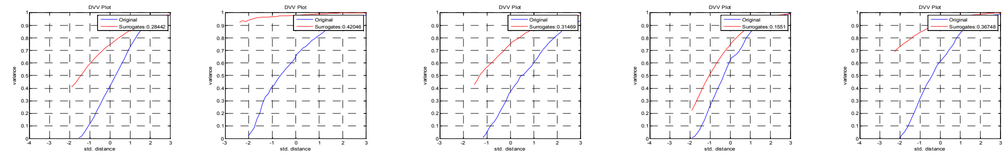

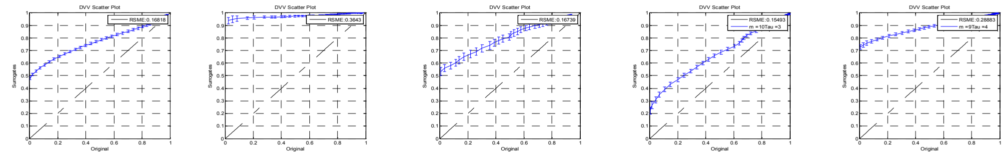

CH1 CH2 CH3 LDVg LDV1

METHOD 2

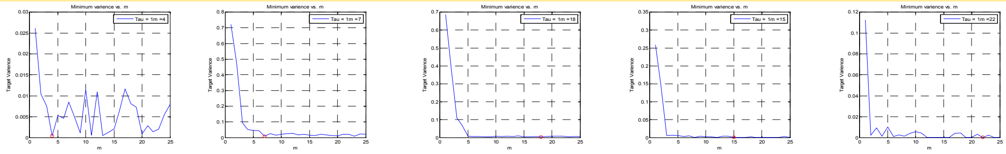

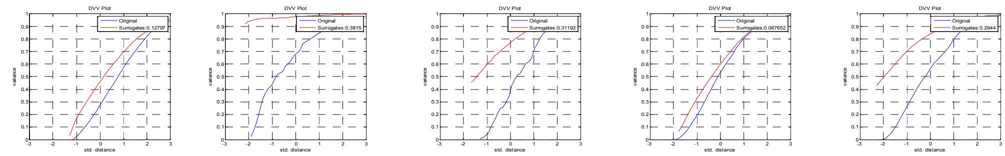

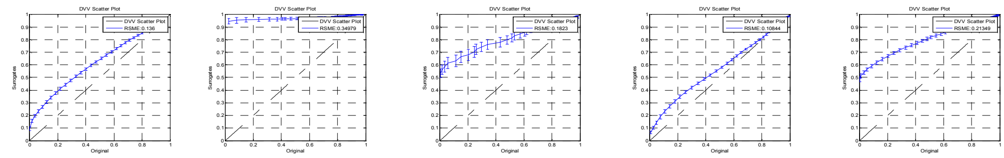

CH1 CH2 CH3 LDVg LDV1

METHOD 3

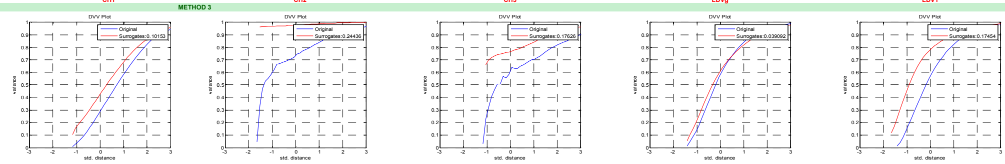

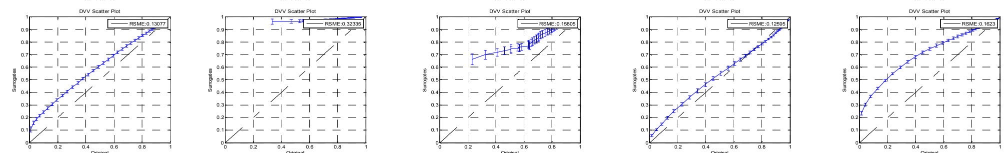

EXPERIMENT	SYSTEM CHARACTERISTCS	VARIABLES		METHOD 1				METHOD 2				METHOD 3			
				best **m**	best **τ**	rsme	RSME	calc **m**	**τ**	rsme	RSME	set **m**	set **τ**	rsme	RSME
10	SDOF CAR attached to fixed supports by 6 calibrated springs (3 on each side)	surface sand paper (rough) number of springs 2 x 3; loading harmonic 2-4-6-8-10 Hz	CH1	3	9	0.2816	0.1670	14	1	0.1980	0.1349	3	1	0.1458	0.1328
			CH2	8	1	0.3732	0.3401	11	1	0.4204	0.3552	3	1	0.2067	0.3402
			CH3	8	1	0.3422	0.1905	12	1	0.3237	0.2037	3	1	0.1902	0.2038
			LDVg	8	5	0.2355	0.1912	11	1	0.0542	0.1181	3	1	0.0303	0.1316
			LDV1	6	5	0.2460	0.1848	12	1	0.2924	0.1828	3	1	0.2012	0.1681

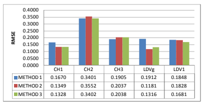

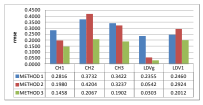

Data recorded 3D Accelerometer

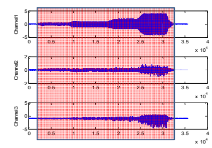

Data analysed 3D Accelerometer

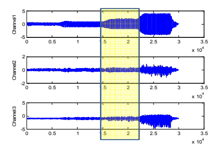

Data recorded LDV

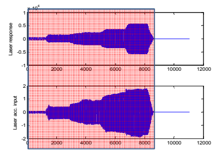

Data analysed LDV

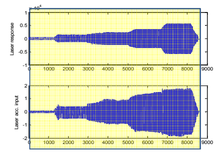

CH1 CH2 CH3 LDVg LDV1

METHOD 1

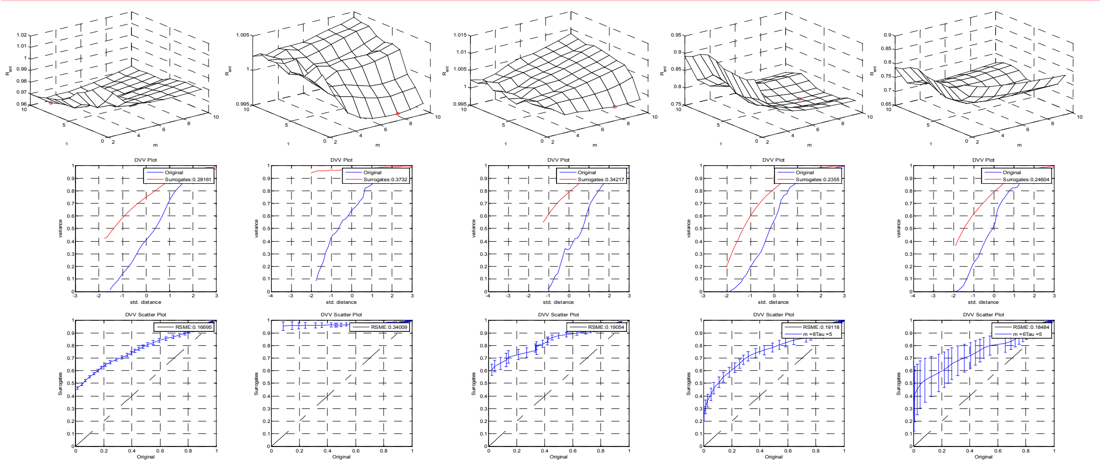

CH1 CH2 CH3 LDVg LDV1

METHOD 2

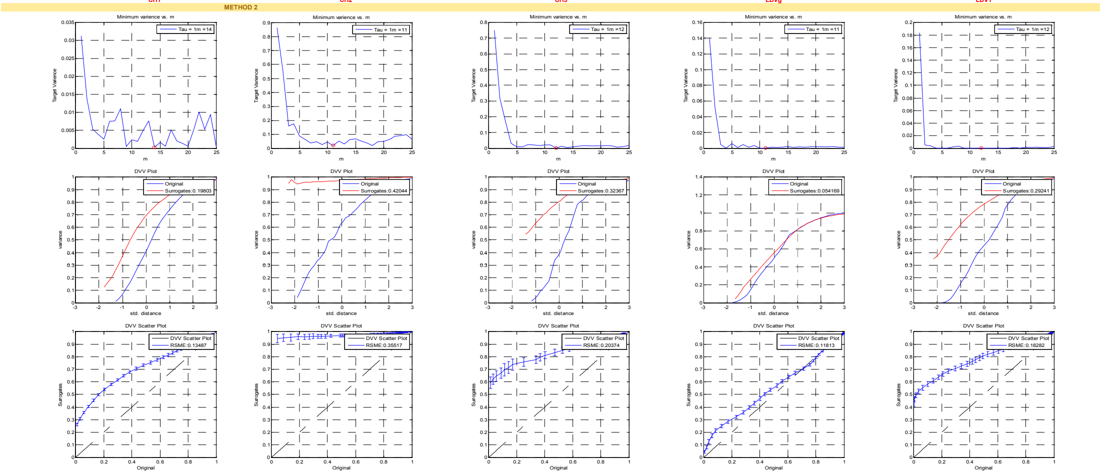

CH1 CH2 CH3 LDVg LDV1

METHOD 3

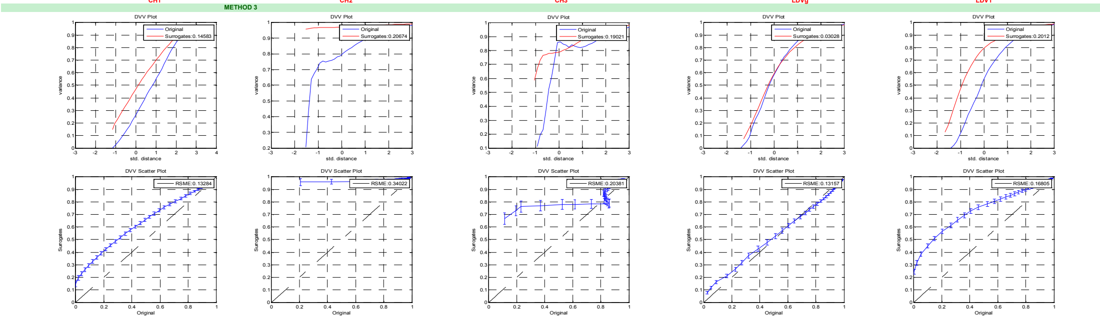

EXPERIMENT	SYSTEM CHARACTERISTCS	VARIABLES		METHOD 1				METHOD 2				METHOD 3			
				best m	best τ	rsme	RSME	calc m	τ	rsme	RSME	set m	set τ	rsme	RSME
11	SDOF CAR attached to fixed supports by 4 calibrated springs (2 on each side)	surface sand paper (rough) Middle spring taken out number of springs 2 x2; loading harmonic 2-4-6-8-10 Hz	CH1	4	10	0.3958	0.2010	10	1	0.2735	0.1514	3	1	0.2079	0.1548
			CH2	10	1	0.6419	0.3674	20	1	0.6193	0.3486	3	1	0.5733	0.3291
			CH3	10	1	0.2980	0.1626	19	1	0.2564	0.1484	3	1	0.3044	0.1883
			LDVg	8	6	0.2343	0.1855	14	1	0.0675	0.1175	3	1	0.0235	0.1102
			LDV1	7	5	0.2680	0.1687	14	1	0.1438	0.1134	3	1	0.0710	0.0978

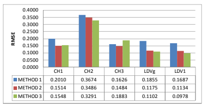

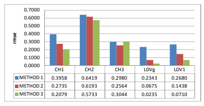

Data recorded 3D Accelerometer **Data analysed 3D Accelerometer** **Data recorded LDV** **Data analysed LDV**

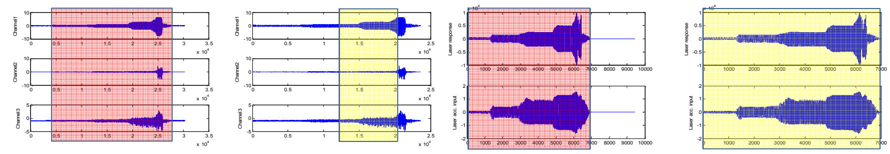

CH1 CH2 CH3 LDVg LDV1

METHOD 1

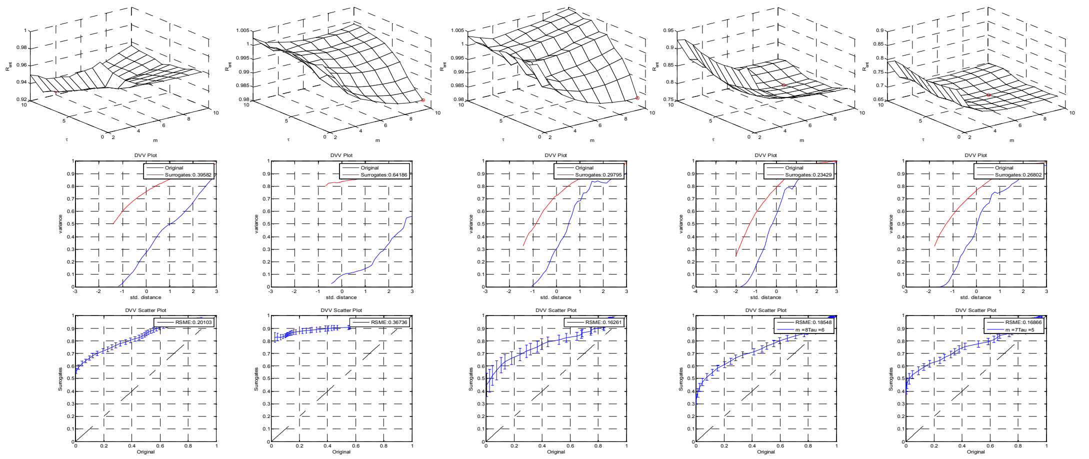

CH1 CH2 CH3 LDVg LDV1

METHOD 2

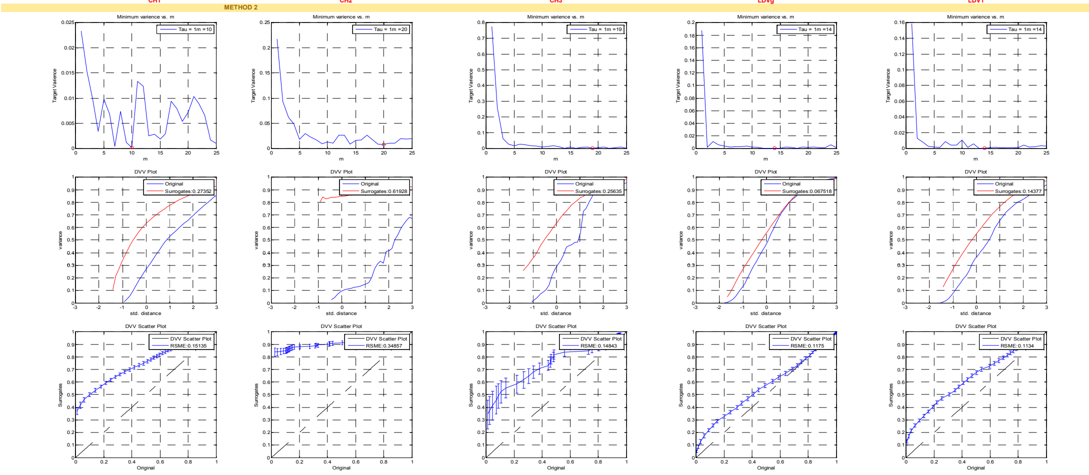

CH1 CH2 CH3 LDVg LDV1

METHOD 3

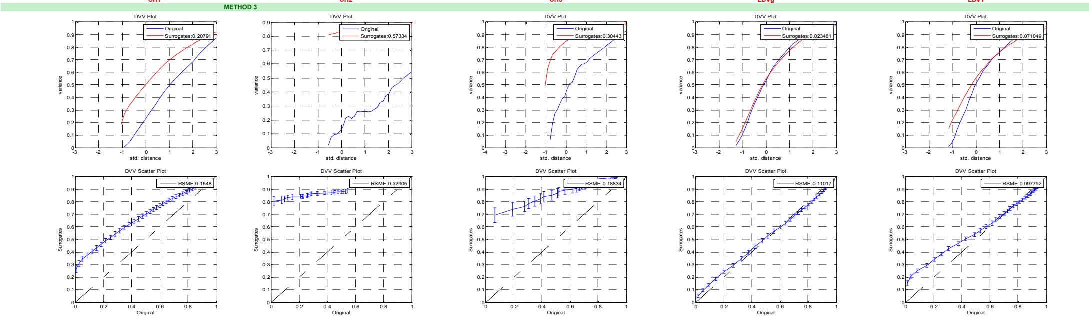

EXPERIMENT	SYSTEM CHARACTERISTCS	VARIABLES		METHOD 1				METHOD 2				METHOD 3			
				best m	best τ	rsme	RSME	calc m	τ	rsme	RSME	set m	set τ	rsme	RSME
12	SDOF CAR attached to fixed supports by 4 calibrated springs (2 on each side)	surface sand paper (rough) Middle spring taken out number of springs 2 x2; loading Sine Sweep	CH1	4	10	0.2691	0.1546	9	1	0.1486	0.1102	3	1	0.1325	0.1415
			CH2	10	3	0.5232	0.2775	15	1	0.5250	0.2838	3	1	0.4094	0.2149
			CH3	10	1	0.3269	0.1693	14	1	0.3390	0.1803	3	1	0.1057	0.1350
			LDVg	8	3	0.1022	0.1263	8	1	0.0302	0.1164	3	1	0.0276	0.1029
			LDV1	7	7	0.1367	0.1063	24	1	0.0805	0.1195	3	1	0.0141	0.0981

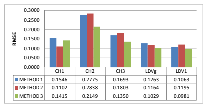

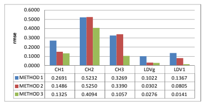

Data recorded 3D Accelerometer

Data analysed 3D Accelerometer

Data recorded LDV

Data analysed LDV

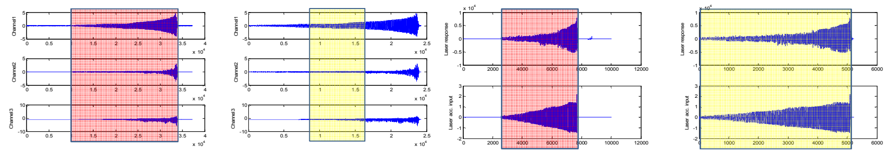

CH1 CH2 CH3 LDVg LDV1

METHOD 1

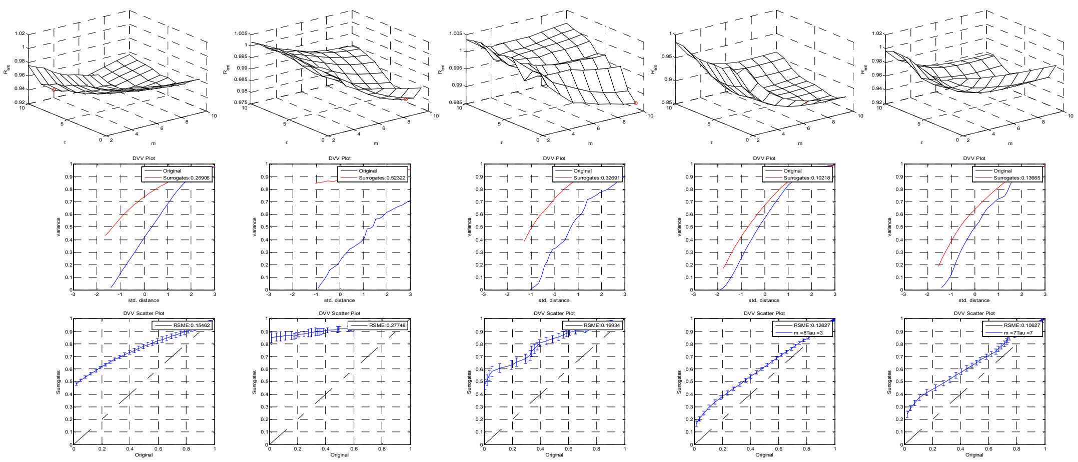

CH1 CH2 CH3 LDVg LDV1

METHOD 2

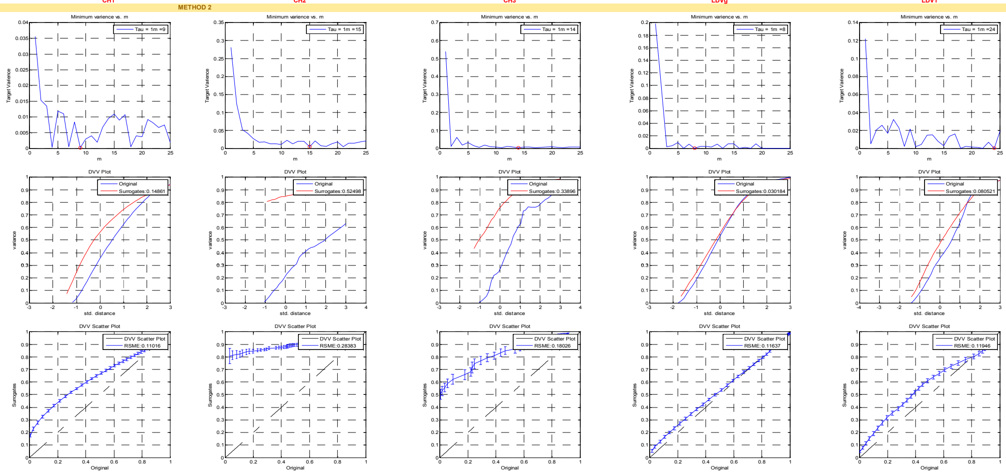

CH1 CH2 CH3 LDVg LDV1

METHOD 3

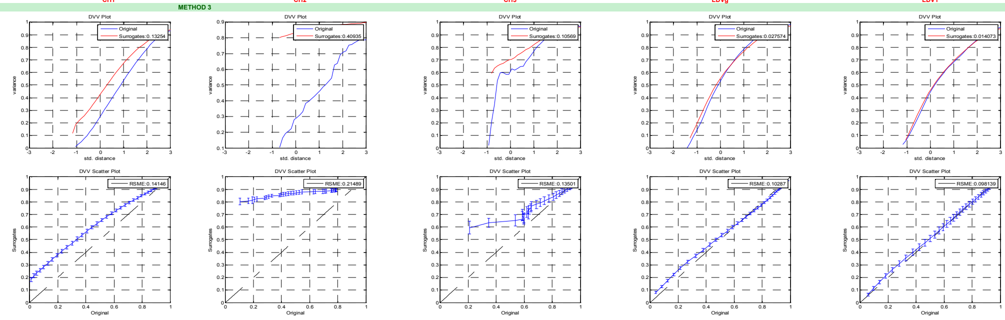

EXPERIMENT	SYSTEM CHARACTERISTCS	VARIABLES		METHOD 1				METHOD 2				METHOD 3			
				best m	best τ	rsme	RSME	calc m	τ	rsme	RSME	set m	set τ	rsme	RSME
13	SDOF CAR attached to fixed supports by 4 calibrated springs (2 on each side) REPEATED EXPERIMENT NO.12	surface sand paper (rough) Middle spring taken out number of springs 2 x2; loading Sine Sweep	CH1	4	10	0.2932	0.1736	19	1	0.1795	0.1250	3	1	0.1026	0.1393
			CH2	10	3	0.4319	0.3034	13	1	0.4338	0.2673	3	1	0.2973	0.2284
			CH3	9	1	0.2023	0.1111	15	1	0.2177	0.1216	3	1	0.1123	0.0981
			LDVg	8	3	0.1056	0.1260	20	1	0.0875	0.1072	3	1	0.0357	0.1047
			LDV1	7	5	0.1701	0.1632	12	1	0.2371	0.1559	3	1	0.1701	0.1410

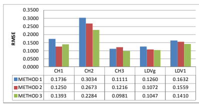

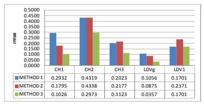

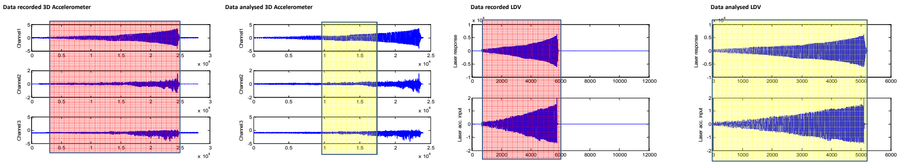

CH1 CH2 CH3 LDVg LDV1

METHOD 1

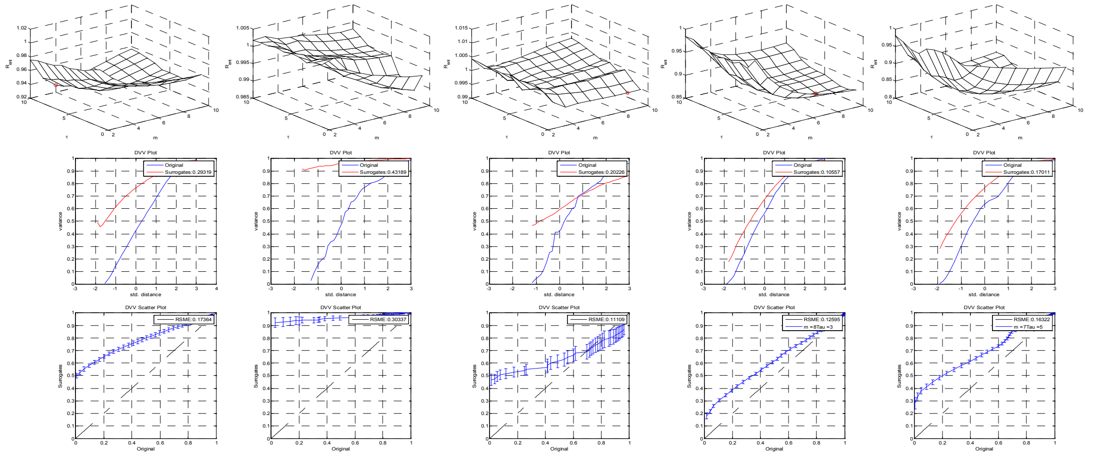

CH1 CH2 CH3 LDVg LDV1

METHOD 2

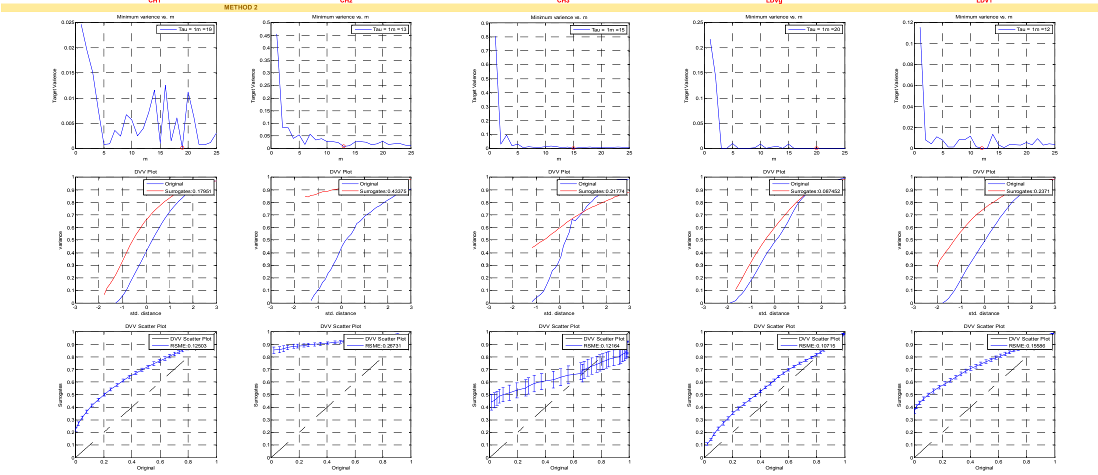

CH1 CH2 CH3 LDVg LDV1

METHOD 3

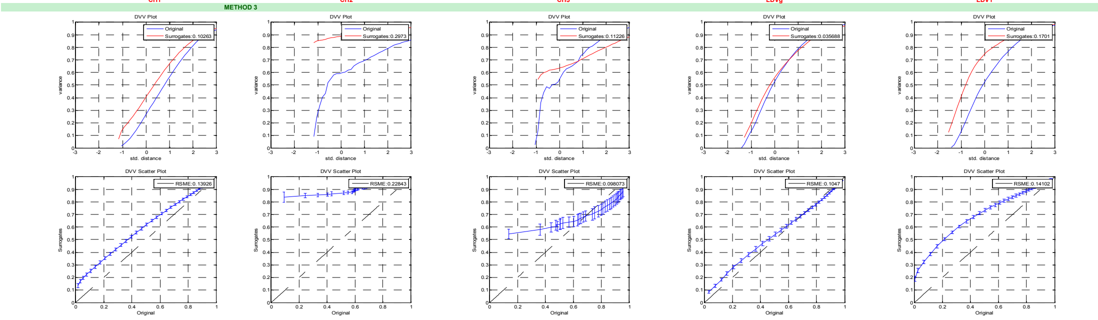

EXPERIMENT	SYSTEM CHARACTERISTCS	VARIABLES		METHOD 1				METHOD 2				METHOD 3			
				best m	best τ	rsme	RSME	calc m	τ	rsme	RSME	set m	set τ	rsme	RSME
14	SDOF CAR attached to fixed supports by 4 calibrated springs (2 on each side)	surface sand paper (rough) Middle spring taken out number of springs 2 x2; loading White Noise	CH1	6	1	0.1597	0.1052	21	1	0.1710	0.1335	3	1	0.1340	0.1064
			CH2	5	1	0.3213	0.3289	14	1	0.4115	0.3509	3	1	0.2359	0.3252
			CH3	3	6	0.0762	0.2905	25	1	0.1015	0.1225	3	1	0.0583	0.1759
			LDVg	6	1	0.0144	0.2840	4	1	0.1934	0.3564	3	1	0.2385	0.3479
			LDV1	4	1	0.2109	0.1760	8	1	0.2282	0.1448	3	1	0.1994	0.1780

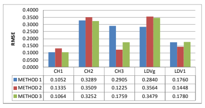

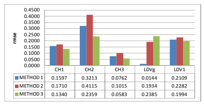

Data recorded 3D Accelerometer | Data analysed 3D Accelerometer | Data recorded LDV | Data analysed LDV

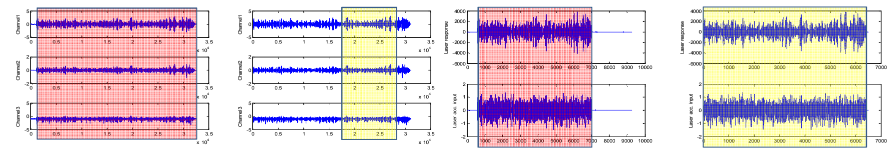

CH1 CH2 CH3 LDVg LDV1

METHOD 1

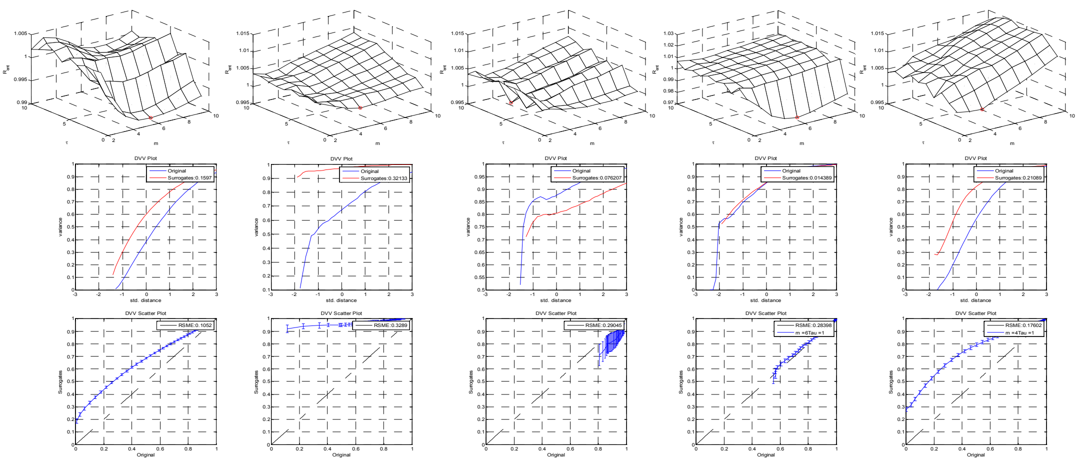

CH1 CH2 CH3 LDVg LDV1

METHOD 2

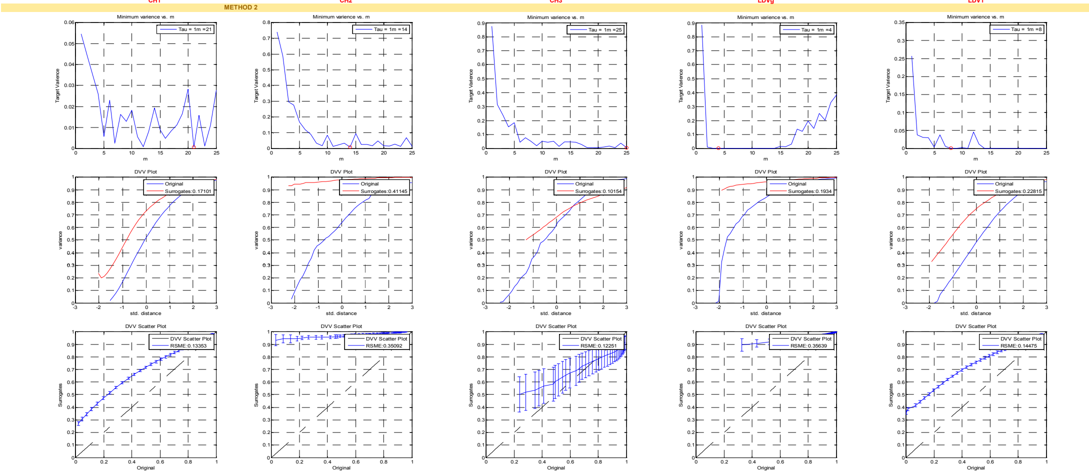

CH1 CH2 CH3 LDVg LDV1

METHOD 3

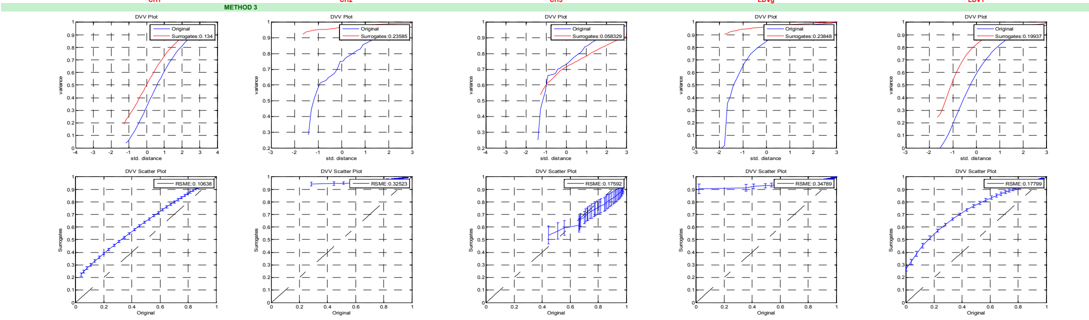

EXPERIMENT	SYSTEM CHARACTERISTCS	VARIABLES		METHOD 1				METHOD 2				METHOD 3			
				best **m**	best **τ**	rsme	RSME	calc **m**	**τ**	rsme	RSME	set **m**	set **τ**	rsme	RSME
15	SDOF CAR attached to fixed supports by 4 calibrated springs (2 on each side)	surface plastic (smooth) Middle spring taken out number of springs 2 x2; loading White Noise	CH1	4	1	0.1428	0.1078	7	1	0.1520	0.1053	3	1	0.1312	0.1118
			CH2	4	5	0.1913	0.3615	19	1	0.3416	0.2899	3	1	0.1730	0.2628
			CH3	8	1	0.2986	0.3386	10	1	0.2631	0.2176	3	1	0.1307	0.2297
			LDVg	6	1	0.0212	0.2731	9	1	0.1961	0.4149	3	1	0.2533	0.3451
			LDV1	2	1	0.1941	0.1550	11	1	0.2138	0.1470	3	1	0.1862	0.1727

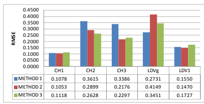

	CH1	CH2	CH3	LDVg	LDV1
METHOD 1	0.1078	0.3615	0.3386	0.2731	0.1550
METHOD 2	0.1053	0.2899	0.2176	0.4149	0.1470
METHOD 3	0.1118	0.2628	0.2297	0.3451	0.1727

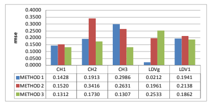

	CH1	CH2	CH3	LDVg	LDV1
METHOD 1	0.1428	0.1913	0.2986	0.0212	0.1941
METHOD 2	0.1520	0.3416	0.2631	0.1961	0.2138
METHOD 3	0.1312	0.1730	0.1307	0.2533	0.1862

Data recorded 3D Accelerometer

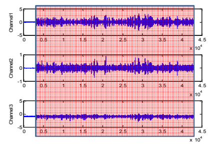

Data analysed 3D Accelerometer

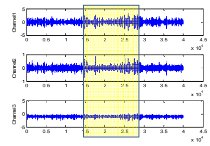

Data recorded LDV

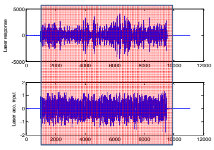

Data analysed LDV

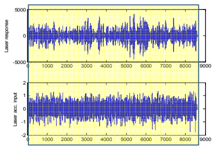

CH1 CH2 CH3 LDVg LDV1

METHOD 1

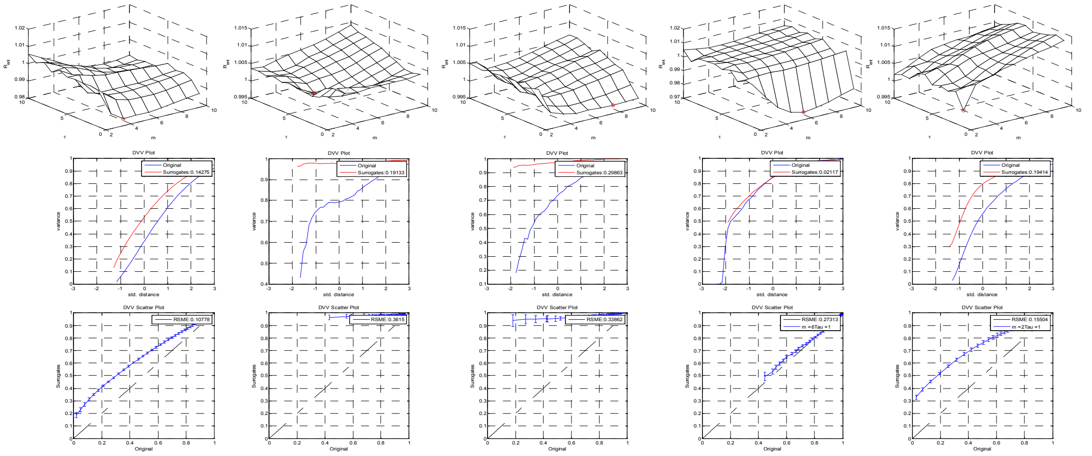

CH1 CH2 CH3 LDVg LDV1

METHOD 2

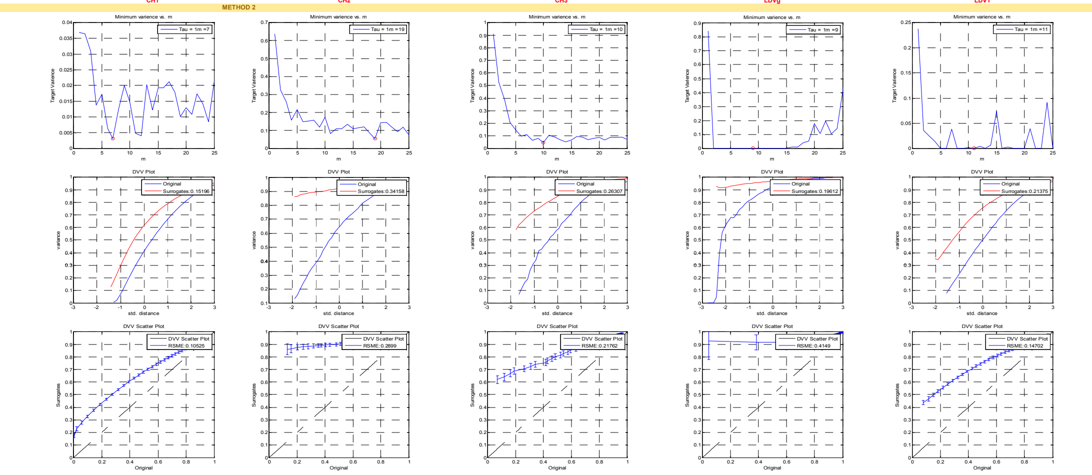

CH1 CH2 CH3 LDVg LDV1

METHOD 3

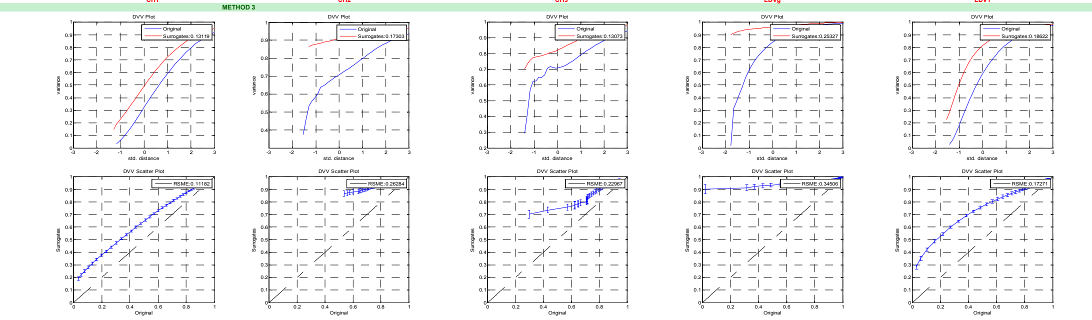

EXPERIMENT	SYSTEM CHARACTERISTCS	VARIABLES		METHOD 1				METHOD 2				METHOD 3			
				best **m**	best **τ**	rsme	RSME	calc **m**	**τ**	rsme	RSME	set **m**	set **τ**	rsme	RSME
16	SDOF CAR attached to fixed supports by 4 calibrated springs (2 on each side)	surface plastic (smooth) Middle spring taken out number of springs 2 x2; loading Sine Sweep	CH1	5	9	0.2767	0.1552	17	1	0.1652	0.1195	3	1	0.0990	0.1493
			CH2	10	2	0.3390	0.2481	13	1	0.3118	0.2162	3	1	0.2198	0.2020
			CH3	10	1	0.3098	0.1654	18	1	0.3506	0.1856	3	1	0.1513	0.1137
			LDVg	8	3	0.0936	0.1236	19	1	0.0688	0.1058	3	1	0.0306	0.1046
			LDV1	8	5	0.1726	0.1714	21	1	0.2837	0.1924	3	1	0.1688	0.1401

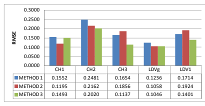

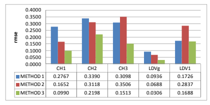

Data recorded 3D Accelerometer **Data analysed 3D Accelerometer** **Data recorded LDV** **Data analysed LDV**

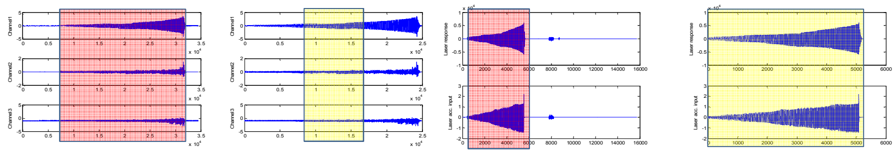

CH1 CH2 CH3 LDVg LDV1

METHOD 1

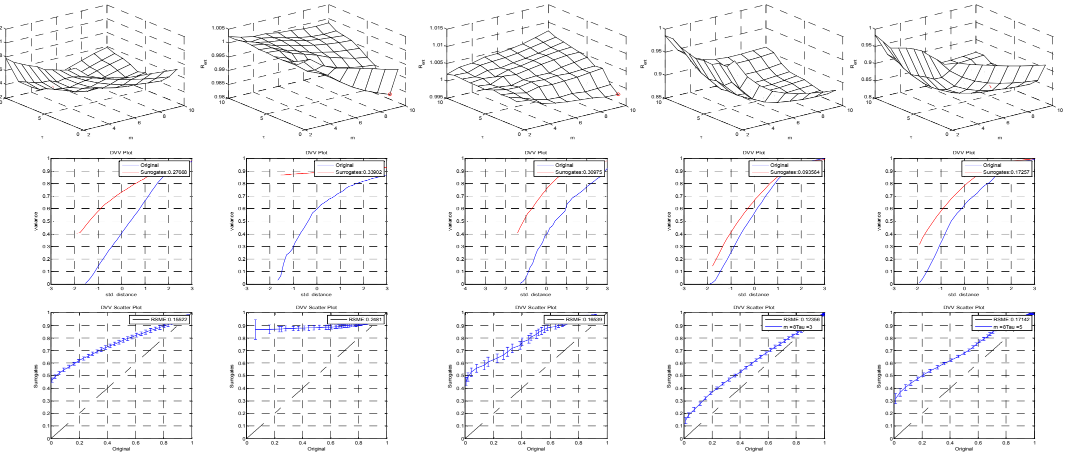

CH1 CH2 CH3 LDVg LDV1

METHOD 2

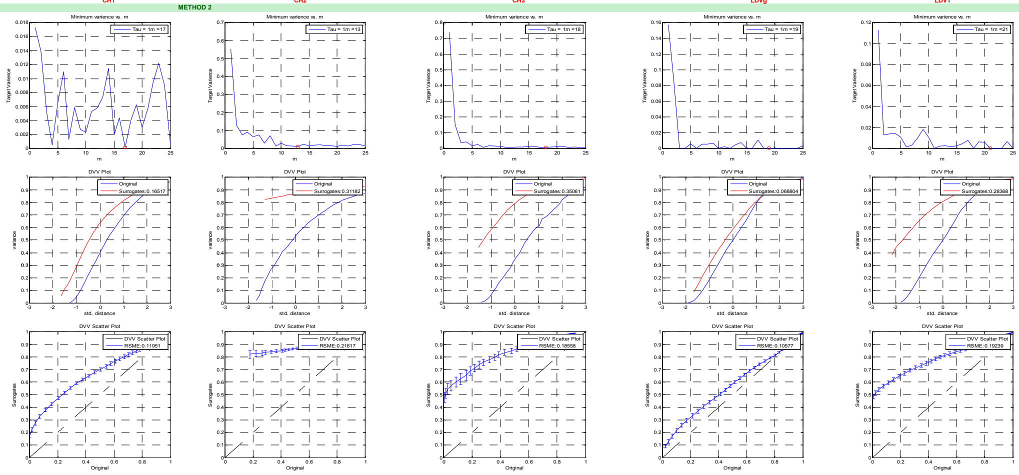

CH1 CH2 CH3 LDVg LDV1

METHOD 3

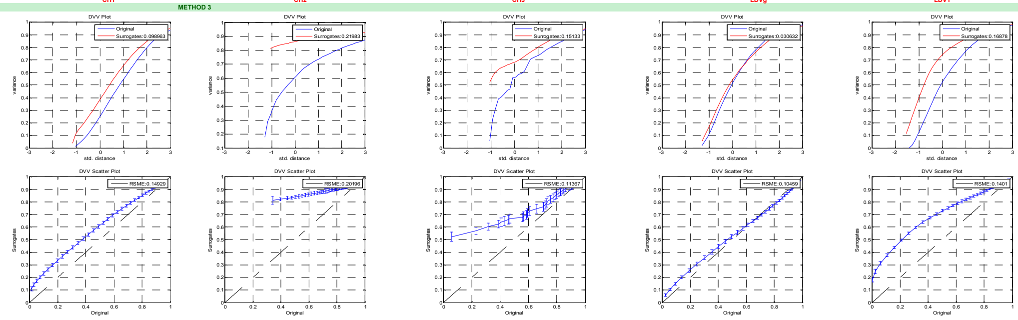

EXPERIMENT	SYSTEM CHARACTERISTCS	VARIABLES		METHOD 1				METHOD 2				METHOD 3			
				best m	best τ	rsme	RSME	calc m	τ	rsme	RSME	set m	set τ	rsme	RSME
17	SDOF CAR attached to fixed supports by 4 calibrated springs (2 on each side)	surface plastic (smooth) Middle spring taken out number of springs 2 x2; loading harmonic 2-4-6-8-10 Hz	CH1						1			3	1		
			CH2						1			3	1		
			CH3						1			3	1		
			LDVg	8	7	0.4169	0.2947	9	1	0.0295	0.1135	3	1	0.0213	0.1132
			LDV1	6	6	0.3819	0.2660	11	1	0.2797	0.1535	3	1	0.2075	0.1473

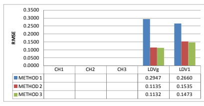

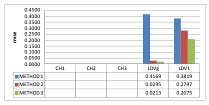

Data recorded 3D Accelerometer

Data analysed 3D Accelerometer

Data recorded LDV

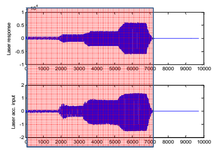

Data analysed LDV

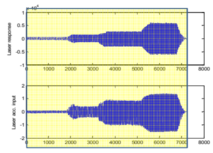

CH1 CH2 CH3 LDVg LDV1

METHOD 1

NO DATA

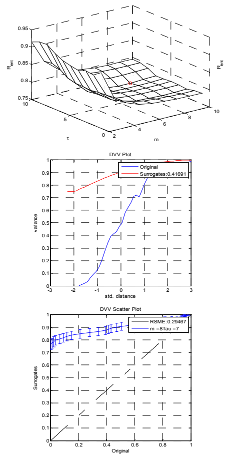

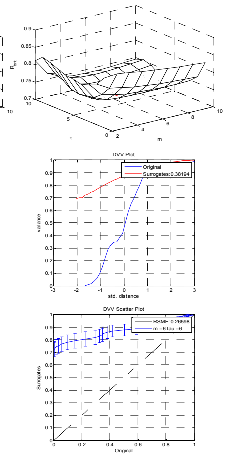

CH1 CH2 CH3 LDVg LDV1

METHOD 2

NO DATA

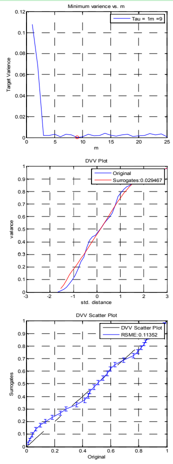

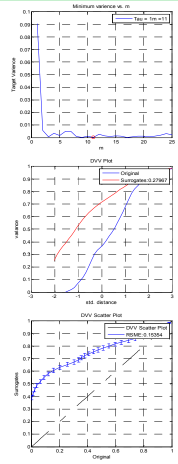

CH1 CH2 CH3 LDVg LDV1

METHOD 3

NO DATA

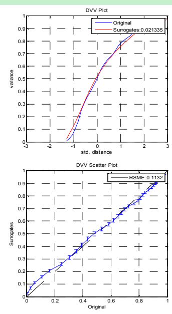

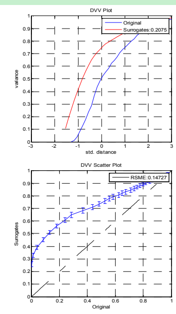

EXPERIMENT	SYSTEM CHARACTERISTCS	VARIABLES		METHOD 1				METHOD 2				METHOD 3			
				best **m**	best **τ**	rsme	RSME	calc **m**	**τ**	rsme	RSME	set **m**	set **τ**	rsme	RSME
18	SDOF CAR attached to fixed supports by 4 calibrated springs (2 on each side)	surface wood Middle spring taken out number of springs 2 x2; loading harmonic 2-4-6-8-10 Hz	CH1	4	10	0.3734	0.1949	2	1	0.2415	0.1973	3	1	0.2609	0.2021
			CH2	9	1	0.6737	0.3737	25	1	0.7082	0.3989	3	1	0.6603	0.3757
			CH3	5	2	0.3453	0.1859	8	1	0.2877	0.1577	3	1	0.2672	0.1497
			LDVg	9	7	0.4325	0.3138	17	1	0.0782	0.1186	3	1	0.0362	0.1067
			LDV1	7	5	0.2536	0.1535	3	1	0.0788	0.0906	3	1	0.0824	0.0909

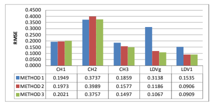

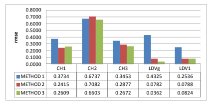

Data recorded 3D Accelerometer **Data analysed 3D Accelerometer** **Data recorded LDV** **Data analysed LDV**

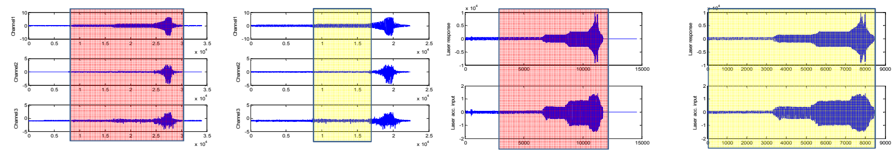

CH1 CH2 CH3 LDVg LDV1

METHOD 1

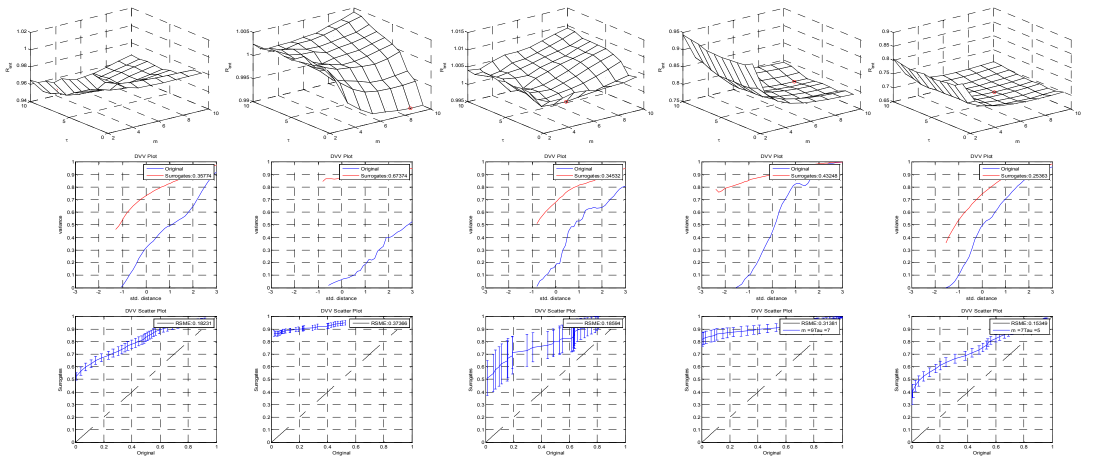

CH1 CH2 CH3 LDVg LDV1

METHOD 2

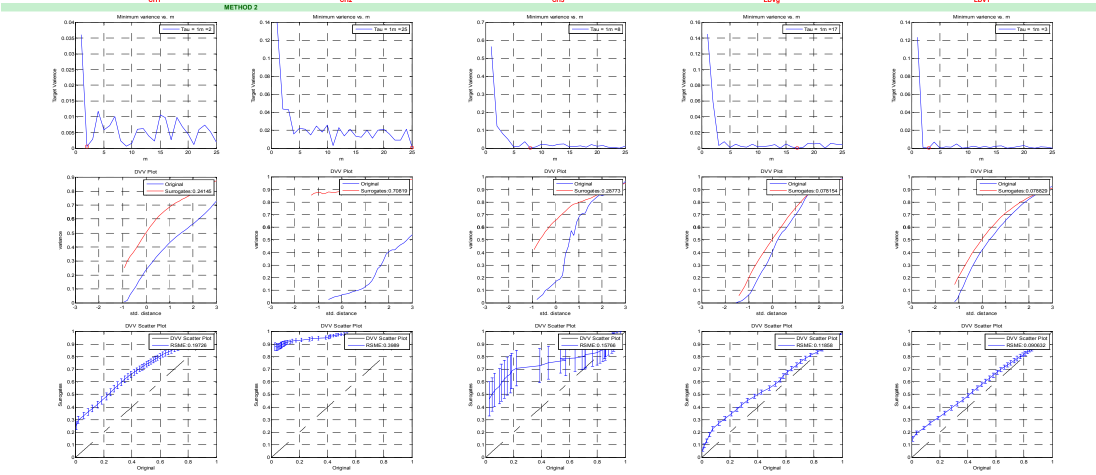

CH1 CH2 CH3 LDVg LDV1

METHOD 3

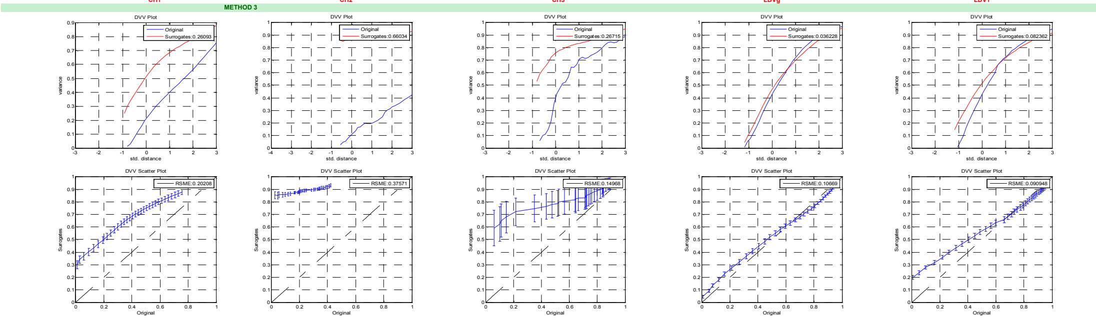

EXPERIMENT	SYSTEM CHARACTERISTCS	VARIABLES		METHOD 1				METHOD 2				METHOD 3			
				best **m**	best **τ**	rsme	RSME	calc **m**	**τ**	rsme	RSME	set **m**	set **τ**	rsme	RSME
19	SDOF CAR attached to fixed supports by 4 calibrated springs (2 on each side)	surface wood Middle spring taken out number of springs 2 x2; loading White Noise	CH1	6	2	0.1763	0.1301	10	1	0.1571	0.1116	3	1	0.1344	0.1141
			CH2	4	1	0.2821	0.3305	22	1	0.4097	0.3801	3	1	0.2458	0.3314
			CH3	4	1	0.2183	0.2895	24	1	0.4016	0.3327	3	1	0.1942	0.2893
			LDVg	6	1	0.2554	0.3742	3	1	0.2775	0.3400	3	1	0.2496	0.3423
			LDV1	2	4	0.2657	0.2551	9	1	0.2023	0.1411	3	1	0.1988	0.1703

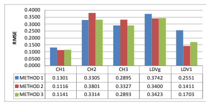

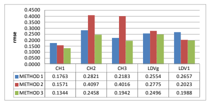

Data recorded 3D Accelerometer

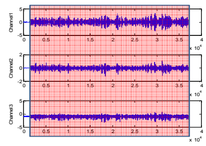

Data analysed 3D Accelerometer

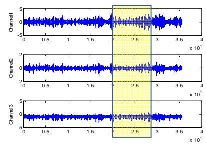

Data recorded LDV

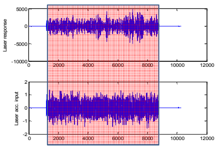

Data analysed LDV

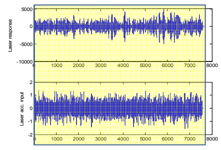

CH1 CH2 CH3 LDVg LDV1

METHOD 1

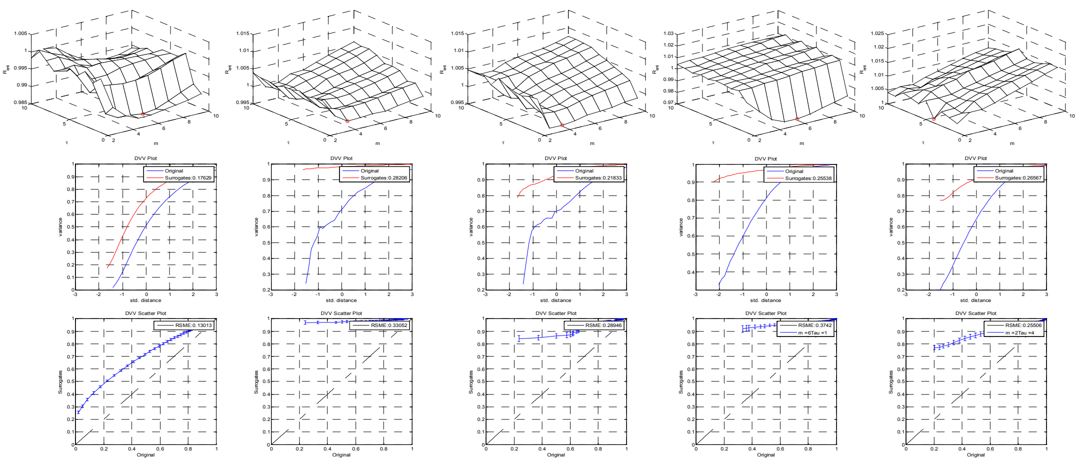

CH1 CH2 CH3 LDVg LDV1

METHOD 2

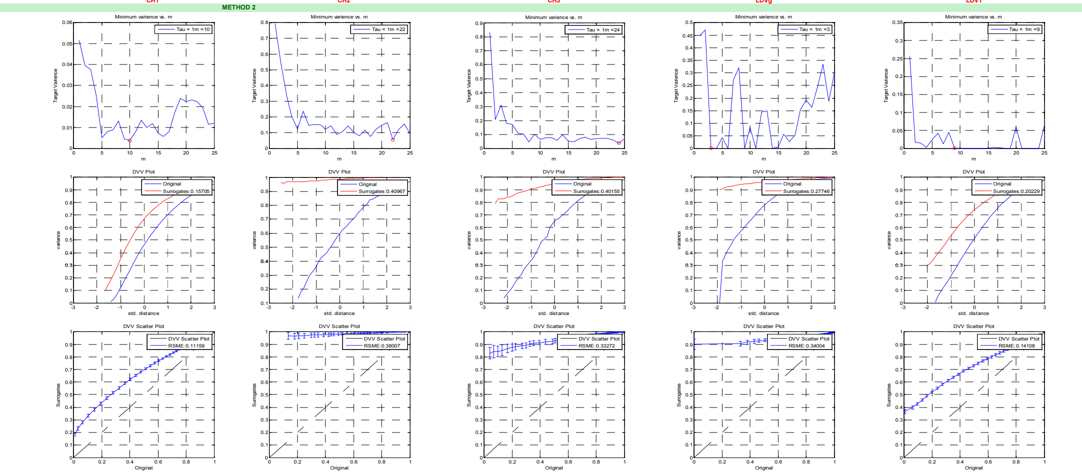

CH1 CH2 CH3 LDVg LDV1

METHOD 3

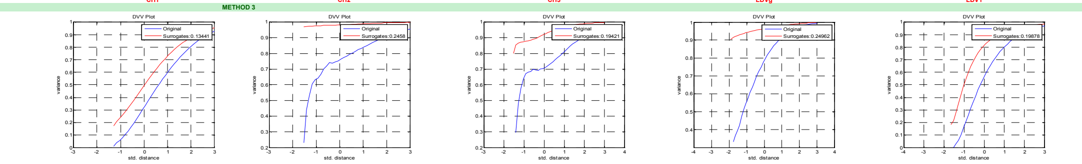

EXPERIMENT	SYSTEM CHARACTERISTCS	VARIABLES		METHOD 1				METHOD 2				METHOD 3			
				best m	best τ	rsme	RSME	calc m	τ	rsme	RSME	set m	set τ	rsme	RSME
20	SDOF CAR attached to fixed supports by 4 calibrated springs (2 on each side)	surface wood Middle spring taken out number of springs 2 x2; loading Sine Sweep	CH1	5	10	0.2834	0.1563	10	1	0.1620	0.1213	3	1	0.1279	0.1515
			CH2	10	1	0.4544	0.3182	12	1	0.4903	0.3278	3	1	0.3329	0.2866
			CH3	4	1	0.3403	0.2314	25	1	0.5086	0.2976	3	1	0.2175	0.2418
			LDVg	9	3	0.1069	0.1251	17	1	0.0593	0.1081	3	1	0.0348	0.1059
			LDV1	8	5	0.1804	0.1634	14	1	0.2493	0.1649	3	1	0.1649	0.1388

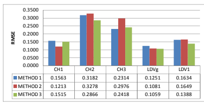

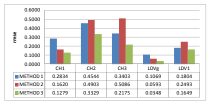

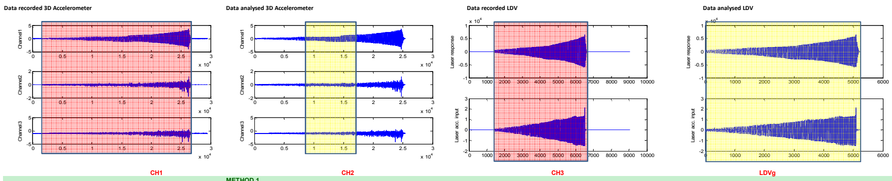

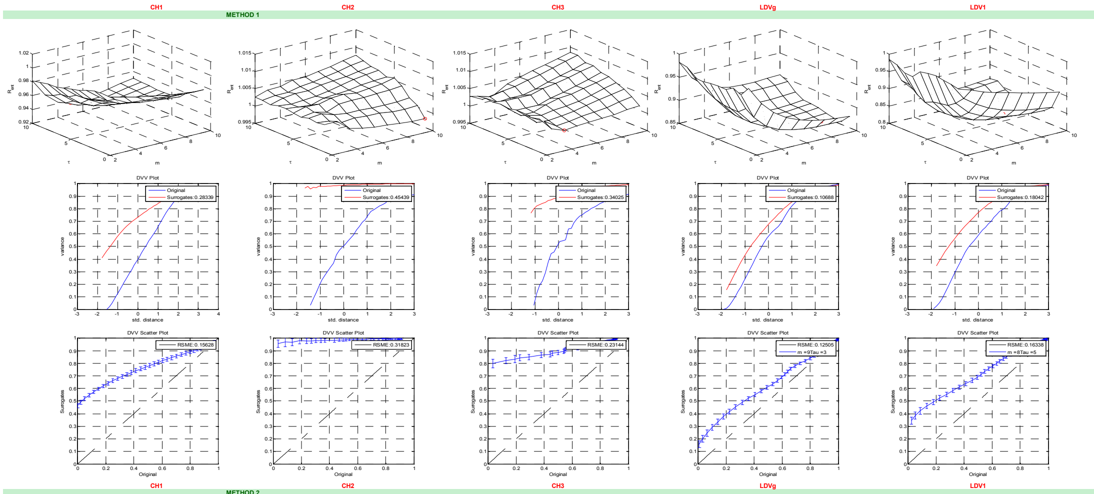

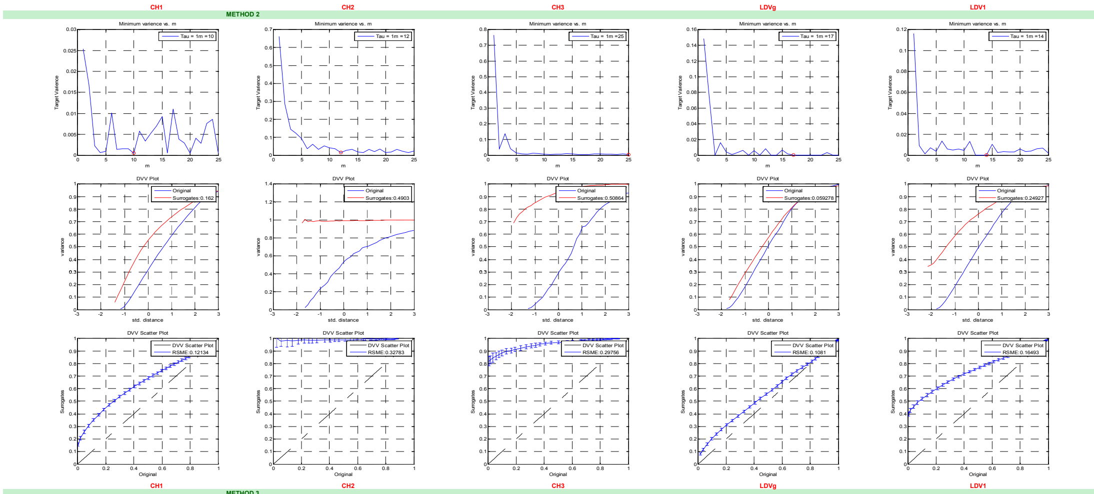

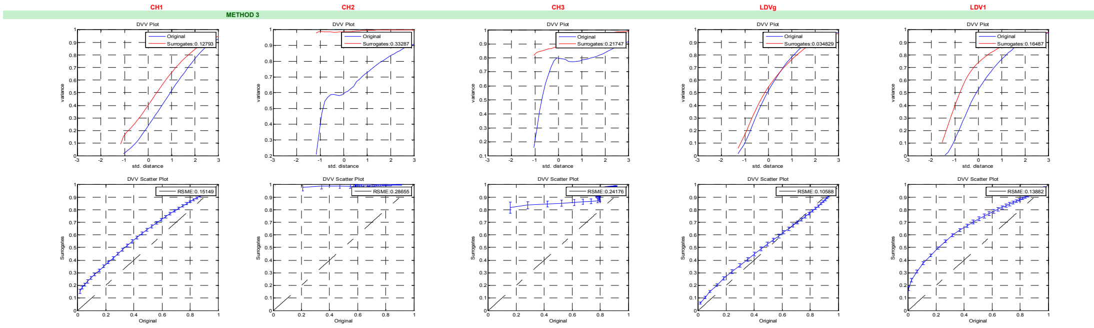

EXPERIMENT	SYSTEM CHARACTERISTCS	VARIABLES		METHOD 1				METHOD 2				METHOD 3			
				best m	best τ	rsme	RSME	calc m	τ	rsme	RSME	set m	set τ	rsme	RSME
21	SDOF CAR attached to fixed supports by 6 / 4 calibrated springs; Two middle springs are glued, detached at 13 sec / 38sec	surface wood Two middle springs are glued, detached at 13 sec / 38sec number of springs 2x3 / 2 x2; loading White Noise	CH1	6	1	0.1562	0.1031	6	1	0.1554	0.1043	3	1	0.1335	0.1079
			CH2	4	4	0.2074	0.3631	19	1	0.3613	0.3404	3	1	0.1947	0.3281
			CH3	3	1	0.1947	0.3281	14	1	0.3901	0.3646	3	1	0.2148	0.3271
			LDVg	6	1	0.1677	0.3935	10	1	0.0412	0.3492	3	1	0.0193	0.2759
			LDV1	2	8	0.0519	0.2460	20	1	0.0448	0.1007	3	1	0.0050	0.1372

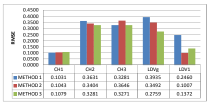

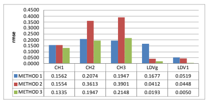

Data recorded 3D Accelerometer

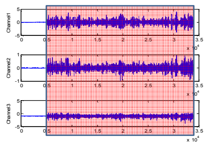

Data analysed 3D Accelerometer

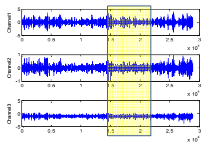

Data recorded LDV

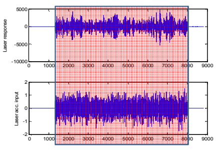

Data analysed LDV

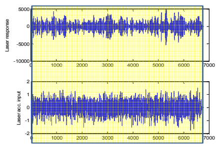

CH1 CH2 CH3 LDVg LDV1

METHOD 1

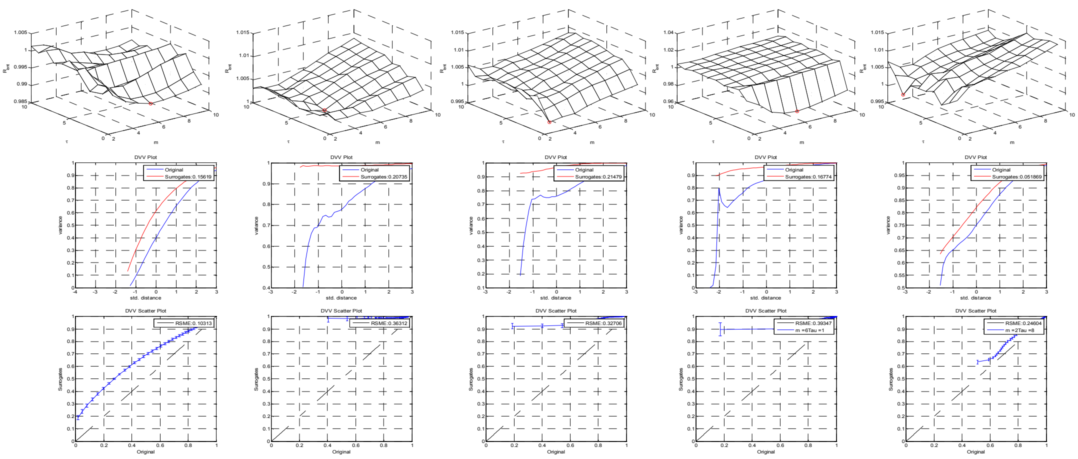

CH1 CH2 CH3 LDVg LDV1

METHOD 2

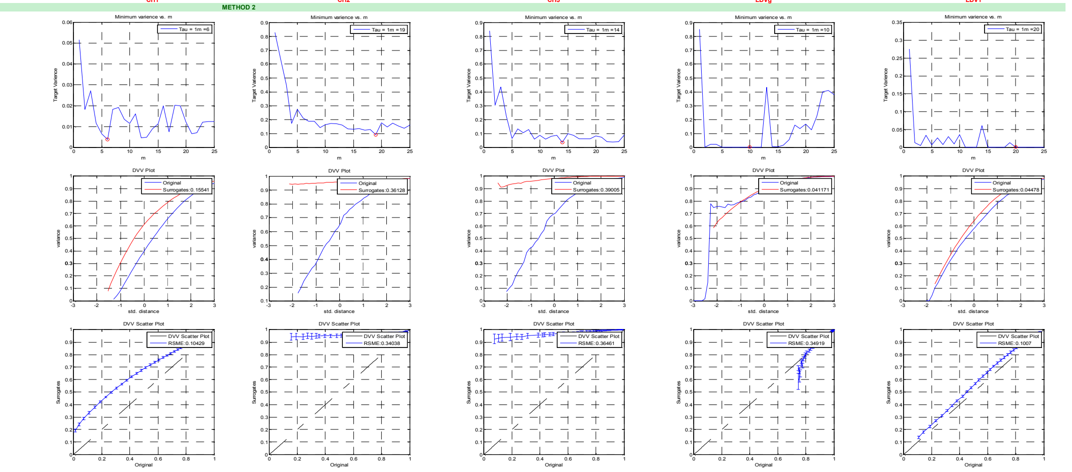

CH1 CH2 CH3 LDVg LDV1

METHOD 3

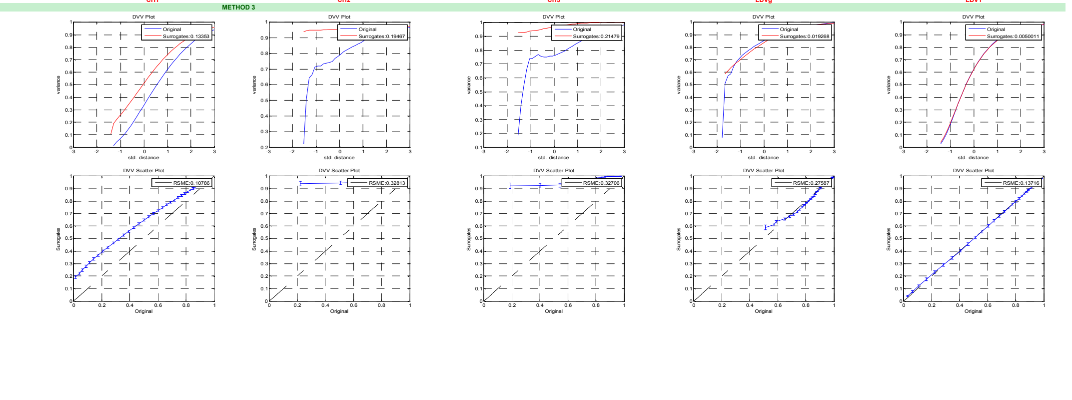

EXPERIMENT	SYSTEM CHARACTERISTCS	VARIABLES		METHOD 1				METHOD 2				METHOD 3			
				best m	best τ	rsme	RSME	calc m	τ	rsme	RSME	set m	set τ	rsme	RSME
HF	SDOF CAR attached to fixed supports by 4 calibrated springs	surface plastic (smooth) number of springs 2 x 3; loading High Frequency	CH1	2	8	0.1395	0.3746	24	1	0.3550	0.3235	3	1	0.2382	0.3390
			CH2	2	4	0.0564	0.4120	22	1	0.4344	0.3732	3	1	0.1624	0.3904
			CH3	2	2	0.0888	0.3616	20	1	0.4163	0.3340	3	1	0.1799	0.3568
			LDVg	5	1	0.3344	0.3091	22	1	0.4547	0.3248	3	1	0.2707	0.2848
			LDV1	2	2	0.0344	0.1209	13	1	0.2846	0.2393	3	1	0.2800	0.2289

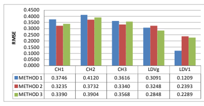

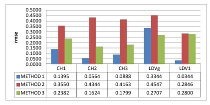

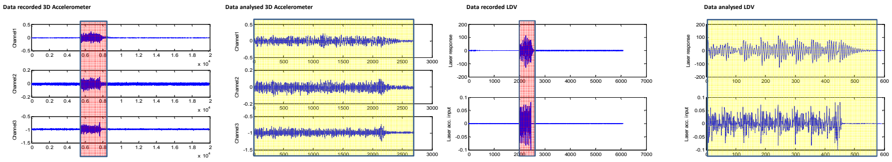

CH1 CH2 CH3 LDVg LDV1

METHOD 1

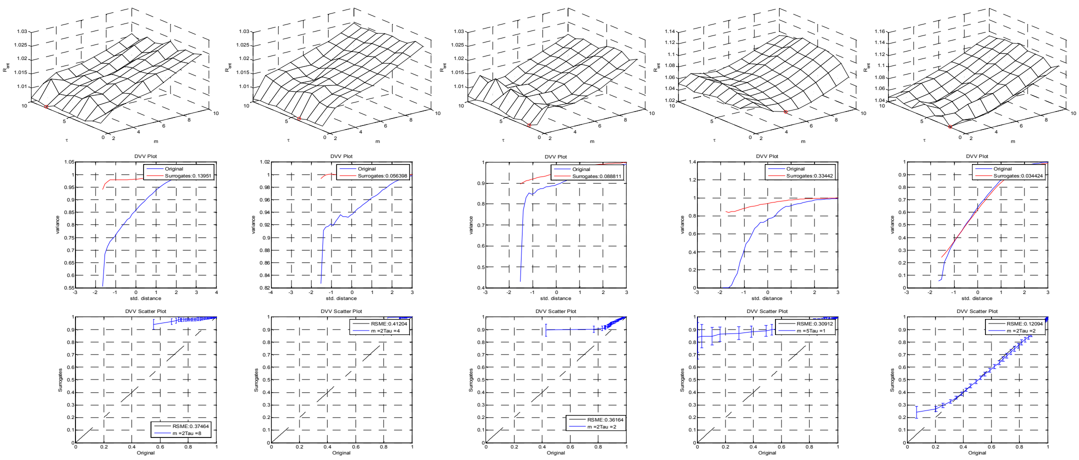

CH1 CH2 CH3 LDVg LDV1

METHOD 2

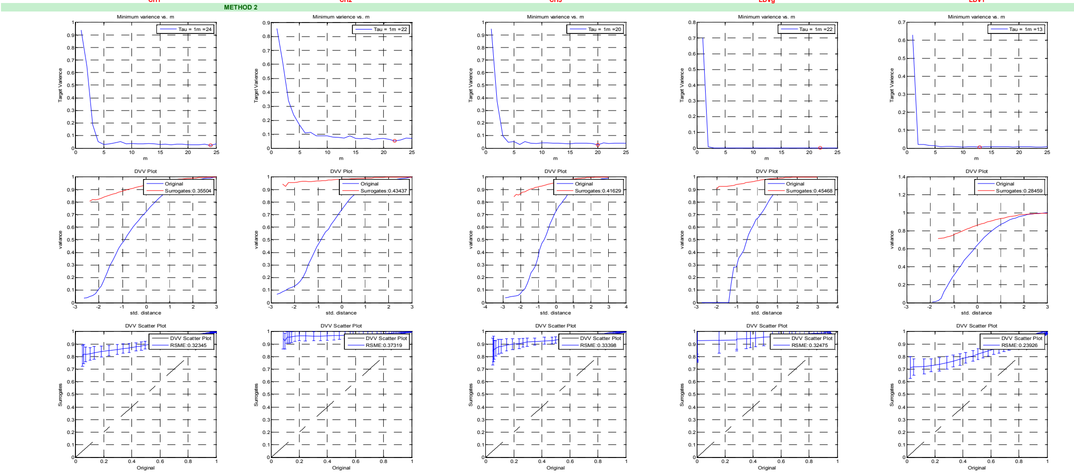

CH1 CH2 CH3 LDVg LDV1

METHOD 3

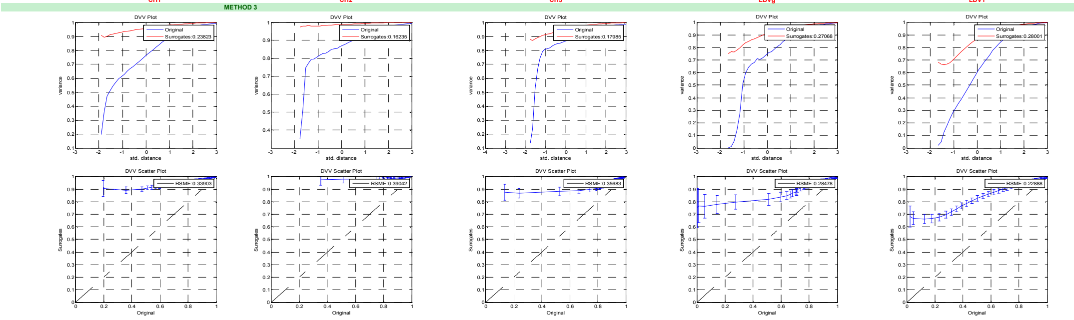

APPENDIX B4

Delay Vector Variance Method WTB Experiment Results

	SYSTEM LOADING	VARIABLES	METHOD 1				METHOD 2				METHOD 3			
			best m	best τ	rsme	RSME	calc m	τ	rsme	RSME	calc m	τ	rsme	RSME
1	Initial exp 4.38 Hz Angle of incidence 8 degree	CH1	6	1	0.7205	0.3879	22	1	0.4213	0.3237	3	1	0.4583	0.2916
		CH2	7	9	0.9878	0.5660	17	1	0.1372	0.6237	3	1	0.3264	0.5585
		CH3	6	1	0.6747	0.4278	23	1	0.6317	0.4002	3	1	0.5505	0.4688
		LDVg	5	5	0.0953	0.3211	5	1	0.5040	0.3054	3	1	0.5773	0.3781
		LDV1	5	1	0.0438	0.3418	24	1	0.0972	0.3084	3	1	0.0412	0.3481
		LDV2	4	2	0.3101	0.2569	6	1	0.3365	0.2308	3	1	0.3086	0.1947
		Strain 1	9	8	0.6131	0.3351	14	1	0.2633	0.2194	3	1	0.3456	0.1875
		Strain 2	8	8	0.5617	0.3094	16	1	0.1099	0.1336	3	1	0.1305	0.1011
		Strain 3	7	7	0.3638	0.2181	17	1	0.0544	0.0697	3	1	0.0233	0.0422
		Strain 4	6	7	0.3284	0.1853	19	1	0.0703	0.0856	3	1	0.0382	0.0543
2	Initial exp Angle of incidence 8 degree	CH1	5	1	0.6093	0.3173	5	1	0.3588	0.2668	3	1	0.4816	0.3171
		CH2	5	8	0.9668	0.5607	23	1	0.3603	0.5924	3	1	0.2699	0.2972
		CH3	5	1	0.8097	0.4405	9	1	0.9294	0.5168	3	1	0.8021	0.4437
		LDVg	4	9	0.9328	0.5527	14	1	0.8386	0.5160	3	1	0.4085	0.3380
		LDV1	6	3	0.0671	0.1716	8	1	0.0213	0.1324	3	1	0.0119	0.1794
		LDV2	5	3	0.1485	0.1734	14	1	0.4531	0.2417	3	1	0.3783	0.1961
		Strain 1	9	8	0.6019	0.3269	19	1	0.2566	0.2387	3	1	0.2918	0.1683
		Strain 2	8	7	0.5645	0.3068	19	1	0.1864	0.1825	3	1	0.0941	0.1157
		Strain 3	8	7	0.4423	0.2436	17	1	0.1131	0.1043	3	1	0.0545	0.0430
		Strain 4	7	7	0.3938	0.2139	19	1	0.1028	0.1161	3	1	0.0666	0.0737
3	FOCUS AT THE ACCELEROMETER	CH1	5	1	0.4504	0.3275	22	1	0.5728	0.3890	3	1	0.3546	0.2426
		CH2	6	1	0.5751	0.4730	12	1	0.4747	0.3636	3	1	0.6560	0.4446
		CH3	5	1	0.5871	0.4145	17	1	0.8665	0.4817	3	1	0.8260	0.4483
		LDVg	4	4	0.3597	0.2869	9	1	0.2614	0.2851	3	1	0.1330	0.4179
		LDV1	6	1	0.1596	0.5475	18	1	0.1519	0.5148	3	1	0.0494	0.5983
		LDV2	5	3	0.4586	0.2360	15	1	0.4340	0.2332	3	1	0.3864	0.2038
		Strain 1	9	1	0.5881	0.3173	12	1	0.2616	0.2070	3	1	0.3687	0.2082
		Strain 2	9	3	0.6479	0.3525	14	1	0.1868	0.1676	3	1	0.1133	0.1077
		Strain 3	9	8	0.5000	0.3055	16	1	0.0878	0.0847	3	1	0.0595	0.0413
		Strain 5	7	10	0.3831	0.2087	23	1	0.1138	0.1097	3	1	0.0591	0.0695
4	with knocks, no movement, best result	CH1	6	2	0.0636	0.1588	24	1	0.0935	0.2328	3	1	0.0541	0.2235
		CH2	6	2	0.2161	0.3215	17	1	0.1887	0.5295	3	1	0.1357	0.4681
		CH3	9	10	0.5314	0.3025	12	1	0.2107	0.1925	3	1	0.3073	0.2552
		LDVg	4	9	0.8576	0.5388	24	1	0.7246	0.5184	3	1	0.1639	0.3749
		LDV1	6	6	0.1467	0.1748	4	1	0.0136	0.1512	3	1	0.0432	0.1841
		LDV2	6	10	0.4526	0.2310	4	1	0.2622	0.1386	3	1	0.2510	0.1401
		Strain 1	7	7	0.2510	0.1820	19	1	0.2288	0.1852	3	1	0.2072	0.1376
		Strain 2	7	7	0.1704	0.1744	22	1	0.1201	0.1642	3	1	0.0469	0.1272
		Strain 3	7	7	0.3900	0.1977	24	1	0.2027	0.1712	3	1	0.1166	0.1391
		Strain 4	6	7	0.3486	0.1778	24	1	0.1359	0.1640	3	1	0.0758	0.1462
5	Harmonic resonance 4.4Hz Focus at accelerometer	CH1	6	10	0.0572	0.1473	13	1	0.0206	0.0943	3	1	0.0154	0.0872
		CH2	6	9	0.2603	0.2511	18	1	0.0178	0.1082	3	1	0.0139	0.1140
		CH3	3	9	0.0311	0.2153	7	1	0.0025	0.1630	3	1	0.0027	0.1741
		LDV	6	9	0.1335	0.2412	15	1	0.0863	0.1701	3	1	0.0595	0.1685
		LDV1	4	1	0.0070	0.1382	4	1	0.0090	0.1386	3	1	0.0031	0.1345
		LDV2	10	10	0.1712	0.1689	15	1	0.1024	0.1561	3	1	0.1424	0.1490
		Strain 1	10	9	0.1363	0.1717	4	1	0.1029	0.1583	3	1	0.1087	0.1381
		Strain 2	10	9	0.1358	0.1728	14	1	0.1973	0.2004	3	1	0.1003	0.1408
		Strain 3	10	9	0.1342	0.1726	4	1	0.1294	0.1608	3	1	0.1163	0.1417
		Strain 4	10	9	0.1340	0.1733	15	1	0.2504	0.2158	3	1	0.1123	0.1423
6	Harmonic resonance 2.0 Hz 2.5 Hz 3.0 Hz 3.5 Hz 4.0 Hz 4.2 Hz 4.3 Hz 4.4 Hz 4.5 Hz 4.6 Hz 5.0Hz 5.5 Hz 6.0 Hz 6.5Hz 7.0Hz Focus at accelerometer	CH1	7	10	0.2275	0.1270	5	1	0.0798	0.1487	3	1	0.0232	0.1595
		CH2	6	10	0.0394	0.1630	25	1	0.0428	0.1091	3	1	0.0170	0.0370
		CH3	5	10	0.0115	0.1307	13	1	0.0120	0.1562	3	1	0.0093	0.1984
		LDVg	9	9	0.2784	0.2324	23	1	0.1238	0.0992	3	1	0.0457	0.0861
		LDV1	6	10	0.1399	0.1412	8	1	0.0647	0.1352	3	1	0.0227	0.1566
		LDV2	10	10	0.3261	0.1723	4	1	0.2445	0.1365	3	1	0.2419	0.1441
		Strain 1	10	9	0.4033	0.2160	8	1	0.2391	0.1495	3	1	0.2333	0.1283
		Strain 2	9	7	0.2962	0.1651	21	1	0.2939	0.1699	3	1	0.2085	0.1367
		Strain 3	8	7	0.3948	0.2094	20	1	0.4380	0.2272	3	1	0.2630	0.1443
		Strain 4	8	7	0.3774	0.1991	5	1	0.2741	0.1440	3	1	0.2032	0.1226

7	Loading Sine sweep 2.0 Hz 6.0 Hz 60 sec Focus at accelerometer	CH1	4	10	0.0464	0.2276	11	1	0.0367	0.2039	3	1	0.0600	0.3182
		CH2	2	6	0.0578	0.2472	19	1	0.0725	0.1439	3	1	0.0688	0.1016
		CH3	4	9	0.0413	0.1323	25	1	0.0384	0.1946	3	1	0.0041	0.2724
		LDVg	10	2	0.3604	0.2572	12	1	0.1016	0.1091	3	1	0.0431	0.1088
		LDV1	6	6	0.3849	0.2246	10	1	0.0405	0.1303	3	1	0.0128	0.1705
		LDV2	8	10	0.0475	0.1453	12	1	0.3114	0.1656	3	1	0.2466	0.1656
		Strain 1	10	10	0.1344	0.1098	7	1	0.2157	0.1395	3	1	0.2384	0.1329
		Strain 2	10	9	0.1039	0.1309	18	1	0.2502	0.1598	3	1	0.1746	0.1363
		Strain 3	10	9	0.3815	0.2012	19	1	0.3918	0.2048	3	1	0.2432	0.1374
		Strain 4	10	9	0.3811	0.1996	23	1	0.3339	0.1717	3	1	0.2277	0.1420
8	Loading White Noise Focus at accelerometer	CH1	4	1	0.0036	0.0732	10	1	0.0160	0.1327	3	1	0.0104	0.0686
		CH2	5	1	0.0435	0.1647	19	1	0.0804	0.1612	3	1	0.0347	0.1264
		CH3	3	1	0.0224	0.0949	16	1	0.0383	0.1911	3	1	0.0168	0.0917
		LDVg	4	1	0.2189	0.3606	19	1	0.0113	0.3882	3	1	0.0444	0.2542
		LDV1	6	10	0.1990	0.1854	12	1	0.0274	0.1337	3	1	0.0057	0.1268
		LDV2	9	10	0.2077	0.2278	14	1	0.3092	0.2399	3	1	0.2351	0.2062
		Strain 1	7	7	0.2163	0.3643	22	1	0.3935	0.3613	3	1	0.2497	0.3134
		Strain 2	7	7	0.1296	0.2625	24	1	0.2236	0.2427	3	1	0.0852	0.2064
		Strain 3	10	6	0.3315	0.2834	17	1	0.1921	0.1646	3	1	0.1455	0.1260
		Strain 4	10	10	0.3392	0.2944	16	1	0.0946	0.1124	3	1	0.0854	0.0854
9	Loading White noise 4.365Hz at the peak Focus at top strain gauge	CH1	2	7	0.0203	0.1421	7	1	0.0114	0.1050	3	1	0.0121	0.0704
		CH2	5	1	0.0394	0.1675	18	1	0.0761	0.1552	3	1	0.0297	0.1257
		CH3	5	1	0.0123	0.1200	25	1	0.0501	0.2024	3	1	0.0222	0.0947
		LDVg	5	1	0.2075	0.3547	15	1	0.0690	0.3539	3	1	0.0522	0.2421
		LDV1	3	9	0.0339	0.1178	15	1	0.0119	0.1097	3	1	0.0071	0.0961
		LDV2	2	1	0.0059	0.1578	17	1	0.2185	0.2670	3	1	0.1820	0.2898
		Strain 1	3	3	0.0082	0.3065	6	1	0.2182	0.3492	3	1	0.2197	0.3364
		Strain 2	2	9	0.0052	0.3211	7	1	0.0842	0.2754	3	1	0.0730	0.2318
		Strain 3	10	6	0.2223	0.2959	23	1	0.1423	0.1939	3	1	0.1275	0.1328
		Strain 4	10	10	0.0073	0.1965	7	1	0.0813	0.1675	3	1	0.0804	0.0913
10	Loading Sine Sweep 2.0 Hz 6.0 Hz 60 sec Focus at top strain gauge	CH1	7	10	0.0696	0.1634	19	1	0.0964	0.2472	3	1	0.0406	0.2608
		CH2	2	8	0.0451	0.2468	20	1	0.0536	0.1117	3	1	0.0443	0.0576
		CH3	5	10	0.0142	0.1677	3	1	0.0102	0.2814	3	1	0.0688	0.3002
		LDVg	10	2	0.3382	0.2526	4	1	0.0559	0.1080	3	1	0.0501	0.0948
		LDV1	6	9	0.3271	0.1985	22	1	0.0585	0.1792	3	1	0.0137	0.1854
		LDV2	8	10	0.1156	0.1703	15	1	0.3039	0.1775	3	1	0.2673	0.1696
		Strain 1	10	10	0.1380	0.1337	14	1	0.4121	0.2053	3	1	0.2496	0.1449
		Strain 2	10	9	0.3985	0.2059	10	1	0.2505	0.1497	3	1	0.2046	0.1533
		Strain 3	10	9	0.4153	0.2148	11	1	0.3410	0.1694	3	1	0.3243	0.1976
		Strain 4	10	9	0.3978	0.2049	12	1	0.3542	0.1764	3	1	0.2607	0.1687
11	Harmonic resonance 2.0 Hz 2.5 Hz 3.0 Hz 3.5 Hz 4.0 Hz 4.2 Hz 4.3 Hz 4.4 Hz 4.5 Hz 4.6 Hz 5.0Hz 5.5 Hz 6.0 Hz 6.5Hz 7.0Hz Focus at top strain gauge	CH1	7	10	0.0832	0.1831	19	1	0.0857	0.2276	3	1	0.0090	0.2512
		CH2	6	10	0.0562	0.1197	22	1	0.0283	0.0817	3	1	0.0116	0.0566
		CH3	4	9	0.0117	0.1400	22	1	0.0071	0.1270	3	1	0.0033	0.1931
		LDVg	10	3	0.1712	0.1685	25	1	0.1249	0.1246	3	1	0.0476	0.1111
		LDV1	8	10	0.1882	0.1488	22	1	0.1733	0.1619	3	1	0.0513	0.1534
		LDV2	10	10	0.3138	0.1713	23	1	0.2482	0.1402	3	1	0.2315	0.1334
		Strain 1	10	10	0.2620	0.1491	17	1	0.4013	0.2202	3	1	0.2123	0.1152
		Strain 2	10	9	0.3953	0.2354	21	1	0.3584	0.1932	3	1	0.2224	0.1279
		Strain 3	10	9	0.3963	0.2366	5	1	0.2270	0.1398	3	1	0.2484	0.1399
		Strain 4	10	9	0.3737	0.2128	19	1	0.4437	0.2166	3	1	0.2365	0.1354
12	Harmonic resonance 2.0 Hz 2.5 Hz 3.0 Hz 3.5 Hz 4.0 Hz 4.2 Hz 4.3 Hz 4.4 Hz 4.5 Hz 4.6 Hz 5.0Hz 5.5 Hz 6.0 Hz 6.5Hz 7.0Hz Focus at mid strain gauge	CH1	2	1	0.1527	0.1006	4	1	0.0109	0.0823	3	1	0.0125	0.0867
		CH2	2	8	0.0106	0.3796	22	1	0.0315	0.2460	3	1	0.0153	0.1746
		CH3	4	4	0.0039	0.1078	1	1	0.0044	0.1585	3	1	0.0020	0.1523
		LDVg	10	2	0.1702	0.1444	22	1	0.1419	0.1289	3	1	0.0433	0.1084
		LDV1	7	9	0.1465	0.1440	2	1	0.0104	0.1702	3	1	0.0289	0.1622
		LDV2	10	9	0.3163	0.1872	24	1	0.2205	0.1337	3	1	0.2131	0.1233
		Strain 1	10	10	0.2410	0.1465	5	1	0.2325	0.1457	3	1	0.2172	0.1187
		Strain 2	10	10	0.2919	0.1654	23	1	0.3287	0.1857	3	1	0.1936	0.1191
		Strain 3	10	9	0.3749	0.2301	18	1	0.4264	0.2194	3	1	0.2271	0.1299
		Strain 4	10	9	0.3499	0.2086	7	1	0.2936	0.1784	3	1	0.2519	0.1433

13	Loading Sine Sweep 2.0 Hz 6.0 Hz 60 sec Focus at mid strain gauge	CH1	3	9	0.0425	0.2044	21	1	0.0639	0.3005	3	1	0.0241	0.2905
		CH2	8	9	0.1169	0.2192	17	1	0.0798	0.1423	3	1	0.0533	0.0738
		CH3	3	8	0.0259	0.1349	22	1	0.0196	0.1741	3	1	0.0227	0.2591
		LDVg	10	2	0.1912	0.1799	7	1	0.1105	0.1670	3	1	0.0619	0.1380
		LDV1	6	6	0.1866	0.2810	5	1	0.0367	0.3386	3	1	0.0668	0.3511
		LDV2	7	7	0.0617	0.2329	24	1	0.5283	0.3078	3	1	0.4848	0.3156
		Strain 1	10	10	0.0882	0.1039	22	1	0.4030	0.2106	3	1	0.2604	0.1358
		Strain 2	9	9	0.0766	0.1423	7	1	0.2112	0.1369	3	1	0.2040	0.1564
		Strain 3	10	9	0.3634	0.1895	5	1	0.2536	0.1320	3	1	0.2723	0.1620
		Strain 4	9	9	0.3700	0.1903	4	1	0.2454	0.1417	3	1	0.2522	0.1643
14	Loading White noise 4.336Hz at the peak next 23Hz Focus at mid strain gauge	CH1	5	1	0.0072	0.0756	24	1	0.0156	0.0853	3	1	0.0080	0.0732
		CH2	5	1	0.0372	0.1616	14	1	0.0489	0.1552	3	1	0.0277	0.1218
		CH3	4	1	0.0190	0.1089	21	1	0.0537	0.1977	3	1	0.0153	0.0961
		LDVg	8	1	0.1692	0.3932	25	1	0.0381	0.4272	3	1	0.0524	0.2549
		LDV1	2	2	0.0030	0.2366	3	1	0.0044	0.1145	3	1	0.0019	0.1134
		LDV2	2	4	0.1031	0.3799	4	1	0.2186	0.2779	3	1	0.2233	0.2656
		Strain 1	2	5	0.0023	0.3227	18	1	0.2176	0.4070	3	1	0.2059	0.3447
		Strain 2	3	5	0.0068	0.2992	22	1	0.0866	0.2729	3	1	0.0637	0.2257
		Strain 3	2	9	0.2249	0.3144	25	1	0.1299	0.1882	3	1	0.1149	0.1277
		Strain 4	7	2	0.2378	0.2272	18	1	0.0800	0.1192	3	1	0.0721	0.0910
15	Loading White noise 4.336Hz at the peak next 23Hz Focus at bottom strain gauge	CH1	4	1	0.0062	0.0692	5	1	0.0066	0.0772	3	1	0.0038	0.0668
		CH2	5	1	0.0321	0.1750	22	1	0.0695	0.1675	3	1	0.0206	0.1353
		CH3	4	1	0.0192	0.1124	17	1	0.0467	0.1979	3	1	0.0168	0.0963
		LDVg	8	1	0.0505	0.3124	9	1	0.0654	0.3185	3	1	0.0442	0.2607
		LDV1	2	10	0.0086	0.1173	19	1	0.0120	0.0846	3	1	0.0041	0.1057
		LDV2	6	1	0.3039	0.3063	18	1	0.3192	0.3524	3	1	0.2591	0.2782
		Strain 1	8	1	0.3199	0.3504	14	1	0.3787	0.3699	3	1	0.2443	0.3280
		Strain 2	7	7	0.1514	0.3172	19	1	0.1445	0.2367	3	1	0.2132	0.2352
		Strain 3	10	6	0.1905	0.2279	18	1	0.1627	0.1652	3	1	0.2765	0.1664
		Strain 4	10	10	0.1453	0.2298	19	1	0.0940	0.1269	3	1	0.2801	0.1815
16	Loading Sine Sweep 2.0 Hz 6.0 Hz 60 sec Focus at bottom strain gauge	CH1	4	10	0.0716	0.1065	25	1	0.0620	0.1974	3	1	0.0354	0.2434
		CH2	2	5	0.0396	0.2383	7	1	0.0333	0.0989	3	1	0.0144	0.0673
		CH3	3	10	0.0141	0.1101	9	1	0.0089	0.1931	3	1	0.0087	0.2193
		LDVg	10	2	0.1700	0.1688	21	1	0.1494	0.1387	3	1	0.0528	0.1211
		LDV1	6	6	0.1758	0.1823	11	1	0.0872	0.1796	3	1	0.0314	0.2079
		LDV2	8	8	0.3659	0.2303	20	1	0.3000	0.1593	3	1	0.2509	0.1316
		Strain 1	10	10	0.1578	0.1270	9	1	0.2749	0.1510	3	1	0.2501	0.1336
		Strain 2	9	9	0.1196	0.1483	6	1	0.2365	0.1597	3	1	0.1830	0.1559
		Strain 3	10	10	0.4309	0.2256	10	1	0.3394	0.1691	3	1	0.2680	0.1610
		Strain 4	9	9	0.3920	0.2015	5	1	0.2818	0.1535	3	1	0.2522	0.1629
17	Harmonic resonance 2.0 Hz 2.5 Hz 3.0 Hz 3.5 Hz 4.0 Hz 4.2 Hz 4.3 Hz 4.4 Hz 4.5 Hz 4.6 Hz 5.0Hz 5.5 Hz 6.0 Hz 6.5Hz 7.0Hz Focus at bottom strain gauge.	CH1	7	10	0.1119	0.1255	22	1	0.1015	0.1965	3	1	0.0530	0.2385
		CH2	6	10	0.0359	0.1084	17	1	0.0197	0.0814	3	1	0.0073	0.0491
		CH3	4	10	0.0191	0.1464	14	1	0.0181	0.1311	3	1	0.0152	0.1867
		LDVg	10	8	0.2920	0.2477	13	1	0.1010	0.0961	3	1	0.0445	0.1009
		LDV1	5	9	0.0212	0.1582	11	1	0.0163	0.1671	3	1	0.0111	0.1873
		LDV2	8	7	0.3506	0.2324	21	1	0.3050	0.1632	3	1	0.2263	0.1206
		Strain 1	10	7	0.3605	0.2185	15	1	0.3875	0.2077	3	1	0.2459	0.1285
		Strain 2	9	7	0.3372	0.1942	10	1	0.2350	0.1589	3	1	0.2011	0.1230
		Strain 3	10	7	0.4138	0.2289	10	1	0.2820	0.1681	3	1	0.2267	0.1304
		Strain 4	9	7	0.3715	0.2099	9	1	0.2784	0.1719	3	1	0.2293	0.1324

* accelerometer placed close to the top of WTB

CH1 - accelerometer channel 1 in the direction of applied vibrations

CH2 - accelerometer channel 2 perpendicular to the direction of applied vibrations

CH3 - accelerometer channel 3 perpendicular to the direction of applied vibrations

LDVg - laser dopler vibrometer (LDV) measurements of accelerometer input

LDV1 - LDV measurements (displacement)

LDV2 - LDV measurements (velocity)

Strain 1 - strain gauge 1 at 1/3 length of WTB from the top

Strain 2 - strain gauge 2 at 2/3 length of WTB from the top

Strain 3 - strain gauge 3 close to bottom of WTB

Strain 5 - strain gauge 5 opposite of 3

EXPERIMENT	VARIABLES		METHOD 1				METHOD 2				METHOD 3			
			best m	best τ	rsme	RSME	calc m	τ	rsme	RSME	set m	set τ	rsme	RSME
1	Initial exp 4.38 Hz Angle of incidence 8 degree	CH1	6	1	0.7205	0.3879	22	1	0.4213	0.3237	3	1	0.4583	0.2916
		CH2	7	9	0.9878	0.5660	17	1	0.1372	0.6237	3	1	0.3264	0.5585
		CH3	6	1	0.6747	0.4278	23	1	0.6317	0.4002	3	1	0.5505	0.4688
		LDVg	5	5	0.0953	0.3211	5	1	0.5040	0.3054	3	1	0.5773	0.3781
		LDV1	5	1	0.0438	0.3418	24	1	0.0972	0.3084	3	1	0.0412	0.3481
		LDV2	4	2	0.3101	0.2569	6	1	0.3365	0.2308	3	1	0.3086	0.1947
		Strain 1	9	8	0.6131	0.3351	14	1	0.2633	0.2194	3	1	0.3456	0.1875
		Strain 2	8	8	0.5617	0.3094	16	1	0.1099	0.1336	3	1	0.1305	0.1011
		Strain 3	7	7	0.3638	0.2181	17	1	0.0544	0.0697	3	1	0.0233	0.0422
		Strain 4	6	7	0.3284	0.1853	19	1	0.0703	0.0856	3	1	0.0382	0.0543

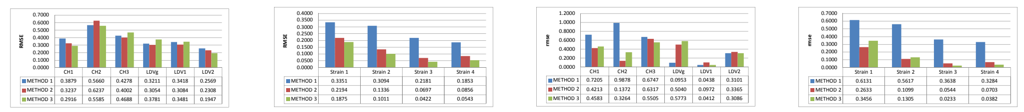

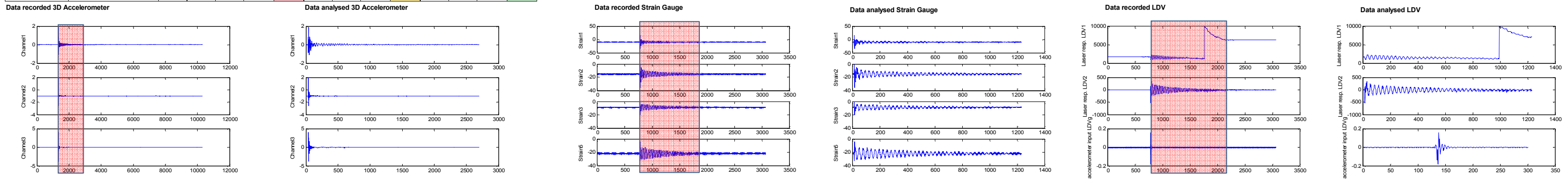

METHOD 1

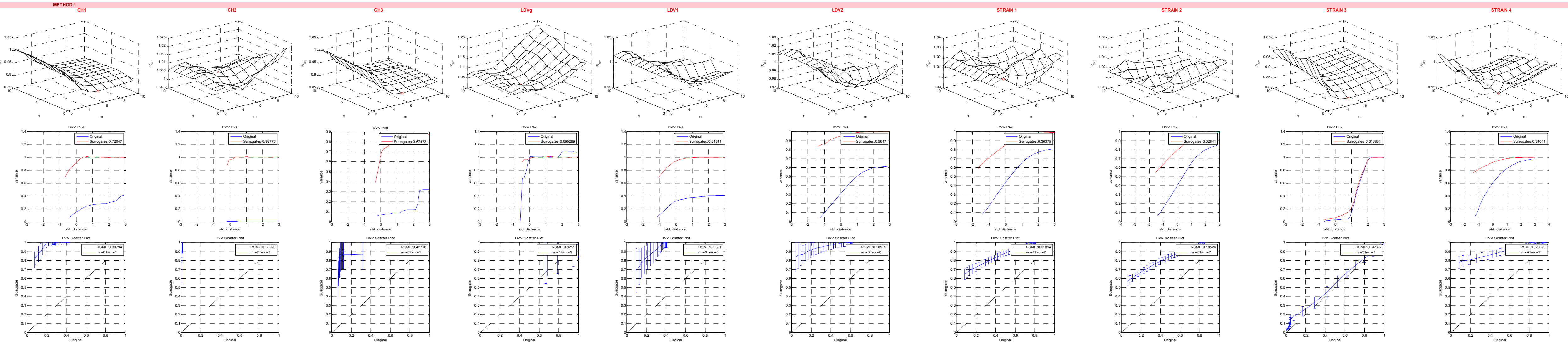

METHOD 2

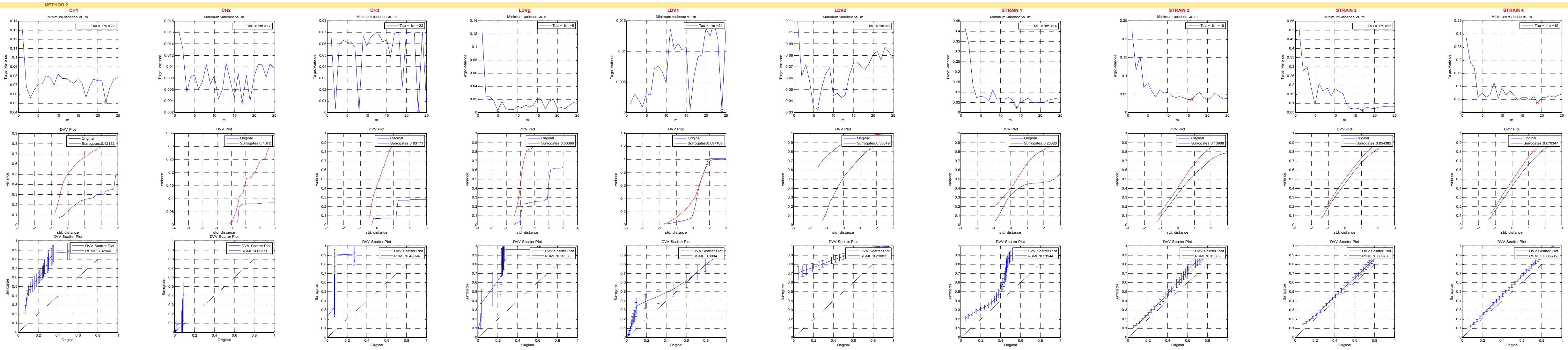

METHOD 3

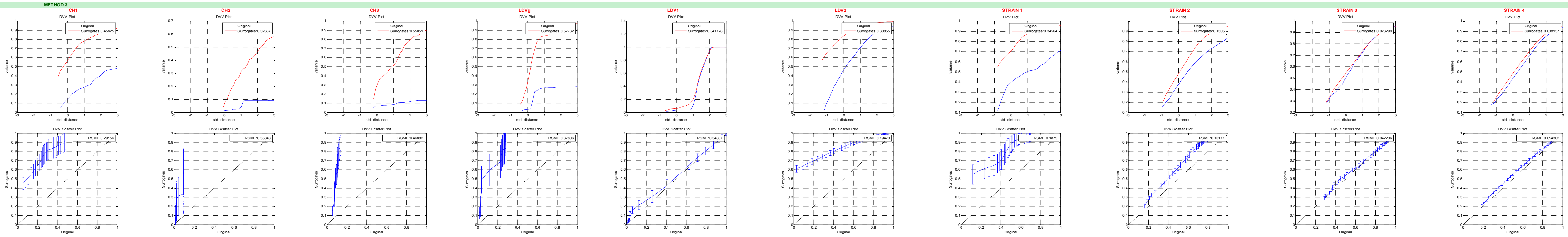

EXPERIMENT	VARIABLES		METHOD 1				METHOD 2				METHOD 3			
			best **m**	best **τ**	rsme	RSME	calc **m**	**τ**	rsme	RSME	set **m**	set **τ**	rsme	RSME
2	Initial exp Angle of incidence 8 degree	CH1	5	1	0.6093	0.3173	5	1	0.3588	0.2668	3	1	0.4816	0.3171
		CH2	5	8	0.9668	0.5607	23	1	0.3603	0.5924	3	1	0.2699	0.2972
		CH3	5	1	0.8097	0.4405	9	1	0.9294	0.5168	3	1	0.8021	0.4437
		LDVg	4	9	0.9328	0.5527	14	1	0.8386	0.5160	3	1	0.4085	0.3380
		LDV1	6	3	0.0671	0.1716	8	1	0.0213	0.1324	3	1	0.0119	0.1794
		LDV2	5	3	0.1485	0.1734	14	1	0.4531	0.2417	3	1	0.3783	0.1961
		Strain 1	9	8	0.6019	0.3269	19	1	0.2566	0.2387	3	1	0.2918	0.1683
		Strain 2	8	7	0.5645	0.3068	19	1	0.1864	0.1825	3	1	0.0941	0.1157
		Strain 3	8	7	0.4423	0.2436	17	1	0.1131	0.1043	3	1	0.0545	0.0430
		Strain 4	7	7	0.3938	0.2139	19	1	0.1028	0.1161	3	1	0.0666	0.0737

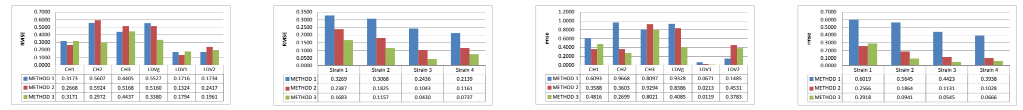

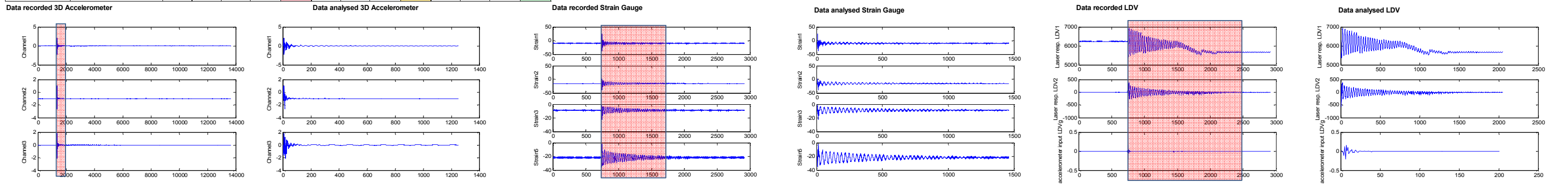

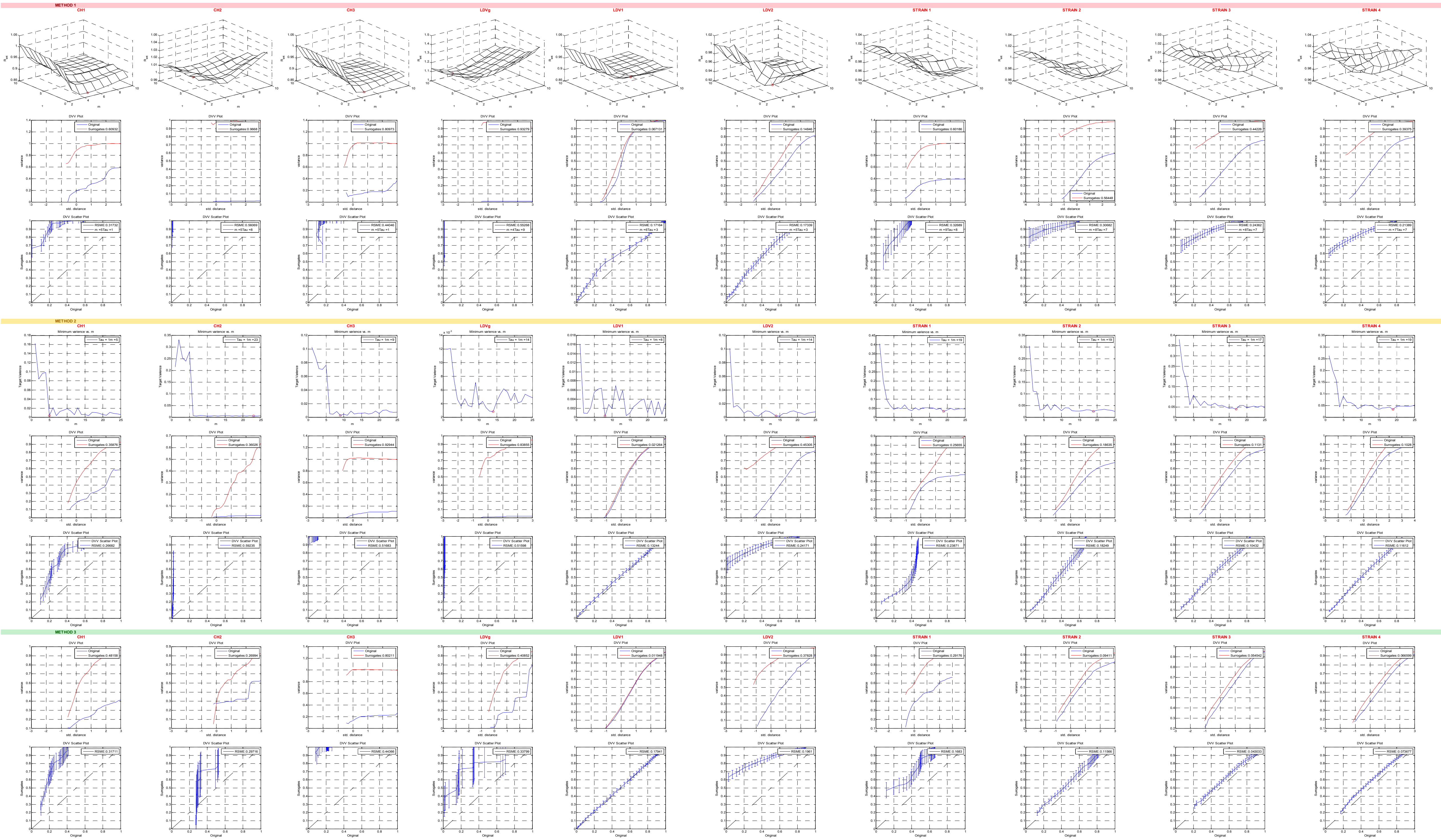

EXPERIMENT	VARIABLES		METHOD 1				METHOD 2				METHOD 3			
			best **m**	best τ	rsme	RSME	calc **m**	τ	rsme	RSME	set **m**	set τ	rsme	RSME
3	FOCUS AT THE ACCELEROMETER	CH1	5	1	0.4504	0.3275	22	1	0.5728	0.3890	3	1	0.3546	0.2426
		CH2	6	1	0.5751	0.4730	12	1	0.4747	0.3636	3	1	0.6560	0.4446
		CH3	5	1	0.5871	0.4145	17	1	0.8665	0.4817	3	1	0.8260	0.4483
		LDVg	4	4	0.3597	0.2869	9	1	0.2614	0.2851	3	1	0.1330	0.4179
		LDV1	6	1	0.1596	0.5475	18	1	0.1519	0.5148	3	1	0.0494	0.5983
		LDV2	5	3	0.4586	0.2360	15	1	0.4340	0.2332	3	1	0.3864	0.2038
		Strain 1	9	8	0.5881	0.3173	12	1	0.2616	0.2070	3	1	0.3687	0.2082
		Strain 2	9	10	0.6479	0.3525	14	1	0.1868	0.1676	3	1	0.1133	0.1077
		Strain 3	9	9	0.5000	0.3055	16	1	0.0878	0.0847	3	1	0.0595	0.0413
		Strain 5	7	7	0.3831	0.2087	23	1	0.1138	0.1097	3	1	0.0591	0.0695

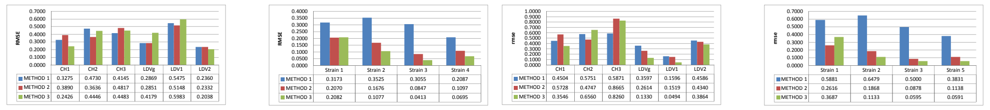

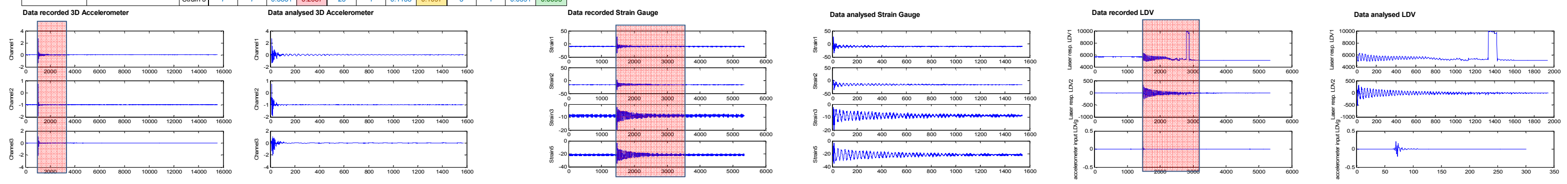

METHOD 1

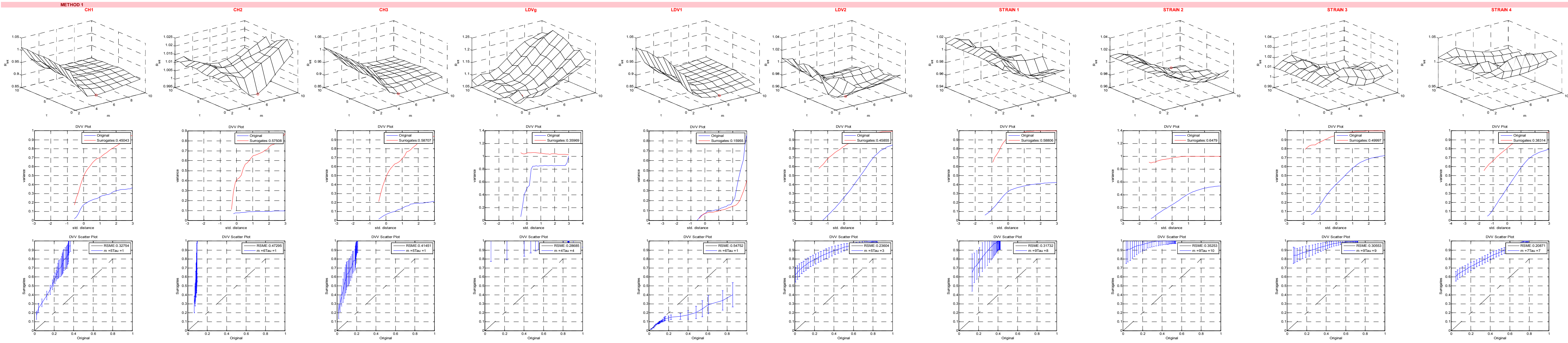

METHOD 2

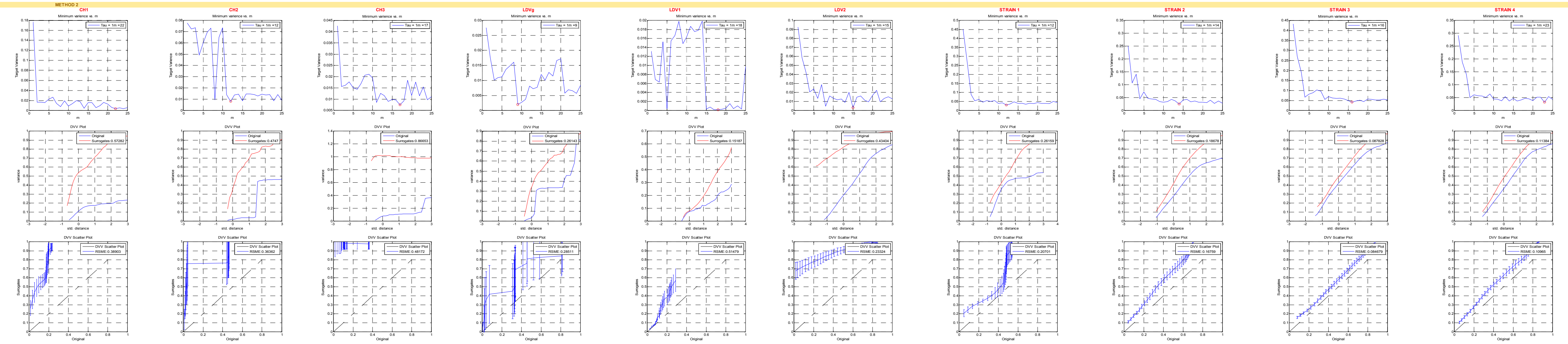

METHOD 3

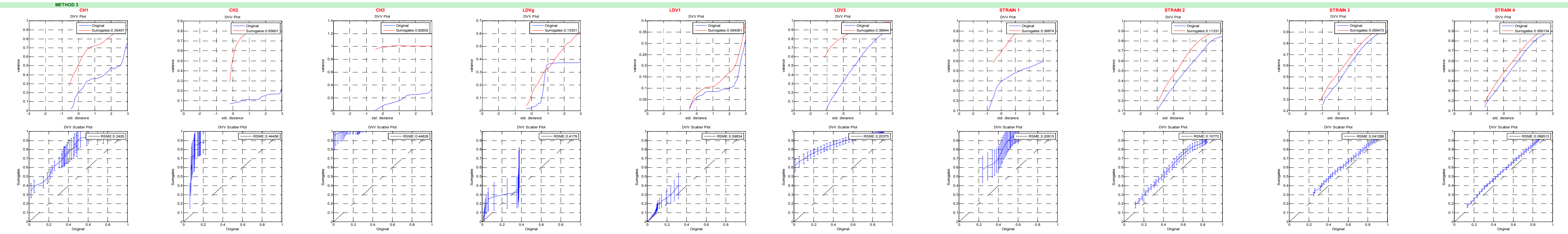

EXPERIMENT	VARIABLES		METHOD 1				METHOD 2				METHOD 3			
			best **m**	best **τ**	rsme	RSME	calc **m**	**τ**	rsme	RSME	set **m**	set **τ**	rsme	RSME
4	with knocks, no movement, best result	CH1	6	2	0.0636	0.1588	24	1	0.0935	0.2328	3	1	0.0541	0.2235
		CH2	6	2	0.2161	0.3215	17	1	0.1887	0.5295	3	1	0.1357	0.4681
		CH3	9	10	0.5314	0.3025	12	1	0.2107	0.1925	3	1	0.3073	0.2552
		LDVg	4	9	0.8576	0.5388	24	1	0.7246	0.5184	3	1	0.1639	0.3749
		LDV1	6	6	0.1467	0.1748	4	1	0.0136	0.1512	3	1	0.0432	0.1841
		LDV2	6	10	0.4526	0.2310	4	1	0.2622	0.1386	3	1	0.2510	0.1401
		Strain 1	7	7	0.2510	0.1820	19	1	0.2288	0.1852	3	1	0.2072	0.1376
		Strain 2	7	7	0.1704	0.1744	22	1	0.1201	0.1642	3	1	0.0469	0.1272
		Strain 3	7	7	0.3900	0.1977	24	1	0.2027	0.1712	3	1	0.1166	0.1391
		Strain 4	6	7	0.3486	0.1778	24	1	0.1359	0.1640	3	1	0.0758	0.1462

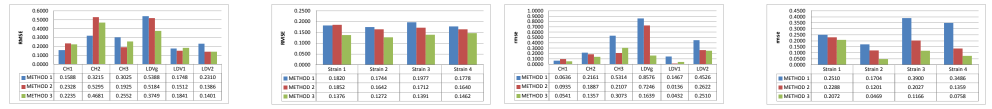

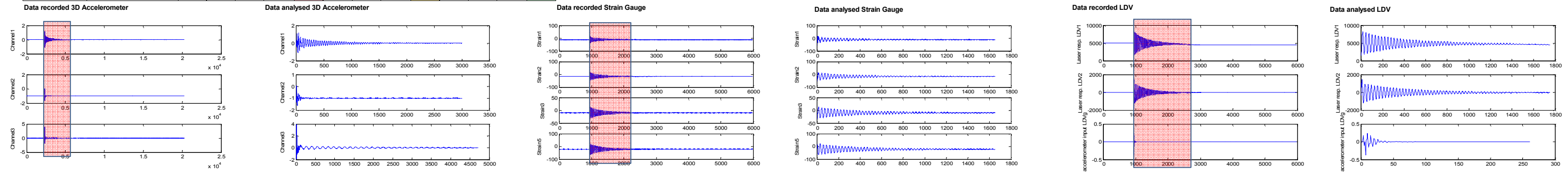

METHOD 1

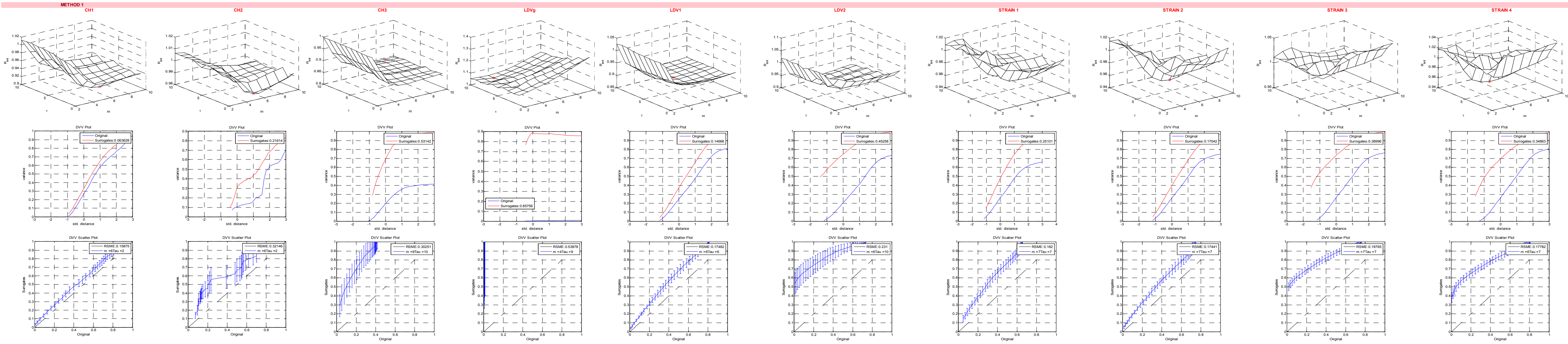

METHOD 2

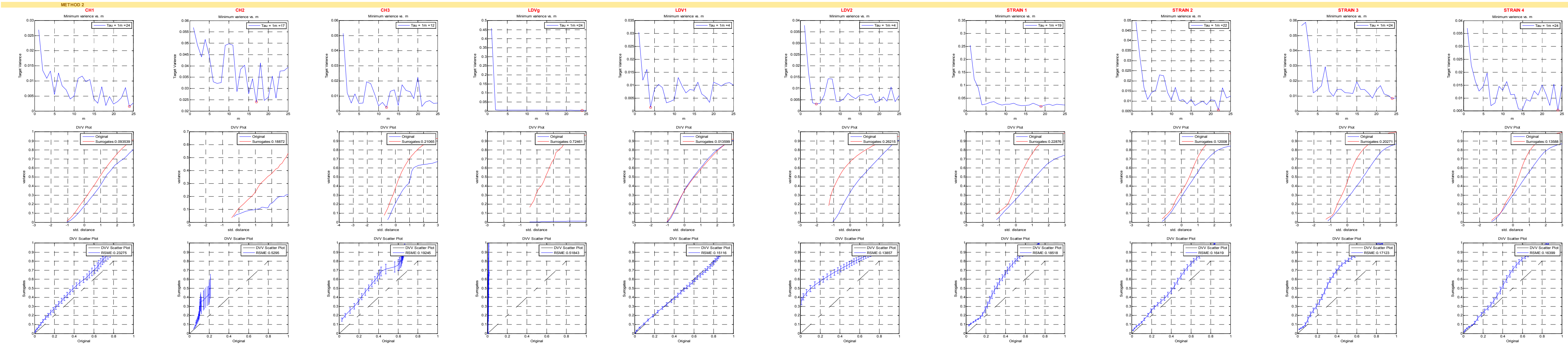

METHOD 3

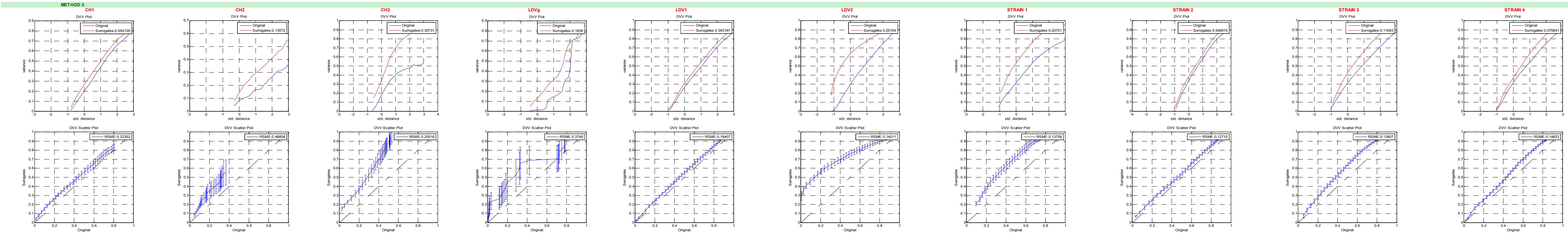

EXPERIMENT	VARIABLES		METHOD 1				METHOD 2				METHOD 3			
			best **m**	best **τ**	rsme	RSME	calc **m**	**τ**	rsme	RSME	set **m**	set **τ**	rsme	RSME
5	Harmonic resonance 4.4Hz Focus at accelerometer	CH1	6	10	0.0572	0.1473	13	1	0.0206	0.0943	3	1	0.0154	0.0872
		CH2	6	9	0.2603	0.2511	18	1	0.0178	0.1082	3	1	0.0139	0.1140
		CH3	3	9	0.0311	0.2153	7	1	0.0025	0.1630	3	1	0.0027	0.1741
		LDV	6	9	0.1335	0.2412	15	1	0.0863	0.1701	3	1	0.0595	0.1685
		LDV1	4	1	0.0070	0.1382	4	1	0.0090	0.1386	3	1	0.0031	0.1345
		LDV2	10	10	0.1712	0.1689	15	1	0.1024	0.1561	3	1	0.1424	0.1490
		Strain 1	10	9	0.1363	0.1717	4	1	0.1029	0.1583	3	1	0.1087	0.1381
		Strain 2	10	9	0.1358	0.1728	14	1	0.1973	0.2004	3	1	0.1003	0.1408
		Strain 3	10	9	0.1342	0.1726	4	1	0.1294	0.1608	3	1	0.1163	0.1417
		Strain 4	10	9	0.1340	0.1733	15	1	0.2504	0.2158	3	1	0.1123	0.1423

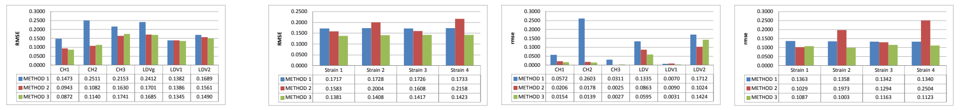

affected by change in amplitude

Data recorded 3D Accelerometer | Data analysed 3D Accelerometer | Data recorded Strain Gauge | Data analysed Strain Gauge | Data recorded LDV | Data analysed LDV

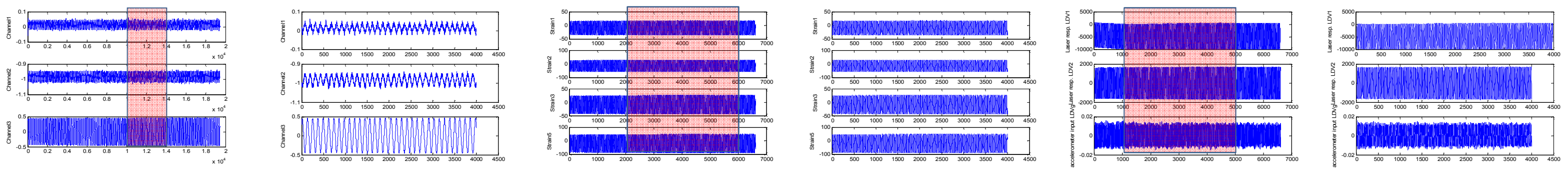

METHOD 1

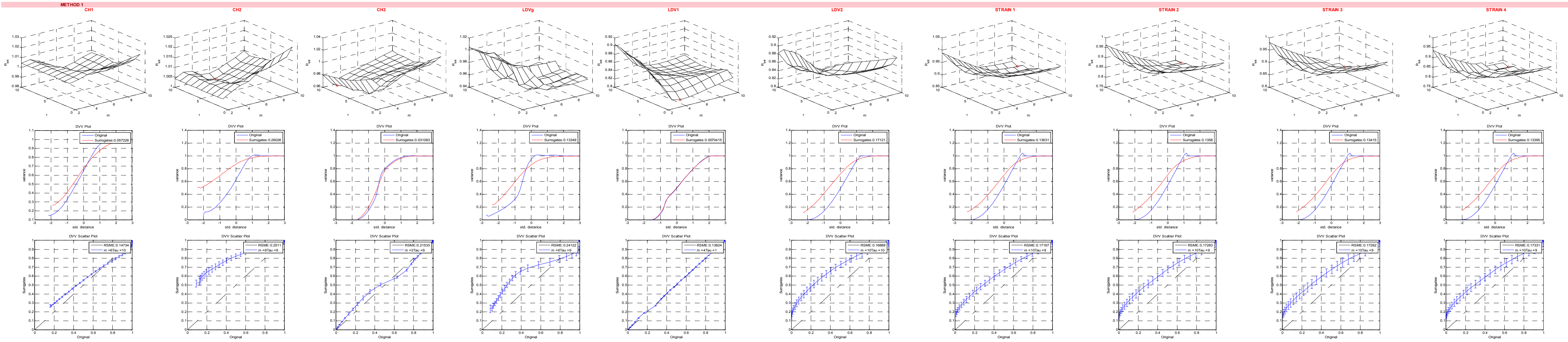

METHOD 2

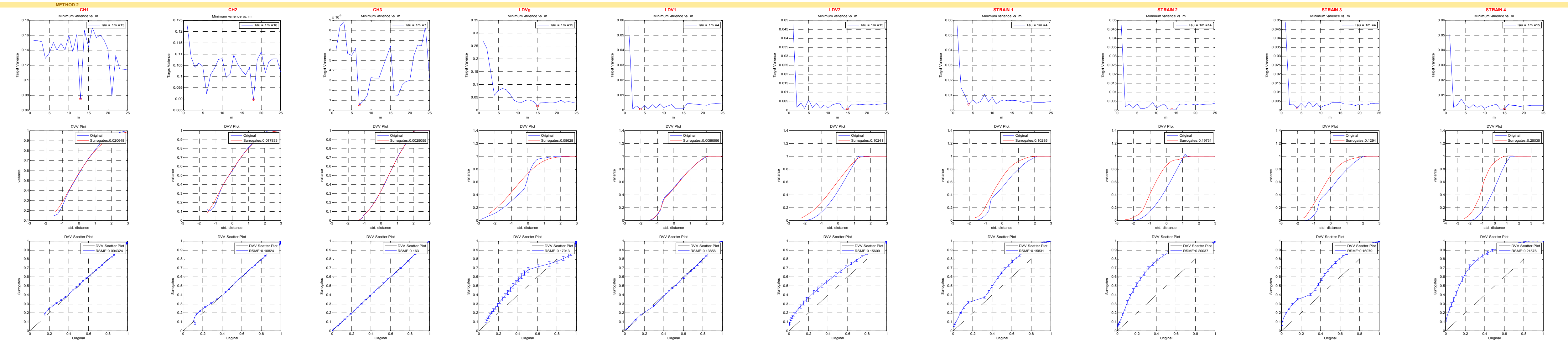

METHOD 3

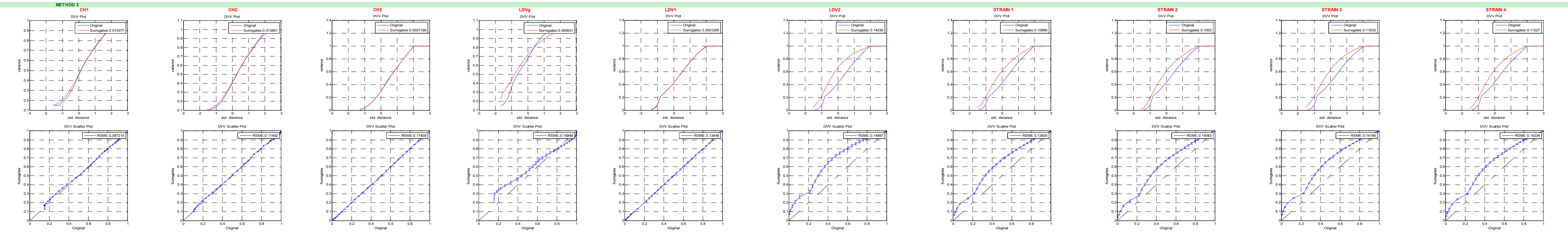

EXPERIMENT	VARIABLES		METHOD 1				METHOD 2				METHOD 3			
			best **m**	best **τ**	rsme	RSME	calc **m**	**τ**	rsme	RSME	set **m**	set **τ**	rsme	RSME
6	Harmonic resonance 2.0 Hz 2.5 Hz 3.0 Hz 3.5 Hz 4.0 Hz 4.2 Hz 4.3 Hz 4.4 Hz 4.5 Hz 4.6 Hz 5.0Hz 5.5 Hz 6.0 Hz 6.5Hz 7.0Hz Focus at accelerometer	CH1	7	10	0.2275	0.1270	5	1	0.0798	0.1487	3	1	0.0232	0.1595
		CH2	6	10	0.0394	0.1630	25	1	0.0428	0.1091	3	1	0.0170	0.0370
		CH3	5	10	0.0115	0.1307	13	1	0.0120	0.1562	3	1	0.0093	0.1984
		LDVg	9	9	0.2784	0.2324	23	1	0.1238	0.0992	3	1	0.0457	0.0861
		LDV1	6	10	0.1399	0.1412	8	1	0.0647	0.1352	3	1	0.0227	0.1566
		LDV2	10	10	0.3261	0.1723	4	1	0.2445	0.1365	3	1	0.2419	0.1441
		Strain 1	10	9	0.4033	0.2160	8	1	0.2391	0.1495	3	1	0.2333	0.1283
		Strain 2	9	7	0.2962	0.1651	21	1	0.2939	0.1699	3	1	0.2085	0.1367
		Strain 3	8	7	0.3948	0.2094	20	1	0.4380	0.2272	3	1	0.2630	0.1443
		Strain 4	8	7	0.3774	0.1991	5	1	0.2741	0.1440	3	1	0.2032	0.1226

*Optimum embeding parameter m and time lag tau are determined as per EXP6b interval

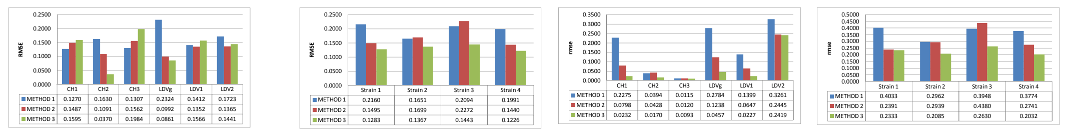

Data recorded 3D Accelerometer

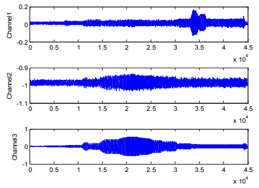

Data recorded Strain Gauge

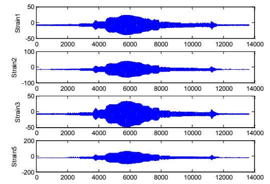

Data recorded LDV

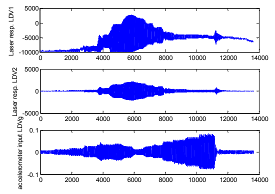

METHOD 1

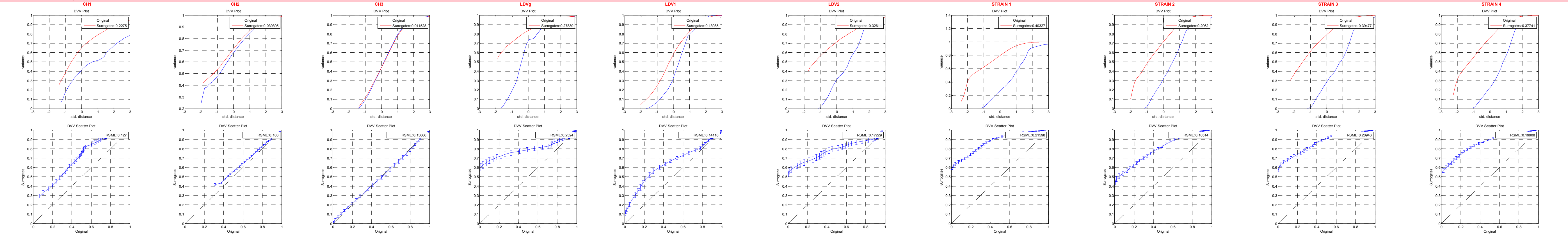

METHOD 2

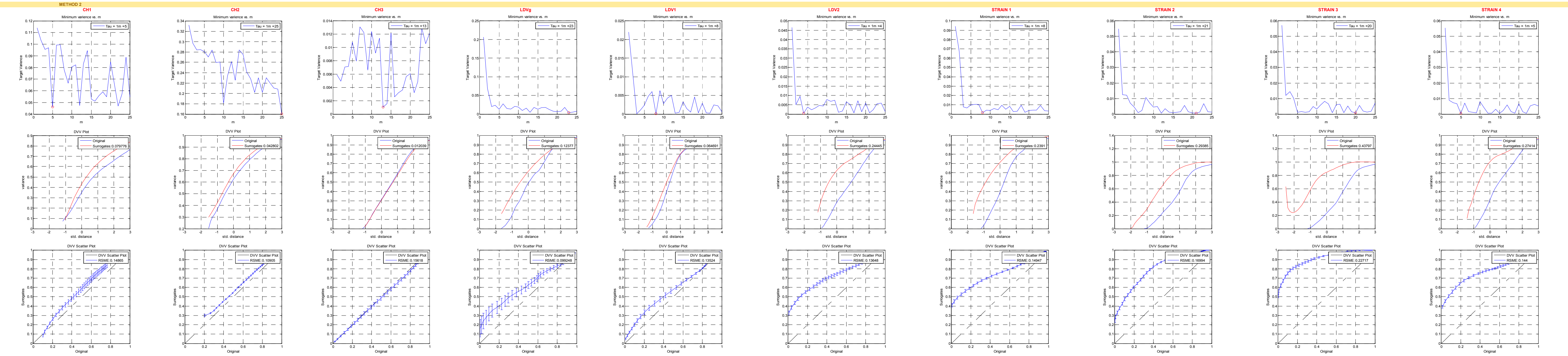

METHOD 3

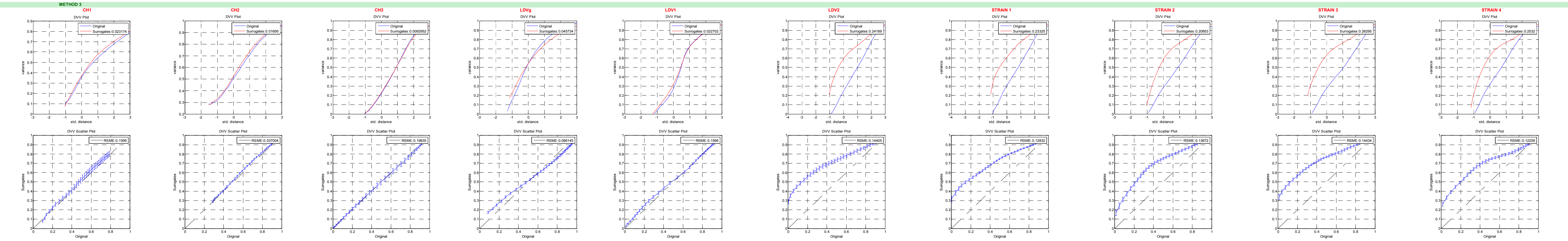

	SYSTEM LOADING	VARIABLES	METHOD 1				METHOD 2				METHOD 3			
			best m	best τ	rsme	RSME	calc m	τ	rsme	RSME	calc m	τ	rsme	RSME
6	Harmonic resonance 2.0 Hz 2.5 Hz 3.0 Hz 3.5 Hz 4.0 Hz 4.2 Hz 4.3 Hz 4.4 Hz 4.5 Hz 4.6 Hz 5.0Hz 5.5 Hz 6.0 Hz 6.5Hz 7.0Hz Focus at accelerometer	CH1	7	10	0.2275	0.1270	5	1	0.0798	0.1487	3	1	0.0232	0.1595
		CH2	6	10	0.0394	0.1630	25	1	0.0428	0.1091	3	1	0.0170	0.0370
		CH3	5	10	0.0115	0.1307	13	1	0.0120	0.1562	3	1	0.0093	0.1984
		LDVg	9	9	0.2784	0.2324	23	1	0.1238	0.0992	3	1	0.0457	0.0861
		LDV1	6	10	0.1399	0.1412	8	1	0.0647	0.1352	3	1	0.0227	0.1566
		LDV2	10	10	0.3261	0.1723	4	1	0.2445	0.1365	3	1	0.2419	0.1441
		Strain 1	10	9	0.4033	0.2160	8	1	0.2391	0.1495	3	1	0.2333	0.1283
		Strain 2	9	7	0.2962	0.1651	21	1	0.2939	0.1699	3	1	0.2085	0.1367
		Strain 3	8	7	0.3948	0.2094	20	1	0.4380	0.2272	3	1	0.2630	0.1443
		Strain 4	8	7	0.3774	0.1991	5	1	0.2741	0.1440	3	1	0.2032	0.1226
6A	Harmonic resonance 2.0 Hz 2.5 Hz 3.0 Hz 3.5 Hz 4.0 Hz 4.2 Hz 4.3 Hz 4.4 Hz 4.5 Hz 4.6 Hz 5.0Hz 5.5 Hz 6.0 Hz 6.5Hz 7.0Hz Focus at accelerometer	CH1	2	8	0.0451	0.2602	12	1	0.0346	0.1640	3	1	0.0201	0.0889
		CH2	2	8	0.0209	0.4342	4	1	0.0345	0.3590	3	1	0.0365	0.3584
		CH3	5	10	0.2956	0.1730	25	1	0.0154	0.1303	3	1	0.0363	0.2280
		LDVg	8	4	0.1653	0.1964	10	1	0.1116	0.1651	3	1	0.0262	0.0919
		LDV1	4	1	0.0251	0.2749	4	1	0.0338	0.2606	3	1	0.0217	0.2688
		LDV2	5	10	0.0849	0.1628	10	1	0.3119	0.1581	3	1	0.2525	0.1640
		Strain 1	8	10	0.4411	0.2438	25	1	0.0705	0.1793	3	1	0.0224	0.1523
		Strain 2	9	10	0.1066	0.1739	24	1	0.0520	0.2481	3	1	0.0335	0.2551
		Strain 3	9	10	0.4509	0.2364	22	1	0.1248	0.2095	3	1	0.1203	0.2259
		Strain 4	8	10	0.4439	0.2331	7	1	0.0130	0.1757	3	1	0.0522	0.2400
6B	Harmonic resonance 2.0 Hz 2.5 Hz 3.0 Hz 3.5 Hz 4.0 Hz 4.2 Hz 4.3 Hz 4.4 Hz 4.5 Hz 4.6 Hz 5.0Hz 5.5 Hz 6.0 Hz 6.5Hz 7.0Hz Focus at accelerometer	CH1	7	10	0.0868	0.2425	23	1	0.0330	0.1818	3	1	0.0090	0.0663
		CH2	6	10	0.0702	0.2041	10	1	0.0153	0.0819	3	1	0.0113	0.0882
		CH3	5	10	0.0432	0.2314	20	1	0.1161	0.1454	3	1	0.0179	0.1676
		LDVg	9	9	0.1207	0.2160	19	1	0.0558	0.1311	3	1	0.0318	0.1222
		LDV1	6	10	0.1001	0.1475	2	1	0.0161	0.1200	3	1	0.0191	0.1093
		LDV2	10	10	0.0196	0.1321	2	1	0.1012	0.1143	3	1	0.1138	0.1222
		Strain 1	10	9	0.0157	0.1296	24	1	0.1030	0.1706	3	1	0.1097	0.1206
		Strain 2	9	7	0.1164	0.1581	11	1	0.1057	0.1872	3	1	0.0995	0.1264
		Strain 3	8	7	0.0086	0.1341	7	1	0.0838	0.1901	3	1	0.1224	0.1333
		Strain 4	8	7	0.1145	0.1517	2	1	0.0932	0.1174	3	1	0.1099	0.1296
6C	Harmonic resonance 2.0 Hz 2.5 Hz 3.0 Hz 3.5 Hz 4.0 Hz 4.2 Hz 4.3 Hz 4.4 Hz 4.5 Hz 4.6 Hz 5.0Hz 5.5 Hz 6.0 Hz 6.5Hz 7.0Hz Focus at accelerometer	CH1	6	8	0.0298	0.1103	15	1	0.0074	0.1218	3	1	0.0037	0.1011
		CH2	2	9	0.0072	0.4444	10	1	0.0196	0.2532	3	1	0.0283	0.1994
		CH3	4	9	0.0485	0.2025	7	1	0.0038	0.1492	3	1	0.0040	0.1646
		LDVg	9	3	0.0496	0.1492	12	1	0.0517	0.1053	3	1	0.0524	0.1270
		LDV1	6	8	0.1697	0.1708	22	1	0.0512	0.0939	3	1	0.0076	0.0956
		LDV2	7	8	0.3454	0.2957	13	1	0.1745	0.1313	3	1	0.1435	0.1218
		Strain 1	10	8	0.1639	0.2684	20	1	0.0390	0.1424	3	1	0.0209	0.0964
		Strain 2	9	7	0.1498	0.2102	5	1	0.0139	0.1415	3	1	0.0086	0.0983
		Strain 3	10	8	0.3593	0.3288	6	1	0.0267	0.1587	3	1	0.0220	0.0904
		Strain 4	9	8	0.3443	0.3145	6	1	0.0121	0.1571	3	1	0.0081	0.0968

* accelerometer placed close to the top of WTB

CH1 - accelerometer channel 1 in the direction of applied vibrations

CH2 - accelerometer channel 2 perpendicular to the direction of applied vibrations

CH3 - accelerometer channel 3 perpendicular to the direction of applied vibrations

LDVg - laser dopler vibrometer (LDV) measurements of accelerometer input

LDV1 - LDV measurements (displacement)

LDV2 - LDV measurements (velocity)

Strain 1 - strain gauge 1 at 1/3 length of WTB from the top

Strain 2 - strain gauge 2 at 2/3 length of WTB from the top

Strain 3 - strain gauge 3 close to bottom of WTB

Strain 5 - strain gauge 5 opposite of 3

EXPERIMENT	VARIABLES		METHOD 1				METHOD 2				METHOD 3			
			best m	best τ	rsme	RSME	calc m	τ	rsme	RSME	set m	set τ	rsme	RSME
6A	Harmonic resonance 2.0 Hz 2.5 Hz 3.0 Hz 3.5 Hz 4.0 Hz 4.2 Hz 4.3 Hz 4.4 Hz 4.5 Hz 4.6 Hz 5.0Hz 5.5 Hz 6.0 Hz 6.5Hz 7.0Hz Focus at accelerometer	CH1	2	8	0.0451	0.2602	12	1	0.0346	0.1640	3	1	0.0201	0.0889
		CH2	2	8	0.0209	0.4342	4	1	0.0345	0.3590	3	1	0.0365	0.3584
		CH3	5	10	0.2956	0.1730	25	1	0.0154	0.1303	3	1	0.0363	0.2280
		LDVg	8	4	0.1653	0.1964	10	1	0.1116	0.1651	3	1	0.0262	0.0919
		LDV1	4	1	0.0251	0.2749	4	1	0.0338	0.2606	3	1	0.0217	0.2688
		LDV2	5	10	0.0849	0.1628	10	1	0.3119	0.1581	3	1	0.2525	0.1640
		Strain 1	8	10	0.4411	0.2438	25	1	0.0705	0.1793	3	1	0.0224	0.1523
		Strain 2	9	10	0.1066	0.1739	24	1	0.0520	0.2481	3	1	0.0335	0.2551
		Strain 3	9	10	0.4509	0.2364	22	1	0.1248	0.2095	3	1	0.1203	0.2259
		Strain 4	8	10	0.4439	0.2331	7	1	0.0130	0.1757	3	1	0.0522	0.2400

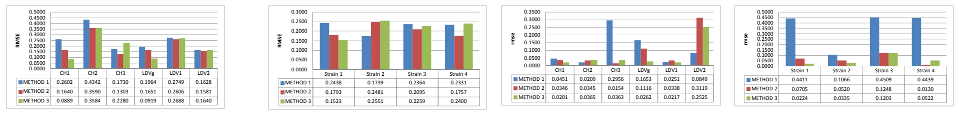

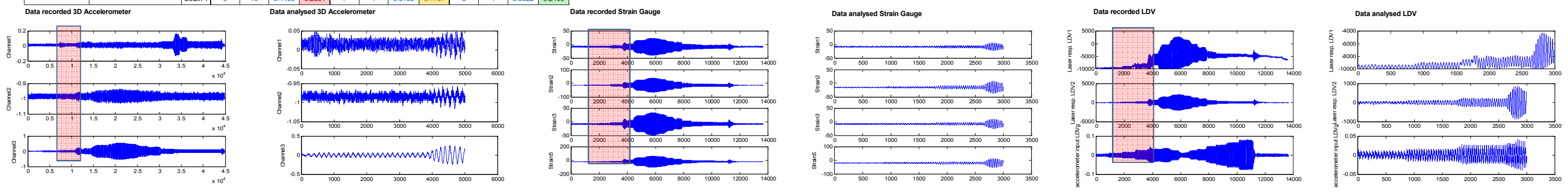

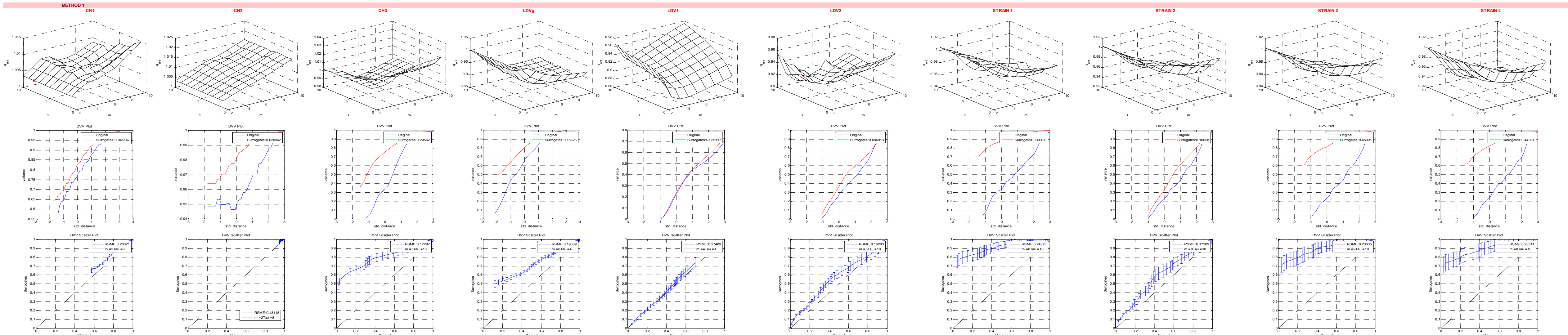

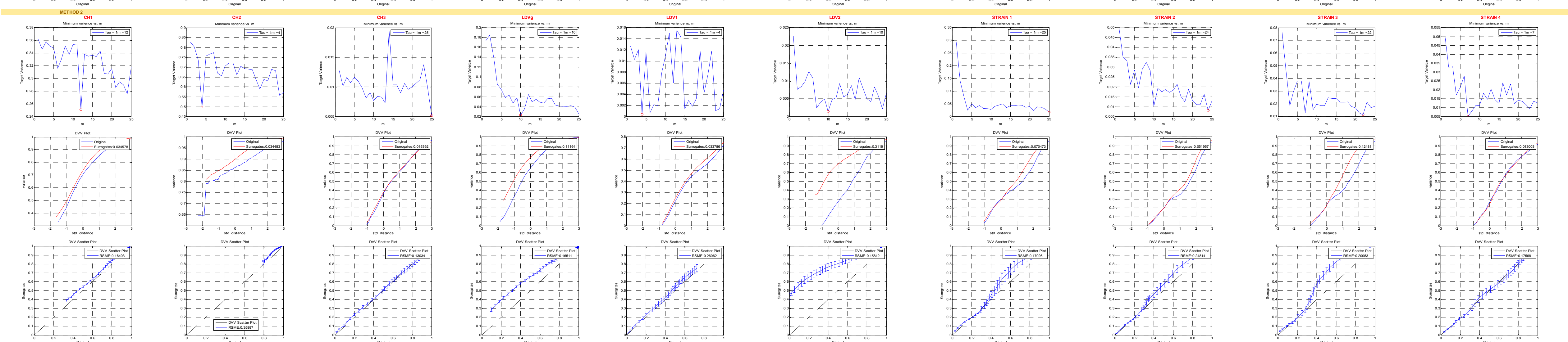

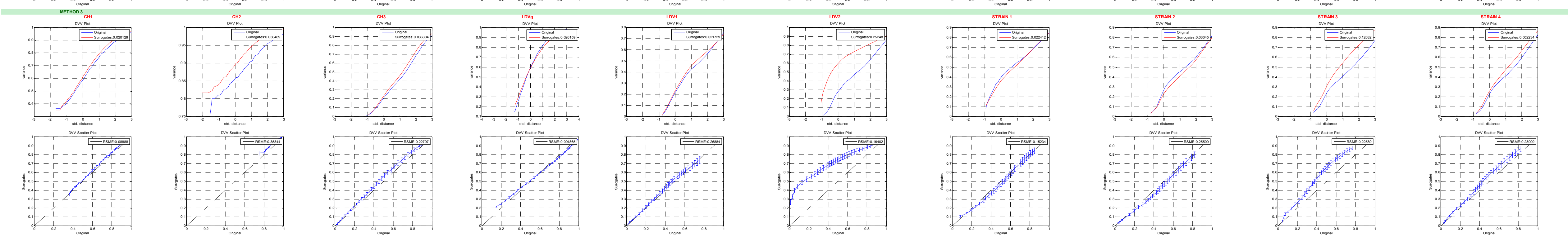

EXPERIMENT	VARIABLES		METHOD 1				METHOD 2				METHOD 3			
			best m	best τ	rsme	RSME	calc m	τ	rsme	RSME	set m	set τ	rsme	RSME
6B	Harmonic resonance 2.0 Hz 2.5 Hz 3.0 Hz 3.5 Hz 4.0 Hz 4.2 Hz 4.3 Hz 4.4 Hz 4.5 Hz 4.6 Hz 5.0Hz 5.5 Hz 6.0 Hz 6.5Hz 7.0Hz Focus at accelerometer	CH1	7	10	0.0868	0.2425	23	1	0.0330	0.1818	3	1	0.0090	0.0663
		CH2	6	10	0.0702	0.2041	10	1	0.0153	0.0819	3	1	0.0113	0.0882
		CH3	5	10	0.0432	0.2314	20	1	0.1161	0.1454	3	1	0.0179	0.1676
		LDVg	9	9	0.1207	0.2160	19	1	0.0558	0.1311	3	1	0.0318	0.1222
		LDV1	6	10	0.1001	0.1475	2	1	0.0161	0.1200	3	1	0.0191	0.1093
		LDV2	10	10	0.0196	0.1321	2	1	0.1012	0.1143	3	1	0.1138	0.1222
		Strain 1	10	9	0.0157	0.1296	24	1	0.1030	0.1706	3	1	0.1097	0.1206
		Strain 2	9	7	0.1164	0.1581	11	1	0.1057	0.1872	3	1	0.0995	0.1264
		Strain 3	8	7	0.0086	0.1341	7	1	0.0838	0.1901	3	1	0.1224	0.1333
		Strain 4	8	7	0.1145	0.1517	2	1	0.0932	0.1174	3	1	0.1099	0.1296

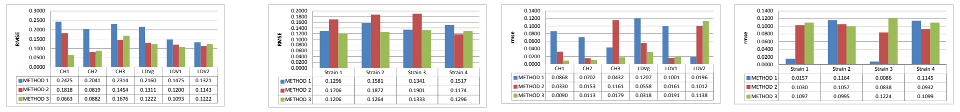

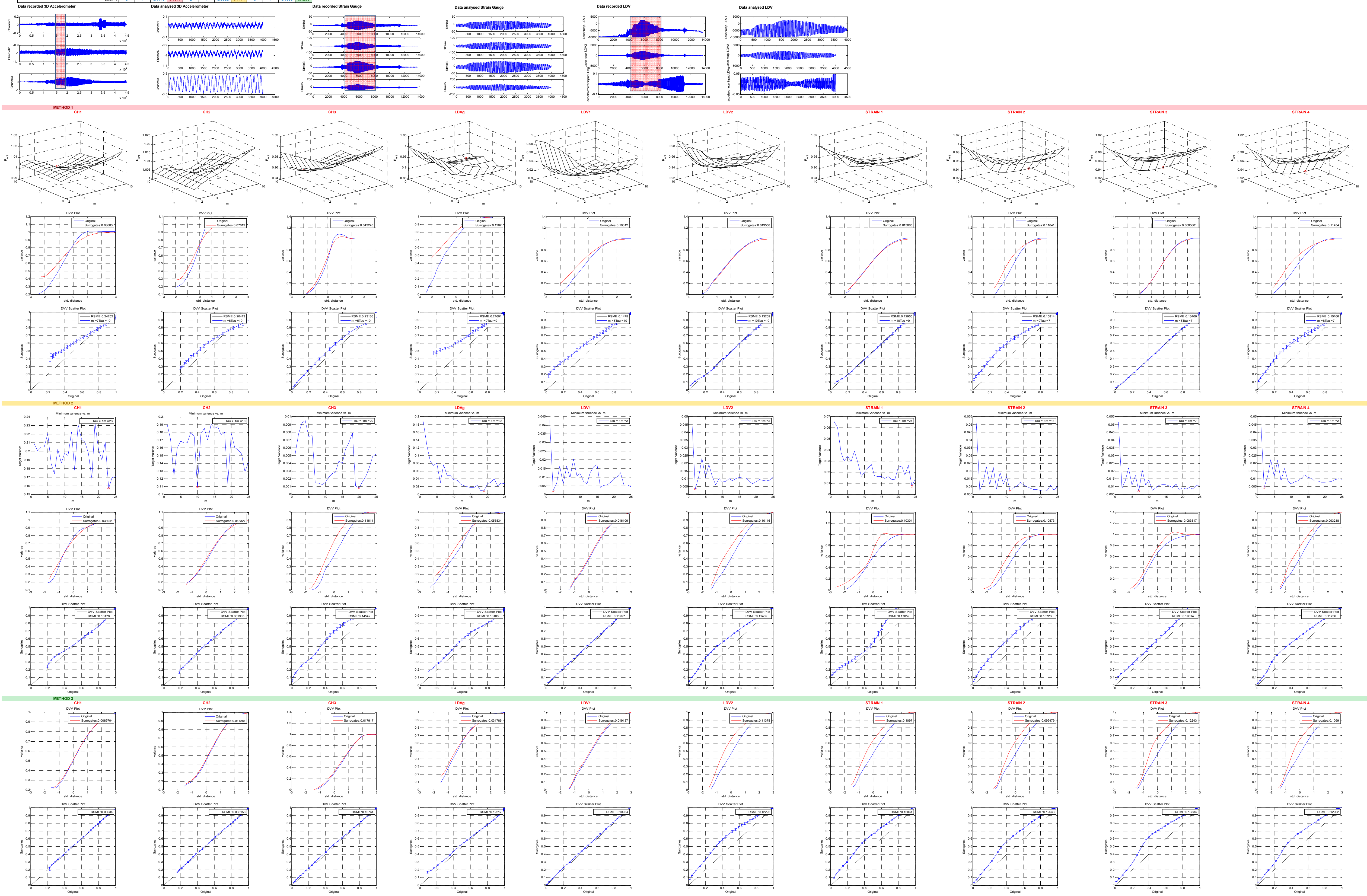

EXPERIMENT	VARIABLES		METHOD 1				METHOD 2				METHOD 3			
			best m	best τ	rsme	RSME	calc m	τ	rsme	RSME	set m	set τ	rsme	RSME
6C	Harmonic resonance 2.0 Hz 2.5 Hz 3.0 Hz 3.5 Hz 4.0 Hz 4.2 Hz 4.3 Hz 4.4 Hz 4.5 Hz 4.6 Hz 5.0Hz 5.5 Hz 6.0 Hz 6.5Hz 7.0Hz Focus at accelerometer	CH1	6	8	0.0298	0.1103	15	1	0.0074	0.1218	3	1	0.0037	0.1011
		CH2	2	9	0.0072	0.4444	10	1	0.0196	0.2532	3	1	0.0283	0.1994
		CH3	4	9	0.0485	0.2025	7	1	0.0038	0.1492	3	1	0.0040	0.1646
		LDVg	9	3	0.0496	0.1492	12	1	0.0517	0.1053	3	1	0.0524	0.1270
		LDV1	6	8	0.1697	0.1708	22	1	0.0512	0.0939	3	1	0.0076	0.0956
		LDV2	7	8	0.3454	0.2957	13	1	0.1745	0.1313	3	1	0.1435	0.1218
		Strain 1	10	8	0.1639	0.2684	20	1	0.0390	0.1424	3	1	0.0209	0.0964
		Strain 2	9	7	0.1498	0.2102	5	1	0.0139	0.1415	3	1	0.0086	0.0983
		Strain 3	10	8	0.3593	0.3288	6	1	0.0267	0.1587	3	1	0.0220	0.0904
		Strain 4	9	8	0.3443	0.3145	6	1	0.0121	0.1571	3	1	0.0081	0.0968

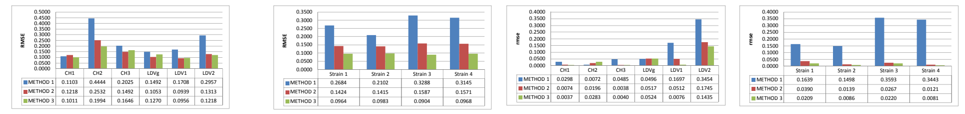

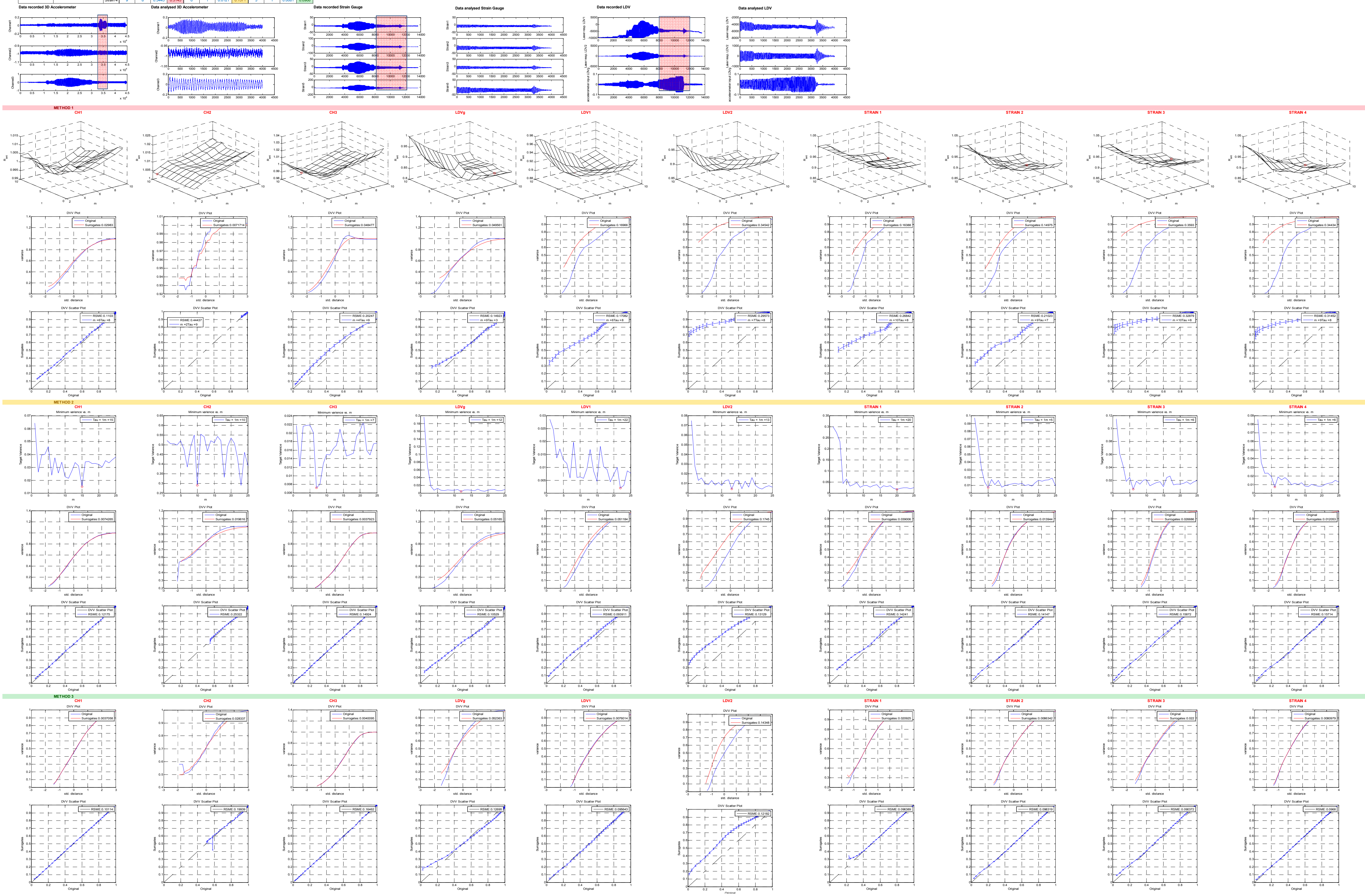

EXPERIMENT	VARIABLES		METHOD 1				METHOD 2				METHOD 3			
			best m	best τ	rsme	RSME	calc m	τ	rsme	RSME	set m	set τ	rsme	RSME
7	Loading Sine sweep 2.0 Hz 6.0 Hz 60 sec Focus at accelerometer	CH1	4	10	0.0464	0.2276	11	1	0.0367	0.2039	3	1	0.0600	0.3182
		CH2	2	6	0.0578	0.2472	19	1	0.0725	0.1439	3	1	0.0688	0.1016
		CH3	4	9	0.0413	0.1323	25	1	0.0384	0.1946	3	1	0.0041	0.2724
		LDVg	10	2	0.3604	0.2572	12	1	0.1016	0.1091	3	1	0.0431	0.1088
		LDV1	6	6	0.3849	0.2246	10	1	0.0405	0.1303	3	1	0.0128	0.1705
		LDV2	8	10	0.0475	0.1453	12	1	0.3114	0.1656	3	1	0.2466	0.1656
		Strain 1	10	10	0.1344	0.1098	7	1	0.2157	0.1395	3	1	0.2384	0.1329
		Strain 2	10	9	0.1039	0.1309	18	1	0.2502	0.1598	3	1	0.1746	0.1363
		Strain 3	10	9	0.3815	0.2012	19	1	0.3918	0.2048	3	1	0.2432	0.1374
		Strain 4	10	9	0.3811	0.1996	23	1	0.3339	0.1717	3	1	0.2277	0.1420

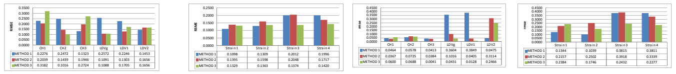

METHOD 1 for data section			
best m	best τ	rsme	RSME
4	10	0.0063	0.1050
2	6	0.0197	0.1682
4	9	0.0260	0.1286

Optimum embeding parameter m and time lag tau are determined using data sqered yellow. Using these parameters RMSE and rmse were calculated for all valid data squered in pink

Data recorded 3D Accelerometer

Data analysed 3D Accelerometer

Data recorded Strain Gauge

Data analysed Strain Gauge

Data recorded LDV

Data analysed LDV

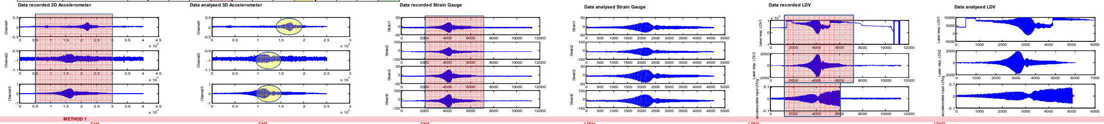

METHOD 1

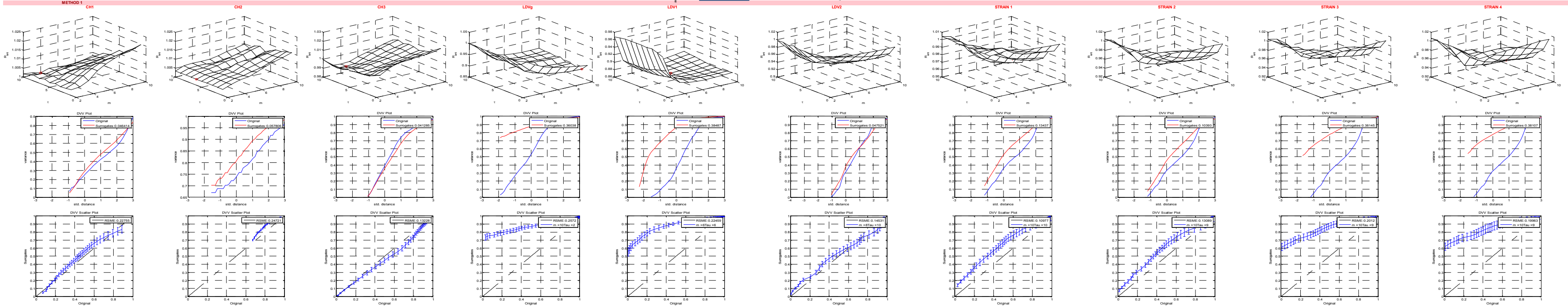

METHOD 2

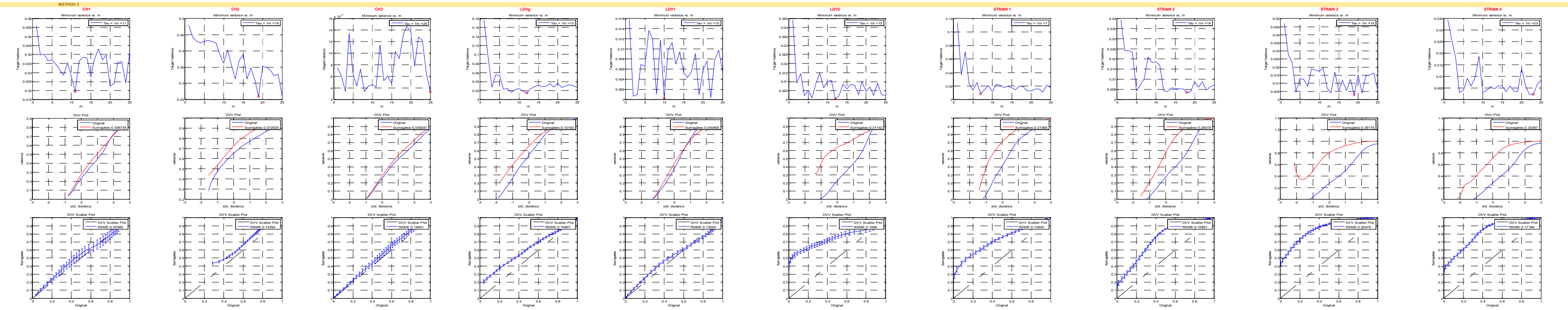

METHOD 3

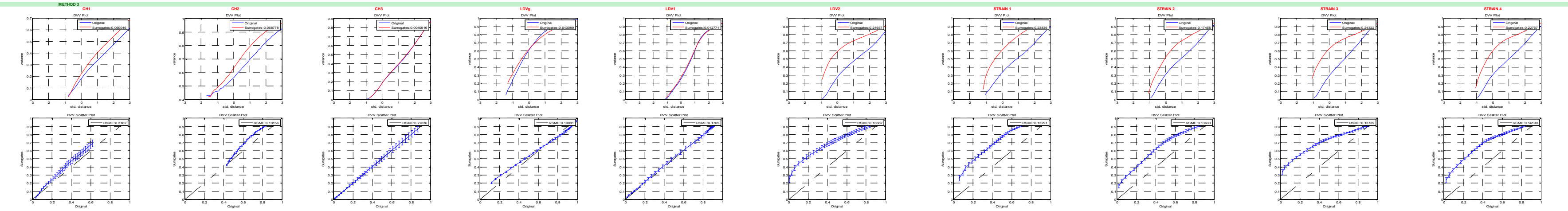

EXPERIMENT	VARIABLES		METHOD 1				METHOD 2				METHOD 3			
			best **m**	best τ	rsme	RSME	calc **m**	τ	rsme	RSME	set **m**	set τ	rsme	RSME
8	Loading White Noise Focus at accelerometer	CH1	4	1	0.0036	0.0732	10	1	0.0160	0.1327	3	1	0.0104	0.0686
		CH2	5	1	0.0435	0.1647	19	1	0.0804	0.1612	3	1	0.0347	0.1264
		CH3	3	1	0.0224	0.0949	16	1	0.0383	0.1911	3	1	0.0168	0.0917
		LDVg	4	1	0.2189	0.3606	19	1	0.0113	0.3882	3	1	0.0444	0.2542
		LDV1	6	10	0.1990	0.1854	12	1	0.0274	0.1337	3	1	0.0057	0.1268
		LDV2	9	10	0.2077	0.2278	14	1	0.3092	0.2399	3	1	0.2351	0.2062
		Strain 1	7	7	0.2163	0.3643	22	1	0.3935	0.3613	3	1	0.2497	0.3134
		Strain 2	7	7	0.1296	0.2625	24	1	0.2236	0.2427	3	1	0.0852	0.2064
		Strain 3	10	6	0.3315	0.2834	17	1	0.1921	0.1646	3	1	0.1455	0.1260
		Strain 4	10	10	0.3392	0.2944	16	1	0.0946	0.1124	3	1	0.0854	0.0854

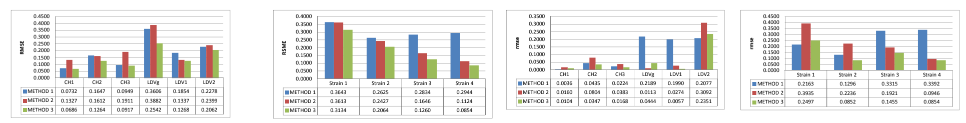

METHOD 1 for data section			
best **m**	best τ	rsme	RSME
4	1	0.0054	0.0738
5	1	0.2186	0.2704
3	1	0.0138	0.0827

Optimum embeding parameter m and time lag tau are determined using data sqered yellow. Using these parameters RMSE and rmse were calculated for all valid data squered in pink

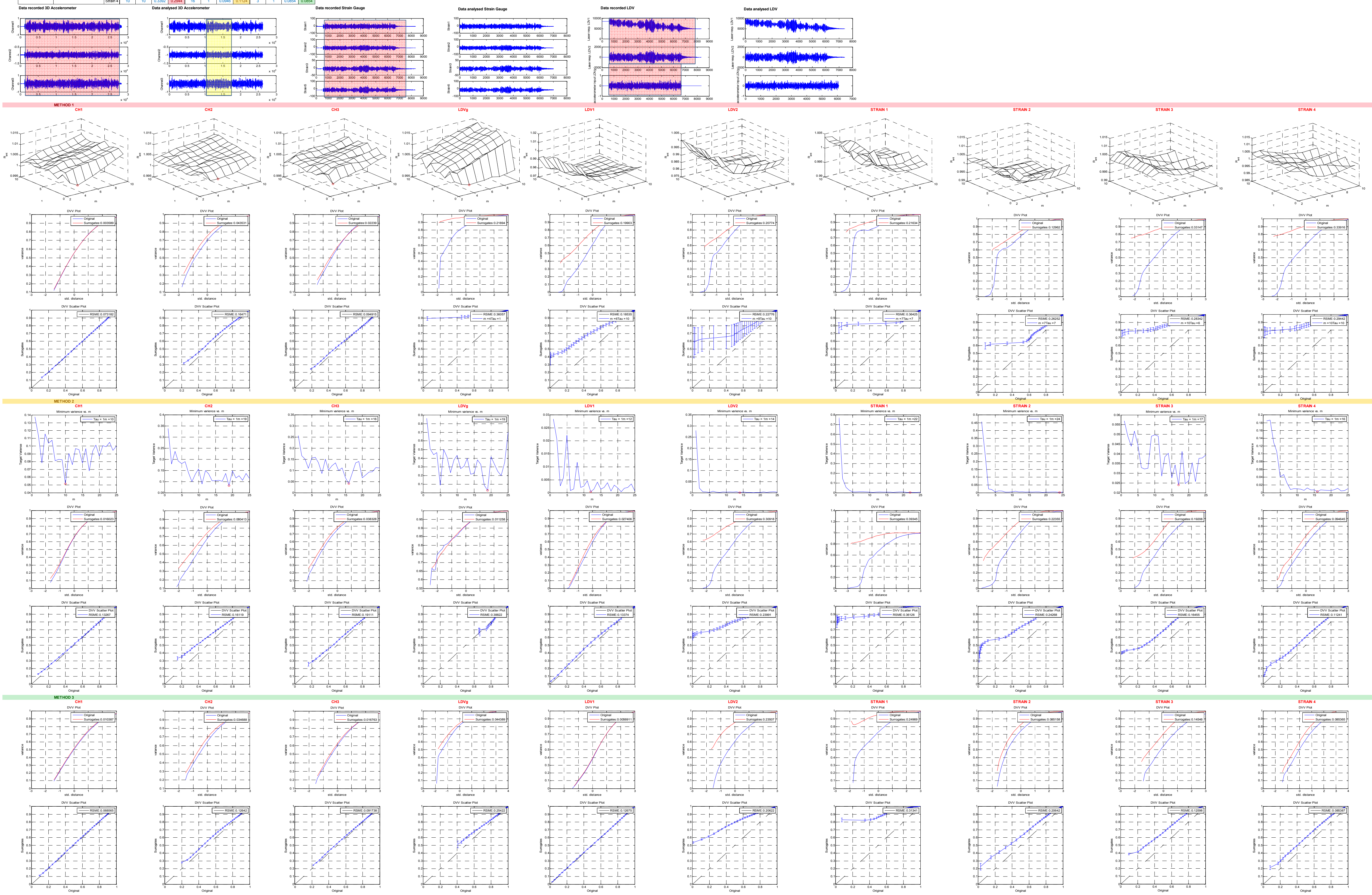

EXPERIMENT	VARIABLES		METHOD 1				METHOD 2				METHOD 3			
			best m	best τ	rsme	RSME	calc m	τ	rsme	RSME	set m	set τ	rsme	RSME
9	Loading White noise 4.365Hz at the peak Focus at top strain gauge	CH1	2	7	0.0203	0.1421	7	1	0.0114	0.1050	3	1	0.0121	0.0704
		CH2	5	1	0.0394	0.1675	18	1	0.0761	0.1552	3	1	0.0297	0.1257
		CH3	5	1	0.0123	0.1200	25	1	0.0501	0.2024	3	1	0.0222	0.0947
		LDVg	5	1	0.2075	0.3547	15	1	0.0690	0.3539	3	1	0.0522	0.2421
		LDV1	3	9	0.0339	0.1178	15	1	0.0119	0.1097	3	1	0.0071	0.0961
		LDV2	2	1	0.0059	0.1578	17	1	0.2185	0.2670	3	1	0.1820	0.2898
		Strain 1	3	3	0.0082	0.3065	6	1	0.2182	0.3492	3	1	0.2197	0.3364
		Strain 2	2	9	0.0052	0.3211	7	1	0.0842	0.2754	3	1	0.0730	0.2318
		Strain 3	10	6	0.2223	0.2959	23	1	0.1423	0.1939	3	1	0.1275	0.1328
		Strain 4	10	10	0.0073	0.1965	7	1	0.0813	0.1675	3	1	0.0804	0.0913

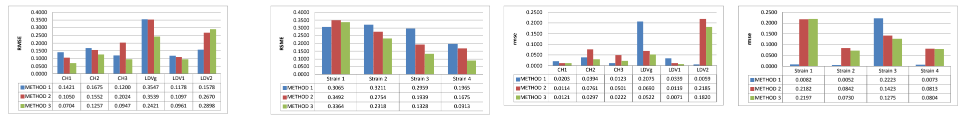

METHOD 1 for data section			
best m	best τ	rsme	RSME
2	7	0.0090	0.1557
5	1	0.2138	0.2550
5	1	0.0167	0.1036

Optimum embeding parameter m and time lag tau are determined using data sqered yellow. Using these parameters RMSE and rmse were calculated for all valid data squered in pink

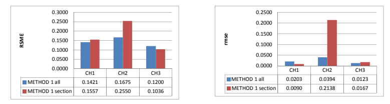

Data recorded 3D Accelerometer / Data analysed 3D Accelerometer / Data recorded Strain Gauge / Data analysed Strain Gauge / Data recorded LDV / Data analysed LDV

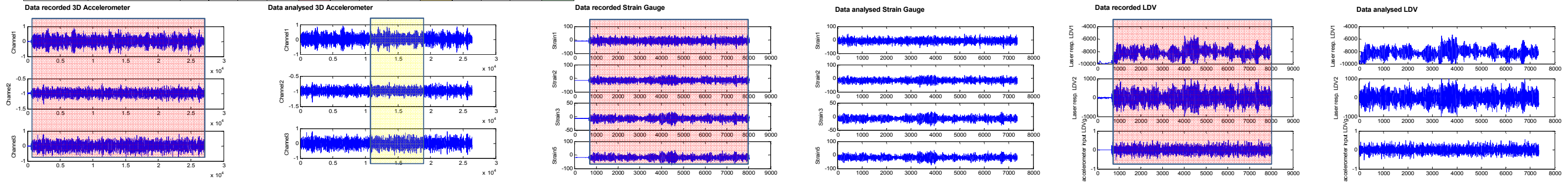

METHOD 1

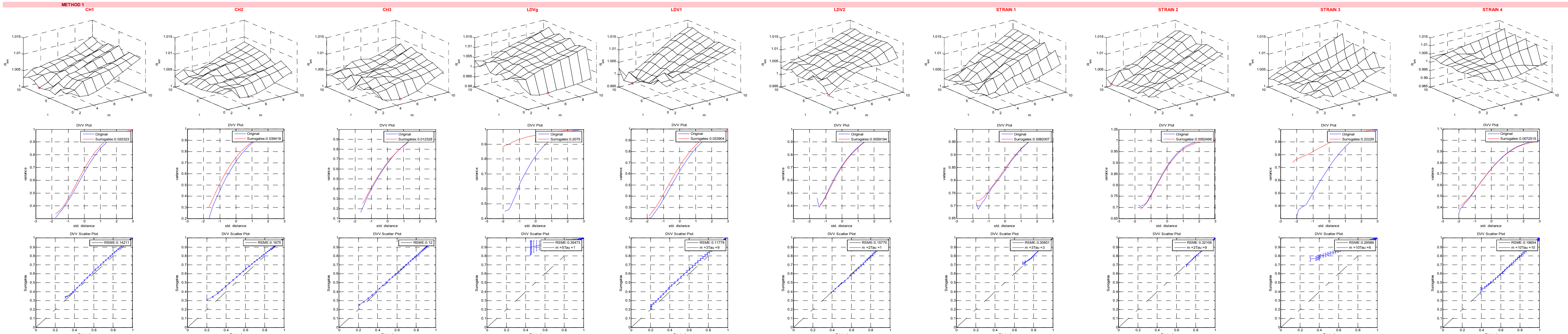

METHOD 2

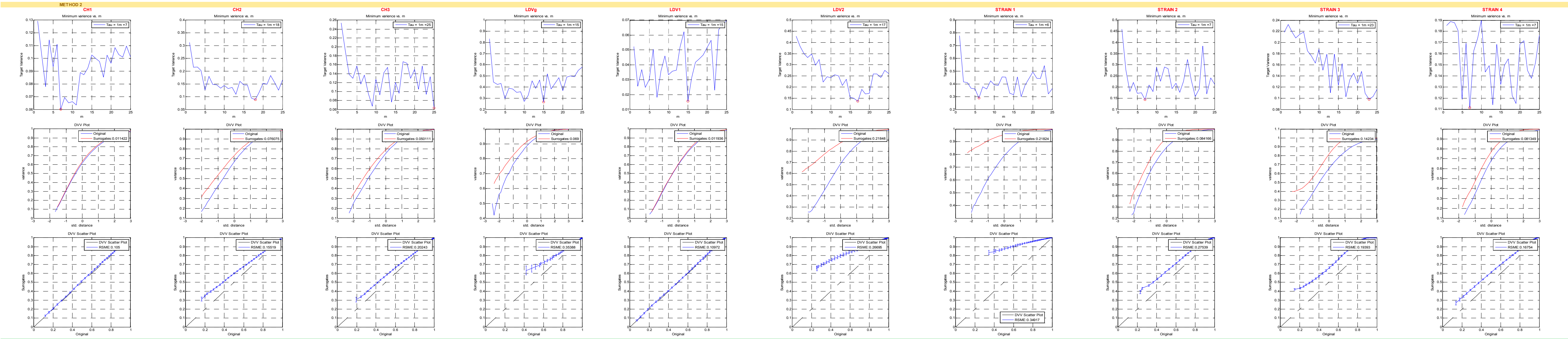

METHOD 3

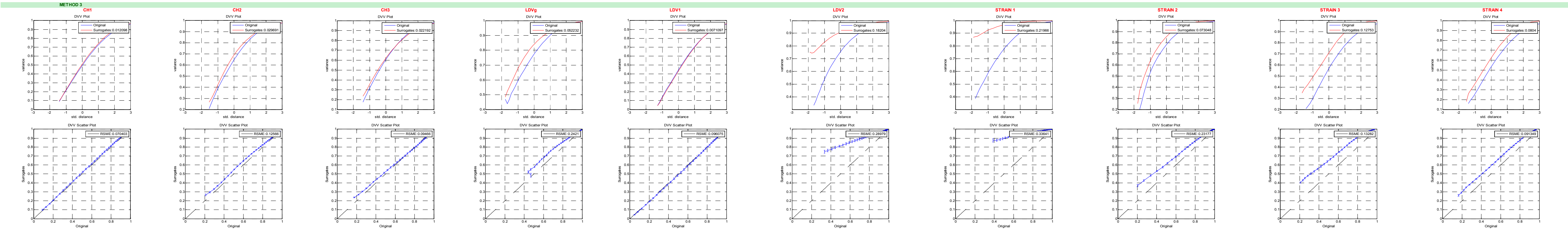

EXPERIMENT	VARIABLES		METHOD 1				METHOD 2				METHOD 3			
			best m	best τ	rsme	RSME	calc m	τ	rsme	RSME	set m	set τ	rsme	RSME
10	Loading Sine Sweep 2.0 Hz 6.0 Hz 60 sec Focus at top strain gauge	CH1	7	10	0.0696	0.1634	19	1	0.0964	0.2472	3	1	0.0406	0.2608
		CH2	2	8	0.0451	0.2468	20	1	0.0536	0.1117	3	1	0.0443	0.0576
		CH3	5	10	0.0142	0.1677	3	1	0.0102	0.2814	3	1	0.0688	0.3002
		LDVg	10	2	0.3382	0.2526	4	1	0.0559	0.1080	3	1	0.0501	0.0948
		LDV1	6	9	0.3271	0.1985	22	1	0.0585	0.1792	3	1	0.0137	0.1854
		LDV2	8	10	0.1156	0.1703	15	1	0.3039	0.1775	3	1	0.2673	0.1696
		Strain 1	10	10	0.1380	0.1337	14	1	0.4121	0.2053	3	1	0.2496	0.1449
		Strain 2	10	9	0.3985	0.2059	10	1	0.2505	0.1497	3	1	0.2046	0.1533
		Strain 3	10	9	0.4153	0.2148	11	1	0.3410	0.1694	3	1	0.3243	0.1976
		Strain 4	10	9	0.3978	0.2049	12	1	0.3542	0.1764	3	1	0.2607	0.1687

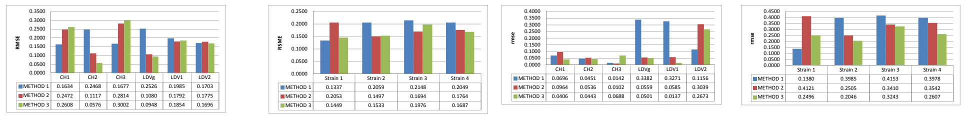

METHOD 1 for data section			
best m	best τ	rsme	RSME
7	10	0.0717	0.2829
2	8	0.1510	0.2165
5	10	0.2099	0.1641

Optimum embeding parameter m and time lag tau are determined using data sqered yellow. Using these parameters RMSE and rmse were calculated for all valid data squered in pink

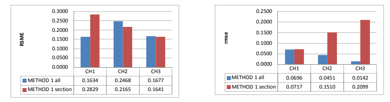

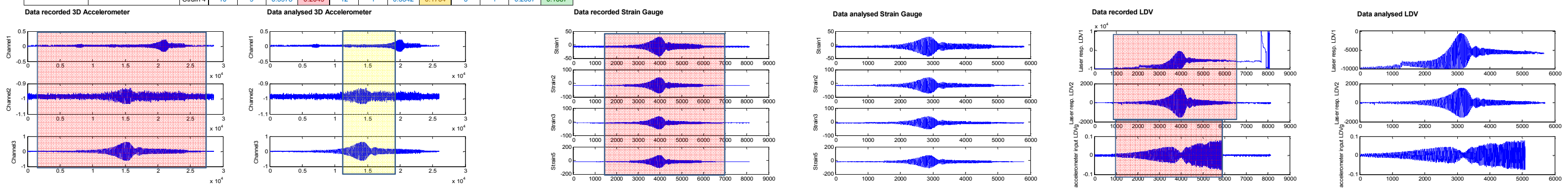

METHOD 1

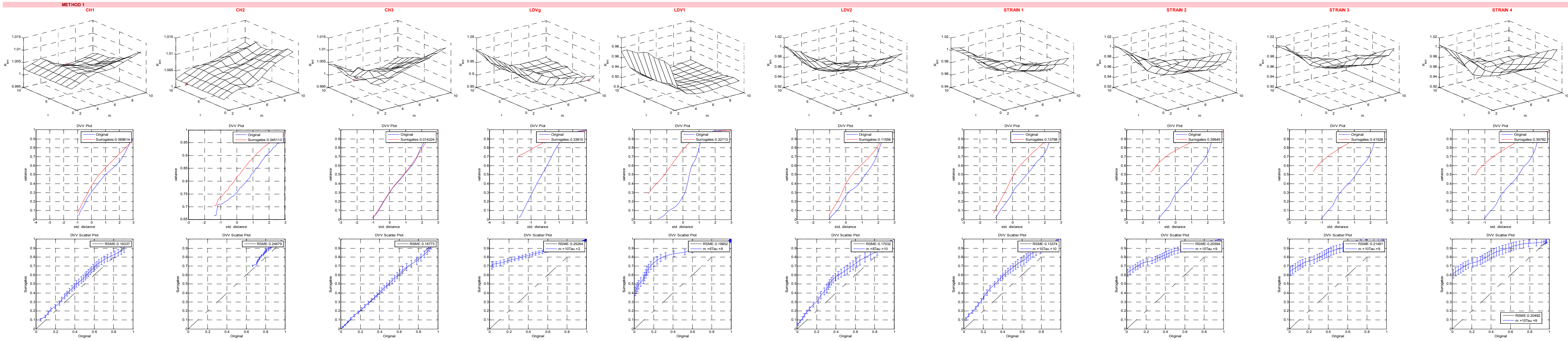

METHOD 2

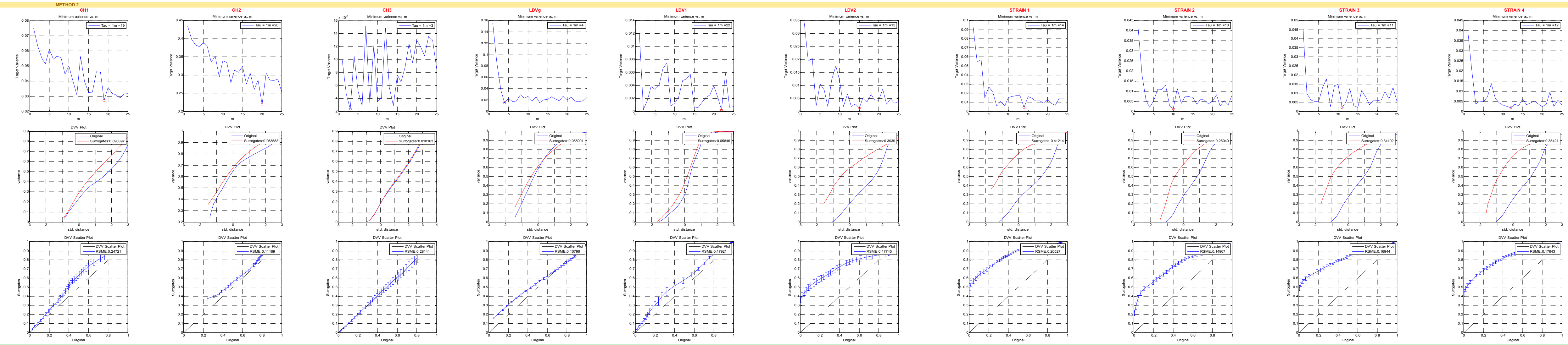

METHOD 3

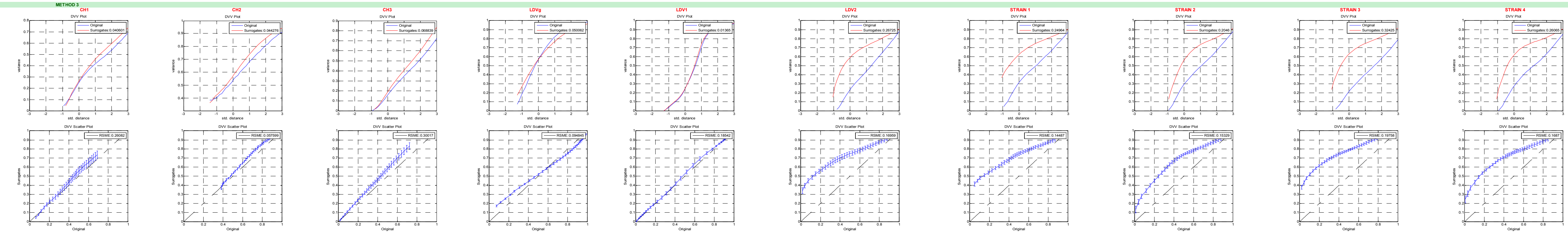

EXPERIMENT	VARIABLES		METHOD 1				METHOD 2				METHOD 3			
			best m	best τ	rsme	RSME	calc m	τ	rsme	RSME	set m	set τ	rsme	RSME
11	Harmonic resonance 2.0 Hz 2.5 Hz 3.0 Hz 3.5 Hz 4.0 Hz 4.2 Hz 4.3 Hz 4.4 Hz 4.5 Hz 4.6 Hz 5.0Hz 5.5 Hz 6.0 Hz 6.5Hz 7.0Hz Focus at top strain gauge	CH1	7	10	0.0832	0.1831	19	1	0.0857	0.2276	3	1	0.0090	0.2512
		CH2	6	10	0.0562	0.1197	22	1	0.0283	0.0817	3	1	0.0116	0.0566
		CH3	4	9	0.0117	0.1400	22	1	0.0071	0.1270	3	1	0.0033	0.1931
		LDVg	10	3	0.1712	0.1685	25	1	0.1249	0.1246	3	1	0.0476	0.1111
		LDV1	8	10	0.1882	0.1488	22	1	0.1733	0.1619	3	1	0.0513	0.1534
		LDV2	10	10	0.3138	0.1713	23	1	0.2482	0.1402	3	1	0.2315	0.1334
		Strain 1	10	10	0.2620	0.1491	17	1	0.4013	0.2202	3	1	0.2123	0.1152
		Strain 2	10	9	0.3953	0.2354	21	1	0.3584	0.1932	3	1	0.2224	0.1279
		Strain 3	10	9	0.3963	0.2366	5	1	0.2270	0.1398	3	1	0.2484	0.1399
		Strain 4	10	9	0.3737	0.2128	19	1	0.4437	0.2166	3	1	0.2365	0.1354

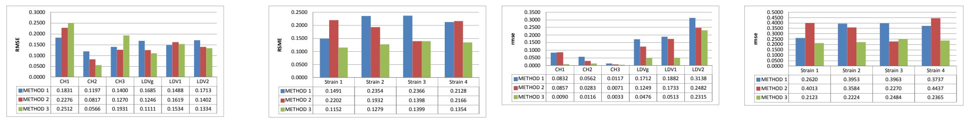

METHOD 1 for data section			
best m	best τ	rsme	RSME
7	10	0.0710	0.3575
6	10	0.0246	0.1636
4	9	0.1533	0.2044
10	3	0.3522	0.2945
8	10	0.1108	0.1557
10	10	0.2648	0.1565
10	10	0.0486	0.1106
10	9	0.2632	0.1558
10	9	0.2716	0.1607
10	9	0.2642	0.1551

Optimum embeding parameter m and time lag tau are determined using data sqered yellow. Using these parameters RMSE and rmse were calculated for all valid data squered in pink

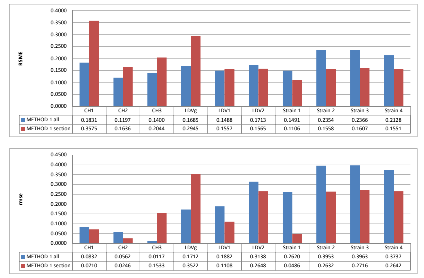

Data recorded 3D Accelerometer

Data analysed 3D Accelerometer

Data recorded Strain Gauge

Data analysed Strain Gauge

Data recorded LDV

Data analysed LDV

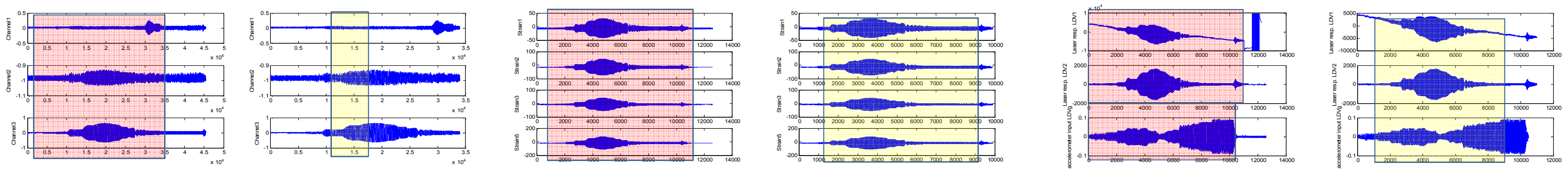

METHOD 1

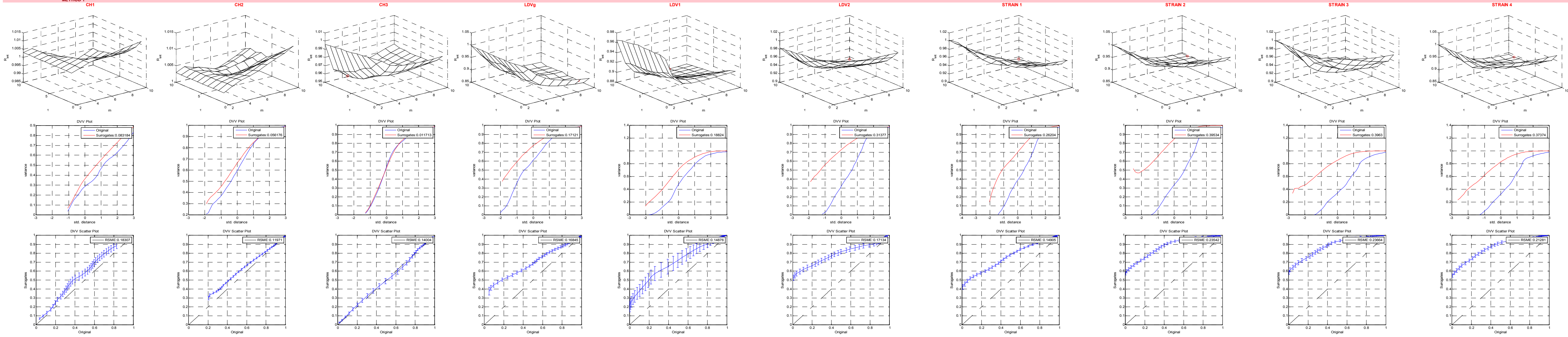

METHOD 2

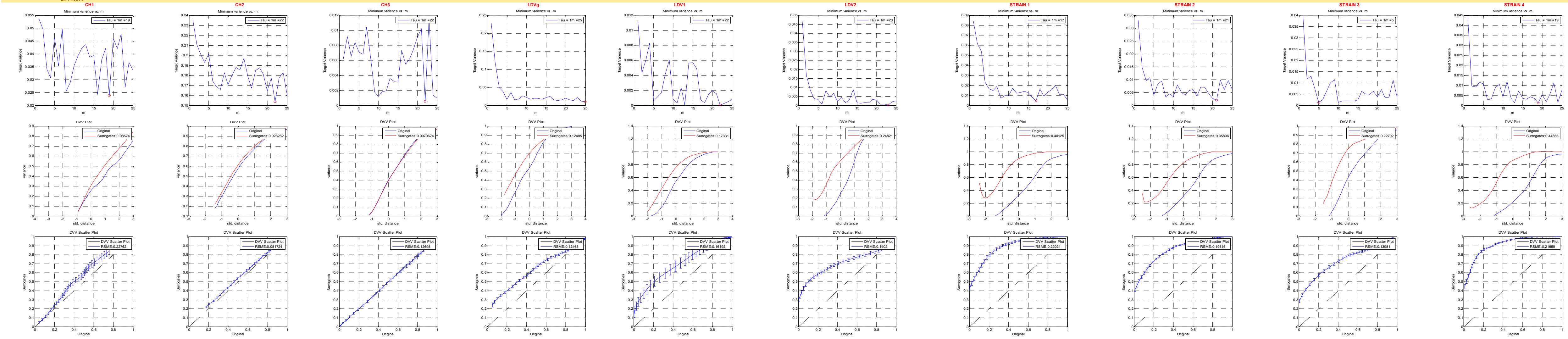

METHOD 3

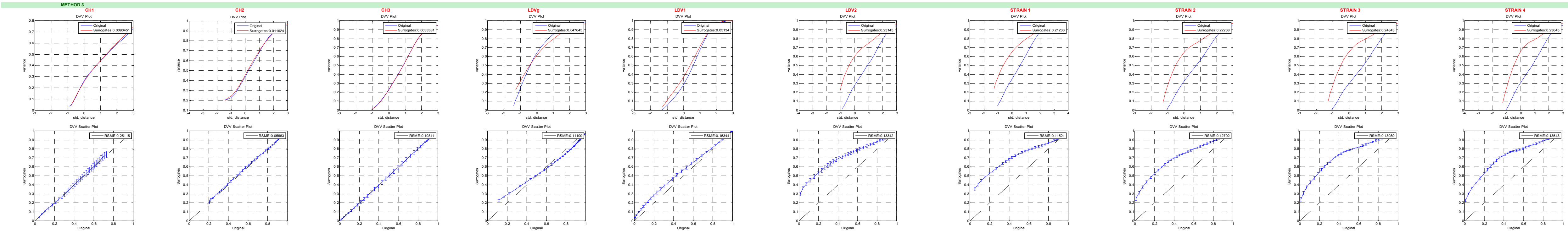

EXPERIMENT	VARIABLES		METHOD 1				METHOD 2				METHOD 3			
			best m	best τ	rsme	RSME	calc m	τ	rsme	RSME	set m	set τ	rsme	RSME
12	Harmonic resonance 2.0 Hz 2.5 Hz 3.0 Hz 3.5 Hz 4.0 Hz 4.2 Hz 4.3 Hz 4.4 Hz 4.5 Hz 4.6 Hz 5.0Hz 5.5 Hz 6.0 Hz 6.5Hz 7.0Hz Focus at mid strain gauge	CH1	2	1	0.1527	0.1006	4	1	0.0109	0.0823	3	1	0.0125	0.0867
		CH2	2	8	0.0106	0.3796	22	1	0.0315	0.2460	3	1	0.0153	0.1746
		CH3	4	4	0.0039	0.1078	1	1	0.0044	0.1585	3	1	0.0020	0.1523
		LDVg	10	2	0.1702	0.1444	22	1	0.1419	0.1289	3	1	0.0433	0.1084
		LDV1	7	9	0.1465	0.1440	2	1	0.0104	0.1702	3	1	0.0289	0.1622
		LDV2	10	9	0.3163	0.1872	24	1	0.2205	0.1337	3	1	0.2131	0.1233
		Strain 1	10	10	0.2410	0.1465	5	1	0.2325	0.1457	3	1	0.2172	0.1187
		Strain 2	10	10	0.2919	0.1654	23	1	0.3287	0.1857	3	1	0.1936	0.1191
		Strain 3	10	9	0.3749	0.2301	18	1	0.4264	0.2194	3	1	0.2271	0.1299
		Strain 4	10	9	0.3499	0.2086	7	1	0.2936	0.1784	3	1	0.2519	0.1433

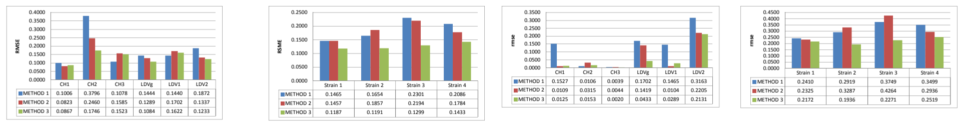

METHOD 1 for data section			
best m	best τ	rsme	RSME
2	1		
2	8		
4	4		
10	2	0.3387	0.3033
7	9	0.2407	0.1863
10	9	0.2408	0.1550
10	10	0.0416	0.1083
10	10	0.0372	0.1125
10	9	0.2355	0.1561
10	9	0.2320	0.1529

Optimum embeding parameter m and time lag tau are determined using data sqered yellow. Using these parameters RMSE and rmse were calculated for all valid data squered in pink

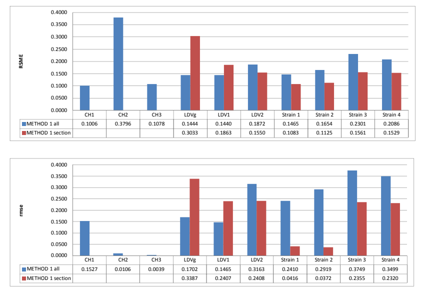

Data recorded 3D Accelerometer

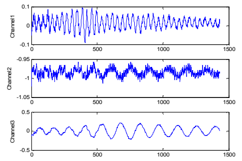

Data analysed 3D Accelerometer

Data recorded Strain Gauge **Data analysed Strain Gauge** **Data recorded LDV** **Data analysed LDV**

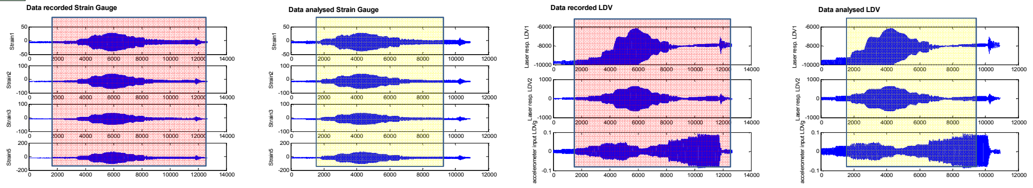

METHOD 1

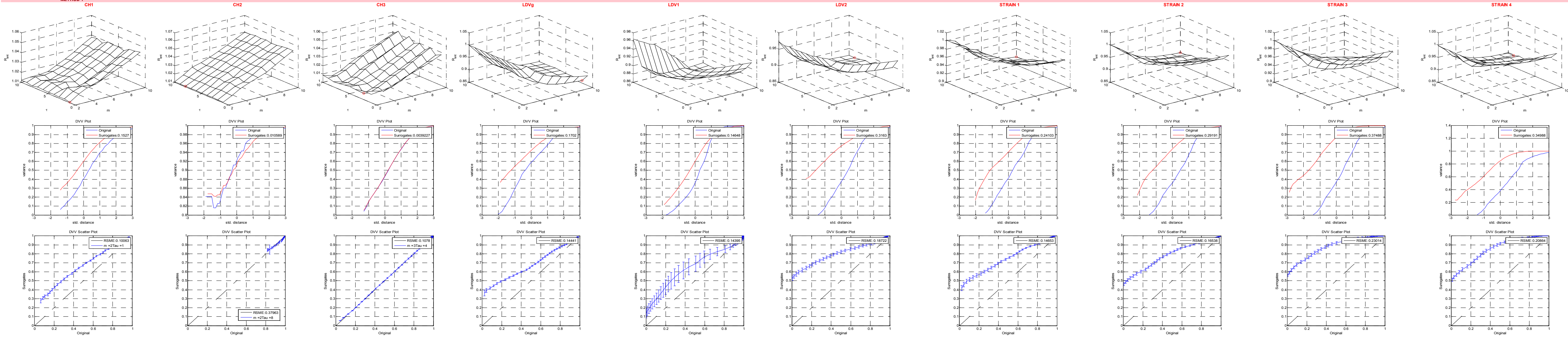

METHOD 2

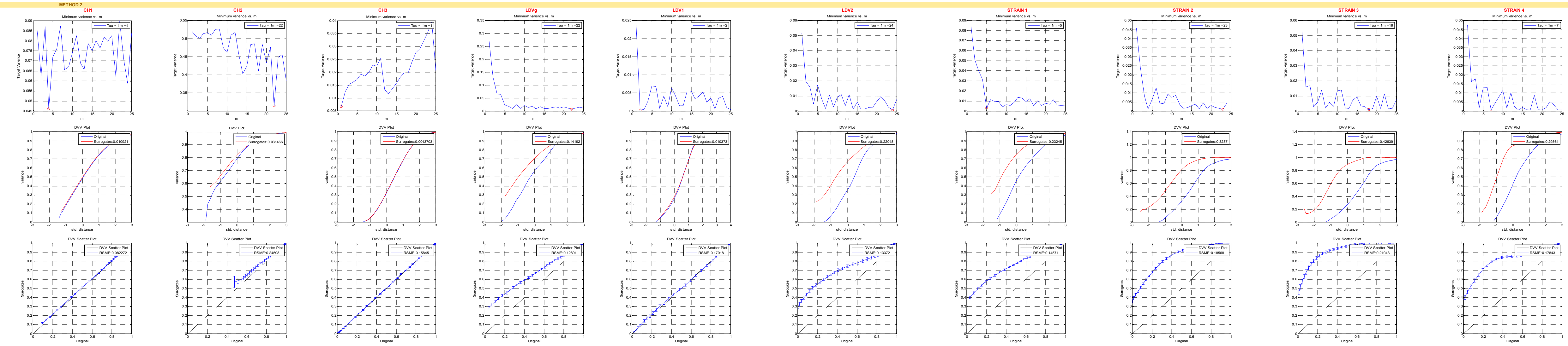

METHOD 3

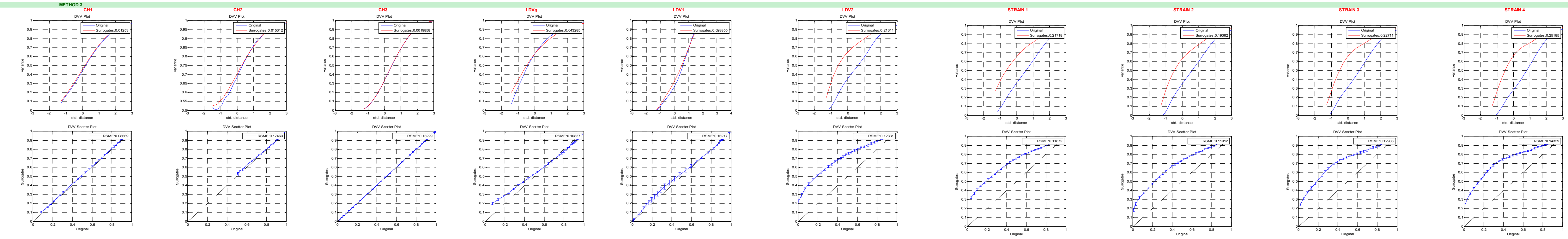

EXP13

EXPERIMENT	VARIABLES		METHOD 1				METHOD 2				METHOD 3			
			best m	best τ	rsme	RSME	calc m	τ	rsme	RSME	set m	set τ	rsme	RSME
13	Loading Sine Sweep 2.0 Hz 6.0 Hz 60 sec Focus at mid strain gauge	CH1	3	9	0.0425	0.2044	21	1	0.0639	0.3005	3	1	0.0241	0.2905
		CH2	8	9	0.1169	0.2192	17	1	0.0798	0.1423	3	1	0.0533	0.0738
		CH3	3	8	0.0259	0.1349	22	1	0.0196	0.1741	3	1	0.0227	0.2591
		LDVg	10	2	0.1912	0.1799	7	1	0.1105	0.1670	3	1	0.0619	0.1380
		LDV1	6	6	0.1866	0.2810	5	1	0.0367	0.3386	3	1	0.0668	0.3511
		LDV2	7	7	0.0617	0.2329	24	1	0.5283	0.3078	3	1	0.4848	0.3156
		Strain 1	10	10	0.0882	0.1039	22	1	0.4030	0.2106	3	1	0.2604	0.1358
		Strain 2	9	9	0.0766	0.1423	7	1	0.2112	0.1369	3	1	0.2040	0.1564
		Strain 3	10	9	0.3634	0.1895	5	1	0.2536	0.1320	3	1	0.2723	0.1620
		Strain 4	9	9	0.3700	0.1903	4	1	0.2454	0.1417	3	1	0.2522	0.1643

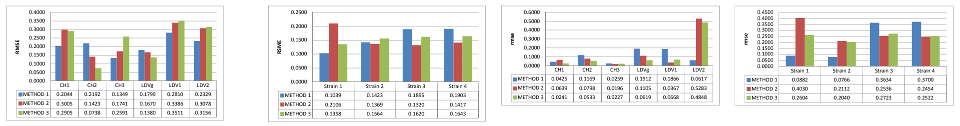

METHOD 1 for data section			
best m	best τ	rsme	RSME
3	9	0.2258	0.1383
8	9	0.1922	0.2875
3	8	0.0145	0.1040

Optimum embeding parameter m and time lag tau are determined using data sqered yellow. Using these parameters RMSE and rmse were calculated for all valid data squered in pink

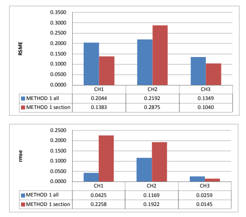

Data recorded 3D Accelerometer

Data analysed 3D Accelerometer

Data recorded Strain Gauge

Data analysed Strain Gauge

Data recorded LDV

Data analysed LDV

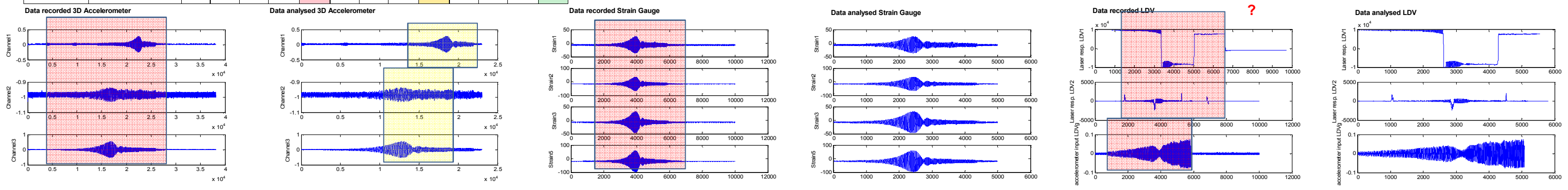

METHOD 1

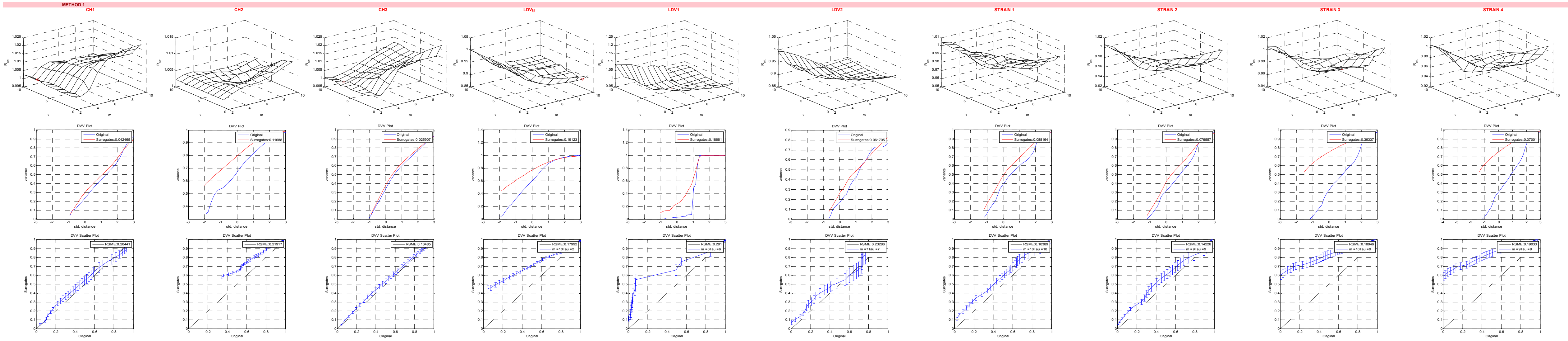

METHOD 2

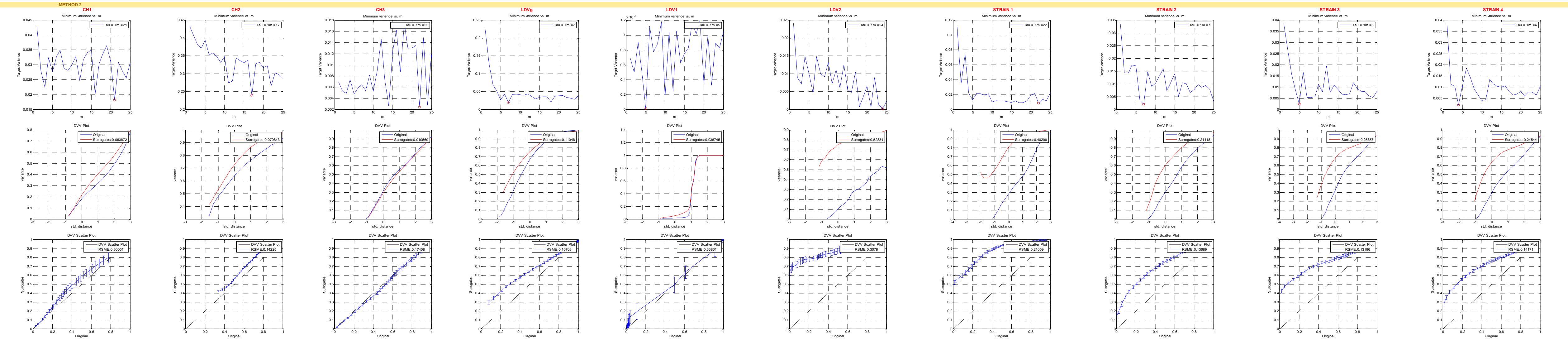

METHOD 3

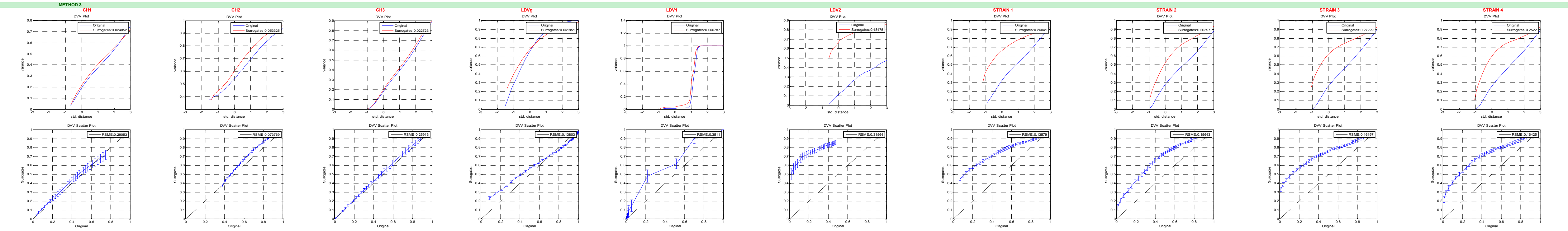

EXPERIMENT	VARIABLES		METHOD 1 best m	METHOD 1 best τ	METHOD 1 rsme	METHOD 1 RSME	METHOD 2 calc m	METHOD 2 τ	METHOD 2 rsme	METHOD 2 RSME	METHOD 3 set m	METHOD 3 set τ	METHOD 3 rsme	METHOD 3 RSME
14	Loading White noise 4.336Hz at the peak next 23Hz Focus at mid strain gauge	CH1	5	1	0.0072	0.0756	24	1	0.0156	0.0853	3	1	0.0080	0.0732
		CH2	5	1	0.0372	0.1616	14	1	0.0489	0.1552	3	1	0.0277	0.1218
		CH3	4	1	0.0190	0.1089	21	1	0.0537	0.1977	3	1	0.0153	0.0961
		LDVg	8	1	0.1692	0.3932	25	1	0.0381	0.4272	3	1	0.0524	0.2549
		LDV1	2	2	0.0030	0.2366	3	1	0.0044	0.1145	3	1	0.0019	0.1134
		LDV2	2	4	0.1031	0.3799	4	1	0.2186	0.2779	3	1	0.2233	0.2656
		Strain 1	2	5	0.0023	0.3227	18	1	0.2176	0.4070	3	1	0.2059	0.3447
		Strain 2	3	5	0.0068	0.2992	22	1	0.0866	0.2729	3	1	0.0637	0.2257
		Strain 3	2	9	0.2249	0.3144	25	1	0.1299	0.1882	3	1	0.1149	0.1277
		Strain 4	7	2	0.2378	0.2272	18	1	0.0800	0.1192	3	1	0.0721	0.0910

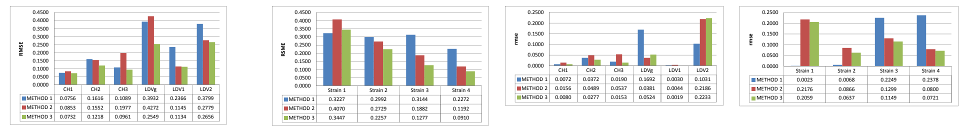

METHOD 1 for data section			
best m	best τ	rsme	RSME
5	1	0.0120	0.0843
5	1	0.2266	0.2818
4	1	0.0218	0.1014

Optimum embeding parameter m and time lag tau are determined using data sqered yellow. Using these parameters RMSE and rmse were calculated for all valid data squered in pink

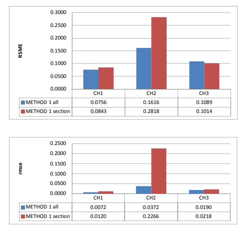

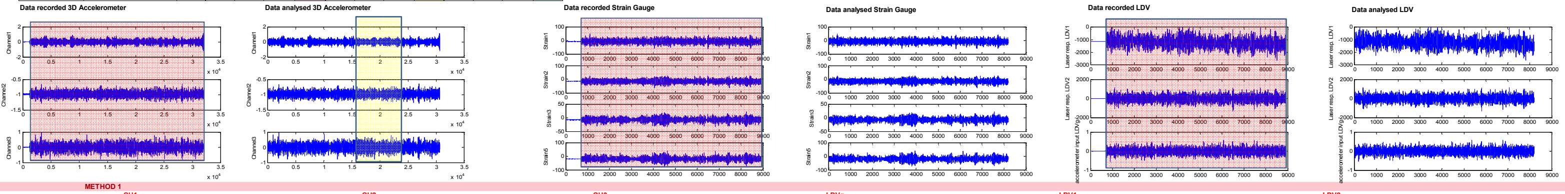

METHOD 1

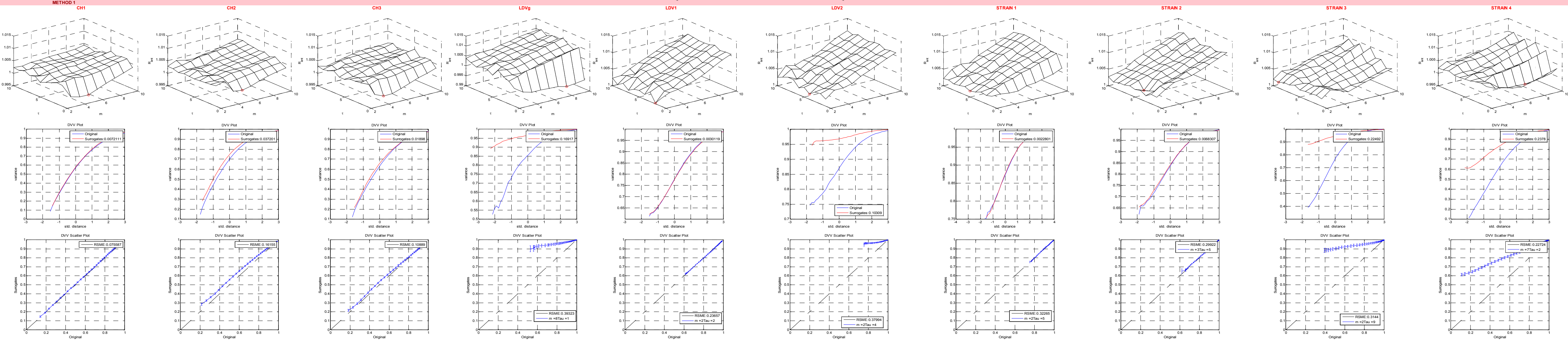

METHOD 2

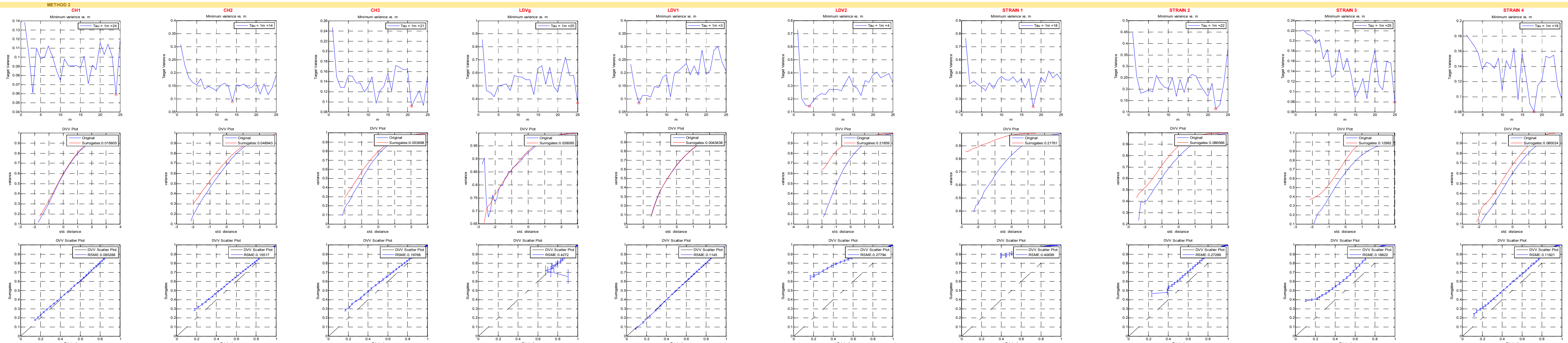

METHOD 3

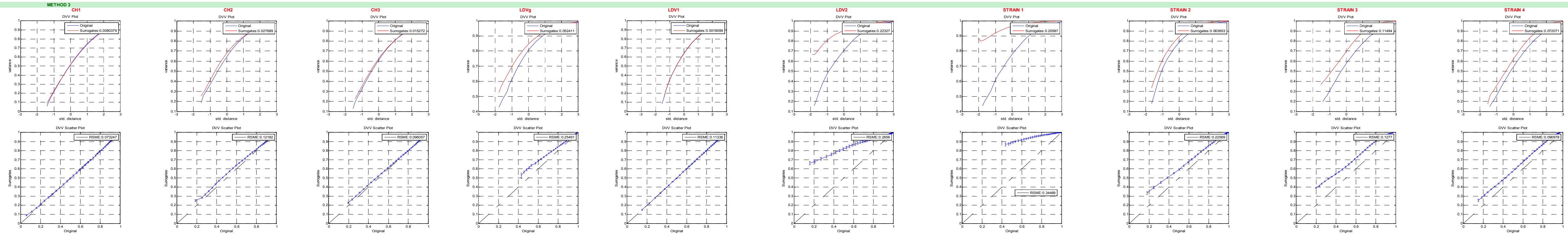

EXPERIMENT	VARIABLES		METHOD 1 best m	METHOD 1 best τ	METHOD 1 rsme	METHOD 1 RSME	METHOD 2 calc m	METHOD 2 τ	METHOD 2 rsme	METHOD 2 RSME	METHOD 3 set m	METHOD 3 set τ	METHOD 3 rsme	METHOD 3 RSME
15	Loading White noise 4.336Hz at the peak next 23Hz Focus at bottom strain gauge	CH1	4	1	0.0062	0.0692	5	1	0.0066	0.0772	3	1	0.0038	0.0668
		CH2	5	1	0.0321	0.1750	22	1	0.0695	0.1675	3	1	0.0206	0.1353
		CH3	4	1	0.0192	0.1124	17	1	0.0467	0.1979	3	1	0.0168	0.0963
		LDVg	8	1	0.0505	0.3124	9	1	0.0654	0.3185	3	1	0.0442	0.2607
		LDV1	2	10	0.0086	0.1173	19	1	0.0120	0.0846	3	1	0.0041	0.1057
		LDV2	6	1	0.3039	0.3063	18	1	0.3192	0.3524	3	1	0.2591	0.2782
		Strain 1	8	1	0.3199	0.3504	14	1	0.3787	0.3699	3	1	0.2443	0.3280
		Strain 2	7	7	0.1514	0.3172	19	1	0.1445	0.2367	3	1	0.2132	0.2352
		Strain 3	10	6	0.1905	0.2279	18	1	0.1627	0.1652	3	1	0.2765	0.1664
		Strain 4	10	10	0.1453	0.2298	19	1	0.0940	0.1269	3	1	0.2801	0.1815

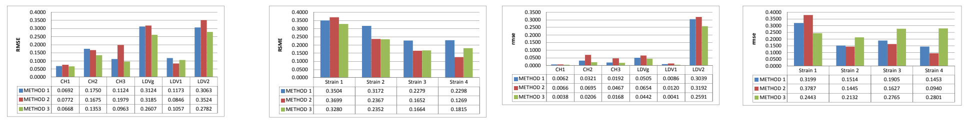

METHOD 1 for data section best m	best τ	rsme	RSME
4	1	0.0048	0.0790
5	1	0.2150	0.2815
4	1	0.0196	0.1121
8	1	0.1910	0.3910
2	10	0.2072	0.2648
6	1	0.0554	0.1961
8	1	0.0619	0.2173
7	7	0.2624	0.3614
10	6	0.2992	0.2897
10	10	0.0531	0.1837

Optimum embeding parameter m and time lag tau are determined using data sqered yellow. Using these parameters RMSE and rmse were calculated for all valid data squered in pink

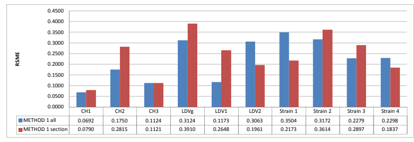

	CH1	CH2	CH3	LDVg	LDV1	LDV2	Strain 1	Strain 2	Strain 3	Strain 4
METHOD 1 all	0.0692	0.1750	0.1124	0.3124	0.1173	0.3063	0.3504	0.3172	0.2279	0.2298
METHOD 1 section	0.0790	0.2815	0.1121	0.3910	0.2648	0.1961	0.2173	0.3614	0.2897	0.1837

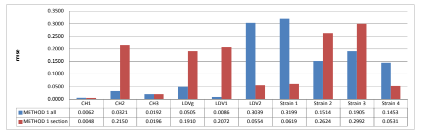

Data recorded 3D Accelerometer

Data analysed 3D Accelerometer

Data recorded Strain Gauge

Data analysed Strain Gauge

Data recorded LDV

Data analysed LDV

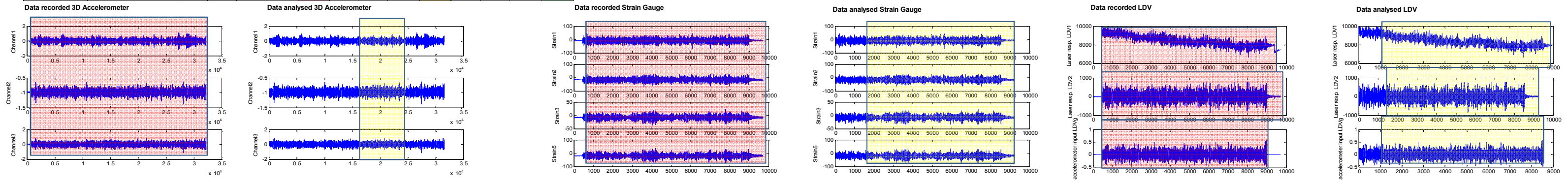

METHOD 1

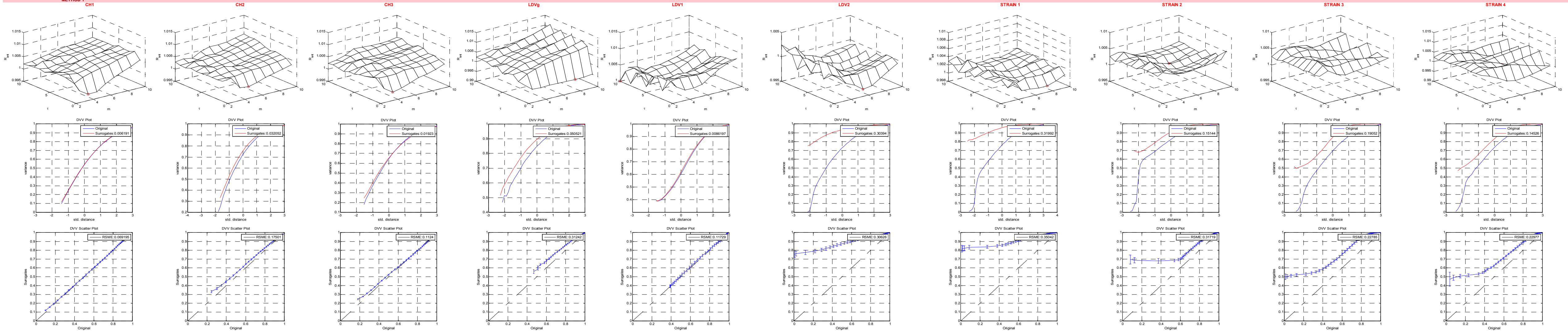

METHOD 2

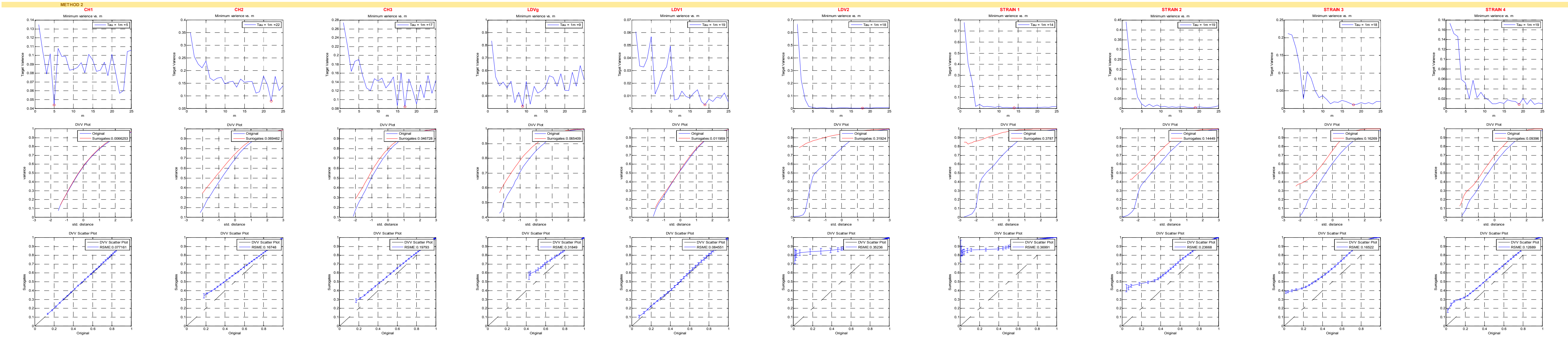

METHOD 3

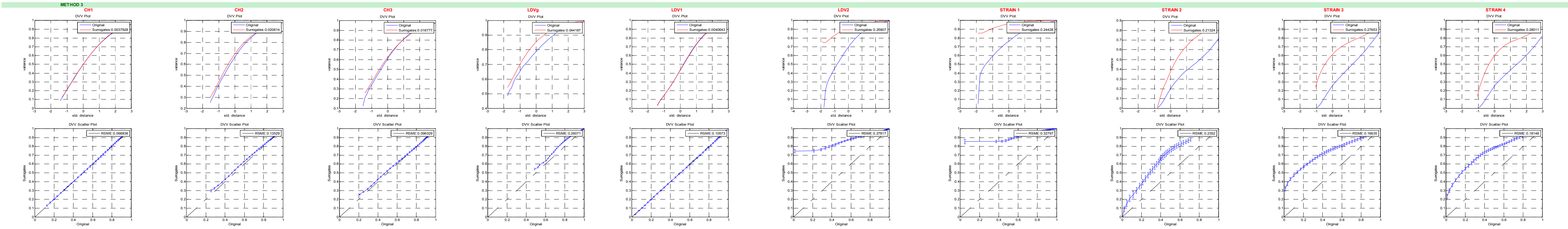

EXPERIMENT	VARIABLES		METHOD 1				METHOD 2				METHOD 3			
			best **m**	best τ	rsme	RSME	calc **m**	τ	rsme	RSME	set **m**	set τ	rsme	RSME
16	Loading Sine Sweep 2.0 Hz 6.0 Hz 60 sec Focus at bottom strain gauge	CH1	4	10	0.0716	0.1065	25	1	0.0620	0.1974	3	1	0.0354	0.2434
		CH2	2	5	0.0396	0.2383	7	1	0.0333	0.0989	3	1	0.0144	0.0673
		CH3	3	10	0.0141	0.1101	9	1	0.0089	0.1931	3	1	0.0087	0.2193
		LDVg	10	2	0.1700	0.1688	21	1	0.1494	0.1387	3	1	0.0528	0.1211
		LDV1	6	6	0.1758	0.1823	11	1	0.0872	0.1796	3	1	0.0314	0.2079
		LDV2	8	8	0.3659	0.2303	20	1	0.3000	0.1593	3	1	0.2509	0.1316
		Strain 1	10	10	0.1578	0.1270	9	1	0.2749	0.1510	3	1	0.2501	0.1336
		Strain 2	9	9	0.1196	0.1483	6	1	0.2365	0.1597	3	1	0.1830	0.1559
		Strain 3	10	10	0.4309	0.2256	10	1	0.3394	0.1691	3	1	0.2680	0.1610
		Strain 4	9	9	0.3920	0.2015	5	1	0.2818	0.1535	3	1	0.2522	0.1629

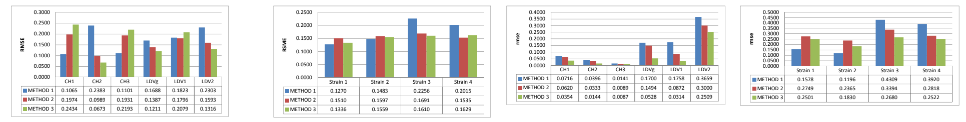

METHOD 1 for data section			
best **m**	best τ	rsme	RSME
4	10	0.0456	0.0875
2	5	0.1540	0.2917
3	10	0.0165	0.1431

Optimum embeding parameter m and time lag tau are determined using data sqered yellow. Using these parameters RMSE and rmse were calculated for all valid data squered in pink

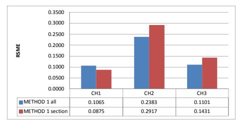

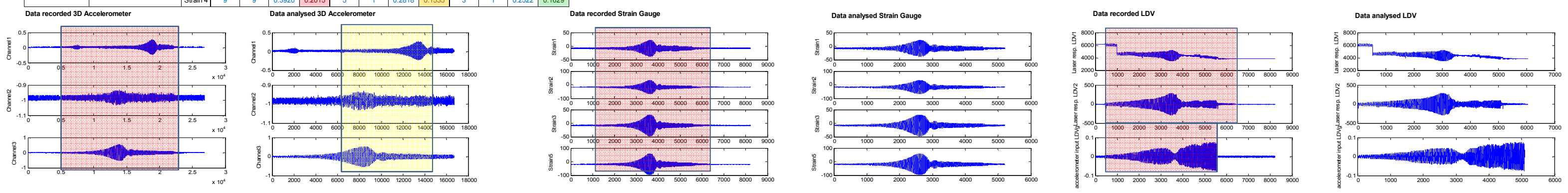

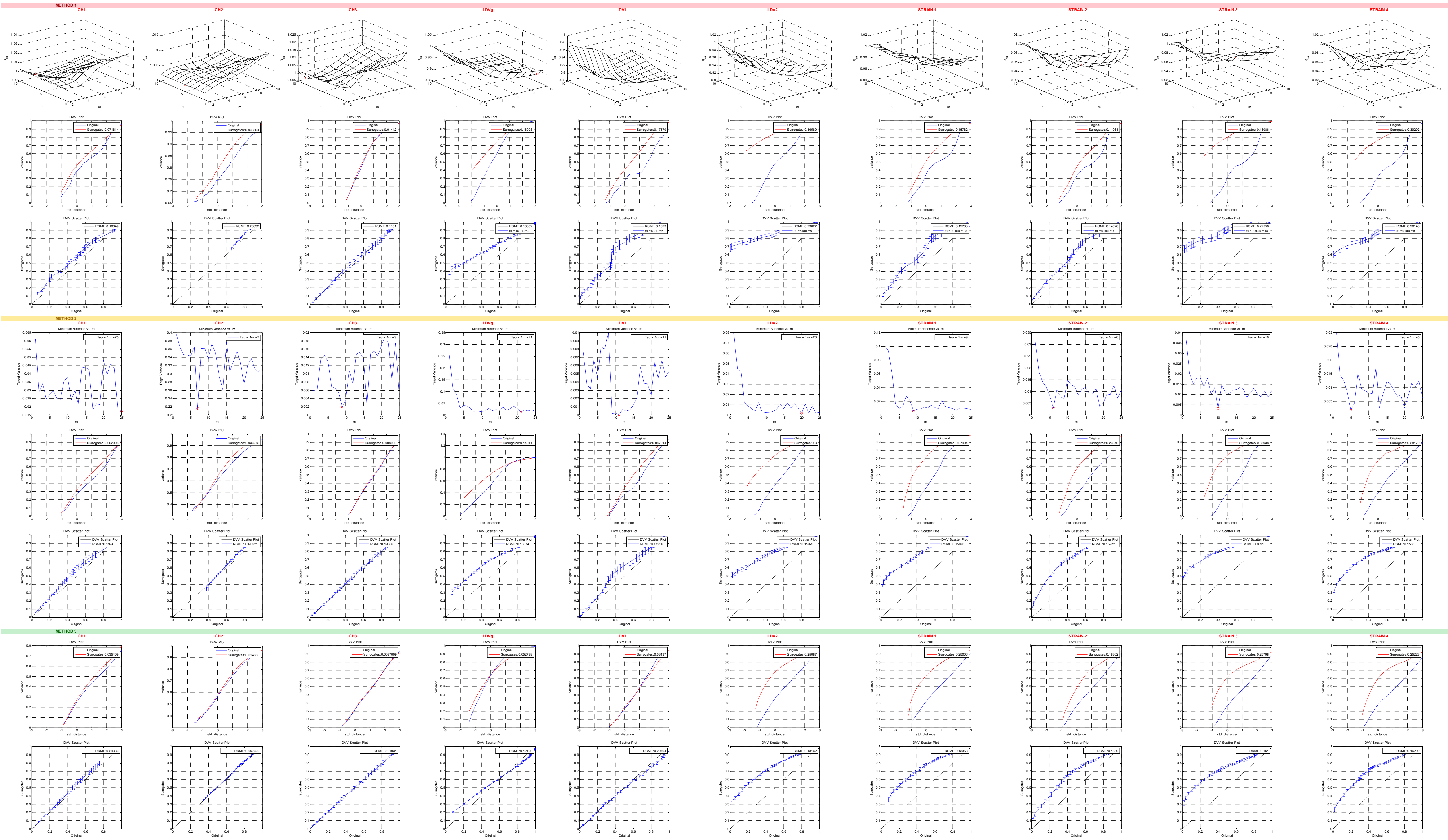

EXPERIMENT	VARIABLES		METHOD 1				METHOD 2				METHOD 3			
			best **m**	best **τ**	rsme	RSME	calc **m**	**τ**	rsme	RSME	set **m**	set **τ**	rsme	RSME
17	Harmonic resonance 2.0 Hz 2.5 Hz 3.0 Hz 3.5 Hz 4.0 Hz 4.2 Hz 4.3 Hz 4.4 Hz 4.5 Hz 4.6 Hz 5.0Hz 5.5 Hz 6.0 Hz 6.5Hz 7.0Hz Focus at bottom strain gauge.	CH1	7	10	0.1119	0.1255	22	1	0.1015	0.1965	3	1	0.0530	0.2385
		CH2	6	10	0.0359	0.1084	17	1	0.0197	0.0814	3	1	0.0073	0.0491
		CH3	4	10	0.0191	0.1464	14	1	0.0181	0.1311	3	1	0.0152	0.1867
		LDVg	10	8	0.2920	0.2477	13	1	0.1010	0.0961	3	1	0.0445	0.1009
		LDV1	5	9	0.0212	0.1582	11	1	0.0163	0.1671	3	1	0.0111	0.1873
		LDV2	8	7	0.3506	0.2324	21	1	0.3050	0.1632	3	1	0.2263	0.1206
		Strain 1	10	7	0.3605	0.2185	15	1	0.3875	0.2077	3	1	0.2459	0.1285
		Strain 2	9	7	0.3372	0.1942	10	1	0.2350	0.1589	3	1	0.2011	0.1230
		Strain 3	10	7	0.4138	0.2289	10	1	0.2820	0.1681	3	1	0.2267	0.1304
		Strain 4	9	7	0.3715	0.2099	9	1	0.2784	0.1719	3	1	0.2293	0.1324

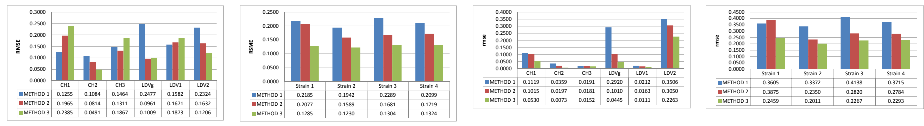

Data recorded 3D Accelerometer **Data analysed 3D Accelerometer** **Data recorded Strain Gauge** **Data analysed Strain Gauge** **Data recorded LDV** **Data analysed LDV**

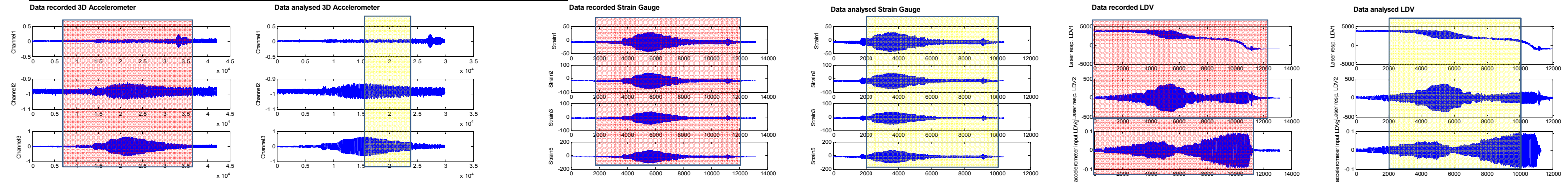

METHOD 1 for data section			
best **m**	best **τ**	rsme	RSME
7	10	0.0674	0.2994
6	10	0.2076	0.2181
4	10	0.1353	0.2228
10	8	0.2923	0.2521
5	9	0.0378	0.1539
8	7	0.0689	0.0970
10	7	0.0340	0.1041
9	7	0.2356	0.1392
10	7	0.2476	0.1467
9	7	0.0235	0.1226

Optimum embeding parameter m and time lag tau are determined using data sqered yellow. Using these parameters RMSE and rmse were calculated for all valid data squered in pink

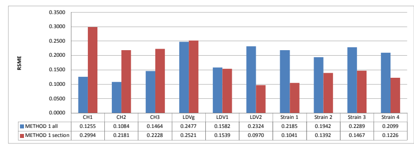

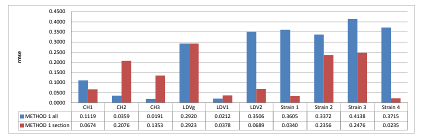

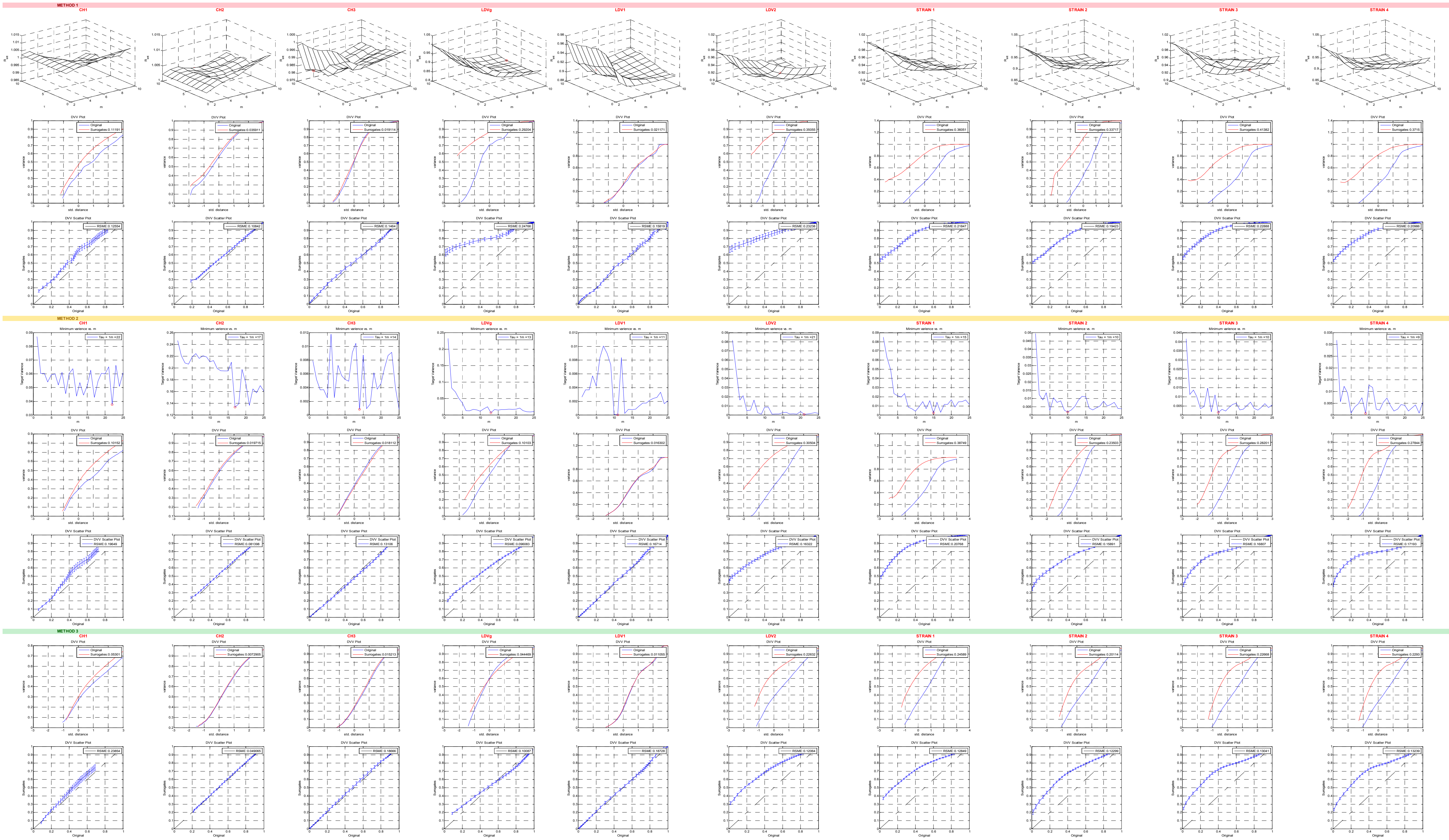

APPENDIX C1

DVV Method Results for An Impact Damaged Prestressed Bridge

1 THERMAL PERIOD

TOP STRAIN GAUGES | SOFFIT STRAIN GAUGES

SECTION E-E (MP4)

SG1

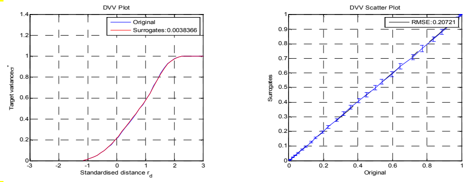

SG2

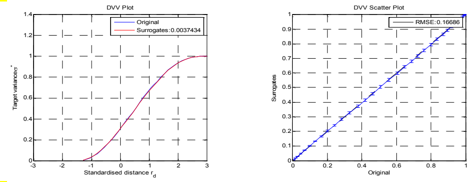

SG4

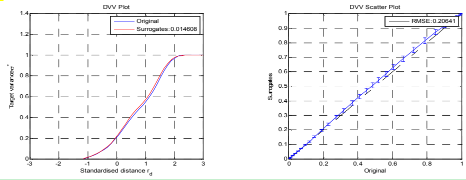

SG3

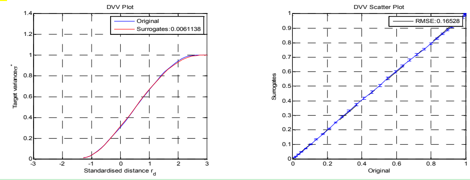

SECTION B-B (MP2)

SG5

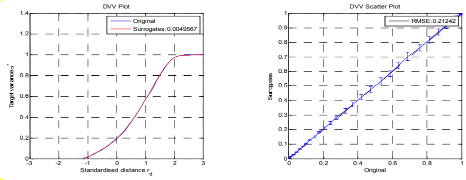

SG10 (DAMAGED)

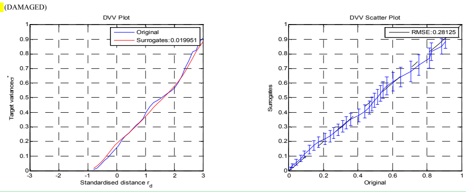

SECTION A-A (MP1)

SG6

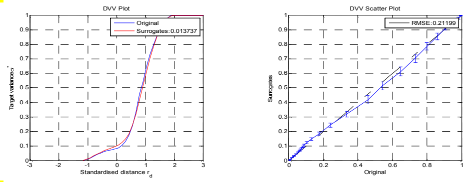

SG7

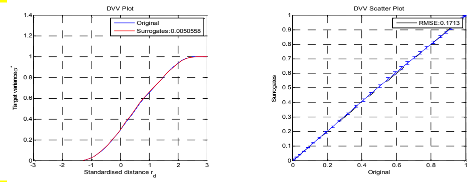

SG9

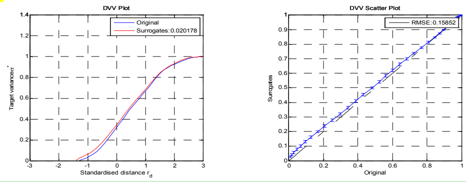

SG8

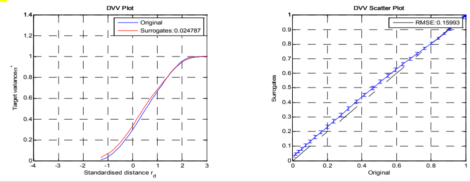

SECTION C-C (MP3)

SG14

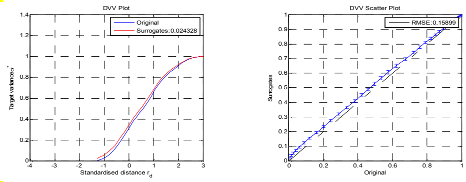

SG15

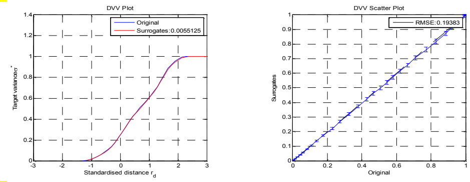

SG17

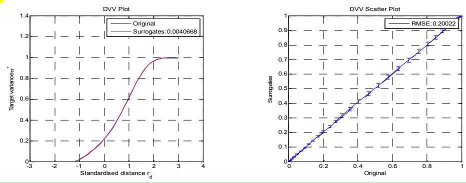

SG16

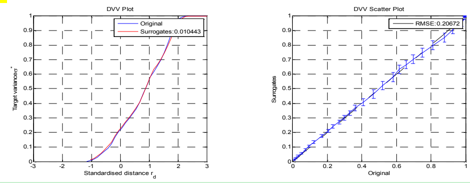

SECTION D-D (MP5)

SG18

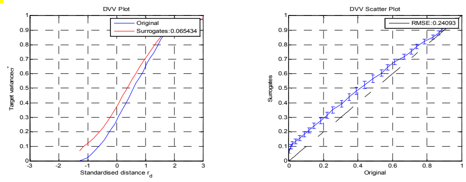

SG19

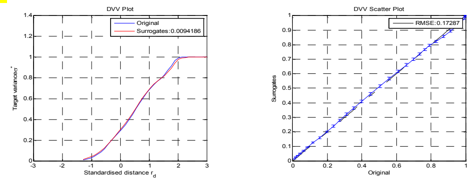

2 PRELOADING PERIOD

TOP STRAIN GAUGES | SOFFIT STRAIN GAUGES

SECTION E-E (MP4)

SG1

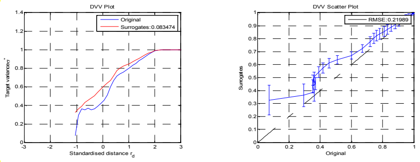

SG2

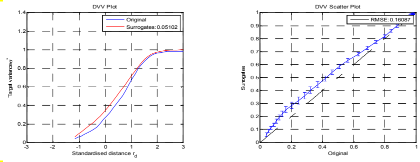

SG4

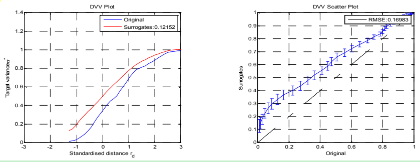

SG3

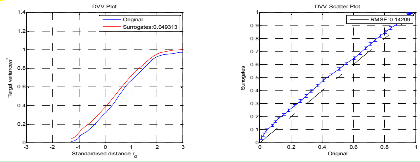

SECTION B-B (MP2)

SG5

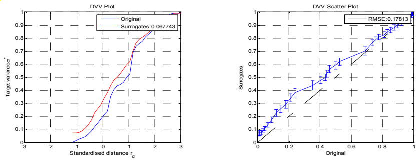

SG11 (EMBEDDED)

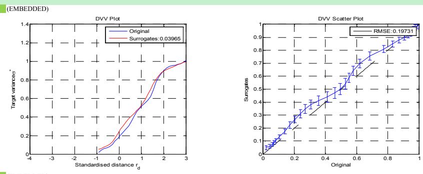

SG12 (EMBEDDED)

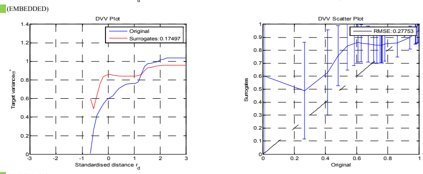

SG10 (DAMAGED)

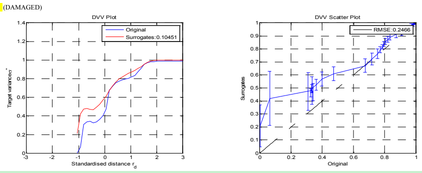

SG13 (EMBEDDED)

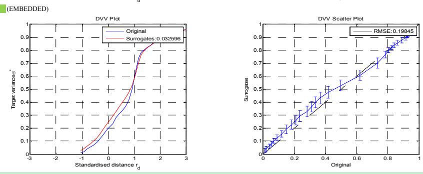

SECTION A-A (MP1)

SG6

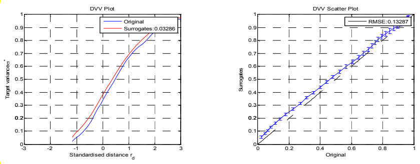

SG7

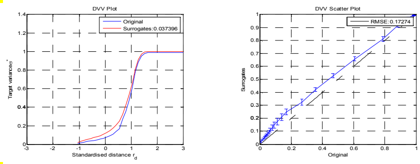

SG9

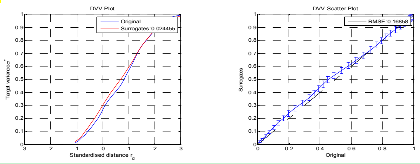

SG8

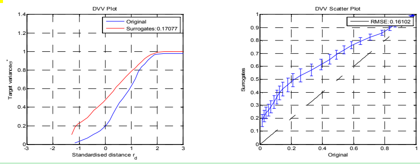

SECTION C-C (MP3)

SG14

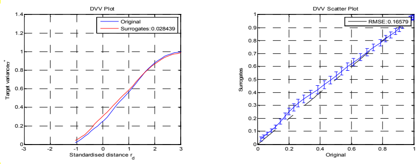

SG15

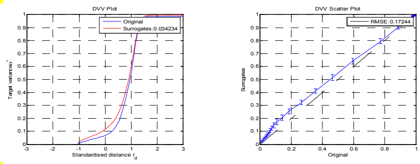

SG17

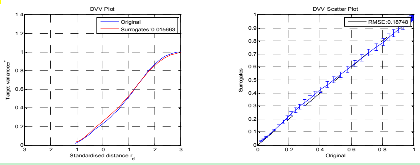

SG16

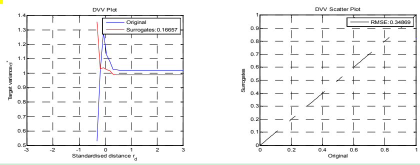

SECTION D-D (MP5)

SG18

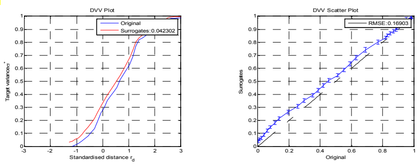

SG19

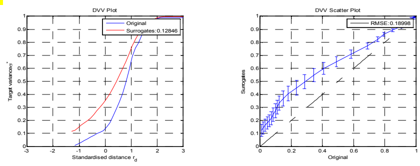

3 HYDRODEMOLITION PERIOD

TOP STRAIN GAUGES | SOFFIT STRAIN GAUGES

SECTION E-E (MP4)

SG1

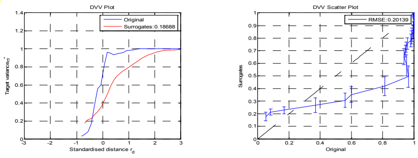

SG2

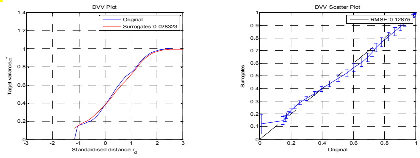

SG4

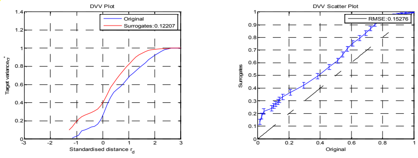

SG3

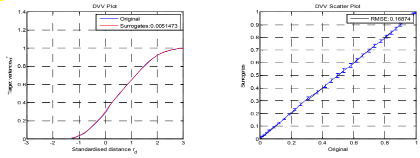

SECTION B-B (MP2)

SG5

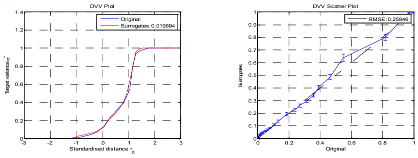

SG11 (EMBEDDED)

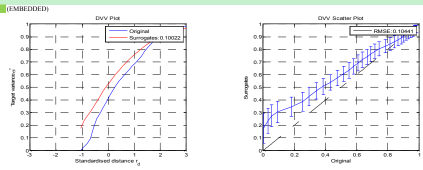

SG12 (EMBEDDED)

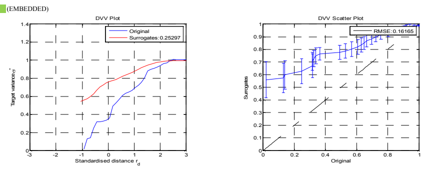

SG10 (DAMAGED)

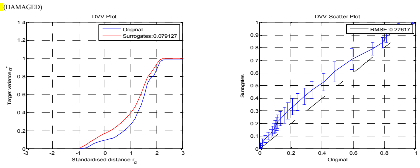

SG13 (EMBEDDED)

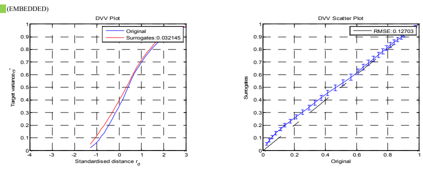

SECTION A-A (MP1)

SG6

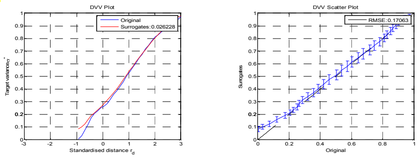

SG7

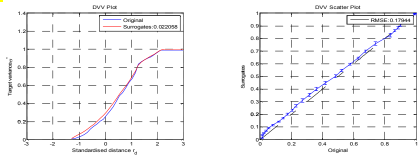

SG9

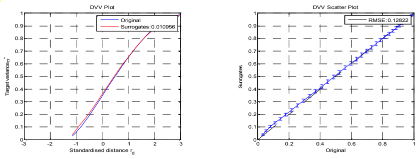

SG8

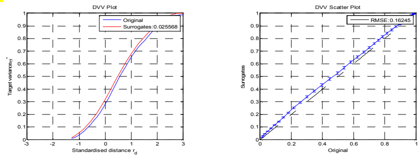

SECTION C-C (MP3)

SG14

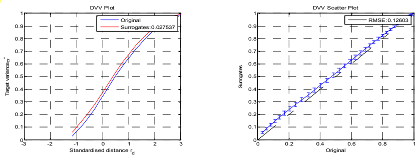

SG15

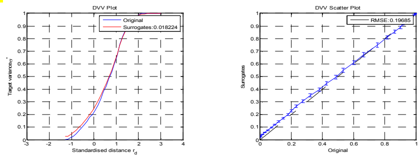

SG17

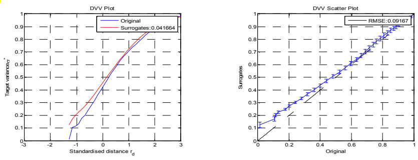

SG16

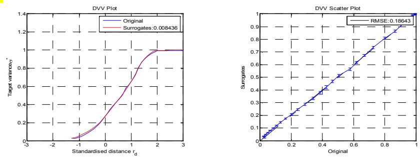

SECTION D-D (MP5)

SG18

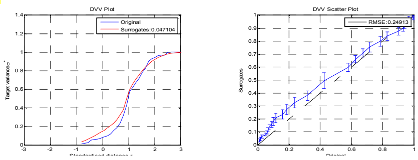

SG19

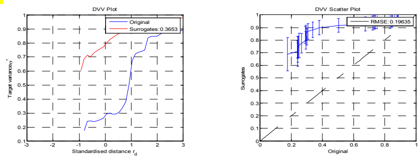

4 FULL LOADING PERIOD

TOP STRAIN GAUGES | SOFFIT STRAIN GAUGES

SECTION E-E (MP4)

SG1

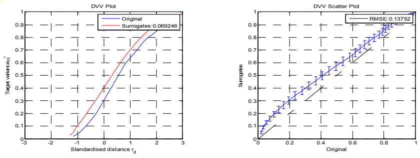

SG2

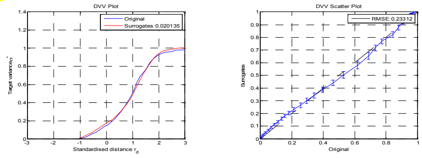

SG4

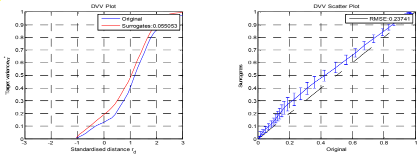

SG3

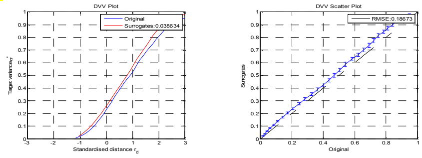

SECTION B-B (MP2)

SG5

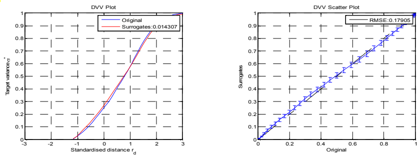

SG11 (EMBEDDED)

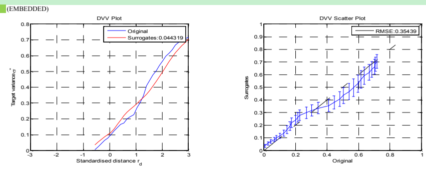

SG12 (EMBEDDED)

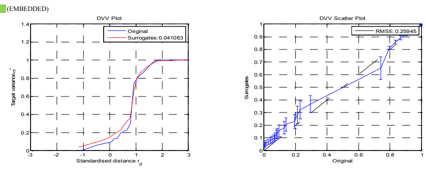

SG10 (DAMAGED)

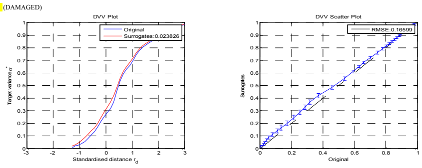

SG13 (EMBEDDED)

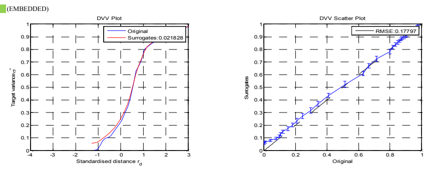

SECTION A-A (MP1)

SG6

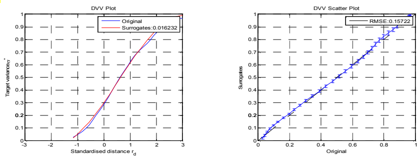

SG7

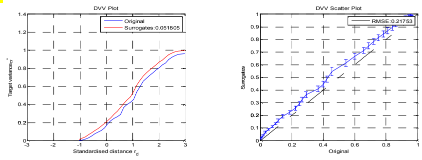

SG9

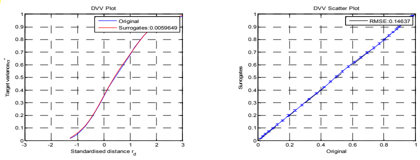

SG8

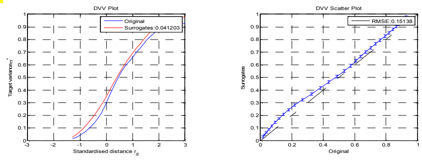

SECTION C-C (MP3)

SG14

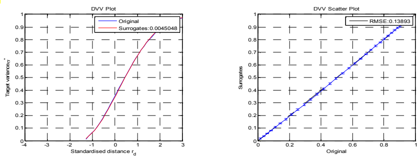

SG15

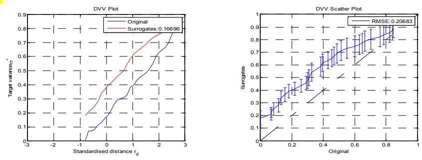

SG17

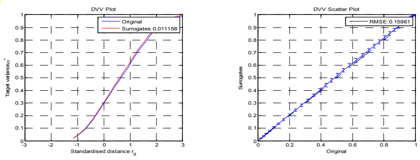

SG16

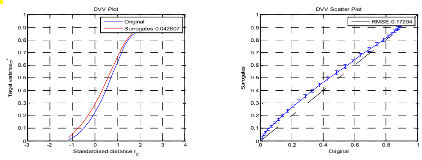

SECTION D-D (MP5)

SG18

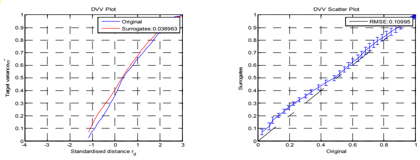

SG19

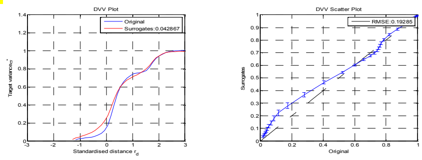

5 SHRINKAGE PERIOD

TOP STRAIN GAUGES | SOFFIT STRAIN GAUGES

SECTION E-E (MP4)

SG1

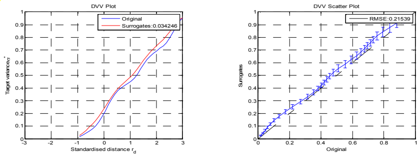

SG2

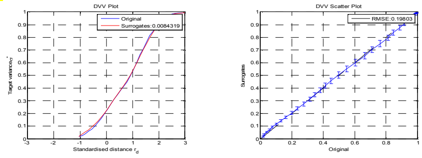

SG4

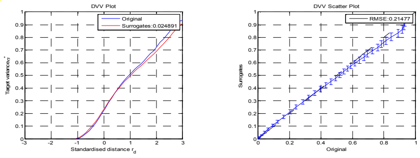

SG3

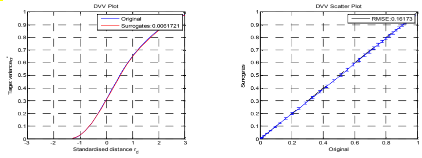

SECTION B-B (MP2)

SG5

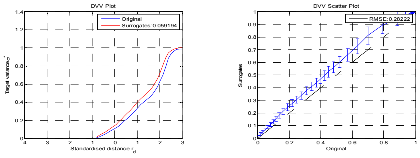

SG11 (EMBEDDED)

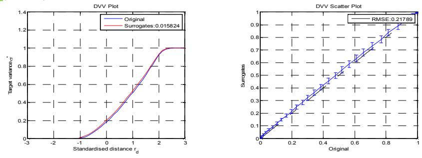

SG12 (EMBEDDED)

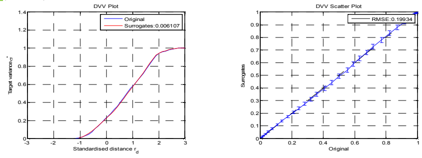

SG10 (DAMAGED)

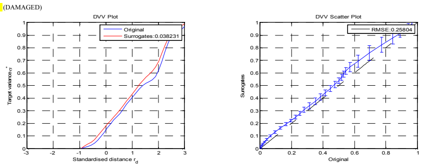

SG13 (EMBEDDED)

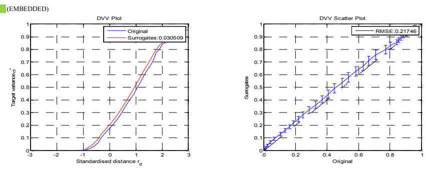

SECTION A-A (MP1)

SG6

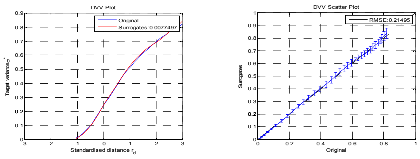

SG7

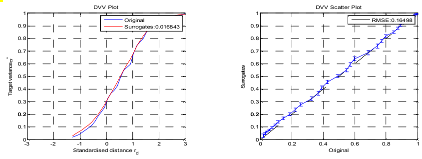

SG9

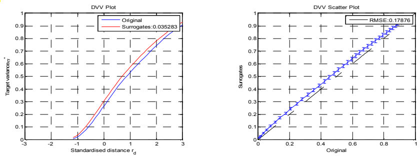

SG8

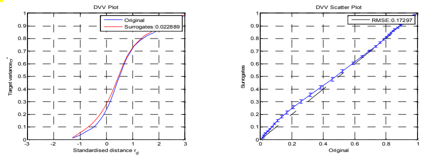

SECTION C-C (MP3)

SG14

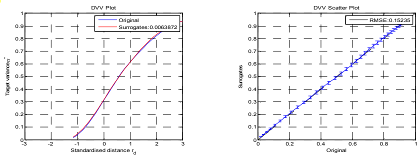

SG15

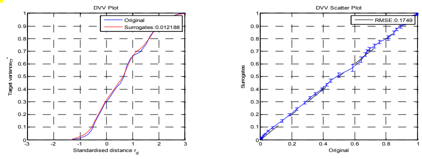

SG17

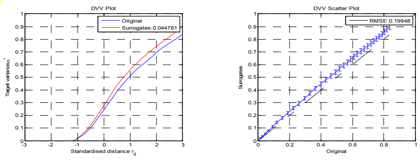

SG16

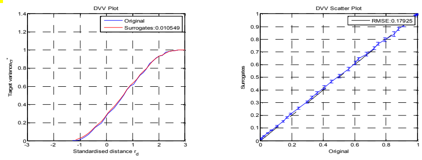

SECTION D-D (MP5)

SG18

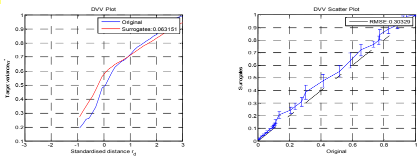

SG19

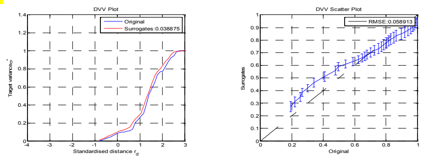

6 UNLOADING PERIOD

TOP STRAIN GAUGES | SOFFIT STRAIN GAUGES

SECTION E-E (MP4)

SG1

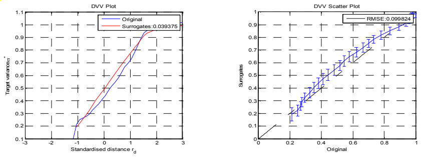

SG2

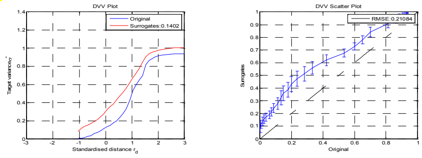

SG4

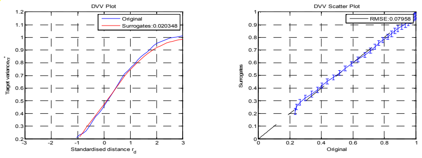

SG3

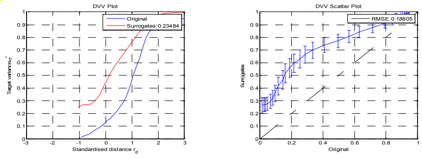

SECTION B-B (MP2)

SG5

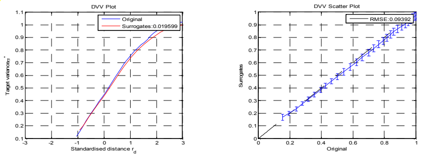

SG11 (EMBEDDED)

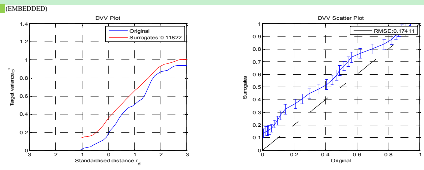

SG12 (EMBEDDED)

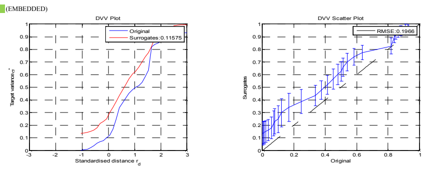

SG10 (DAMAGED)

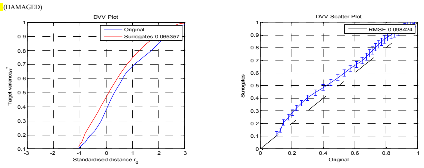

SG13 (EMBEDDED)

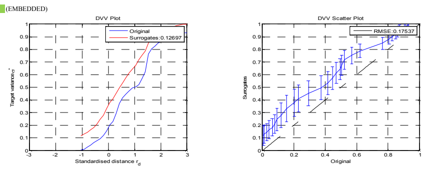

SECTION A-A (MP1)

SG6

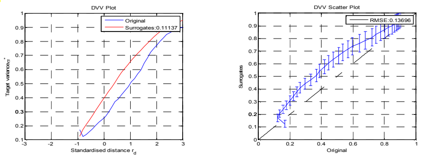

SG7

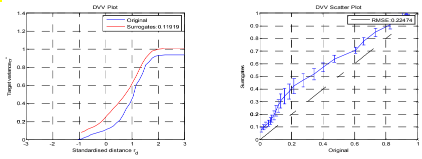

SG9

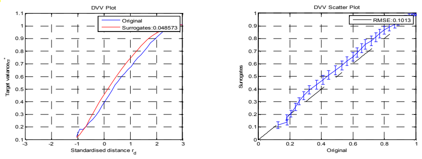

SG8

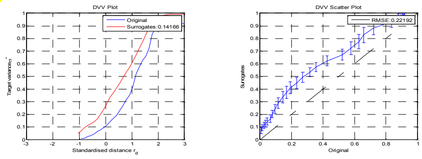

SECTION C-C (MP3)

SG14

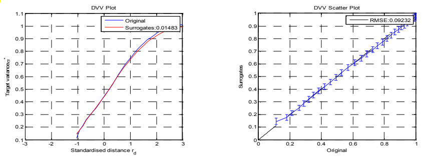

SG15

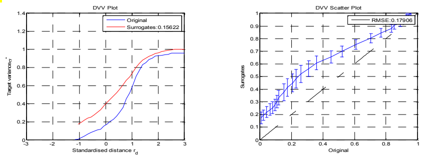

SG17

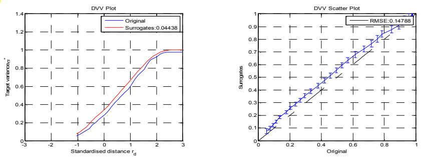

SG16

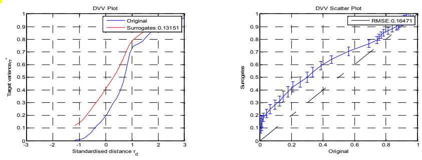

SECTION D-D (MP5)

SG18

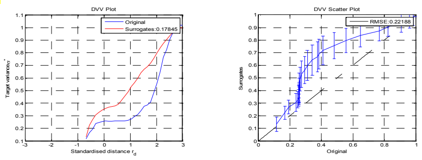

SG19

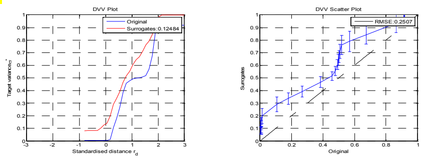

7 STRENGTH GAIN PERIOD

TOP STRAIN GAUGES | SOFFIT STRAIN GAUGES

SECTION E-E (MP4)

SG1

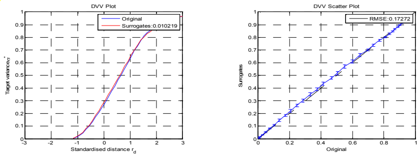

SG2

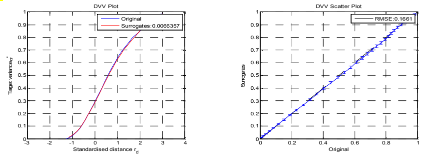

SG4

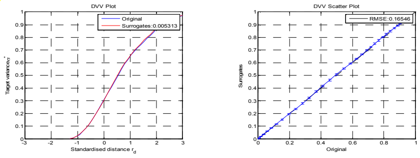

SG3

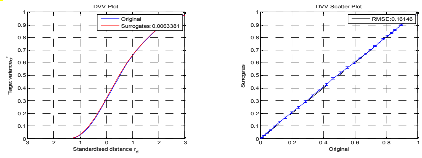

SECTION B-B (MP2)

SG5

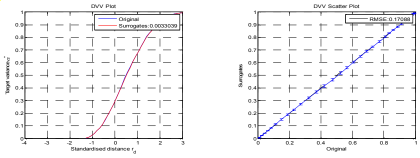

SG11 (EMBEDDED)

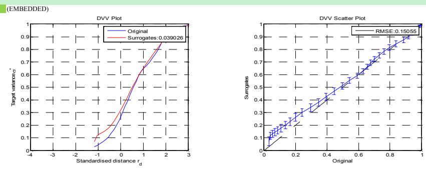

SG12 (EMBEDDED)

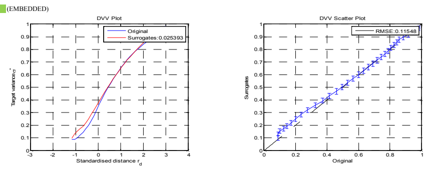

SG10 (DAMAGED)

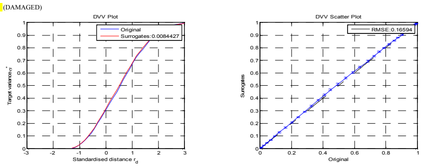

SG13 (EMBEDDED)

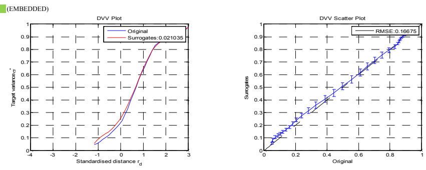

SECTION A-A (MP1)

SG6

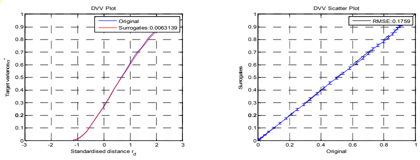

SG7

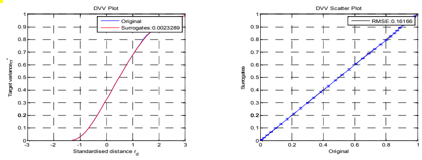

SG9

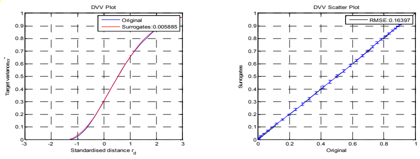

SG8

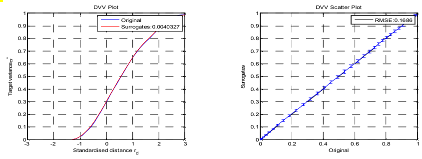

SECTION C-C (MP3)

SG14

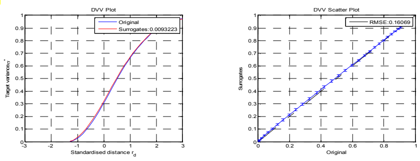

SG15

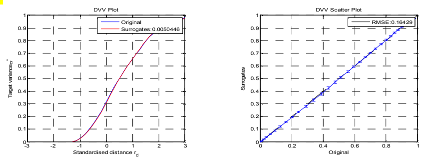

SG17

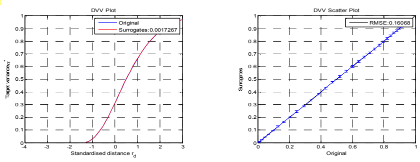

SG16

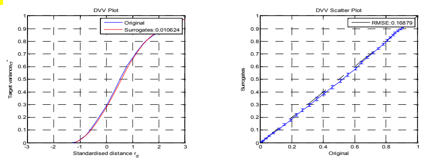

SECTION D-D (MP5)

SG18

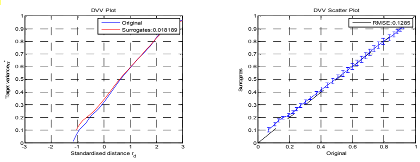

SG19

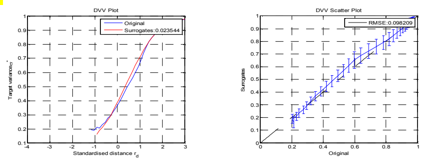

APPENDIX C2

DVV Method Results for A Single Span Steel-Concrete Composite Bridge

TRAIN 1

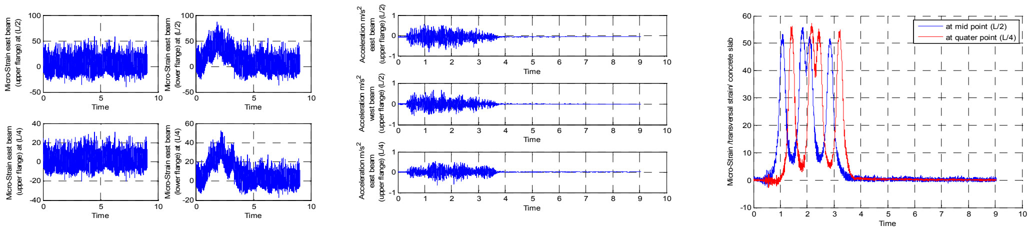

Strain East Beam L/2 Top Flange

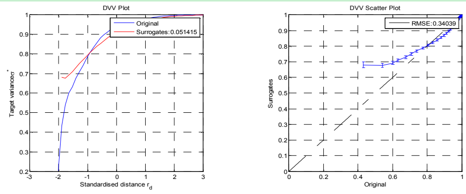

Strain East Beam L/2 Bottom Flange

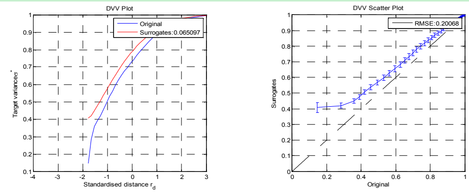

Strain East Beam L/4 Top Flange

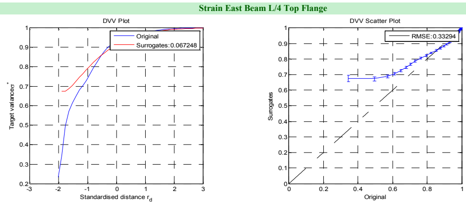

Strain East Beam L/4 Bottom Flange

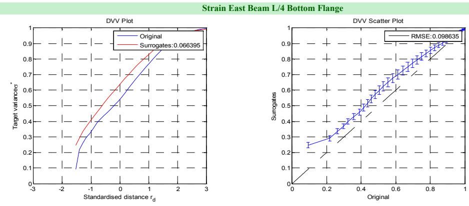

Acceleration East Beam L/2 Top Flange

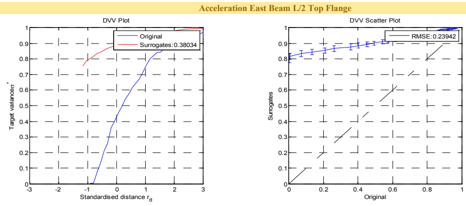

Acceleration East Beam L/4 Top Flange

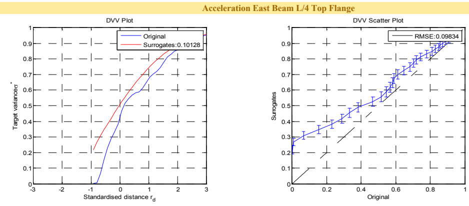

Acceleration West Beam L/2 Top Flange

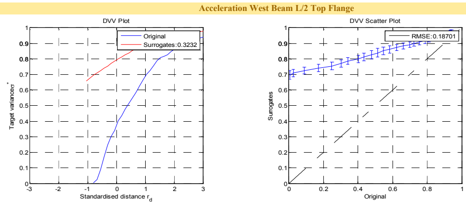

Transversal Strain Slab L/2

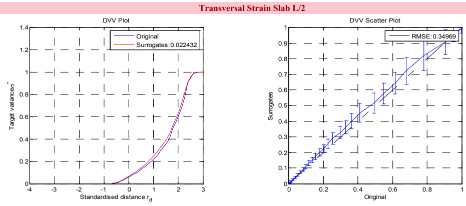

Transversal Strain Slab L/4

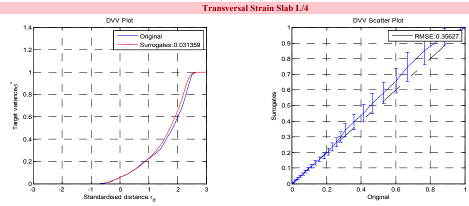

TRAIN 2

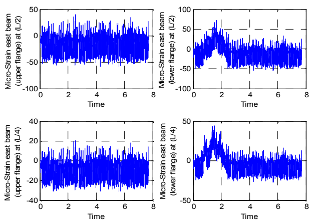

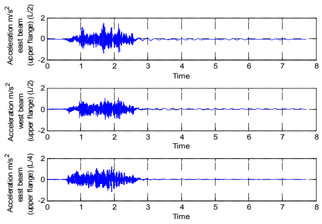

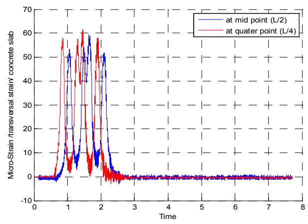

Strain East Beam L/2 Top Flange

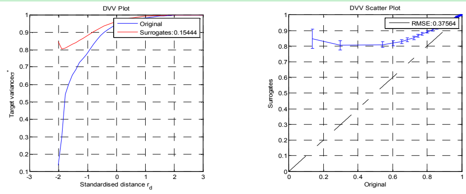

Strain East Beam L/2 Bottom Flange

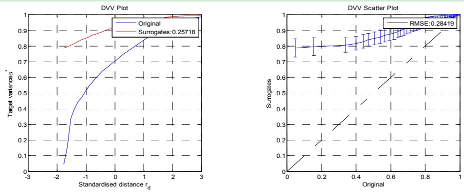

Strain East Beam L/4 Top Flange

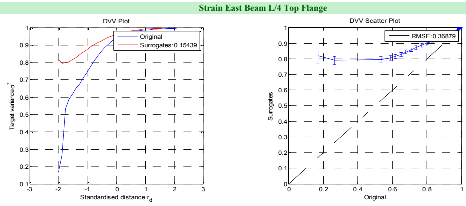

Strain East Beam L/4 Bottom Flange

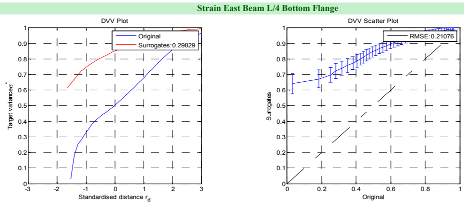

Acceleration East Beam L/2 Top Flange

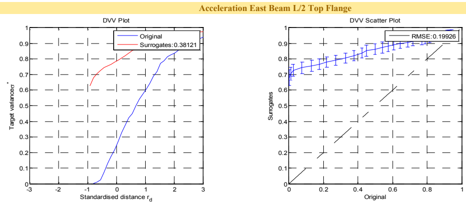

Acceleration East Beam L/4 Top Flange

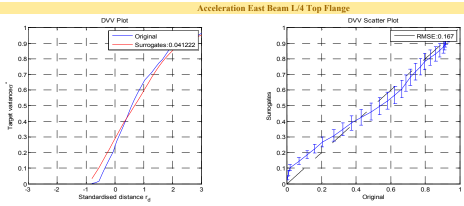

Acceleration West Beam L/2 Top Flange

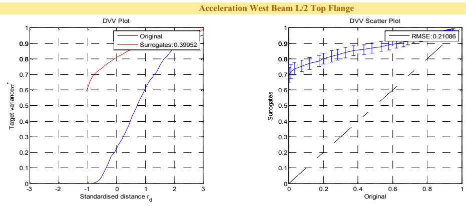

Transversal Strain Slab L/2

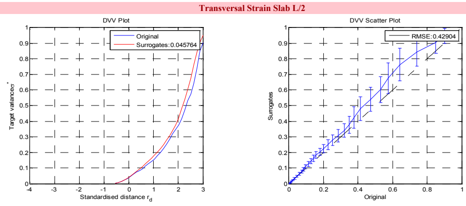

Transversal Strain Slab L/4

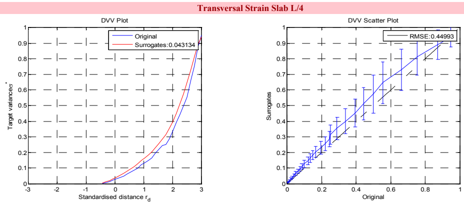

TRAIN 3

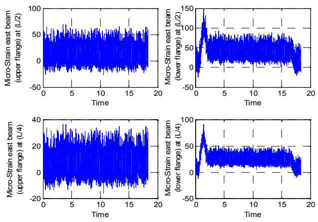

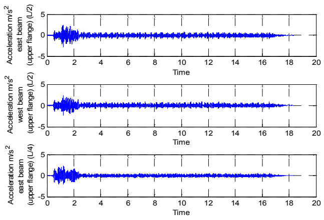

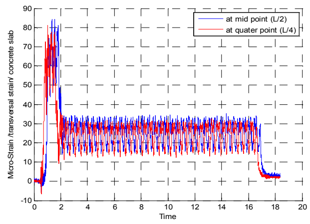

Strain East Beam L/2 Top Flange

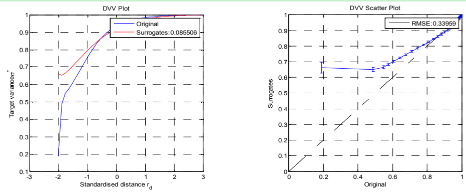

Strain East Beam L/2 Bottom Flange

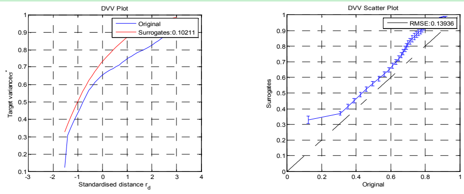

Strain East Beam L/4 Top Flange

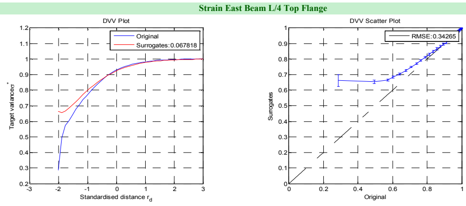

Strain East Beam L/4 Bottom Flange

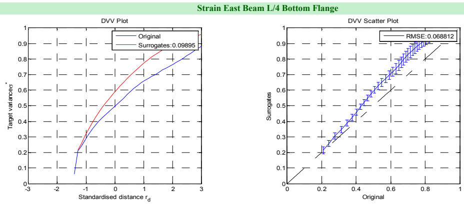

Acceleration East Beam L/2 Top Flange

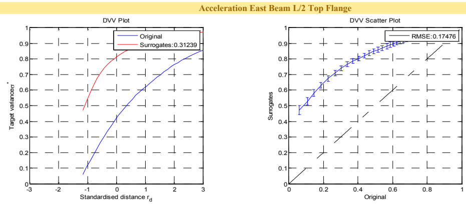

Acceleration East Beam L/4 Top Flange

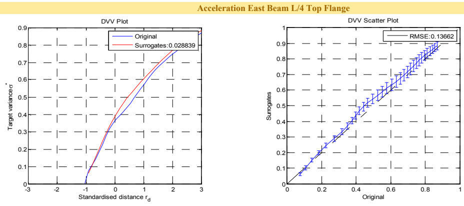

Acceleration West Beam L/2 Top Flange

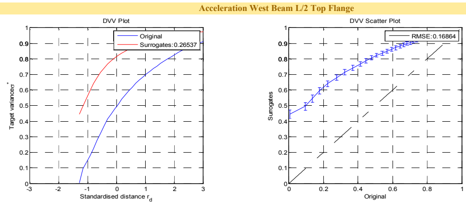

Transversal Strain Slab L/2

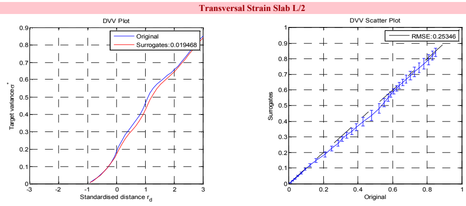

Transversal Strain Slab L/4

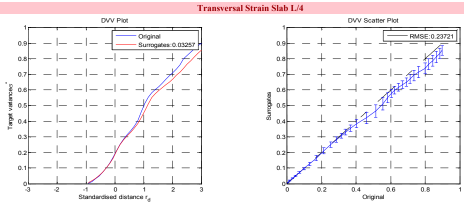

TRAIN 4

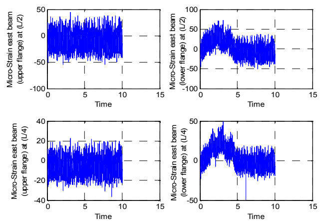

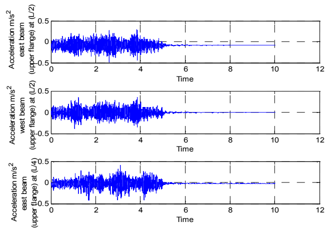

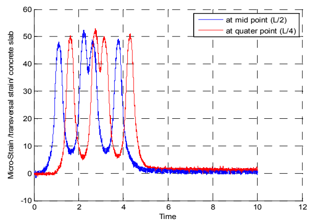

Strain East Beam L/2 Top Flange

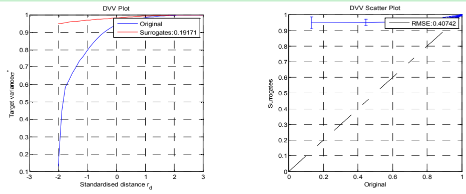

Strain East Beam L/2 Bottom Flange

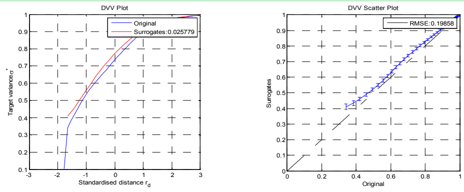

Strain East Beam L/4 Top Flange

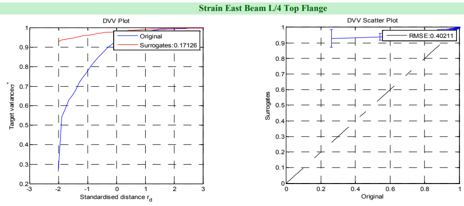

Strain East Beam L/4 Bottom Flange

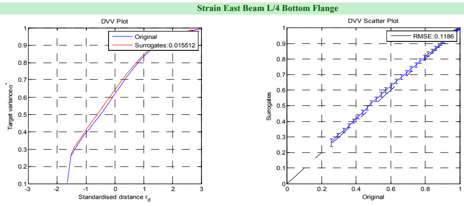

Acceleration East Beam L/2 Top Flange

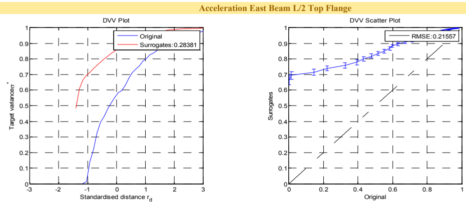

Acceleration East Beam L/4 Top Flange

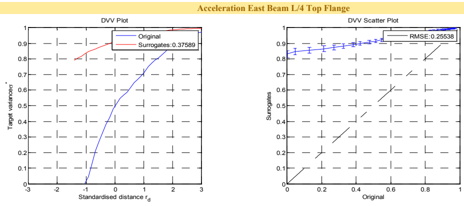

Acceleration West Beam L/2 Top Flange

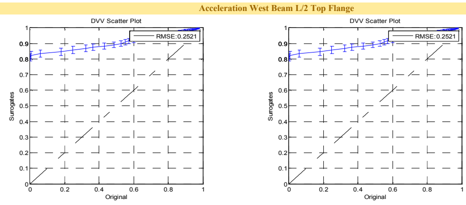

Transversal Strain Slab L/2

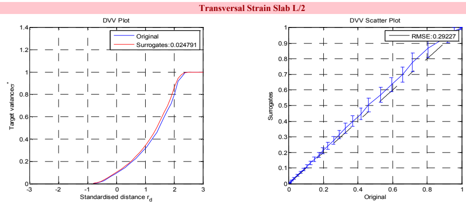

Transversal Strain Slab L/4

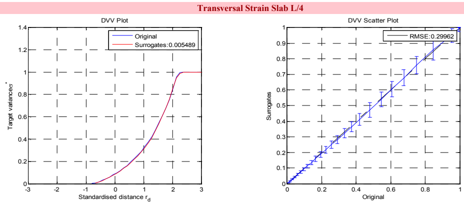

TRAIN 5

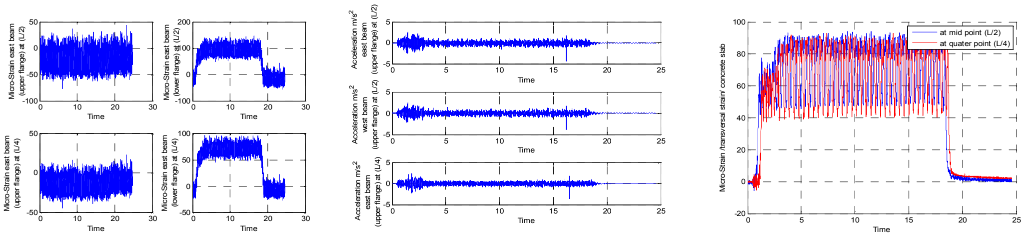

Strain East Beam L/2 Top Flange

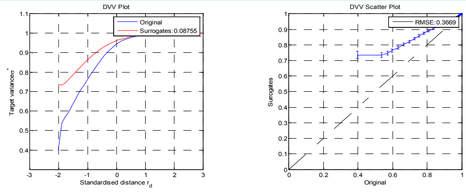

Strain East Beam L/2 Bottom Flange

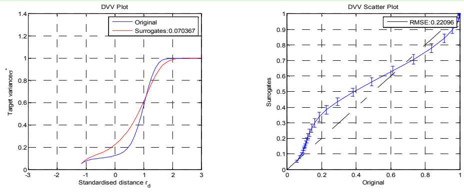

Strain East Beam L/4 Top Flange

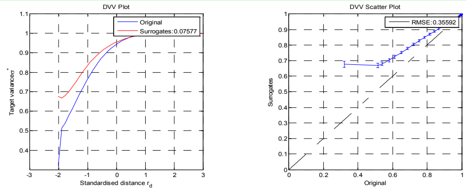

Strain East Beam L/4 Bottom Flange

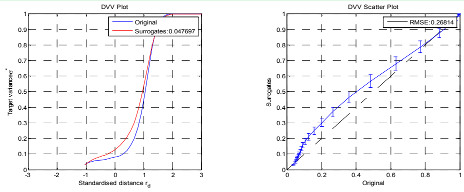

Acceleration East Beam L/2 Top Flange

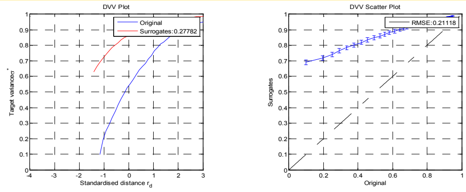

Acceleration East Beam L/4 Top Flange

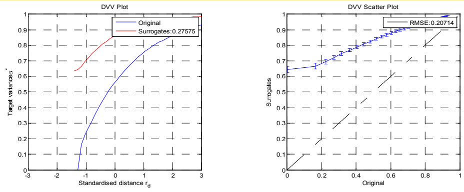

Acceleration West Beam L/2 Top Flange

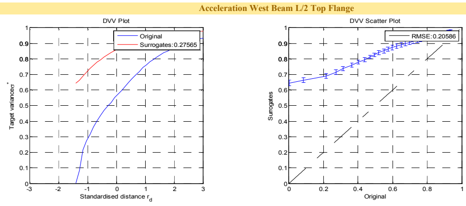

Transversal Strain Slab L/2

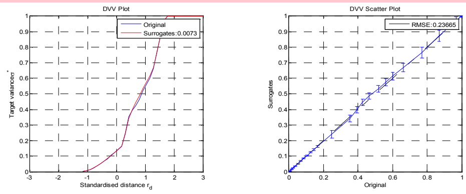

Transversal Strain Slab L/4

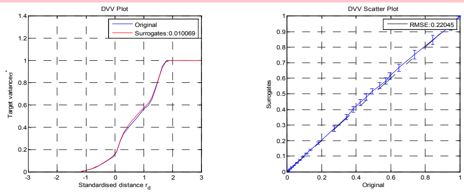

TRAIN 6

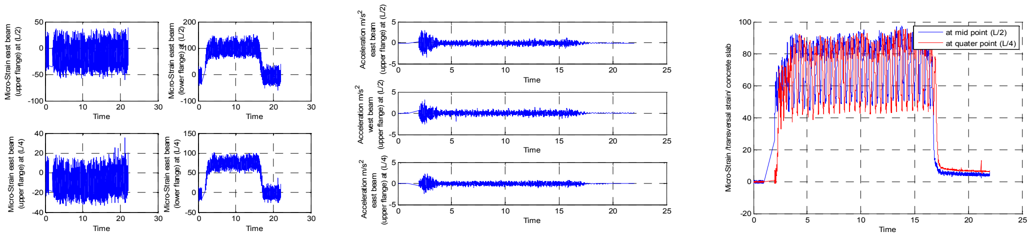

Strain East Beam L/2 Top Flange

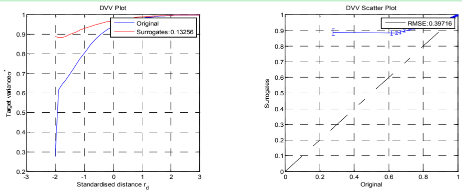

Strain East Beam L/2 Bottom Flange

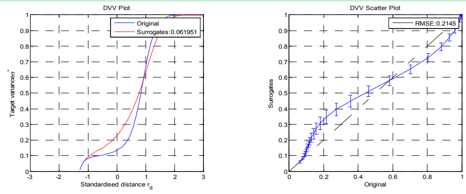

Strain East Beam L/4 Top Flange

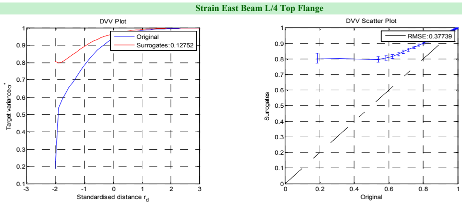

Strain East Beam L/4 Bottom Flange

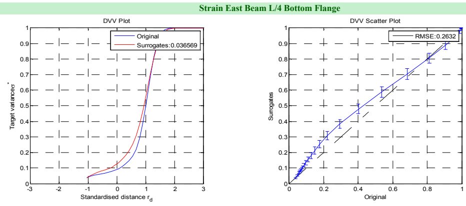

Acceleration East Beam L/2 Top Flange

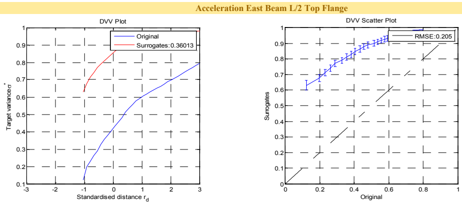

Acceleration East Beam L/4 Top Flange

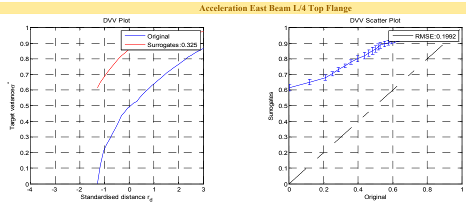

Acceleration West Beam L/2 Top Flange

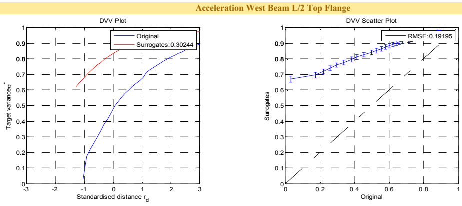

Transversal Strain Slab L/2

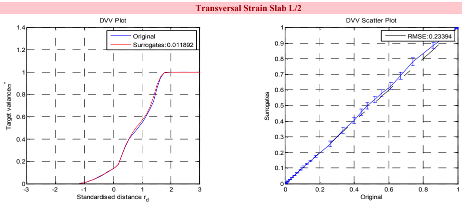

Transversal Strain Slab L/4

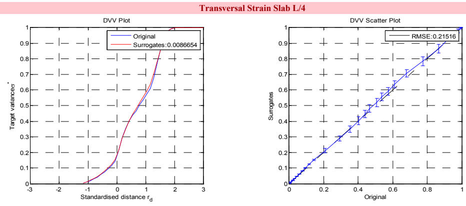

TRAIN 7

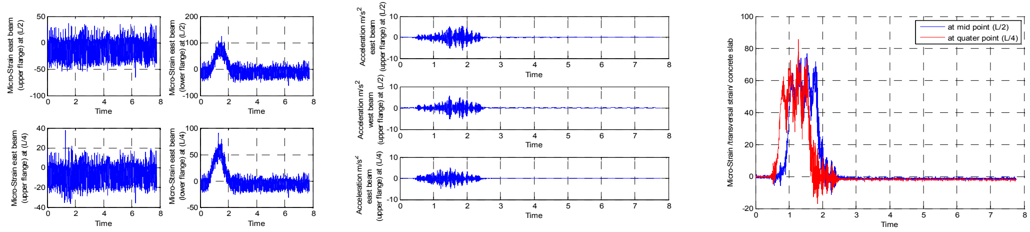

Strain East Beam L/2 Top Flange

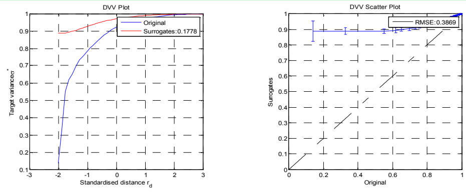

Strain East Beam L/2 Bottom Flange

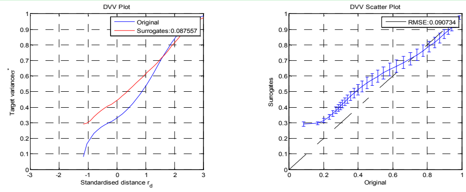

Strain East Beam L/4 Top Flange

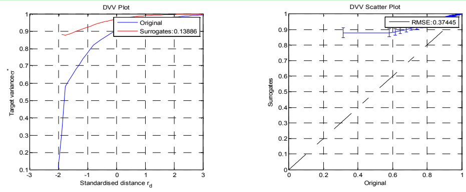

Strain East Beam L/4 Bottom Flange

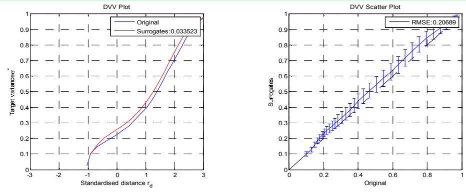

Acceleration East Beam L/2 Top Flange

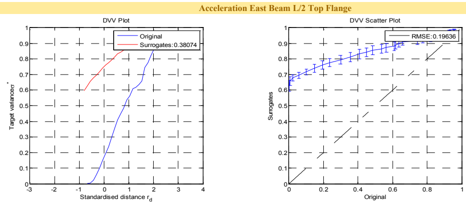

Acceleration East Beam L/4 Top Flange

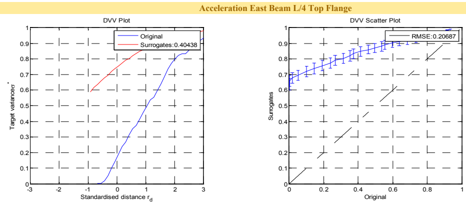

Acceleration West Beam L/2 Top Flange

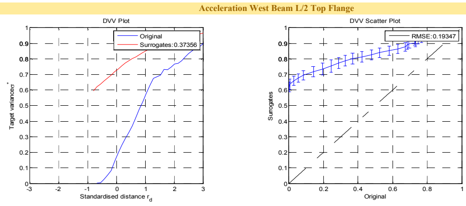

Transversal Strain Slab L/2

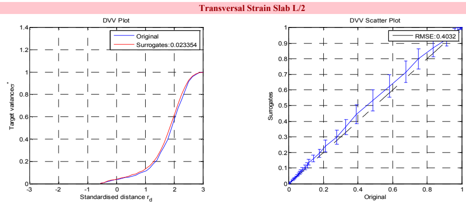

Transversal Strain Slab L/4

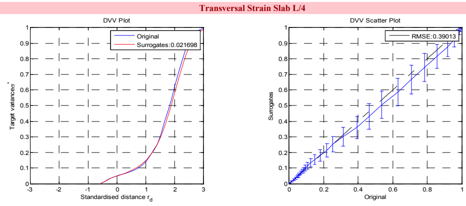

TRAIN 8

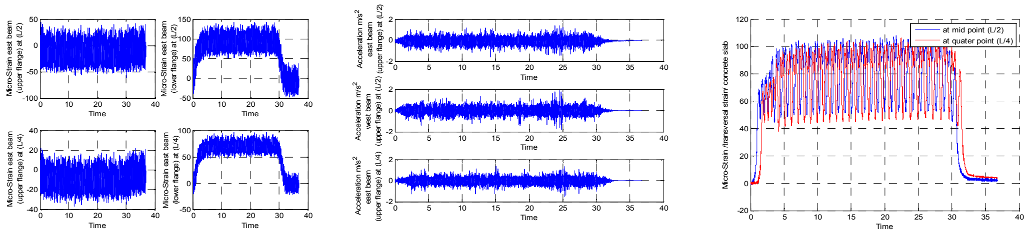

Strain East Beam L/2 Top Flange

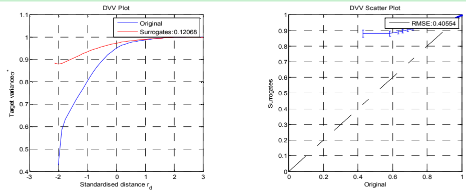

Strain East Beam L/2 Bottom Flange

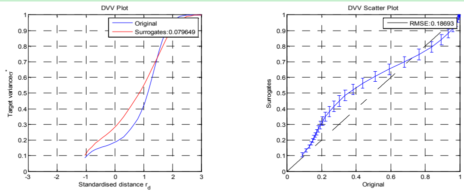

Strain East Beam L/4 Top Flange

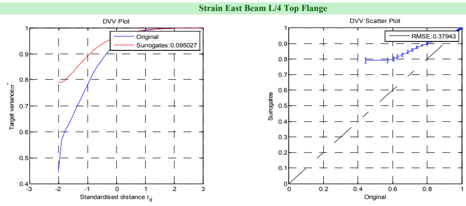

Strain East Beam L/4 Bottom Flange

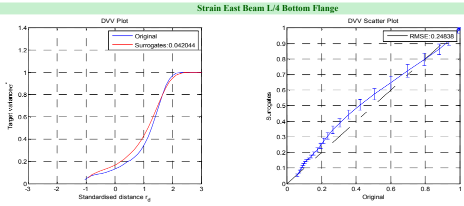

Acceleration East Beam L/2 Top Flange

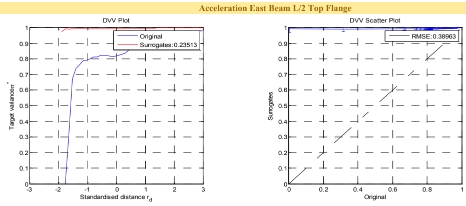

Acceleration East Beam L/4 Top Flange

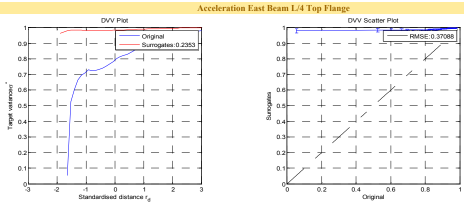

Acceleration West Beam L/2 Top Flange

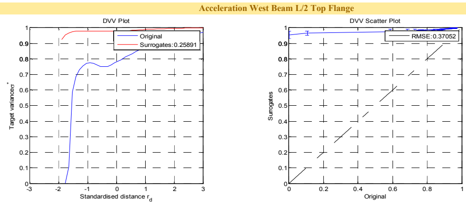

Transversal Strain Slab L/2

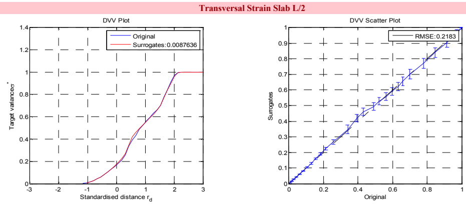

Transversal Strain Slab L/4

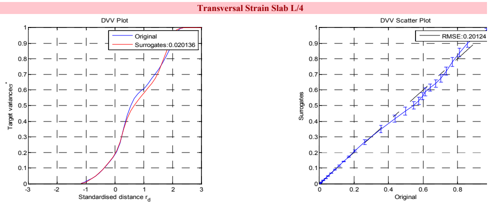

TRAIN 9

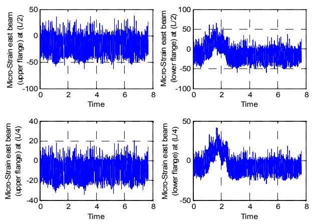

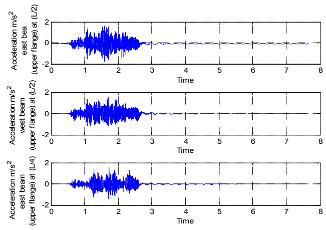

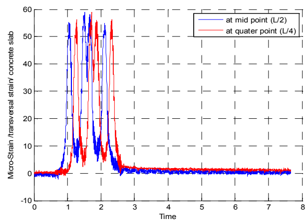

Strain East Beam L/2 Top Flange

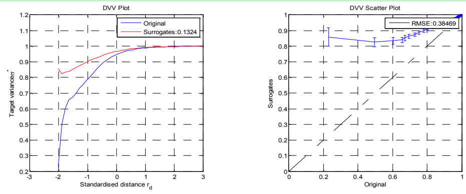

Strain East Beam L/2 Bottom Flange

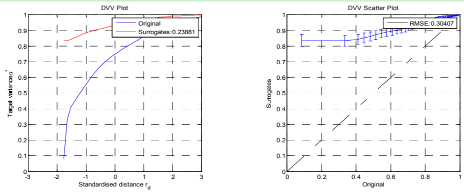

Strain East Beam L/4 Top Flange

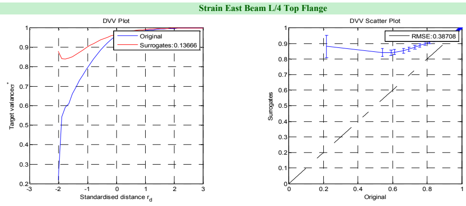

Strain East Beam L/4 Bottom Flange

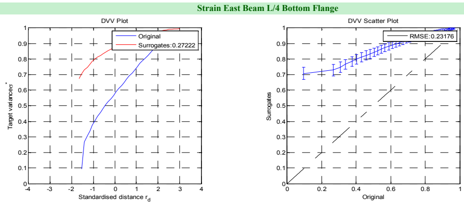

Acceleration East Beam L/2 Top Flange

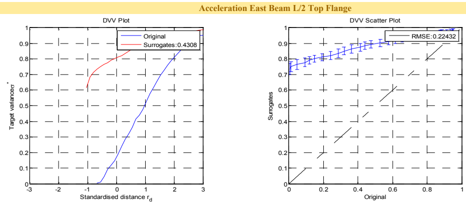

Acceleration East Beam L/4 Top Flange

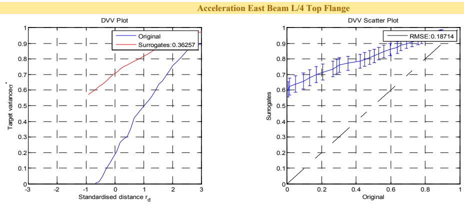

Acceleration West Beam L/2 Top Flange

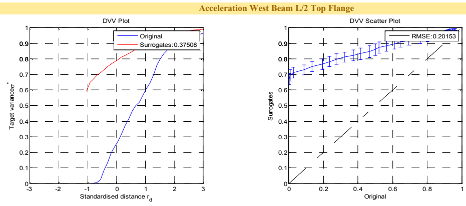

Transversal Strain Slab L/2

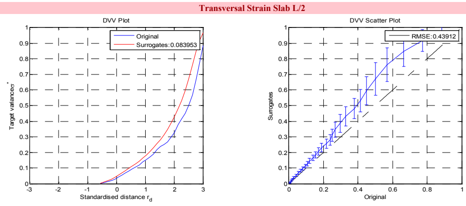

Transversal Strain Slab L/4